UNIVERSIDAD COMPLUTENSE DE MADRID

FACULTAD DE CIENCIAS GEOLÓGICAS
DEPARTAMENTO DE PETROLOGÍA Y GEOQUÍMICA

TESIS DOCTORAL

Thermal and sedimentary modelling of an intraplate extensional basin (Cameros basin, North of Spain):
application for a hydrocarbon prospecting

Modelización de la evolución sedimentaria y térmica de una cuenca extensional intraplaca (Cuenca de Cameros):
aplicación a la prospección de hidrocarburos

MEMORIA PARA OPTAR AL GRADO DE DOCTOR

PRESENTADA POR

Silvia Omodeo Salé

Directores

José Arribas Mocoroa
José Ramón Mas Mayoral

Madrid, 2014

Departamento de Petrología y Geoquímica
Facultad de Ciencias Geólogicas
Universidad Complutense de Madrid

Tesis Doctoral

Thermal and Sedimentary Modelling of an Intraplate Extensional Basin (Cameros Basin, North of Spain): Application for a Hydrocarbon Prospecting

Modelización de la Evolución Sedimentaria y Térmica de una Cuenca Extensional Intraplaca (Cuenca de Cameros): Aplicación a la Prospección de Hidrocarburos

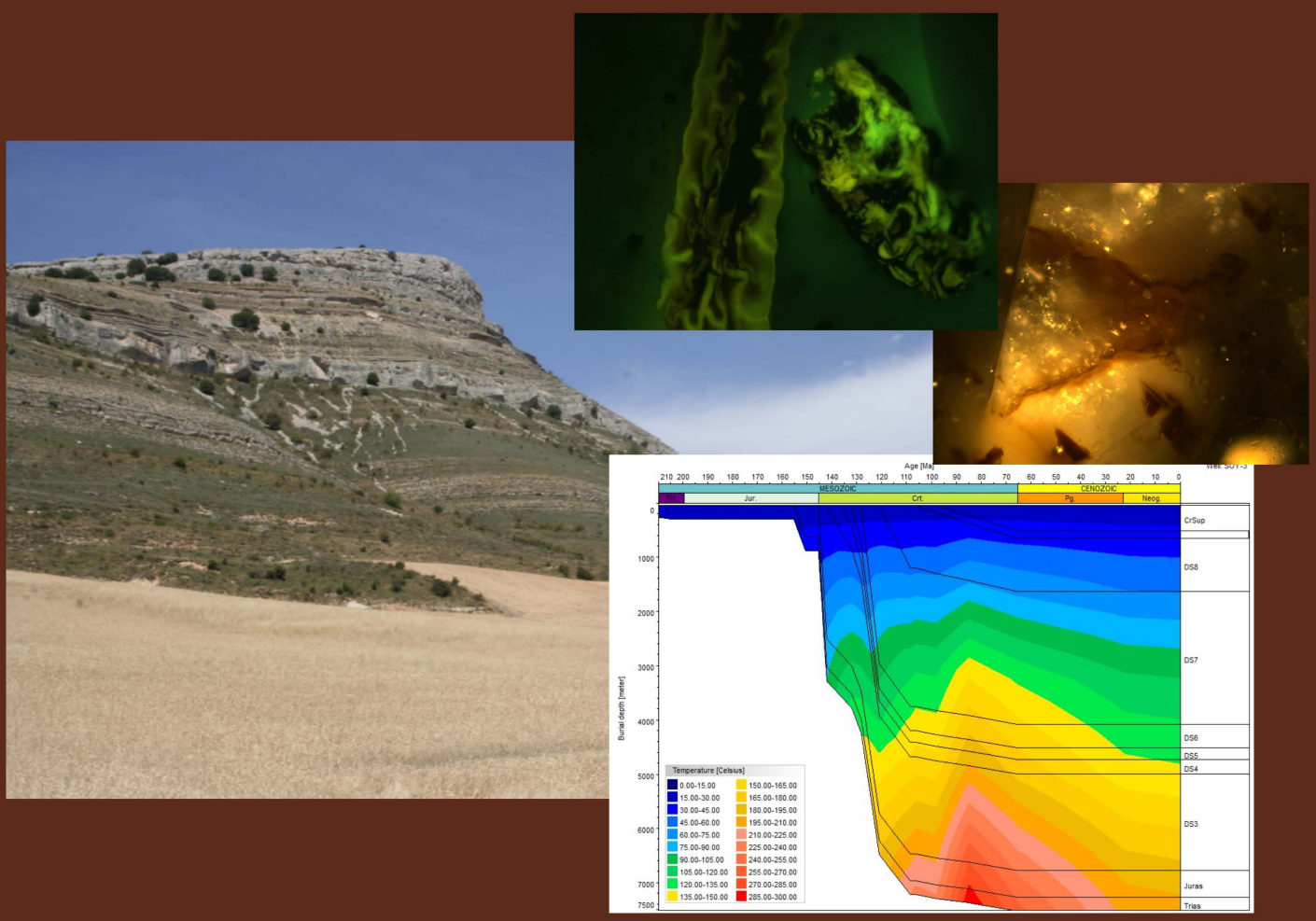

Silvia Omodeo Salé

Departamento de Petrología y Geoquímica
Facultad de Ciencias Geológicas
Universidad Complutense de Madrid

TESIS DOCTORAL

Thermal and Sedimentary Modelling of an Intraplate Extensional Basin (Cameros Basin, North of Spain): Application for a Hydrocarbon Prospecting

MODELIZACIÓN DE LA EVOLUCIÓN SEDIMENTARIA Y TÉRMICA DE UNA CUENCA EXTENSIONAL INTRAPLACA (CUENCA DE CAMEROS): APLICACIÓN A LA PROSPECCIÓN DE HIDROCARBUROS

Departamento de Petrología y Geoquímica
Facultad de Ciencias Geológicas
Universidad Complutense de Madrid

TESIS DOCTORAL

Thermal and Sedimentary Modelling of an Intraplate Extensional Basin (Cameros Basin North of Spain): Application for a Hydrocarbon Prospecting

Modelización de la Evolución Sedimentaria y Térmica de una Cuenca Extensional Intraplaca (Cuenca de Cameros): Aplicación a la Prospección de Hidrocarburos

MEMORIA PARA OPTAR AL GRADO DE DOCTOR
PRESENTADA POR

Silvia Omodeo Salé

Departamento de Petrología y Geoquímica
Facultad de Ciencias Geológicas
Universidad Complutense de Madrid

TESIS DOCTORAL

Modelización de la Evolución Sedimentaria y Térmica de una Cuenca Extensional Intraplaca (Cuenca de Cameros): Aplicación a la Prospección de Hidrocarburos

MEMORIA PARA OPTAR AL GRADO DE DOCTOR
PRESENTADA POR

Silvia Omodeo Salé

Madrid, 2014

Esta Tesis Doctoral ha sido realizada en el Departamento de Petrología y Geoquímica de la Universidad Complutense de Madrid, bajo la dirección de los profesores José Arribas Mocoroa y José Ramón Mas Mayoral

V^{o}B^{o}

Prof. José Arribas Mocoroa

V^{o}B^{o}

Silvia Omodeo Salé

Prof. J. Ramón Mas Mayoral

A Noi...

AGRADECIMIENTOS

Madrid, 5 de julio 2014

Al final de este largo viaje, que ha representado la realización de esta tesis doctoral, muchísimas son las personas que quiero agradecer, por haber compartido, participado o tal vez solamente observado, mi lento pero incansable caminar que me ha hecho llegar al día de hoy hasta aquí. No ha sido un camino rápido, ni fácil, ni siempre soleado. Muchas nubes han pasado, nubes blancas, nubes negras. Muchas tormentas han caído, tormentas de todos tipos, a veces tan fuertes que me han hecho dudar de poder seguir caminando. Pero aquí, increíblemente, hoy estoy, y si he llegado hasta aquí es sin duda también gracias a todas aquellas queridas presencias que me han acompañado en este largo camino.

Mis primeros agradecimientos son para mis directores de tesis, Prof. José Arribas y Prof. Ramón Mas. A vosotros un Gracias sentido por la confianza, el apoyo, la ayuda que me habéis dado desde el primer momento hasta el final de esta tesis. Gracias por haber confiado en mí cuando todavía no me conocíais, para encargarme el tema de esta tesis, entonces para mi tan nuevo, tan complejo, tan desconocido. Gracias por haber confiado siempre en mis capacidades. Gracias por haberme animado siempre en cada instante de este largo y complejo viaje. Gracias por haberme ayudado siempre cariñosamente a disolver mis miedos e incertidumbres. Gracias por haberme siempre apoyado y aconsejado en cada elección que tenía que tomar sobre cómo avanzar en el trabajo de la tesis. Gracias por haberme dejado tanta libertad en seguir las líneas de investigación que más me gustaban y por las que sentía más afinidad e interés. Gracias por haber estado siempre tan abiertos y dispuestos a discutir los nuevos resultados que salían desde mi trabajo. Gracias por haber estado siempre dispuestos a aceptar las nuevas líneas de trabajo y metodologías que continuamente iban surgiendo. Gracias por haberme repuesto en el buen camino cuando me perdía en dificultades y problemas inútiles y/o inexistentes. Gracias por haberme sabiamente aconsejado siempre sobre cómo actuar en las relaciones "diplomáticas". Gracias por haberme animado a seguir adelante en los muchos momentos de dificultad y de desaliento que he tenido en estos años. Un gracias especial a José por haberme ayudado siempre a organizar el enredo de datos, informaciones y dudas que tenía y a planificar mi trabajo de forma ordenada y sintética, y otro a Ramón por haberme ayudado a poner meticulosamente orden a todas la información de la cuenca de Cameros. En fin, un gracias infinito a los dos por

haberme mostrado siempre, ante todo, vuestro lado humano, comprensivo, cercano y cariñoso. Estas cualidades vuestras son las que siempre recordaré de vosotros, las que siempre me llevaré conmigo. Gracias.

Además de mis dos directores quiero dar gracias especiales a las personas que en estos años han colaborado activamente en la realización de esta tesis: Prof. Joan Guimerà y Prof. Ramón Salas de la Universidad de Barcelona, Prof. Luis Martínez de la Universidad de Nancy y de Estrasburgo, Dr Isabel Suárez-Ruiz del Instituto Nacional del Carbón de Oviedo y Dr. Robert Ondrak del GFZ de Potsdam. Gracias a todos vosotros por vuestra colaboración, por vuestro tiempo, por vuestro compromiso, por haber compartido conmigo vuestro saber y por haberme ayudado a resolver y comprender las problemáticas de la cuenca de Cameros. Un agradecimiento especial a Joan por tu paciencia y dedicación en enseñarme las herramientas para construir un corte geológico y su restitución. Mil gracias a Ramón por mostrarme como realizar un análisis de subsidencia y del flujo de calor y por transmitirme pacientemente tus sabios consejos y enseñanzas sobre cómo publicar. A Luis unas inmensas gracias por haberme dado durante toda la tesis utilísimos consejos, ánimos, opiniones y discusiones. Gracias por haber siempre compartido conmigo todo tu conocimiento e ideas. Un gracias especial a Luis también por tu disponibilidad y amable acogida tanto en Nancy como en Estrasburgo, haciendo posible que mis estancias allí hayan sido siempre tan bonitas y emocionantes. A Isabel un gracias muy especial por haberme enseñado tanto sobre el estudio de la materia orgánica, por haber compartido tanto conmigo su conocimiento y sobretodo su amor y su pasión por la materia. Gracias por haber hecho posible que yo me apasionara tanto en un tema tan sorprendentemente interesante, tema para mí antes completamente desconocido. Gracias Isabel también por la acogida, disponibilidad y confianza que me diste desde el primer momento en el laboratorio del INCAR. Muchísimas gracias a Robert por haberme ayudado y enseñado a construir un modelo térmico tan complejo de la cuenca. Gracias por haberme acogido en tu despacho y en tu centro en los meses que estuve allí, gracias por la simpatía y espíritu alegre con los cuales acompañaste las horas que compartimos juntos durante mi estancia.

Agradezco también a todas las personas que han hecho posible la realización de esta tesis, a través de su trabajo. Gracias al equipo del laboratorio de Petrología de la UCM. Gracias a Dionisio y José Ramón del laboratorio del INCAR de Oviedo por la ayuda que me dieron y por los buenos momentos pasado juntos. A Dionisio un gracias especial por el cuidado, la dedicación y la paciencia con la cual me preparó mis miles y miles de muestras de materia orgánica. Gracias a la Prof. Maribel Benito por haberse encargado con tanta dedicación de toda la gestión económica del proyecto de Cameros, y por haberme siempre apoyado en todas mis actividades, estancias, congresos, etc.. Gracias a la Prof Rosa Tejero por su ayuda y consejo durante la realización del corte de la cuenca. Miles y miles de gracias a Pepa por haber revisado tan cuidosamente el inglés de una parte de los capítulos de esta tesis. Muchísimas gracias a

Rebeca por haberme ayudado y enseñado a maquetar mi tesis. Gracias a todo el personal del departamento de Petrología y Geoquímica por haberme apoyado en estos años de mi trabajo. Gracias a todo el equipo de la Facultad de Ciencias Geológicas, del Rectorado de la UCM, del Ministerio de Ciencia y Innovación (antes) y de Economía y Competitividad (ahora), por haber hecho posible que yo realizara una tesis doctoral aquí en este país, por haberme concedido una beca pre-doctoral, por haberme dado todos los medios económicos y técnicos que necesitaba para realizar esta tesis. Gracias a Agustín Pieren por haberme ayudado en resolver todos los trámites burocráticos para conseguir una beca aquí en España.

Un sentido gracias a todas las personas con las cuales he compartido este largo y intrincado camino. Algunas de ellas han caminado a mi lado durante todo el camino, viviendo intensamente cada instante de este proceso. Otras sólo han compartido partes de este viaje, algunas las cuestas arriba, otras las cuestas abajo. Otras simplemente han sido observadoras de mi viaje, quedándose al margen del camino, nada más mirándome pasar…A todas les agradezco de haber estado presentes en mi vida en estos años, todas han sido importantes, todas me han regalado unas palabras, una sonrisa, una mirada, un abrazo, una enseñanza… Gracias a todos, sin vosotros este viaje no habría sido como ha sido. Gracias por haberme acompañado.

Gracias a todos aquellos que han compartido conmigo los momentos y las emociones tan intensas que nacieron durante la realización de esta tesis. En Nancy, gracias a Silvia, Arvid, a Antonio, a Silvana, a Charlotte, a David, a Francisco C., a Francisco De la O., a Josué, a Pablo, a Jon, a Clemence, a Lidia y a Nadia. En Potsdam, gracias a Pablo, a mis chicas queridas, Janina, Ana y Christina, y también gracias a Diego, por haber cruzado tan intensamente mi vida. En Oviedo, a Veneranda, a Belén, a Marian, a Miguel, a los amigos de Mieres y a todo el maravilloso equipo del INCAR. En Barcelona, a Pablo y a Marco. Gracias a todos los compañeros de la facultad de Madrid, Cristina, Elena, Quique, Maricarmen, Rebeca, Miguel, Laurita, Pepa, José Ignacio, Inma, David, Andrea, Richard, Pablo, Emma, Sara, Ángela, Emilio, Alicia, Ainara. Gracias infinitas a todo el grupo de petrofísica, por haberme siempre acogido cariñosamente y aceptado con entusiasmo, y en fin, gracias a todo el departamento de Petrología por el cariño que siempre me ha demostrado en estos años.

Un gracias muy especial a las amistades tan importantes que me han acompañado a lo largo de todos estos años. Gracias por haberme siempre apoyado, comprendido, escuchado y alentado. Gracias por haber estado siempre a mi lado, en los momentos malos y buenos, por haberme acompañado tanto en la alegría como en la tristeza, por haber compartido conmigo tanto la risa como las lágrimas. Gracias a Giada, a Marina, a Simona, a Chiara, a Katia, a Lia, a Barbara, a Liliana, a todos los amigos de la Pandilla de Madrid (Buenri amigos), a las constelaciones familiares, al grupo de meditación, a todo el grupo de Biodanza, a la biodanza, por haberme enseñado a tener fe y esperanza en la vida y ayudado a buscar (y encontrar) el equilibrio, a todo el grupo del tango, al tango, por hacerme emocionar tanto y por ser capaz de hacerme olvidar

de todos los problemas y a estar tan presente en el momento. A Emi, gracias por haberme acompañado y ayudado en la última parte de este viaje, tan atormentada y confusa.

Gracias a todos aquellos que en estos años han creído en mis posibilidades, que me han apoyado y animado, tanto a empezar como a acabar este hermoso pero a veces tan difícil viaje. Gracias a mis profesores de la universidad de Parma y a todo el equipo Engeo de Parma por haberme animado y ayudado a empezar este viaje. Unas gracias especiales a toda mi familia entera, y en especial gracias a mi padre Angelo, a mi madre Angela y a mi hermana Marina, por haberme apoyado, comprendido y acompañado en la realización de este largo viaje. Gracias por haber creído tanto en mí.

Unas gracias infinitas e inmensas a Silvio, por haber estado allí, a mi lado, siempre,…. apoyándome, animándome, escuchándome, aconsejándome,….en cada momento, en cada elección, en cada caída, en cada gratificación, con tu amor y con tu ternura, con tu paciencia, y con tu presencia. Gracias por haber siempre apoyado y aceptado mis elecciones, decisiones, necesidades,….también las que hicieron que nuestros caminos se fueron alejando. Gracias por haberme dejado siempre ser yo misma. Gracias por tu amor. Gracias a Nuestro Amor, a Él dedico esta tesis, gracias a Él he empezado, gracias a Él ahora he llegado hasta aquí. Gracias por lo que fue, gracias por aquello en lo cual se transformará. Gracias a este Nuestro Amor, por haber estado siempre sencillamente ahí, tan puro y transparente, tan sincero y maravilloso.

En fin, agradezco a este país, a su gente, a sus lugares, a su cielo, a sus nubes, a su Sol… gracias por haberme acogido tanto y por haberme siempre hecho sentir tan querida, gracias por haberme enseñado tanto, gracias por haberme hecho crecer tanto. Vino una Silvia y se va otra Silvia, distinta, creo mejor, más serena, más segura, más tranquila, más agradecida. Gracias por haberme hecho ser una persona mejor.

Silvia

Index

Abstract / Resumen

I. ABSTRACT

Thermal and Sedimentary Modelling of an Intraplate Extensional Basin (Cameros Basin, N of Spain): Application for a Hydrocarbon Prospecting

I.1 Introduction

The Cameros Basin is an inverted extensional basin located in the north-western part of the Iberian Chain (North of Spain). It was formed during the Mesozoic Iberian Rifting (Late Jurassic-Early Cretaceous) and was inverted during the Alpine Orogeny (Mas et al., 1993, Guimerà et al., 1995 and Salas et al., 2001). The Cameros Basin has been the object of numerous multidisciplinary studies that focused on the reconstruction of the geologic evolution of the basin, characterizing with detail the structure, stratigraphy, sedimentology and petrology of the basin infill. These studies highlighted that this basin is characterized by a very singular tectono-stratigraphic and thermal history. Furthermore, several data indicate that during the evolution of the basin a petroleum system was activated.

I.2 Objetives

The main objective of this thesis is to obtain a complete and detailed basin scale study, taking into account the geometry and structure of the basin, the thermal evolution, and the sedimentological, petrological and geochemical features of the basin infill

I.3 Methodology

To achieve the main objective, a multidisciplinary approach was carried out. Six main disciplinary areas weredeveloped, each one focused to solve one specific aspect of the evolution of the basin: 1) Reconstruction of the geometry and structure of the basin; 2) Subsidence analysis and heat flow estimation; 3) Reconstruction of the thermal history of the basin; 4) Characterization of the most relevant organic matter accumulation of the basin; 5) Definition of the kinetic parameters of the immature kerogen of the basin; and 6) Modelling of the petroleum system of the basin.

I.4 Results

In the first section, by defining the geometry and architecture of the basin infill, a complete reconstruction of the tectono-stratigraphic evolution of the Cameros Basin is provided. By the results performed in this thesis, the characterization of the geometry and architecture of the basin, as well as the understanding of the mechanisms that governed the extensional tectonic processes and their relationship with sedimentation trends, were improved. Due to its peculiar geometry and structures, the Cameros Basin is interpreted as an extensional ramp syncline

basin, which formed over a south-dipping ramp joining two flats of a blind extensional fault located deep in the basement.

In a second step, the subsidence analysis was determined by reconstructing the burial evolution of the basin over time together with its essential basin forming mechanisms. During the extensional stage of the basin, two cycles of rapid and decelerated subsidence phases were determined. These cycles were recorded diachronously in the basin, as a consequence of the lateral migration of the areas where new accommodation space was formed. By distinguishing the initial and thermal subsidence phases and by determining the relative magnitudes, a maximum heat flow peak at the end of the extensional stage was calculated. The estimated heat flow is lower that the heat flow estimated in typical rift areas (Allen and Allen, 2009). This data is interpreted as the result of the reduced lithosphere stretching in the Cameros Basin area during the extensional stage.

Furthermore than a singular tectono-stratigraphic evolution, the Cameros Basin experienced a complex thermal history. Throughout the basin, remarkable variations of the thermal conditions have been determined, by the record of anomalous trends of organic and inorganic geothermometer. The origin and distribution of these thermal anomalies has been the subject of much debate in recent years. In the third section of this thesis, to improve the understanding of the thermal evolution of the Cameros Basin, a 2D thermal modelling was undertaken. To reconstruct the thermal history of the Cameros Basin, the most important variables that play a major role in the thermal evolution of a basin, (i.e., heat flow and burial of sediment load) were considered. Thus, the results of the subsidence analysis and heat flow estimations of the Cameros Basin area were taken into consideration. To validate the calculations obtained from the model, vitrinite reflectance was mostly used. Additionally, fluid inclusions data were used to clarify the interpretation of the thermal history of the basin, as far as they are the unique direct evidence of paleofluids circulation. The discussion of the thermal model results determines that the anomalous temperatures recorded in the basin are a consequence of the circulation of hot fluid during the evolution of the basin. Hot fluids circulation heated the sediments to anomalously high temperatures, regardless of their stratigraphic position. Circulation of hot fluids is attributed to the metamorphic events that affected the central and northern sector of the basin during the post-extensional stage and the Alpine compressive phase.

In the last sections of the thesis the evolution of the petroleum system of the basin is modeled. To model the evolution of the petroleum system is firstly necessary to define and to characterize the potential source rocks in the basin. Due to the strong thermal alteration of the basin infill rocks, very little research has been performed in the past to identify potential source rocks in the Cameros Basin petroleum system. In the fourth section of this thesis, a detailed petrographic and geochemical study of the organic matter of the basin was performed. It was determined the amount and type of organic matter presently preserved in the basin, the causes of the scarce

organic matter preservation, the source rocks in the Cameros Basin petroleum system and the hydrocarbon potential, today and in the past. Overmatured spent source rocks were identified in the pre-extensional and syn-extensional stratigraphic record cropping out in the northern sector of the basin, whereas immature to mature potential source rocks were identified in the southern sector. An original Type II kerogen is suggested for the pre-extensional source rock, whereas a Type I and Type III kerogen is considered for the syn-extensional source rocks.

Another important data that was necessary to define and model the evolution of the petroleum system in the basin, is the kinetic of the kerogen transformation into oil and gas. In the fifth section of this thesis, bulk kinetic parameters for the immature kerogen of the Cameros Basin were calculated. Kinetic parameter calculations are based on a mathematical computational modeling of the S2 peak of the pyrolysis Rock-Eval results. Mathematical computational modeling resulted satisfactory, as a correct reproduction of the S2 peak measured in the pyrolysis was performed by the model. Frequency factor and sets of activation energies, describing the thermal cracking of the analyzed kerogens, were determined. Comparison of the calculated kinetic parameters with the parameters of classical Type I, Type II and Type III kerogens (Tissot et al., 1987; Behar et al., 1997) indicates a different kerogen behavior respect to what was expected considering only pyrolysis data. These differences are explained as a consequence of the presence of sulfur in the structure of the kerogens and due to a mixture of different types of kerogen. The obtained results were used to choose in the literature compositional kinetics that have a kinetic behavior similar to the Cameros Basin kerogen.

Finally, in the last section of this monography, the collection of all previously described data and results were used to reconstruct the complete evolution of the petroleum system of the Cameros Basin. The structure and geometry of the basin previously determined were used to reconstruct the geologic conceptual model, as well as the sedimentological and chronostratigraphical data. Temperature variations in the basin over time, as well as the paleoheat flow, were obtained from the previously reconstructed and calibrated thermal model. The geochemical data of the potential source rocks were introduced in the model, considering the results of the organic matter characterization carry out in this thesis. Finally, bulk kinetics calculated for the Cameros Basin kerogen, as well as appropriate compositional kinetics chosen fom the literature, were assigned to the proposed source rocks. By gathering and interpreting the model results, the elements and processes that compose the petroleum system (sensu Magoon and Down, 1994) were determined. The maximum hydrocarbons generation peak was reached at the end of the extensional stage. During this phase, the syn-extensional Berriasian coastal-lacustrine black-shale facies (Valdeprado Fm) was the source rock that mostly contributed to the generation of hydrocarbons, followed by the pre-extensional Jurassic marine black-shales facies. A secondary hydrocarbon generation peak occurred during the inversion stage, formed mostly as consequence of the thermal transformation of the kerogen of the Jurassic marine source rocks,

located in the south of the basin. The most relevant hydrocarbon accumulation in the basin formed at the end of the post-extensional stage, in the post-extensional unit sandstone bodies (Utrillas Fm). A secondary hydrocarbon accumulation in these deposits was formed during the inversion stage, as structural traps originated during the inversion process. The major part of the hydrocarbons was lost during the extensional phase due to outflowing to the surface, firstly caused by the absence of a seal or trap. However, even during the inversion phase, hydrocarbons continued to be lost, as a consequence of the uplift and erosion of the reservoirs. Concluding two petroleum systems can be recognized in the basin: the first one in the northern sector of the basin and primarily active during the extensional and post-extensional phases and the second located in the southern sector of the basin, active primarily during the post-extensional and inversion phases. Source rocks of these systems are syn-extensional lacustrine black-shales facies (Berriasian) in the first system and pre-extensional marine black-shales (Callovian) in the second.

I.4 Conclusions

This thesis represents a multidisciplinary characterization of the geological evolution of the Cameros Basin, which makes a synthesis of all the structural, sedimentological, petrological, geochemical and thermal issues of the basin. The results obtained in this thesis clarify the numerous debates about the structural and thermal evolution of the basin, as well as the functionality of its petroleum system.

II. RESUMEN

Modelización de la Evolución Sedimentaria y Térmica de una Cuenca Extensional Intraplaca (Cuenca de Cameros): Aplicación a la Prospección de Hidrocarburos

II.1 Introducción

La Cuenca de Cameros es una cuenca extensional invertida, localizada en el sector noroccidental de la Cordillera Iberica (Norte de España). La Cuenca de Cameros se formó durante el Rift Mesozoico Ibérico (Jurásico superior-Cretácico inferior) y su inversión se produjo durante la orogenia Alpina (Mas et al., 1993, Guimerà et al., 1995 and Salas et al., 2001).

La cuenca de Cameros ha sido objeto de numerosos estudios multidisciplinares, enfocados principalmente a la reconstrucción de la evolución geológica de la cuenca, donde se han caracterizado con detalle la estructura, estratigrafía, sedimentología y petrología de su relleno sedimentario. Estos estudios han puesto de manifiesto que la cuenca de Cameros tiene una evolución tectónica, estratigráfica y térmica muy peculiar y distinta a la de otras cuencas típicas de rift. Además, existen numerosas evidencias que demuestran que durante su evolución se activó y funcionó un sistema petrolífero.

II.2 Objetivos

Esta tesis se propone como objetivo principal, hacer un estudio detallado y completo de la Cuenca de Cameros, que tenga en cuenta la geometría y la estructura de la cuenca, su evolución térmica y las características sedimentológicas, petrológicas y geoquímicas de su relleno .

II.3 Metodología

Los objetivos propuestos en esta tesis se han alcanzado a través de un enfoque multidisciplinar. Se desarrollan seis áreas temáticas, cada una focalizada en resolver un aspecto específico de la evolución de la cuenca. Estas áreas son: 1) Reconstrucción de la geometría y estructura de la cuenca; 2) Análisis de la subsidencia y estimación del flujo de calor; 3) Reconstrucción de la historia térmica de la cuenca; 4) Caracterización de los restos de materia orgánica contenidos en los depósitos de la cuenca; 5) Cálculo y definición de los parámetros cinéticos que caracterizan el kerógeno inmaduro de la cuenca y 6) Modelización del sistema petrolífero.

II.4 Resultados

En el primer apartado de la tesis se reconstruye la evolución tectono-estratigráfica completa de la Cuenca de Cameros a través de la definición de la geometría y arquitectura de su relleno . En este apartado se determina el espesor y geometría del relleno de la cuenca, tanto en el

momento actual, como durante los momentos previos a los procesos de inversión y erosión. Los resultados obtenidos en esta tesis contribuyen a caracterizar con más detalle la geometría y arquitectura de la cuenca y a comprender los mecanismos que gobernaron los procesos tectónicos extensionales y sus relaciones con los procesos de sedimentación. La cuenca de Cameros se interpreta como una cuenca de bloque de techo de rampa extensional, que se formó sobre una rampa con buzamiento hacia el sur y que unía dos rellanos de una falla extensional profunda, localizada en el basamento.

En el segundo apartado de la tesis se analiza la subsidencia de la cuenca, mediante la reconstrucción de la evolución del enterramiento a lo largo del tiempo y de los mecanismos geodinámicos que intervinieron. Durante la fase extensional se reconocen tres etapas, una inferior y otra superior de subsidencia rápida, así como otra etapa intermedia de subsidencia decelerada. Estas etapas con diferentes velocidades de subsidencia se registran de forma diacrónica en la cuenca, como consecuencia de la continua migración lateral de las áreas donde se forma nuevo espacio de acomodación. Diferenciando la subsidencia inicial y la subsidencia térmica, y calculando sus relativas magnitudes, se calcula el pico máximo de flujo de calor registrado al final de la fase extensional. El valor de flujo de calor estimado resulta bajo si se consideran los valores estimados en una cuenca de rift típica en el sentido expresado por Allen and Allen (2009). Este dato se explica considerando el reducido estiramiento de la litosfera que se registra durante la fase extensional, en el área de la cuenca de Cameros.

Además de la peculiar evolución tectono-estratigráfica de la cuenca de Cameros, ésta se caracteriza también por una compleja historia térmica. A lo largo de la cuenca, se han observado notables variaciones de las condiciones térmicas registradas en los sedimentos, obtenidas tanto por geotermómetros orgánicos como inorgánicos. El origen y la distribución de estas anomalías térmicas han sido objeto de númerosos debates en las últimas décadas. En el tercer apartado de la tesis, y para aclarar la evolución térmica de la cuenca, se desarrolla un modelo térmico 2D a escala de cuenca. Para reconstruir la historia térmica de la cuenca, fue necesario considerar las variables que principalmente condicionan la evolución térmica de la cuenca (ej. Flujo de calor y enterramiento de la carga de sedimentos). Como consecuencia, en la realización del modelo térmico, se tienen en cuenta los resultados previamente obtenidos del análisis de la subsidencia y de la estimación del flujo de calor. Los modelos térmicos se han calibrado utilizando la reflectancia de la vitrinita como paleotermómetro principal. En algunos casos específicos, para ayudar en la interpretación de los resultados del modelo, se utilizaron también datos de inclusiones fluidas. La discusión de los resultados del modelo térmico determina que las anomalías de temperatura registradas en la cuenca son consecuencia de la circulación de fluidos calientes durante la evolución de la cuenca. La circulación de fluidos calentó los sedimentos hasta temperaturas anómalamente altas, independientemente de su posición estratigráfica. La circulación de fluidos calientes se atribuye a los eventos metamórficos que afectaron a la cuenca,

en los sectores septentrional y central, durante la fase post-extensional y la fase contractiva Alpina.

En la segunda parte de la tesis se modeliza la evolución del sistema petrolífero de la cuenca. Para ello fue necesario, en primer lugar, definir y caracterizar las rocas madres potenciales. Por esta razón en el cuarto apartado de la tesis se ha realizado un detallado estudio petrográfico y geoquímico de los restos de materia orgánica de los depósitos de la cuenca. En este apartado se determina la cantidad y el tipo de materia orgánica preservada y las causas por las cuales sólo se han conservado una escasa cantidad de dicha materia. Asimismo, se caracterizan las rocas madres del sistema petrolífero de la cuenca y su potencial generador de hidrocarburos, tanto en la actualidad como en el pasado. En el sector septentrional de la cuenca, en el registro estratigráfico pre-extensional y sin-extensional (edad Jurásico superior y Berriasiense, respectivamente) se identifican rocas madres supermaduras, mientras en el sector sur de la cuenca se identifican rocas madres inmaduras y parcialmente maduras en el registro estratigráfico sin-extensional (edad Barremiense superior-Aptiense inferior). Teniendo en cuenta datos sedimentológicos, petrográficos y geoquímicos, se ha deducido un kerógeno de Tipo II para las rocas madres pre-extensionales, mientras que se ha deducido un kerógeno Tipo I y III para las rocas madres sin-extensionales.

Otro dato importante que es necesario tener en cuenta a la hora de modelizar la evolución del sistema petrolífero de la cuenca son las cinéticas con las que el kerógeno de las rocas madre se transforma en petróleo y gas. Con este fin, en la quinta parte de la tesis, se calculan los parámetros cinéticos de los kerógenos inmaduros de la cuenca. El cálculo de estos parámetros se basa en un modelo matemático donde se reconstruye el pico S2 obtenido del análisis de pirólisis Rock-Eval. Los resultados de la modelización matemática se consideran satisfactorios en cuanto que se reproduce correctamente el pico S2 medido en el análisis Rock-Eval. A partir de estos resultados, se obtiene un factor de frecuencia y un conjunto de energías de activación que representan el comportamiento cinético del kerógeno analizado. Comparando los parámetros cinéticos calculados con los parámetros del kerógeno clásico de Tipo I, Tipo II y Tipo III (Tissot et al., 1987; Behar et al., 1997), se puede observar un comportamiento cinético de los kerógenos distinto respecto a lo que se espera considerando sólo los datos de la pirólisis. Estas diferencias pueden explicarse debidas a la presencia de sulfuros en la estructura del kerógeno y también como consecuencia de la mezcla de distintos tipos de kerógenos. Los resultados obtenidos se utilizan para elegir en la bibliografía las cinéticas composicionales que tengan un comportamiento parecido al kerógeno de la cuenca de Cameros.

En la última parte de esta tesis, se reconstruye la evolución del sistema petrolífero de la cuenca, a través de la integración de todos los datos y resultados obtenidos en los apartados anteriores. Combinando los resultados del modelo con los datos geológicos de la cuenca, se determinan los elementos y los procesos que constituyen el sistema petrolífero de la cuenca

(sensu Magoon and Dow, 1994). El pico máximo de generación de hidrocarburos se alcanza al final de la etapa extensional. Durante esta fase la roca madre, que principalmente contribuye a la generación de hidrocarburos, está constituida por las facies de black-shales costero-lacustres, formadas durante la fase extensiva (DS3, Valdeprado Fm – Berriasiense), seguida por la facies constituida por black-shales marinas, formadas durante la fase pre-extensional (Pozalmuro Fm – Calloviense). Un segundo momento de generación de hidrocarburos ocurre durante la fase de inversión de la cuenca, principalmente como consecuencia de la transformación del kerógeno de las rocas madres pre-extensionales, localizadas en el sur de la cuenca. La acumulación de hidrocarburos más relevante se forma durante la fase post-extensional, en cuerpos canalizados de la primera unidad (Utrillas Fm). Una segunda acumulación se forma durante la inversión de la cuenca, gracias a trampas estructurales que se forman en esta etapa. La mayor parte de los hidrocarburos producidos se perdieron durante la fase extensional, fluyendo a la superficie, y como consecuencia de la falta de un sello efectivo. En la fase de inversión de la cuenca parte de los hidrocarburos generados y acumulados siguen perdiéndose, como consecuencia del levantamiento y erosión de los almacenes formados previamente. En resumen, en la cuenca de Cameros se pueden identificar dos sistemas petrolíferos; uno localizado en el sector norte-central de la cuenca, principalmente activo durante las fases extensional y post-extensional; y otro localizado en el sector sur-central de la cuenca, principalmente activo en las fases post-extensional y durante la inversión de la cuenca. Las rocas madres son principalmente las facies de black-shales lacustres (Berriasiense) en el primer sistema petrolífero y las facies de black-shales marinas (Calloviense) en el segundo sistema.

II.4 Conclusiones

Esta tesis representa una caracterización multidisciplinar de la evolución geológica de la cuenca de Cameros, realizando una síntesis de todos los aspectos estructurales, sedimentológicos, petrológicos, geoquímicos y térmicos de la cuenca. Los resultados obtenidos contribuyen a aclarar los numerosos debates tanto sobre la evolución estructural y térmica de la cuenca, así como la caracterización y evolución de su sistema petrolífero.

Chapter 1

1. Introduction

In the last decades the Cameros Basin has been object of numerous multidisciplinary researches that have focused on the reconstruction of the geologic evolution of the basin, characterising in detail the structure, stratigraphy, sedimentology and petrology of the basin infill. These studies have highlighted that the Cameros Basin is characterised by a very singular tectono-stratigraphic and thermal evolution, and that a petroleum system was activated during its evolution. Despite of the numerous researches carry out on the Cameros Basin, there is a lack of a complete and detailed basin scale study taking into account the geometry and structure of the basin, the thermal evolution, and the sedimentological, petrological and geochemical features of the basin infill.

The Cameros Basin is an inverted extensional basin, located in the north-western part of the Iberian Chain (NE of Spain). It was formed during the Mesozoic Iberian Rifting (Late Jurassic-Early Cretaceous) and it was inverted during the Alpine Orogeny (Mas et al., 1993; Guimerà et al., 1995 and Salas et al., 2001). A very thick sedimentary succession was deposited during the extensional stage, being the stratigraphic record mostly composed by continental and coastal deposits, predominantly fluvial, deltaic and lacustrine. The peculiar geometry and tectonic structures that characterise the Cameros Basin clearly suggest a different extensional model to the typical half-graben rift model (Gibbs, 1987; McClay, 1990; Schlische, 1991; Gawthorpe and Leeder, 2000), where accommodation space is formed by a basin border-bounding normal fault that simply reactivated during the

compressive phase. Over the last few decades the extensional mechanisms that formed the basin, have been the subject of several debates (Mas et al., 1993; Casas-Sainz and Gil-Imaz, 1994; Guimerà et al., 1995; Mata et al., 2001; Casas et al., 2012; González-Acebrón et al., 2012; Omodeo Salé et al., 2014). Despite of that a detailed reconstruction of the tectono-stratigraphic evolution of the basin would help understanding the genetic model of the basin, it has not been performed yet.

Furthermore than a singular tectono-stratigraphic evolution, the Cameros Basin experienced a complex thermal history. Throughout the basin remarkable variations of the thermal conditions have been determined, by the analysis of anomalous trends of organic and inorganic geothermometers (Barrenechea et al. 1995; Alonso-Azcárate et al. 1999; Mantilla-Figueroa et al. 1999; Mata et al., 2001; Del Río et al., 2009; González-Acebrón et al., 2011). Additionally a number of petrological studies have demonstrated that in some areas of the basin the syn-extensional deposits have been affected by low to very low metamorphism (Casquet et al. 1992; Alonso-Azcárate et al. 1995, 1999; Barrenechea et al. 1995, 2001; Mata et al., 2001; Mantilla-Figueroa et al. 2002; Mas et al. 2003, Ochoa et al., 2007; Del Río et al., 2009; González-Acebrón et al., 2011, 2012; Casas et al., 2012). The origin and distribution of these thermal anomalies have been the subjects of much debate in recent years. Despite of several previous works, a complete reconstruction of the thermal history of the Cameros Basin, indicating the paleo-temperature variations over geological time and space would permit to improve the comprehension of the thermal anomalies that have been recorded in the basin infill.

Another relevant feature of the Cameros Basin is the imprint on the deposits that gives evidences of the generation, migration and accumulation of hydrocarbons during the basin evolution. The mayor exploitable resources, generated as a consequence of the setting of this petroleum system, are located at small tar sandstone accumulations in the Utrillas Fm (a post-extensional unit), that crop out in the southern sector of the Cameros Basin, and in the Escucha Fm (last syn-extensional unit), located in a small satellite half-graben basin to the south of the main Cameros Basin (Mas et al., 2002, 2003). Presently some hypotheses have been suggested to determine the main elements of the petroleum system of the basin, as well as to explain the processes responsible for its evolution (Mas et al., 2002, 2003; Ochoa et al., 2007). However, a complete and detailed reconstruction of the elements and processes that characterise the petroleum system of the basin has not been defined yet.

In the Cameros Basin there have been few works to identify the potential source rocks of its petroleum system. It has been suggested that the original organic matter was mostly completely altered (Mas et al., 2003), due to the strong thermal alteration of the basin infill rocks. Therefore, up to now, the potential source rocks have mainly been identified based on sedimentary features (Mas et al., 2003), whereas no detailed petrographic and geochemical analysis of the organic matter of the basin has been carried out. Furthermore, another important variable needed to

reconstruct the petroleum system evolution, is the kinetic of the kerogen transformation into hydrocarbons. Moreover, it is necessary to evaluate the timing of the kerogen thermal degradation and hydrocarbon formation, as a consequence of the progressive temperature increase during burial of the source rock. In the Cameros Basin, up to now, no research has been performed about the kinetic of the source rock.

These numerous unsolved topics about the tectono-sedimentologic and thermal history of the Cameros Basin, as well as the evolution of its petroleum system, makes this basin very interesting for a basin scale analysis. Thus, in this thesis, by means of a multidisciplinary approach, a synthesis of the evolution of the Cameros Basin is proposed. The results of this thesis contribute to clarify several debates about the structural and thermal evolution of the basin, as well as the functionality of its petroleum system. Thus, this work can be considered a very important and relevant advance in the knowledge of the Cameros Basin, as well as on the understanding of inverted extensional basins evolution and of their related petroleum systems. The data presented herein represent a solid base for future research on the basin and on the geodynamic evolution of the study area.

Chapter 2

2. Objectives

This thesis is the result of a multidisciplinary study that aims to determine the tectono-stratigraphic and thermal hystory of the Cameros Basin, as well as the petroleum system evolution within the basin. The primary objectives of the present work are organized in six main disciplinary areas that compose the research activity developed in this thesis.

1) Geometry and Structure

In this section the geometry and architecture of the basin was characterised, by means of the reconstruction of the basin tectono-stratigraphic evolution. The definition of these data can help to understand the mechanisms governing the extensional tectonic processes and their relationship with the sedimentation trends. To achieve these objectives the following tasks were developed:

- Revision of the geological map of the area of study;
- Definition of the present-day thickness of the units deposited under the extensional regime;
- Definition of the geometry and architecture of the units deposited under the extensional regime:
- Definition of the main structural elements of the basin;

- Reconstruction of the eroded thickness of the basin infill;
- Reconstruction of the geometry and thickness of the basin before the inversion:
- Reconstruction of the change of position of the basin depocentres during the different evolution stages;
- Definition of a genetic extensional model more coherent with the geometrical reconstruction herein performed.

2) Subsidence analysis and heat flow estimation

To reconstruct the thermal history of the Cameros Basin, two of the most important variables playing a major role in the basin thermal evolution are the basal heat flow and the burial degree generated by the sediment load. Thus, in this thesis it was carried out subsidence analysis and heat flow estimation of the Cameros Basin area. To achieve these objectives, in this section, the following tasks were developed:

- Calculation of the basin Total Subsidence;
- Calculation of the basin Tectonic Subsidence;
- Definition of the rapid and decelerated subsidence phases recorded in the basin;
- Calculation of the maximum heat flow recorded at the end of the extensional stage;
- Definition of the heat flow trend recorded during the entire evolution of the basin.

3) Thermal modelling

Temperature is possibly the most critical parameter since it affects not only hydrocarbon generation but also many physical properties of sediments and fluids. Therefore, a realistic reconstruction of the temperature history is crucial to model the basin thermal evolution and to understand the very complex processes that took place and their interactions during the basin development. One crucial point in the reconstruction of the thermal history of a basin is to calibrate the modelling results using reliable paleothermometers, in order to provide direct data of the maximum thermal conditions recorded in the sediments of the basin infill. To achieve these objectives a thermal modelling of the basin was performed by means of the following tasks:

- Definition of the temperature variation in the sediment over time;
- Definition of the maximum temperature accomplished by each stratigraphic unit and establishment of the relative time;
- Definition of the sectors of the basin where the highest temperatures were attained;

- Characterisation of thermal anomalies recorded in the basin infill:
- Model calibration.

4) Organic Matter Characterisation

To reconstruct the petroleum system evolution within the basin, it is necessary to determine the amount and type of organic matter presently preserved and its hydrocarbon potential, currently and in the past, as well as to identify potential source rocks. These objectives were achieved developing the following tasks:

- Definition of the organic matter rich levels within the basin;
- Petrographical and geochemical characterisation of the organic matter rich levels;
- Definition of the thermal maturity of the deposits analyzed;
- Definition of the type and amount of organic matter preserved at the present-day in the basin;
- Definition of the potential and/or spent source rocks of the basin;
- Definition of the hydrocarbons potential of the source rocks of the basin.

5) Kinetic calculation and definition

The kinetic behaviour of the kerogen contained within the source rock need to be taken into consideration, as kinetic determines the influence of time and temperature in the process of kerogen maturation. In this section bulk kinetic parameters for the immature kerogen of the Cameros Basin were calculated. This objective was achieved developing the following tasks:

- Definition of the organic matter layer with suitable characteristic to be used for kinetic calculation;
- Modelling of the pyrolysis Rock-Eval data;
- Definition of the frequency factor and activation energies distribution;
- Calibration of the calculated parameters;
- Comparison of the kinetic calculated for the basin with literature kinetics.

6) Modelling of the petroleum system

Petroleum system modelling reconstructs the timing and volume of hydrocarbon generation as well as migration and accumulation. In the case of paleopetroleum systems, the main processes and elements can be determined taking into account the entire geological evolution of the basin. The evolution of the Cameros Basin petroleum system was modelled, developing the following

tasks:

- Definition of the source rocks thermal maturity in the basin;
- Definition of the source rocks that mostly contributes to the generation of hydrocarbons during the basin evolution;
- Definition of the times of hydrocarbons migration, generation and accumulation;
- Definition of the reservoirs of the petroleum system;
- Definition of the time of formation of seals and/or traps;
- Estimation of the amount of hydrocarbons generated, migrated and accumulated;
- Establishment of causes of the lack of the preservation of the hydrocarbons accumulations.

Chapter 3

3. Methodology

In order to achieve the objectives proposed in this thesis, it is necessary to make a basin scale study of the Cameros Basin. The basin-scale study was handled by means of a multidisciplinary approach. Six main disciplinary areas were dealt (Fig. 3.1), each one focused to solve one specific aspect of the evolution of the basin: 1) Reconstruction of the geometry and structure of the basin; 2) Subsidence analysis and heat flow estimation; 3) Reconstruction of the thermal history of the basin; 4) Characterisation of the most relevant organic matter accumulations in the basin; 5) Definition of the kerogen kinetic parameters in the basin and 6) Modelling of the petroleum system in the basin. In this monograph, each disciplinary area was dealt in independent sections. The results obtained in each section are the source data of the next sections (Fig. 3.1). As a consequence there is a strong interconnectivity between all sections.

A brief description of the six sections in which this work has been subdivided is presented here.

1. Geometry and structure of the basin

This section firstly aims to determine the geometry, thickness and architecture of the basin infill, as well as to determine the eroded thickness through the reconstruction of a balanced geological cross section and its restorations. Furthermore it is determined the depositional trend recorded during the extensional phase and its relationship with the extensional tectonic activity that affect

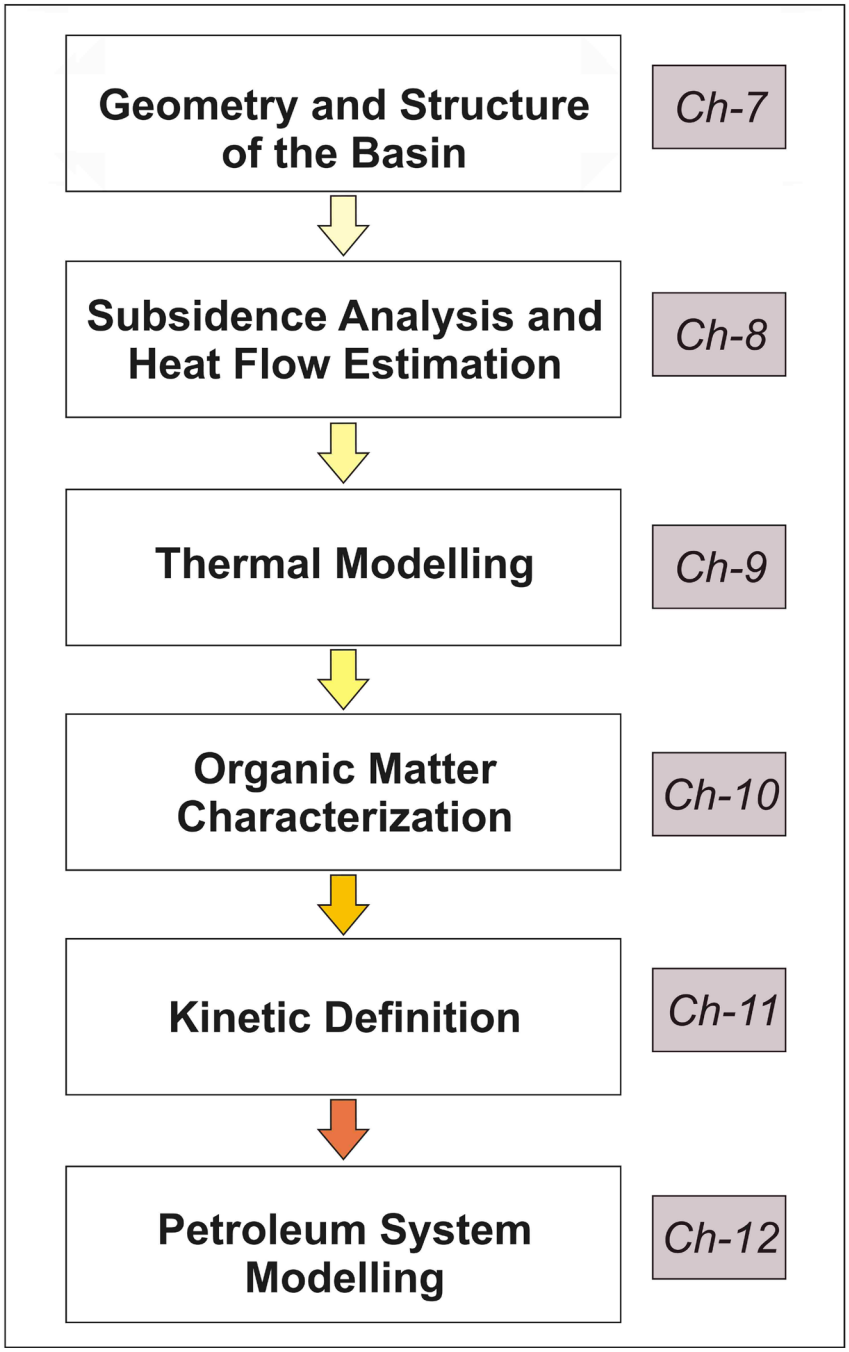

Fig. 3.1 Main disciplinary areas in which the work realized in this thesis was subdivided

the basin during the extensional stage. Finally, in this section, an hypothesis of the possible extensional mechanisms which formed the basin are proposed.

2. Subsidence analysis and heat flow estimation

This section aims to perform a subsidence analysis of the basin infill, determining: sources

of sediment supply and burial evolution over time, accommodation space formation trend and amount and type of subsidence that have affected the basin. In a second step subsidence analysis data were used to estimate the maximum heat flow affecting the basin at the end of the extensional stage, consequence of the lithosphere stretching and of e asthenosphere upraise.

3. Thermal modelling of the basin

In this section 1D and 2D thermal models of the basin were reconstructed determining paleo-temperature sover geological time and its spatial variation in the basin. To reconstruct a thermal model it was taken into account the geohistory of the basin (depositional and erosional events), the geometry of the basin infill and the heat flow affecting the basin area. 1D thermal models were reconstructed on virtual wells defined on the restored section of the basin, whereas the entire restored section was modelled in the 2D thermal model. Calibration of the thermal model was performed by vitrinite reflectance data. Fluid inclusions were as well used to test the interpretation of the thermal history of the basin. Several calibration runs were made until the model results approximated the measured data. Thus, calibration of the heat flow estimated in the previous section was obtained.

4. Organic matter characterisation

In this section a detailed petrological and geochemical characterisation of the organic matter present in the basin was realized. Analyses were addressed to determine: thermal maturity accomplished by sedimentary rocks, quantitative and qualitative amount of organic matter, macerals abundance and features, type of kerogen and hydrocarbon potential of the basin. From these data, the potential source rocks of the basin were identified, as well as the effects of the thermal evolution of the basin (burial and/or hydrothermalism) on the organic matter preservation.

5. Kinetics definition

In this section it was calculated the bulk kinetic parameters of the kerogen, that form the original source rocks of the petroleum system of the basin. Calculations were performed on immature organic matter samples and they were based on a mathematical computational modelling of the S2 peak of the pyrolysis Rock-Eval. Results were compared with classical kinetics proposed in the literature, in order to interpret the thermal alteration behavior of the kerogen of the Cameros Basin. The results allows choosing in the literature compositional kinetic appropriate for the kerogen of the Cameros Basin.

6. Modelling of the petroleum system of the basin

In this section a modeling of the petroleum system of the basin was performed, by means of a 2D thermal model. In the model, a synthesis of the geological history of the basin was

performed, including structural deformation history, stratigraphy, chronostratigraphy, burial history, paleogeography, paleotemperature, paleoheat flow, petrophysical properties of the rocks, kinetics parameters, organic petrology and geochemistry data. For this purpose the whole data and results obtained and determined in the previous sections were used to reconstruct a reliable and complete model. The elements and processes of the petroleum system were reconstructed.

Previously to handle the thematic section, it was developed a detailed alphanumeric and geographic data base of the geological and geographical data of the study area. This data base was performed at the beginning of the research and it was based on the very abundant previous bibliography, data and information. The resultant data-base represented a solid base and reference during the progress of the entire work.

A detailed flow chart of the methodology used in each section is shown in Fig. 3.2 and it is extensively explained in the next corresponding chapters. Each section is organized in different parts, which commonly are: introduction, methodology, results, discussion and conclusions. As a consequence, discussion of the results obtained in this thesis is treated separately for each discipline area, instead of drawing up a unique discussion chapter. Instead, a final conclusion chapter is presented, adding-up the partial conclusions of each section. A unique geological setting (**Chapter 5**) is placed before the six previously described sections. In some case, when it can help to understand the data used and the discussion of the results performed, a synthesis of the geological section is provided inside the chapters.

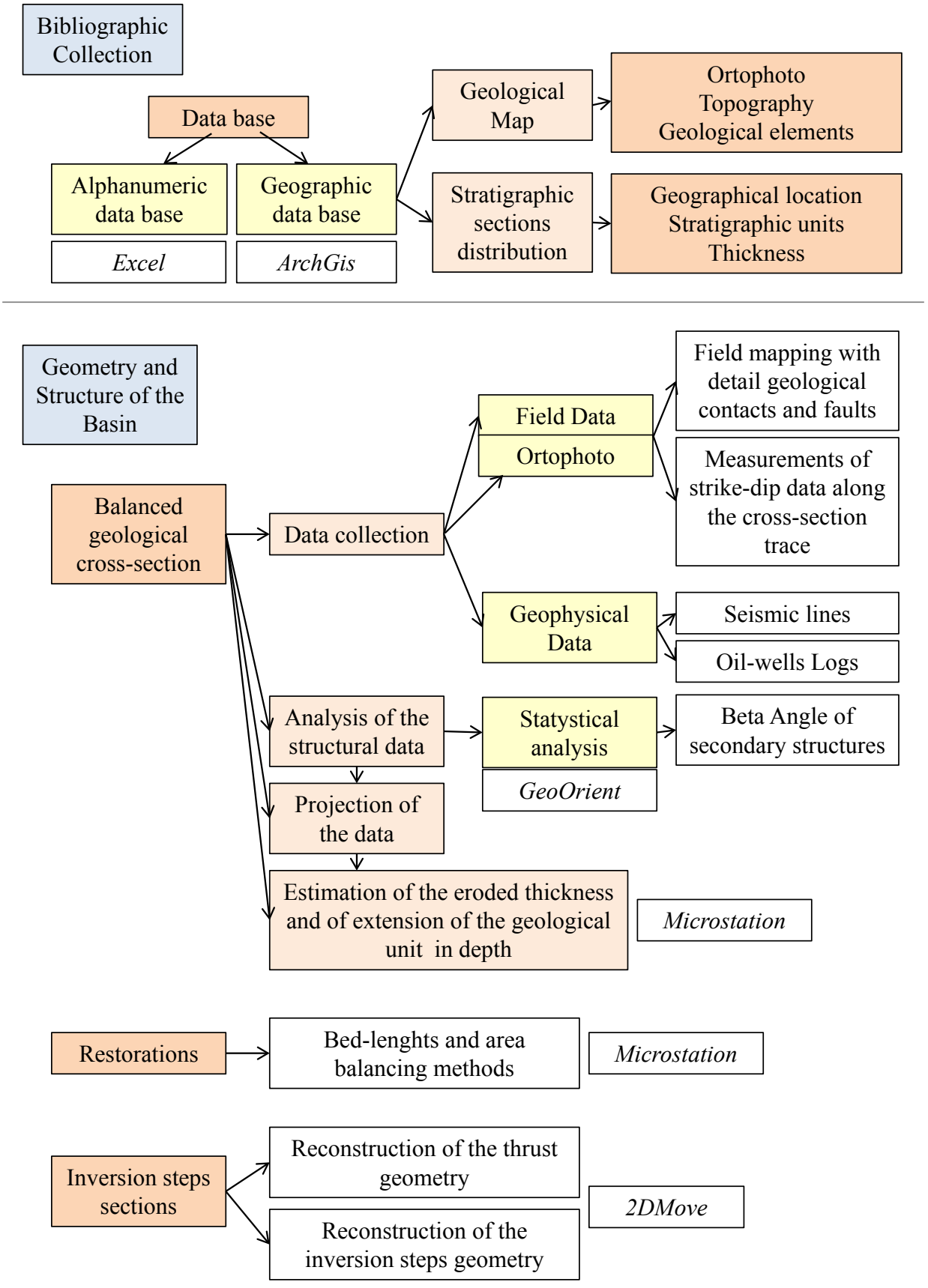

Fig. 3.2 (Part 1) - Detail of the methodology used in each disciplinary area - Continues

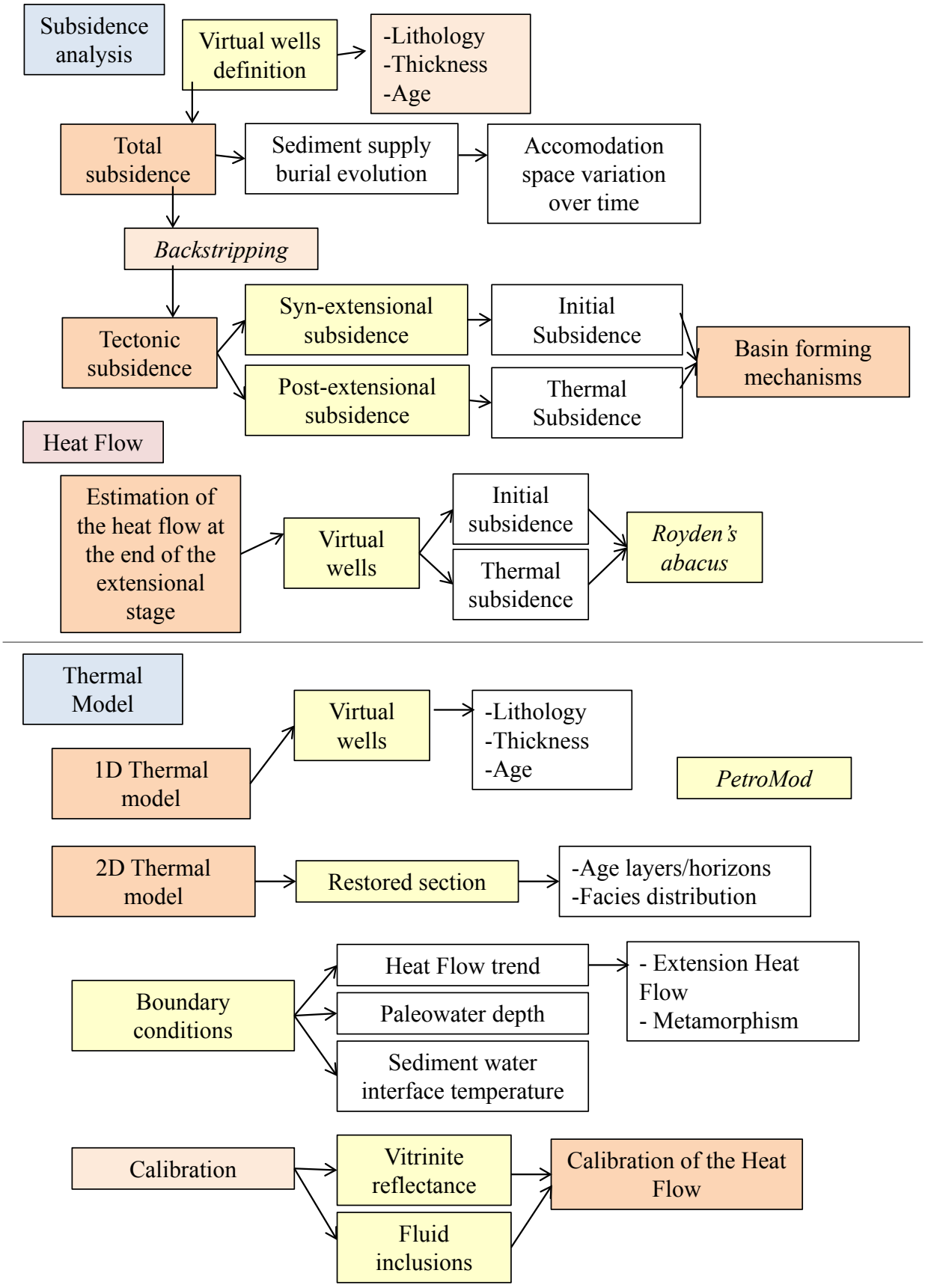

Fig. 3.2 (Part 2) - Detail of the methodology used in each disciplinary area - Continues

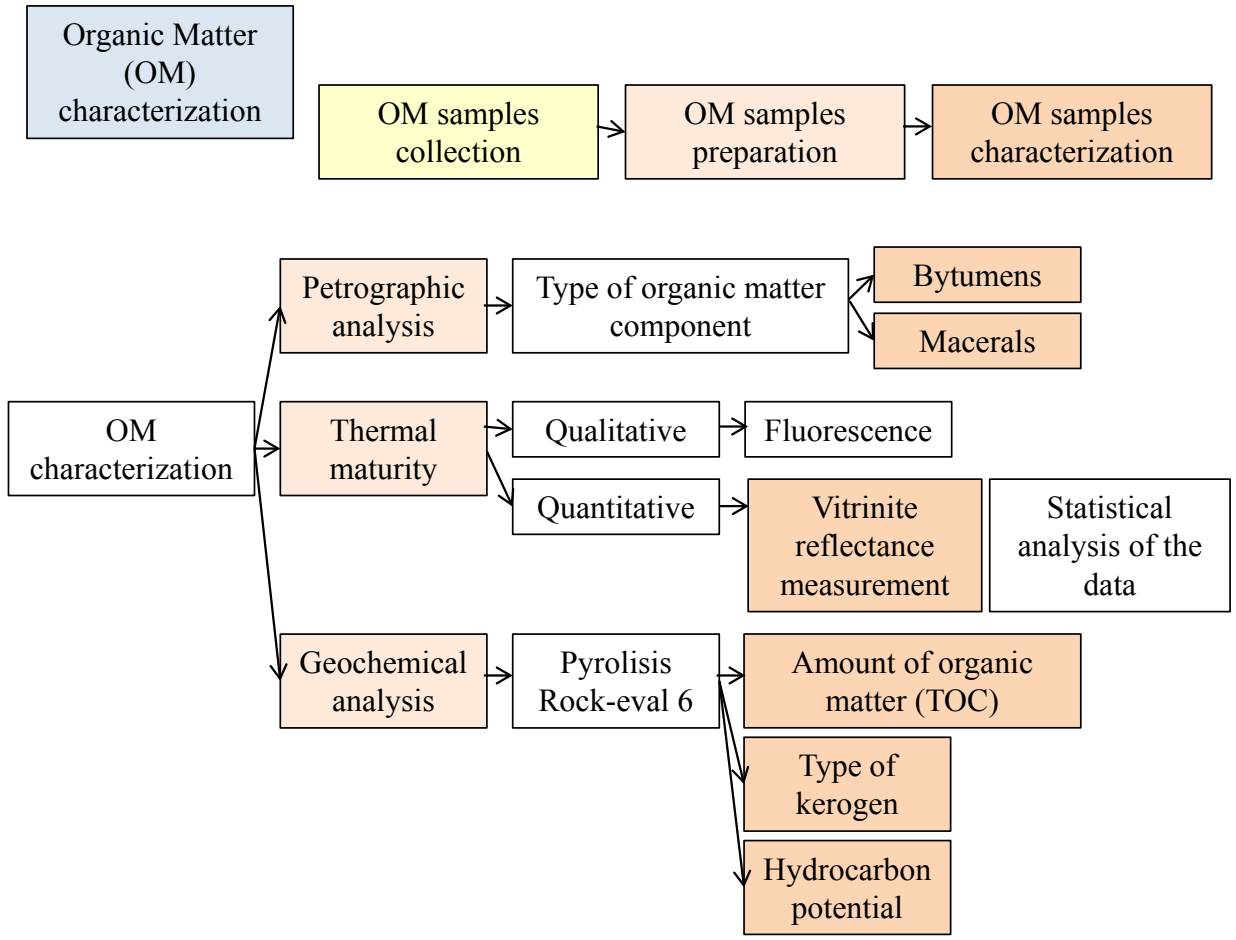

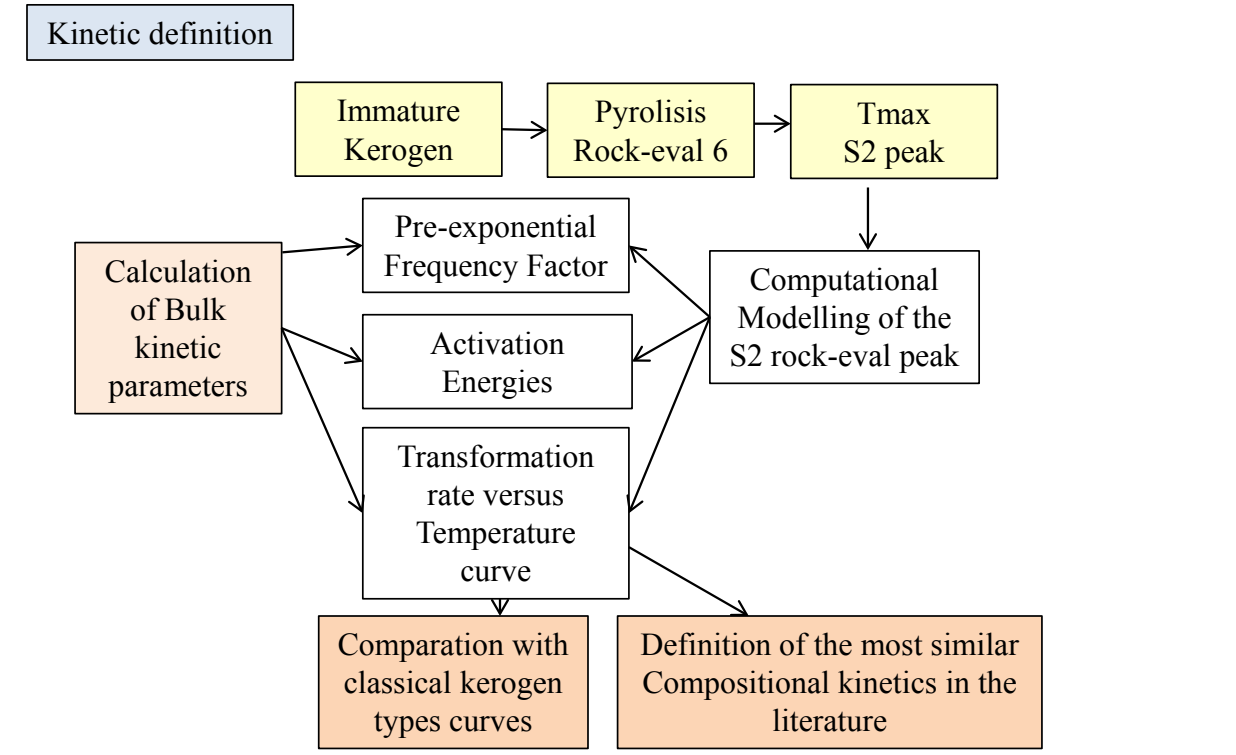

Fig. 3.2 (Part 3) - Detail of the methodology used in each disciplinary area - continues

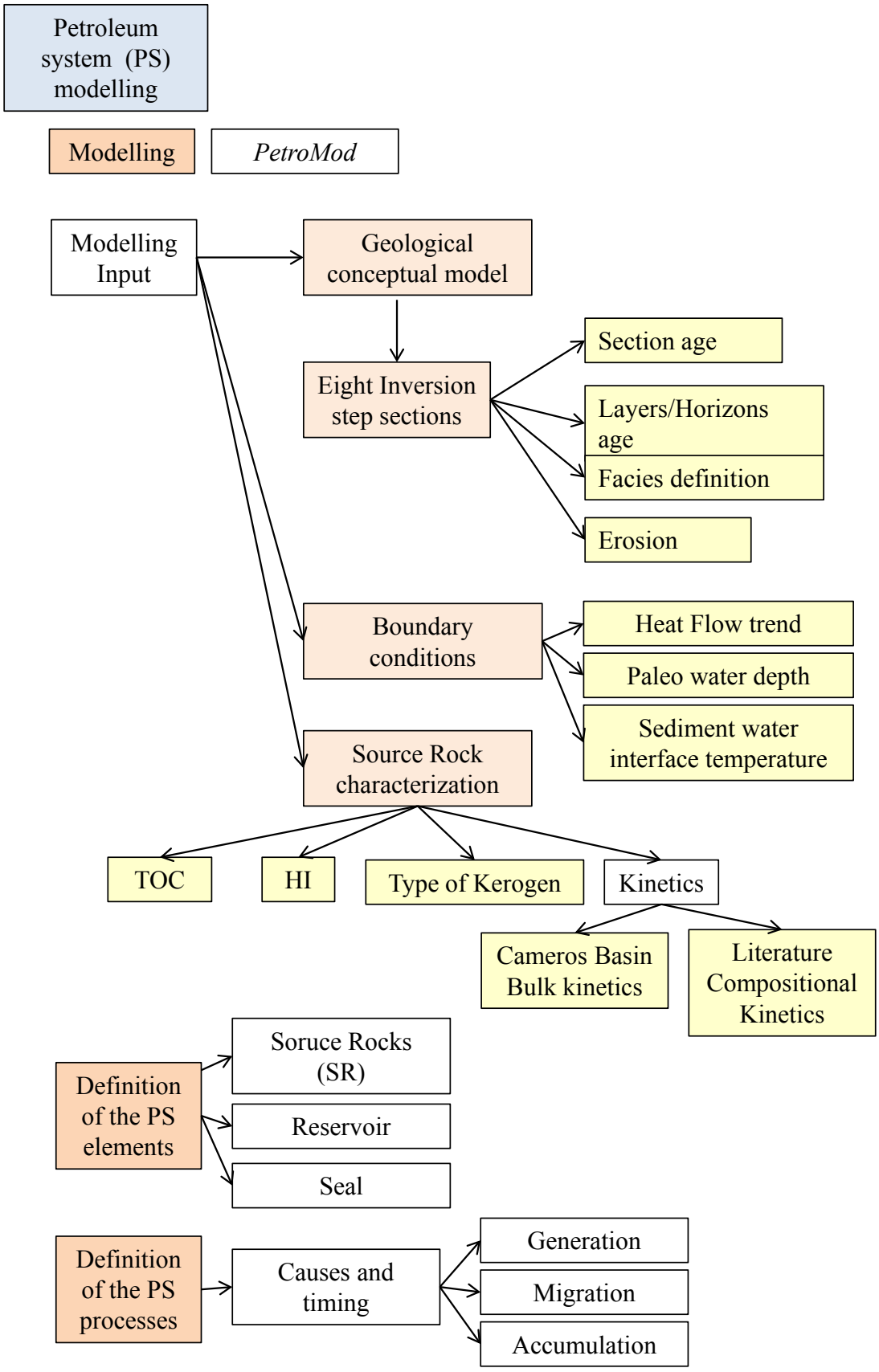

Fig. 3.2 (Part 4) - Detail of the methodology used in each disciplinary area

Chapter 4

4. Previous Studies

4.1. INTRODUCTION

The Cameros Basin has been the object of numerous multidisciplinary studies in the last centuries, due to the relevant tectonic, sedimentological and petrological features that it presents. Furthermore, the good stratigraphic record preservation of the Cameros Basin and its peculiar marginal position within the Iberian Chain makes the understanding of the Cameros Basin geological evolution a major task for the complete comprehension of the whole Iberian Rift System.

Previous works realized in the Cameros Basin have been mainly organized in three main chronological groups:

- works realized in XIX century,
- works realized between 1900 and 1980
- works realized from 1980 to present day

4.2. WORKS REALIZED IN THE XIX CENTURY

Very general geographical and regional works in the areas of Burgos, Soria and Logroño (Esquerra, 1841, Aranzazu, 1877) were performed during this time period. During these years a first geological map of Spain was realized and the first description of the mineral resources and fossils of the area were reported by Urrutia (1978) and Mallada (1884, 1885 and 1887).

Palacios and Sánchez Lozano (1885) made a description of the main geological facies present in the area, which partially corresponded to the Purbeck, Weald and Urgo-Aptian facies later recognized by others authors (Tischer, 1966). Palacios-Sáenz (1890) described the geology of the Soria province in the memory of a geological map of the area, and in 1892, realized a geological study in the south of the Zaragoza province. Sánchez Lozano (1894), for the first time, divided the Cretaceous continental formations of the area in five groups, similarly to the currently used stratigraphic subdivision.

At the end of this century, basic stratigraphic data of the Iberian area (provinces of Burgos, Soria, Logroño, Álava and Aragón) were provided by Chudeau (1896), Larrazet (1896) and Derreims (1898).

4.3. WORKS REALIZED FROM 1900 TO 1980

During this time interval more detailed studies were done, which aimed to describe the landscape, geological, botanical and hydrological features of the Iberian Chain, as well as of the Cameros Basin (Mallada, 1904; Ritcher; 1930, Navás, 1931). General features about the stratigraphy, tectonic and paleogeography of the Iberian Chain were provided by Richter (1933), whereas more detailed studies about the stratigraphy of the Cameros Basin were reported by Sáenz García (1942). Aitken (1942, 1946) studied the structure of the northern border of La Demanda Chain.

An important work of this period was provided by Tischer (1965, 1966) which studied the Weald facies outcropping in the eastern part of the Cameros Basin. He defined five lithological main groups (Tera, Oncala, Urbión, Enciso and Oliván) that are still used at present-day. These deposits were generally interpreted as fluvio-deltaic. Differently, in the western part of the basin the Weald and Utrillas facies were studied by Beuther (1966).

The chronostratigraphic framework of the basin was based firstly on biostratigraphic data, and more specifically on ostracods biozones, proposed by Kneuper-Haack (1966), which determined a Kimmeridgian-Valanginian age for the basin infill. Later, using ostracods dating, Brenner (1976) extended the upper stratigraphic limit up to the Barremian.

The I.G.M.E. (1971a, 1971b) published the geological maps of Logroño and Soria at scale 1:200.000, and Álvaro et al. (1979) explained the Cameros Basin within the context of an aulacogen model that was established for the entire Iberian Basin.

4.4. WORKS REALIZED FROM 1980 TO PRESENT-DAY

The relevance of the studies carried out during this period of time is their multidisciplinary focuses and approaches, willing to characterise in deep detail all the different features that characterise the Cameros Basin (sedimentology, stratigraphy, tectonic, petrology, mineralogy, diagenesis, etc.,).

Furthermore, in the first decade of this period, a large number of geological maps at scale 1:50.000 were produced (Plan MAGNA of the Instituto Geológico y Minero de España – (IGME): Rey and Rivera, 1981; Cámara and Durantez, 1982; Durantez et al. 1982; Navarro Vázquez et al. 1991a,b), improving the knowledge about the stratigraphy, sedimentology, paleontology and tectonic of both the eastern and western sectors of the basin.

4.4.1. Stratigraphy, sedimentology and basin analysis

During this period relevant stratigraphic syntheses of the Cameros Basin deposits were performed.

Salomon (1982a, b, 1983a, b) produced a synthesis of the Cameros Basin stratigraphy, defining with clarity three facies Weald, Urgon and Utrillas. The eastern and the western sectors of the basin were differentiated, based on their different stratigraphic-sedimentological trends.

Guiraud (1983), and Guiraud and Seguret (1985) proposed the first tectono-sedimentary model of the basin, characterising the stratigraphic record from the Kimmeridgian to the Aptian. The same five groups recognized by Tischer (1965) were only slightly modified. They interpret the entire stratigraphic record of the basin composed by material that represent a broad fluvial delta.

Others basin-scale studies allowed important advances in the knowledge of the tectonic and sedimentological evolution of the basin. Schudack (1987) and Schudack and Schudack (1989) defined a new tectonic and paleogeographic model of the basin and they go back over the ages of the stratigraphic units, which have been previously defined by Salomon (1982b). Alonso and Mas (1988) characterised Lower Cretaceous outcrops in the south of the Moncayo Chain and they mention for the first time the presence of Aptian marine facies directly on top of Late Jurassic continental facies. Díaz Martínez (1988) defined the stratigraphic framework of the lithological

units outcropping in the northern border of the basin, while Platt (1989a, b) realized a tectonic and sedimentological study of the western sector of the basin.

A more modern synthesis of the tectono-stratigraphic evolution of the Cameros Basin with detailed sedimentological description of the basin infill was provided by Mas et al. (1993). In this work the lithostratigraphic units forming the syn-extensional stratigraphic record were organized in several depositional sequences, bounded by unconformities and their related conformities, organized in a chronostratigraphic framework. Dating of this framework was provided by Martín i Closas and Alonso Millán (1998), which realized a biostratigraphic study of the western syn-extensional depositional sequences, based on charophyte biozones, correlating them with the eastern sector depositional sequences.

Salas et al. (2001) developed a more general work of the tectono-stratigraphic and paleogeographical evolution of the entire Iberian Chain. A correlation between the stratigraphic record and the tectono-sedimentary stages of all Late Jurassic-Early Cretaceous Iberian Basins, including the Cameros Basin, was proposed.

Mas et al. (2002, 2003) provided new data of the Jurassic substratum, the stratigraphy of the basin infill, the genesis and characteristics of the metamorphism affecting the basin and the possible tectonic models that could explain the basin formation and inversion mechanisms. They presented the first detailed hypothesis of the petroleum system formed in the Cameros Basin area.

Within this time period, a very large number of detailed works were realized to improve the knowledge on the sedimentological, petrographical and mineralogical characteristics of the syn-extensional deposits of the basin. A synthetic compilation of these studies is presented in Table 4.1, where works involving the syn-extensional units are grouped by disciplinary areas.

The deposits of the eastern sector have been studied in detail by numerous authors (Alonso et al., 1986, 1987, 1989; Wygrala, 1988; Alonso and Mas, 1990; Gómez Fernández, 1992; Barrenechea, 1993; Mas et al., 1993, 1997, 2002, 2003, 2009, 2011; Gómez-Fernández and Meléndez, 1994; Barrenechea et al., 1995; Alonso-Azcárate, 1997; Benito and Mas, 2001; Benito et al., 2003, 2005, 2006; Arribas et al., 2003, 2007; González-Acebrón et al., 2007; González-Acebrón, 2009; Quijada et al., 2010, 2013a,b; Suárez-González et al., 2010, 2013, 2014).

Differently, the deposits of the western sector of the basin have been characterised by a reduced number of works: Clemente and Alonso (1990); Platt (1990, 1995); Clemente and Pérez Arlucea (1993); Mas et al. (1993); Martín i Closas and Alonso Millán (1998) and Arribas et al. (2001, 2003).

Arribas et al. (2002, 2003, 2007, 2013); Najarro de la Parra, (2005); Ochoa et al. (2005, 2007); Ochoa (2006); González-Acebrón (2009); González-Acebrón et al. (2007, 2011, 2012, 2013) have

presented detailed studies about the petrography, provenance and diagenesis of the syn-extensional deposits outcropping in the western sector of the basin and of the Tera and Urbión Groups from the eastern sector.

4.4.2. Tectonic evolution of the basin

The Cameros Basin geometry and structure have been the subject of debates trying to find a reliable extensional and inversion genetic model.

Guiraud (1983) and Guiraud and Seguret (1985) proposed a "pull-apart" model, formed by two main km-scale sinistral strike-slip faults with a NE-SW orientation. In this context, during the extensional phase, the strike-slip tectonic would create a WNW-ESE oriented normal fault in the northern basin margin, which movement forms a south-dipping half graben within the basement. The main normal fault was slightly inverted during a Tertiary compressional phase, creating the current Cameros Basin structure.

Casas-Sainz and Simón-Gómez (1992) and Casas-Sainz (1993) explained the Cameros Basin evolution as a result of the inversion and overthrust of the basin on the Ebro foreland. The inversion plane was a lystric fault which was interpreted to be the same normal fault forming the basin during the extensional phase. This model was later confirmed and completed by Gil-Imaz et al. 1995, Casas-Sainz and Gil-Imaz (1998), Casas-Sainz et al. (2000), Mata et al. (2001), Soto et al. (2007), Casas et al. (2009, 2012). The gradual motion along the lystric normal fault caused the sedimentary infill to be passively folded by bending (Mata et al., 2001), creating a basin-scale syncline geometry. Increasing accumulation space was generated in the core of the syncline, allowing the vertical superimposition of syn-extensional depocenters (Mata et al., 2001). Casas-Sainz and Gil-Imaz (1998) recognized that, at the end of the Lower Cretaceous, the basin underwent contraction, manifested as gentle folds containing axial-plane cleavage. This contraction is coeval to the onset of oceanic spreading in the Bay of Biscay. Paleomagnetic and rock magnetic data analyses were provided by Villalaín et al. (2003) and Casas et al. (2009), which reconstructed the original geometry of the northern basin border before the inversion. These studies confirmed the synclinal geometry of the basin, associated with a large-scale syn-sedimentary normal fault drag with a minor roll-over anticline.

A different interpretation was provided by Mas et al. (1993) and Guimerà et al. (1995), where the Cameros Basin was interpreted as an extensional-ramp basin produced over an S-dipping ramp linking two flats of an extensional fault, located some kilometers deep in the basement. The extensional displacement of the fault produced a synclinal basin which progressively widened with time. The depocenters of the successive depositional sequences were always located above the ramp and migrated laterally to the north, inside the basin, as a result of the hangingwall

displacement to the south. The inversion occurred along a thrust plane located on the Upper Triassic beds (Keuper).

A recent study (Omodeo Salé et al., 2014) has proposed a comprehensive reconstruction of the tectono-stratigraphic evolution of the Cameros Basin, presenting a synthesis and an integration of previous studies of the structure and geometry of the basin. This study is very useful as a basis for future basin-scale research and for the modelling of the ancient petroleum system of the basin.

4.4.3. Metamorphism and thermal evolution

Guiraud (1983) and Guiraud and Seguret (1985) have been the first authors that recognized that the deposits of the northern part of the basin were affected by metamorphism. They interpreted this metamorphism as caused by burial of the basin infill. A maximum temperature of 420-520ºC was estimated based on the mineral paragenesis.

Goldberg et al., (1988) realized the first dating of the metamorphic event that affected the basin (98.5 My). After this work it has been considered that the metamorphism was contemporaneous with the basin formation.

Casquet et al. (1992) defined the Cameros Basin metamorphism processes as hydrothermal. A maximum temperature of 350ºC and a pressure of 1 kbar have been estimated by these authors, based on mineral paragenesis. K-Ar dating of illites provided a Middle Cretaceous age, 81-86 My (Albian to Coniacian) for the metamorphism.

Barrenechea (1993) and Barrenechea et al. (1995) studied the mineralogy and clay mineral crystallinity of the deposits affected by the metamorphism, determining an inverse-with-depth thermal gradient and circulation of hot fluids throughout the sedimentary succession.

Alonso-Azcárate et al. (1995, 1999), Alonso-Azcárate (1997) studied the pyrite deposits of the basin and the metamorphic conditions of the upper syn-extensional depositional sequences. They proposed a metamorphic genetic model for the pyrite formation (Alonso-Azcárate et al., 1999), defining a formation temperature approximately of 370ºC. In Alonso-Azcárate et al. (1995, 1997, 1999), Alonso-Azcárate (1997) and Barranechea et al. (2001) confirmed as well a hydrothermal origin of the metamorphism. These studies demonstrated that the illite cristallinity was mainly controlled by the carbonate presence and the permeability of the sediment. In addition, a decrease-with-depth trend of the illite cristallinity values was recognized in the central sector of the basin.

Mantilla-Figueroa et al., (1998, 1999) and Mantilla-Figueroa (1999) recognized as well that the metamorphism in the Cameros Basin was hydrothermal. In these studies the hydrothermal

flow properties have been characterised, as well as theirs relationship with the basin infill and the tectonic basin evolution. The maximum temperatures reached in the rocks were estimated by secondary fluid inclusions in quartz veins (220-240ºC). An inversion of the temperature-with-depth trend was determined even in these works. Mantilla-Figueroa et al. (2002) established geochronological sequence of events by K-Ar dating of autigenic illites and identified two metamorphic events: the first produced at a time period between 90-100 My, during the post-extensional phase, and a second event at 40 My, produced during the basin inversion.

Ochoa (2006) and Ochoa et al. (2007) studied the mineralogy and sandstone petrology and thermal evolution of the Urbión Gr. Numerous hydrothermal mineral facies were found in the sandstone cements located in the northern sector of the basin. Primary fluid inclusions found in quartz overgrowths allowed to determine the diagenetic temperatures for these deposits.

Mata-Campo, (1997), Mata et al. (2001), Del Río (2009), Del Río et al. (2009a,b) and Casas et al. (2012) studied the thermal evolution of the Cameros Basin, with the aim to assess the implication of the thermal history in the tectonic and structural evolution of the area.

Mata-Campo (1997) and Mata et al. (2001) interpreted the metamorphism of the Cameros Basin as a burial metamorphism, result of an anomalous geothermal gradient produced during the extensional stage. This event has been correlated to a more general heating event that took place in the north-eastern part of the Iberian plate. A normal increase-with-depth trend was determined by primary fluid inclusions measurements in quartz veins.

Del Río-Bermejo (2009) studied the thermal evolution of the Cameros Basin using fission tracks thermochronology and (U-Th)/He analysis or SHRIMP U-Pb for dating. A metamorphic event was recognized in the central sector of the basin, which was suggested to be controlled by burial. Del Río et al., (2009a) described the textural relationships and geochemical aspect of authigenic and/or metamorphic monazite. Two metamorphic peaks were recognized which were dated as 119-107 My and 106-86 My using U-Pb SHRIMP analyses on authigenic monazite.

González-Acebrón (2009) and González-Acebrón et al. (2011, 2012) realized a detailed study on the diagenetic processes affecting the deposits of the first depositional sequences of the syn-extensional phase (Tera Gr). A metamorphic hydrothermal alteration was recognized in the south-eastern area of the basin (El Pégado anticline), using petrography and SEM-CL combined with microthermometry of fluid inclusions and isotopic analyses. Two hydrothermal metamorphic events were recognized by these authors, the first taking place during the mid-Cretaceous and the second during the Eocene.

4.4.4. The petroleum system of the area

In 1964 Hispanoil developed several oil-wells in the Iberian Range area for exploration, some of them located in the Cameros Basin. The basin infill stratigraphic record and the depth and nature of the syn-extensional substratum were determined. In 1984 ENIEPSA performed several seismic lines to explore the Cameros Basin area and the surroundings. These seismic lines and the related interpretations have been placed openly available online by I.G.M.E in recent years. Wells logs of the area appear compiled in Lanaja (1987).

Muñoz-Recio (1993) modeled the hydrocarbon potential of the NW Iberian Chain. In the Cameros Basin area a very low hydrocarbon potential was deduced, based on the reduced thickness of the source rocks (Permian and Lower Jurassic) and the low heat flow affecting the area, which did not allow source rocks thermal maturation.

Mas et al. (2002, 2003) realized a first synthesis of the petroleum system of the Cameros Basin and the surrounding sub-basins (Rioja and Bigornia throughs), defining its possible elements (source rocks, reservoirs and seals) and processes. As potential source rocks in the Cameros through were identified the Callovian deposits forming the Marine Jurassic substratum and the syn-extensional Berriasian lacustrine organic-rich shales deposits. The Urbión Group sandstone bodies were identified as the best potential reservoir of the basin. Following these authors, hydrocarbons generation occurred in two stages: the first during the Albian, by burial, and the second in the Late Cretaceous, induced by the abnormal heat flow caused by the first hydrothermal event.

Ochoa (2006) and Ochoa et al. (2007) reconstructed the physico-chemical properties of the Urbión Gr as a possible reservoir of the Cameros Basin petroleum system. In the central sector of the basin, these authors identified hydrocarbon fibers lying between quartz grains of the sandstone bodies, which were probably deposited during the mesodiagenetic phase and before the quartz cementation.

Mas et al. (2003) and Ochoa et al. (2007) suggested that in the northern and central areas of the basin the hydrothermal metamorphism destroyed the reservoirs by generating metamorphic hydrothermal mineral cements.

Table 1 - Synthetic compilation of the studies realised from 1980 to present-day, including the syn-extensional units grouped by disciplinary areas

Unit	Sedimentology/Stratigraphy/Basin analysis	Petrology/Diagenesis/Metamorphism	Tectonic evolution
Marine Jurassic	Alonso et al., 1986-1987 Alonso and Mas, 1990 Benito-Moreno, 2001 Benito and Mas, 2001, 2006 Benito et al., 2003, 2005 and 2006	Mas et al., 1997 Benito-Moreno, 2001 Benito and Mas, 2001, 2006 Benito et al., 2003, 2005 and 2006	Casas-Sainz and Simón-Gómez,1992 Casas-Sainz, 1993 Mas et al., 1993 and 1997 Miegebielle et al., 1993 Guimerà et al., 1995 Gil-Imaz, 1998
DS1+2	Gómez-Fernández, 1992 Gómez-Fernández and Meléndez, 1994 Mas et al., 1993, 2002, 2003 and 2011 González-Acebrón et al., 2007 González-Acebrón, 2009	Mantilla-Figueroa, 1999 Mantilla-Figueroa et al., 1999 Arribas et al., 2003 González-Acebrón, 2009 González-Acebrón et al., 2007, 2011, 2012 and 2013	Casas-Sainz, et al., 2000 Casas et al., 2009 and 2012 Mata et al., 2001 Salas et al., 2001 Gil-Imaz et al., 1995
DS3	Gomez-Fernandez ,1992 Mas et al., 1993, 1997, 2002, 2003 and 2011 Gómez-Fernández and Meléndez, 1994 Quijada et al., 2010, 2011 and 2013a,b	Mantilla-Figueroa, 1998, 1999 Barrenechea et al., 2001 Del Rio et al., 2009a, b Arribas et al., 2003	Villalain et al., 2003 Guimerà et al., 2004 Soto et al., 2007 González-Acebrón et al., 2012
(DS4+5+6) Urbión Gr	Barrenechea, 1993 Mas et al., 1993, 2002, 2003 and 2011 Ochoa-Rodríguez, 2006	Barrenechea, 1993 Barrenechea et al., 1995, 2001 Mantilla-Figueroa, 1999 Mata et al., 2001 Arribas et al., 2003 Ochoa-Rodríguez, 2006 Ochoa et al., 2007 Del Río et al., 2009	
DS6 Pantano Fm	Clemente-Alonso, 1990 Clemente and Pérez-Arlucea, 1993 Martín i Closas and Alonso Millán, 1998 Arribas et al., 2003	Arribas et al., 2003 Arribas et al., 2013	
DS7 Enciso Gr	Mas et al., 1993, 2002, 2003 and 2011 Alonso-Azcarate, 1997 Suárez-González et al., 2010, 2013 and 2014	Alonso-Azcarate, 1997 Alonso-Azcarate et al., 1995, 1997 and 1999 Mantilla-Figueroa, 1999 Ochoa-Rodríguez, 2006 Mata et al., 2001 Ochoa et al., 2007 Del Río, 2009a, b	
DS7 Abejar Fm	Martín i Closas and Alonso Millán, 1998 Arribas et al., 2003	Arribas et al., 2003 Arribas et al., 2013	
DS8	Mas et al., 2002, 2003, 2009 and 2011		

Chapter 5

5. Geological Setting

5.1. INTRODUCTION

Before starting with the description of the geological setting of the Cameros Basin, it is important to indicate that, throughout this monograph memory, terminology ascribing the Cameros Basin to a particular type of extensional basin will be avoided. Thus, when being referring to the stratigraphic record of the Cameros Basin, the use of terms such as “Syn-rift”, “Post-rift” or “Rifting” was avoided. Differently, in this report it was preferred to use terms related to the subsidence regime type that was dominated at the time of formation of the different phases that composed the stratigraphic record. Therefore, the terms "extensional" phases and "post-extensional” phases were used respectively depending on which of them prevailed, a purely extensional subsidence regime ("extensional" phase) or a predominant thermal subsidence regime ("post-extensional" phase). Furthermore, in the case of "extensional phases" they appear distinguished as "rapid extensional" stages and "decelerated extensional" stages, depending on the higher or lower subsidence rate (Omodeo-Salé et al., in rev.1).

The above clarification is motivated by the special characteristics of the Cameros Basin observed throughout this research. This fact has been shown in very recent publications (Omodeo Salé et al., 2014; Omodeo-Salé et al., in rev.1) and is particularly evident throughout **Chapters 7, 8 and 9** respectively devoted to “Geometry and Structure of the basin”, “Subsidence and Heat flow” and

"Thermal modeling". These special features observed in the basin indicate that there are some doubts about the direct assignment of the Cameros Basin to a Rift basin as it has been attributed in numerous studies (Platt, 1989; Clemente and Alonso, 1990; Casas Sainz and Simón Gómez, 1992; Mas et al., 1993, 2002, 2003, 2011; Gómez-Fernández and Meléndez, 1994; Guimerà et al., 1995; Martín-Closas and Alonso Millán, 1998; Salas et al., 2001; Mata et al., 2001; Arribas et al., 2003, 2013; Villalaín et al., 2003; Soto et al., 2007, Casas et al., 2009, 2012; Del Río et al., 2009, 2013; Clemente, 2010; Omodeo Salé et al., 2014). However, it is relevant to stress that Mas et al. (1993) and Guimerà et al. (1995) already stated the following idea: "The Cameros Basin is an extensional-ramp basin, formed during the late Malm and early Cretaceous, over a roughly south-dipping ramp in a buried horizontal extensional fault several kilometres deep. The south-displacement of the hangingwall of this fault produced the basin over the ramp and increased the basin size progressively". Thus, thirty years ago, the Cameros Basin was classified as an singular type of extensional basin, which has only few analog models (McClay, 1990; Roure et al., 1992). However, to simplify, at this time the Cameros Basin was included within the context of rift basin.

5.2. GEOLOGICAL FRAMEWORK

The Cameros Basin is located in the northern part of the Iberian Peninsula (Fig. 5.1) and it covers part of the Soria, La Rioja and Burgos provinces (Fig. 5.2). It is a Mesozoic basin that has been inverted during the Alpine contractional phase. At the present-day it forms part of the north-western Iberian Chain, an intraplate compressional chain that extends over the eastern, central and northern area of the Iberian Peninsula (Fig. 5.1 and Fig. 5.2).

The Cameros Basin was formed in the Mesozoic Iberian Basin (Iberian Rift System of Casas and Salas 1992; Salas and Casas 1993; Salas et al., 2001). During the Mesozoic, the Iberian plate was repeatedly affected by extensional tectonics, as a consequence of the opening of the Western Tethys, the North Atlantic domain and the Bay of Biscay. Different basins were formed (from west to east, Cameros Basin, Maestrazgo Basin, Columbretes Basin and South Iberian Basin) (Fig. 5.1), accumulating thick sequences of continental and shallow marine siliciclastics, carbonates and minor evaporites (Mas et al., 1993; Guimerà et al., 1995; Salas et al., 2001). Mesozoic sediments lay unconformably on the Variscan basement. The Cameros Basin is the northwesternmost sub-basin of the Iberian Basin and it was filled from the Late Jurassic (Tithonian) to the Early Cretaceous (early Albian) (Mas et al., 1993; Salas et al., 2001).

During the Paleogene (Eocene to early Miocene), the whole Mesozoic Iberian Basin was completely inverted, under a regional NNE-SSW direction, building the Iberian and Catalan Coastal Chains (Casas and Salas 1992; Salas and Casas 1993; Salas et al., 2001) (Fig. 5.1 and Fig.

5.2).The contractional intraplate deformation results from the interaction of deformations located in both borders of the Iberian Plate during the Alpine collisional event: the Pyrenean Orogeny

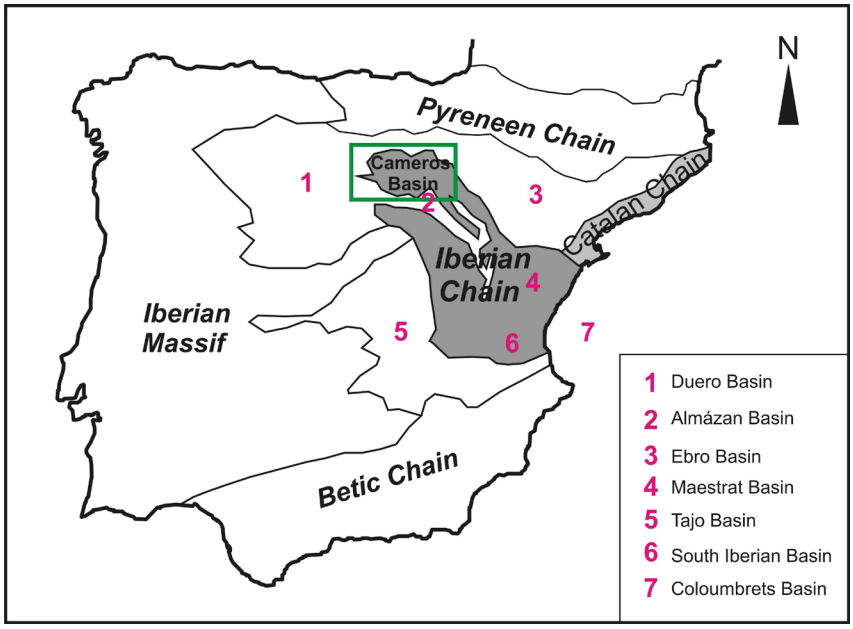

Fig. 5.1 - Location of the Cameros Basin in the Iberian Peninsula

(Guimerà, 1984; Guimerà and Alvaro, 1990; Vergès and Garcia-Senz, 2001) and the contemporaneous early phase of the Betic Orogeny (Guimerà and Alvaro, 1990; Vera et al., 2001). Within the Iberian Chain, two detachment levels have been recognized as acting during the inversion (Guimerà 1984; Viallard 1989; Guimerà and Alvaro, 1990; Guimerà et al., 1995), one within the Triassic evaporitic levels and a second deeper one in the basement. The Ebro and Duero Basins are the northern foreland basins of the Iberian Chain, while the Tajo Basin is the southern one (Salas et al., 2001) (Fig. 5.1).

5.3. STRATIGRAPHIC FRAMEWORK

According to the subsidence type the Mesozoic stratigraphic record of the Iberian Basin can be divided into two main extensional phases that are separated by post-extensional thermal subsidence phases (Syn-rift and Post-rift phases of the Mesozoic Rift System of Salas et al., 2001 and Mas et al., 2003). The first extensional phase lasted from Late Permian to Late Triassic times, followed by a Jurassic post-extensional shallow marine carbonate episode; the second extensional phase lasted from Late Jurassic to Early Cretaceous (Tithonian to Early Albian) followed by a more uniform Late Cretaceous post-extensional carbonate deposits (Mas et al., 1993; Guimerà et al., 1995; Salas et al., 2001) (Fig. 5.3). Each one of these active phases can be considered as a supersequences that appear separated by regional unconformities (Salas et al., 2001; Mas et al., 2003).

The Cameros Basin originated during the second extensional phase (Tithonian to Early Albian) that affected the Mesozoic Iberian Basin (Mesozoic Iberian Rift System of Mas et al.,

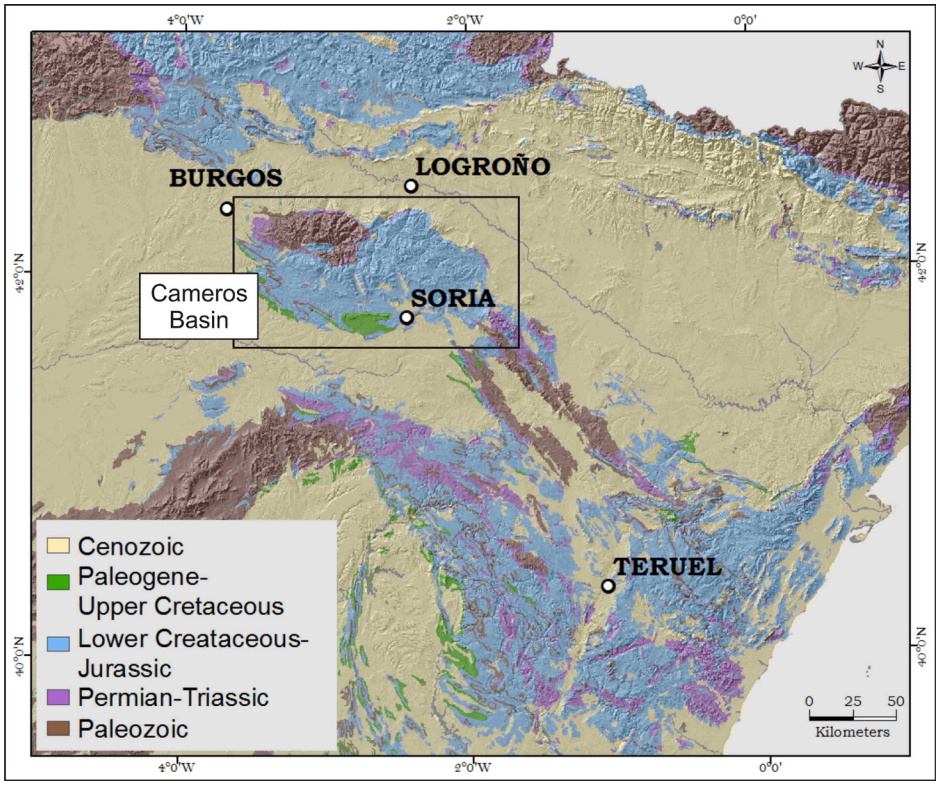

Fig. 5.2 - Location of the Cameros Basin in a simplified geological map of the North-Eastern Iberian Peninsula

1993, Guimerà et al., 1995 and Salas et al., 2001), when most of the basin infill was deposited (Fig. 5.3). Late Permian, Triassic and Jurassic deposits of the first extensional and post-extensional phases represent the substratum of the basin. The syn-extensional deposits that fill the Cameros Basin, Late Jurassic-Early Cretaceous in age, form a supersequence bounded by regional unconformities (Mas et al., 1993, 2002, 2003, 2011; Guimerà et al., 1995, 2004; Salas et al., 2001) (Fig. 5.3). The basal unconformity, the Kimmeridgian regional unconformity, is a time-gap that varies from Late Kimmeridgian to Early Tithonian age in the central sector of the basin, although it appears to be Late Kimmeridgian to Early Barremian age in the northern sector (Mas et al., 1993, 2003). The Kimmeridgian regional unconformity separates the syn-extensional deposits from the underlying pre-extensional deposits. The top unconformity is the intra-Albian regional unconformity, which has a more uniform age throughout the basin (Mas et al., 1993; Guimerà et al., 1995; Mas et al., 2003). The Albian regional unconformity separates the syn-extensional Late Jurassic-Early Cretaceus deposits from the post-extensional late Albian-Late Cretaceous deposits (Upper Cretaceous sequence of Alonso et al., 1993 and García and Mas, 2004).

5.3.1. Basement of the basin

The Variscan Basement of the basin crops out only in the northwest area of the basin, in the Sierra de La Demanda and in the Moncayo area, to the south-east of the basin (Fig. 5.4). It is formed by a thick series (between 3500 and 4000 m thick) that includes rocks aged from

Cambrian to early Ordovician, lying on schists attributed to the Precambrian (Lozte, 1929, 1961; Colchen, 1974). It is predominantly composed of an alternating succession of meta-sediments (quartzite, meta-arenites, shales and occasional dolomites). Prior to the deposits that constitute the substrate of the Cameros Basin (first extensional and post-extensional phases of the Iberian Basin) in the Sierra de la Demanda area appear Upper Westphatian B deposits that post-date

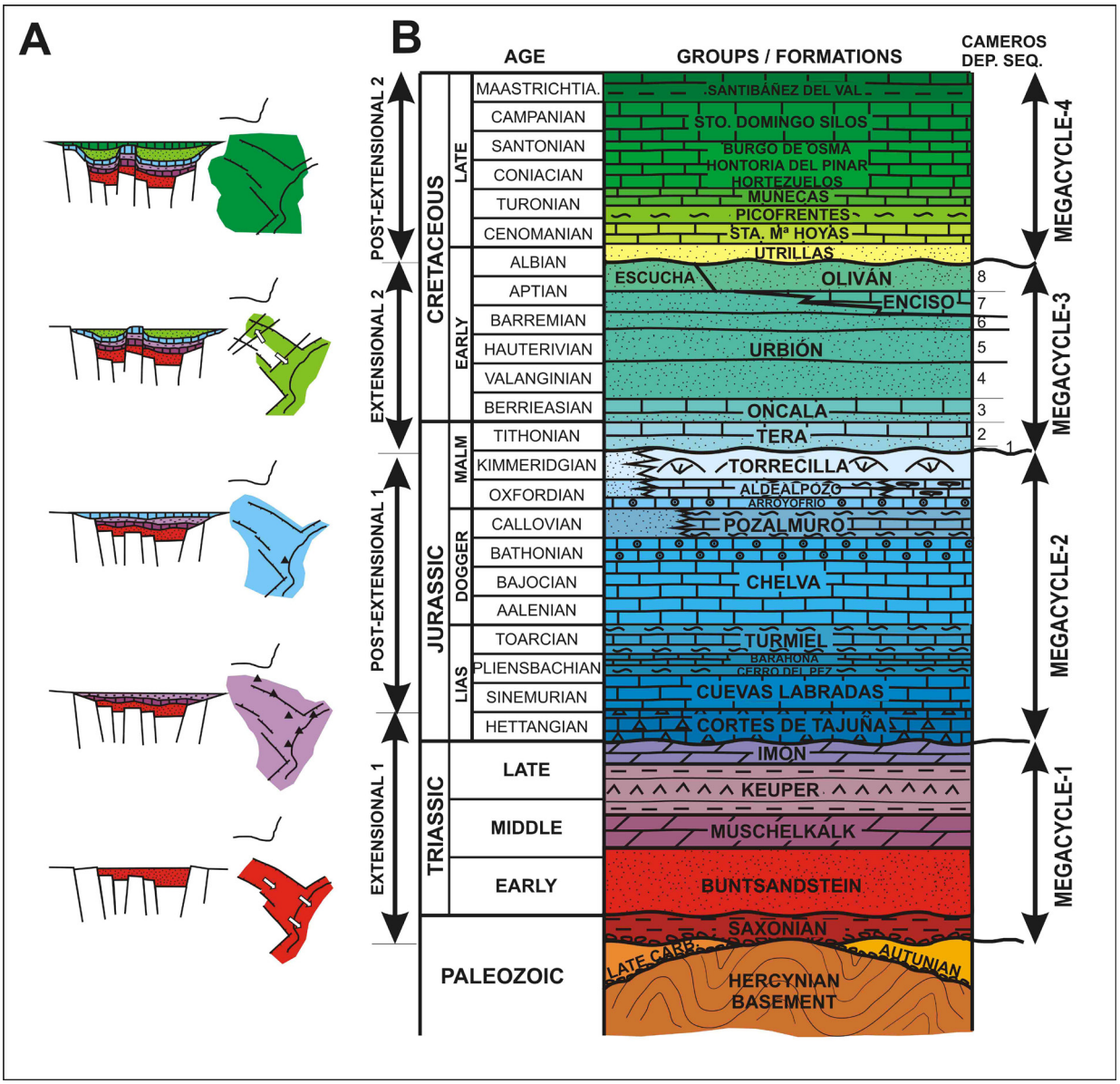

Fig. 5.3 - (a) Extensional and Post-Extensional phases on the evolution of the Iberian Basin (Salas et al., 2001). The Cameros Basin formed during the second extensional phase. (b) Synthetic stratigraphic section of the entire late Paleozoic and Mesozoic stratigraphic record that crop out in the Cameros Basin. The first extensional and post-extensional phases represent the substratum of the basin, whereas most of the basin infill was deposited during the second extensional-phase (Tithonian to Early-Albian). (Modified from Mas et al., 2003).

Variscan structures (Perez Estaun et al., 1990) and locally, in the Moncayo area, an Autunian volcanoclastic unit lies unconformable on the Hercynian Basement (Arribas, 1985; Rey and Ramos, 1990).

5.3.2. Substratum of the basin

The sedimentary record deposited during the Late Permian to Triassic extensional phase and in the related post-extensional phase (Early to Late Jurassic) (first syn-rift and post-rift phases of Salas et al., 2001 and Mas et al., 2003), form part of the substratum of the basin (Fig. 5.4).

5.3.2.1. Late Permian to Triassic extensional phase

This time span correspond to the moment at which the Iberian Basin started developing, with reactivation of late-Variscan faults. They overlaid the Variscan basement unconformably (in La Demanda and Moncayo areas). In the Moncayo area, a first Saxonian (Late Permian) clastic continental unit lies unconformable on both the Hercynian basement and the Autunian volcanoclastic unit (when the latter is locally present). In La Demanda and Cameros areas, as well as in the most of the Iberian basins, the first deposits formed in this period are Triassic and correspond to continental environments (Buntsandstein Facies) that evolved progressively to shallow marine and coastal carbonate environments (Muschelkalk Facies) and coastal evaporitic environments (Keuper Facies) towards the top of the succession (Salas et al., 2001). The Keuper facies act as the detachment level during the Alpine Inversion in most of the Iberian Range (Guimerà, 1984). In the Cameros Basin it crops out in both the northern (nearly 500 m) and southern (nearly 100 m) borders of the basin (Fig. 5.4).

5.3.2.2. Early to Late Jurassic post-extensional phase

At this time period the Iberian Basin area underwent regional thermal subsidence, giving rise to the formation of broad carbonate platforms (Salas et al., 2001). The sedimentary record is largely made up of marine deposits, mainly carbonates, which suggest a period of rising global sea level (Vail, 1977; Vail et al., 1984; Haq et al., 1988) that affected the Iberian and northern Tethys domain (Alonso and Mas 1990; Aurell and Meléndez 1993; Leinfelder 1994; Bádenas and Aurell 2001; Benito et al., 2005).

In the Cameros Basin the deposits formed during this period crop out, with a maximum thickness of 650 m, along the entire northern border of the basin and along part of the southern border, in contact with the main thrust plane (Fig. 5.4). In the basin area six sequences have been recognized, with ages ranging between the Early and Middle Jurassic, whereas there are three

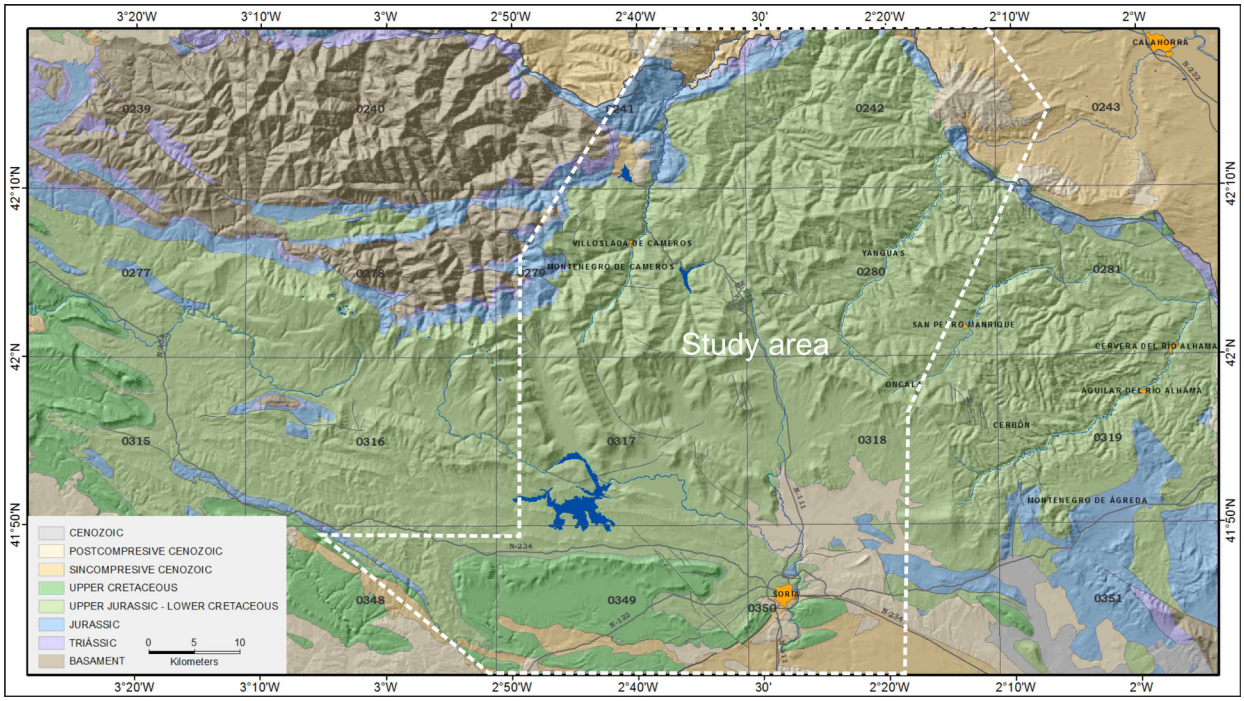

Fig. 5.4 - Simplified geological map of the Cameros Basin. The dashed white line indicates the area studied in detail in this work

with Late Jurassic age (Mas et al., 2003). The Late Jurassic marine record (Early Oxfordian to Early Kimmeridgian) is well represented in the basin, as it generally constitutes the substratum of the Late Jurassic-Early Cretaceous syn-extensional deposits that fill up the Cameros Basin (Mas et al., 2003).

5.3.3. Syn-extensional stage infill (Tithonian to Early Albian)

The syn-extensional deposits constitute the main infill of the Cameros Basin and range from the Tithonian to the Early Albian. They were formed when the Iberian Basin as a whole was affected by a second extensional phase and new extensional basins were formed (Salas et al., 2001). The syn-extensional sediments overlie unconformably Late Jurassic marine carbonates (Mas et al., 1993; Salas et al., 2001).

The syn-extensional sedimentary record is mainly composed of continental deposits, predominantly fluvial and lacustrine, with coastal deposits that indicate the existence of marine incursions (Mas et al., 1993, 2003, 2011; Quijada et al., 2013; Suárez-González et al., 2013). Lithostratigraphically, Beuther (1966) and Tischer (1966 a, b) divided this extensional basin infill into five Groups (Tera, Oncala, Urbión, Enciso and Oliván) whose limits were later on redefined by Mas et al., (1993). Generally, Tera, Urbion and Oliván Groups are mostly constituted by

clastic deposits, with some carbonate levels, sedimented mainly in fluvial, lacustrine and deltaic systems (Mas et al., 1993, 2003 and 2011). Differently, Oncala and Enciso Groups have a dominance of carbonate and evaporite deposits, resulting from the development of lacustrine, palustrine and coastal systems (Mas et al., 1993, 2003 and 2011). The lower lithostratigraphic units (Formations) have been defined by several authors (see Mas et al. 2003 and references therein).

As regards the genetic units, the syn-extensional deposits have been divided into eight depositional sequences (DS) (Mas et al., 1993; Martín i Closas and Alonso Millán, 1990; Mas et al., 2002, 2003; Arribas et al., 2003) (Fig. 5.5) each one separated by unconformities and their relative conformities. These sequences are usually organized in sedimentary cycles, starting with clastic deposits at the base that change to carbonates towards the top (Mas et al., 1993; Gómez Fernández and Meléndez, 1994; Mas et al., 2002, 2003; Arribas et al., 2003). The reconstruction of the chronostratigraphy of the basin infill is not easy because there is generally a poor fossil record. Scattered data has been obtained using charophites, ostracods and palynological associations from the continental record, and dasycladacean algae and some few foraminfera from the marine incursion deposits (Brenner, 1976; Salomon, 1982b; Guiraud and Seguret, 1985; Schudack, 1987; Martín i Closas, 1989; Clemente et al., 1991; Alonso and Mas, 1993; Martín i Closas and Alonso Millán, 1998; Suaréz-González et al., 2010). Given the scarcity of fossil content, the ages of the depositional sequence boundaries refer to an approximate interval of time rather than to an exact absolute age.

5.3.3.1. Lithological and sedimentological features of the syn-extensional deposits

Here is reported a brief description of the eight depositional sequences in which the Cameros Basin syn-extensional infill has been subdivided in the study area, with references from several previous studies. The lithological Formations and Groups units herein described refer mainly to the deposits cropping out in the study area of this thesis, which correspond to the central sector of the basin (Fig. 5.4). Additional and/or different lithological units, constituting the basin infill in the eastern and western sectors of the basin, are not described in this section.

- **Depositional sequence 1 (DS1)** (EarlyTithonian): It represents the beginning of the extensional phase, when several small isolated sub-basins were formed. Its spatial distribution is very discontinuous and mainly confined along the basin borders. Thicknesses recorded are generally less than 100m, but occasionally may reach up to 400m. The SD1 basal boundary is the regional Early Tithonian unconformity. In the study area this sequence is represented by the Agreda Fm, composed of conglomerates passing upwards into coarse-medium grained sandstones, interbedded with reddish mudstones and limestone beds with reduced lateral extension (Mas et al., 1993; Gómez Fernández and Meléndez, 1994; Mas et

al., 2003; Gonzálesz-Acebrón et al., 2007). These facies were deposited in a meandering-channel and mud flat environment, in a distal alluvial fan system (Mas et al., 1993; Gómez Fernández and Meléndez, 1994; González-Acebrón et al., 2007).

- **Depositional sequence 2 (DS2)** (Tithonian – Early Berriasian): It is recorded in a more uniform area and it has a greater extension than the previous sequence, localized mainly in the western and southern basin sectors. Its thickness ranges from 200m to 1400m. It is mainly composed of the Magaña Fm, that generally passes upwards to the Matute Fm, with a lateral and vertical transition. The Magaña Fm is composed of sandy channel-fill and crevasse deposits interbedded with floodplain mudstones rich in paleosol levels (Mas et al., 1993; González-Acebrón et al., 2007). This sequence was formed by a proximal to distal meandering fluvial depositional system (Mas et al., 1993; Gómez Fernández and Meléndez, 1994; Mas et al., 2003; González-Acebrón et al., 2007). Matute Fm is composed of thick tabular carbonate beds of grey wackestone microfacies (Gómez Fernández and Meléndez, 1994; González-Acebrón et al., 2007) and represents a lacustrine-palustrine depositional system. The set of DS1 and DS2 is equivalent to the Tera lithological Group. Because the difficulties to distinguish in the study area DS1 from DS2, in this study it has been considered a unique unit, defined as DS1+2.

- **Depositional sequence 3 (DS3)** (Berriasian): It is a generally very thick sequence (that commonly reaches over 1000m but to the east even reaches a thickness of 2500m) which crops out extensively in the central-eastern sector of the basin. This sequence is composed of siliciclastic deposits, formed in a fluvio-deltaic and a palustrine depositional systems that pass gradually to laminated carbonate-marls deposits, laterally and vertically. Frequently, and mainly to the east, these laminated deposits are interbedded with gypsum levels, generated in lacustrine-sabkha and playa-lake depositional systems (Mas et al., 1993; Gómez Fernández and Meléndez, 1994; Quijada et al., 2013a, b). Siliciclastic deposits constitute the Huerteles Fm, while carbonates belong to the Valdeprado Fm Black-shales levels, with abundant organic matter content, crop-out in the central-eastern sector of the basin. Evidences of marine influence have been found in different levels of the sequence (Quijada et al., 2013b). The whole DS3 is equivalent to the Oncala lithological Group.

- **Depositional sequence 4 (DS4)** (Late Berriasian – Early Valanginian): It has a thickness that varies between 100 m and 300 m, being its areal extension limited to the north-eastern sector of the basin. The basal unconformity is an important regional unconformity (Latest Berriasian unconformity), that marks tectonic, stratigraphic and depocentral significant changes in the basin (Mas et al., 1993; Mas et al., 2003; Arribas et al., 2003 and 2007). In the study area DS4 is essentially represented by channelized sandstones with lateral accretion surfaces, sedimented by a meandering fluvial systems (Mas et al., 2003; Ochoa et al., 2007). These deposits belong to the Urbion Group and have been defined as "Urbion

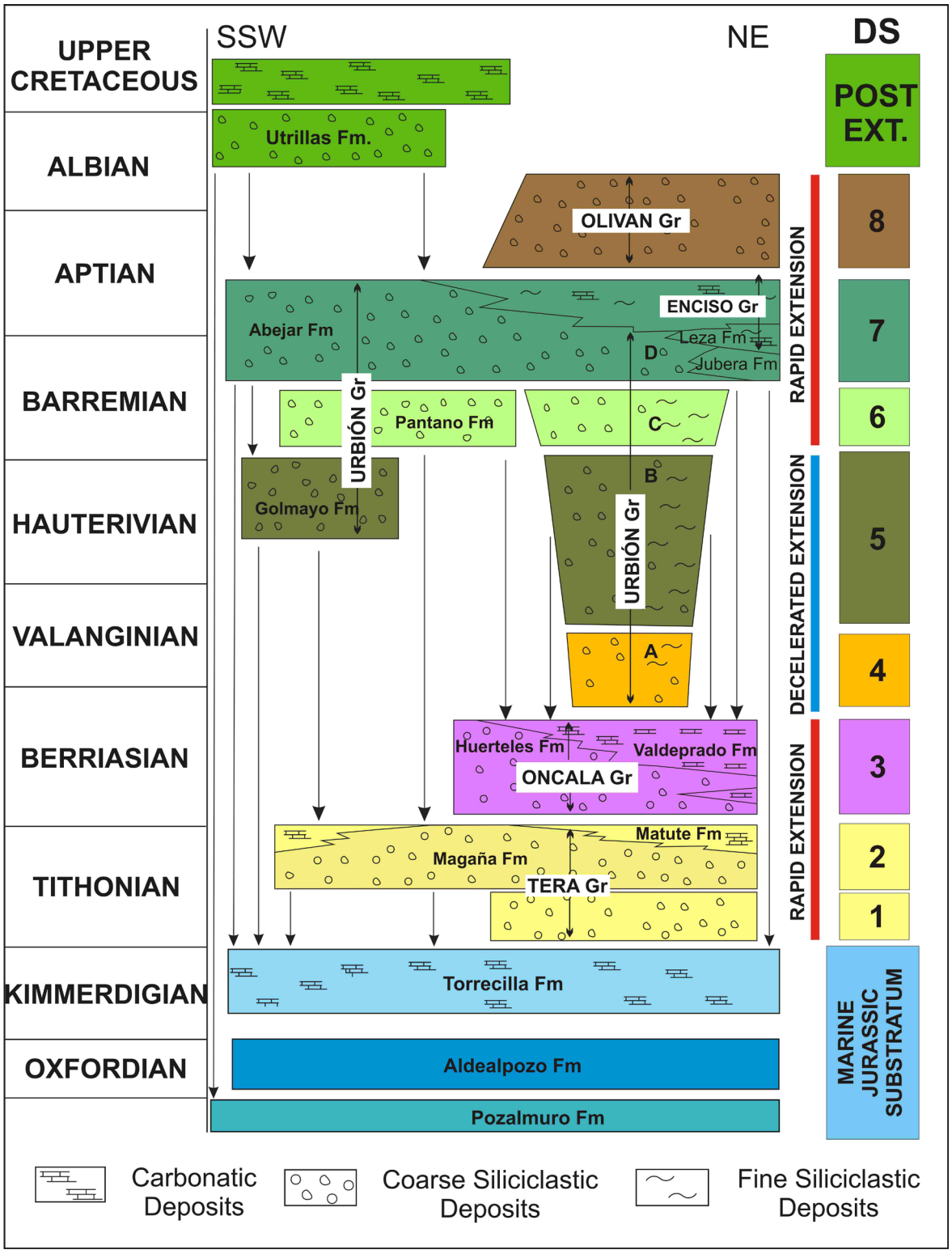

Fig. 5.5 - Chrono-stratigraphic framework of the Cameros Basin infill (modified from Mas et al., 2002, 2003 and 2011, with new data from Quijada et al., (2013). The syn-extensional deposits have been subdivided in 8 depositional sequences (DS), composed of different lithological Groups and Formations. In this framework, only the lithological units cropping out in the study area (Fig. 5.4) are indicated

Group – Unit A" by Barrenechea et al., (1995).

- **Depositional sequence 5 (DS5)** (Late Valanginian – Late Hauterivian): It reaches its maximum thickness (nearly 700m) in the southern and western areas of the basin. In the study area DS5 is represented by the Golmayo Fm in the southern sector, and by the Urbion Group – Unit B in the north-eastern sector (Mas et al., 1993; Barrenechea et al., 1995). The Golmayo Fm consists of channelized fluvial sandstone bodies, interbedded with limestone and red limestone beds (Arribas et al., 2003). Abundant remains of faunas (fish fragments, dinosaur bones fragments and ostracodes) and flora (charophytes and pollen) have been found (Clemente y Alonso, 1990a). The Golmayo Fm was formed in fluvio-lacustrine depositional system (Martín i Closas and Alonso Millán, 1998; Arribas et al., 2003). The Urbion Group – Unit B is made mainly by grey and green lutites that were sedimented in a fluvial flood plain depositional system (Mas et al., 1993; Barrenechea et al., 1995; Ochoa et al., 2004 and 2006).

- **Depositional sequence 6 (DS6)** (Early-Late Barremian): It crops out in the south-central sector of the basin, with the deposition of a succession that is more than 1500 m thick. In the north-eastern sector DS6 is confined to a reduced depositional area, with no more than 600 m of thickness. A Late Barresian or Late Tithonian unconformity represents its basal boundary, except in the north-eastern sector where it lies conformably on the previous DS5 Early Valanginian-Late Hauterivian deposits. The top of DS6 is bounded by the Late Barremian regional unconformity. Towards the south-central sector, DS6 is represented by the siliciclastic Pantano Fm (Clemente and Alonso, 1990a; Clemente and Pérez-Arlucea, 1993), constituted by channelized sandstone bodies, interbedded with conglomerates, lutites and scarce limestones beds. It has been interpreted as a basin-parallel alluvial braided system, with a complex multi-channel system migrating in a wide alluvial flood plain (Clemente and Pérez Arlucea; 1993; Martín i Closas and Alonso Millán; 1998; Arribas et al., 2003). In the north-eastern sector the DS6 depositional sequence is formed by channelized coarse-grained sandstones, with lateral accretion surface, passing upwards to grey and green lutites with isolated fine-grained sandstone beds. These deposits represent the Urbion Group-Unit C (Barrenechea et al., 1995; Mas et al., 1993; Mas et al., 2003; Ochoa et al., 2004 and Ochoa-Rodríguez, 2006) and are interpreted as deposits generated in a meandering fluvial system.

- **Depositional sequence 7 (DS7)** (Late Barremian-Early Aptian) records an important change in the basin depositional trend. In fact a generalized and important subsidence affects the entire basin with the deposition of thick sedimentary successions (Mas et al., 1993; Salas et al., 2001; Mas et al., 2003). The maximum thickness is reached in the northern sector, being up to 3000 m. The DS7 basal boundary is an important regional unconformity (Late Barremian) recorded in the whole Iberian Range. It marks a re-activation of the

tectonic activity with a generalized increment of subsidence and sedimentary accumulation rate in the sedimentary basins (Mas et al., 1993; Salas et al., 2001; Mas et al., 2003). Its time-gap could range from Early Berrasian to Early Barremian. DS7 is constituted by the Abejar Fm (Urbión Gr.) in the southern and western basin sectors, by Urbion Group-Unit D in the central sector, and by Enciso Gr., Leza Fm and Jubera Fm (Urbión Gr.) in the North-eastern sector. The lateral transition from one formation to another generally is produced by a change from proximal to middle-distal facies (Mas et al., 2003; Ochoa et al., 2004 and Ochoa-Rodríguez, 2006). The Abejar Fm consists of conglomerates and white sandstone bodies, alternated with clay intervals rich in pedogenetic levels. Pollen and flora have been found (Clemente and Alonso, 1990a, b). It has been interpreted as braided fluvial channels in a complex basin-transverse unconfined alluvial system (Clemente and Alonso, 1990a; Martín i Closas and Alonso Millán, 1998; Arribas et al., 2003; Ochoa-Rodríguez, 2006). The Urbion Group-Unit D is formed by coarse-grained sandstone bodies that correspond to a braided fluvial system in the west and a proximal meandering fluvial system in the north-east (Mas et al., 1993; Barrenechea et al., 1995; Mas et al., 2003; Ochoa-Rodríguez, 2006). This unit generally displays a basal sharp erosive contact. The Enciso Group is a mixed clastic-carbonate unit characterised by the cyclical alternation of limestone, sandstone and clay to siltstone beds. Organic matter-rich levels are also common (Alonso-Azcárate et al., 1995 and 1999). These cycles formed in a fluvio-lacustrine, palustrine depositional system. The Jubera Fm is a siliciclastic unit formed by unconfined basin-transverse alluvial-fan deposits, which consist of conglomerate bodies rich in carbonate clasts (Mas et al., 2003; Ochoa-Rodríguez, 2006; Suárez-González et al., 2010, 2013). Generally this formation passes upward to the Leza Fm, composed mainly by black limestone and dolomitic limestone beds (Mas et al., 2003; Suárez-Gonzáles et al., 2010, 2013). Stromatolites, charophites, ostracods, dasycladacean and other floral and faunal remains have been found (Alonso and Mas, 1993; Suárez-González et al., 2010, 2013). This unit was formed in a coastal lacustrine depositional system with frequent marine influence (Alonso and Mas, 1993; Mas et al., 2003; Suárez-Gonzáles et al., 2010, 2013). Small-scale normal syn-sedimentary faults strongly controlled the sedimentation of the last two Formations, limiting their extension to the northern basin border. Laterally and vertically these units pass gradually to the Enciso Group, (Mas et al, 2003; Suárez-González et al., 2013).

- **Depositional Sequence 8 (DS8)** (Late Aptian-Early Albian): It is the last syn-extensional sequence and records a new important tectonic and erosional phase, which produced a large amount of terrigeneous sediments. DS8 is only present in the north-eastern border of the basin, generally accumulating more than 2000 m of material, and up to 2800 m at its depocentre. The basal boundary is the middle Aptian unconformity while the top one is the middle Albian unconformity, that generally separates the syn-extensional deposits

from the post-extensional ones (Late Cretaceous Cycle; Alonso et al., 1993). DS8 is formed by the Olivan Group, a prevalently siliciclastic unit formed by sandstone channelized facies, lutite, crevasse splays and shallow ephemeral carbonate beds (Mas et al., 2009). These deposits were sedimented in a distal to medial-proximal meandering fluvial system, with sporadic lacustrine episodes (Mas et al., 2009).

In each defined depositional sequence, from south to north, generally a transition between proximal to distal facies can be observed (Mas et al., 2003; Mas et al., 2009). In more detail, the proximal facies appear concentrated in the southwestern margins of the basins and are represented by fluvial braided systems. These proximal facies laterally pass to deposits sedimented by meandering fluvial system, particularly developed in the central sector of the basin. In the northeastern sector, more distal deposits, such as lacustrine carbonates and shales, are dominant, representing lacustrine-palustrine environments with sporadic marine influences.

5.3.4. Post-extensional stage infill (Late Albian-Late Cretaceous)

Cretaceous Upper Megacycle (Alonso et al., 1993) represents the post-extensional phase of the Late Jurassic-Early Cretaceous extensional phase (Salas et al., 2001; Mas et al., 2003) with a stratigraphic record extending from the late Albian to the Late Cretaceous and part of the Paleocene. At that time, the whole of the Iberian Basin area became tectonically quiescent and its evolution until Maastrichtian times was controlled by thermal relaxation of the lithosphere and eustatically rising sea-levels. Large part of the Northwestern Iberia was covered by marine platform (Haq et al., 1988; Platt, 1989b; Alonso et al., 1993; Salas et al., 2001). In the Cameros Basin, the post-extensional deposits are preserved only in the southern sector of the basin, whereas in the rest of the basin they have been eroded out during the inversion stage (Fig. 5.4).

The first unit forming the stratigraphic record of the post-extensional deposits is siliciclastic Utrillas Fm, which unconformably lies on the extensional infill of the basin (Alonso et al., 1982; Platt, 1989b). Towards the top there is a transgressive sequence (Cenomanian-Coniacian) formed by limestone and marl, that were deposited in marine platforms (Alonso et al., 1993; Salas et al., 2001; García and Mas, 2004). The subsequent Santonian-Paleocene sequence has a marked shallowing upwards character with an upward gradation from open marine to fresh-water carbonates (Alonso et al., 1994, Salas et al., 2001). A maximum thickness of 650 m has been estimated to be deposited on the Cameros Basin during this phase (Alonso et al., 1993; García and Mas, 2004).

Chapter 6

6. Geological and Geographical Data-Base

6.1. INTRODUCTION

The Cameros Basin has been the object of several research studies during more than 30 years. Thus, there is an abundant and copious geological data of the basin. In order to plan a multidisciplinary basin scale study, which is the object of this thesis, it is necessary to build up a strongly articulated data base, which integrates schematically all the different disciplinary available data and to set them within a geographical context. For this reason in this work the geological data of the Cameros Basin have been implemented in ArcGIS 10.0, a Geographic Information System.

The reconstruction of the spatial data base of the Cameros Basin could be considered a great improvement of the utility of the available scientific data of the basin. The possibility to combine different data types has increased considerably. Furthermore, the integration of different levels of information (geological, geographical, stratigraphical, lithological) in a geographical representation permits a better understanding of the distribution and variation of the basin characteristics.

6.2. METHODS AND DATA

The spatial data base of the Cameros Basin was developed considering data from data from different disciplines, which were integrated in a sole spatial data base (Fig. 6.1). Firstly the geological information of the Cameros Basin was organized in an alphanumerical data base. ArchGIS software was subsequently used to implement these data into a Geographic Information System.

The first step to reconstruct the spatial data base of the Cameros Basin was to create a geo-referenced geological map of the basin. The areal distribution of the basin infill units and the position of the stratigraphic contacts and faults were taken from previous published and unpublished data (Beuther, 1966; Tischer, 1966b; Guiraud, 1983; Platt, 1989b; Clemente and Alonso, 1990; Gómez-Fernández, 1992; Casas Sainz and Simón Gómez, 1992; Mas et al., 1993; 2002, 2003, 2011; Guimerà et al., 1995; Barrenechea, 1993; Quijada et al., 2013; Suárez-González et al., 2013 and the following MAGNA geological maps (I.G.M.E.): Hoja 239 – Pradoluengo (Boquera-Fillol et al., 1978a), Hoja 240 – Ezcaray (Boquera-Fillol et al., 1978b), Hoja, 241 – Anguiano (Ramírez-Merino et al., 1990), Hoja 242 – Munilla (Hernández-Samaniego et al., 1990), Hoja 243 – Calahorra (Castiella-Muruzábal et al., 1977), Hoja 277 – Salas de Los Infantes (Gil-Serrano et al., 1978), , Hoja 278 – Canales de la Sierra (Gil-Serrano and Zubieta-Freire, 1978), Hoja 279 – Villoslada de Cameros (Cámara-Rupelo and Durántez-Romero, 1982), Hoja 280 – Enciso (Cámara-Rupelo and Durántez-Romero, 1981), Hoja 281 – Cervera Del Río Alhama (Durántez et al., 1982), Hoja 315 – Santo Domingo de Silos (Quintero-Amador and Mansilla-Izquierdo, 1982), Hoja 316 – Quintanar de la

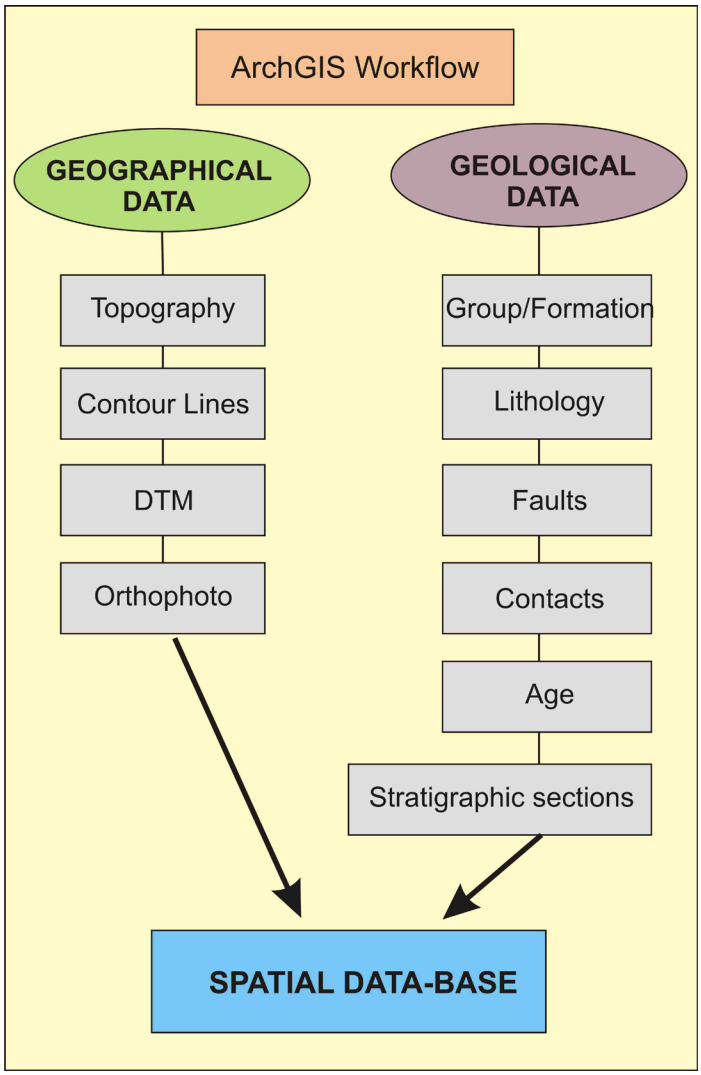

Fig. 6.1 - Workflow used to reconstruct the spatial data-base of the Cameros Basin with ArchGIS

Sierra (Quintero-Amador and Mansilla-Izquierdo, 1986), Hoja 317 – Vinuesa (Quintero-Amador and Mansilla-Izquierdo, 1988), Hoja 318 – Almarza (Rey de la Rosa and Rivera-Navarro, 1981a), Hoja 319 – Agreda (Rey de la Rosa and Rivera-Navarro, 1981b), Hoja 348 – San Leonardo de Yagüe (Quintero-Amador and Mansilla-Izquierdo, 1981), Hoja 349 – Cabrejas del Pinar (Beltrán-Cabrera et al., 1980), Hoja 350 – Soria (Navarro-Vázquez, 1991) and Hoja 351 – Olvega (Esnaola-Gómez and Martín-Fernández, 1973). Hand-drawn geological maps were digitalized and geo-referenced using ArchGIS. All data have been geo-referenced respect the U.T.M. ETRS89 reference system. Orthophotos of "Plan Nacional de Ortofotografía Aérea", and the Digital Terrain Model and National Topographic Base of "Centro Nacional de Información Geográfica" of the Spanish "Instituto Geográfico Nacional – I.G.N." were used as auxiliary spatial information.

The geological contacts digitalized were originally traced in maps at different scales, which were subsequently unified in a unique scale map. Thus, in some cases, geological maps contacts do not correspond exactly with the geological contacts observable in ortophotos. As a consequence, in these study areas of the thesis, as a high detail geological map is necessary, the exact position of stratigraphical contacts and faults were revised during field work and data obtained from MAGNA geological maps (I.G.M.E.) and ortophotos.

In order to enforce the comprehension of the geological data, stratigraphic sections information (i.e. spatial localization, stratigraphic unit's names and thickness, top and bottom contacts of stratigraphic units, author, etc.) have been incorporated to the spatial data base in a schematic way. Stratigraphic sections information was taken from previous published and unpublished studies (Gómez-Fernández, 1992; Barrenechea, 1993; Mas et al., 1993, 2002, 2003; Alonso-Azcárate, 1997; Arribas et al., 2003; Ochoa-Rodríguez, 2006 and González-Acebrón, 2009), which were performed before year 2010. Stratigraphic sections measured in the next years were not introduced in the data-base.

6.3. RESULTS

The reconstruction of a spatial referenced geological map of the Cameros Basin is one of the most relevant results performed in this thesis (Fig. 6.2). Different levels of information were implemented in the maps: stratigraphic contacts of the basin infill units, position of the main faults, topography, contour lines and DTM. A map of the 1.50000 and 1.25000 sheets of the I.G.N. that were used to make the reconstruction of the geographical data base of the basin is shown in Fig. 6.2.

Another relevant result of this thesis is the incorporation, in the geological map, of the information compiled from the stratigraphic sections measured by previous authors. Only were considered the stratigraphic sections characterising the syn-extensional deposits of

the basin were considered, whereas stratigraphic sections of the pre-extensional and post-extensional deposits were not implemented. For each stratigraphic section the following data were collected: 1) author that measured and/or published the data; 2) geographical location (latitude, longitude); 3) total measured thickness; 4) stratigraphic units composing the measured stratigraphic succession; 5) thickness of each stratigraphic unit and 6) location of the base and top contacts of the stratigraphic section. A synthesis of all these data is reported in Table 6.1. The thickness of the stratigraphic unit that composed each stratigraphic section measured is reported in **Appendix 1**.

The compiled data was integrated in a geographic information system (ArchGis) as complementary data of the geological map (Fig. 6.3). Each stratigraphic section was represented as a point in the map (geographical coordinates indicating the location of the section base and top). Associated with the geographical point a vertical bar-diagram was built up for each section, indicating the stratigraphic units forming the section, and their related thickness (Fig. 6.3).

The resultant maps are very useful synthesis of the geological and stratigraphic available information of the basin. It allows to determine very easily in which parts of the basin it is available detailed stratigraphic information of the syn-extensional units, units cropping out in a particular area, their stratigraphic thickness and finally the source (thesis, publication, etc.) from where more detailed data of the stratigraphic sections (i.e., lithology, facies, sedimentary structures, etc.,) can be obtained.

6.4. CONCLUSIONS

In this first part of the thesis geological and geographical information were combined to reconstruct a spatial data base by the use of the ArchGis Software. The reconstruction of a geographical-spatial data base of the geological information of the Cameros Basin represents a fundamental solid base that allowed to reconstruct, with high precision and reliability the geometry, and structure of the basin. Thus, the geographical data base reconstructed herein was used in every section of this work for several purposes, among them: to determine the spatial distribution of the basin deposits, to locate the collected samples, to reconstruct the areal distribution of geochemical properties, etc.

Fig. 6.2 (on the right) - Geological map of the Cameros Basin build using ArcGis software

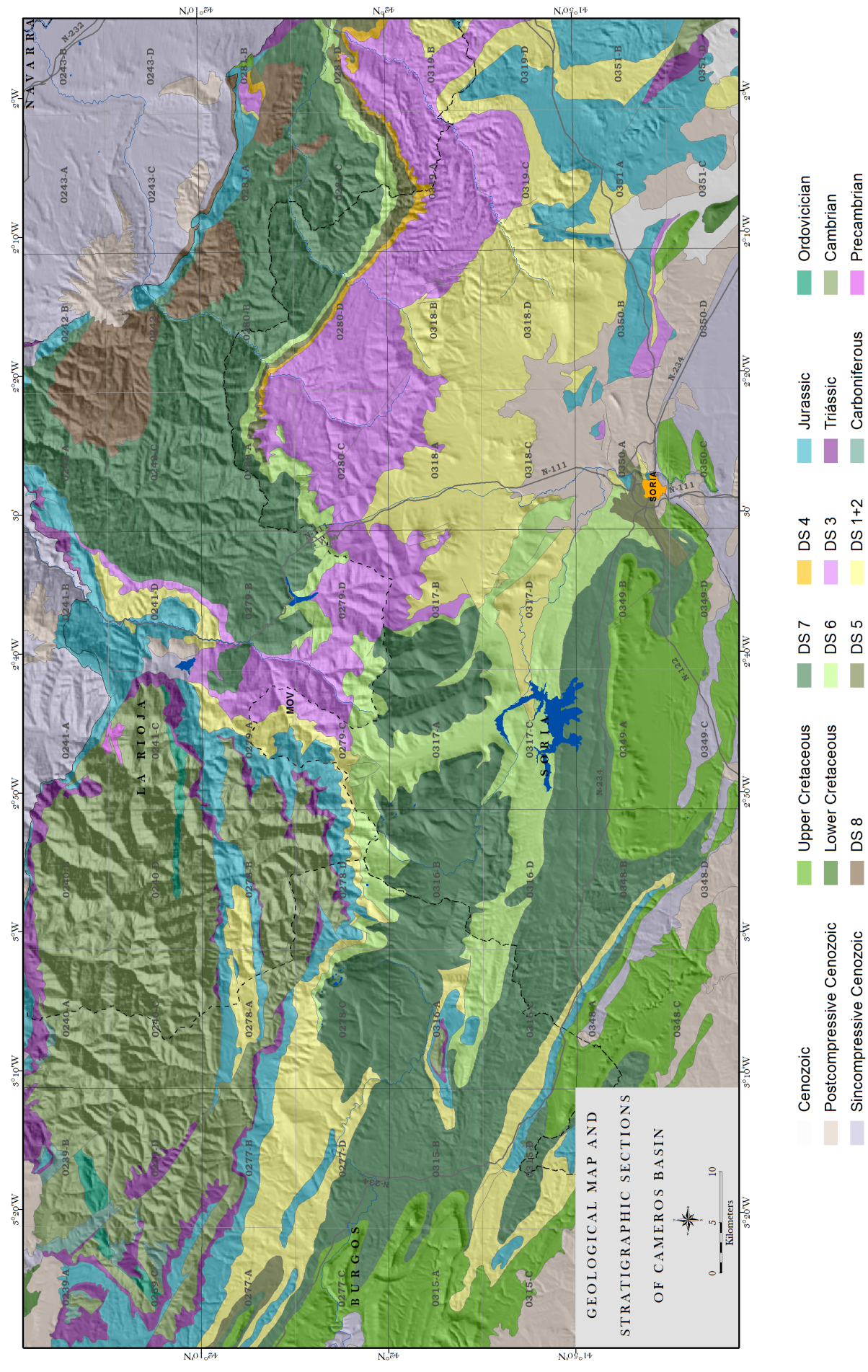
GEOLOGICAL MAP AND
STRATIGRAPHIC SECTIONS
OF CAMEROS BASIN
Kilometers
0
5
10
Cenozoic
Postcompressive Cenozoic
Sincompressive Cenozoic
Upper Cretaceous
Lower Cretaceous
DS 8
DS 7
DS 6
DS 5
DS 4
DS 3
DS 1+2
Jurassic
Triássic
Carboniferous
Ordovicician
Cambrian
Precambrian
NAVARRA
LA RIOJA
BURGOS
SORIA
MOV
N-232
N-111
N-234
N-122

ID Section	Section Name	Basal contact	Top contact	Font
RUP	Rupelo	Callovian	Covered	
CML	Campolara	Dogger-Callovian	Covered (Castrillo Fm?)	
TRR	Terrazas1	Callovian	Uncertain	
TRZ	Terrazas2	Callovian	Uncertain	
CTV	Castrovido	Jaramillo Fm	Covered (Abejar Fm?)	
CON	Contreras	Covered	Utrillas Fm	
MON2	Moncalvillo	Dogger-Callovian	Covered	
GAN	La Gallega Norte	Covered	Covered (Castrillo Fm?)	
GAS1	La Gallega Sur	Kimmiridigian (Talveila Fm)	Abejar Fm-Castrillo Fm	Arribas et al. 2003
PEÐ3	Peñacoba	Peñacoba Fm	Abejar Fm	
HIN	Hinojosa	Peñacoba Fm	Abejar Fm	
TAL	Talveila	Torrecilla Fm	Abejar Fm	
CID	Cidones	Pantano Fm (Fault)	Abejar Fm	
ABJ	Abejar Fm	Uncertain	Covered	
HYM	Hoya del Moro	Abejar Fm Fm (Fault)	Abejar Fm	
MUR	Muriel	Pinilla de Los Moros	Utrillas Fm	
CUB	Cubillejas	Uncertain	Abejar Fm	
ALMA_ARZA	Almarza de Cameros	Torrecilla Fm	Huerteles Fm	
PRA	Pradillo-Villanuova de Cameros	Torrecilla Fm	Covered	
MOV	Montenegro-Villoslada de Cameros	Torrecilla Fm	Huerteles Fm	
POV	Póveda	Covered	Covered	
POR	Portelrubio	Torrecilla Fm	Covered	
CAS	Castelfrío de la Sierra	Torrecilla Fm	Huerteles Fm	
ALM	Almajano	Torrecilla Fm	Covered	
ESP	El Espino	Torrecilla Fm	Covered	
MAG	Magaña Fm	Covered	Huerteles Fm	González-Acebrón, 2009
CSP	Collado de San Pedro	Covered	Huerteles Fm	
AGE	Ágreda Est	Torrecilla Fm	Covered (Agreda Fm - West)	
AGO	Ágreda Oeste	Covered (Agreda Fm - Est)	Cenozoic	
BLA	San Blas	Torrecilla Fm	Covered	
1SAN	San Felices 1	Covered	Uncertain	
2SAN	San Felices 2	Uncertain	Uncertain	
3SAN	San Felices 3	Uncertain	Oncala Gr	
VUR	Valdegutur	Torrecilla Fm	Covered	
EN	Enciso	Urbión Gr	Oliván Gr	
MU	Munilla	Urbión Gr	Oliván Gr	
AM	Ambasaguas	Urbión Gr	Oliván Gr	
GR	Gravalos	Urbión Gr	Oliván Gr	Alonso-Azcarate, 1997
AR	Arnedillo	Jubera Fm	Oliván Gr	
PR	Préjano	Jubera Fm	Oliván Gr	
LE	Leza	Jubera Fm	Enciso Gr	
SA	San Andres	Oncala Gr	Covered	
YA	Yanguas	Oncala Gr	Covered	Barrenechea, 1993
SP	San Pedro Manrique	Oncala Gr	Covered	
VM	Valdemadera	Valdeprado Fm	Covered	
1	Torrecilla en Cameros	Torrecilla Fm	Covered	
2	Almarza de Cameros	Torrecilla Fm	Covered	
3	Ortigosa	Torrecilla Fm	Covered	
4	Montenegro-Villoslada	Torrecilla Fm	Covered (conglomerate)	
5	Peña Negra	Torrecilla Fm	Covered (conglomerate)	
6	Emb. De Cuerda del Pozo	Conglomerate (?)	Covered (conglomerate)	
7	Rollamienta	Covered	Covered (conglomerate)	
8	Puerto de Piqueras	Covered	Covered (conglomerate)	
9	Sta. Cruz de yanguas	Covered	Covered (conglomerate)	
10	Espejo de Tera	Magaña Fm	Covered (conglomerate)	Gómez-Fernandéz, 1992
11	ValdehuÚrteles	Huerteles Fm Fm	Covered (conglomerate)	
12	Yanguas	Uncertain	Covered (conglomerate)	
13	Portelrubio	Torrecilla Fm	Magaña Fm	
14	Cerro de San Juan	Magaña Fm	Eroded	
15	Las Casas	Torrecilla Fm	Covered (sandstone)	
16	Almajano	Torrecilla Fm	Quaternary	
17	Serie Castelfrío de la Sierra	Torrecilla Fm	Covered	
18	Valtarejos	Magaña Fm	Eroded	
19	Matasejun	Magaña Fm	Covered	

Table 6.1 (Part 1) - Synthesis of the information compiled of the stratigraphic section of the syn-extensional infill of the basin (DS1-DS8), measured by previous authors

ID Section	Section Name	Basal contact	Top contact	Font
20	Aldealpozo	Torrecilla Fm	Covered	
21	Valdege±a	Torrecilla Fm	Magaña Fm	
22	El Espino	Torrecilla Fm	Covered	
23	Suellacabras	Covered	Covered (sandstone)	
24	Magaña Fm	Covered	Covered	
25	Corral de la Severa	Covered	Valdeprado Fm	
26	Aguilar del Río Alhama	Uncertain (limestone?)	Valdeprado Fm	
27	Navaj·n	Huerteles Fm	Covered (limestone?)	
28	Cervera del Río Alhama	Uncertain (limestone?)	Covered (limestone?)	
29	Fitero	Torrecilla Fm	Covered	
30	Puerto del Madero	Marine Jurassic	Magaña Fm	
31	Corrales de TrÚvego	Torrecilla Fm	Magaña Fm	Gómez-Fernandéz, 1992
32	Débanos	Torrecilla Fm	Covered	
33	Valdegutur	Torrecilla Fm	Covered	
34	Cerro de San Blas	Torrecilla Fm	Magaña Fm	
35	Agreda Fm Est	Torrecilla Fm	Matute Fm	
36	Agreda Fm Oeste	Covered	Eroded	
37	Litago	Uncertain (shales?)	Eroded	
TRE	Trevijano	Torrecilla Fm	Leza Fm	
JUR	Jubera-Robres	Torrecilla Fm	Leza Fm	
ARN	Arnedillo	Torrecilla Fm	Leza Fm	
PRE	Préjano	Turmiel Fm (Jurassic)	Leza Fm	
SAN	San Andrés	Oncala Gr	Eroded	Ochoa, 2006
YNG	Yanguas-Las Ruedas	Oncala Gr	Enciso Gr	
SPM	San Pedro Manrique	Oncala Gr	Covered	
VLM	Valdemadera	Oncala Gr	Covered	
TFC	Trinchera del Ferrocarril	Golmayo Fm	Utrillas Fm	

Table 6.1 (Part 2) - Synthesis of the information compiled of the stratigraphic section of the syn-extensional infill of the basin (DS1-DS8), measured by previous authors

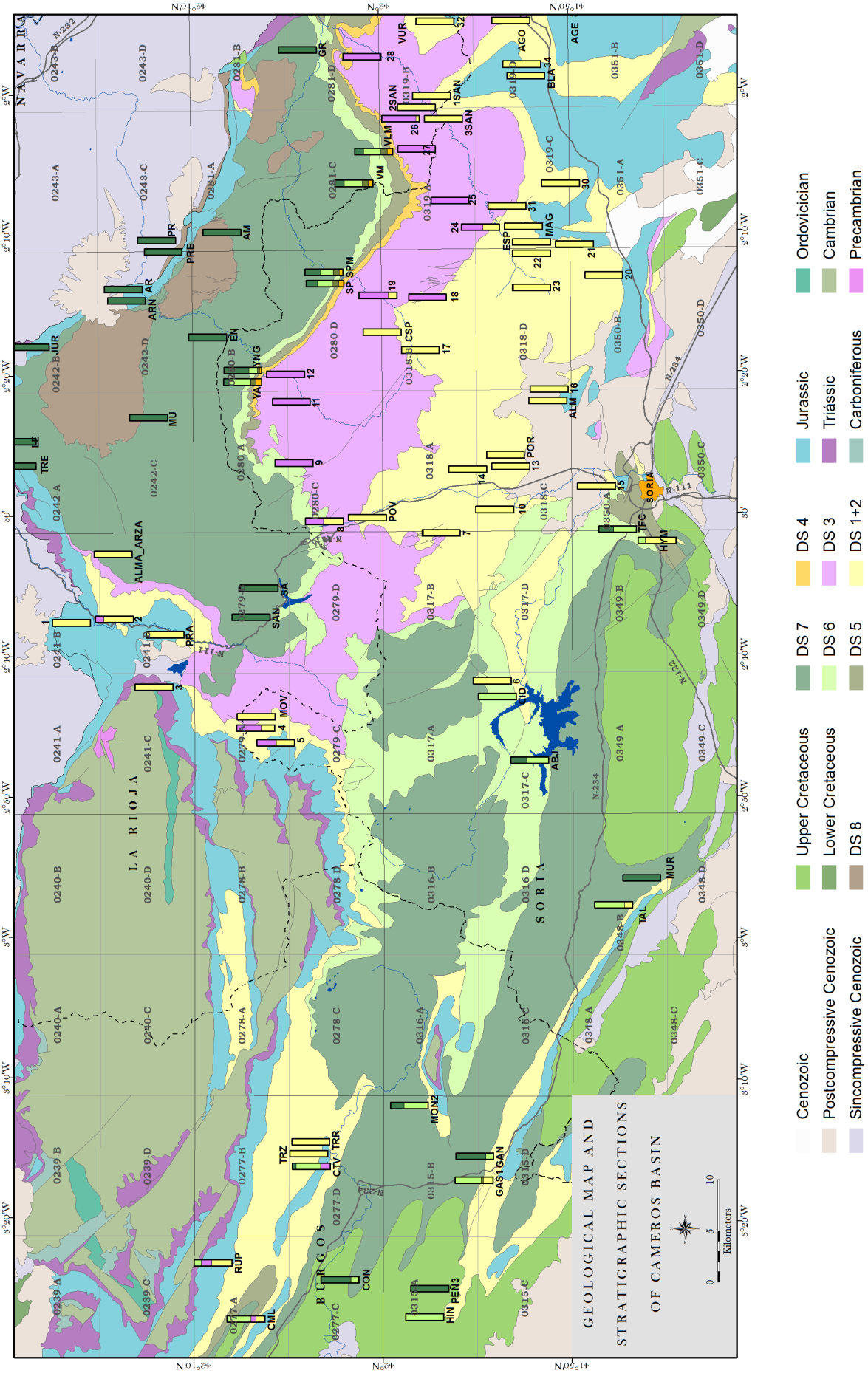
GEOLOGICAL MAP AND
STRATIGRAPHIC SECTIONS
OF CAMEROS BASIN
N A V A R R A
L A R I O J A
S O R I A
B U R G O S
Kilometers
Cenozoic
Upper Cretaceous
Lower Cretaceous
Postcompressive Cenozoic
Sincompressive Cenozoic
DS 7
DS 6
DS 5
DS 4
DS 3
DS 1+2
DS 8
Jurassic
Triássic
Carboniferous
Ordovicician
Cambrian
Precambrian

Fig. 6.3 - Geological map of the Cameros Basin where information of the stratigraphic sections of the syn-extensional deposits of the basin (DS1-DS8), measured by previous authors, are indicated

Chapter 7

7. Geometry and Structure of the Basin

7.1. INTRODUCTION

Extensional basins are generally characterised by high to medium subsidence rates, which allow constant formation of accommodation space and the accumulation of thick sedimentary successions (i.e., Busby and Ingersoll, 1995). Extensional basins provide the most important record of the history of the stretching of the crust, for they contain structure that were active during sedimentation and strata that provide the necessary chronologic constraints for dating the structures" (Schlische, 1991). Thus, by studying extensional basin successions, an understanding of the mechanisms that govern the extensional tectonic processes and their relationship with sedimentation trends can be gained (Gawthorpe et al., 2000). Unfortunately, in the case of extensional basins that have experienced a high degree of inversion, the original structures and geometry can be modified and/or eroded (Schlische, 1991), and consequently, the evolution of the basin can barely be interpreted. Thus, in these cases, a reliable reconstruction of the geometry of the basin before the inversion is fundamental in determining its tectono-stratigraphic evolution.

The reconstruction of the original structure and geometry of the basin represents an essential base for basin-scale studies, e.g., subsidence analysis, thermal modelling and petroleum system play reconstruction (Allen and Allen, 2009). The amount of erosion must be determined to calculate the

maximum burial of the basin as consequence of the sediment load, which is a fundamental key for determining the thermal maturity of the source rocks. Furthermore, the reconstruction for the different steps of the basin evolution (from the beginning of the infill process to the inversion and erosion processes) of the geometry of the basin infill can be useful for determining the main migration paths of the hydrocarbons and their possible accumulations (Allen and Allen, 2009).

7.2. GEOMETRY AND STRUCTURE OF THE CAMEROS BASIN

The geometry of the Cameros Basin infill, as well as the extensional mechanisms that formed the basin, have been the subject of debates over the last few decades (Mas et al., 1993; Casas-Sainz and Gil-Imaz, 1994; Guimerà et al., 1995; Mata et al., 2001; Casas et al., 2012; González-Acebrón et al., 2012). The most controversial issues concern the estimation of the maximum burial depth, the geometry of the syn-extensional units and the nature of the normal fault that formed the accommodation space during the extensional phase. In fact, the peculiar geometry and structures of the Cameros Basin clearly suggest a different extensional model than a typical half-graben rift model (Gibbs, 1987; McClay, 1990; Schlische, 1991; Gawthorpe and Leeder, 2000), where accommodation space is formed by a basin border-bounding normal fault transecting the sedimentary cover that is simply reactivated during the compressive phase.

The main aim of this work is to provide an accurate reconstruction of the geometry and architecture of the basin infill. Secondarily, a model that could better explain the structure and geometry of the basin is proposed. To determine the geometry and structure of the Cameros Basin, a basin-wide balanced cross-section and its partial restorations were reconstructed, based mainly on field data, geophysical and subsurface data, such as seismic lines and well-logs.

The results performed in this part of the thesis represent the fundamental geological base necessary to develop the next sections of the thesis. Areal distribution, geometries and thicknesses of the basin infill herein reconstructed represented in fact the fundamental input data in the subsidence and heat flow analyses calculation. Additionally these data allow determining with precision the depth and location of the analyzed organic matters samples. Finally they were used to define the geological conceptual model of the thermal and petroleum system models of the basin.

To help the comprehension of methods, results and discussion presented herein to reconstruct the geometry and the architecture of the basin infill, as well as to determine the most reliable extensional model of the basin, in this chapter a brief synthesis of the main relevant aspects of the geological setting of the basin is presented. Data refer to the numerous previous studies carried out on the geologic evolution of the Cameros Basin.

7.3. GEOLOGICAL FRAMEWORK

The Cameros Basin is the westernmost Iberian Rift System basin and it was formed under a regional N-S to NNE-SSW extension direction. The basin records the greatest subsidence of the Mesozoic Iberian System, with a vertical thickness in the depocentral area of more than 6500 m (Mas et al., 2011). The basin infill was deposited in approximately 46 Ma, from the late Jurassic (Tithonian) to the early Cretaceous (early Albian) (Mas et al., 1993; Salas et al., 2001). During the Eocene to early Miocene, the whole Mesozoic Iberian Rift System was inverted under a regional NNE-SSW contraction, building the Iberian Ranges and Catalan Coastal Chains (Guimerà and Alvaro, 1990; Casas and Salas 1992; Salas and Casas 1993; Salas et al., 2001) (Fig. 7.1a).

7.3.1. Basin structure

The Cameros Basin is contained in the Cameros thrust-sheet (Guimerà et al., 1995), which includes the extensional and post-extensional sedimentary infill of the Cameros Basin and also its Jurassic and Triassic substratum and the Hercynian Basement (cropping out mainly in the Sierra de la Demanda, in the Northwest sector of the basin) (Fig. 7.1).

The Cameros thrust sheet thrusts northward onto the Ebro Basin foreland, with nearly 28 km of horizontal displacement, and southwards, with a back-thrust system, onto the local Almazán Basin with a smaller displacement of nearly 5 km (Guimerà et al., 1995). These features define the Cameros tectonic unit as a pop-up structure (Guimerà et al., 1995) (Fig. 7.1).

The northern main thrust (the Cameros Thrust) is oriented E-W along the Sierra de la Demanda and the central part of the basin, where it is almost continuously exposed for 120 km (Fig. 1a). To the SE, it continues for more than 150 km under a cover of post-tectonic Tertiary rocks (as observed in several oil wells), forming the boundary between the Iberan Chain and the Ebro Basin (Guimerà et al., 2004). The southern border of the basin is defined by a nearly 150 km-long conjugate south-verging thrust-system with imbricate thrusts and thrust propagation folds (Platt, 1990; Casas-Sainz,1992; Miegebielle et al., 1993; Guimerà et al., 1995) (Fig. 7.1a and Fig. 7.1b).

In the Northern Cameros area, the main thrust is located within the evaporitic Upper Triassic beds (Keuper facies), whereas, in the southern area, and to the west, north of the Sierra de la Demanda, it is located deeper in the Hercynian basement (Guimerà et al., 1995). These two detachment levels are joined by means of an oblique to frontal ramp (Fig. 7.1b). The shortening direction during the basin inversion has been estimated to be between N-S and NNE-SSW (Guimerà et al., 1995). At the regional scale, the Cameros Basin has a gently folded synclinal geometry (Fig. 7.1b).

7.3.2. Basin infill and stratigraphy

The Cameros Basin infill is related to the second extensional phase of the Mesozoic Rift System (Salas et al., 2001). The stratigraphic record of the basin spans from the Tithonian to the early

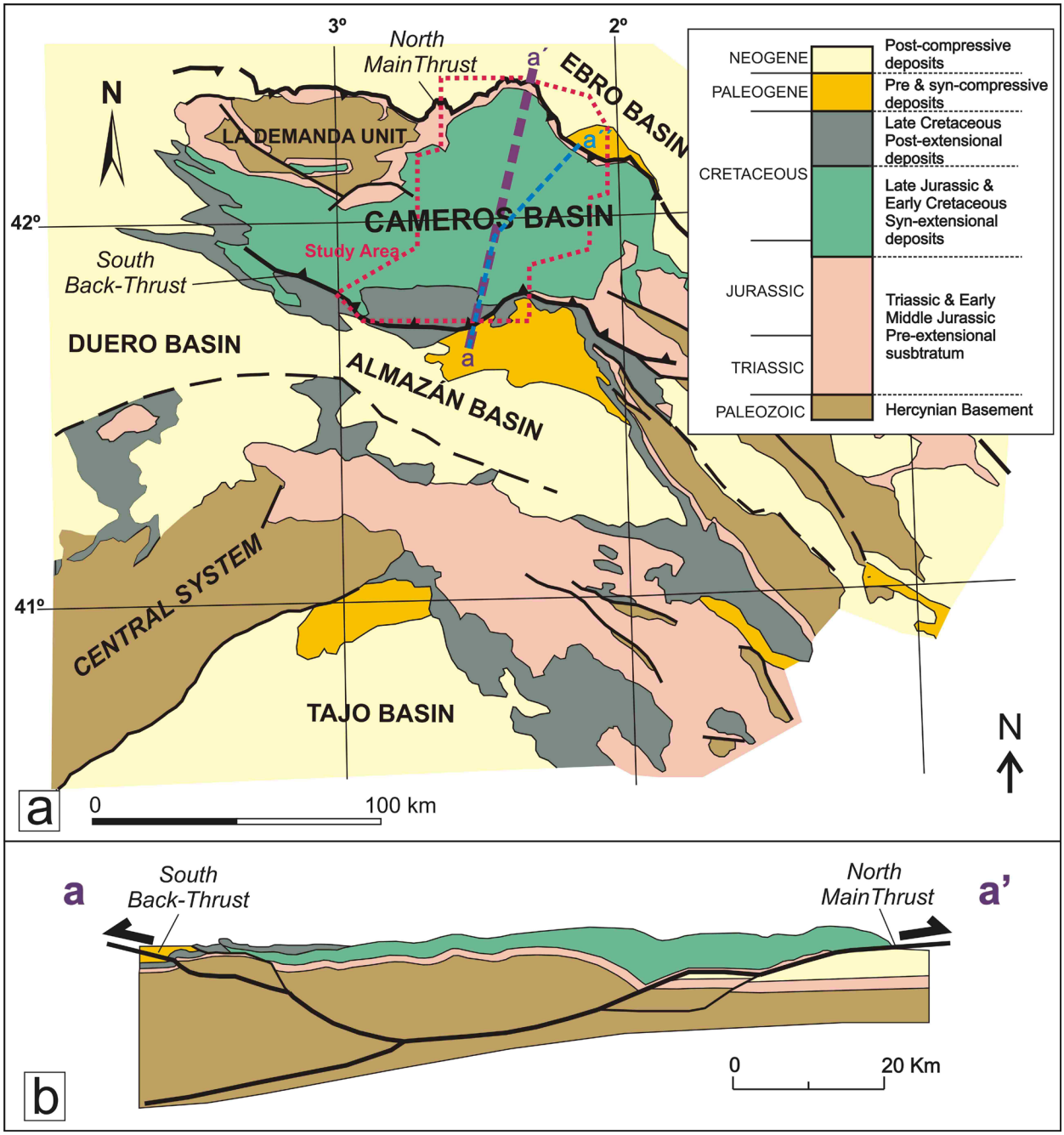

Fig. 7.1 - (a) Geological setting of the Cameros Basin (after Guimerá et al., 2004). (a-a') indicates the trace of the section shown in Fig. 7.2b, whereas (a-a'') indicates the trace of the balanced geological cross-section reconstructed in this work (Fig. 7.13); (b) The Cameros tectonic unit shows a "pop-up" structure, characterised by a main thrust in the northern basin border and a secondary back-thrust in the southern one (after Guimerà et al., 1995).

Albian. The syn-extensional deposits have been subdivided in the Tera, Oncala, Urbión, Enciso and Oliván lithostratigraphic Groups (Beuther, 1966; Tischer, 1966a, b) and in eight depositional sequences (Mas et al., 1993; Arribas et al., 2003; Mas et al., 2003). The syn-extensional deposits are dominated by fluvial and lacustrine continental deposits, with episodic marine incursions (Mas et al., 1993, 2003, 2011). Due to the scarce paleontologic dating the age limits assigned to each depositional sequence refer more to an interval of time than to an exact boundary dating.

In this chapter the syn-extensional deposits were analyzed considering the eight depositional sequence defined by Mas et al., (2003), as well as the lithological Group and Formation units in which they are subdiveded. The stratigraphic framework of the basin infill analysed in the study area of this work is shown in Fig. 7.2.

A brief description of the sedimentological characteristics of the syn-extensional deposits outcropping in the study area is given in Table 7.1, based mainly on Meléndez and Vilas (1980); Clemente and Alonso (1990); Mas et al. (1993, 2003 and 2009); Gómez Fernández and Meléndez (1994); Barrenechea, (1993); Martín i Closas and Alonso Millán (1998); Arribas et al. (2003 and 2007); Ochoa-Rodríguez, (2006); González-Acebrón et al. (2007); Mas et al. (2009); Quijada et al. (2010 and 2013) and Suárez-González et al. (2010 and 2013).

7.4. PROPOSED GENETIC MODELS

Although the geometry and structure of the Cameros Basin have been debated, no agreement has been reached yet. Three main genetic models have been proposed:

1) Guiraud and Séguret (1985) (Fig. 7.3i) interpreted the Cameros Basin as a releasing solitary overstep of two NE-SW strike-slip faults. In this context, NW-SE extensional faults would develop inside the step area, allowing the formation of the basin, whereas NW-SE compressional structures formed outside it, producing uplifted areas. Associated with the forward migration of each tip of the major strike-slip faults, the normal faults would be successively initiated SW and NE of the overstep. Consequently, the basin lengthened, and the depocentres migrated to the NE. Moreover, these authors assume that the extensional faults involve only the Variscan basement, with the Mesozoic cover detached at the Keuper (Upper Triassic) level and stretched only by smaller-scale faults (see Guiraud and Séguret, 1985, figs 8 and 9). According to these authors, the main normal fault in the north was slightly inverted during the Tertiary contraction, creating the present-day Cameros Basin structure.

2) Casas-Sainz and Simón-Gómez (1992), Casas-Sainz (1993), Casas-Sainz and Gil-Imaz (1998), Casas-Sainz et al. (2000), Mata et al. (2001) and Casas et al. (2009) (Fig. 7.3ii) explain the Cameros basin as formed by the action of a listric south-dipping normal fault located in the

evaporitic Triassic beds and limiting the basin northwards. The gradual motion along the listric normal fault causes the sedimentary infill to be passively folded by bending (Mata et al., 2001), creating a basin scale syncline geometry. Increasing accumulation space is generated in the core of the syncline, allowing the vertical superimposition of the syn-extensional depocentres (Mata et al., 2001). The fault movement stretched the pre-extensional Jurassic substratum but without loss of its longitudinal continuity (Casas et al., 2009). The complete inversion of the Mesozoic

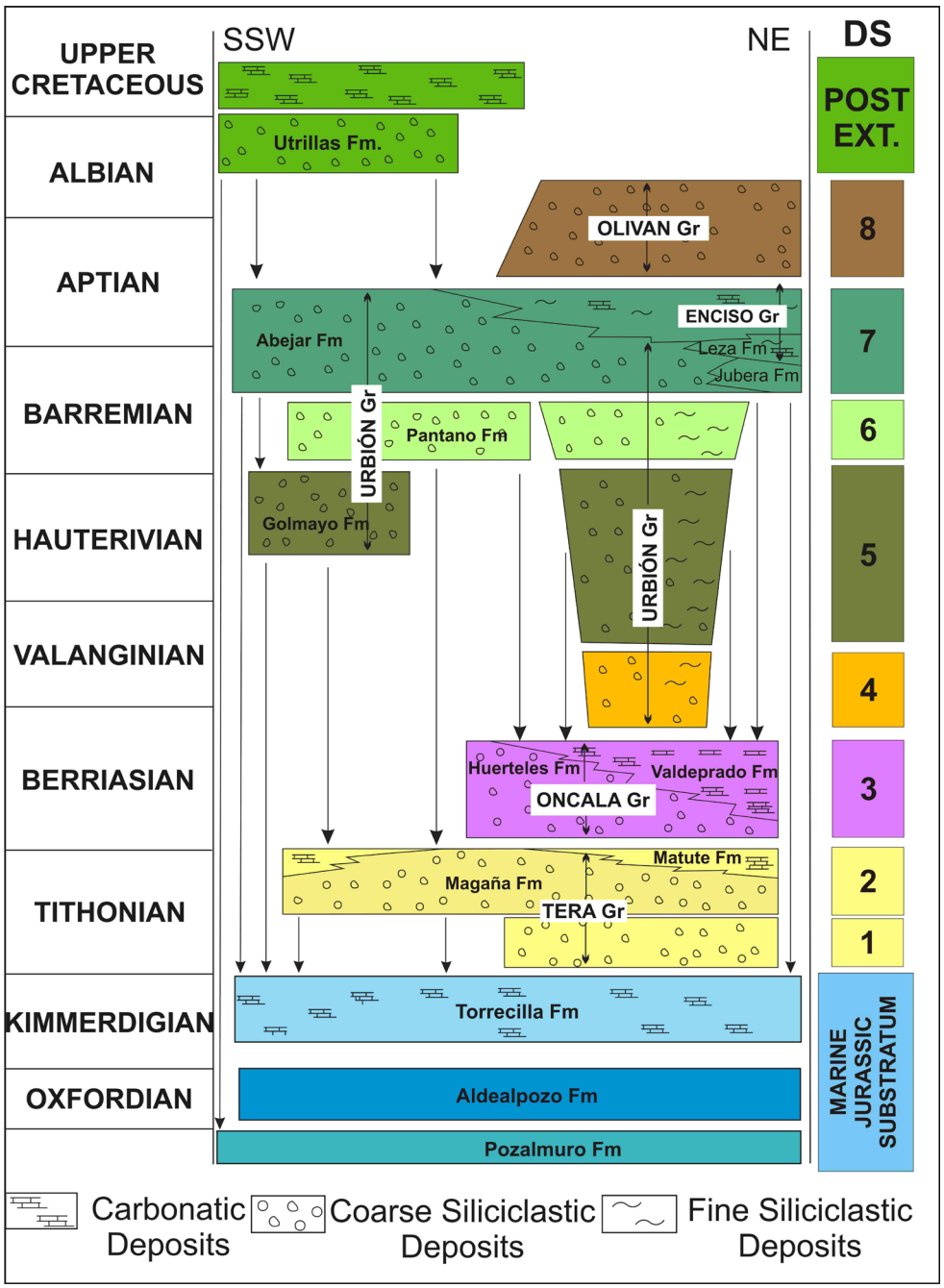

Fig. 7.2 - Chrono-stratigraphic framework of the Cameros Basin infill (modified from Mas et al., 2003). The syn-extensional deposits have been subdivided in 8 depositional sequences (DS), composed by different lithological Groups, which distribution in the study-area varies from SSW to NE (see Fig. 7.4)

Age (My)		Unit	Group/Formation	Lythology	Depositional System
From	To				
121	108.7	DS8	Olivan Gr	Channelized sandstone bodies, interbedded by shales and carbonate beds	Medial-proximal meandering fluvial system, sporadically passing to lacustrine systems
127	121	DS7	Enciso Gr	Mixed clastic-carbonate unit characterized by the cyclical alternation of limestone, sandstone and clay to siltstone beds	Fluvio lacustrine-palustrine system to coastal-lagoons and tidal flat
			Urbión Gr	Coarse-medium grained channelized sandstone bodies grading to shales	Meandering fluvial system
			Abejar Fm	Conglomerates and white sandstone bodies, alternated with clay intervals rich in pedogenetic levels	Braided fluvial channels in a unconfined alluvial palustrine-lacustrine system
129	127	DS6	Urbión Gr	Channelized coarse-grained sandstone, grading upward to grey and green shales	Meandering fluvial system
			Pantano Fm	Lenticular sandstone bodies, interbedded with conglomerates and shales	Alluvial braided system migrating in wide alluvial flood plains
136.7	129	DS5	Urbión Gr	Coarse-medium grained channelized sandstone bodies grading to shales	Meandering fluvial system
			Golmayo Fm	Channelized fluvial sandstone bodies, interbedded with limestone and red limestone beds	Fluvial-lacustrine system
142.3	136.7	DS4	Urbión Gr	Coarse-medium grained channalized sandstone	Meandering fluvial system
145.5	142.3	DS3	Valdeprado Fm	Laminate carbonate-marls interbedded with gypsum levels	Lacustrine-sabkha and playa-lake system
			Huerteles Fm	Thin beds of fine-grained sandstone interbedded with shale and marls	Fluvial-palustrine to deltaic system
150.8	145.5	DS1+2	Matute Fm	Tabular carbonate beds of grey wackestone	Lacustrine-palustrine system
			Magaña Fm	Conglomerates grading into coarse-medium grained sandstones, interbedded with reddish mudstones beds.	Alluvial fan system and Proximal to distal meandering fluvial system

Table 7.1 - Synthesis of the lithological and sedimentological characteristics of the eight depositional sequences, into which the syn-extensional infill of the basin has been subdivided

extensional fault movement took place during the Alpine contractional phase, with a maximum displacement of 30 km (Casas-Sainz and Simón-Gómez, 1992).

3) Mas et al. (1993), Guimerà et al. (1995), Mas et al. (2002), Mas et al. (2003) and Mas et al. (2011) (Fig. 7.3iii) interpreted the Cameros Basin as an extensional-ramp basin produced over an S-dipping ramp of an extensional fault, located deep in the basement. The extensional

displacement on the fault produced a synclinal basin that progressively widened with time. The depocentres of the successive depositional sequences were always located above the ramp and migrated to the north, inside the basin, as a result of the hangingwall displacement to the south. Therefore, the Cameros Basin is a synclinal basin, and no major faults bounded it during its development (Mas et al. 2011). The extension localised in the basement allows the marine Jurassic substratum to experience a mild deformation during the entire extensional stage (Guimerà et al., 1995). During the Alpine compression, a thrust formed in the north basin margin at the weakness zone of the Upper Triassic (Keuper) beds. The thrust gradually expanded to the north and to the south during the deformation, until linking at depth with the Mesozoic extensional fault flat.

7.5. METHODOLOGY AND DATA ACQUISITION

This work focuses on the basin infill located in the central-eastern sector of the Cameros Basin (Fig. 7.1). In this area crops out the entire stratigraphic record of the basin (Fig. 7.4): the pre-extensional deposits (the substratum of the basin), all the syn-extensional depositional sequences and the post-extensional deposits. Furthermore, in this area the syn-extensional units reach their maximum stratigraphic thickness, allowing a reliable reconstruction of the depocentral areas in the basin.

To characterise the geometry, the structure and the real thickness of the syn-extensional deposits, a balanced geological cross-section was constructed and restored to various stages within the evolution of the basin. The proposed section traverses the basin from the northern main thrust to the southern back-thrust, intersecting the whole extensional succession (Fig. 7.4). To maintain the section perpendicular to the main contractional structures, the cross-section was divided into two segments: a northern one, NE-SW-oriented, and a southern one, NNE-SSW-oriented. The total length of the section is nearly 70 km. To develop the balanced geological cross-section, we have integrated both new and revised field, geophysical and subsurface data.

Restoration of the obtained balanced cross-section was performed using constant bed-length and area balancing methods (Suppe 1983, Mitra et al., 1989, Rouby et al., 1996) via a CAD program (Microstation). The first step was to restore the section to its undeformed state previous to Alpine contraction. To that end, the base of the post-extensional unit (Upper Cretaceous) was flattened

Fig. 7.3 - Sketch of the three most widely accepted hypotheses of the genetic model of the basin, which explain the structure and geometry of the basin (modified from Mas et al., 1993 and Mata et al., 2001). For each model (a) illustrate the proposed position, depth and detachment level of the main normal fault, relative to the extensional phase, whereas (b) represents the position and detachment level of the thrust forming during the inversion of the basin

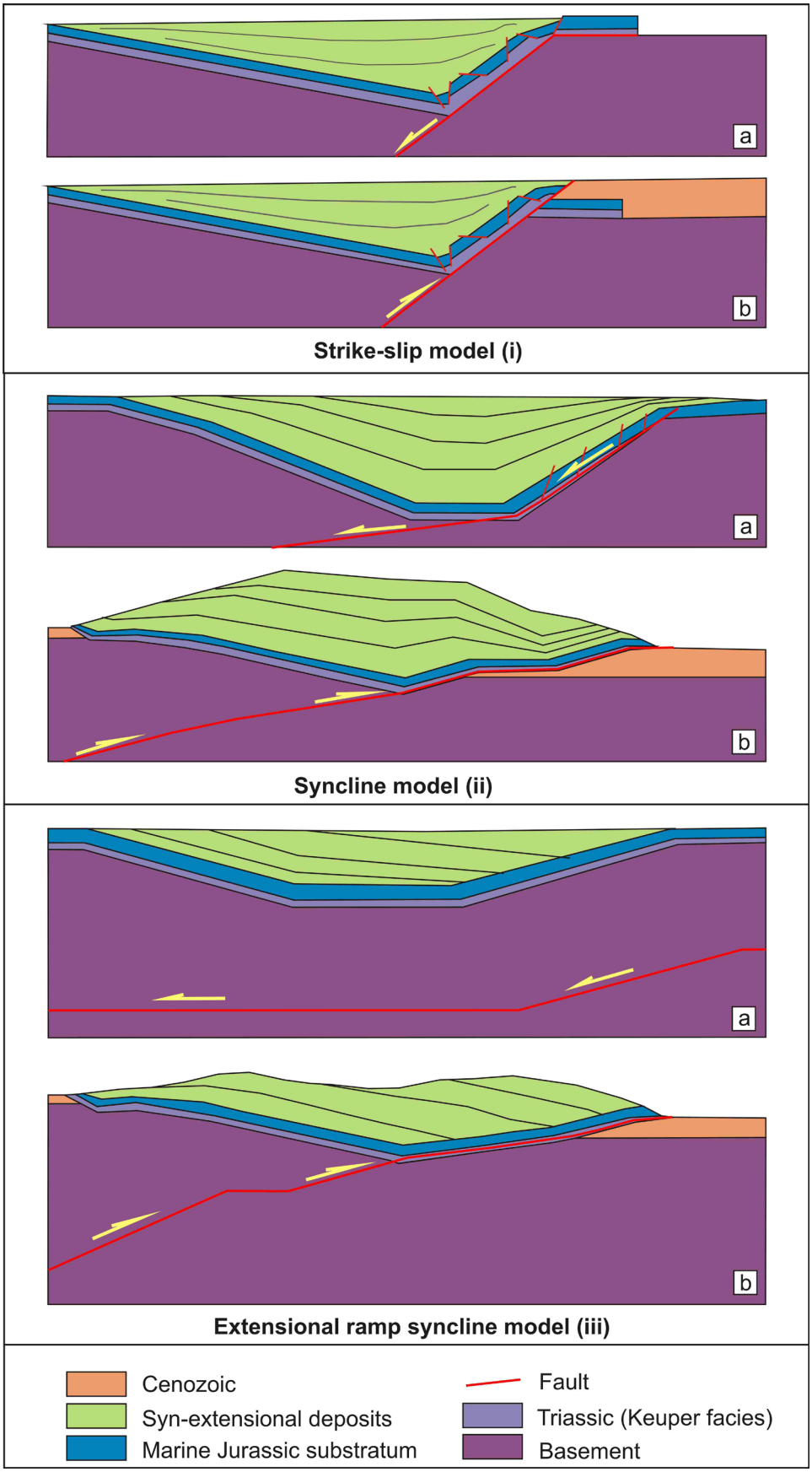
a
b
Strike-slip model (i)
a
b
Syncline model (ii)
a
b
Extensional ramp syncline model (iii)
Cenozoic
Syn-extensional deposits
Marine Jurassic substratum
Fault
Triassic (Keuper facies)
Basement

and taken as reference level. Subsequently, the geometry of the lower units was reconstructed, maintaining for every unit the bed-length and the section area. In a second step, additional restored sections, corresponding to the geometry of the basin at the end of the deposition of each depositional sequence, were drawn. Each restored section was achieved by flattening the top of the correspondent DS and taking it as reference level; the geometry of the lower section was reconstructed with maintenance for every unit of the bed-length and the section area of the previous restored section.

To calculate the amount of displacement that occurred during the basin inversion process, as well as the geometry of the associated inversion structures, the younger restored section was forward modelled with Move software, considering the base of the Upper Cretaceous as reference level. The restored section was introduced as input of the model, whereas the geometry of the fault planes, along which the section was displaced and the amount of displacement were considered as variables. These variables were changed until the restored section introduced achieved a deformation style similar to the post-inversion structure, represented in the balanced section reconstruct in this work. A coaxial deformation in a 2D plane was assumed. To simplify, erosion was not considered in this process.

7.5.1. Field data

Systematic field work focused on details in a 20-km-wide band across the section (approximately 10 km on either side). Digital orthophotos (PNOA, scale 1:5000, 0.5 m per pixel) assisted and clarified field observations. In particular, field work consisted of the following: i) determining the areal distribution of extensional deposits (Fig. 7.4, Fig. 7.5, Fig. 7.6 and Fig. 7.7), revising the pre-existing geological maps and integrating all of the data in a new GIS-based geological mapping of the study sector (Omodeo-Salé et al., 2012); ii) characterising the main structural elements intersecting the cross-section and iii) collecting a large number (430) of strike-and-dip measurements of bedding along the cross-section **(Appendix 2)**. The collected field data were gathered in the detailed geological maps of Fig. 7.5, Fig. 7.6 and Fig. 7.7, where only the most representative strike and dip directions are represented. Strike-and-dip data were grouped into different dip domains, with every domain comprising strike-and-dip data belonging to the same fold (Fig. 7.8). The axis of the fold (β) was found by plotting the strike-and-dip measurements of bedding in a stereographic projection and fitting a great circle to the data (Fig. 7.9). The strike-and-dip data of every domain were projected onto the cross-section in the direction of the calculated β axis (Fig. 7.8).

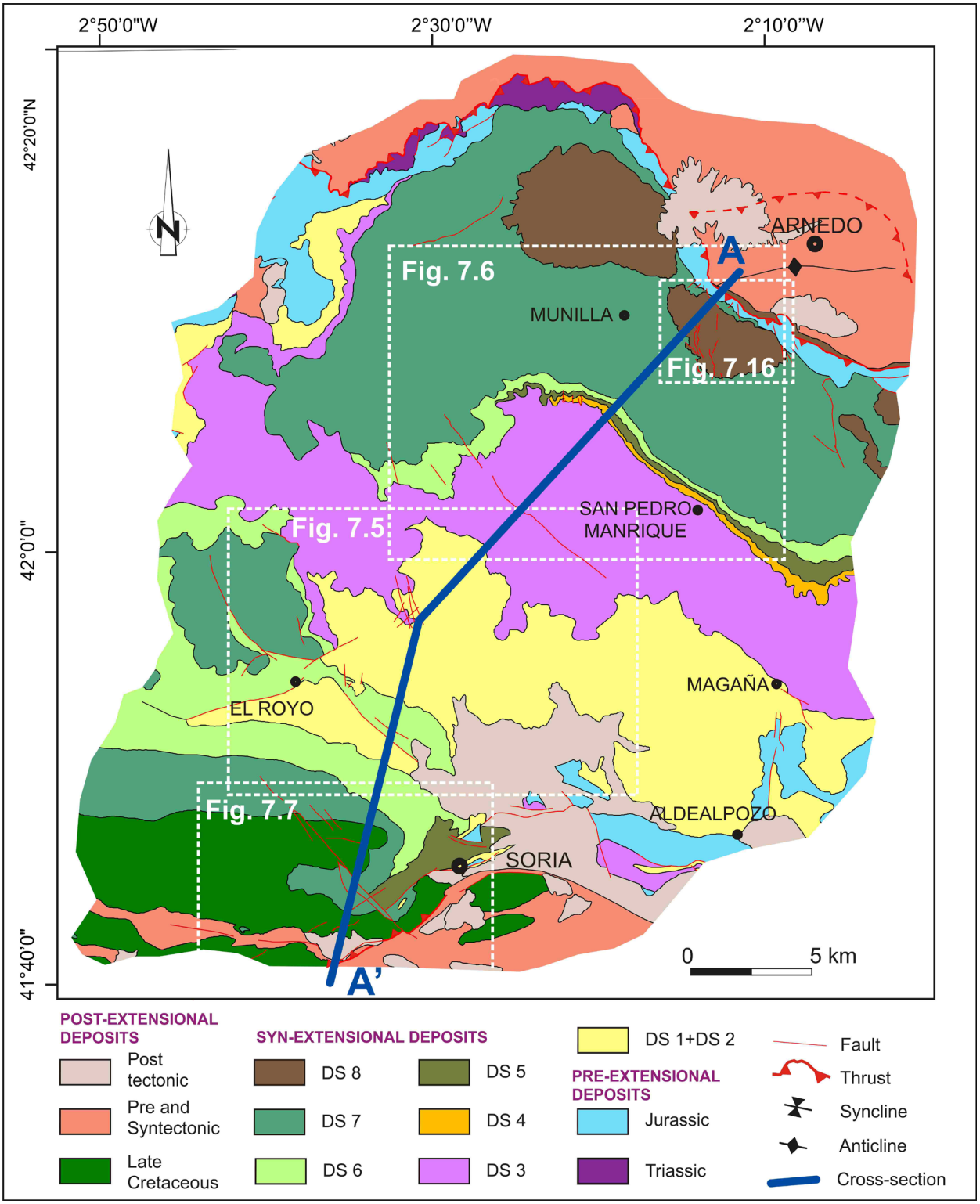

Fig. 7.4 - Geological map of the study area analysed to reconstruct the geometry and architecture of the Cameros Basin infill. In this area crop out all the syn-extensional depositional sequences, as well as the pre-extensional (substratum of the basin) and post-extensional deposits of the basin.

7.5.2. Geophysical and subsurface data

Geophysical and subsurface data enhanced the understanding of the deep structure of the basin and the areal distribution of the extensional-deposits in depth. Geophysical data refer to the interpretation of two seismic lines (TOR84-05 and TOR84-06) (Fig. 7.10, Fig. 7.11 and Fig. 7.12), acquired by ENIEPSA in 1984. A shot was performed with a 15-kg explosive, and 36 geophones were arranged. Coverage was 12-fold and the record length 6000 ms, with a sampling of 2 ms, filters used range between 8 and 125 Hz. Static and dynamic correction were applied. Second, subsurface data, represented by logs of oil wells, were used. The wells analysed (Fig. 9) were drilled by "Hispanoil" in 1964 for oil exploration.

TOR84-05 is perpendicular to the main structures of the northern basin border, crossing the main basin thrust (Fig. 7.10). Although TOR84-05 does not intersect the cross-section trace, interpretation of this seismic line was useful in determining the relationship between the Jurassic substratum and the syn-extensional deposits at the northern border of the basin (Fig. 7.11). TOR84-06 crosses the section line (Fig. 7.10) and facilitates the differentiation of the Jurassic substratum from the basin infill formed during the extensional phase (Fig. 7.12). Because of the limited quality of the lines and the scarcity of well correlation data, boundaries between the various syn-extensional depositional sequences are not readily recognisable. As a consequence, TOR84-06 was used mainly to evaluate the Jurassic substratum depth at the intersection of the seismic line with the cross-section, converting the TWT to depth.

The Castilfrío-1 well, located at nearly 6 km from the cross-section, was used to determine the nature of the substratum of the extensional deposits in the central part of the basin (Fig. 7.10). The Aldehuela-1 well, located at nearly 15 km from the cross-section trace, was used to determine the areal extension of extensional deposits and the variation in their thickness in the southern sector of the basin (Fig. 7.10). The Quintana-Redonda-1 well, located at nearly 5 km from the cross-section trace, south of the southern Cameros thrust, was used to limit the extension of the extensional deposits (Fig. 7.10). The Ucero-1 well, located more than 30 km from the cross-section trace, SW of the southern current border and thus outside the Cameros Basin (Fig. 7.10), was used to limit the extension of the extensional deposits.

7.6. RESULTS

The detailed revision of the geological map (Fig. 7.4, Fig. 7.5, Fig. 7.6 and Fig. 7.7), the collected structural data (Fig. 7.8) and the geophysical and subsurface data interpretations (Fig. 7.10, Fig. 7.11 and Fig. 7.12) facilitated the construction of a balanced geological cross-section and its restoration (Fig. 7.13). From an interpolation of the geometric reconstruction and

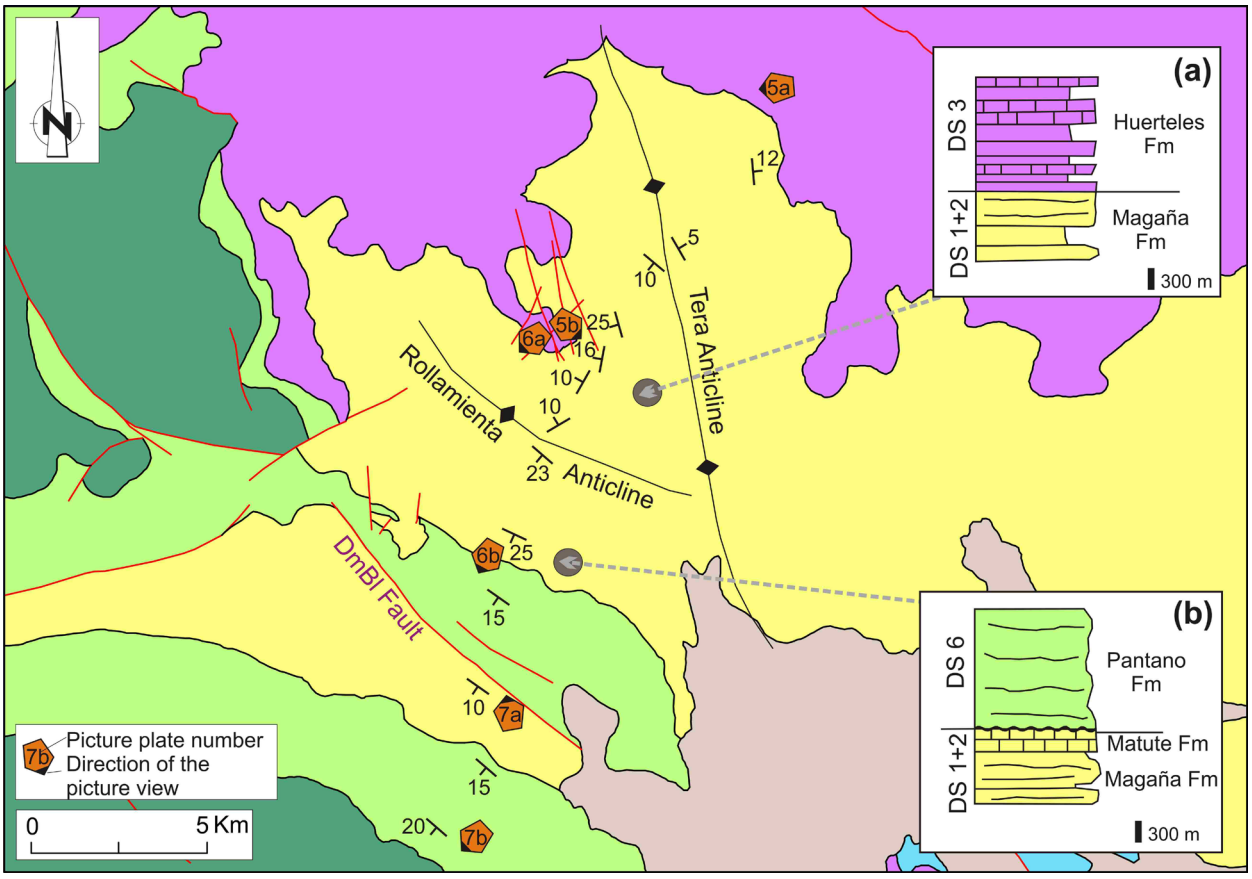

Fig. 7.5 - Detailed geological map of the central sector, showing the main structural elements (only the most representative strike-and-dip data are shown). (a) Schematic sketch of the typical stratigraphic succession of the area northern to the Rollamienta Anticline. (b) Schematic sketch of the area southern to the Rollamienta Anticline. For location and legend see Fig. 7.4. Panoramic views of the area are shown in the pictures of Plate 7.5, Plate 7.6 and Plate 7.7

geological map data, the geometry and thickness of eroded strata were obtained, as shown in Fig. 7.13b. The geometry of the contractional structures and the basin infill architecture in depth, herein reconstructed, is presented in Fig. 7.13b. Restorations of the balanced cross-section to the undeformed state before the Alpine contraction are shown in Fig. 7.13c. Partial restorations, corresponding to the geometry of the basin at the end of each depositional sequence, are presented in Fig. 7.14. The levels that have been flattened and used as reference level to restore each partial restored section are indicated in Fig. 7.14. In the restoration processes, the average of the balancing error ranges from 2% to 4%, which was calculated considering the difference in the bed-length and section area values obtained respect the previous section. The amount of displacement that occurred during the basin inversion process, as well as the geometry of the associated inversion structures was obtained with Move software (Fig. 7.15). Geometries and structures of the intermediate steps of the inversion process was also determined (Fig. 7.15).

Interpretation of the balanced geological cross-sections and its restorations and the collected

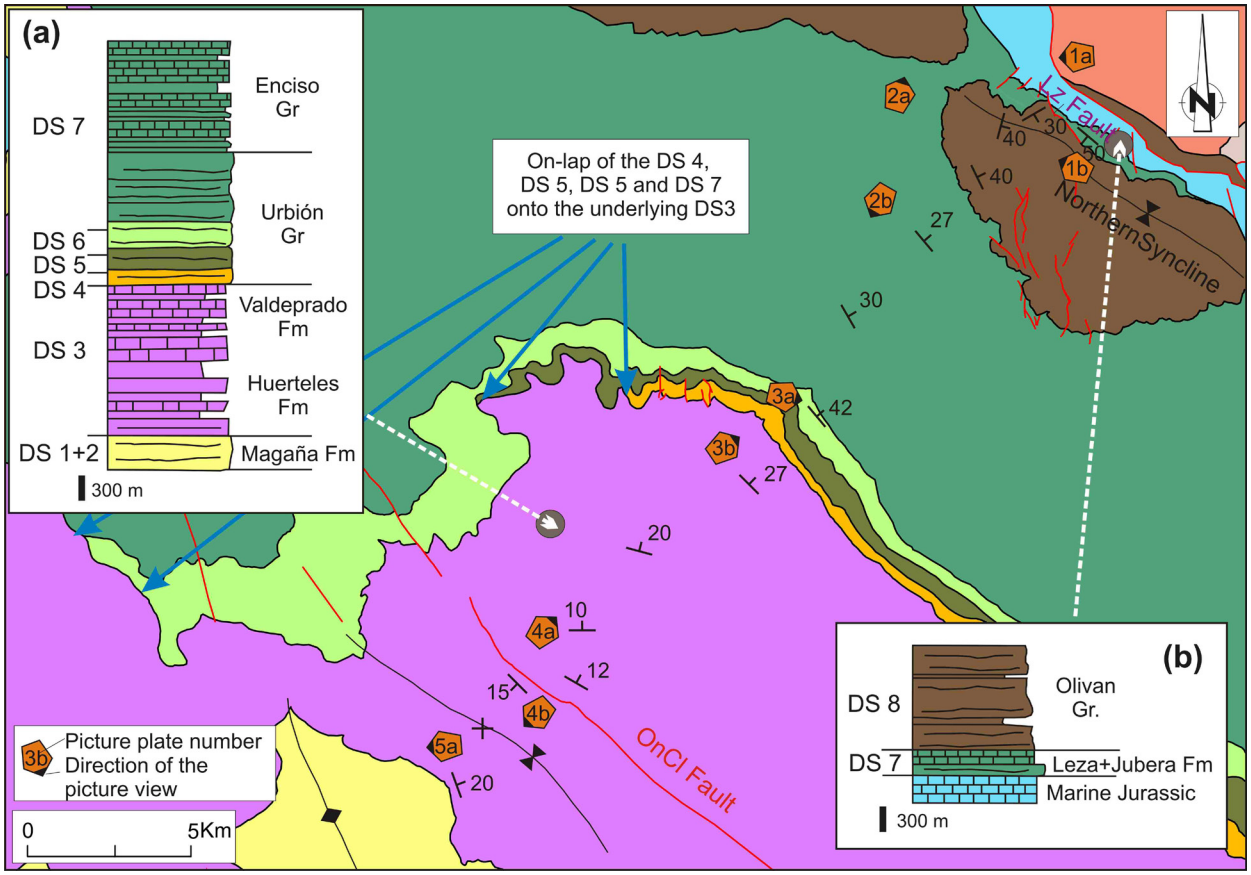

Fig. 7.6 - Detailed geological map of the northern sector, showing the main structural elements (only the most representative strike-and-dip data are shown). (a) Schematic sketch of the typical stratigraphic succession of the monocline northern to the Tera Anticline. (b) Schematic sketch of the northernnost basin border. On-lap of the DS4, DS5 and DS6 on the underlying DS3 is marked. For location and legend see Fig. 7.4. Panoramic views of the area are shown in the pictures of Plate 7.1, Plate 7.2 and Plate 7.3, Plate 7.4 and Plate 7.5

field and geophysical-subsurface data allow a detailed discussion of the areal distribution, structure and geometry of the syn-extensional infill of the basin.

7.6.1. Areal distribution and geometry of the syn-extensional deposits

Throughout the whole basin, the syn-extensional deposits are folded to form gentle synclines and anticlines that are oriented approximately 120º-140º N along the northern cross-section segment and 280º N along the southern cross-section segment (Fig. 7.4, Fig. 7.5, Fig. 7.6 and Fig. 7.7). The oldest syn-extensional deposits (DS1 and DS2) crop out in a complex antiform located in the centre of the basin (Fig. 7.5 and Fig. 7.13a). The antiform is constituted by two anticlines, whose axes are oriented N340 (the northern Tera Anticline) and N270 (the southern Rollamienta Anticline) and separated by a narrower syncline. In the northern limb of the Tera anticline, DS2

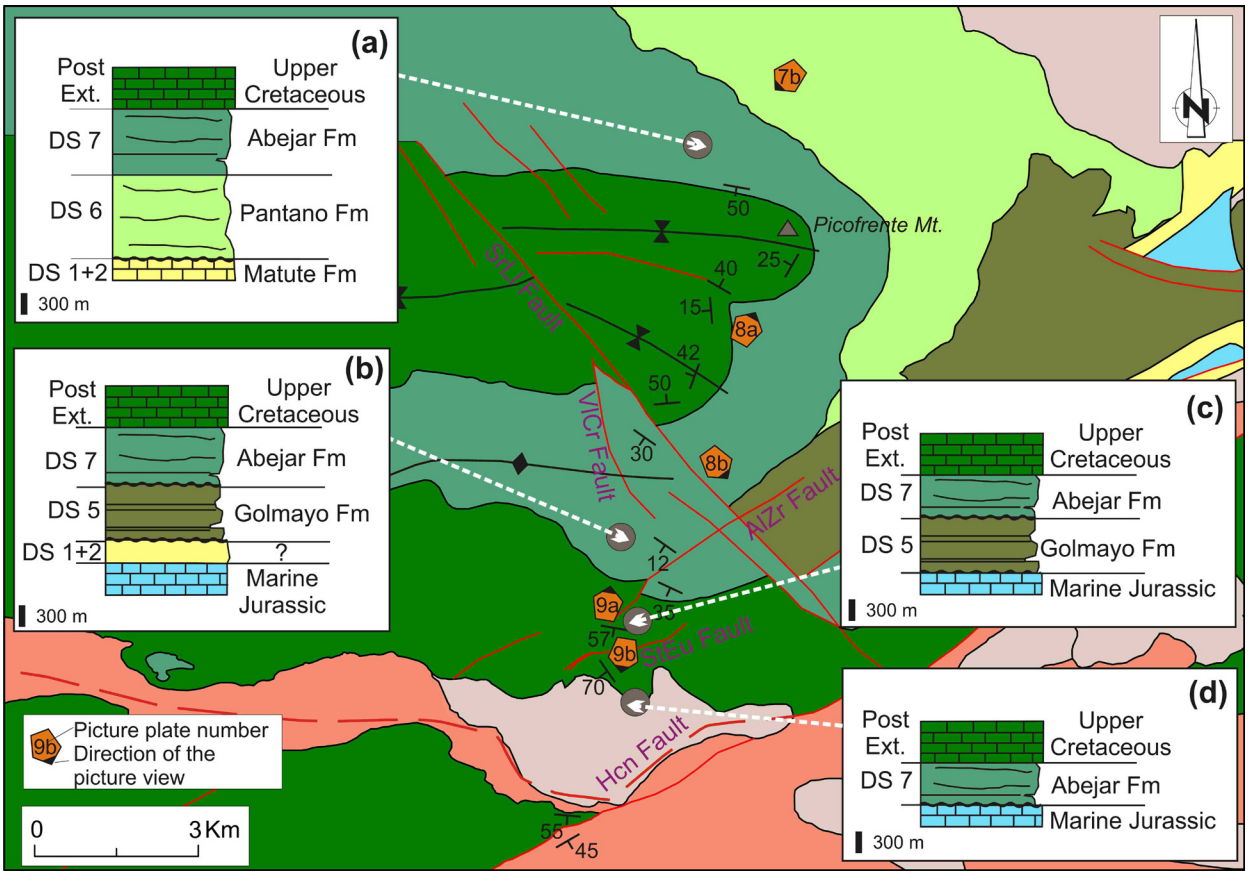

Fig. 7.7 - Detailed geological map of the southern sector, showing the main structural elements (only the most representative strike-and-dip data are shown). (a) Schematic sketch of the typical stratigraphic succession of the area northern to the Sierra Llana (SrLl) Fault. (b) Schematic sketch of the typical stratigraphic succession of the area included between SrLl Fault and the Alto de Zorraquín (AlZr) Fault. (c) Schematic sketch of the typical stratigraphic succession of the area included between the AlZr Fault and the Santa Eulelia (StEu) Fault. (d) Schematic sketch of the typical stratigraphic succession southern to the StEu Fault. For location and legend see Fig. 7.4. Panoramic views of the area are shown in the pictures of Plate 7.7, Plate 7.8 and Plate 7.9.

(Magaña Fm) is topped by DS3 (Huerteles Fm). DS3 is folded into a gentle syncline and into an anticline whose core is faulted by a nearly vertical post-extensional fault (Oncala Fault) and oriented NW-SE and extending on a basin scale (Fig. 7.6).

From the Oncala Fault, a large 25-35º dipping monocline extends until the northern border of the basin, where the whole syn-extensional succession crops out (from DS3 to DS8, Fig. 7.6 and Fig. 7.13a). The dominant carbonate facies of the uppermost DS3 (Valdeprado Fm) are topped by a siliciclastic unit, the Urbión Group, that in this part of the basin belongs to DS4, DS5, DS6 and to the lowermost DS7 (Fig. 7.2, Fig.7. 6a and Fig. 7.13a). The uppermost part of DS7 is formed by a mixed carbonate and siliciclastic unit, corresponding to the Enciso Group (Fig. 7.2 and Fig. 7.6a). On the top of DS7 lies DS8 (Olivan Gr.) (Fig. 7.6b and Fig. 7.13a). DS8 deposits are folded by an asymmetrical syncline (Northern Syncline) oriented WNW-ESE (Fig. 7.6 and

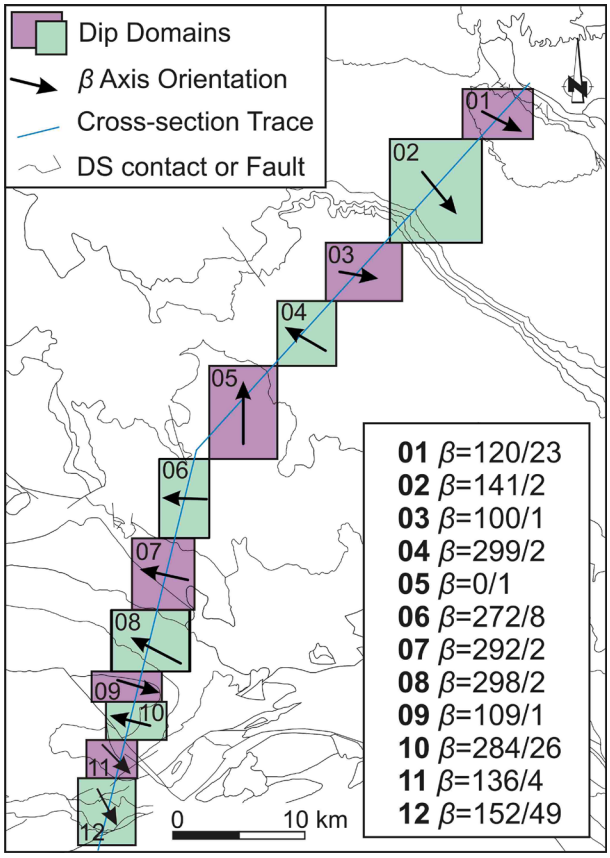

Fig. 7.8 - The 430 strike and dip data collected along the cross-section trace were grouped in 12 dip domains, characterised by a similar strike and dip value. β represents the axis of the fold in which lie the strata planes of every domain. Strike and dip data have been projected on the cross-section plane parallel to the β axis direction. Stratigraphic contacts refer to Fig. 7.4

Fig. 7.16), which can be traced along the entire northeastern basin border. The southern limb is wider and contains the thicker DS8 sedimentary succession, which is generally more than 2000 m thick, whereas the northern syncline limb is narrower and contains no more than 400 m of DS8 deposits (Fig. 7.16c). In the northern syncline limb, DS7 (Leza Fm and Jubera Fm) outcrops, with a south-dipping sedimentary succession just 200 m thick, which lies unconformably on the Jurassic substratum (Fig. 7.16). The difference in thickness between the two syncline limbs can be explained by the peculiar geometry of DS8. Orthophoto analysis and field panoramic views demonstrate that the lower part of the DS8 onlaps northward onto DS7 and that it thins northward (Fig. 7.16a and Fig. 7.16c). In addition, the northern syncline limb (close to the basin boundary) displays variation in the thickness of the upper part of the DS8, in correspondence with a normal fault (Fig. 7.16a). Thus, the deposition of the uppermost DS8 was influenced by the activity of a syn-sedimentary normal fault.

Fig. 7.9 - Strike-and-dip data were grouped into different dip domains, with every domain comprising strike-and-dip data belonging to the same fold. The axis of the fold (β) was found by plotting the strike-and-dip measurements of bedding in a stereographic projection and fitting a great circle to the data

Domain 1
Beta(°) = 120/23

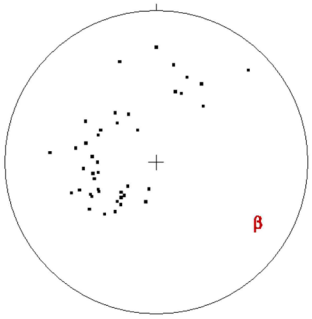

Domain 2
Beta(°) = 141/2

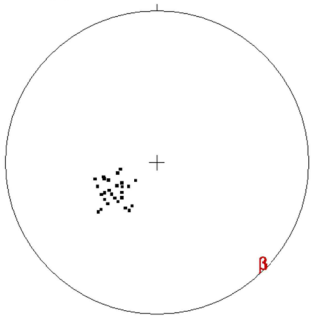

Domain 3
Beta(°) = 100/1

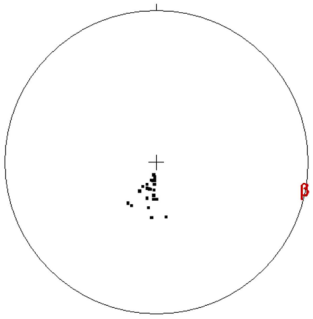

Domain 4
Beta(°) = 299/2

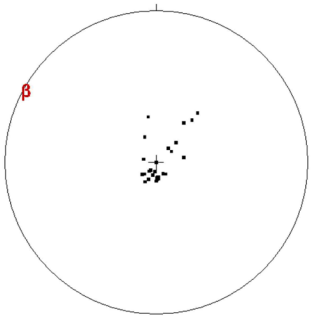

Domain 5
Beta(°) = 0/1

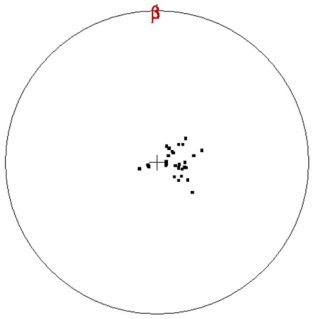

Domain 6
Beta(°) = 272/8

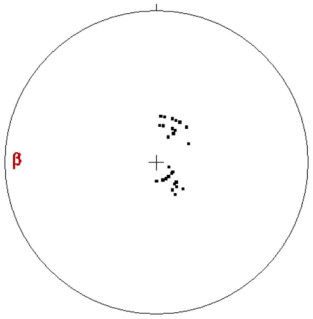

Domain 7
Beta(°) = 292/2

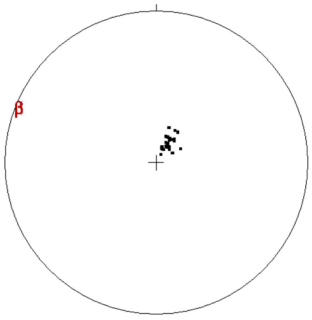

Domain 8
Beta(°) = 298/2

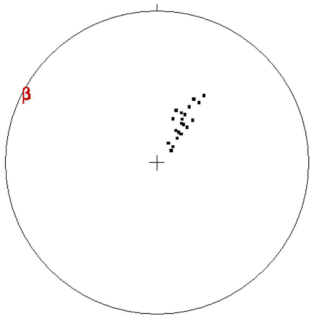

Domain 9
Beta(°) = 109/1

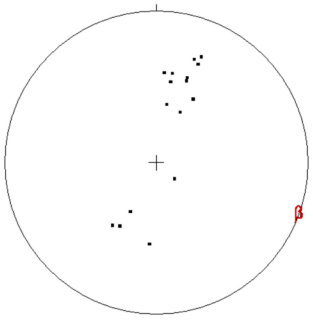

Domain 10
Beta(°) = 284/26

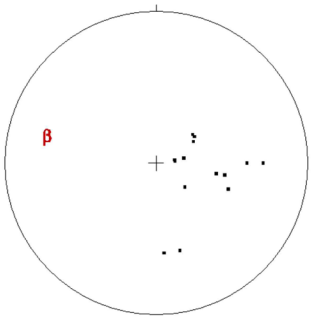

Domain 11
Beta(°) = 136/4

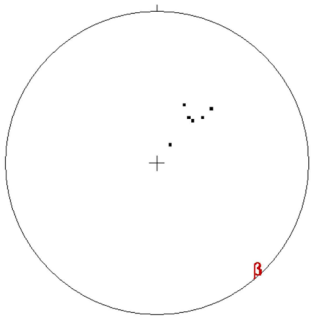

Domain 12
Beta(°) = 152/49

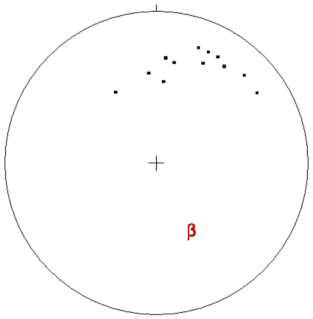

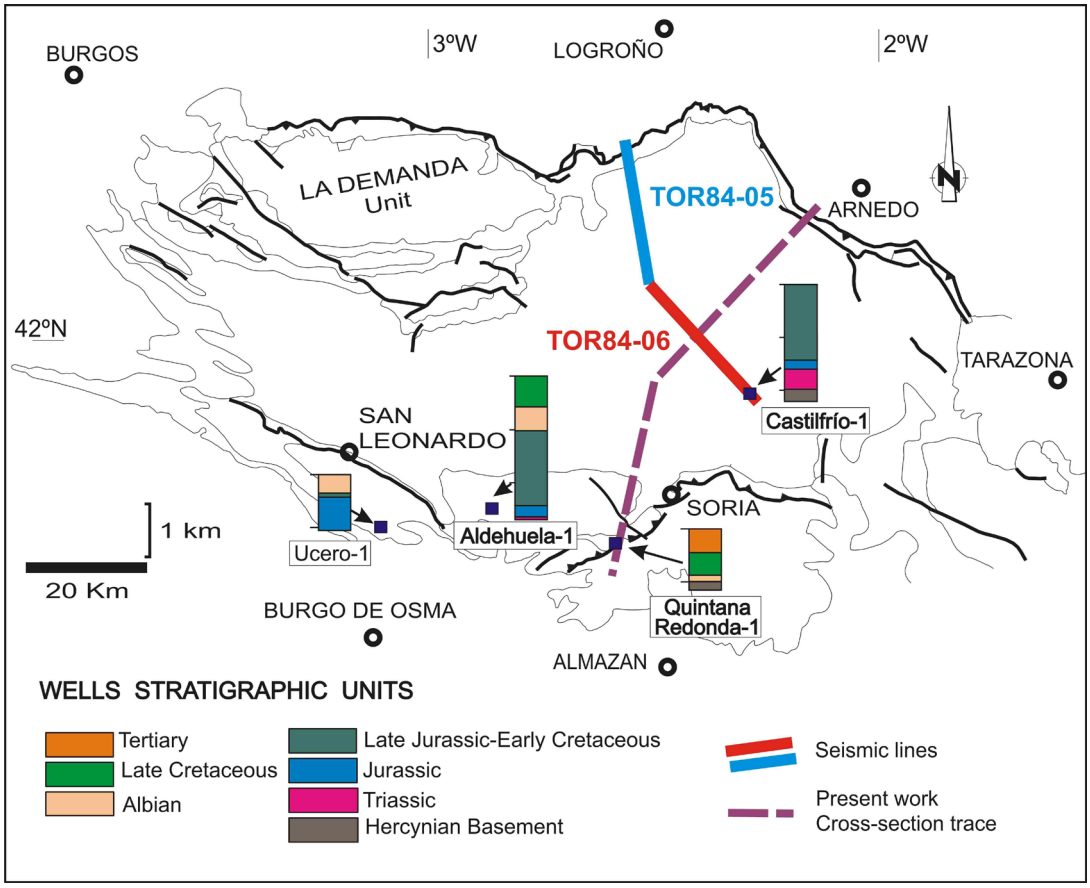

Fig. 7.10 - Location of two seismic lines and of the four oil wells analyzed in this work. Geological contacts refer to Fig. 7.1a

In the northern basin border, the Jurassic substratum, together with the uppermost syn-extensional deposits (DS7 and DS8), are folded by an anticline and thrusted over the foreland on a 50º thrust plane located in the Upper Triassic evaporitic beds (Keuper facies) (Fig. 7.16c). In the footwall of the thrust, it outcrops a reduced thickness of the last depositional sequence (DS8), which is unconformably covered by Cenozoic deposits. These footwall DS8 deposits represent the lateral continuity of the uppermost DS8 stratigraphic levels outcropping in the hangingwall. The interpretation of this thrust plane is discussed in the next section.

In the southern sector of the basin, the uppermost depositional sequences (DS5, DS6 and DS7) lie directly on the oldest one (DS1+2), marking an important stratigraphic and time gap (Fig. 7.5 and Fig. 7.7a,b,c,d). This contact, first outcropping in the southern limb of the Rollamienta Anticline, is repeated to the south due to a nearly vertical NW-SE normal fault (the Dumbellas Fault) (Fig. 7.5 and Fig. 7.13a). In this area the DS2 is formed by tabular limestone beds (Matute Fm), whereas the DS6 by coarse-grained channelized sandstone bodies (Pantano Fm). From the Dumbellas Fault towards the south, DS6 (Pantano Fm) outcrops with continuity for nearly 4 km, with a constant strata orientation of 210ºN azimuth and 20-25º dip (Fig. 7.7).

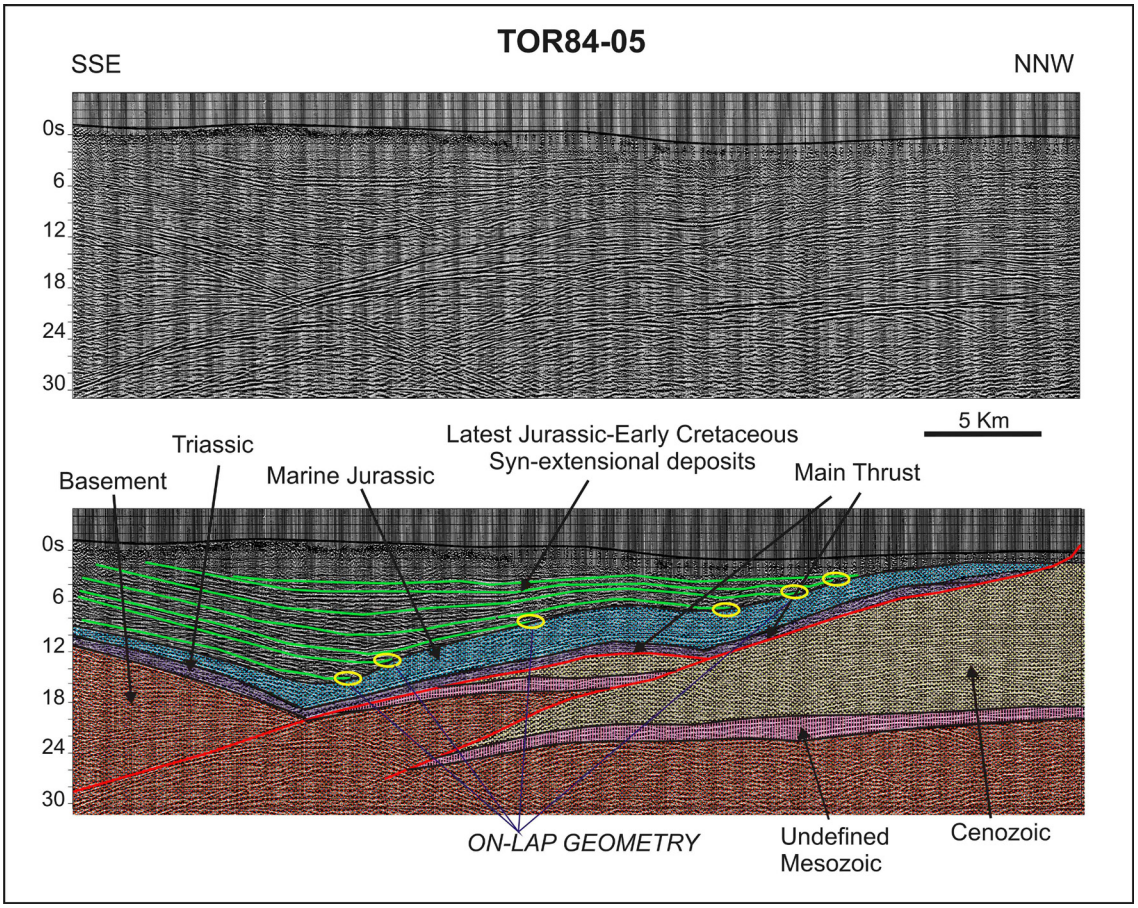

Fig. 7.11 - TOR84-05 seismic profile (above) and its interpretation (below). For location see Fig. 7.9. In this seismic line the main northern thrust of the basin can be traced. A short-cut of the thrust is recognized in the basement. Green lines represent seismic units boundaries (Strata Genetic Increments) in the syn-extensional sedimentary record, displaying an on-lap geometry on the marine Jurassic substrate. The different syn-extensional depositional sequences are difficult to distinguish accurately in this seismic line.

To the southeast, DS6 thins abruptly and closes on the underlying DS5 (Golmayo Fm) (Fig. 7.7). The latter depositional sequence is present only in the southernmost sector of the basin (Fig. 7.7), whereas northwards, it tends to disappear (Fig. 7.4). DS5 and DS6 are overlain by DS7, which is a sandstone-conglomerate alluvial unit (Abejar Fm) that extends quite uniformly in all of the southern and western sectors of the Cameros Basin. DS7 is unconformably topped by the Upper Cretaceous deposits (Albian-Aptian unconformity) (Fig. 7.2, Fig. 7.7 and Fig. 7.13a), representing the post-extensional cycle (Upper Cretaceous Megacycle of Alonso et al. (1993). In the cross-section area, in the Picofrente Mountain, both the syn-extensional DS7 (Abejar Fm) and the post-extensional Upper Cretaceous deposits are folded by two synclines, oriented WNW-ESE (Fig. 7.7 and Fig. 7.13a). A NW-SE 15-kilometre-long fault, the Sierra Llana fault (SrLl in Fig. 7), joins these synclines with an anticline of equal orientation, where DS7 (Abejar Fm) outcrops at its core. The anticline is cut by another near-vertical fault, the Villaciervos fault (VlCr in Fig.

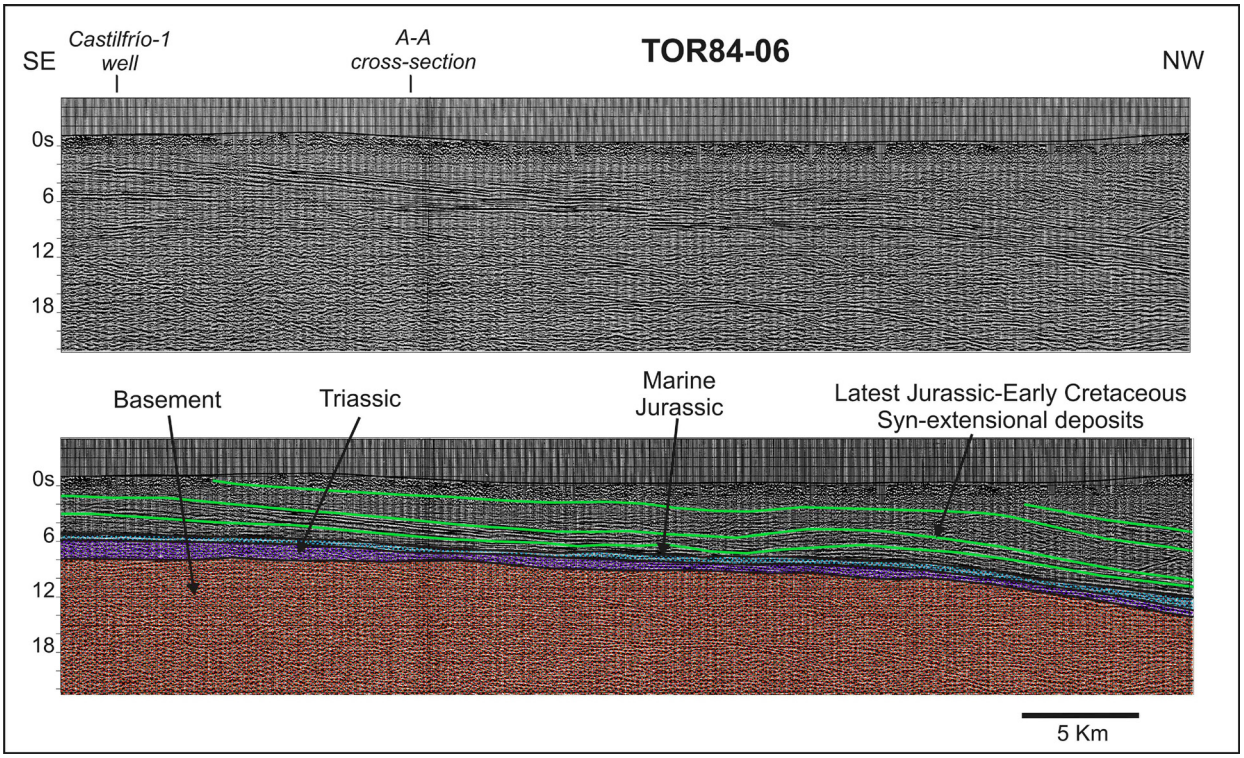

Fig. 7.12 - TOR84-06 seismic profile (above) and its interpretation (below). For location see Fig. 7.9. In this seismic line the depth of the marine Jurassic substratum with respect to the present topographic profile can be obtained. Green lines represent seismic unit boundaries (Strata Genetic Increments) in the syn-extensional sedimentary record, having an on-lap geometry on the marine Jurassic substrate. The different syn-extensional depositional sequences are difficult to distinguish accurately in this seismic line.

7.7), which has an orientation similar to the previous one.

South of this area, only faulted and gently folded post-extensional deposits outcrop. The faults are mainly NE-SW-oriented, perpendicular to the direction of most of the faults that affect the rest of the basin. The post-extensional carbonates of the Upper Cretaceous thrust onto the Cenozoic Duero Basin deposits, by means of a NE-SW-oriented thrust system.

7.6.2. Structural elements

The thrusts that bounded the Cameros Structural Unit to the north and to the south are the most relevant structural features in the study area (Guimerà et al., 1995) (Fig. 7.4). Modelling performed using the Move software allowed us to reconstruct the main thrust ramp-and-flat geometry, with a ramp dipping of approximately 20-30º (Fig. 7.13b). The back-thrust, dipping 30º N, joins the flat of the main thrust deep in the basement (approximately 10 km deep) (Fig. 7.13b). To reproduce the present-day structure, a displacement of the undeformed section (Fig. 7.13c) of 30 km along the main northern thrust and of 3 km along the southern back-thrust was

determined (Fig. 7.15). A very similar displacement has been previously estimated by Guimerà et al. (1995).

In the north, the Cameros Structural Unit thrusts onto the thick syn-contractive Cenozoic succession of the Ebro Basin (Fig. 3), which lies on a Mesozoic substratum (Fig. 7.13). This substratum has been interpreted (Mas et al., 1993, 2003) as being formed by the Lower and Middle Jurassic unconformably covered by the post-extensional Upper Cretaceous deposits. It is relevant to stress that the thrust surface cropping out in the cross-section area (oriented NW-SE and with a dip of nearly 50º SW) (Fig. 7.4 and Fig. 7.16) is not the main thrust surface, but a secondary splay (sensu McClay, 1992) that emerges from the main thrust fault. In fact, in the footwall of this thrust, only a reduced thickness of the last depositional sequence (DS8) crops out, which represents the lateral equivalent of the uppermost DS8 stratigraphic levels (Oliván Gr) cropping out in the hangingwall. Thus, the displacement produced by this thrust is reduced, and as a consequence, it cannot be considered to be the main thrust responsible for the basin inversion, whose displacement has been estimated to be 30 km. The main thrust can be recognised all along the northern border of the Cameros unit (Fig. 7.1 and Fig. 7.4). Nevertheless, in the section area, the main thrust is blind, and it can be located approximately in front of the Arnedo anticline (Fig. 7.4), covered by the Cenozoic deposits (see also Casas Sainz, 1993 and Fig. 3 of Mata et al., 2001).

In the cross-section area, three basin-scale normal faults were recognised, Oncala (OnCl), Dumbellas (DmBl) and Sierra Llana (SrLl), with a reduced strike-slip component and with similar orientation that of the main northern thrust (NW-SE) (Fig. 7.4). The Oncala and the Dumbellas faults, located in the northern and central sectors, respectively (Fig. 7.4, Fig. 7.5 , Fig. 7.6 and Fig. 7.13a), are not associated with variation of the sedimentary record from one side to the other, and it is interpreted as post-sedimentary. The third basin-scale fault, the Sierra Llana fault (Fig. 7.7 and Fig. 7.13a), located in the southern sector of the basin, can be interpreted as active also before the Alpine compression because different deformation styles were observed in the two sides of the faults: on the left side sediments are deformed in a fold with a NW-SE axe, whereas on the right side sediments are deformed in a fold with an E-W axis (Fig. 7.7).

Close to the northern and southern basin margins, several faults were identified as syn-sedimentary because a different depositional record was recognised in the two sides of the faults. In the north, a normal NW-SE-oriented fault, the Lázaro fault (Lz), produces a sharp contact between the DS8 and the DS7 (Leza Fm) sequences (Fig. 7.16). The DS8 thickness changes abruptly from one side of the fault to the other (Fig. 7.16c), suggesting that this fault was active during at least the DS8 deposition stage. In the northern border of the basin, several hectometric-to kilometric-scale normal faults have been mapped (Díaz-Martínez, 1988; Alonso and Mas, 1990; Suárez-González et al., 2013), with vertical displacements of several hundred of meters. It has to be stressed that no major normal faults of deca-kilometric scale that are active during the

Mesozoic extensional phase have been recognised (Mas et al., 1993, Guimerà et al., 1995; Díaz-Martínez, 1988; Suárez-González et al., 2013), as expected in a typical rift basin (Gibbs, 1987, McClay, 1990). In the southern sector, a series of faults were interpreted as syn-sedimentary faults: the Alto de Zorraquín fault (AlZr), the Santa Eulalia fault (StEu) and the Hocino fault (Hcn) (Fig. 7.7 and Fig. 7.14). The syn-sedimentary nature of the Alto del Zorraquín and Santa Eulalia faults was deduced from geometric reconstructions and well data, which demonstrate that these faults limited the sedimentation towards the south, on their foot-wall side. In fact to the south of the AlZr fault DS1+2 was not deposited, and DS5 (Golmayo Fm) has a reduced thickness than in the hanging-wall, whereas, to the south of the StEu fault, DS5 was not deposited (Fig. 7.7 and Fig. 7.14). The AlZr and StEu faults are oriented similarly to the southern back-thrust (NW-SE) (Fig. 7.7), suggesting that they were reactivated during Alpine contraction. It is suggested that the southernmost syn-sedimentary fault, the Hocino fault (Hcn), actually covered by Cenozoic deposits (Fig. 7.7), was acting as southern boundary of the basin during the sedimentation of the syn-extensional deposits. In fact, to the south of this fault, no syn-extensional deposits outcrop and the post-extensional deposits of the Upper Cretaceous Megacycle lie directly on the Jurassic substratum (Fig. 7.7 and Fig. 7.14).

7.6.3. Basin infill substratum

From field observation, geophysical and subsurface data interpretation, it can be deduced that the marine Jurassic (generally Late Jurassic) constitutes the substratum of the syn-extensional deposits all along the basin. In the northern basin border, DS7 (Leza Fm and Jubera Fm) lies directly on the marine Jurassic deposits (Fig. 7.6b), as can be observed in outcrop (ellipse on the right in Fig. 7.17a and Fig. 7.17b). In the central and southern sectors of the basin, the marine Jurassic nature of the syn-extensional substratum is deduced from the stratigraphy of the Castilfrío-1 and Aldehuela-1 wells (Fig. 7.10). Interpretation of seismic lines provides the same results, further indicating the continuity of the marine Jurassic substratum below the extensional basin infill (Fig. 7.11 and Fig. 7.12). Interpreting the TOR-84-06 seismic line (Fig.

Fig. 7.13 - (a) Cross-section of the Cameros Basin at the present topographic profile. Location of the main structures of the basin infill is indicated. Location of these structures in the geological map is indicated in (Fig. 7.4, Fig. 7.5, Fig. 7.6 and Fig. 7.7. (b) Balanced geological cross-section with the reconstruction of the eroded part and of the deeper part. The short-cut and the foreland stratigraphic succession refer to the TOR-84-05 seismic line interpretation (see Fig. 7.11). The onlap geometry of the DS onto the underlying Juassic substratum is indicated. (c) Restoration of the cross-section (A-A') to the undeformed state previous to the Alpine contraction and to the deposition of the post-extensional Upper Cretaceous unit. The trace of the section is shown in Fig. 7.4

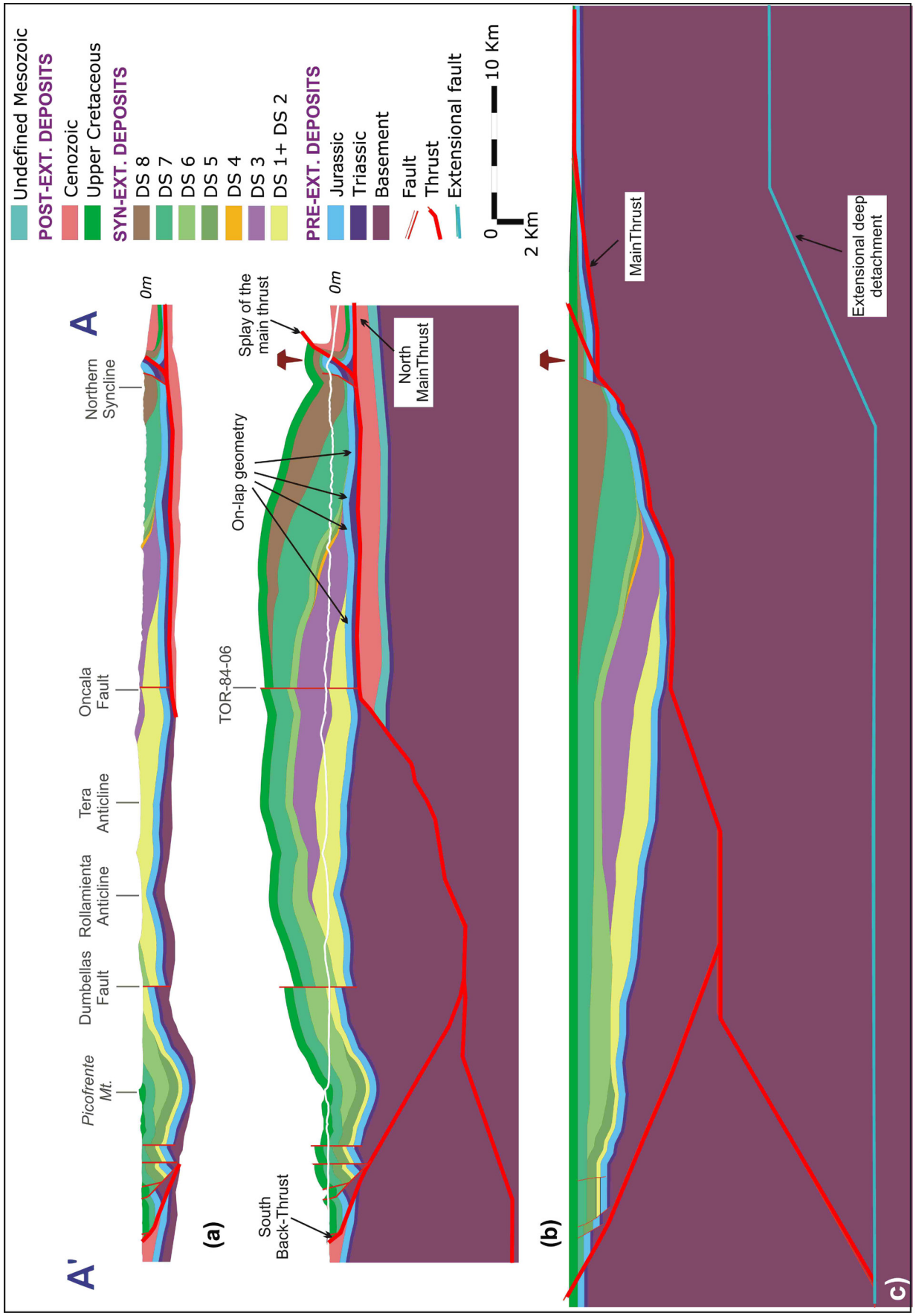
Undefined Mesozoic
POST-EXT. DEPOSITS
Cenozoic
Upper Cretaceous
SYN-EXT. DEPOSITS
DS 8
DS 7
DS 6
DS 5
DS 4
DS 3
DS 1+ DS 2
PRE-EXT. DEPOSITS
Jurassic
Triassic
Basement
Fault
Thrust
Extensional fault
0
2 Km
10 Km
A
A'
Picofrente Mt.
Dumbellas Fault
Rollamienta Anticline
Tera Anticline
Oncala Fault
Northern Syncline
0m
(a)
TOR-84-06
On-lap geometry
Splay of the main thrust
North MainThrust
South Back-Thrust
(b)
MainThrust
Extensional deep detachment
c)

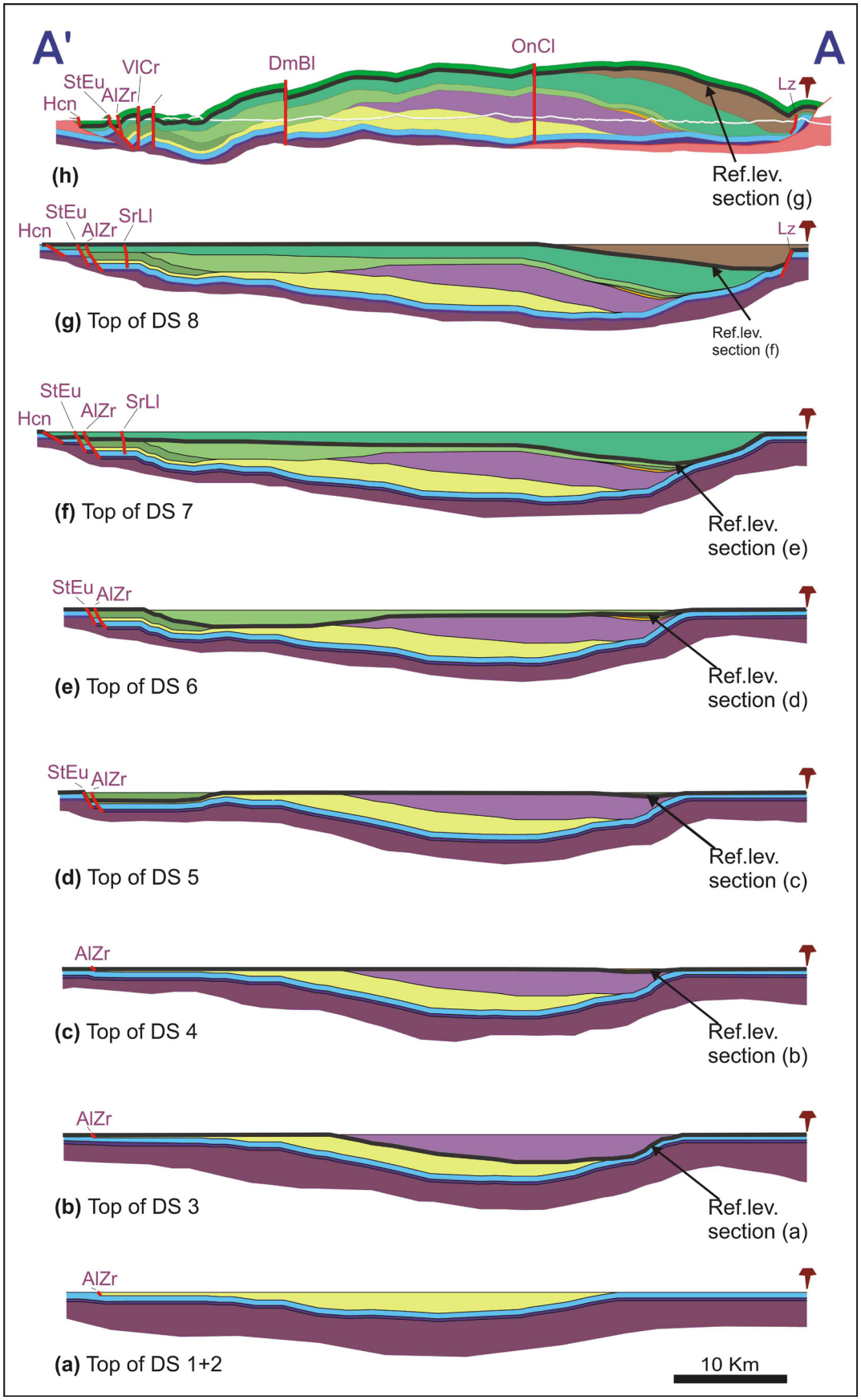
A'
A
VlCr
DmBl
OnCl
StEu
AlZr
Hcn
Lz
(h)
Ref.lev.
section (g)
StEu
SrLl
Hcn
AlZr
Lz
(g) Top of DS 8
Ref.lev.
section (f)
StEu
SrLl
Hcn
AlZr
(f) Top of DS 7
Ref.lev.
section (e)
StEu
AlZr
(e) Top of DS 6
Ref.lev.
section (d)
StEu
AlZr
(d) Top of DS 5
Ref.lev.
section (c)
AlZr
(c) Top of DS 4
Ref.lev.
section (b)
AlZr
(b) Top of DS 3
Ref.lev.
section (a)
AlZr
(a) Top of DS 1+2
10 Km

7.12), a substratum depth of 1550 m from the present topographic surface was deduced in the intersection of the seismic line with the cross-section traces (Fig. 7.13b).

7.6.4. Depositional sequence architecture

The onlap of the depositional sequence onto the underlying pre-extensional substratum (marine Jurassic), represented in the balanced geological cross-section and in the restored sections (Fig. 7.13), was deduced from geological map and seismic lines. The geological map indicates that in the northern sector of the basin, only the youngest units (DS7 and DS8) crop out, making a stratigraphic contact with the marine Jurassic substratum (Fig. 7.13b and the right ellipse in Fig. 7.17a and Fig. 7.17b; see also discussion in the section 7.6.1). In the northwestern border area of the basin, from south to north, progressively younger deposits lie on the Jurassic substratum (see the left ellipse detail in the Fig. 7.17a). This means that during the evolution of the basin, the youngest depositional sequences northwards progressively onlapped (sensu Schlische, 1991) onto the pre-extensional Jurassic substratum. The TOR-84-05 seismic line (Fig. 7.11) indicates that the syn-extensional deposits reflections (green layers in Fig. 7.11) pinchout to the north onto the Jurassic substratum, with typical onlap geometry (Mitchum, 1977; Vail, 1987; Schlische, 1991), characterised by a progressive up-dip termination of the depositional sequences against the underlying substratum surface.

Two other features of the depositional sequences geometry are considered relevant. The first is observed in the northern sector (geological map in Fig. 7.6), where the set of depositional sequences DS4, DS5 and DS6 north-westward onlap onto the underlying DS3. The second is observed in the northernmost sector of the basin, where DS8 displays an onlap geometrical relationship with DS7 (see in Fig. 7.16 how the strata of the Lower DS8 gradually onlap northward onto the underlying DS7 surface).

7.6.5. Thickness distribution of depositional sequences

Interpretation of the balanced cross-section and related restored sections define the variation

Fig. 7.14 - (g) Restorations of the balanced section A-A' (h) to the undeformed state previous to Alpine contraction (g), using as reference level the base of the Upper Cretaceous unit. (f-a) restoration to the end of each depositional sequence in which the syn-extensional basin infill has been subdivided. The lines which have been flattened and used as reference level to restore each section are indicated on the sections. Syn-sedimentary (Hcn, StEu, AlZr, SrLl and Lz) and post-sedimentary (DmBl, OnCl and VlCr) normal faults are indicated on the sections. For the legend see Fig. 7.13

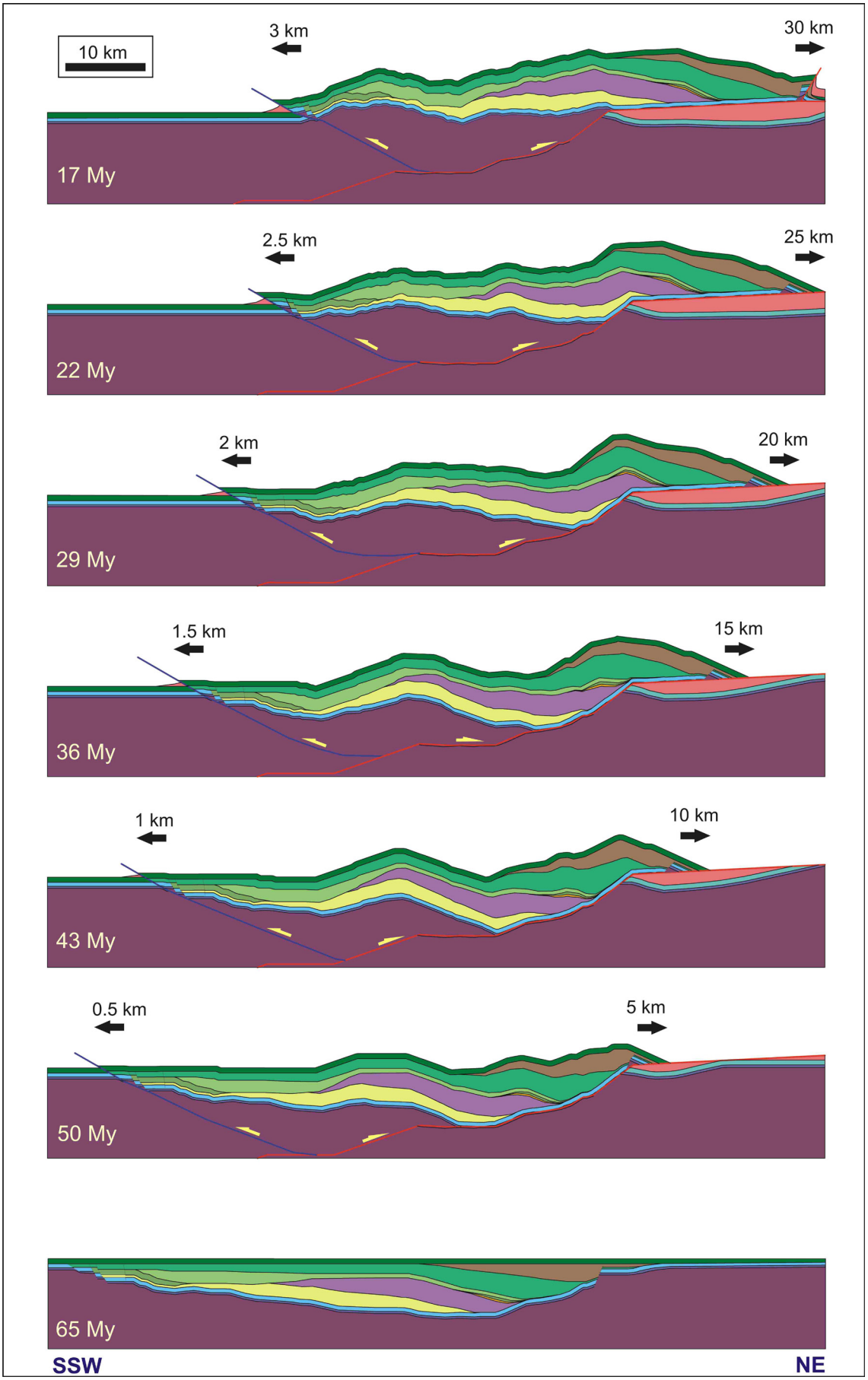
10 km
3 km
30 km
17 My
2.5 km
25 km
22 My
2 km
20 km
29 My
1.5 km
15 km
36 My
1 km
10 km
43 My
0.5 km
5 km
50 My
65 My
SSW
NE

of the basin depocentral areas throughout time (Fig. 7.18), suggesting a possible depositional scenario for each depositional sequence in which the Cameros Basin extensional phase infill was subdivided.

During the deposition of DS1+2, the depocentral area was located in the central part of the basin, in the Tera Anticline core (Fig. 7.14a and Fig. 7.18a). A maximum thickness of 1895 m was obtained from geometrical reconstructions. Northwards, DS1+2 thin and end abruptly on the Jurassic substratum. Southwards, DS1+2 thin considerably, although a thickness of 300 m is maintained until the end of the section (Fig. 7.14a). Field data and the Aldehuela-1 well indicate that DS1+2 were not deposited south of the NE-SW-oriented Altos del Zorraquín Fault (Fig. 7.10 and Fig. 7.7b), as a consequence of the early activation of this fault.

The DS3 depocentral area was localised in the northern sector of the basin, just north of the Oncala Fault (Fig. 7.18b). A maximum thickness of 2445 m can be seen in the cross-section (Fig. 7.14b).

The areal extension of DS4 is very limited, as seen only in the cross-section area, which records a reduced thickness of 230 m (Fig. 7.14c and Fig. 7.18c). The DS4 depocentral area was located to the north of DS3. Field and well data (Fig. 7.7 and Fig. 7.10) confirm the absence of DS3 and DS4 records in the southern sector of the basin.

During the deposition of DS5, sedimentation took place only in two sectors of the basin (Fig. 7.14d). The most relevant depositional area was in the south (Golmayo Fm) (Fig. 7.18d), where a thickness of 715 m was estimated from well data (Aldehuela-1 well, Fig. 7.10). The second depositional area, north of DS4, was recorded as having a reduced thickness of 290 m (Urbión Gr) (Fig. 7.14d). Most likely, no deposition took place between these two sectors. To the south, DS5 continues with a constant thickness until the Santa Eulalia Fault (Fig. 7.14d), sealing the Altos de Zorraquín Fault, which most likely stopped its activity at this time. There is no evidence of the presence of the DS5 on the southern side of the Santa Eulalia Fault. Hence, this fault most likely limited the deposition in the southern area of the basin during the DS5 sedimentation.

The main DS6 depocentral area was located in the southern sector of the basin (Pantano Fm), with a maximum thickness of 1545 m in the cross-section (Fig. 7.14e and Fig. 7.18e). To the north, the thickness of the DS6 (Urbión Gr) abruptly decreased to less than 500 m (Fig. 7.14e). Because of the absence of the previous units in the central part of the basin, DS6 lies directly on the DS1+2 sequences, with an important depositional hiatus (Fig. 7.14e).

Fig. 7.15 - Intermediate steps of the inversion process obtained with Move software. A displacement to the north of 30 km an to the south of 5 km along the thrust surfaces was determined

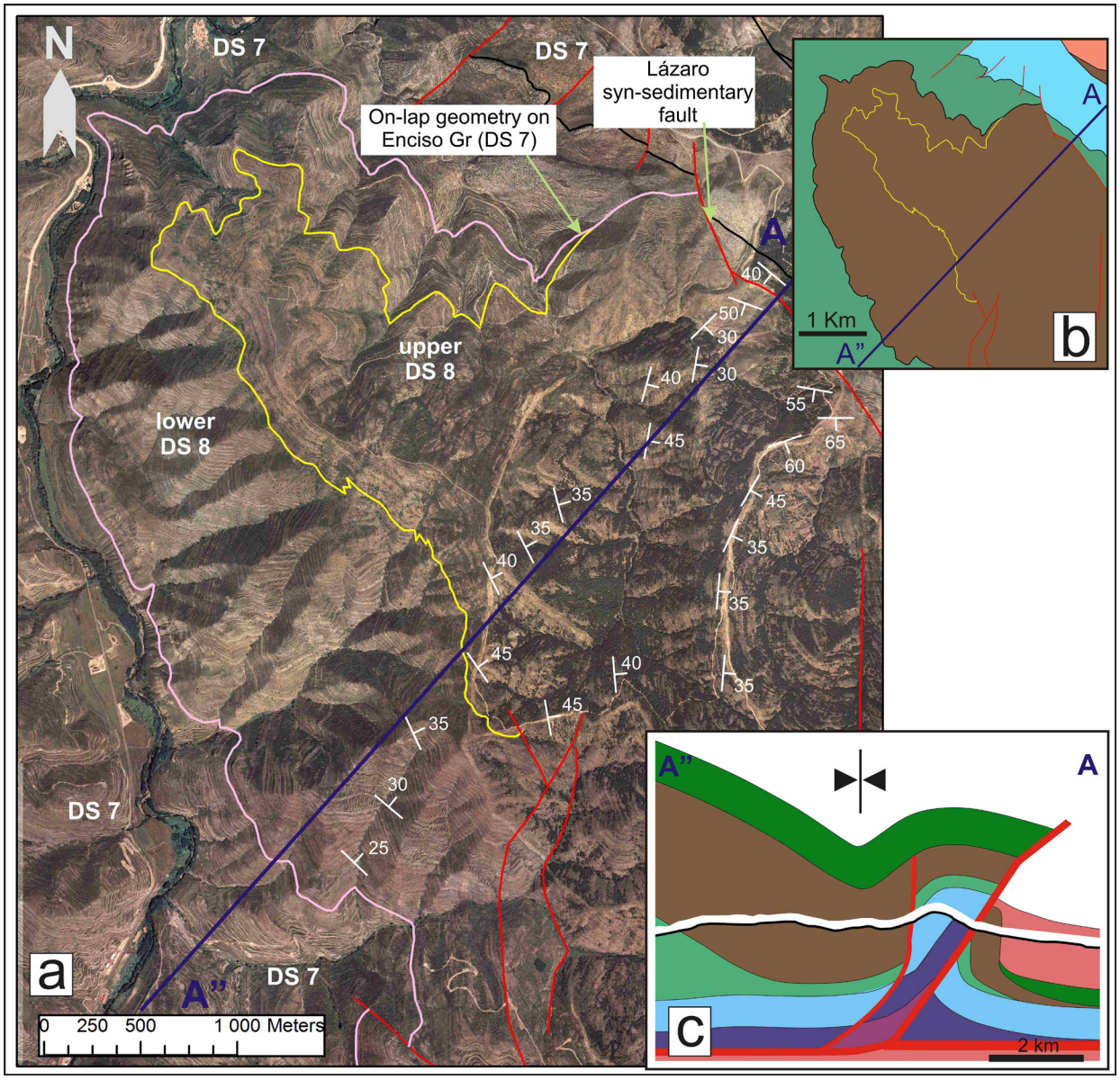

Fig. 7.16 - Ortophoto (a) and geological map (b) of the northern border of the basin and its structure along the cross-section (for location and legend see Fig. 7.3). In (a) the contact between DS7 (Enciso Gr) and DS8 (Olivan Gr) is represented in pink, while in (a) and (b) the yellow line represents the contact between the lower and upper parts of the DS8. The lower DS8 unit to the north onlaps on the DS7, whereas the upper DS8 unit ends against a syn-sedimentary fault. As a consequence of these geometries the southern syncline limb is thicker and wider than the northern one (c)

As stated previously (see section 7.6.4), the set of depositional sequences DS4, DS5 and DS6 onlap onto DS3 (Fig. 7.6). This geometry is correlated with the reduction in the formation of accommodation space in the northern sector of the basin during the deposition of these units, even expressed by the southward migration of the depocentral areas of DS4 and DS5. In fact, the absence of new accommodation space in the northern area explains why, at that time, these sequences exceeded only slightly the northward extension limit of the DS3 and onlap it.

DS7 was deposited along the entire cross-section area but with a variable thickness. The depocentral area in the cross-section was recorded in the northern sector of the basin (2900 m) (Fig. 7.14f and Fig. 7.18f). To the north, DS7 thins abruptly to only 200 m in the northern basin border area (Enciso Gr.) (Fig. 7.6b). In this area, DS7 lies directly on the marine Jurassic substratum (Fig. 6b and Fig. 15). Southwards, DS7 thins more gradually in the central sector of the basin (Urbión Gr), where a thickness of 1220 m was estimated (Fig. 7.14f). Another thickness reduction can be observed in the Picofrentes mountain area, where a thickness of 912 m was measured (Abejar Fm). Considering the Aldehuela-1 well data, south of the Alto de Zorraquín Fault, only 450 m was estimated for DS7 (Fig. 7.7d and Fig. 7.14f). DS7 extension is limited to the south by the Hocino Fault, covered by post-extensional Cenozoic deposits (Fig. 7.14f). South of this fault, the post-extensional deposits overlie the marine Jurassic substratum, whereas no syn-extensional deposits are preserved (Fig. 7.7 and Fig. 7.14). Hence, the Hocino Fault delimits the Cameros basin in the cross-section area.

DS8 deposits appear only in the northern basin sector, where the main depocentral area was located during this stage (Fig. 7.14g and Fig. 7.18g). A maximum thickness of 2220 m was reconstructed along the cross-section. To the north (northern side of the anticline), DS8 thins abruptly, partially pinching-out with an onlap onto the older DS7 and partially against the syn-sedimentary Lázaro normal fault (Fig. 7.16 and see discussion in sections 7.6.1 and 7.6.2). The DS8 thickness above the DS7 in the northern side of the anticline was estimated to be at least 450 m. South of the Cameros Northern Thrust, the contact between DS8 and the Upper Cretaceous top unit is not preserved. Therefore, the thickness of DS8 could not be completely estimated.

The syn-extensional infill of the Cameros Basin was overlain by the post-extensional Upper Cretaceous Megacycle deposits, with a thickness of 530 m (Picofrentes Mountain area) (Fig. 7.13a). Taking into account data from other Iberian coeval basins, a maximum thickness of 650 m was estimated for the Upper Cretaceous Megacycle (siliciclastic Utrillas Fm plus marine carbonate Late Cretaceous units) (García and Mas, 2004) (Fig. 7.13b).

The amount of erosion estimated along the section is variable: a maximum of 5500 m in the northern-central part of the section, 1400 m in the northern extreme and from 150 to 1000 m in the southern extreme of the section.

7.7. DISCUSSION

The reconstruction of a balanced geological cross-section and its restorations, as well as the revision of the geological map and of the geophysical and subsurface data, represents the most relevant advance in this work on the knowledge of the Cameros Basin tectono-stratigraphic evolution. In fact, as extensively presented in section 5, these results provide a detailed and

precise reconstruction of the following features: 1) the areal distribution of the infill deposits, 2) the present-day structure and thickness of the infill of the basin, 3) the amount of erosion, 4) the architecture of the syn-extensional units, 5) the geometry of the basin in the different evolution stages and 6) the main structural elements that have influenced the present geometry and architecture of the basin infill. Interpretation and discussion of these new data allow the proposal of a synthesis of the sedimentary architectural model of the basin infill during the extensional stage and the identification of a genetic model more coherent with the structure and geometry of the basin. The synthesis herein proposed can integrate data and interpretations presented by previous studies on the structure and geometry of the basin (Guiraud and Séguret, 1985; Mas et al., 1993; Guimerà et al., 1995; Mata et al., 2001; Casas et al., 2009). In addition, it can be an useful basis for future basin- and plate-scale research.

7.7.1. Sedimentary architectural model of the syn-extensional deposits

The variation of the geometry, thickness and areal distribution of the depocentres (Fig. 7.13 and Fig. 7.16), together with sedimentological information (Table 7.1), allow us to present a synthesis of the sedimentary architectural evolution of the basin during the syn-extensional phase (Late Jurassic to Early Cretaceous).

At the beginning of the extensional phase, during the Tithonian-early Berriasian (deposition of the DS1 and DS2), the basin depocentre was located in the central sector. A reduced thickness was deposited in the southern sector of the basin, whereas no sedimentation is recorded in the northern sector. Proximal-distal fluvial systems predominated, with alternating fine- and coarse-grained siliciclastic deposits (Magaña Fm). Tabular limestone (Matute Fm), deposited in a lacustrine depositional system, tops this first interval of the extensional phase. During the Berriasian (deposition of the DS3), the basin was characterised by a rapid subsidence, with the accumulation in the basin of a thick depocentre. The depocentre was located north of the depocentre of the previous stage, during which fluvial-deltaic and lacustrine playa-lake depositional systems were predominant (Huerteles Fm and Valdeprado Fm respectively). In the next stage, the Late Berriasian – Early Valanginian (DS4, Urbión Gr), reduced accommodation space was formed in the basin. A small depocentre formed north of DS3 depocentral area, with deposition of dominantly siliciclastic deposits. From the Late Valanginian to the Early Barremian (DS5 and DS6), the depositional area of the basin migrated southward. The formation of depocentres in this area could be a consequence of the tectonic activity of normal faults, which increased the subsidence rate. Fluvial to alluvial depositional systems developed with the formation of very thick sandstone bodies alternated with lutitic intervals (Golmayo Fm and Pantano Fm). From the Late Barremian to the Early Aptian (deposition of the DS7), the subsidence became again very rapid. In fact, during this stage, the depositional area extended

over most of the basin. In the southern sector, fluvial braided depositional systems developed (Abejar Fm), evolving to meandering fluvial systems towards the central sector (Urbión Gr) and to lacustrine-wet land environments toward the northern one (Enciso Gr). Tidal flats developed in the northernmost area (Leza Fm). The depocentral area was again located in the northern

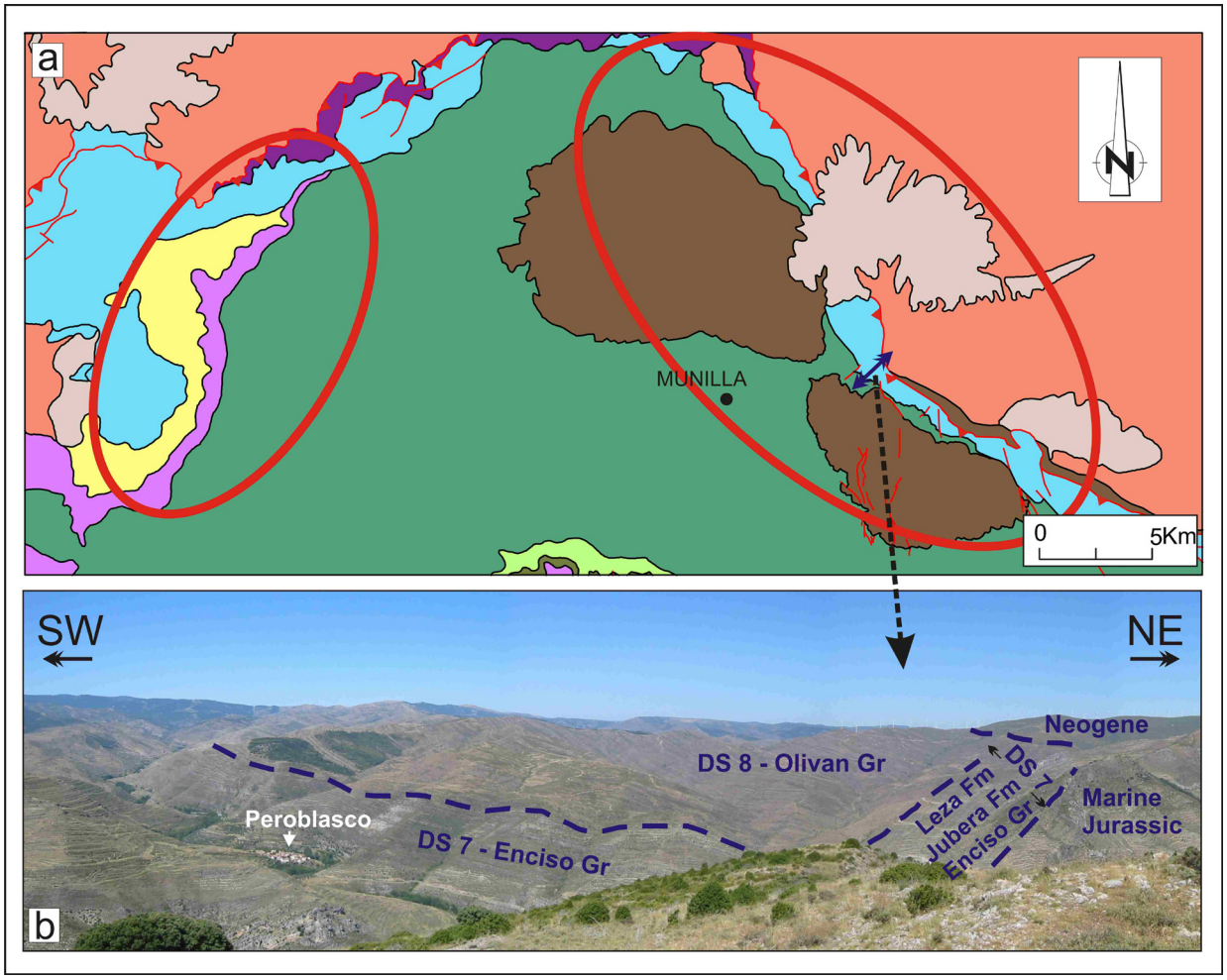

Fig. 7.17 - (a) Geological map of the northern basin border whereas it is indicated: 1) the DS1+2 and DS3 on-lap onto the underlying Marine Jurassic substratum (in the left ellipse) and 2) the northward abruptly thinning of the DS7, which lies directly on the marine Jurassic substratum (right ellipse). For legend and location see Fig. 7.4. (b) Panoramic view from Peñalmonte peak (La Rioja) where the DS7 (Enciso Gr) contact with the underlying Jurassic substratum can be observed

sector, to the north of the DS3 depocentral area. From the Late Aptian to the Early Albian (deposition of the DS8), which is the last syn-extensional stage, an accommodation space formed only in the northernmost sector of the basin, where a thick areally limited depocentre formed. At that time, large amounts of terrigenous sediments were produced, with the reactivation of fluvial depositional systems that deposited thick sandstone bodies, alternating with fine facies (Oliván Gr).

The sedimentary architectural evolution reconstructed herein reflects, during the basin infill, a cyclical transition from a dominant fluvial to a dominant lacustrine and also coastal-marine depositional setting, as a consequence of the combination of tectonic and sedimentological factors (Schlische ad Olsen, 1990; Schlische, 1991). In the Cameros Basin, lacustrine depositional settings developed mostly during DS3 and DS7 (Gr Oncala and Gr Enciso, respectively), which can be related to an increase in the capacity of the basin and of the subsidence rate, as a consequence of the extension, together with a decrease in the available volume of sediment (Schlische, 1991). A future accurate subsidence analysis study of the basin infill would be necessary to determine a more precise relationship between subsidence/tectonic processes and sedimentological and architectural features.

The accurate reconstruction of the basin infill geometry performed in this work determines a maximum vertical thickness at the basin depocentre of 6500 m, similar to the thickness estimated by Mas et al. (2011). The maximum erosion is estimated in the central and northern sector of the basin, whereas it decreases abruptly towards the south. The detailed reconstruction of the basin infill thickness obtained in this work would allow future precise subsidence and thermal maturity analyses.

Concerning the extensional mechanisms, which created the stratigraphic architecture observed, It is relevant to stress that no evidence of major normal faults of the deca-kilometric scale, which may be responsible of the formation of accommodation space during the extensional stage, was found in the border of the basin. This makes difficult to explain the syn-extensional architecture observed in the Cameros Basin with a typical rift model (Ziegler, 1978; Gibbs, 1987; McClay, 1990), where accommodation space is formed by a series of listric normal faults bounding the basin during the extension. In the latter case, because of the extensional fault movement, the extensional deposits would lie onto progressively older units until they reached the basin basement (Leeder and Gawthorpe, 1987; Gibson et al., 1989; Schlische and Olsen, 1990). In contrast, in the Cameros Basin, the stratigraphic evolution reconstructed herein shows that during the extensional stage, all of the depositional sequences onlap to the north directly onto the marine Jurassic substratum, which, as indicated by field and seismic lines observations, does not display relevant stretching. Thus, the Cameros Basin cannot be considered a typical half-graben rift basin (Schlische, 1991, Gawthorpe and Leeder, 2000), and a different model is needed to explain its tectono-stratigraphic evolution.

7.7.2. Basin formation genetic model

Despite the extensive research on the structure of the Cameros Basin (see section 3), an agreement on the formation mechanisms that could explain the peculiarity of the basin has not yet been achieved. The data and results presented in this work can help to define the main

critical points of the models proposed up to now.

The main drawbacks of the strike-slip basin model of Guiraud and Séguret (1985) (see section 7.4 and Fig. 7.3i) can be summarised as follows: 1) the compressional structures outside the proposed releasing areas developed during the Cenozoic, that is when the Cameros basin was already fully formed; 2) the extension needed in the basement is larger than that deduced from the normal faults involving the Mesozoic cover; 3) the Cameros Basin extends further west (south of La Demanda massif) and east (Moncayo area) of the supposed location of the releasing strike-slip faults; 4) no evidence of the two NE-SW strike-slip faults suggested by this model has been found in the Cameros Basin area.

The syncline basin model, proposed by Casas-Sainz and Simón-Gómez, (1992), Casas-Sainz (1993), Casas-Sainz and Gil-Imaz (1998), Casas-Sainz et al. (2000), Mata et al. (2001) and Casas et al. (2009) (see section 7.4 and Fig. 7.3ii) does not explain some of the data presented in this work and in several previous studies (Mas et al., 1993; Guimerà et al., 1995; Mas et al., 2002, 2003 and 2011, Suaréz-González et al., 2010, 2013). The most significant drawbacks can be summarised as follows. 1) Field observation and seismic line interpretations indicate that all of the depositional sequences in the north lie directly on the marine Jurassic substratum, displaying an onlap geometry. As a result, in the northern basin border area, only the younger syn-extensional deposits can be found (Fig. 7.13 and Fig. 7.17). This onlap geometry was not accepted by the "syncline model" authors, who assumed that the older syn-extensional units are present in the northern border area of the basin. 2) The northward lateral migration of the depocentres during the extensional stage was not accepted either by Casas-Sainz and Simón-Gómez (1992), Casas-Sainz (1993), Casas-Sainz and Gil-Imaz (1998), Casas-Saínz et al. (2000), Mata et al. (2001) and Casas et al. (2009), who assumed that the depocentres of every stratigraphic unit were superimposed vertically instead

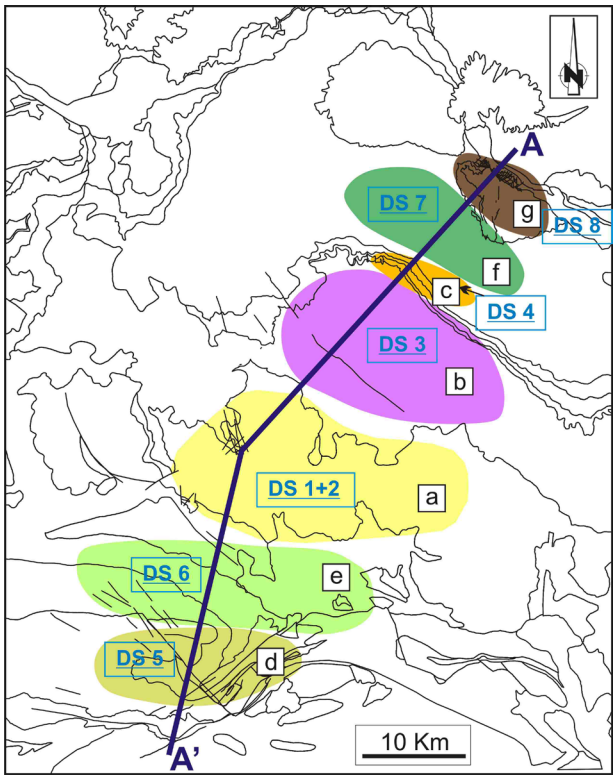

Fig. 7.18 - Location of the syn-extensional depocentral areas. Geological map contacts and legend refer to Fig. 7.4, whereas letters of the depocentral areas refer to Fig. 7.14. The depocentral areas shapes represented in this figure are indicative, showing only the supposed position of the depocenters at the time of deposition of the different depositional sequences

of laterally. 3) The continuity of the extensional phase substratum and its integrity along the basin was acknowledged by these authors, who stated that the fault movement stretched the pre-extensional Jurassic substratum by means of small-scale normal faults (Casas et al., 2009) but maintaining a more or less longitudinal continuity in the direction of the extension (Casas et al., 2009) (Fig. 7.3ii). In fact, these authors (i.e., Fig 3B in Mata et al, 2001) drew isolated blocks separated by a set of normal faults of hectometric displacement (171 m to 1334 m) and one major fault (with a displacement of 4385 m) bounding the basin to the north. Most of these faults should have been apparent in the seismic profile analysed previously (Fig. 7.11 and Fig. 7.12), where it is clear that the pre-extensional substratum maintains its integrity and continuity all along the profile. 4) The absence in the northern border area of the older depositional sequences is a very important key to understanding the geometry and evolution of the Cameros Basin. In the geological maps presented in Mata et al. (2001), Villalaín et al. (2003) and Casas et al. (2009), the lower depositional sequences (DS1, DS2 and DS3) appear in the northern border area of the basin. This would be the evidence of a vertical depocentre superposition, a crucial element of the syncline basin model. The present work, together with several previous works (Mas et al. 2003; Suárez-González et al., 2010, 2013), demonstrates that this assumption is based on misinterpretation of these outcrops and of the basin stratigraphy. In fact, Casas et al. (2009) and references therein consider that the Oncala Gr. (DS3) appears in the northern border area, with both carbonate and conglomeratic facies. These carbonate and the conglomeratic units correspond to various facies of the Urbión and Enciso Groups (DS7) (Alonso and Mas, 1993; Suárez-González et al., 2010, 2013) (Fig. 7.6). Panoramic views (Suárez-González et al., 2013) clearly indicate that the carbonate unit outcropping in the northern border area is a facies lateral change of the Enciso Gr. (DS7), the Leza Fm, and consequently cannot be considered to belong to the DS3. The dating of this carbonate unit as Barremian-Aptian (Suaréz-González et al., 2010, 2013) reinforced this attribution. The drawbacks of the "Syncline basin model" were recently exhaustively discussed in detail by González-Acebrón et al. (2012), where implications for the metamorphism recorded in the Cameros Basin of the different genetic models are also considered.

Conversely, the extensional ramp syncline model, proposed by Mas et al. (1993), Guimerà et al. (1995), Mas et al. (2002), Mas et al. (2003) and Mas et al. (2011) (see section 7.4 and Fig. 7.3iii) is the model best supported by the new data and evidence presented in this work. 1) The absence of a main extensional fault in the basin border area and the limited extension in the extensional substratum support the location of the extension in the middle-lower crust instead of in the Mesozoic cover. 2) The lateral migration of all of the depocentres and their onlap geometry on the extensional substratum can be explained by the movement along the deep detachment fault that produces the extension.

The geometry of the extensional fault was modelled by Guimerà et al. (1995) (represented in

Fig. 7.13c), as well as the intermediate steps of the evolution of the basin due to the hangingwall displacement to the south (Fig. 7.19). In this evolutionary model, the depocentral areas of the depositional sequences are generally located above the detachment ramp. As a result of the hangingwall displacement to the south, the depocentral areas migrate laterally to the north, lapping on the pre-extensional substratum (Gibbs, 1987, Leeder and Gawthorpe, 1987, Gibson et al., 1989, Schlische and Olsen, 1990) (Fig. 7.19b). As a consequence of the depocentral area lateral migration, instead of being vertically superimposed, the maximum vertical thickness recorded in the basin is significantly less than the complete stratigraphic record thickness (sum of the maximum thickness of each sequence in the cross-section) (Mas et al., 1993, 2011). The formation of depocentres in the southern sector of the basin during the Late Valanginian-Early Barremian (sequences DS5 and DS6) can be explained by the activation of antithetic faults in the southern basin border area creating localised accommodation space (Fig. 7.19c). In the southern margin, fault control of sedimentation was recognised by Arribas et al. (2002, 2003) during this interval of time. Activity of the main deep detachment fault became again dominant during the last stages, and a renewed northward migration of the depocentres (DS7 and DS8) was produced (Fig. 7.19c). The basin was inverted by a main thrust generated and located in the weakness zone of the Upper Triassic (Keuper) beds that branched in depth with the Mesozoic extensional fault flat (Fig. 7.13c and Fig. 7.19d). The geometry and architecture of the syn-extensional deposits

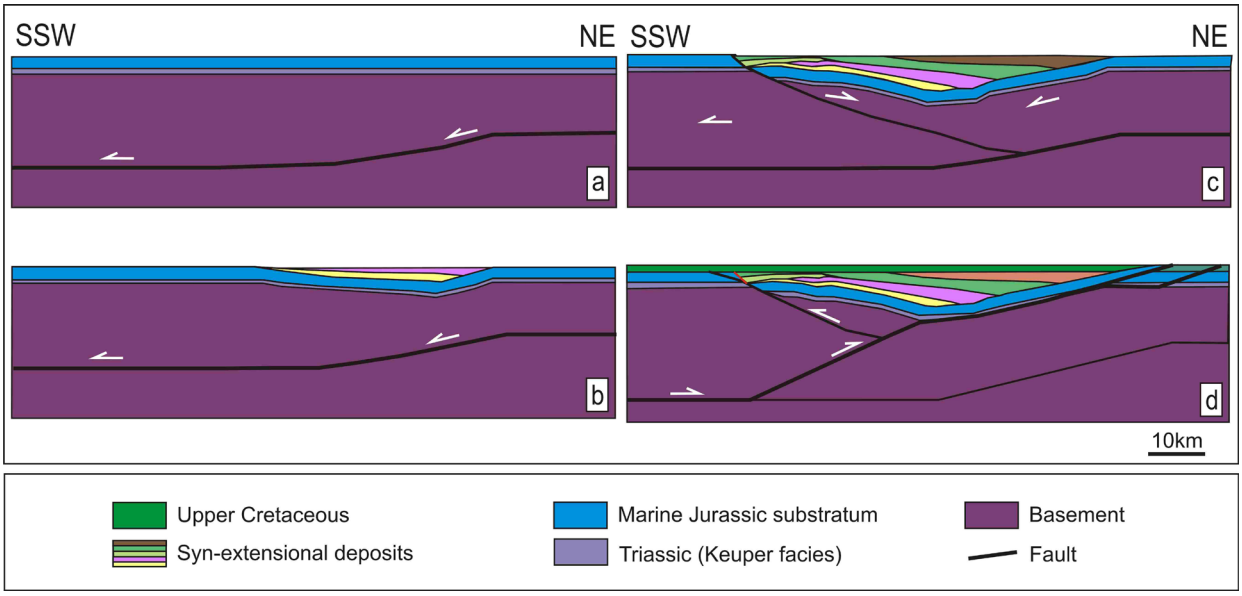

Fig. 7.19 - Evolution of the Cameros Basin as proposed by the "Extensional ramp syncline model" and confirmed by this work (modified from Mas et al., 1993). (a) Formation during the extensional phase of a deep detachment fault; (b) As a result of the hangingwall displacement to the south, depocentral areas migrated laterally to the north, onlapping onto the Jurassic substratum; (c) The activation of antithetic faults in the south, during the Late Valanginian-Early Barremian, forms secondary depocenters even in the south; (d) A thrust, located in the Upper Triassic beds and branching to the Mesozoic extensional fault flat, inverted the basin

reconstructed by the computer simulation of Guimerà et al. (1995) (Fig. 7.19) is very similar to the geometries obtained in the restorations sections performed in the present work (Fig. 7.14).

Summing up the previous discussion, the genetic model proposed by Mas et al. (1993), Guimerà et al. (1995) and Mas et al. (2002, 2003, 2011) appears to be the most coherent with the basin infill geometry and evolution reconstructed in this work and with the structural elements known today. Thus, the Cameros Basin can be considered a singular example of inverted extensional basin, where the inversion processes did not occur by reactivation of the extensional fault during the contractive phase (as in Jackson and Larsen, 2008 and Mora et al., 2009) but instead via a newly formed thrust. The accommodation space was formed by an extensional deep detachment instead of by a basin-bounding normal fault, which did not affect the sedimentary cover, which typically occurs in the most common rift basins (Ziegler, 1978; Gibbs, 1987; McClay 1990).

An unresolved issue with the "extensional ramp syncline model" is the correlation of the proposed extensional mechanism with the Iberian structural context. In fact, the formation of an extensional flat-ramp basin has to be linked to the north with a rift half-graben basin, where the ramp-flat deep detachment crops out (Gibbs 1987, McClay 1990; Roure et al., 1992). A plausible hypothesis is correlating the ramp and flat deep detachment with the listric normal faults that bounded the rift basins of the Basco-Cantabrian Chain (Rat, 1988; García-Mondejar et al., 1996; García-Mondejar et al., 2004; Pujalte et al., 2004), a western prolongation of the Pyrenees. These basins were formed during the early Cretaceous rifting, affecting this area and all of the Pyreneean domains (Rat, 1988; García-Mondéjar et al., 1996; Rosales et al., 2002). As a consequence of this hypothesis, the formation of the Cameros Basin could be correlated on a larger scale with the Pyreneean extensional geodynamic context. Thus far, the deep structural relationships that could explain this geodynamic link have not yet been well defined. To address these critical points and to define a more accurate genetic model for the Cameros Basin, the structural features of the basin in the context of the geodynamic mechanisms that govern the Mesozoic Iberian rift at plate scale should be taken into account in an exhaustive work.

7.8. CONCLUSIONS

A combination of field, geophysical and subsurface data with sedimentological information (facies changes and depositional environments) allowed the establishment of the evolution of the basin during the extensional stage and the original thickness of the syn-extensional units. The first phase of the extension is Tithonian-Early Berriasian (deposition of the DS1, DS2 and DS3), which is characterised by a rapid subsidence rate, with the formation of thick depocentres in the central-northern sector of the basin (1895 m for the DS1+2 and 2445 m for DS3, in the

basin cross-section A-A'). The deposition at the beginning of this first extensional phase was prevalently siliciclastic (DS1 and DS2) in a fluvial system environment. Towards the top, carbonate deposits (DS3) sedimented in lacustrine environments became dominant. The Late Berriasian-Early Barremian stage (deposition of the DS4, DS5 and DS6) is characterised by a decelerating subsidence rate. The thickest deposits of this phase were located in the southern sector of the basin (715 m for the DS5 and 1545 m for the DS6, in the basin cross-section A-A'). The deposits are dominantly siliciclastic and were generated by fluvial systems. From the Late Barremian to the Early Aptian (deposition of the DS7), the whole basin was characterised by an increased subsidence rate. The depocentre was located in the northern sector (2900 m), where the maximum thickness of the entire Cameros basin extensional stage was recorded. During this phase, fluvial-system siliciclastic deposits were dominant in the southern and central sector while mixed siliciclastic and carbonate deposits, which are related to palustrine-lacustrine depositional environments, dominated in the northern one. The last phase of the extensional phase is Late Aptian-Early Albian in age (deposition of the DS8), recording another high-subsidence stage. Deposition was confined to the northernmost sector of the basin where a thick depocentre (2220 m) was located. In this last phase of the extensional phase, siliciclastic deposits sedimented by a fluvial system were strongly dominant. The maximum vertical thickness measured at the basin depocentre is 6500 m. The maximum amount of erosion, which occurred as consequence of the inversion of the basin during the Cenozoic, is 5500 m.

During the extensional phase, a northward lateral migration of the depocentres occurred. This trend was inverted during the Late Valanginian-Early Barremian stages (DS5 and DS6) when the depocentres were located in the southern sector of the basin. As a general result, the overall stratigraphic architecture of the eight depositional sequences (DS) displays an onlap geometry toward the north onto the underlying marine Jurassic substratum.

In the basin boundaries, there is no evidence of major normal faults that could have been active during the extensional stage. The extensional substratum (marine Jurassic deposits) appears to be continuous throughout the whole basin and consequently was not affected by any major stretching.

The extensional-ramp model proposed by Mas et al. (1993), Guimerà et al. (1995) and Mas et al. (2002; 2003 and 2011) better explains the basin infill geometry and evolution reconstructed in this work. Thus, the Cameros Basin formed over a south-dipping ramp joining two flats of a blind extensional fault located deep in the basement. The inversion of the basin was produced by a main thrust generated and located in the weakness zone of the Upper Triassic (Keuper) beds, which branched in depth with the Mesozoic extensional fault flat.

The results presented in this work represent a geological basis for the next basin studies presented herein in the next chapters, such as subsidence analysis, thermal and petroleum

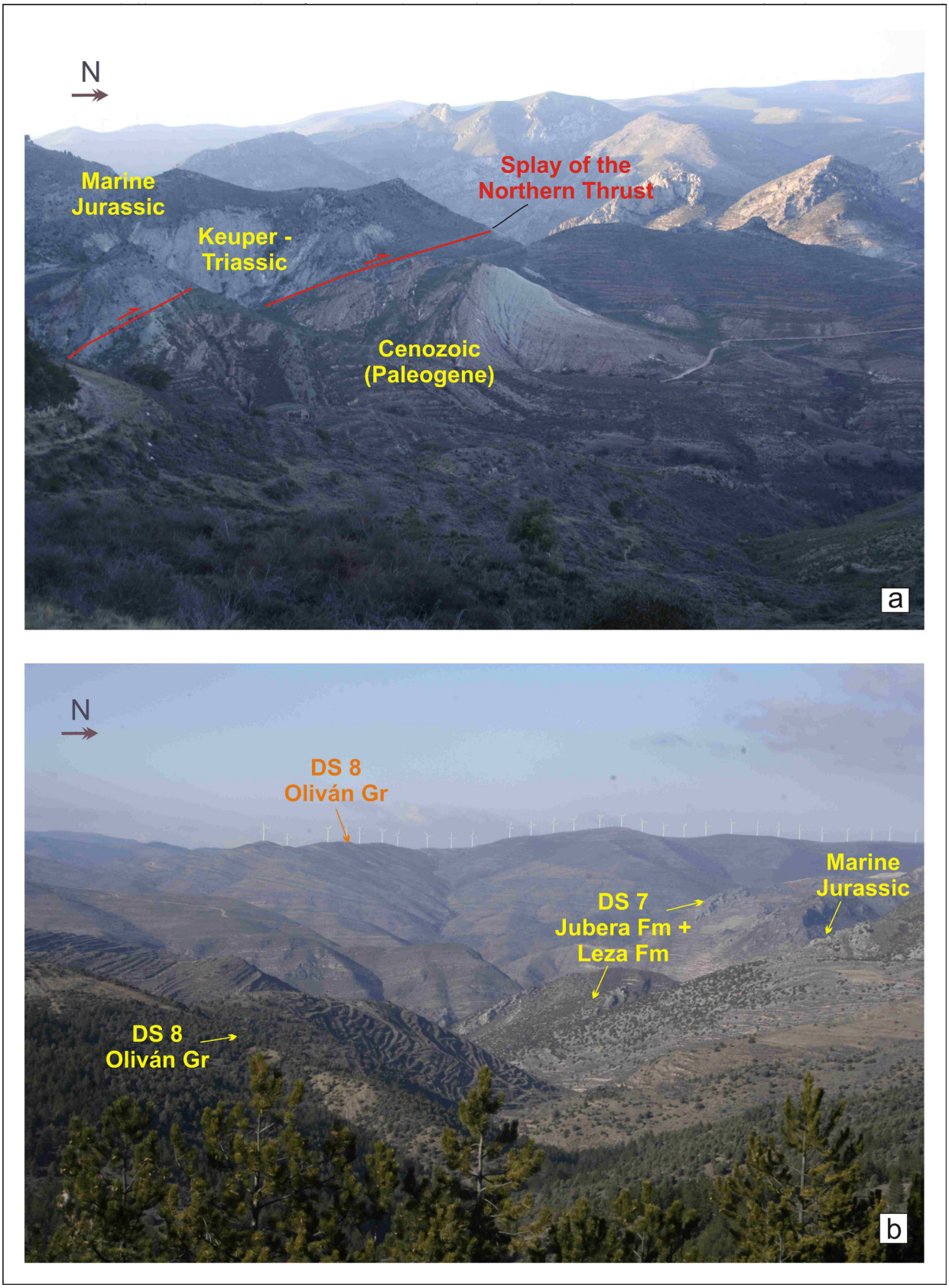

Plate 7.1 – Northern border of the basin: (a) splay of the main north thrust which makes crop out the Jurassic substratum and it creates an anticline in the footwall; (b) latest syn-extensional units which lye directly on the Jurassic substratum of the basin; Location of the points from where pictures were taken is indicated in Fig. 7.6

Plate 7.2 – (a) Northern border of the basin: latest syn-extensional units DS7 (Enciso Gr) and DS8 (Oliván Gr); (b) Large monocline cropping out in the northern sector of the basin, DS7 (Enciso Gr). Location of the points from where pictures were taken is indicated in Fig. 7.6.

Plate 7.3 – Large monocline cropping out in the northern sector of the basin: (a) DS6 (Urbión Gr); (c) DS3 (Valdeprado Fm) and the uppermost stratigraphic contact with the DS4 (Urbión Gr). Location of the points from where pictures were taken is indicated in Fig. 7.6

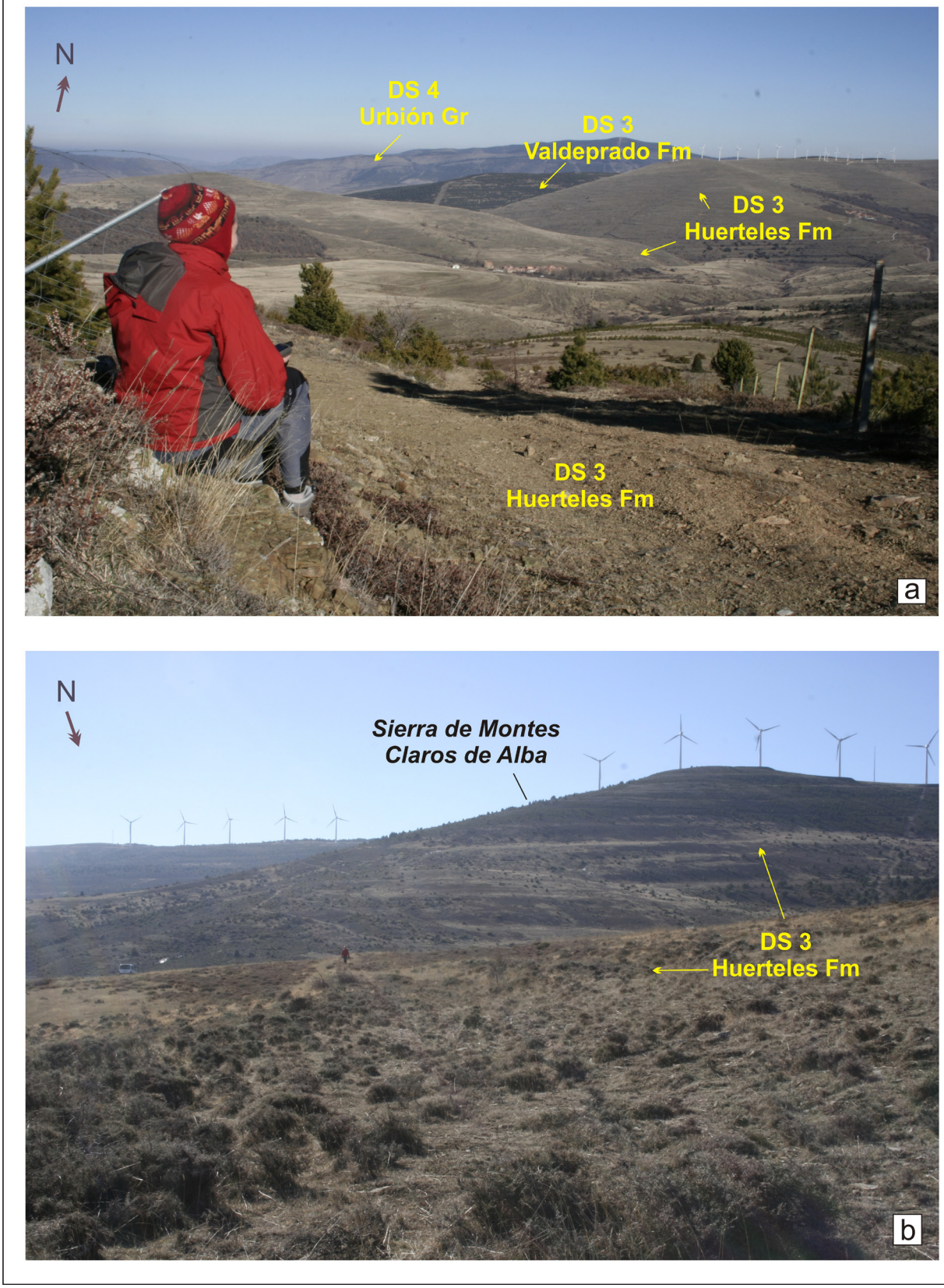

Plate 7.4 - Northern-central sector of the basin: (a) Large stratigraphic succession of the DS3 (Valdeprado Fm and Huerteles Fm) from the central sector of the basin toward the uppermost stratigraphic contact with the DS4 (Urbión Gr) to the north; (b) DS3• (Huerteles Fm) deposits in the central sector of the basin. Location of the points from where pictures were taken is indicated in Fig. 7.6

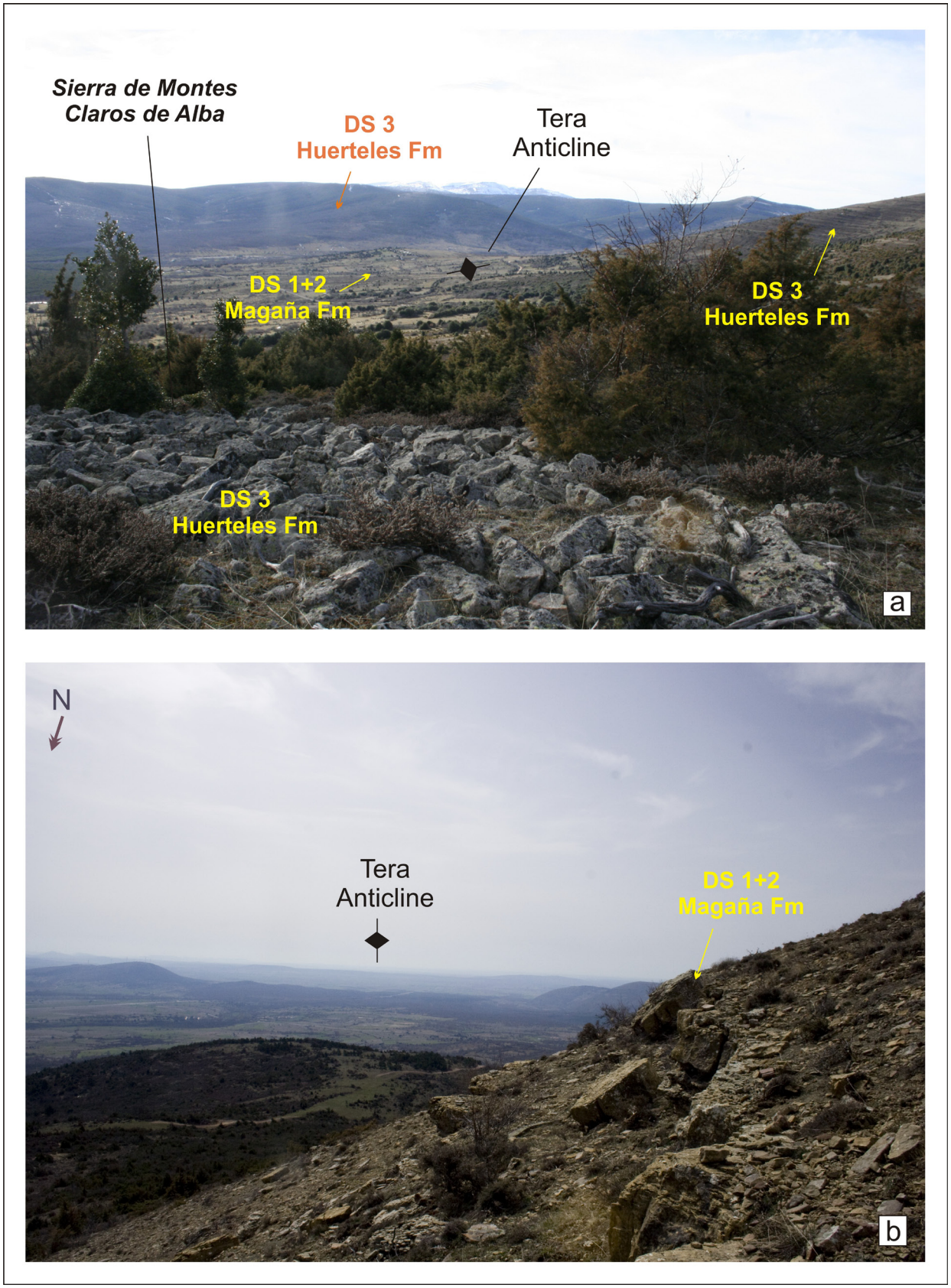

Plate 7.5: Central sector of the basin: (a) View of the northern Tera Anticline core; (b) View of the southern Tera Anticline core. Location of the points from where pictures were taken is indicated in Fig. 7.5

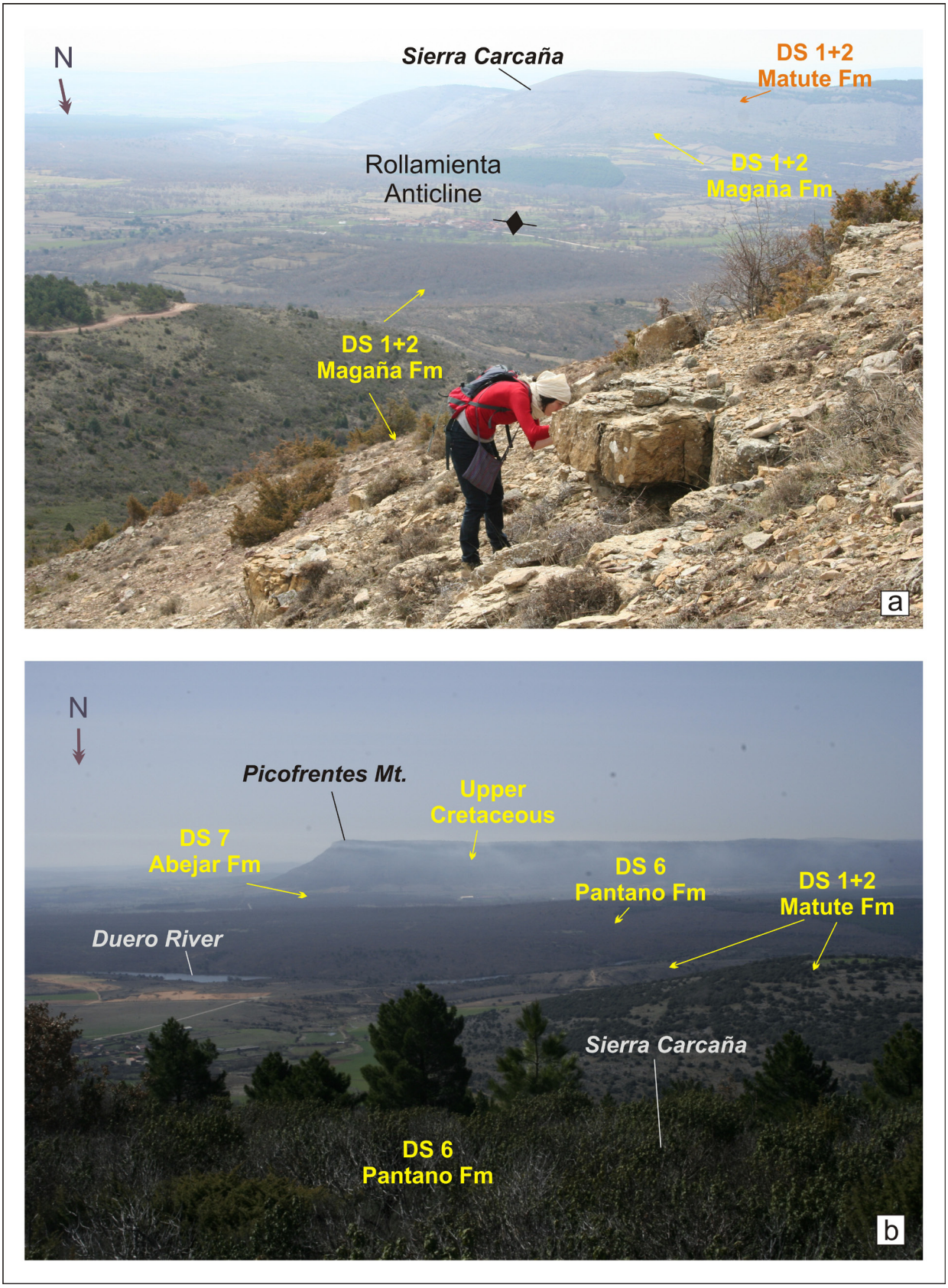

Plate 7.6 – Central sector of the basin: (a) View of the southern Tera Anticline core; (b) View of the Rollamienta anticline core. Location of the points from where pictures were taken is indicated in Fig. 7.5

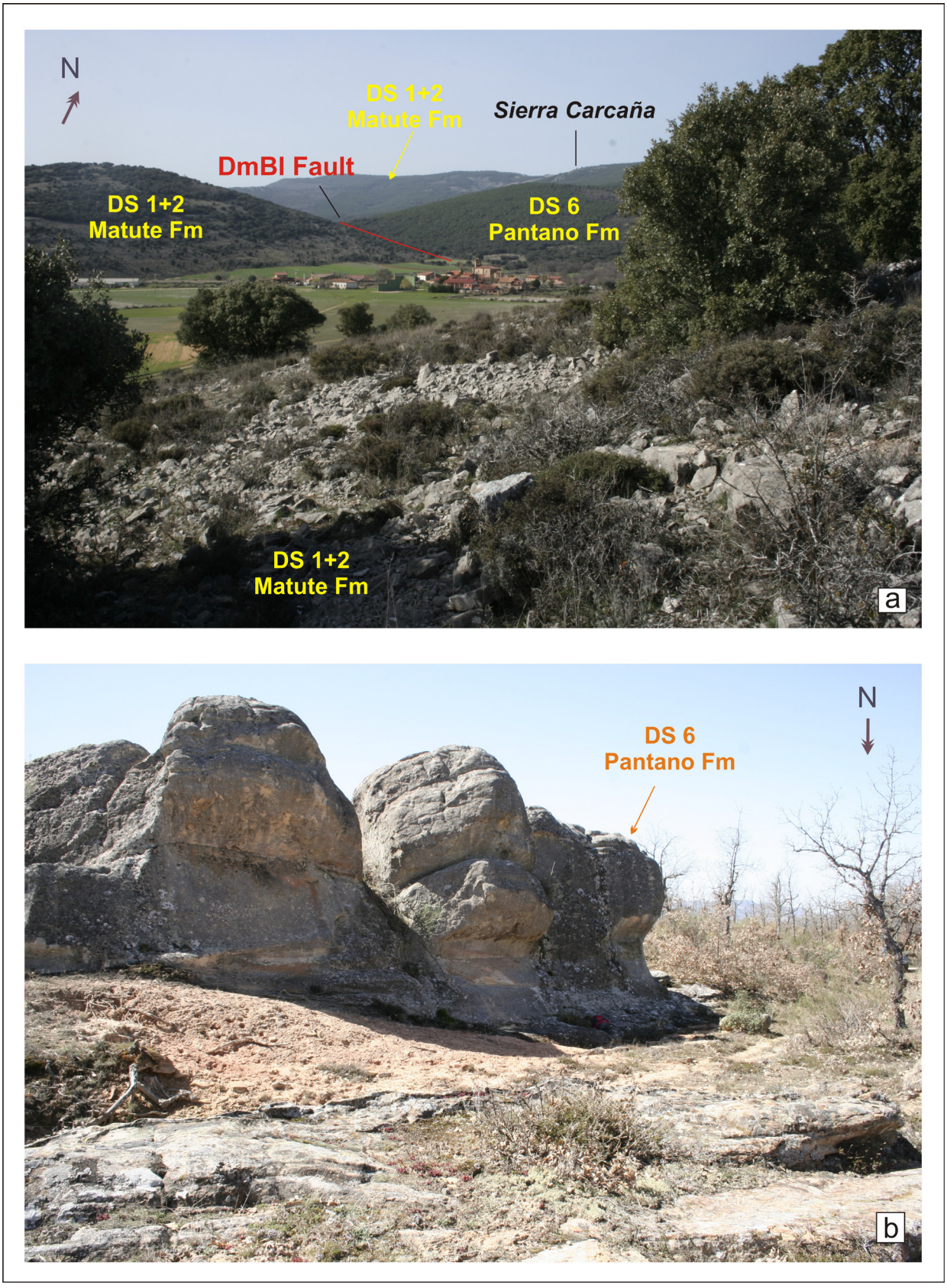

Plate 7.7 – Central-southern sector of the basin: (a) Post-sedimentary normal fault (DmBl Fault) that put in contact the Pantano Fm (DS6) with the Matute Fm (DS2); (b) Pantano Fm sandstone channel bodies. Location of the points from where pictures were taken is indicated in Fig. 7.5 and Fig. 7.7

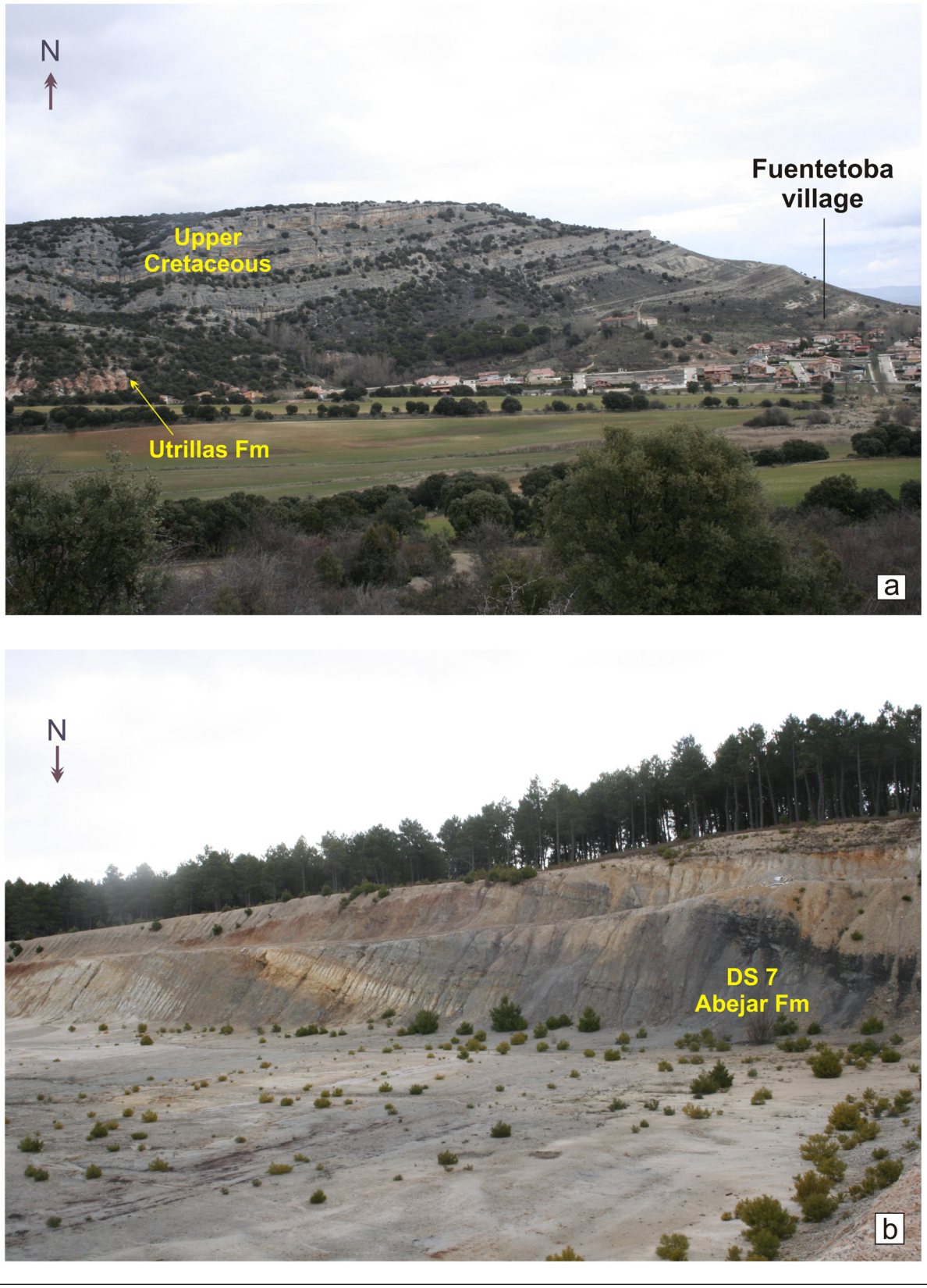

Plate 7.8: Southern sector of the basin: (a) Upper Cretaceous sequence; (b) Abejar Fm (DS7) in the Golmayo area. Location of the points from where pictures were taken is indicated in Fig. 7.7

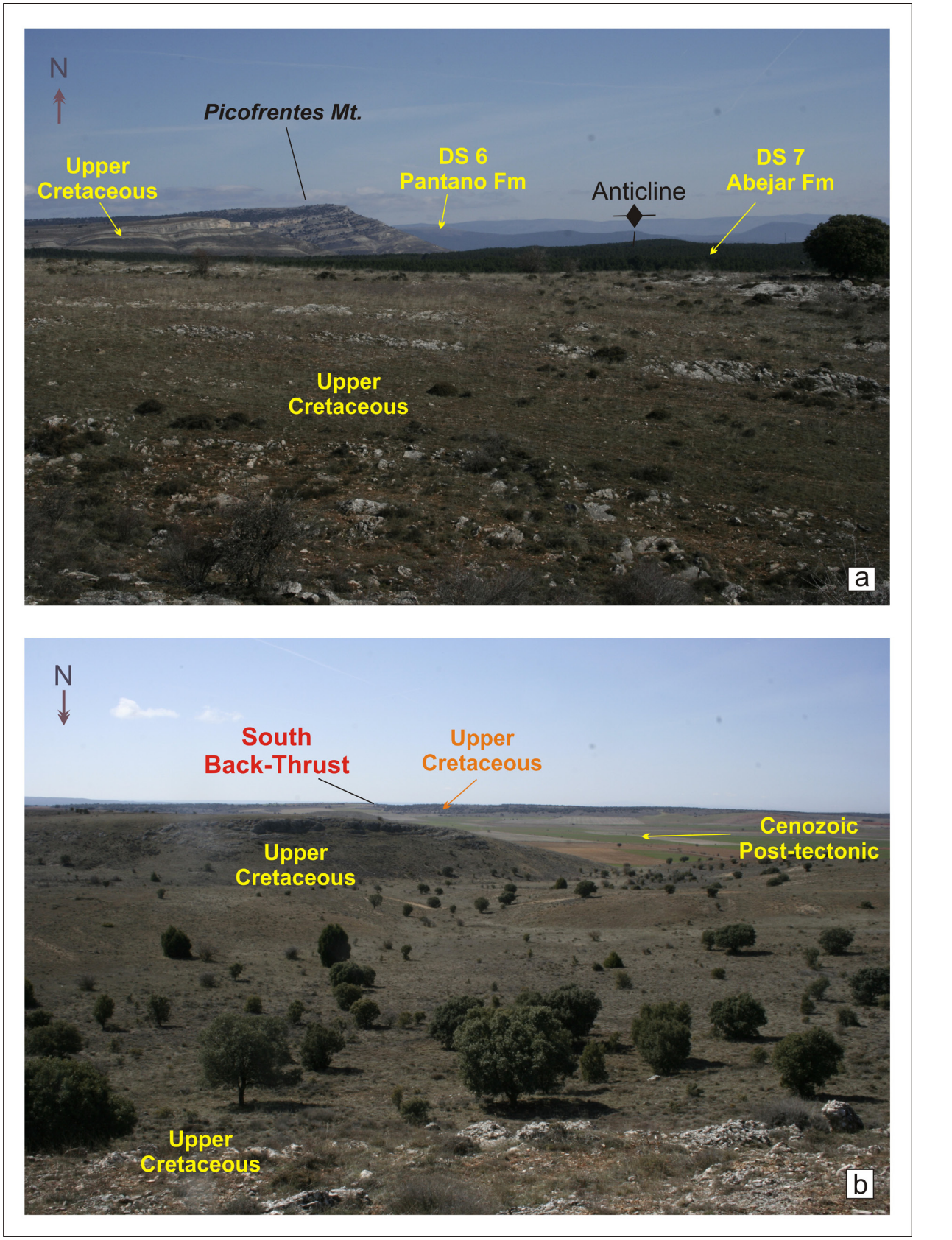

Plate 7.9: Southern border of the basin: (a) View of the latest units cropping out in the south of the basin; (b) View of the southern border of the basin, where the Upper Cretacesous units are unconformably covered by Cenozoic post-tectonic deposits. Location of the points from where pictures were taken is indicated in Fig. 7.7

Chapter 8

8. Subsidence Analysis and Heat Flow Estimation

8.1. INTRODUCTION

Crustal behavior is the main cause of basin subsidence and uplift, and determines much of the heat flow budget and temperature history. Thus for the purpose of modelling the thermal and geologic history of a basin the tectonic origin and the plate-tectonic position of the basin need to be considered. A characteristic thermal behavior can be assigned at each position with respect the tectonic plates, and these data can be used to estimate heat flow history associated with the basin evolution (McKenzie, 1978; Poelchau et al., 1997; Allen and Allen, 2009).

"Subsidence and uplift history can be derived from crustal models such as that of McKenzie (1978). However, these models require knowledge of crustal thickness and, in the case of extensional basins, the stretching factor (β). This means that in many cases an analysis of the stratigraphic column and sediment succession probably gives a more accurate subsidence history and heat flow estimation than that predicted by the theoretical models" (Poelchau et al., 1997). Royden and Keen (1980) and Royden (1986) demonstrate how surface heat flow within a basin can be deduced directly from its subsidence history. These authors consider that subsidence history depends basically from two factors: the crust thinning drive by tectonic forces and the heat flow affecting the lithosphere during the extension. As a consequence subsidence history and heat flow are strongly linked in an

extensional basin setting.

8.1.1. Basin subsidence

The evolution of a sedimentary basin is influenced by three factors: 1) the sediment accumulation and compaction, 2) the basement movement and 3) the base level changes (eustasy) (Burton et al., 1987). The play of these three factors determines the subsidence history of a basin (or geohistory of Allen and Allen, 2009). Subsidence history of a basin can be subdivided in two separated stages (Sleep, 1971; Watts and Ryan, 1976; McKenzie, 1978; Keen, 1979; Watts and Steckler, 1981; Royden and Keen, 1980; Royden, 1986; Allen and Allen, 2009). The first one corresponds to the "extensional stage" and it is characterised by a crust and mantle thinning for stretching and by a consequent replacement by hot asthenosphere. The isostatic response to this net density changes is expressed by a rapid change in elevation. "The initial elevation change in response to extension can be uplift or subsidence, depending on the predominance of density increase processes (relative to crustal rock replaced by denser mantle material) or of density decrease processes (relative to replace of colder denser mantle lithosphere with hotter less dense asthenosphere" (Royden, 1986). "The possible occurring subsidence is called initial subsidence and the depth immediately after extension is called the initial depth. Initial subsidence is a response to active extensional processes in the lithosphere and the area of subsidence is usually well localized and fault bounded. Sediments deposited during this phase are often deposited very rapidly, usually contain synsedimentary faults and may have rotated bedding" (Royden, 1986). The second stage of subsidence corresponds to a long term thermal cooling of the lithosphere that follows the extensional phase (from 50 to 200 My) (Allen and Allen, 2009, Royden, 1986). "This process is called thermal subsidence. Its duration it depends mostly from the heat distribution in the lithosphere, whereas it is independent of crustal thickness. Thermal subsidence is usually of greater areal extent than initial subsidence and is not usually confined o fault bounded. Sediments are relatively flat-lying and undisturbed, often extended over the entire basin area, onlapping onto basement rocks adjacent to the initial rifts" (Royden, 1986).

The sum of the initial and thermal subsidence perform a subsidence curve through time, which is called Total or Tectonic subsidence depending if sediment load has been removed (Allen and Allen, 2009, Royden, 1986). In order to obtain a subsidence curve, three corrections to the present stratigraphic thickness need to be carried out (Allen and Allen, 2009):

- Decompaction: present-day stratigraphic thickness must be corrected to account for the progressive loss of porosity with depth of burial;

- Paleobathymetry: the water depth at the time of deposition determines its position relative to a datum (such as present-day sea level);

- Absolute sea level fluctuations: changes in the paleo sea-level throughout time.

"The addition of a sediment load to a sedimentary basin causes additional subsidence of the basement. This is a simple consequence of the replacement of water, air or sediment. The total subsidence is therefore portioned into that cause by the tectonic driving force and that due to the sediment load. The way in which this portioning operates depends on the isostatic response of the lithosphere. The simplest assumption is that any vertical column of load is compensated locally (Airy isostasy). This implies that the lithosphere has no strength to support the load. Alternatively, the lithosphere may transmit stresses and deformation laterally by regional flexure.

The technique whereby the effects of the sediment load are removed from the total subsidence to obtain the tectonic contribution is called backstripping. Principles and methodology of the backstripping technique are explained in the methodology paragraphs of this chapter (8.2.1). Backstripped subsidence curves are useful in investigating the basin-forming mechanisms (Allen and Allen, 2009).

8.1.2. Basin basal heat flow calculation

"In order to calculate the amount of crustal attenuation and the amount of heating that occur during formation of a sedimentary basin, it is necessary to consider the following: 1) to distinguish accurately between the initial and thermal phases of basin formation; 2) to determine the magnitude of the initial subsidence; 3) to determine rates of thermal subsidence and heat flow and 4) to estimate the pre-extensional thermal structure (or thickness of the lithosphere)" (Royden, 1986).

"In order to calculate the subsidence and heat flow histories of an extended region, crustal thinning and lithospheric heating need to be described by simple parameters. Crustal thinning can easily be described by a thinning factor δ (so that if the crustal thickness before stretching is (h), the thickness after stretching is (h/δ). The thinning factor describes the net crustal thinning. The amount of heat distributed throughout the lithosphere is described by two parameters: δ to describe the assumed post-rift geotherm in the crust and β to describe the assumed post-rift geotherm in the mantle lithosphere. δ describes also the crustal thinning, so crustal heating and crustal thinning are linked. Differently the mantle heating is independent from the crustal thinning" (Royden, 1986)

A series of different equations that give an analytical solution to the initial and thermal subsidence and to the relative heat flow, considering the parameters β and δ, was performed by Royden (1986). "Equations are calibrated with oceanic data. After that equations are presented in a graphical form, to allow simple and fast determinations of extension in a sedimentary basin.

All the plots presented assume h/l = 0.35 (h = 35 km and l = 125 km), where (h) is the crustal thickness before stretching and (l) the lithosphere thickness. Errors in (1-h/l)2 of about 20% are introduced when (h) is taken to be 25 or 45 km. Error is zero when $\beta - \delta = 0$. All subsidence must be water loaded, so that corrections for sediment loading and compaction are already assumed (Sclater and Christie, 1980)" (Royden, 1986).

The reconstructed graphs show initial depth, thermal subsidence and surface heat flow as function of β and δ parameters. The combined use of these plots can performs a fast determination of the extension parameters in a basin like the surface heat flow recorded after the extensional phase. In this work especially attention has been focused on the heat flow determination. Initial subsidence and thermal subsidence data performed by the subsidence history analysis have been used.

8.2. SUBSIDENCE ANALYSIS AND HEAT FLOW ESTIMATION IN THE CAMEROS BASIN

The extensional Cameros Basin, formed during the Mesozoic Iberian Rifting period (Late Jurassic-Early Cretaceous) and inverted during the Alpine Orogeny, underwent a striking tectonic, sedimentary and thermal evolution, which makes this basin a very interesting subject for a basin scale analysis.

The Cameros Basin is a singular example of a basin where the accommodation space was formed by an extensional deep detachment instead of by a basin-bounding normal fault (Mas et al., 1993; Guimerà et al., 1995; Omodeo Salé et al., 2014). As a result of the hangingwall displacement along the deep detachment, the depocentral areas migrate laterally, instead of being vertically superimposed, lapping on the pre-rift substratum (Mas et al., 1993; Guimerà et al., 1995; Omodeo Salé et al., 2014). Consequently the maximum subsident area in the basin change throughout the time, following the movement along the extensional deep detachment. In the Mesozoic Iberian Rifting context the Cameros Basin experienced the highest subsidence (Salas et al., 2001), with the deposition in the maximum vertical thickness of 6500 m of sediments, of a mainly continental fluvial-lacustrine nature, in less than 50 My (Omodeo Salé et al., 2014). These features make the Cameros Basin an interesting object for a basin analysis study, where the related results can help to determine the basin infill pattern and the basin forming-mechanisms.

Besides to influence the subsidence trend, the extensional basin forming-mechanism could have important consequence on the heat flow affecting the basin during its evolution. In fact the basal heat flow of a basin strictly depends on the amount of lithosphere stretching and initial thickness (Royden and Keen, 1980; Royden, 1986). The stretching of the lithosphere would determine the depths of asthenosphere upraise, which determine the amount of the heat flow.

Thus the result of the heat flow calculation can perform interesting discussion on the extensional basin mechanisms. Calculation of the basal heat flow affecting the basin during its evolution represents an important achieve if the thermal history of the basin would be modelled. Basal heat flow is in fact the most important heat input into a sedimentary basin (Poelchau et al., 1997). Therefore definition of the basal heat flow is one of the most important variables which need to be determined when the thermal history of a basin want to be modelled (Poelchau et al., 1997).

In this chapter a subsidence analysis of the basin and a estimation of the maximum heat flow recorded at the end of the extensional stage were performed. Results would improve the understanding of the crustal behavior and the extension forming mechanism in the Cameros Basin area.

8.3. METHODS AND DATA

The degree of burial and the tectonic deformation forming the basin were calculated from subsidence analysis and were subsequently used to determine the heat flow affecting the basin.

Analyses were carried out in the central part of the basin, where geometry, structure and basin infill thickness were calculated in the previous **Chapter 7** (Fig. 8.1). In this area pre-extensional, syn-extensional and post-extensional units crop out with their maximum thickness. Thus, a reliable estimation of the burial history and maximum heat flow which characterise the basin can be obtained analyzing data collected in this area. Lithological Group and Formation forming the pre-extensional, syn-extensional and post-extensional units in the study area are summarized in the chronostratigraphic framework shown in Fig. 8.2. More detail on the sedimentology and depositional environments of these units are described in the **Chapter 7**.

The structure and geometry of the basin infill used for calculation were deduced from the balanced geological cross-section and its restoration prior to the Alpine inversion performed in **Chapter 7** (Fig. 8.3). The balanced geological cross-section (Fig. 8.3a) represents the inverted basin infill thickness before erosion, whereas the restored section (Fig. 8.3b) shows the basin infill geometry and thickness before the inversion. Given that the main aim of this work is to reconstruct the subsidence of the basin and heat flow affecting the basin during its formation and infill processes, the subsidence analysis was directly based on the restored cross-section, without considering the inversion process. The most relevant erosion event occurred during the inversion stage (Eocene to Early Miocene), when the basin was uplifted. During the basin infill phase, corresponding to the pre-rift, syn-extensional and post-extensional stages, relevant erosion events were considered. The amount of the erosion occurred in the inversion stage was estimated considering the data provided by the balanced geological cross-section (Omodeo Salé et al., 2014, **Chapter 7**). A maximum vertical thickness erosion of 5500 m has been calculated in

the central part of the section, which gradually decreases toward the southern and northern end of the section (Omodeo Salé et al., 2014) (Fig. 8.3). Similar erosion amount has been previously estimated by Muñoz et al., (1997) and Casas-Sainz and Gil-Imaz (1998)

8.3.1. Subsidence analysis

For the subsidence analysis the contribution of the sediment load and the tectonic deformation that produce stretching of the lithosphere must be separated. Thus, curves for the sediment accumulation rates over time of total subsidence (sediment loaded) and for the tectonic subsidence (sediment unloaded) were calculated from eight virtual wells that were introduced into the restored cross-section for this purpose (Fig. 8.3b). Data of the virtual wells are displayed in Fig. 8.4, where the specific age, thickness and lithology corresponding to each unit are represented.

The number of units into which the basin infill was divided depends on the data available for dating. In the pre-extensional stage only one unit was considered, comprising the Jurassic (Kimmeridgian) carbonate deposits, which forms the syn-extensional substratum throughout the basin (Mas et al., 1993; Mas et al., 2003; Mas et al., 2011; Omodeo Salé et al., 2014). A representative thickness of 100 m and a depositional age ranging from 155.6 to 150.8 My were assumed. For the syn-extensional stage, the subsidence analysis units correspond to the depositional sequences defined by Mas et al. (2002, 2003, 2011). Depositional sequences (DS) represent the lower order units whose boundaries can be dated and traced throughout the basin. Since precise ages are necessary for a subsidence analysis and thermal model calculation, the DS age assignation was simplified. One example of this simplification is the age assignment applied to the DS3 upper boundary. DS3 has an essentially Berriasian or "Berriasian s.l." age (Mas et al., 2003); on the other hand, the DS4 lower boundary is Late Berriasian although the exact age is approximate. As a consequence, DS3 was considered to have been deposited in the Early Berriasian, whereas DS4 was assigned partially to the Late Berriasian. Finally, the post-extensional stage was divided into two units: a 100 m unit largely made up of clastic deposits (mainly sandstone), corresponding to the Utrillas Fm (Late Albian?), and a 550 m unit mainly made up of carbonates, spanning the Late Cretaceous. In this work, the latter unit was defined as "Upper Cretaceous".

The absolute age of the unit horizons used in this work (Fig. 8.1, Fig. 8.2 and Table 8.1) refers to the Stage dating reported by the Geological Time Scale of Gradstein et al., (2004) and Ogg et al., (2008).

To simplify the process of lithological assignation, each Formation and Group was represented by percentages of three main lithologies (limestone, sandstone and shale, Table 8.1). When a unit in a virtual well is formed by more than one Formation or Group, the resulting simplified

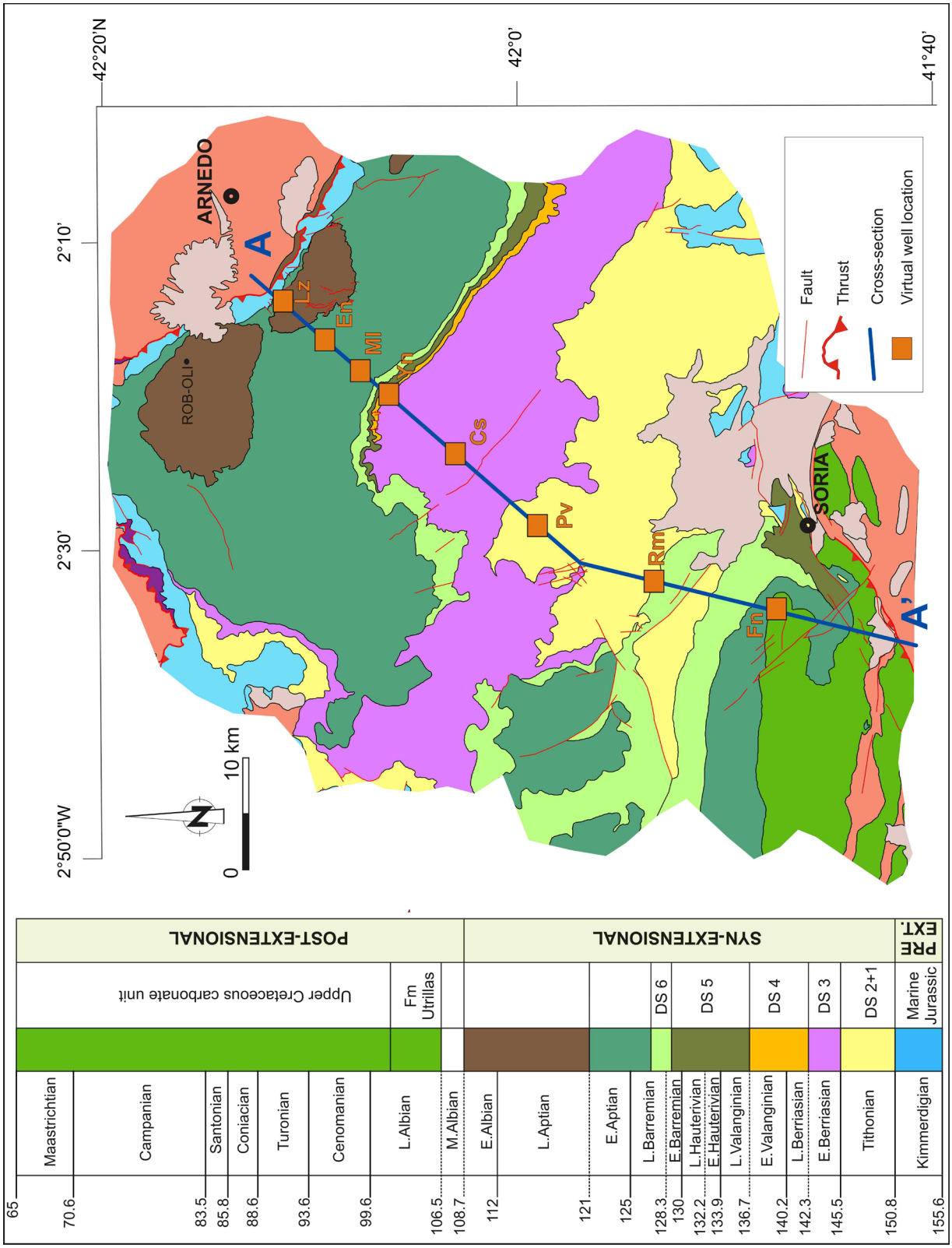

Fig. 8.1 Study area where data for the subsidence and heat flow analyses were collected. The geometry, structure and basin infill thickness of this area were determined by the reconstruction of the balanced geological cross-section (trace A-A') and its restoration (Fig. 8.2). Location of the virtual well used for subsidence and heat flow analyses is indicated: (Lz)-Lazaro, (En)-Enciso, (Ml)-Molino, (Yn)-Yanguas, (Cs)-Castillejo, (Pv)-Poveda, (Rm)-Rollamienta and (Fn)-Fuentetoba

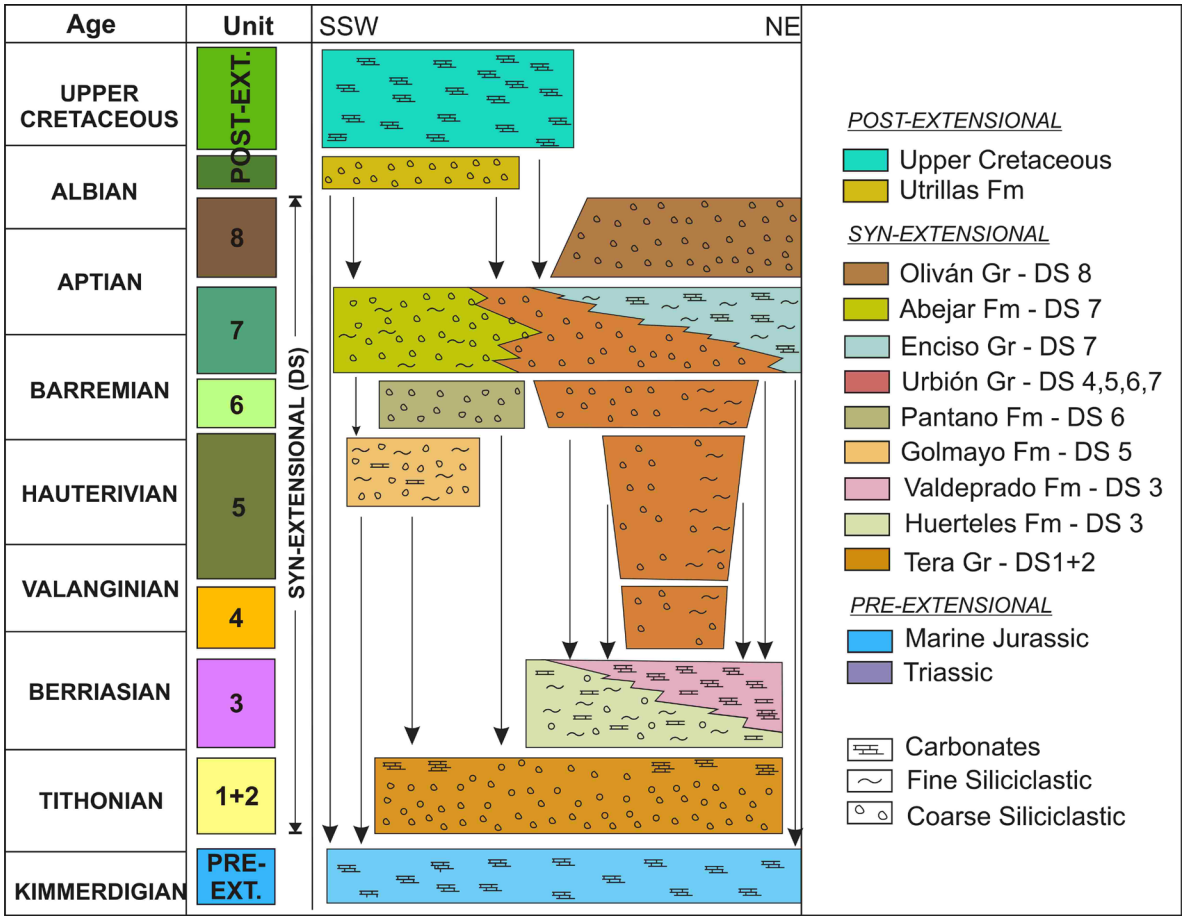

Fig. 8.2 - Chrono-stratigraphic sketch of the Cameros basin infill and distribution of the syn-extensional depositional sequences (DS) and the relative lithological units (Groups and Formations)

lithology was proportionally calculated with respect to the thickness of the Formation or Group considered (Table 8.2).

The burial history diagrams were obtained using the subsidence software of Waltham (2001). The variation in thickness and palaeo-depth of each sediment layer over time was sequentially calculated by removing the overlying layers and decompacting each layer in accordance with Allen and Allen (2009). Decompaction was calculated using empirical porosity/depth equations (Sclater and Christie, 1980) for the specific lithology of each layer:

$$\Phi y = \Phi 0 \exp(-cy)$$

where Φy is the sediment porosity at a certain depth (y), $\Phi 0$ is the initial porosity and c is the compaction factor which is constant for each lithology. Φ and c used in this work refer to the values proposed by Sclater and Christie (1980) and Schmoker and Halley (1982) for each main lithology. The porosity and compaction factors were proportionally calculated with respect to the lithological composition of each unit (Table 8.2).

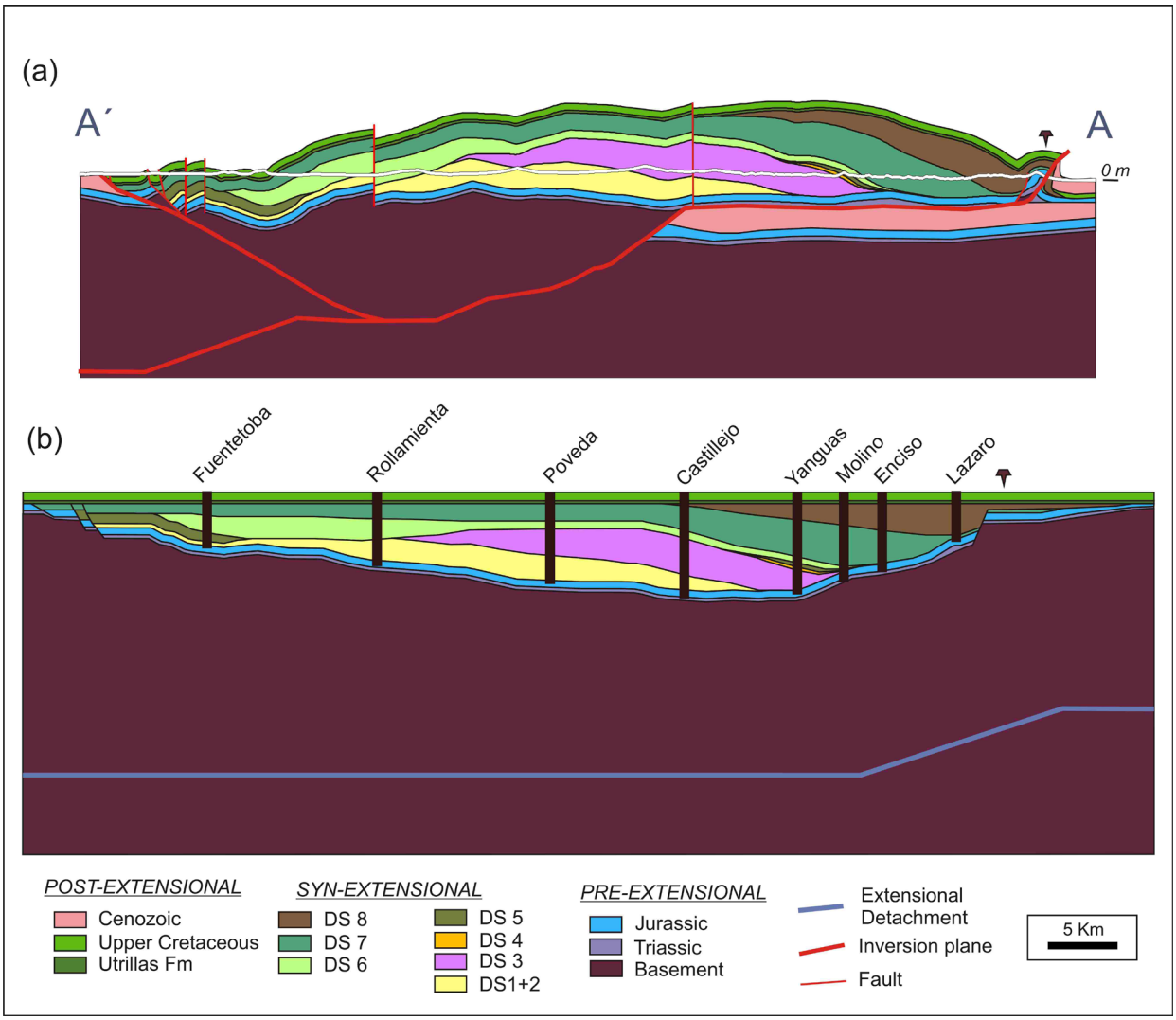

Fig. 8.3 - Balanced geological cross-section (a) and its restoration (b). In (b) is indicated the location of the virtual wells used for the subsidence and heat flow analyses

A curve for each virtual well was obtained to provide information about the thickness and burial variations of the units with time. The lowest curve represents the bottom of the basin where sedimentation started (basin basement or substratum). This curve is defined as "Total subsidence" and gives information about the accommodation space formed over time. The amount of total subsidence, obtained from the burial history diagram, generally requires palaeobathymetry and eustasy corrections, in order to obtain an accommodation curve (Allen and Allen, 2009). In this work, these corrections were not performed because of the continental to very shallow coastal nature of the deposits.

The tectonic subsidence was obtained by backstripping the total subsidence curves, eliminating the effect of the sediment load. The backstripping equation used is the one proposed by Watts and Ryan (1976), assuming a local compensation (Airy model):

$$Y = S\,[(\rho m-\rho s)/(\rho m-\rho w)]+Wd$$

where Y is the basement depth in the absence of sediment cover, S is the total sediment thickness, ρm, ρs and ρw are the densities of the mantle, sediments and water and Wd is the water sedimentation depth , respectively

8.3.2. Heat flow

The heat flow (mW/m^2) at the end of the extensional stage was estimated by means of the graphical approach method developed by Royden and Keen (1980) and Royden (1986) for which the initial depth and thermal subsidence values were used. The initial depth and thermal subsidence correspond to the syn-extensional and the post-extensional stages of the tectonic subsidence of the basin.

Initial depth and thermal subsidence values were extrapolated from the subsidence curves. Thus, corrections for paleobatimetry and isostasy were already taken into account. The obtained values have been plotted in the graphs proposed by Royden that express the following (Fig. 8.5): in (a) the initial depth after stretching as a function of the upper and lower lithosphere extension parameters (δ and β) and in (b) the thermal subsidence that occurs in a time interval ranging from immediately after stretching and 10 My after stretching, as a function of the upper and lower lithosphere extension parameters (δ and β). The intersected area, resulting from the superimposition of the value plotted in graph (a) with the one plotted in graph (b), has been plotted in graph (c) that express the surface heat flow at 10 My after stretching, as a function of the upper and lower lithosphere extension parameters (δ and β). An initial crustal thickness before stretching of 35 km and a lithosphere thickness of 125 km were considered (Simancas et al., 2003). A heat flow value that represents the amount of heat flow affecting the basin at the end of the rift stage was obtained. The corresponding estimations were made for each virtual well defined in Fig. 8.3b.

Fig. 8.4 - Virtual wells plotted onto the restored cross-section. For every unit considered, age (My), thickness (m) and lithology (%) are indicated. Thk = thickness; Lithol = lithology; Lm = limestone; Sn = sandstone; Sh = shale

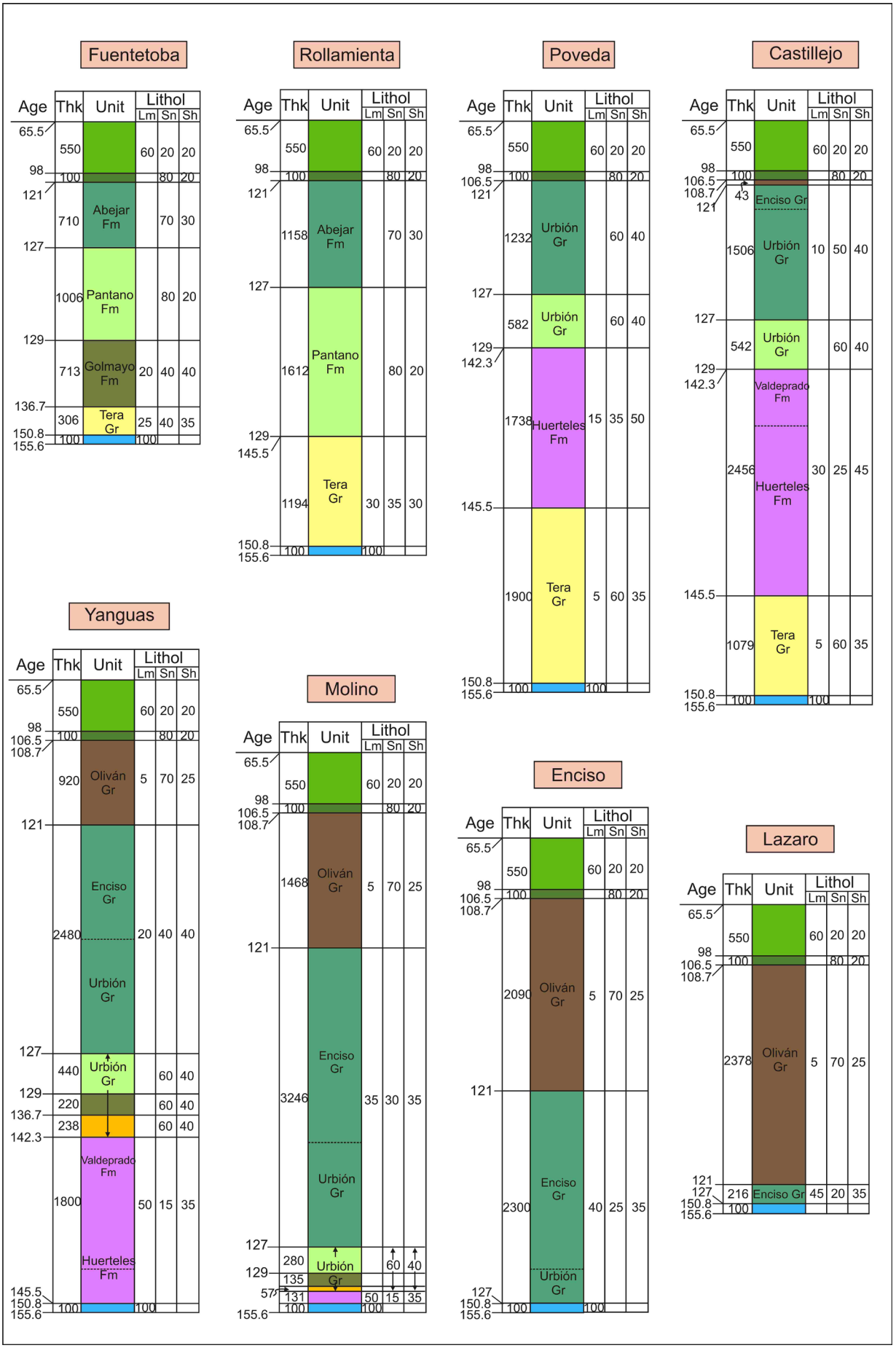
Fuentetoba
Age Thk Unit Lithol Lm Sn Sh
65.5
550 60 20 20
98
100 80 20
121
710 Abejar Fm 70 30
127
1006 Pantano Fm 80 20
129
713 Golmayo Fm 20 40 40
136.7
306 Tera Gr 25 40 35
150.8
100 100
155.6
Rollamienta
Age Thk Unit Lithol Lm Sn Sh
65.5
550 60 20 20
98
100 80 20
121
1158 Abejar Fm 70 30
127
1612 Pantano Fm 80 20
129
145.5
1194 Tera Gr 30 35 30
150.8
100 100
155.6
Poveda
Age Thk Unit Lithol Lm Sn Sh
65.5
550 60 20 20
98
106.5
100 80 20
121
1232 Urbión Gr 60 40
127
582 Urbión Gr 60 40
129
142.3
1738 Huerteles Fm 15 35 50
145.5
1900 Tera Gr 5 60 35
150.8
100 100
155.6
Castillejo
Age Thk Unit Lithol Lm Sn Sh
65.5
550 60 20 20
98
106.5
100 80 20
108.7
121
43 Enciso Gr
1506 Urbión Gr 10 50 40
127
542 Urbión Gr 60 40
129
142.3
Valdeprado Fm
2456 Huerteles Fm 30 25 45
145.5
1079 Tera Gr 5 60 35
150.8
100 100
155.6
Yanguas
Age Thk Unit Lithol Lm Sn Sh
65.5
550 60 20 20
98
106.5
100 80 20
108.7
920 Oliván Gr 5 70 25
121
Enciso Gr
2480 20 40 40
Urbión Gr
127
440 Urbión Gr 60 40
129
220 60 40
136.7
238 60 40
142.3
Valdeprado Fm
1800 50 15 35
Huerteles Fm
145.5
150.8
100 100
155.6
Molino
Age Thk Unit Lithol Lm Sn Sh
65.5
550 60 20 20
98
106.5
100 80 20
108.7
1468 Oliván Gr 5 70 25
121
Enciso Gr
3246 35 30 35
Urbión Gr
127
280 Urbión 60 40
129
135 Gr
57
131 50 15 35
155.6
100 100
Enciso
Age Thk Unit Lithol Lm Sn Sh
65.5
550 60 20 20
98
106.5
100 80 20
108.7
2090 Oliván Gr 5 70 25
121
2300 Enciso Gr 40 25 35
Urbión Gr
127
150.8
100 100
155.6
Lazaro
Age Thk Unit Lithol Lm Sn Sh
65.5
550 60 20 20
98
106.5
100 80 20
108.7
2378 Oliván Gr 5 70 25
121
127
216 Enciso Gr 45 20 35
150.8
100
155.6

Age (My)		Unit	Group/Formation	Lithology		
From	To			Limestone	Sandstone	Shale
65.5	98	Post-extensional	Upper Cretaceous	60	20	20
98	106.5		Utrillas Fm	0	80	20
121	108.7	DS8	Olivan Gr	5	70	25
127	121	DS7	Leza Fm	-	-	-
			Enciso Gr	45	20	35
			Urbión Gr	0	60	40
			Abejar Fm	0	70	30
129	127	DS6	Urbión Gr	0	60	40
			Pantano Fm	0	80	20
136.7	129	DS5	Urbión Gr	0	60	40
			Golmayo Fm	40	40	20
142.3	136.7	DS4	Urbión Gr	0	60	40
145.5	142.3	DS3	Valdeprado Fm	60	4	36
			Huerteles Fm	15	35	50
150.8	145.5	DS1+2	Tera Gr	5	60	35
150.8	164.7	Pre-extensional	Marine Jurassic	100	0	0

Table 8.1 - Lithology composition as a percentage of three main lithologies (limestone, sandstone, shale) for each unit considered in the subsidence analysis calculations

8.4. RESULTS

8.4.1. Subsidence analysis

Total and tectonic subsidence curves for every virtual well defined on the restored cross-section were obtained (Fig. 8.6). Total subsidence curves determine the amount of accommodation space formed in the different sectors of the basin at the different times. At the end of the syn-extensional and post-extensional sedimentation stages (65.5 My) the areas of maximum accommodation space correspond to the Castillejo and Yanguas wells, that show a total subsidence of 6833 and 6868 m, respectively (Fig. 8.6). The area corresponding to the Lazaro and Fuentetoba wells is where the lowest accommodation space was formed (3300 and 3700 m of total subsidence, respectively), whereas intermediate values of subsidence were recorded

Table 8.2 - Thickness, lithologies, Φ and values of parameter c attributed to units of each well

Virtual Wells/Units	Thickness (m)	Limestone (%)	Sandstone (%)	Shale (%)	Φ	c
Fuentetoba						
Upper Cretaceous	550	60	20	20	0.53	0.000468
Utrillas Fm	100	-	80	20	0.518	0.000318
DS7	710	-	70	30	0.532	0.000342
DS6	1006	-	80	20	0.518	0.000318
DS5	713	20	40	40	0.55	0.000416
DS1+2	306	25	40	35	0.544	0.0004165
Rollamienta						
Upper Cretaceous	550	60	20	20	0.53	0.000468
Utrillas Fm	100	-	80	20	0.518	0.000318
DS7	1158	-	70	30	0.532	0.000342
DS6	1612	-	80	20	0.518	0.000318
DS1+2	1194	30	35	30	0.5135	0.0004035
Poveda						
Upper Cretaceous	550	60	20	20	0.53	0.000468
Utrillas Fm	100	-	80	20	0.518	0.000318
DS7	1232	-	60	40	0.546	0.000366
DS6	582	-	60	40	0.546	0.000366
DS3	1738	15	35	50	0.563	0.0004275
DS1+2	1900	5	60	35	0.54	0.0003665
Castillejo						
Upper Cretaceous	550	60	20	20	0.53	0.000468
Utrillas Fm	100	-	80	20	0.518	0.000318
DS8	43	5	70	25	0.526	0.0003425
DS7	1463	10	50	40	0.548	0.000391
DS6	542	-	60	40	0.546	0.000366
DS3	2456	30	25	45	0.559	0.000453
DS1+2	1079	5	60	35	0.54	0.0003665
Yanguas						
Upper Cretaceous	550	60	20	20	0.53	0.000468
Utrillas Fm	100	-	80	20	0.518	0.000318
DS8	920	5	70	25	0.526	0.0003425
DS7	2480	20	40	40	0.55	0.000416
DS6	440	-	60	40	0.546	0.000366
DS5	220	-	60	40	0.546	0.000366
DS4	238	-	60	40	0.546	0.000366
DS3	1800	50	15	35	0.549	0.000479
Molino						
Upper Cretaceous	550	60	20	20	0.53	0.000468
Utrillas Fm	100	-	80	20	0.518	0.000318
DS8	1468	5	70	25	0.526	0.0003425
DS7	3246	35	30	35	0.546	0.0004415
DS6	280	-	60	40	0.546	0.000366
DS5	135	-	60	40	0.546	0.000366
DS4	57	-	60	40	0.546	0.000366
DS3	131	50	15	35	0.549	0.000479
Enciso						
Upper Cretaceous	550	60	20	20	0.53	0.000468
Utrillas Fm	100	-	80	20	0.518	0.000318
DS8	2090	5	70	25	0.526	0.0003425
DS7	2300	40	25	35	0.547	0.000454
Lazaro						
Upper Cretaceous	550	60	20	20	0.53	0.000468
Utrillas Fm	100	-	80	20	0.518	0.000318
DS8	2090	5	70	25	0.526	0.0003425
DS7	3600	45	20	35	0.548	0.0004665

close to the Poveda (6147 m), Molino (5680 m), Rollamienta and Enciso (4700 m) wells (Fig. 8.6).

The tectonic curves displayed in all the virtual wells a succession of steep and smooth slopes during the syn-extensional stage (from 150.8 to 108.7 My) (Fig. 8.7). Two main cycles of steep/smooth slopes can be identified in the curves. The first one ranges from the Tithonian to the Early Barremian (from 150.8 to 129 My), whereas the second one ranges from the Early Barremian to the Middle Albian (from 129 to 108.7 My) (Fig. 8.7). Steep slope curve correspond to period of rapid subsidence, whereas smooth slope curve represent periods of decelerated subsidence, where considerable time-gap in the sedimentary successions can be formed. In both these two cycles rapid and decelerated subsidence phases were not recorded synchronously in the basin (Fig. 8.8). In the first cycle the rapid subsidence phase was recorded from 150.8 My to 145.5 My in the Fuentetoba and Rollamienta wells, from 150.8 My to 142.3 My in the Poveda and Castillejo wells, from 145.5 My to 142.3 My in the Yanguas and Molino wells, whereas was not recorded at all in the the Enciso and Lazaro wells (Fig. 8.8). In the second cycle the rapid subsidence phase was recorded from 129 My to 127 My in the Fuentetoba and Rollamienta wells, from 129 My to 121 My in the Poveda, Castillejo, Yanguas and Molino wells and from 127 My to 108.7 My in the Enciso and Lazaro wells. As a consequence, in both cycles, even the duration of the two related decelerated subsidence phases were variable in the different virtual wells (Fig. 8.8).

Considering along the entire basin a medium tectonic subsidence of 1 km (Fig. 8.7) and an initial crustal thickness variable between 30 and 35 km, it is possible to calculate the vertical elongation (ve) in the basin as:

$$ve = (\text{final elongation} - \text{initial elongation})/(\text{initial elongation})$$

thus, for an initial crustal thickness of 30 km (ve) = -0.033, whereas for an initial crustal thickness of 35 km (ve) = -0.029, which average value is -0.03.

The vertical crustal stretching (vcs) can be calculated as:

$$vcs = 1 + (ve)$$

thus, in the Cameros Basin (vcs) = 0.97, which correspond to a 3% of vertical crustal stretching.

8.4.2. Heat flow

A heat flow value (mW/m^2) at the end of the syn-extensional phase for each virtual well was estimated using Royden's graphical method. Results of the estimation of the heat flow plotting the initial and thermal subsidence of each well on the abacus proposed by Royden is shown in in Table 8.3 and in Fig.8.9. The Heat flow values obtained are similar for all the virtual wells and range from 60 to 65 mW/m^2.

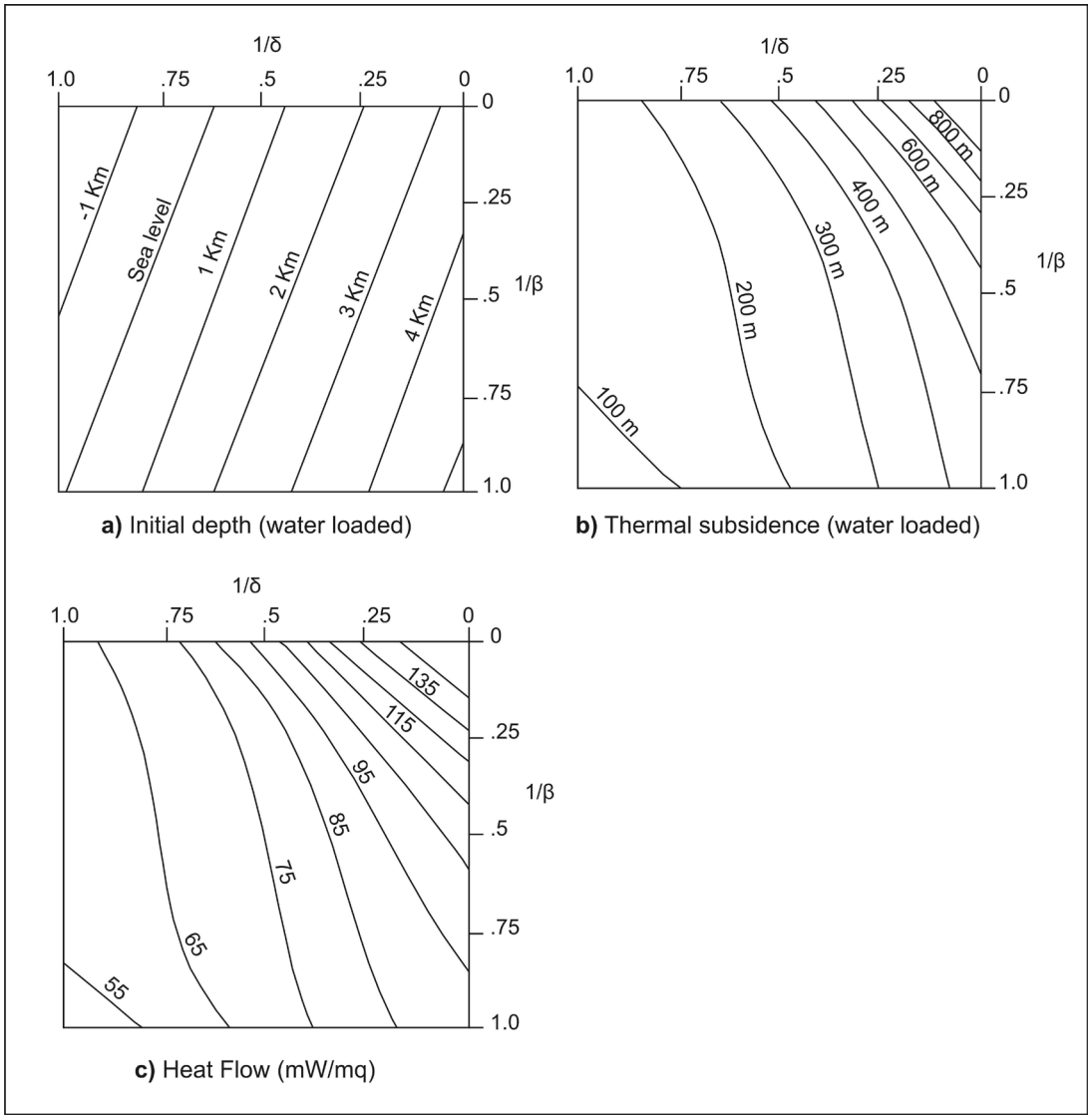

Fig. 8.5 - Abacus proposed by Royden (1986) to determine the maximum heat flow value (mW/m^2), recorded the end of the extensional stage, using subsidence analysis data. (δ) is the crustal thinning whereas (β) is the subcrustal thinning. Meaning and use of the abacuss is explained with detail in the text (Methods and Data section)

From this result the reconstruction of a paleoheat flow trend for the Cameros Basin, from the extensional stage to the present-day, was reconstructed. An average value of 64 mW/m^2 was considered to be the maximum value at the end of the extensional stage (108.7 My). Given that a gradual cooling of the lithosphere commenced in the post-extensional stage, a value of 50-55mW/m^2 was assumed in accordance with Allen and Allen (2009) (Fig. 8.10). Under present-day conditions, a heat flow of 60 mW/m^2 was adopted taking in account the commercial oil-well heat flow data located in the area (Castilfrio oil-well, see Fig. 7.10 for location) (Fernández et al. 1998) (Fig. 8.10).

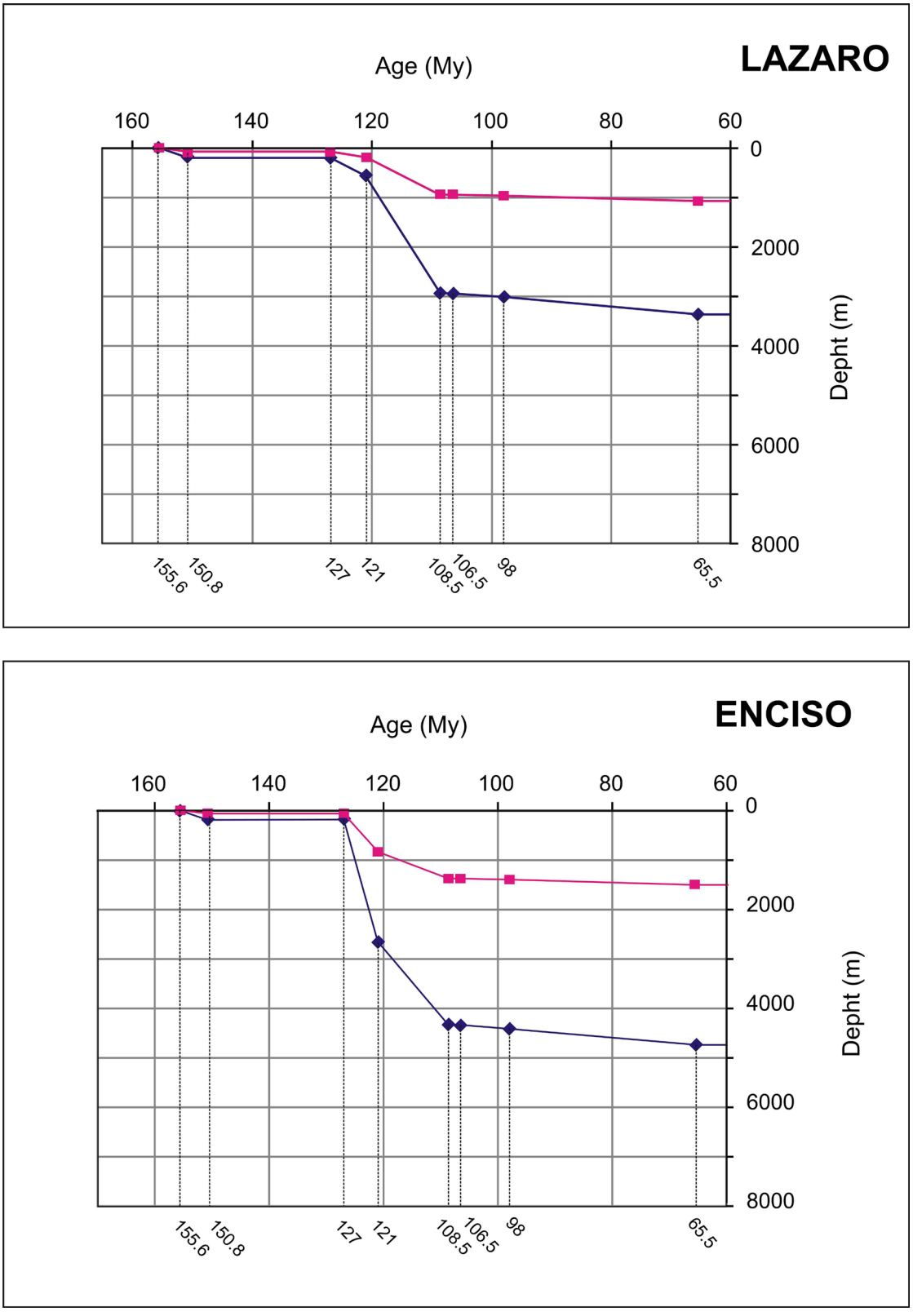

Fig. 8.6 (Part 1) - Total (blue) and Tectonic (pink) subsidence curves obtained for each well

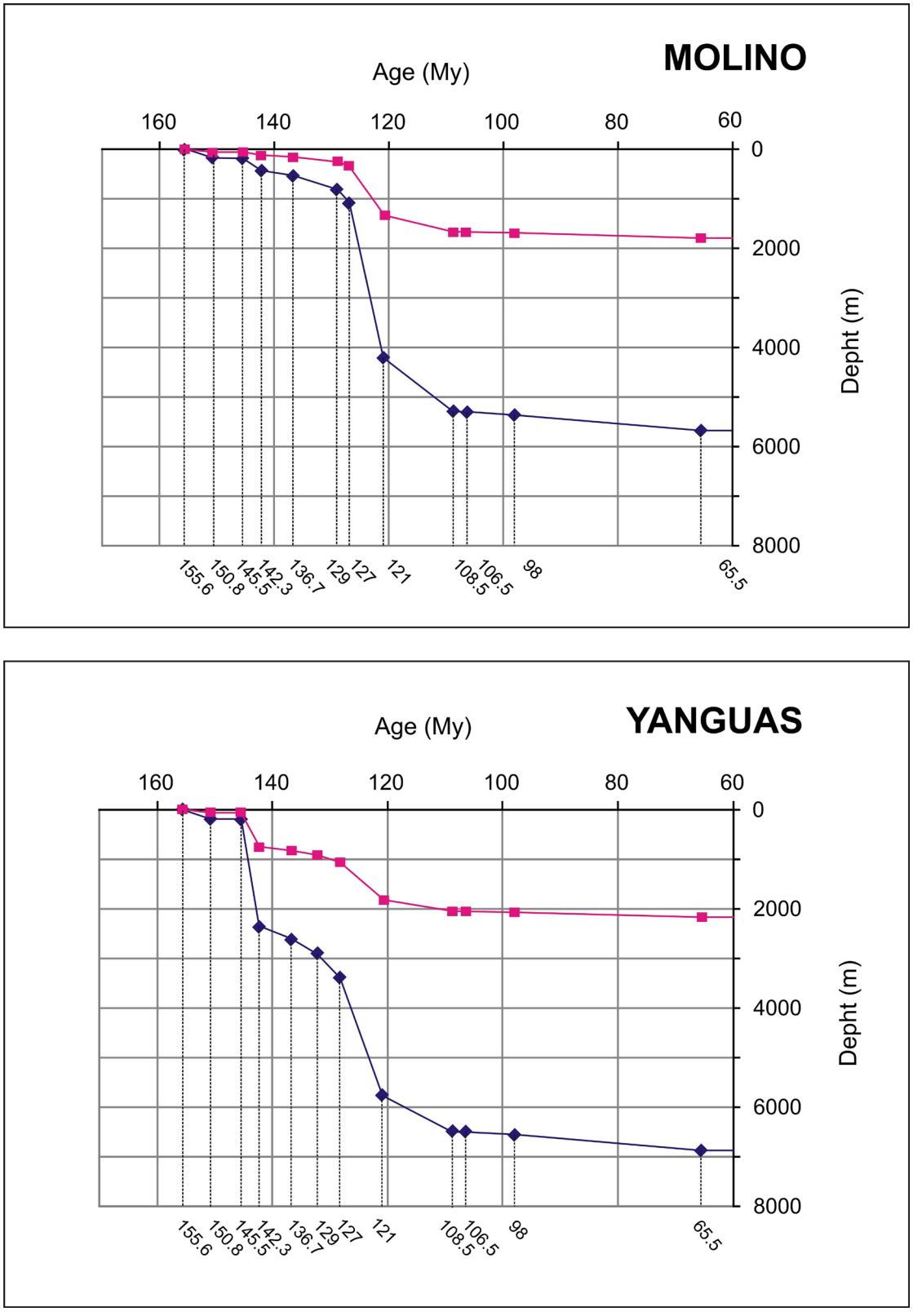

Fig. 8.6 (Part 2) - continued

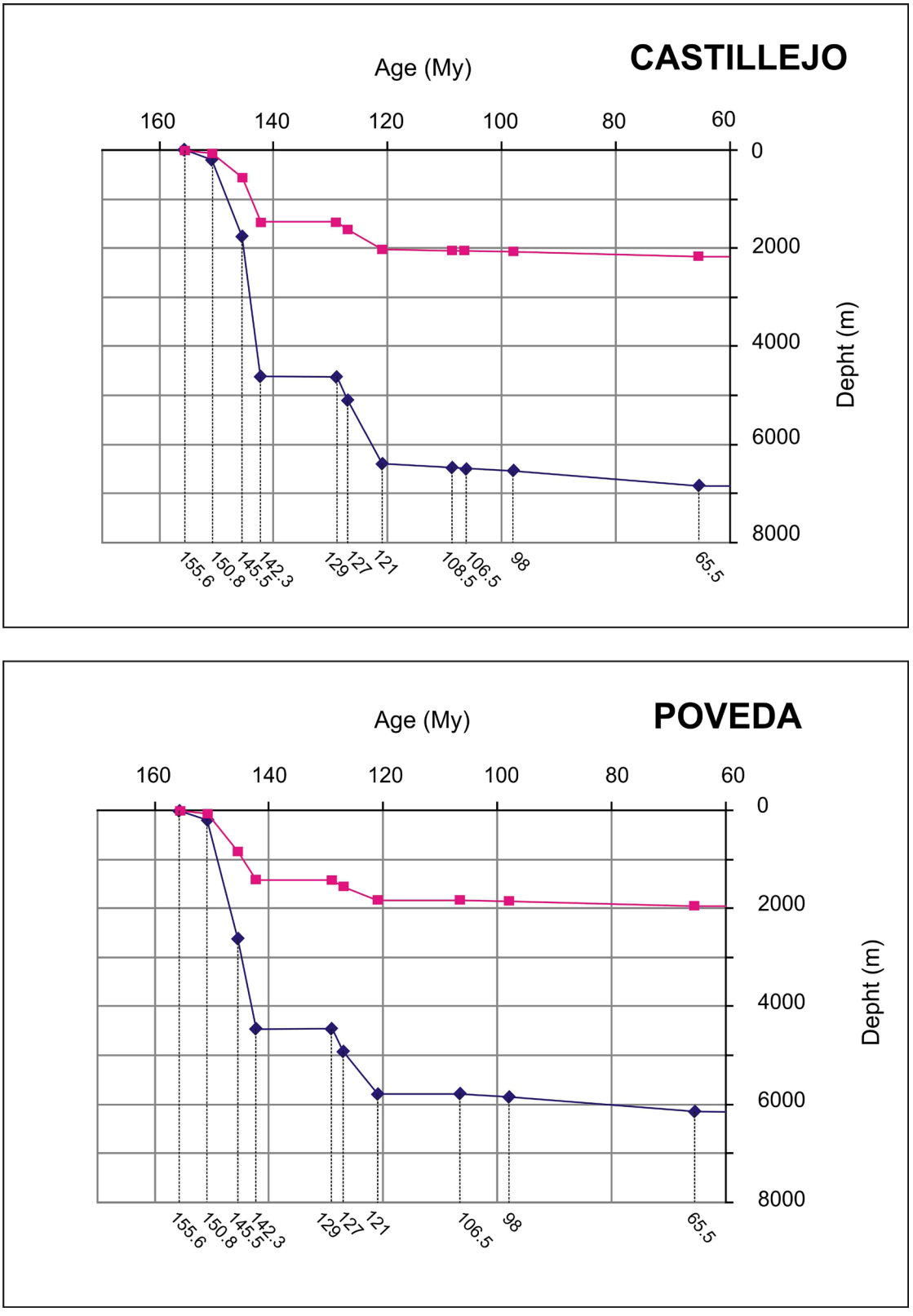

Fig. 8.6 (Part 3) - Total (blue) and Tectonic (pink) subsidence curves obtained for each well

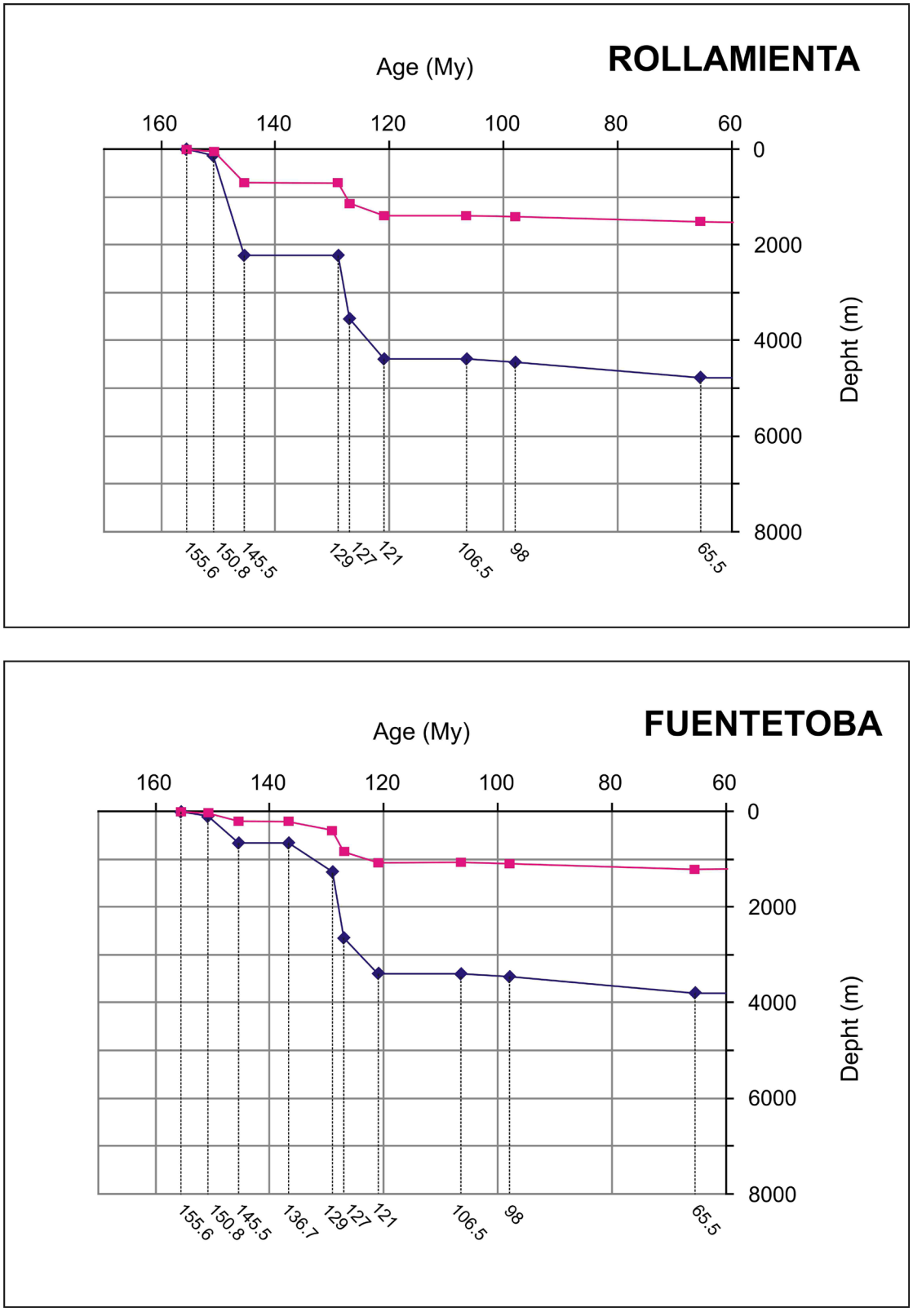

Fig. 8.6 (Part 4) - continued

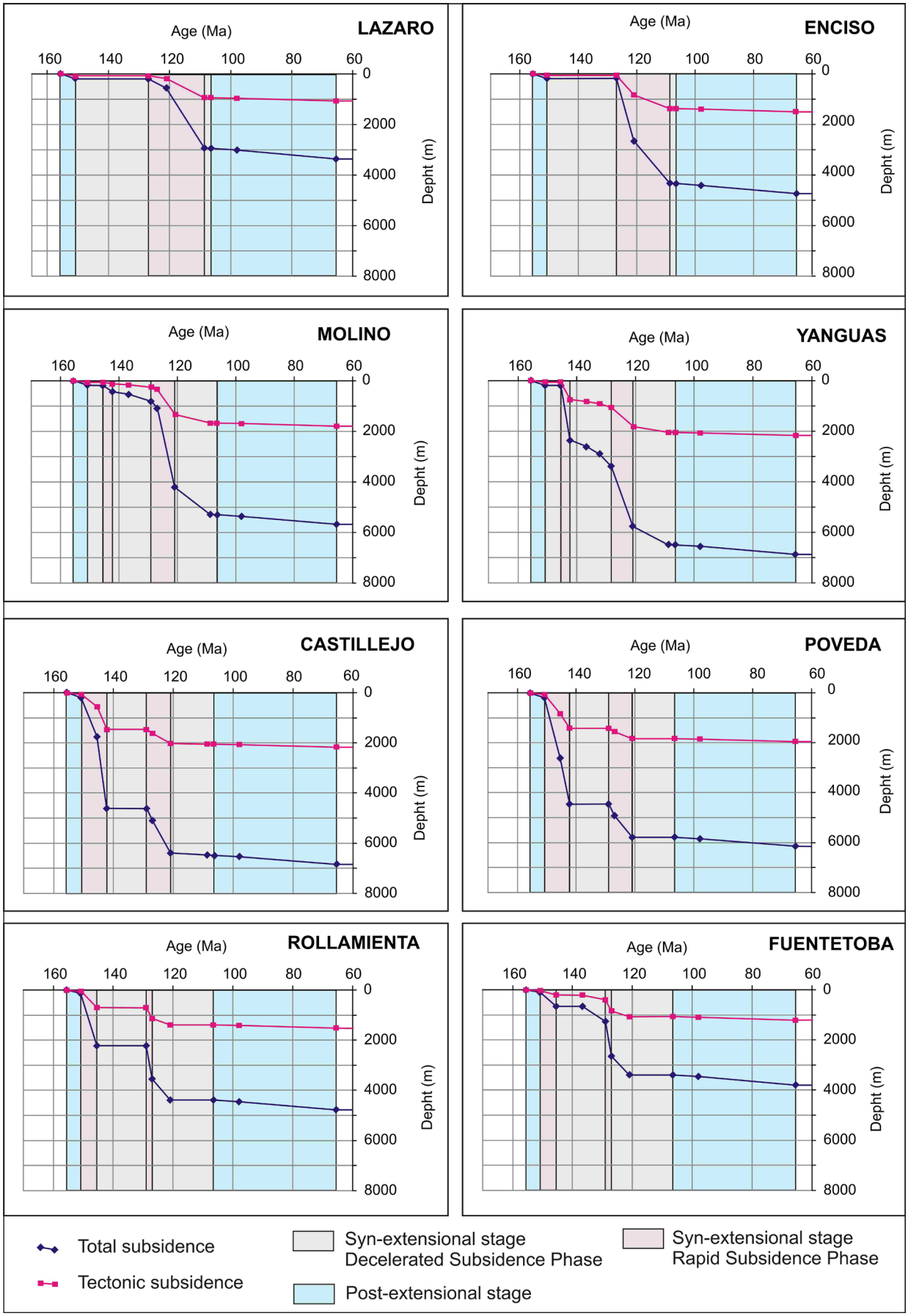
LAZARO
ENCISO
MOLINO
YANGUAS
CASTILLEJO
POVEDA
ROLLAMIENTA
FUENTETOBA
Age (Ma)
160
140
120
100
80
60
0
2000
4000
6000
8000
Depht (m)
Total subsidence
Tectonic subsidence
Syn-extensional stage
Decelerated Subsidence Phase
Syn-extensional stage
Rapid Subsidence Phase
Post-extensional stage

8.5. DISCUSSION

8.5.1. Subsidence and accommodation space

Tectonic subsidence analysis yields fresh insights into the basin subsidence trend and causes, eliminating the effect of the sediment load. The most remarkable feature obtained from the tectonic subsidence curves is the succession of steep and smooth slopes displayed in the curves from 150.8 to 108.7 My (Fig. 8.7). In general, this trend has been interpreted as a succession of syn-extensional and post-extensional stages, which is typical of intra-cratonic basins. These basins were formed during periods of repeated mechanical crustal stretching followed by periods of thermal relaxation (Allen and Allen, 2009). This mechanism has been considered to be responsible of the alternation of rapid and decelerated subsidence phase in a coeval Iberian Basin, the Maestrat Basin (Salas and Casas, 1993; Salas et al., 2001). However, if we consider the geometry of the basin infill before the inversion (Fig. 8.3b) a different interpretation must be found for the Cameros Basin. The geometry of all the units from DS1 to DS8 (150.8 My to 108.7 My) indicates that they were deposited during a syn-extensional regime, whereas the planar geometry, expansive overlap and the uniform thickness of the upper Utrillas Fm and Upper Cretaceous units (Fig. 8.3b), implicates the interpretation that all these units (from 108.7 My to 65.6 My) are post-extensional deposits (Bally and Snelson, 1980; Vail, 1987; Bott, 1992). Thus, the successions of steep and smooth slopes of the tectonic subsidence curve were interpreted as cycles of rapid and decelerated subsidence phases that occurred during the syn-extensional stage (Fig. 8.7, legend). The fact that the rapid/decelerated cycles were recorded diachronously along the section (Fig. 8.8) means that they were simultaneously rapid or decelerated subsidences in different parts of the basin. In the extensional-ramp syncline model these accelerated and decelerated subsident phases can be explained by accelerations or deceleration of the displacement over the deep fault.

The evolution of the accommodation space can be inferred from the total subsidence curves. The maximum accommodation space in the basin was reached in the central-northern sector at the end of the basin infill (65.5 My). Accommodation space gradually decreased towards the south of the basin, whereas it decreased more abruptly to the north. During the first rapid/decelerated subsidence cycle, the largest accommodation space was formed in the central sector of the basin (Castillejo, Poveda, Yanguas and Rollamienta wells) whereas in the second cycle, the largest accommodation space was formed in the northern sector of the basin (Lazaro, Enciso,

Fig. 8.7 - Total (blue) and Tectonic (pink) subsidence curves obtained for all the wells. Rapid and decelerated subsidence trend, corresponding with steep and smooth curves slopes, are indicated

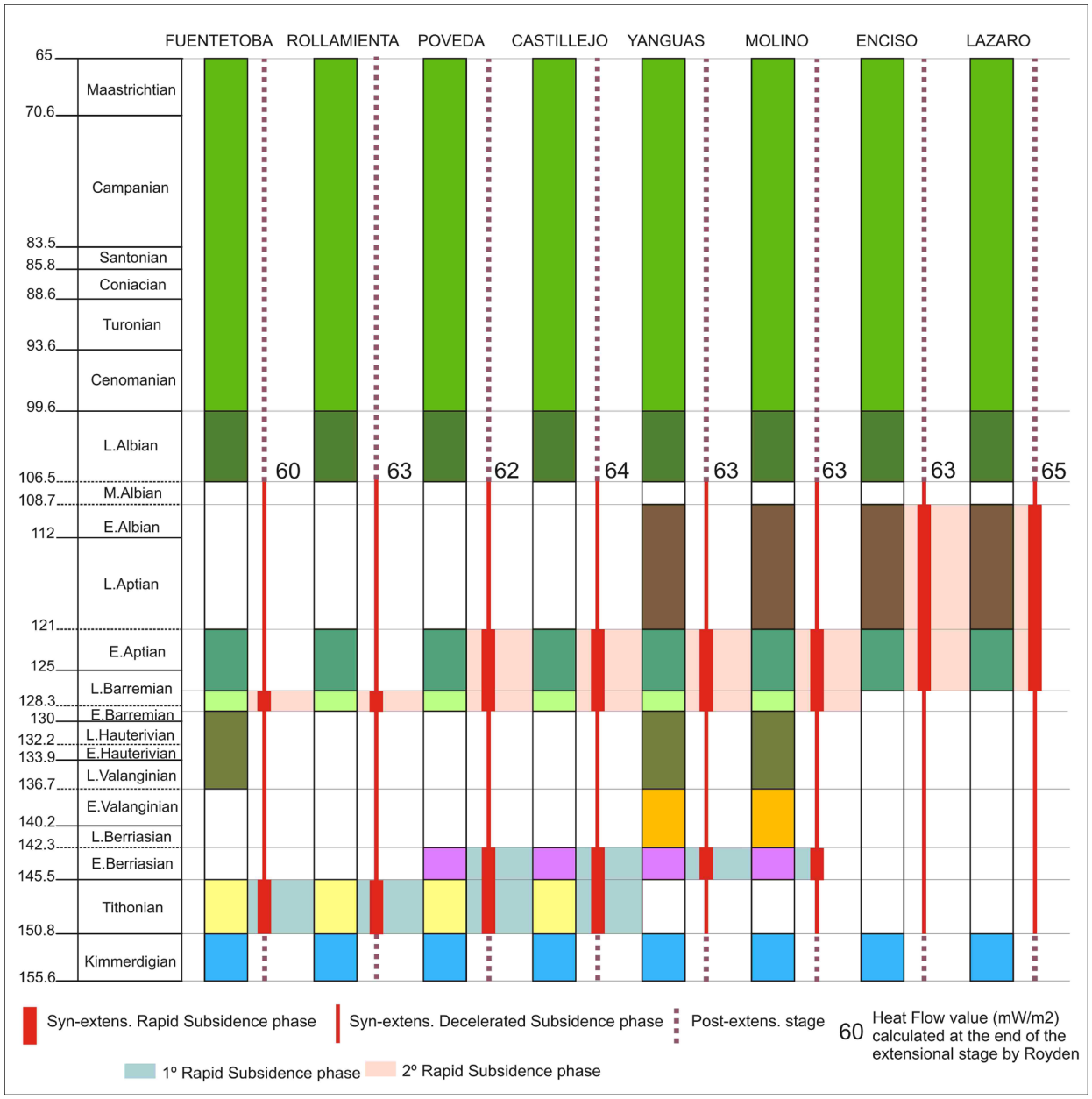

Fig. 8.8 - Synthesis of the subsidence history of the Cameros basin deduced from the interpretation of the tectonic subsidence curves obtained from the defined virtual wells. Heat flow values calculated at the end of each syn-extensional rapid subsidence phase are indicated

Molino and Yanguas wells).

The formation of a new accommodation space trend, as well as the diachronous record along the section of the rapid/decelerated subsidence cycles, can be related to the extensional mechanisms which form the basin. The hangingwall displacement toward the south, along the deep extensional detachment, caused the gradual lateral migration toward the north of the depocentres, thus north of the areas where new accommodation space formed. Furthermore the lateral migration of the depocenters can explain the diachronous record along the section

LAZARO well			HF (mW/m^2)	ENCISO			HF (mW/m^2)
Intial Subsidence (m)		**867**	**65**	Intial Subsidence (m)		**1315**	**63**
Time (My)	Subsidence (m)			Time (My)	Subsidence (m)		
150.8	58			150.8	60		
108.7	925			108.7	1375		
Thermal Subsidence (m)		**133**		Thermal Subsidence (m)		**124**	
Time (My)	Subsidence (m)			Time (My)	Subsidence (m)		
108.7	925			108.7	1375		
65.5	1058			65.5	1499		
MOLINO well			HF (mW/m2)	YANGUAS			HF (mW/m2)
Intial Subsidence (m)		**1617**	**63**	Intial Subsidence (m)		**1996**	**63**
Time (My)	Subsidence (m)			Time (My)	Subsidence (m)		
150.8	60			150.8	61		
108.7	1677			108.7	2057		
Thermal Subsidence (m)		**120**		Thermal Subsidence (m)		**116**	
Time (My)	Subsidence (m)			Time (My)	Subsidence (m)		
108.7	1677			108.7	2057		
65.5	1797			65.5	2173		
CASTILLEJO well			HF (mW/m^2)	POVEDA			HF (mW/m^2)
Intial Subsidence (m)		**1989**	**64**	Intial Subsidence (m)		**1771**	**62**
Time (My)	Subsidence (m)			Time (My)	Subsidence (m)		
150.8	60			150.8	60		
108.7	2049			108.7	1831		
Thermal Subsidence (m)		**113**		Thermal Subsidence (m)		**114**	
Time (My)	Subsidence (m)			Time (My)	Subsidence (m)		
108.7	2049			108.7	1831		
65.5	2162			65.5	1945		
ROLLAMIENTA well			HF (mW/m^2)	FUENTETOBA			HF (mW/m^2)
Intial Subsidence (m)		**1356**	**63**	Intial Subsidence (m)		**1041**	**60**
Time (My)	Subsidence (m)			Time (My)	Subsidence (m)		
150.8	31			150.8	31		
108.7	1387			108.7	1072		
Thermal Subsidence (m)		**124**		Thermal Subsidence (m)		**129**	
Time (My)	Subsidence (m)			Time (My)	Subsidence (m)		
108.7	1387			108.7	1072		
65.5	1511			65.5	1201		

Table 8.3 - Initial and thermal subsidence values determined from the tectonic subsidence curves for each virtual well together with the heat flow (mW/m2), estimated by using Royden's graph approach

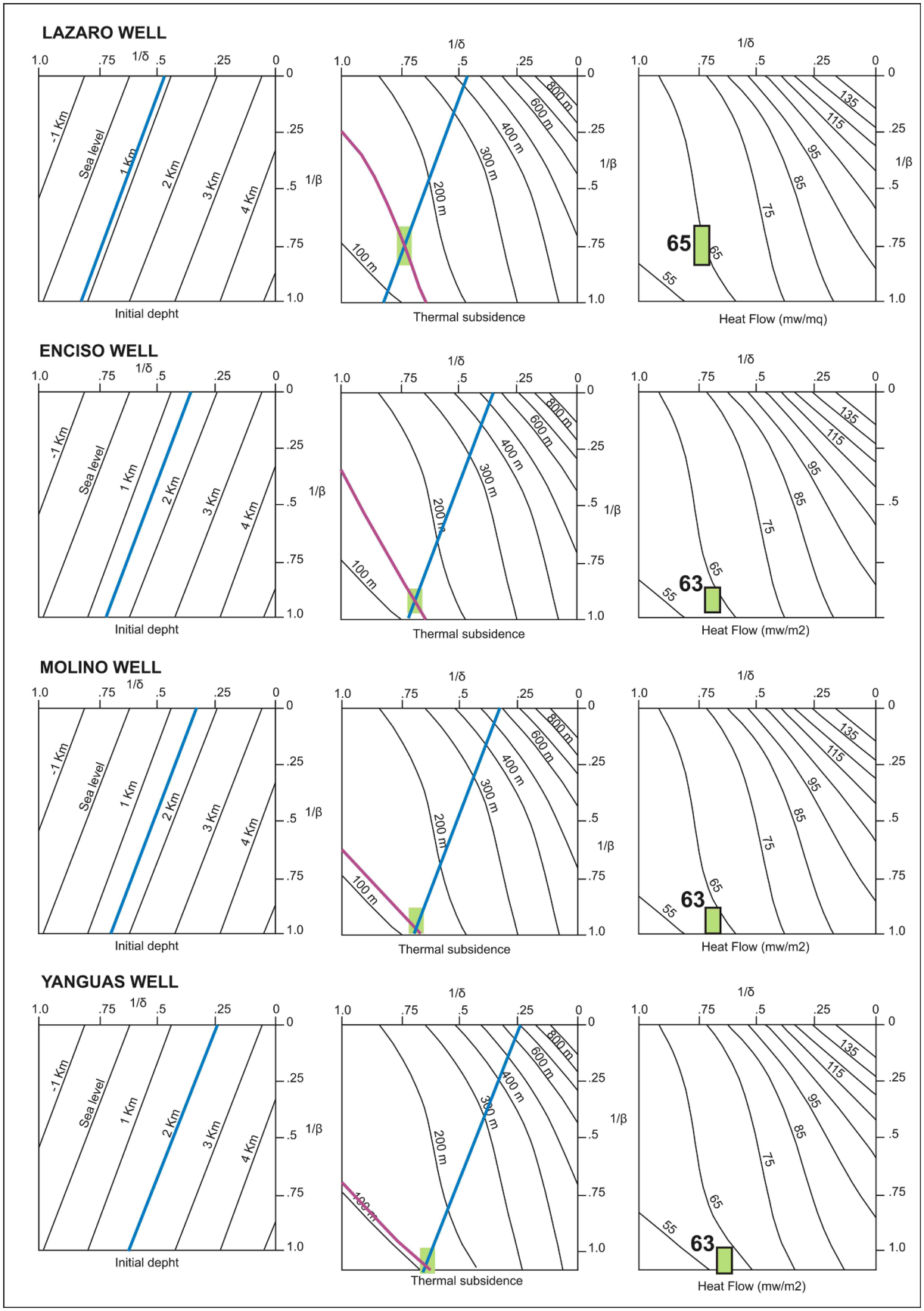

Fig. 8.9 (Part 1) - Estimation of the heat flow at the end of the extensional stage, plotting on the graphs the initial and thermal subsidence values determined for each virtual well (Table 8.3)

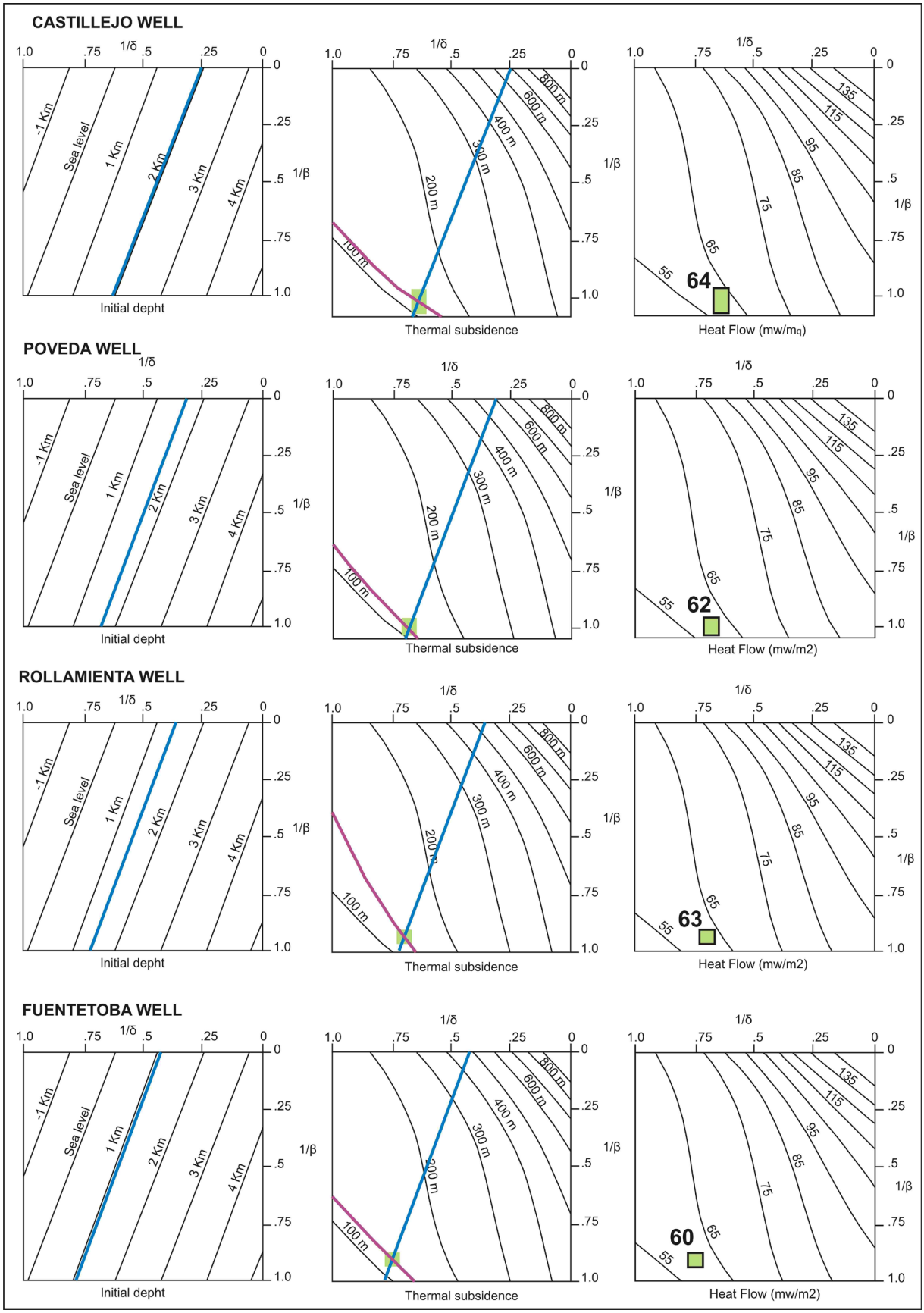

Fig. 8.9 (Part 2) - continued

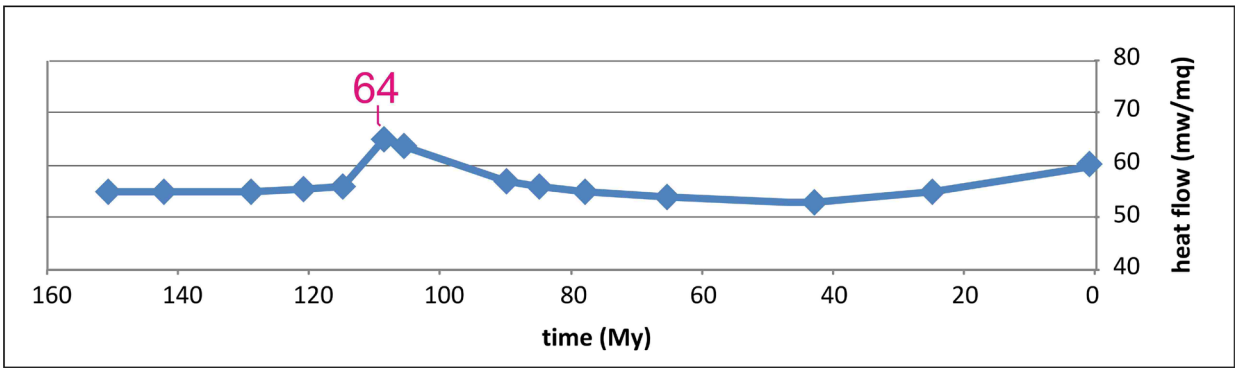

Fig. 8.10 - Heat flow trend defined for the Cameros Basin. A maximum peak of 64 mW/m² was estimated at the end of the syn-extensional stage (108.7 My)

of the rapid/decelerated subsidence cycles. In fact, if the lateral movement of the depocenters occurred during the same rapid subsidence phase, larger accommodation space would be formed partially at one point of the basin and partially in lateral points, determining the diachronous record of the subsidence cycles. This is evident that in both cycles the rapid subsidence phase ended earlier in the south and gradually later to the north (Fig. 8.8), due to the northward lateral displacement trend of the depocenters occurring during the same rapid/decelerated subsidence cycle.

The vertical crustal stretching estimated during the crustal thinning (0.97) is very small taking into account that the value of 1 corresponds to the undeformed state. In the syncline extensional model the maximum lithosphere thinning would be placed far away, toward the south of the basin.

8.5.2. Heat flow

The heat flow during the evolution of the basin is one of the most important variables that must be considered when reconstructing a thermal model of a basin. The estimates of the basinal heat flow at the end of the syn-extensional stage range from 60 to 65 mW/m². The heat flow at the end of the extension stage, was constant for all basin sectors (Table 8.3), despite their different subsidence histories.

The heat flow estimated for the Cameros Basin at the end of the extension stage falls within the lower heat flow ranges proposed for an active rift (63 to 105 mW/m²) (Allen and Allen, 2009) (Fig. 8.11). Such low values can be explained considering the extensional mechanisms which are suggested to have formed the basin (Mas et al., 1993; Guimerà et al., 1995; Omodeo Salé et al., 2014). In fact, as the basin formed on a detachment located deep in the basement, the lithosphere

extension would be limited in the basin area, and consequently it can be suggested a reduced asthenosphere uprising. Thus, lower heat flow values have to be expected than in the case of an active rift, where a considerable extension of the lithosphere occurred and oceanic crust formed (Ebinger and Casey, 2001; Kendall et al., 2006; Kurz et al., 2007). In the syncline extensional model higher heat flow values would be reached far away, toward the south of the basin, where the maximum lithosphere thinning would be placed. When low heat flow anomalies occur after stretching, only a small amount of subsequent thermal subsidence will affect the basin. Indeed, in the Cameros Basin the post-extensional deposits are not more than 650 m, which corresponds to a thermal subsidence of about 120 m (see tectonic subsidence curves in Fig. 8.7).

Although the results obtained contribute to understand crustal and mantle thermal phenomena and to estimate the maximum heat flow value in the stretching phase they cannot be sufficient to provide a precise heat flow variation over time (Yalçin et al., 1997). In fact the model proposed cannot take into account additional heat input by metamorphic events and/or advective heat transport like heat transported by hydrothermal hot fluids. Therefore the heat flow estimated herein must be considered a "conservative-estimate" parameter, which would need a different modelling approach in combination with the calibration with other temperature sensitive parameters. Calibration of the estimated heat flow with measured paleotemperature data is performed in the next chapter.

8.6. CONCLUSIONS

Subsidence analysis was employed to reconstruct the burial evolution of a basin over time together with its essential basin forming mechanisms. Total and Tectonic subsidence obtained from the subsidence analysis indicate the variation in accommodation space in the basin over time and the subsidence evolution resulting from the stretching of the lithosphere.

In the Cameros Basin two cycles of rapid and decelerated subsidence phases during the mechanical subsidence of the syn-extensional stage were determined by analysis of the tectonic subsidence. The first cycle ranges from the Tithonian to the Early Berriasian (from 150.8 to 142.3 My), whereas the second one ranges from the Early Barremian to the Early Albian (from 129 to 108.7 My). These two rapid/decelerated cycles were not recorded synchronously in the basin, coherently with the extensional-ramp syncline model. The maximum depth in the basin was attained in the central-northern sector of the basin. The depth decreases gradually towards the south, whereas it is more abrupt towards the north, coherently with the extensional-ramp syncline model.

A maximum heat flow peak for the end at the syn-extensional stage (108.7 My) was calculated by distinguishing the initial and thermal subsidence phases and by determining the relative

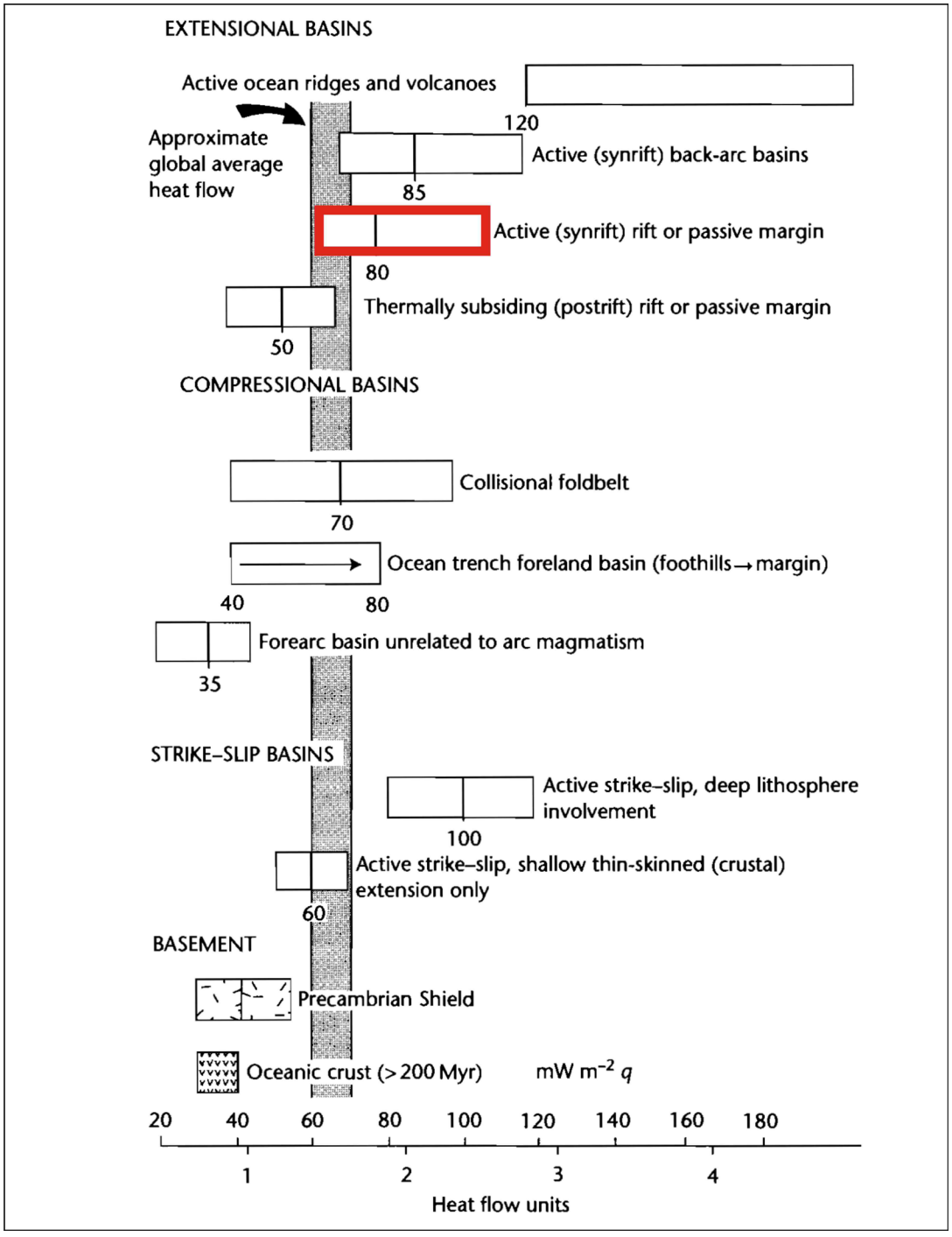

Fig. 8.11 - Summary of the typical heat flow associated to sedimentary basins of various type proposed by Allen and Allen, (2009). For an active rift it is proposed and heat flow ranging from 63 to 105 mW/m² (from Allen and Allen, 2009)

magnitudes. The maximum heat flow peak ranges from 60 to 65 mW/m², which is related to the maximum heat flow recorded as consequence of the thinning of the lithosphere and to the upwelling of the hot asthenosphere. The heat flow is similar in all the virtual wells, indicating that the heat flow affecting the basin at the end of the syn-extensional is constant in all the

basin sectors, despite slight differences of subsidence. The low heat flow value calculated for the Cameros Basin can be explained considering the reduced lithosphere extension in the basin area, which determined a reduced asthenosphere uprising. The paleoheat-flow trend from the rift stage to the present-day was reconstructed for the Cameros Basin area, considering calculated and litterature data.

Chapter 9

9. Thermal Model of the Basin

9.1. INTRODUCTION

9.1.1. Basin modelling

The term basin modeling has acquired a meaning referring mostly to "simulating the thermal history of a basin for a given geological and depositional history and, associated with it, to determine the timing and volume of hydrocarbon generation as well as migration and accumulation" (Welte and Yalçin, 1988; Poelchau et al., 1997; Ungerer et al., 1990).

"The basin thermal model depends on a well-defined conceptual model which is based on the integrated sum of all available geological data. The simulation is then performed on the discretized, numerical representation of the conceptual model. Output of the simulation is compared with the input and with independent calibration parameters, and if necessary the conceptual model is adjusted or modified to lead to a better match between simulation and calibration data" (Poelchau et al., 1997).

"The conceptual model follow the steps which the model builder must take from describing the architecture or geometry of the basin, defining the physical stratigraphy, chronology and the physical properties of the basin infill, identifying the post-depositional processes, their timing and

kinetics, to finding the various temperature and maturation measures needed for calibrating the model and the final output of temperature history and hydrocarbons generation" (Poelchau et al., 1997).

Basin and petroleum system modelling take into consideration geological processes at several scales and levels of complexity, depending on its spatial dimension. One-dimensional modelling (1D) examines burial history at a point location; two-dimensional modelling (2D) reconstruct thermal history and hydrocarbons generation, migration and accumulation along a cross section and three-dimensional modelling (3D) reconstructs the thermal history and petroleum system at basin scale and it has the property to display the output data in 1D, 2D or 3D, and through time.

Models results allow to determine several features of a basin history: 1) the burial history of the basin infill; 2) the variation of the physical properties of the sediments (porosity, permeability, compaction, etc.,) over time; 3) the temperature variations in the basin in time and space; 4) the calibration of a basal heat flow; 4) the thermal maturity of the sediments; 5) the petroleum system elements and boundaries; 6) the timing of hydrocarbon generation, migration and trap formation.

This chapter discusses methods and results of the modelling of the thermal history of a sedimentary basin, demonstrating the role of various parameters and boundary conditions on the temperature distribution. Principle, methods and results of the hydrocarbons generation, migration and accumulation modelling is considered in a next chapter (**Chapter 12**).

9.1.2. Thermal modelling

Crucial for thermal modelling is the reconstruction of paleo-temperature over geologic time and its spatial variation in the basin (Poelchau et al., 1997). "Temperature is possibly the most critical parameter since it affects not only hydrocarbon generation but also many physical properties of sediments and fluids. Consequently many processes during basin evolution, such as compaction and fluid flow, are controlled directly by the temperature itself. Therefore a realistic reconstruction of temperature history is crucial for the modelling of basin evolution and for understanding the very complex processes and their interactions during basin development" (Yalçin et al., 1997).

The thermal history of a basin is affected by several geological processes, among them: 1) deposition, 2) non deposition; 3) erosion; 4) faulting; 5) thrusting/overthrusting, 6) compaction; 7) pressure; 8) heat transfer; 9) sediment physical properties. Vice versa the temperature history controls the following processes: 1) kinetics of chemical reactions; 2) maturation of organic matter; 3) oil and gas generation and 4) expulsion. In the thermal modelling most of these factors are contemplated (Yalçin et al., 1997). In fact, during the calculation procedures of the

modelling routine parameters as thermal conductivity, specific heat, density, compressibility, permeability, initial porosity of sediments of different lithotypes, viscosity and density of pore fluids are considered (Yalçin et al., 1997).

"To model the reconstruction of the thermal history of a sedimentary basin a forward modelling approach is used, which means that processes during basin evolution are modeled from past to present assuming starting conditions according to the geological principle "the present is the key to the past" (Yalçin et al., 1997). Thus a deterministic model is performed, which determine a unique result whereas no probabilities are involved (Yalçin et al., 1997). A numerical modelling technique is applied, and hence numerical values of all input parameters are required" (Yalçin et al., 1997).

"The model starts running at a given time in the geological past and simulates the temporal development until the present. As a consequence the input data must be prepared in an appropriate way so that the entire temporal development is represented by the data. This requires a systematic consideration of the geological history using all available data. However some of the paleoparameters can be estimated only using indirect approaches. Estimation of paleoheat flow and paleoclimatic conditions or erosional amounts are typical examples. Therefore prior to the mathematical model a conceptual model must be designed (Welte and Yalçin, 1987). The conceptual model forms the basis for the model input and must be calibrated by comparing the simulation results with observed data. In most cases an iterative approach is needed to reach an acceptable fit between simulated and observed results" (Yalçin et al., 1997). Other details of the system and its modeling aspects are provided by Welte and Yalçin (1987, 1988), Wygrala (1988) and Yalçin (1991).

9.1.2.1. The conceptual basin model

"The evolutionary history of a geologic sedimentary basin consists of a sequence of events in time during which a large number of physical processes have acted on the basin materials in three dimensional spaces. The computer simulation requires the quantification of all defining parameters, and the conceptual model provides the temporal framework which is needed to structure the input data (Wygrala, 1988). The conceptual model is a condensed description of the geologic evolution of the basin (Welte and Yalçin, 1987)" (Poelchau et al., 1997).

"For all types of basin simulation (1D, 2D and 3D) the design of a conceptual model of basin history is the first and most critical step. The conceptual model is a formulation, suitable for numerical treatment (discretization) of the principal elements of a basin history. It must be based on the interpretation of conventional geologic, geophysical and geochemical observational data placed in a temporal framework. Stratigraphic analysis provides the most crucial input to the conceptual model. From such analysis, basin history is subdivided into an interrupted sequence

of events, of specified age and duration, which takes place during the evolution of the basin. Each stratigraphic event represents a time span during which one of the three basin geologic processes prevailed, i.e., accumulation of a layer (deposition), non-deposition (hiatus), or uplift and erosion (unconformity). Similarly, structural and tectonic events, as folding, faulting, thrust, etc., may be included in the conceptual model when reasonable geologic age limits and durations can be assigned. The resulting conceptual model of the geologic basin history provides the numerical "pattern" both physical and temporal, which provides the essential input for the basin simulation program (Poelchau et al., 1997).

"Stratigraphic history modeled as a sequence of events is the most basic and common requirement for the design of all basin models. However, the conceptual model has certain shortcomings when used in more advanced basin modeling systems where a multitude of post-depositional processes are considered which can change or add parts of the stratigraphic section. This concerns, for instance, diagenetic alteration of only parts of selected layers such that a new physical stratigraphic entity is created long after deposition. Other examples are interstratal hydrothermal deposits or intrusive sills" (Poelchau et al., 1997). Therefore the "conceptual model" idea must be refined and adjusted to the requirements of the modelled basin history.

9.1.2.2. Boundary conditions setting

"In order to compute heat transfer in basin infill, physical and thermal conditions at the base and the top of the sedimentary basin must be considered, which consist in: water depths, heat flow at the base of the system and surface or sediment/water interface temperature at the top. The lower boundary condition is determined by the heat flux density, which controls heat input into a basin. The upper boundary is determined by temperatures prevailing at the surface sediment/water interface (sea bottom) or subaerial surface temperatures of the sedimentary package" (Yalçin et al., 1997).

Heat input into a sedimentary basin comes mostly from its base (subcrustal heat flow), therefore definition of the basal heat flow is one of the most important variable which need to be determined in the model (Yalçin et al., 1997). Basal heat flow strictly depends on the geodynamic context of a basin and it can be related with the position of the basin in the tectonic plates (Allen and Allen, 2009). Although it is risky to generalize, an assignment of heat flow values to basin types is possible (Yalçin et at., 1997). "However to reconstruct the temperature history of sedimentary basin, not only the present values of heat flow needs to be considered but also the ancient values (paleoheat flow) must be known. Several attempts have been made to estimate paleoheat flow in a basin considering the amount of stretching of the lithosphere (McKenzie, 1978, Sclater and Christie, 1980; Wernicke 1985; Royden, 1986; Burrus and Bessis, 1986). By these authors the period of stretching and thinning of the lithosphere and uprising

of the asthenosphere is associated with an increase in the heat flow, which is quantitatively determined as a function of stretching factor and time. The so-called thermal subsidence period following the termination of stretching is represented by a decrease in the heat flow over time due to the relaxation of lithospheric isotherms to their original position before stretching" (Yalçin et al., 1997) (see **Chapter 8**).

Although these models contribute to understand crustal and mantle thermal phenomena and to estimate the maximum heat flow value in the stretching phase they cannot be sufficient to provide a precise heat flow variation over time. In fact crustal model cannot take into account regional heat flow variability, such as regional tectonic evolution, basalt intrusion, metamorphic events, hydrothermal hot fluids circulation (Yalçin et al., 1997). "Therefore the history of the basal heat flow must be considered a "best-estimate" parameter, which can be adjusted with the help of other temperature-sensitive parameters" (Yalçin et al., 1997). Calibration of the output model with measured paleotemperature data represents one of the most fundamental tools to assess the reliable of the heat flow estimation (Yalçin et al., 1997).

9.1.2.3. Calibration of the model

The typical outputs of the model for each event consists of thickness, porosity, pore pressure, temperature, maturity, level of hydrocarbon generation, amount of generated hydrocarbons, and the expulsion efficiency as a function of time. Almost all of these parameters can be used directly or indirectly for calibration purposes by comparing the values calculated by the simulation for the present time with the measured data. The use of several calibration parameters would be the ideal and most comprehensive manner of thermal history calibration (Yalçin et al., 1997).

"The calibration process is based on modification of the conceptual model, as permitted by relevant field and laboratory data, and on the adjustment of the respective parameters on the input data. However, original input such as thickness of the layers, type, age, and duration of various events, timing of tectonic movements, depositional environment and related water depths, basin type, and thermophysical properties of different lithologies are based on real observation and measurements and therefore cannot be significantly modified for calibration purposes. Consequently only sea bottom temperatures, heat flow, timing and duration of erosional events, and original thickness of eroded units are input data which can be adjusted within geologically acceptable ranges to establish a fit between calculated and measured parameters. However there are limitations in the adjustment of these parameters as physical, chemical and geological data and principles place severe constraints on the procedure" (Yalçin et al., 1997).

Vitrinite reflectance is the most common maturity indicators used to calibrate the model, although organic maturity indicators have a high sensitivity to thermal history (Yalçin et al.,

1997). The combination of more independent sets of calibration parameters, as ones derived from maturation indices Rock-Eval pyrolysis data (Tmax), as well as geothermometry (fluid inclusions measurements, fission-track studies and illite crystallinity), can perform a reliable temperature history reconstruction (Lischner et al., 1993). The combination of vitrinite reflectance with inorganic data is very useful when complex thermal history want to be modelled (repeated uplift, erosion and subsidence events, hydrothermalism, basalt intrusions, etc.,) (Yalçin et al., 1997). "After calibration of the conceptual model a sensitivity analysis can be performed by changing selected input parameters within geologically justifiable ranges and by simulating again the basin evolution with these values" (Yalçin et al., 1997).

9.2. THERMAL MODEL OF THE CAMEROS BASIN

One of the most relevant features of the Cameros Basin is its complex thermal history. The basin in fact was characterised by a differentiated subsidence trend from a sector to the other, which determines differences in the burial heating (**Chapter 8**). Furthermore, the basin infill deposits have been affected by low to very low metamorphism, which recorded anomalously high temperatures, the origin and distribution of which have been the subjects of much debate in recent years. Some authors (Guiraud et al. 1985, Golberg et al. 1988, Casas-Sainz et al. 1992, Mata et al. 2001, Del Río et al. 2009, Casas et al. 2012) have attributed this metamorphism to heating resulting from burial of the deepest areas of the basin. However, other authors (Casquet et al., 1992; Barrenechea et al., 1995, 2001; Mantilla-Figueroa et al. 1998; Alonso-Azcárate et al. 1999; Ochoa et al., 2007; González-Acebrón et al., 2011, 2012) have interpreted this metamorphism as hydrothermal and allochemical processes.

The aim of this chapter is to reconstruct the thermal history of the Cameros basin, by means of the reconstruction of a 2D thermal model. To achieve this objective, the present study considers the most important variables that play a major role in the thermal evolution of a basin, i.e., heat flow and burial of sediment load, circulation of fluids.

In this chapter the thermal model of the basin is reconstructed from the age of formation of the basin until the end of the infill processes, which correspond to the syn-extensional and post-extensional stages, whereas inversion and erosion processes were not considered. The reconstruction of a 2D thermal model of the basin allows taking into account all the geological and geophysical variables which influence the thermal history of the basin and it helps to determine the following aspects: 1) the basin infill temperature variation over the time and space, 2) to calibrate the basal heat flow of the basin, calculated in the previous **Chapter 8** by means of Royden's method and 3) to determine the origin of the thermal events which affected the basin during its evolution

Vitrinite reflectance was mostly used to calibrate the calculation obtained from the model. Additionally fluid inclusions data were used to clarify the interpretation of the thermal history of the basin, as far as they are the unique direct evidence of circulation of paleofluids (Goldstein and Reynolds, 1994).

9.3. METHODOLOGY

By combining geological, geophysical and thermodynamic data, a numerical thermal model can be created with the result that the processes leading to the thermal evolution of the basin can be quantified (Welte and Yükler, 1981; Tissot et al., 1987; Welte and Yalçin, 1988; Yalçin and Welte, 1988; Welte et al., 1997 and Littke et al., 2008). The principles and applications of these simulations are exposed in the previous sections and they have been explained by Welte and Yalçin (1987, 1988); Wygrala (1988); Yalçin and Welte (1988); Yalçin (1991); Büker et al. (1995); Poelchau et al. (1997) and Yalçin et al. (1997).

Numerical simulations were performed using the Petro Mod software of Schlumberger. 1D and 2D thermal models of the thermal history of the basin were performed. 1D thermal model determine the temperature variation versus time and burial depth for a given point of the basin. On the other hand 2D thermal model allows the temperature variation throughout the section to be determined in different ages.

The heat flow affecting the basin was estimated from the geodynamic setting of a rift as a consequence of the stretching of the lithosphere (McKenzie, 1978; Royden, 1986; Allen and Allen, 2009) (**Chapter 8**). Vitrinite reflectance (%Ro) was primarily used to calibrate the models. Punctually homogenization temperatures (Th) measured in primary fluid inclusions was used to support the discussion of the calibration results.

9.3.1. Modelling input

9.3.1.1. Geological conceptual model

To determine the geological conceptual model of the basin, data provided by the balanced geological cross-section of the basin and its restoration were used (Fig. 9.1 and Fig. 9.2). In fact, as the trace of the cross-section intersects the main depocentral areas of the basin (Fig. 9.1), this section performs a reliable reconstruction of the maximum burial depth which experienced the basin.

Because most of the relevant thermal events of the basin was recorded during the extensional and post-extensional stages, to determine the thermal history of the basin the model was

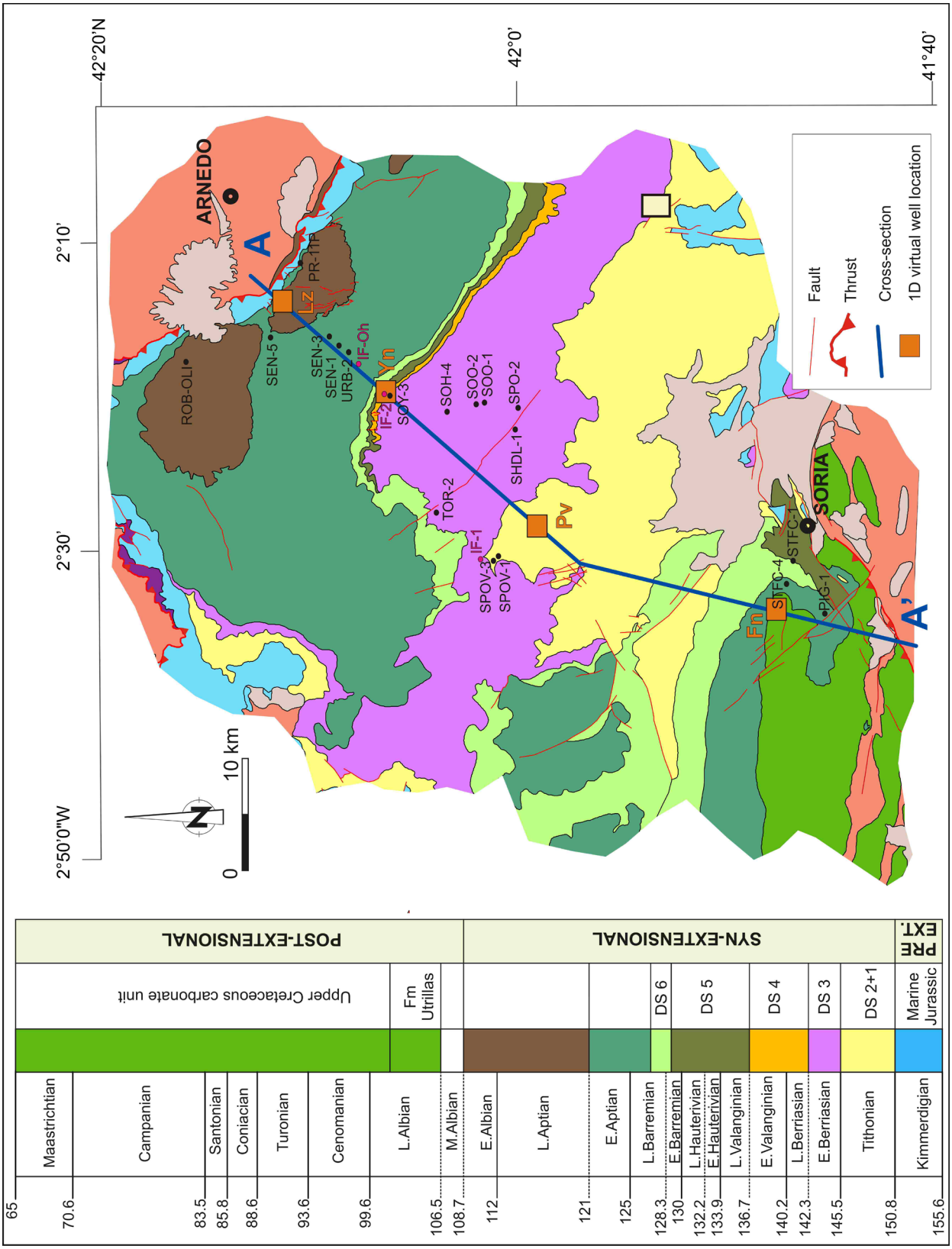

Fig. 9.1 - Trace of the cross-section used to determine the geometry and structure of the basin in the reconstruction of the geological conceptual model. Position of the virtual well used for the 1D thermal models is indicated. Location of the samples collected for vitrinite reflectance measurements and fluid inclusions data (González-Acebrón et al., 2013 and Ochoa-Rodríguez, 2006) are shown

reconstructed directly on the restored cross-section (Fig. 9.2). Thus erosion was not considered as a variable in the model, as the restored section represent the basin infill geometry, thickness and structure at the end of the post-rift stage (65.5 My), before the inversion and erosion of the basin infill. In the 1D model four virtual wells were defined on the restored section, whereas the entire restored section was used in the 2D model (Fig. 9.2). Age, facies and lithology of the stratigraphic units in which the basin infill has been subdivided is represented in Fig. 9.3 and Table 9.1.

To reconstruct a geological conceptual model, the basin history was subdivided into an interrupted sequence of events (deposition, no-deposition and/or erosion) of a specified age (Table 9.2). Ages and units representing the subsequent depositional events of the basin refer to

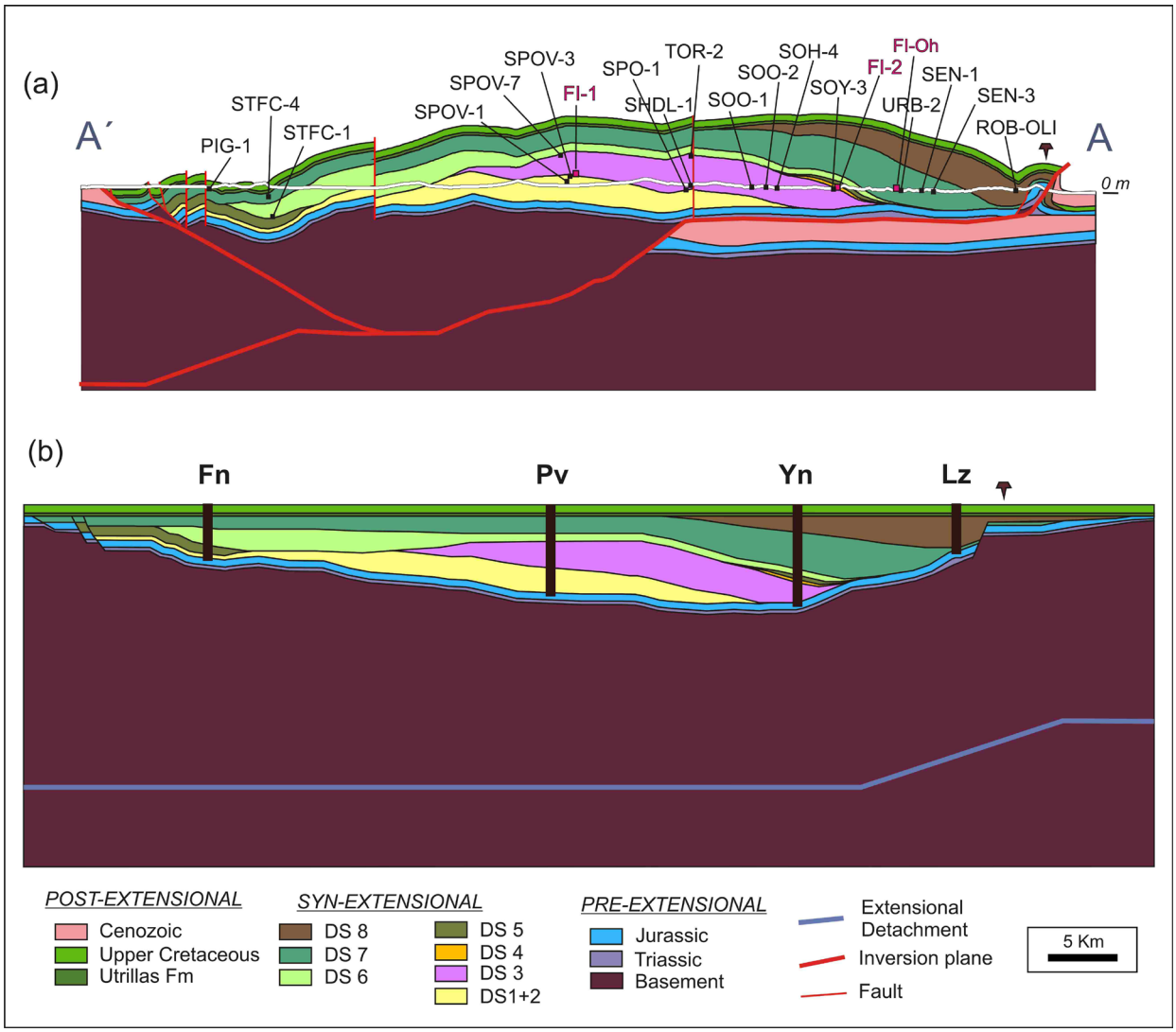

Fig. 9.2 - (a) Balanced geological cross-section showing location of organic matter and fluid inclusions samples. Samples are located in accordance with their geographical and stratigraphical position. (b) Restored cross-section used as geological conceptual model in the 2D thermal model and location of virtual wells used for 1D thermal modelling

Table 9.1 and Table 9.2). Since precise ages are necessary for thermal model calculation, the DS age assignation was simplified (see subsidence analysis methods in **Chapter 8**).

For each unit a specific lithological facies was assigned (Table 9.1). Facies defined refer to the Formations and Groups lithological units in which the basin infill has been subdivided (Fig. 9.3). Facies were built in terms of percentage of lithological composition (Table 9.1). Petrophysical properties of the defined facies were provided by the modeling package (Table 9.3). Facies were assigned to the restored section, considering areal distribution of the Formations and Groups (Mas et al., 1993, 2003, 2011) (Fig. 9.4). In Fig. 9.5 a synthesis of the input data introduced in the four 1D model (unit, thickness, ages and lithology) is performed.

9.3.1.2. Boundary conditions

To prepare the model for simulation boundary conditions need to be established. The boundary conditions define variation during the time in the thermal history, paleogeography,

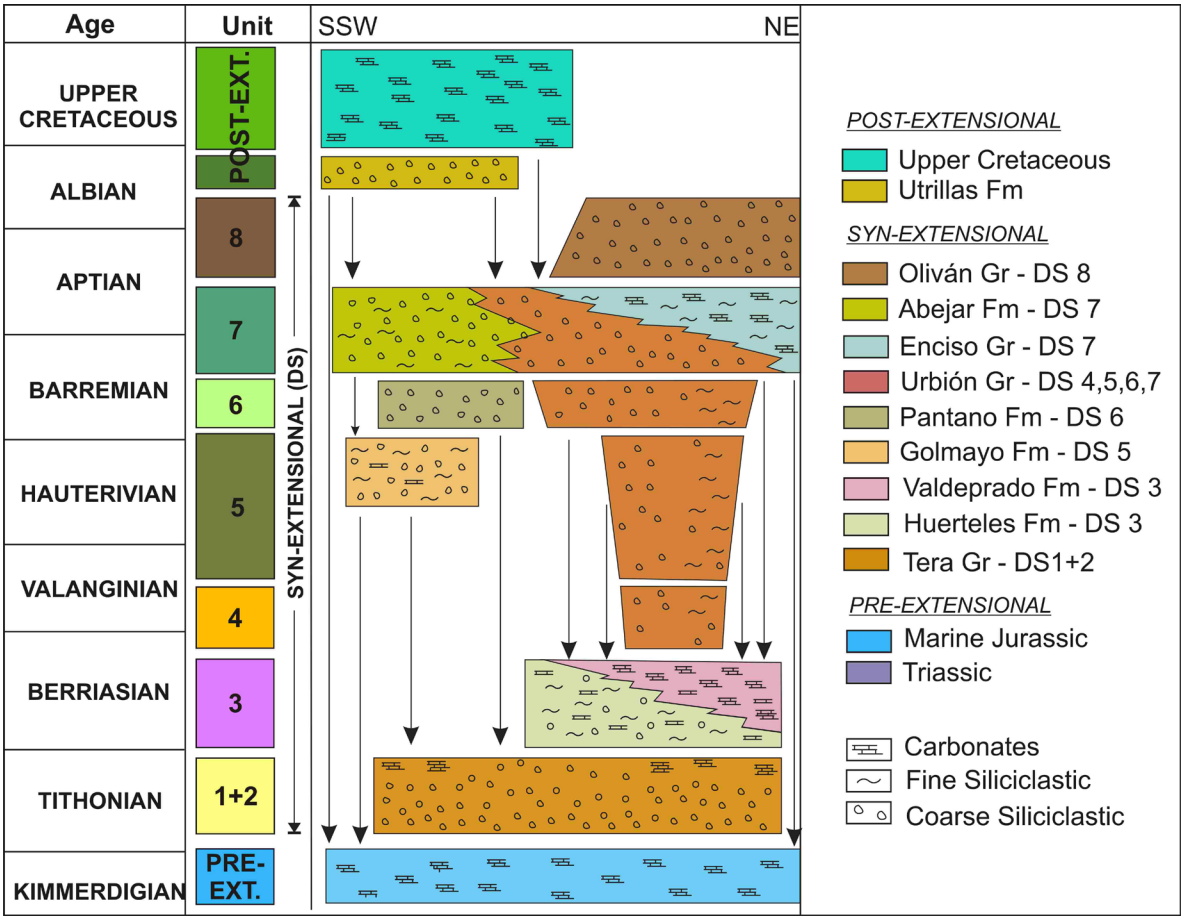

Fig. 9.3 - Chrono-stratigraphic sketch of the Cameros Basin infill and distribution of the syn-extensional depositional sequences (DS) and the relative lithological units (Groups and Formations) (Modified from Mas et al., 2002, 2003 and 2011)

Age (My)		Unit	Group/Formation	Facies assigned in	Lithology		
From	To				Limestone	Sandstone	Shale
65.5	98	Post-extensional	Upper Cretaceous	UpCretac	60	20	20
98	106.5		Utrillas Fm	Utrillas	0	80	20
121	108.7	DS8	Olivan Gr	Olivan	5	70	25
127	121	DS7	Leza Fm	-	-	-	-
			Enciso Gr	Enciso	45	20	35
			Urbión Gr	Urbión	0	60	40
			Abejar Fm	Abejar	0	70	30
129	127	DS6	Urbión Gr	Urbión	0	60	40
			Pantano Fm	Pantano	0	80	20
136.7	129	DS5	Urbión Gr	Urbión	0	60	40
			Golmayo Fm	Golmayo	40	40	20
142.3	136.7	DS4	Urbión Gr	Urbión	0	60	40
145.5	142.3	DS3	Valdeprado Fm	Valdeprado	60	4	36
			Huerteles Fm	Huerteles	15	35	50
150.8	145.5	DS1+2	Tera Gr	Tera	5	60	35
150.8	164.7	Pre-extensional	Marine Jurassic	Jurassic	100	0	0

Table 9.1 - Age, facies and lithologies of the basin infill units, which were used to reconstruct the geological conceptual model

Age at the base (My)	Event number	Event Type	Layer
65.5	16	Hiatus	Hiatus 65.5_0
98	15	Deposition	Upp_Cretaceous
106.5	14	Deposition	Utrillas
108.7	13	Hiatus	Hiatus 108.7_106.5
121	12	Deposition	DS8
127	11	Deposition	DS7
129	10	Deposition	DS6
136.7	9	Deposition	DS5
142.3	8	Deposition	DS4
145.5	7	Deposition	DS3
150.8	6	Deposition	DS1+2
164.7	5	Deposition	Jurassic
205	4	Hiatus	Hiatus 205_164.7
245	3	Deposition	Triassic
380	2	Hiatus	Hiatus 380_245
500	1	Deposition	Basement

Table 9.2 - Events defined in the geological conceptual model reconstructed for both 1D and 2D thermal models

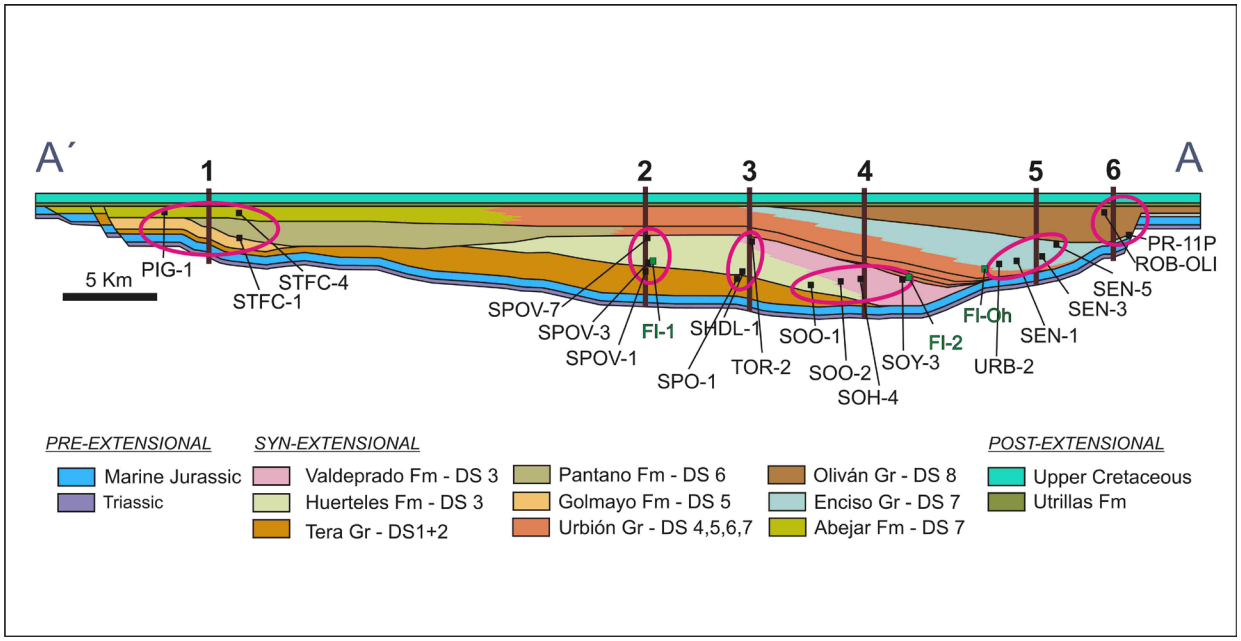

Fig. 9.4 - Facies distribution in the restored section of the Cameros Basin. The organic matter samples, where %Ro was measured, are depicted at the calculated original paleo-depth. To calibrate the 2D thermal model, the measured %Ro values were grouped and projected on six calibration wells, arranged along the section

topography and bathymetry of the basin (Poelchau et al., 1997). In the computational model three main boundary conditions need to be considered: Paleo water depth (PWD), sediment water interface temperature (SWIT) and heat flow (HF).

In the Cameros Basin, sea-level fluctuations during the time were ignored, because the continental or very shallow coastal-marine nature of most of the deposits. Thus paleowater depth correction was not considered. Correction of the sediment water interface temperature was done automatically by the PetroMod software (Wygrala, 1988), which takes into account SWIT variation over the geological past for a given geographical location. SWIT variation during the time calculated by the model, for the Cameros Basin area that at the present-day is located in the northern hemisphere at 42º latitude, is indicated in Fig. 9.6. In a first attempt the heat flow trend introduced in the model refer to the heat flow trend determined in **Chapter 8**, characterised by a maximum peak of 64 mW/m^2 at the end of the syn-extensional stage (108.7 My), a value of 50-55mW/m^2 in the post-extensional stage and a present-day value of 60 mW/m^2, as indicated by Fernández et al., (1998) (Fig. 9.7). After that, different heat flow scenarios were tested to calibrate the model and to obtain a good match between modelled and measured %Ro data.

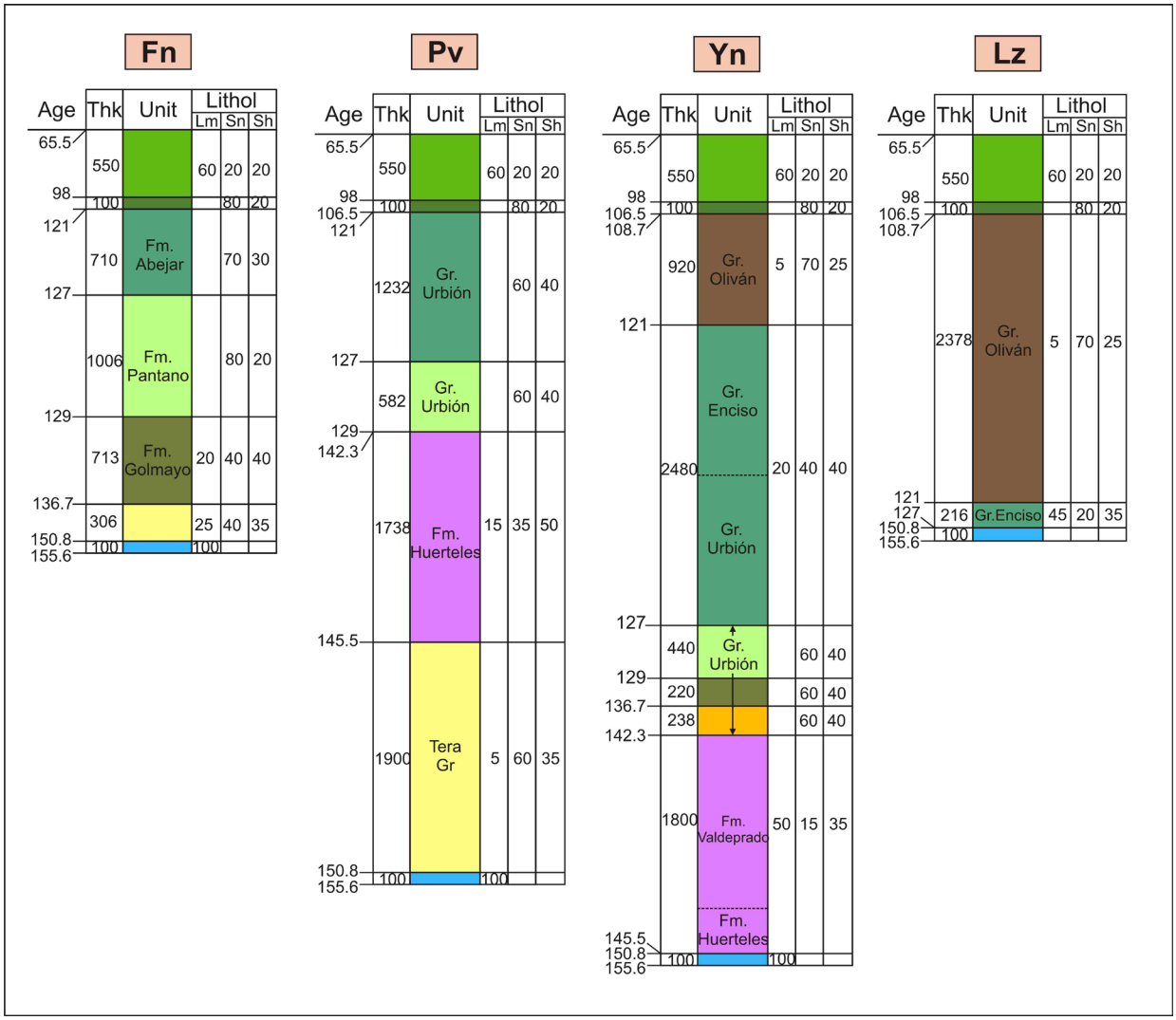

Fig. 9.5 - Input data introduced in the 1D thermal models: Unit, age (My), thickness (m) and lithology (%). Thk = thickness; Lithol = lithology; Lm = limestone; Sn = sandstone; Sh = shale. For legend of the stratigraphic units see Fig. 9.2

9.3.2. Calibration

Thermal model were mostly calibrated by comparing the measured vitrinite reflectance data (%Ro) with the vitrinite reflectance values calculated with the EASY %Ro model (Sweeney and Burnham, 1990) and punctually with the Th from fluid inclusions. Random vitrinite reflectance (%Ro) measurements were performed at the INCAR-CSIC Petrology laboratory (Oviedo, Spain). Nineteen polished sections from outcrops of fine sediment samples (see Fig. 9.1 for location of the samples) were prepared and analysed, using a MPV-Combi-Leitz microscope fitted with an oil immersion objective (50x), following the ISO7404–2 (2009) and ISO 7404–5 (2009) norms, respectively, and ICCP nomenclature (ICCP, 1998, 2001; Sýkorova et al., 2005). A random statistical orientation of macerals or organic particles was applied to ensure accurate

Facies	Initial Porosity (%)	Density (Kg m^{-3})	Permeability at porosity of (log mD)		Heat Capacity (Kcal kg^{-1} K^{-1})		Thermal Conductivity (W m^{-1} K^{-1})	
			25%	45%	20ºC	100ºC	20ºC	100ºC
Up Cretac	51	2710	1	1.52	0.2	0.23	3	2.69
Utrillas Fm	40	2760	2	3.62	0.21	0.24	3.35	2.95
Oliván	49	2667	1.4	3.55	0.21	0.24	3.75	3.24
Enciso	51	2704	-0.36	1.10	0.21	0.24	2.13	2.05
Abejar	46	2700	1.7	4.37	0.2	0.23	4.21	3.58
Pantano	47	2684	1.8	3.88	0.21	0.24	3.74	3.23
Golmayo	51	2700	0.89	2.09	0.2	0.24	2.54	2.35
Urbión	53	2664	0.6	2.93	0.21	0.24	3.73	3.22
Valdeprado	55	2670	-0.81	0.28	0.21	0.24	2.01	1.96
Huerteles	50	2714	1.2	2.97	0.2	0.24	3.03	2.71
Tera	51	2673	0.76	3.48	0.21	0.24	3.37	2.96
Jurassic	51	2680	0.73	1.00	0.2	0.23	2	1.96
Triassic	10	2540	-	-	0.19	0.21	4.69	3.91
Basement	5	2750	-	-	0.19	0.22	2.72	2.35

Table 9.3 - Petrophysical properties of the facies assigned in the model

measurements, because of the high anisotropy of the optical properties in the stages of high organic maturity. A microscope equipped with a 1λ retarder plate and polarized light was used to identify the anisotropy and to distinguish high reflectance vitrinite from inertinite and/or solid bitumen particles. Vitrinite reflectance measured for every samples analyzed is presented in Table 9.4. The representative %Ro mean value indicated in Table 9.4 for each sample is estimated considering both %Ro mean value and %Ro frequency distribution (standard deviation). More data on the vitrinite reflectance measurements are reported in the **Appendix 3.**

Fluid inclusions (FI) data were obtained from González-Acebrón et al., (2013) and Ochoa-Rodríguez (2006). In González-Acebrón (2013) the following FI data were used: 1) a primary FI, measured in quartz syntaxial overgrowth of a sample located in the base of the DS3 deposits, at the central sector of the basin (FI-1) (Fig. 9.1); 2) a primary FI, measured in hydrothermal quartz veins fracturing the Urbión Gr (DS4) deposits in the northern sector of the basin (FI-2) (Fig. 9.1). In Ochoa-Rodríguez (2006) Th measurements correspond to fluid inclusions from quartz overgrowths in the Urbión Gr (DS7), cropping-out in the modelled section area (FI-Oh) (Fig. 9.1). Additionally, data from Th measured in diagenetic fluid inclusions of the Urbión Gr were taken into account to interpret the model results, despite of they were not measured in the modelled area. Thus, location of the latter Ochoa-Rodríguez (2006) samples was not indicated in the map (Fig. 9.1) and in the sections (Fig. 9.2 and Fig. 9.4). A synthesis of the most relevant data performed by fluid inclusions measurements are indicated in (Table 9.5).

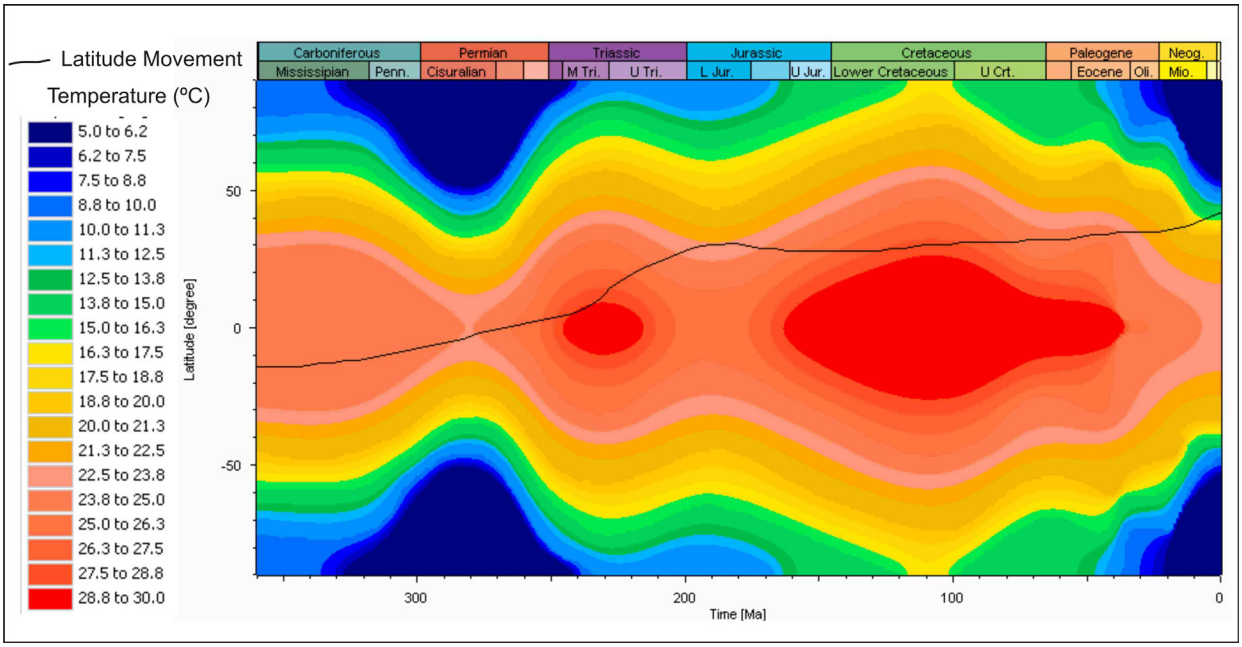

Fig. 9.6 - Water interface temperature variation (SWIT) during the time for the Cameros Basin area, at the present-day located at 42° N of latitude (based on Wygrala, 1989)

To ensure a correct calibration of the model %Ro samples were plotted on the balanced cross-section of the basin, in accordance with their geographical and stratigraphical positions (Fig. 9.1 and Fig. 9.2a) and then on the modeled restored section, at the calculated original paleo-depth (Fig. 9.4). Subsequently the measured %Ro values were grouped and projected onto 6 calibration wells, at the corresponding depth, calculated on the basis of the distance of the stratigraphic level of the samples from the bottom of the subsequent unit and/or from the top of the previous unit (Fig. 9.4). The calibration wells were used to calibrate both 1D and 2D thermal models. The thermal model was considered as "calibrated" when the modeled vitrinite reflectance-depth

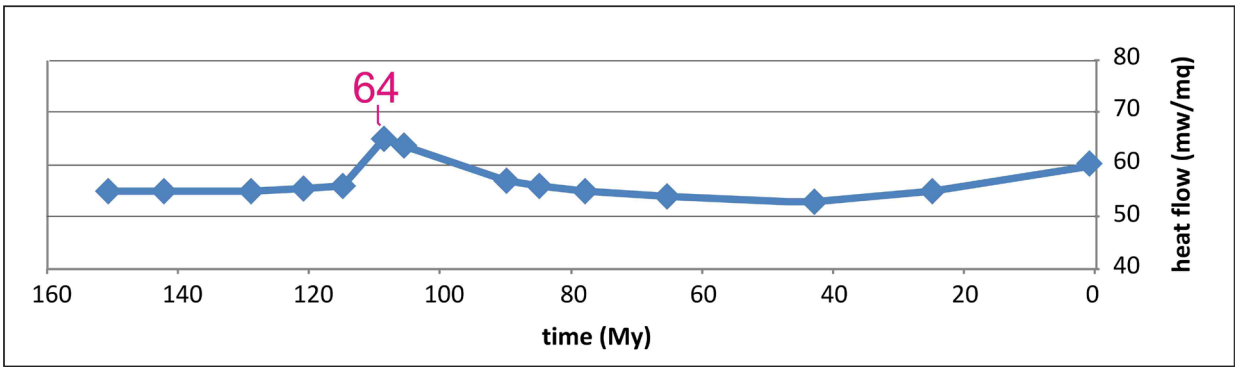

Fig. 9.7 Heat flow trend defined for the Cameros Basin. The maximum peak calculated by Royden's method, recorded at the end of the syn-extensional stage (108.7 Ma), is estimated to be around 64 mW/m²

ID_sample	Unit	%Ro_Mean	%Ro_Min	%Ro_Max
ROB-OLI	DS8 - Oliván Gr	3.20	3.03	3.52
PR-11P	DS7 - Leza Fm	3.50	1.94	5.60
SEN-5	DS7 - Enciso Gr	2.40	2.20	5.10
SEN-3	DS7 - Enciso Gr	3.88	3.10	5.70
SEN-1	DS7 - Enciso Gr	2.09	1.80	2.30
URB-2	DS7 - Urbión Gr	3.20	3.00	3.90
SOY-3	DS3 - Valdeprado Fm	3	2.4	4.3
SOH-4	DS3 - Valdeprado Fm	2.7	2.4	3.5
SOO-2	DS3 - Valdeprado Fm	2.00	1.7	3.2
SOO-1	DS3 - Valdeprado Fm	1.9	1.55	2.8
TOR-2	DS3 - Huerteles Fm	4.6	3.7	6
SHDL-1	DS3 - Huerteles Fm	2.9	2.7	3.2
SPO-1	DS1+2 Tera Gr	3.5	3.1	3.7
SPOV-7	DS3 - Huerteles Fm	3	2.07	3.47
SPOV-3	DS1+2 Tera Gr	2	1.3	2.8
SPOV-1	DS1+2 Tera Gr	2.2	1.7	2.4
PIG-1	DS7 - Abejar Fm	0.47	0.3	0.9
STFC-4	DS7 - Abejar Fm	0.50	0.4	0.6
STFC-1	DS6 - Pantano Fm	0.57	0.40	0.65

Table 9.4 - Vitrinite reflectance measured for each simple. The %Ro mean value is estimated considering both %Ro mean value and %Ro frequency distribution (standard deviation)

curve approaches the measured vitrinite reflectance data. On the other hand, if the measured %Ro values differ markedly from the trend represented by the curve, the model was considered as "not calibrated". In this case the burial history variables (depositional thickness or erosion) and/or the heat flow trend needed to be adjusted until the %Ro values calculated by the model approximated the measured values. In case the modeling results do not reflect the observations there are three likely causes: (1) the observations are wrong, (2) the input and/or calibration data are insufficient, or (3) the simulation technique is not suitable.

Homogenization temperatures (Th) measured in primary fluid inclusions, were punctually used to complement and to discuss the result of the model calibration using vitrinite reflectance. The Th measured in fluid inclusions were compared with the temperatures determined by the model at the corresponding depth. Two separated calibration wells were defined to analyse the fluid inclusions data (Fig. 9.4).

ID_Sample	Unit	Location	Nºmeasure/sample	Origin	Author
IF-1	DS3 - Huerteles Fm	Poveda section	19	Primary	González-Acebrón et al., 2013
IF-2	DS4 - Urbión Gr	Yanguas section	25	Primary	González-Acebrón et al., 2013
IF-Oh	DS7 - Urbión Gr	Yanguas section	28	Primary - Hydrothermal	Ochoa-Rodríguez, 2006
None	Urbión Gr	Northern sector	-	Primary - Diagenetic	Ochoa-Rodríguez, 2006
ID_Sample	**Type**	**System**	**Th min [ºC]**	**Th max [ºC]**	**Th mean [ºC]**
IF-1	Quartz overgrowths	NaCl+H_2O	111	168	120
IF-2	Quartz vein	NaCl+H_2O	121	299	290
IF-Oh	Quartz overgrowths	NaCl+H_2O	133	184	165
None	Quartz overgrowths	NaCl+H_2O	100	115	112

Table 9.5 - Fluid inclusions data used to calibrate the 2D thermal model

9.4. RESULTS

9.4.1. Temperature distribution

The results of the 1D and 2D thermal model were calculated assuming a basal heat flow for an extensional geodynamic setting and show: 1) the variation in sediment temperature during time, 2) the maximum temperature for each stratigraphic unit and relative time, and 3) the sectors of the basin where the highest temperatures were attained. In Fig. 9.8 burial diagram versus temperature obtained for the four 1D models are represented, whereas Fig. 9.9 shows the temperature distribution throughout the restored section from the beginning to the end of the basin infill.

The resulting output graphs of both 1D and 2D models show that the bottom of the basin reaches the maximum temperatures in the central-northern sector of the basin, whereas temperatures decrease towards the borders (Fig. 9.8 and Fig. 9.9). Maximum temperatures are reached at the end of the syn-extensional stage (108.7 My) (Fig. 9.9), coinciding with the maximum heat flow peak used (Fig. 9.7).

To compare the 1D and 2D model outputs, burial history versus temperature diagrams were extracted from the 2D thermal model (Fig. 9.10) at the same virtual well positions as used for 1D modeling. Comparison of the results shows that, for a same virtual well location, the 2D thermal models yield higher temperatures than the 1D thermal models (Fig. 9.10).

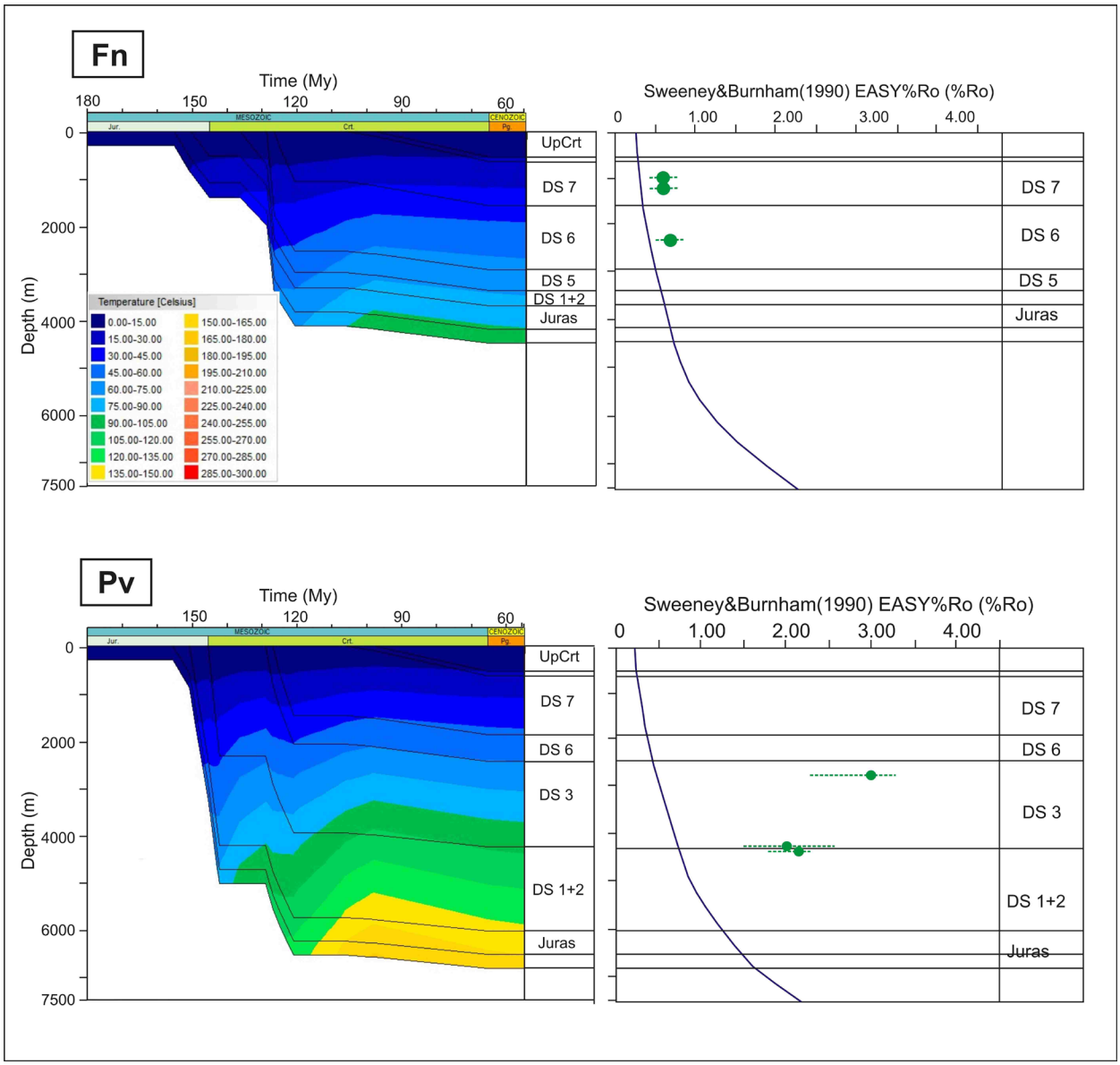

Fig. 9.8 (Part 1) - 1D thermal models output of the virtual wells indicated in Fig. 9.2, obtained using the Royden's method: On the left – Burial diagram versus temperature plots; On the right – Calibration plot of the 1D thermal model comparing measured vitrinite reflectance and calculated trend (Sweeney and Burnham, 1990)

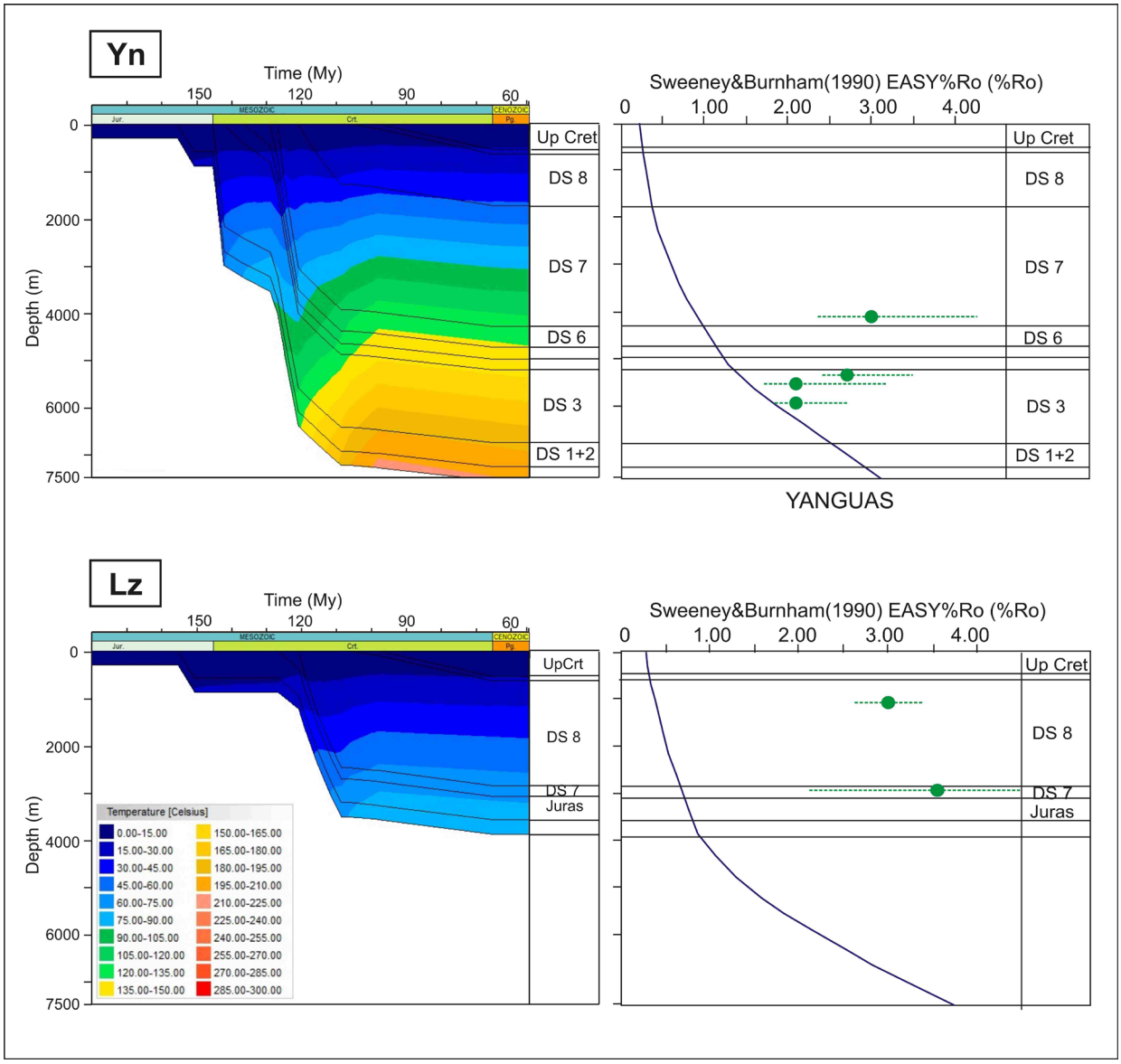

Fig. 9.8 (Part 2) - 1D thermal models output of the virtual wells indicated in Fig. 9.2, obtained using the Royden's method: On the left – Burial diagram versus temperature plots; On the right – Calibration plot of the 1D thermal model comparing measured vitrinite reflectance and calculated trend (Sweeney and Burnham, 1990)

9.4.2. Calibration results

Results of the 1D thermal model calibration indicate that none of the 1D thermal models can be considered as calibrated. In fact in the vitrinite/depth distribution graphs the %Ro measured values are in all the cases higher than the ones proposed by the model theoretical curves (Fig. 9.8). On the other hand calibration of the 2D model indicate that the model is calibrated only in the southern part of the section (calibration-well 1), whereas the model is not calibrated in the rest of the section (Fig. 11).

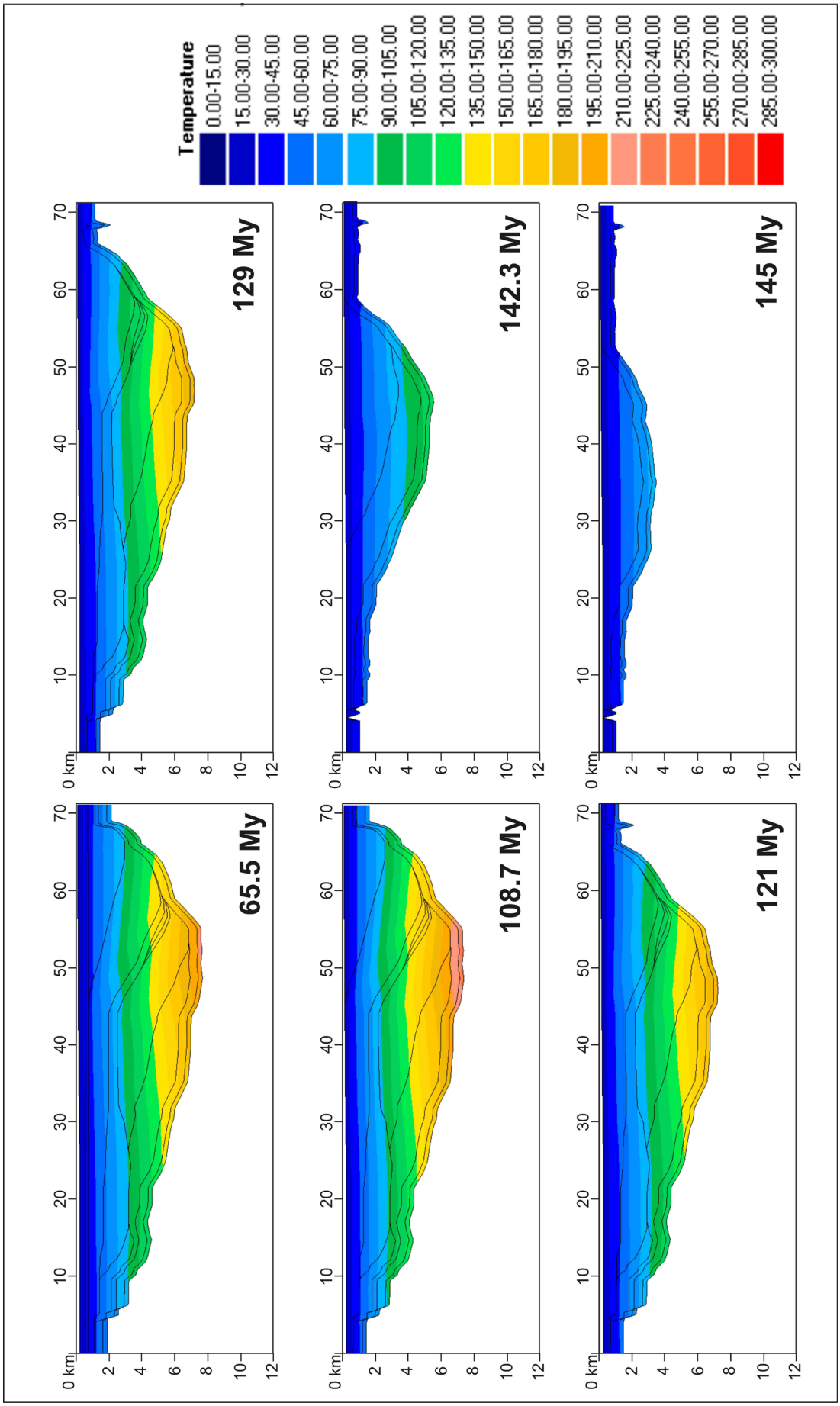
Temperature
0.00-15.00
15.00-30.00
30.00-45.00
45.00-60.00
60.00-75.00
75.00-90.00
90.00-105.00
105.00-120.00
120.00-135.00
135.00-150.00
150.00-165.00
165.00-180.00
180.00-195.00
195.00-210.00
210.00-225.00
225.00-240.00
240.00-255.00
255.00-270.00
270.00-285.00
285.00-300.00
129 My
142.3 My
145 My
65.5 My
108.7 My
121 My
0 km
10
20
30
40
50
60
70
2
4
6
8
10
12

Calibration of the 2D model (Fig. 9.11) shows that the model is well calibrated only in the southern part of the section (calibration-well 1). By contrast, the model is not calibrated in the rest of the section because the measured vitrinite reflectance values are higher than the ones proposed by the theoretical curves of the model. In the central part of the section (calibration-wells 2, 3 and 4), the highest %Ro values measured are related to the samples located at the top of the DS3, whereas the %Ro values measured decrease toward the base of the unit (Fig. 9.11). In the northern part of the section (calibration-well 5), no specific %Ro-with-depth trend is observed since high values were measured in both the upper and lower stratigraphic levels of the DS7 (Fig. 9.11). In the northernmost part of the section (calibration-well 6), the measured %Ro value is markedly higher than the theoretical value predicted by the model (Fig. 9.11).

Other several calibration runs were done to reach a better fit of measured and calculated data, increasing the maximum heat flow peak at the end of the extensional phase from the value of 64 mW/m2 to higher values of 80-100 mW/m^2, which are more typical for an active rift basin (Allen and Allen, 2009). Calibration results did not improve consistently from the previous run, as even in these models the central and northern sectors of the basin still result not calibrated (Fig. 9.11).

Fluids inclusions data indicate that in the central area, temperatures measured in in the hydrothermal quartz veins (Th of 121-290 ^{o}C) are dramatically higher than the temperature reconstructed by the model (120-135 ^{o}C) (Fig. 9.12). Similarly Th values from hydrothermal fluid inclusions in Ochoa-Rodríguez (2006), in the Urbión Gr (DS7) cropping out in this area are higher (133-184^{o}C) than temperatures calculated by the model (Fig. 9.11). On the other hand Th measured in Ochoa-Rodríguez (2006) in the diagenetic fluid inclusions of the Urbión Gr are consistent with the model (100-115^{o}C). However, as the latter were not measured exactly in the modelled area, it cannot be plotted on the burial history versus temperature diagram of Fig. 9.11. In the northernmost part of the section (calibration-well 6), the measured %Ro value is markedly higher than the theoretical value predicted by the model.

Fig. 9.9 - 2D thermal model output using the heat flow calculated by Royden's method: temperature distribution throughout the restored section from the beginning to the end of the basin infill temperature evolution at different times

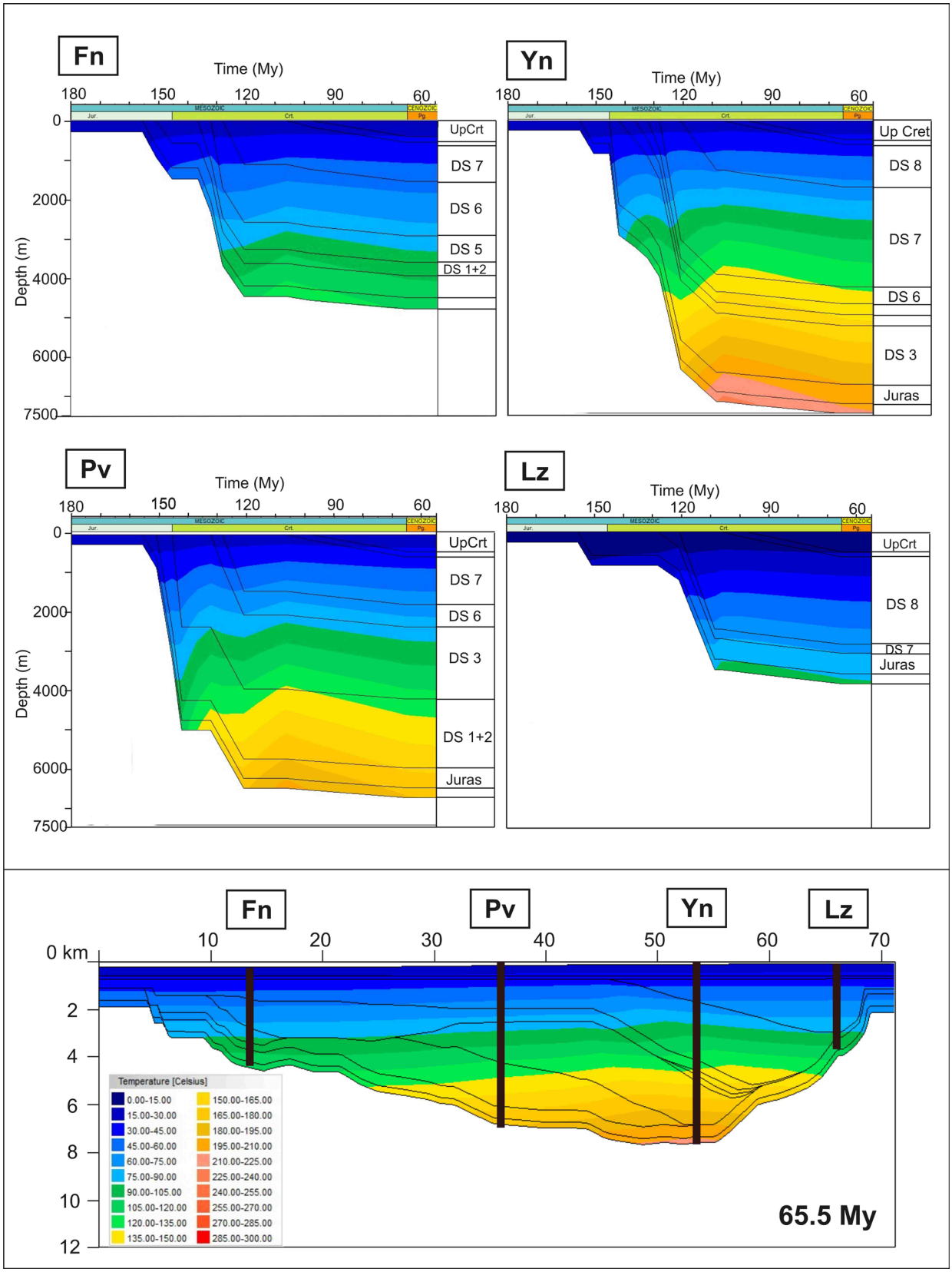

Fig. 9.10 - Burial history versus temperature diagrams obtained from the 2D thermal model at the same virtual well position as used for 1D modelling (Fig. 9.2 and Fig. 9.8). At the same location the 2D thermal models yield higher temperatures than the 1D thermal models

9.5. DISCUSSION

9.5.1. Temperature distribution and 1D-2D thermal model result comparison

Since, in the thermal modelling, the same calculated heat flow trend, characterised by a peak of 64 mW/m^2 at the end of the rift stage, was assumed for the entire section as a boundary condition, the burial depth exerted most influence on the temperature distribution in the modelling results. Thus, both 1D and 2D models indicate that the highest temperatures were reached at the end of the extensional stage in the section sectors where the maximum accommodation space was attained (central-northern sector, corresponding with the Pv and Yn 1D virtual wells), while temperatures decrease toward the borders (Fig. 9.8 and Fig. 9.9). Maximum temperatures are reached at the end of the syn-extensional stage (106.8 My), coinciding with the maximum heat flow peak introduced in the model.

Although the 1D and 2D thermal model outputs show similar temperature distribution trends throughout the basin with time, the 1D models predict lower temperatures for the basin infill than the 2D ones (see comparison between 1D model burial history versus temperature plots - Fig. 9.8 - with the plots extracted at the same section point from the 2D model -Fig. 10). Differences of the results obtained from 1D and 2D thermal models can be attributed to the fact that 2D thermal model takes into account fluid flow and heat conduction also in a lateral direction, not only in a vertical one (Carter and Lerche, 1991). On the other hand 1D thermal model cannot simulate heat flow lateral transport. Thus, it can be considered that the 2D thermal models reconstruct a thermal history of the basin more coherent than the 1D model. Confirms this assumption the fact that none of the 1D models is calibrated (Fig. 9.10), whereas 2D model is calibrated at least in the southern sector of the basin (Fig. 9.11) and that, in the central sector of the basin, fluid inclusion temperature are consistent with the model (Fig. 9.12).

9.5.2. Discussion of the thermal anomalies

Calibration of the model, where the estimated heat flow, characterised by a peak of 64 mW/m^2 at the end of the extensional stage, was assumed for the entire section as a boundary condition, demonstrated that the results were correct only in the southern sector of the basin, whereas %Ro values were generally higher than those calculated by the model in the central and northern sectors of the basin (Fig. 9.11). Increasing the maximum heat flow peak at the end of the extensional stage to higher values (80-100 mW/m2) did not perform a satisfactory calibration (Fig. 9.11). Thus, these data indicate that the temperatures recorded in the sediments in the central and northern sectors of the basin were higher than those calculated from the combination of the burial process and the heat flow of the extension.

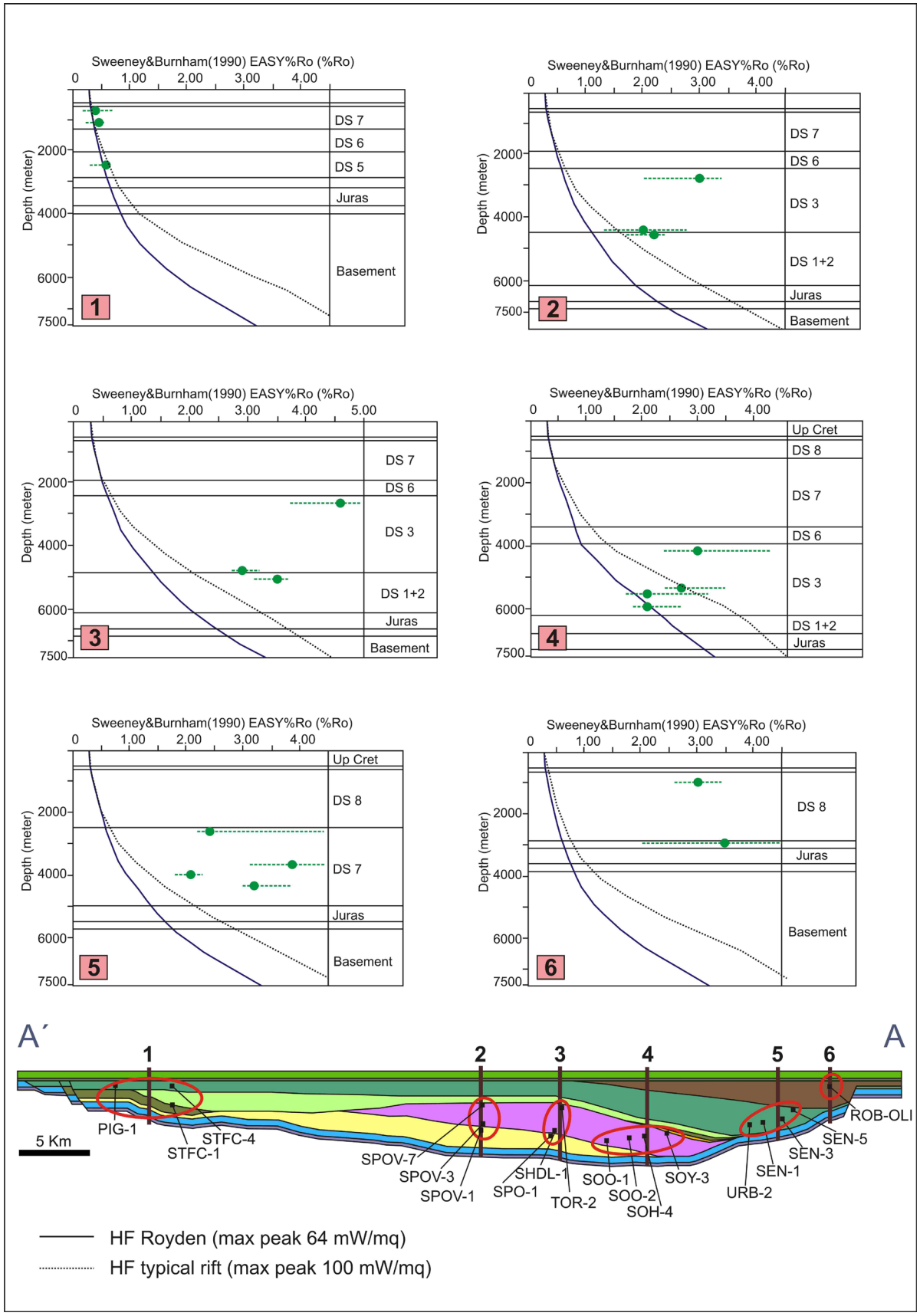

Fig. 9.11 - Calibration of the 2D thermal model obtained using the heat flow calculated by Royden's method along the entire section. Vitrinite reflectance data were used to calibrate the model. For the legend of the restored section see Fig. 9.2

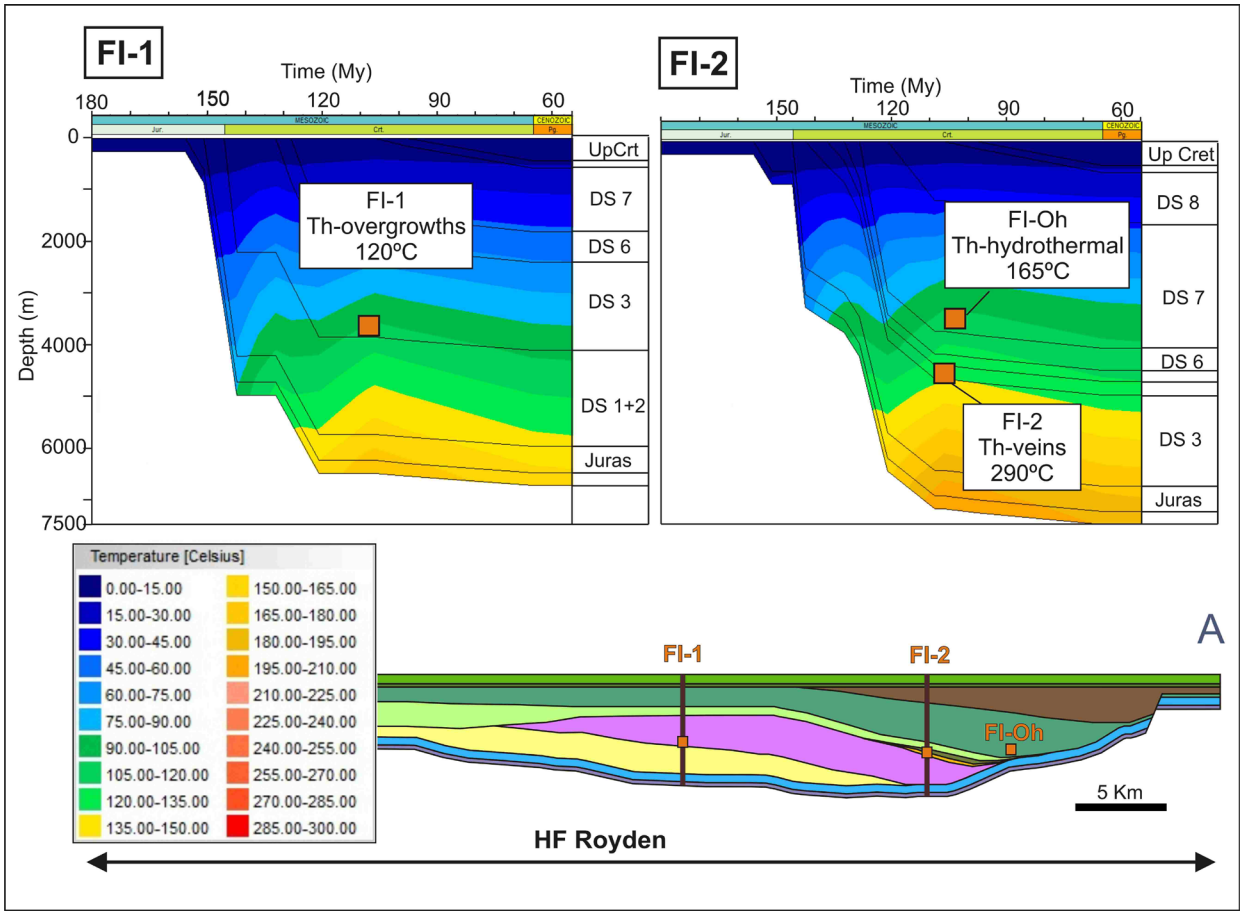

Fig. 9.12 - Burial diagram versus temperature plot extracted from the 2D thermal model at the site in the section where FI-1 and FI-2 fluid inclusion samples are located (Fig. 9.2 and Fig. 9.4). FI-Oh data is plotted on the same FI-2 sample, at the extrapolated stratigraphic depth. In the model the heat flow calculated by Royden's method was used for the entire section. In the burial diagram FI samples were located at the correspondent stratigraphical position. Temperature measured in FI-1 is consistent with the model, whereas the temperature measured in FI-2 is dramatically higher than in the model. For the legend of the restored section see Fig. 9.2

Analysis of the calibration results can help to explain the causes of the inconsistency of the model. Generally, the %Ro values along the section showed a decrease in %Ro with depth, which is not consistent with those expected in a sedimentary basin (Teichmüller and Teichmüller, 1982; Sweeney and Burnham, 1990; Allen and Allen, 2009). This may be observed in the vitrinite/ depth distribution graphs of the calibration-wells 2, 3 and 4 of Fig. 9.11, which show the highest %Ro values at the top of DS3. Anomalous values show a less clear trend in the upper depositional sequences, DS7 and DS8, where the %Ro values range from 2 to 4, regardless of their stratigraphic position. Other data are the high %Ro measured in the DS7 and DS8 deposits (%Ro > 3), shown in the calibration-well 6 (Fig. 9.11), when the modelled %Ro value for the samples range from 0.3% to 0.7%, because it is located in the upper levels of the basin infill, with an overburden of only 650 m of sediments.

The anomalous distribution of the vitrinite reflectance with depth in the central and northern sectors cannot be explained by increasing burial, considering higher erosion thickness (as in the case of the Lower Saxony Basin, (Adriasola Muñoz et al., 2007), nor by taking into account a higher heat flow (e.g., regional metamorphic event, as suggested for the Cameros Basin by Mata et al., 2001; Del Río et al., 2009; Casas et al., 2012) because this would result only in an increase of vitrinite reflectance with depth. Thus, a more successful calibration cannot be achieved increasing the maximum heat flow peak at the end of the rift to higher values (80-100 mW/m^2), more typical for a active rift basin (Allen and Allen, 2009) (Fig. 9.11). Furthermore the very high vitrinite reflectance values measured in the basin (%Ro >3) are not usually reached through subsidence in rift regions of normal geothermal gradients (Teichmüller and Teichmüller, 1982). To obtain such high values an additional heating needs to be considered in the area. Several examples of continental rift basins characterised by anomalous vitrinite reflectance trend are reported in the literature, where anomalies were caused by deep-lying magmatic bodies and/or dike intrusions (e.g. Alston Block, north-eastern England; Creaney, 1980; Illinoise Basin, Stewart et al., 2005), by magmatic activity during the evolution of the basin (e.g. Pannonian and Styrian Basins, Sachsenhofer, 1994; Yalçin et al., 1997) and by the presence of salt diapirism and/or thick evaporitic units (e.g. Adana Basin, Yalçin et al., 1997; Lower Saxony Basin, Adriasola Muñoz et al., 2007). However, in the Cameros Basin, no evidences of intrusion of magmatic bodies in the shallow sedimentary cover, magmatic activity and of relevant salt diapirism were found.

One hypothesis, which could account for the thermal anomalies observed in the Cameros Basin, is the circulation of hot fluids during the evolution of the basin. These fluids could have heated the sediments to temperatures higher than those expected of a normal rift, with a trend regardless of their stratigraphic position. In such a case, the permeability of the sediments is the most important variable in the determination of the anomalous temperatures. The original high permeability of the sandstone DS8 deposits would allow the circulation of hot fluids, giving rise to high temperatures in the sediments despite their stratigraphic position. Moreover, since this unit is located near the border of the basin, circulation of hot fluids could be facilitated by the numerous faults which affected this area (Fig. 9.1 and Fig. 9.2). In DS7, abundant sandstone bodies intercalated with shale and carbonate deposits could also facilitate hot fluid circulation, leading to higher temperatures along the whole stratigraphic succession (Fig. 9.11). The anomalous trend recorded along DS3 characterised by an increase in %Ro values toward the top could be attributed to the presence of a thick sandstone succession at the upper part of the DS3 unit (Fig. 9.3). This succession corresponds to the Urbión Gr (DS4, DS5, DS6 and part of DS7), whose deduced original high permeability (Arribas et al., 2013) facilitated the circulation of hot fluids. It may be assumed that temperatures recorded in sediments would gradually decrease from these upper sandstone bodies toward the bottom of the DS3 unit (Fig. 9.11, calibration-well 4). Finally, hot fluid circulation could be facilitated along the faults, with the record of anomalous high temperatures in sediments close to the fault (e.g. samples located close to the

NW-SE post-sedimentary faults - Fig. 9.1, grouped in the calibration-well 2 and 3 - Fig. 9.11).

Fluid inclusions provide useful data to clarify interpretation on the thermal history of the basin, as they provide different types of thermal information than vitrinite reflectance. Fluid inclusion homogenization temperature (Th) indicates the minimum temperature at which the inclusion was trapped, giving us direct information about burial temperatures and thermal pulses (Goldstein and Reynolds, 1994). On the other hand vitrinite reflectance indicates the maximum thermal conditions affecting the sediments (Taylor et al., 1998). Different information was performed from primary fluid inclusions in quartz overgrowths (FI-1), and generated during burial diagenesis, than those from quartz veins fracturing the sedimentary record (FI-2), during a later stage of diagenesis.

Fluid inclusions Th confirm that in the central and northern sector of the basin circulation of hot fluids need to be considered in the post-diagenetic stage. In the central sector of the basin temperatures measured in the primary fluid inclusions, trapped in the quartz overgrowths of the sandstone of the central sector of the basin (FI-1) (Huerteles Fm, DS3), are in agreement with the temperatures determined in this sector by the model (Fig. 9.12). Thus, it can be suggested that during the diagenesis stage, DS3 deposits located in the central sector of the basin were heated to temperature around 120 ºC, as correctly reconstructed by the thermal model (Fig. 9.12). However the high vitrinite reflectance measured in this area (SPOV-1, SPOV-3 and SPOV-7 samples - %Ro of 2.0-3.0) (Fig. 9.11, calibration-well 2 and Table 9.4) indicates that higher temperature is required in the post-diagenetic stages. In the northern sector of the basin, fluid inclusions measurements in the FI-2 sample (Urbión Gr, DS4) indicate higher temperature than those calculated by the model (Fig. 9.12). Considering that FI-2 fluid inclusions were measured in quartz veins, it can be deduced that fluids circulating in this part of the basin could reach temperature of 290 ºC. This data is coherent with the very high vitrinite reflectance measured in the deposits located in this area (SOY-3 sample, %Ro of 3.0) (Fig. 9.11, calibration-well 4 and Table 9.4). Lower temperatures were calculated by the model (Fig. 9.12), which considers only the effects of burial and a heat flow typical of an extensional setting. This model result is consistent with the Ochoa-Rodríguez (2006) fluid inclusion data, which determine for the diagenetic fluid inclusions of the Urbión Gr Th of 100-115ºC. However it has to take into account that the latter were not measured exactly in the modelled area. On the other hand Th measured in Ochoa-Rodríguez (2006) (Fig. 9.12) in the hydrothermal fluid inclusions are considerably higher than the model result, indicating that in this area circulated fluids with higher temperatures considerably higher than those reached only by burial.

The circulation of hot fluids could be attributed to the two hydrothermal metamorphic events which affected the Cameros Basin (Casquet et al., 1992; Alonso-Azcárate et al., 1999; Mas et al., 2003; Ochoa et al., 2007; González-Acebrón et al., 2011; González-Acebrón et al., 2012). On the basis of mineral transformations, these hydrothermal metamorphic events have been classified,

by the authors mentioned-afore, as very low grade metamorphism to low grade metamorphism, including anchizone interval (sensu Winkler, (1979). According to Kisch (1987) and Taylor et al. (1998), the anchizone grade corresponds to a vitrinite reflectance between 2.5 % and 4%, which is consistent with the values measured in the central and northern sectors of the basin.

Origin and flow path of the hydrothermal hot fluids is a still controversial and unsolved topic. A hypothesis could be that during the extension hydrothermal hot fluids rise from the depth along the deep detachment fault. Fracturing of the basement rocks in close to the ramp of the detachment could favorite circulation of the hot fluids up to the basin infill, affecting especially the sediments located in the depocentral areas located close to the ramp. During the inversion stage circulation of hydrothermal hot fluids could be facilitated along the thrust plane. However more detailed tectonic and petrologic studies would be necessary to clarify this topic in the future.

9.5.3. Recalibration of the model

In an attempt to reproduce the metamorphic events in the model, two extra heat flow peaks of short duration (1 My) of 200 mW/m^2 and 180 mW/m^2 were introduced into the northern sector of the modelled section and into part of the central sector. Peaks were introduced at 85 My and 45 My, which are the representative approximate ages for the two metamorphic-events (Fig. 9.13). The variations of the 2D model outputs with respect to the previous model in accordance with Royden´s heat flow estimations for the whole basin are shown in (Fig. 9.14).

The introduction of additional heat flows permitted a better calibration of the model (Fig. 9.15) than the previous attempt (Fig. 9.11). In fact, an additional heat flow, at 85 and 45 My in the northern and central sectors, does not modify the satisfactory calibration obtained for the southern sector, thereby allowing an improved calibration of the northern and central sectors (Fig. 9.15). Thus, in calibration-wells 2, 3 and 5 the lowermost measured %Ro values are correctly fitted to the theoretical curve. In calibration-well 4, the theoretical curve is consistent with the high values of the samples located in the uppermost stratigraphic levels of DS3, whereas the values measured in the lowermost samples are now lower than those of the theoretical curve (Fig. 9.15) in contrast to the previous calibration (Fig. 9.11). In the burial diagram versus temperature plot extracted from this new model at the FI-1 sample position, it is now clear that temperatures measured in the primary fluid inclusions in the quartz overgrowths were recorded before the metamorphic event (85 My) (Fig. 9.16), and they can be attributed to diagenetic burial process. On the other hand temperatures deduced in this new model in the FI-2 sample position now better approximate temperature measured in the primary fluid inclusions in the quartz veins (Fig. 9.16), which can be attributed to the circulation of the hot hydrothermal fluids trough fractures. Even the Th calculated by Ochoa-Rodríguez (2006) in the hydrothermal fluid inclusions of the

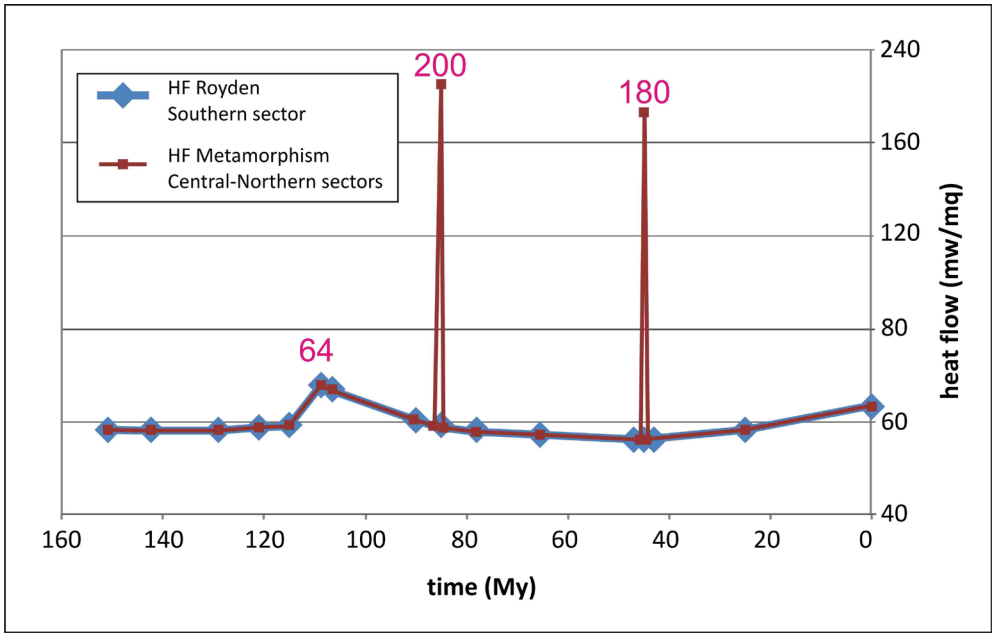

Fig. 9.13 - Heat flow trends defined for the Cameros Basin in attempt to reproduce the metamorphic events in the model. The blue curve represents the heat flow where the maximum peak is calculated by Royden's method. In the 2D model the blue curve heat flow trend was applied to the southern sector of the section, whereas the red curve to the northern and central sectors

Urbión Gr (DS7) cropping out in the section modelled area (145-184ºC) are coherent with the model (Fig. 9.11).

However, despite the more satisfactory results obtained, the new model cannot be considered totally calibrated. In fact, for the samples located in the uppermost stratigraphic levels of calibration-wells 2, 3, and 5 and for the samples of calibration-well 6, theoretical values are still markedly lower than the measured %Ro values (Fig. 9.15). Unfortunately, a better calibration cannot be performed using conductive heat flow as the only process of heat transport, which is a limitation of traditional basin modelling software. For this reason, heat flow is transmitted from the bottom to the top of the basin with the result that the highest temperatures are recorded in the deepest part of the basin. Consequently, advective heat transport, which could focus heat transport and thus high temperatures into the uppermost stratigraphic layers of the model, cannot be simulated.

An attempt to reproduce in the model the inversion of the vitrinite reflectance with depth trend was done using the "intrusion" tools provided by the PetroMod software. This tool allowed simulating the effect of intrusion of high temperature bodies at different levels of the stratigraphic record. Thus, the temperature anomalies created by the intrusions would allow reproducing the effects of the circulation of hot fluids even in the uppermost stratigraphic levels. In the model lithology and temperature of the intrusion bodies need to be assigned. For the

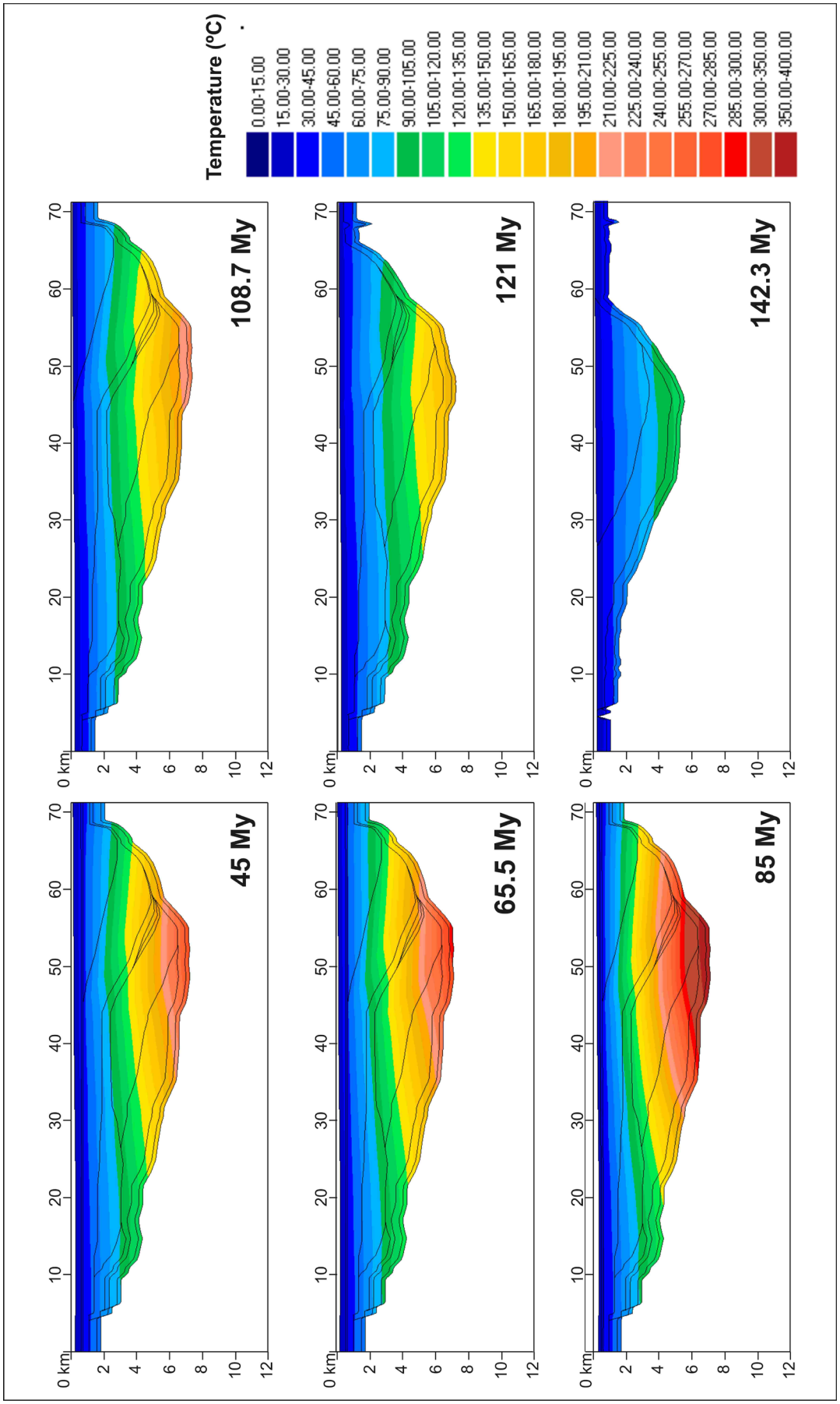

Fig. 9.14 - Output of the 2D thermal model that attempts to reproduce the metamorphic events, obtained adding in the northern and central sectors of the basin, a heat flow of short duration (1 My) at 85 My and at 45 My of 200 mW/m2 and 180 mW/m2, respectively

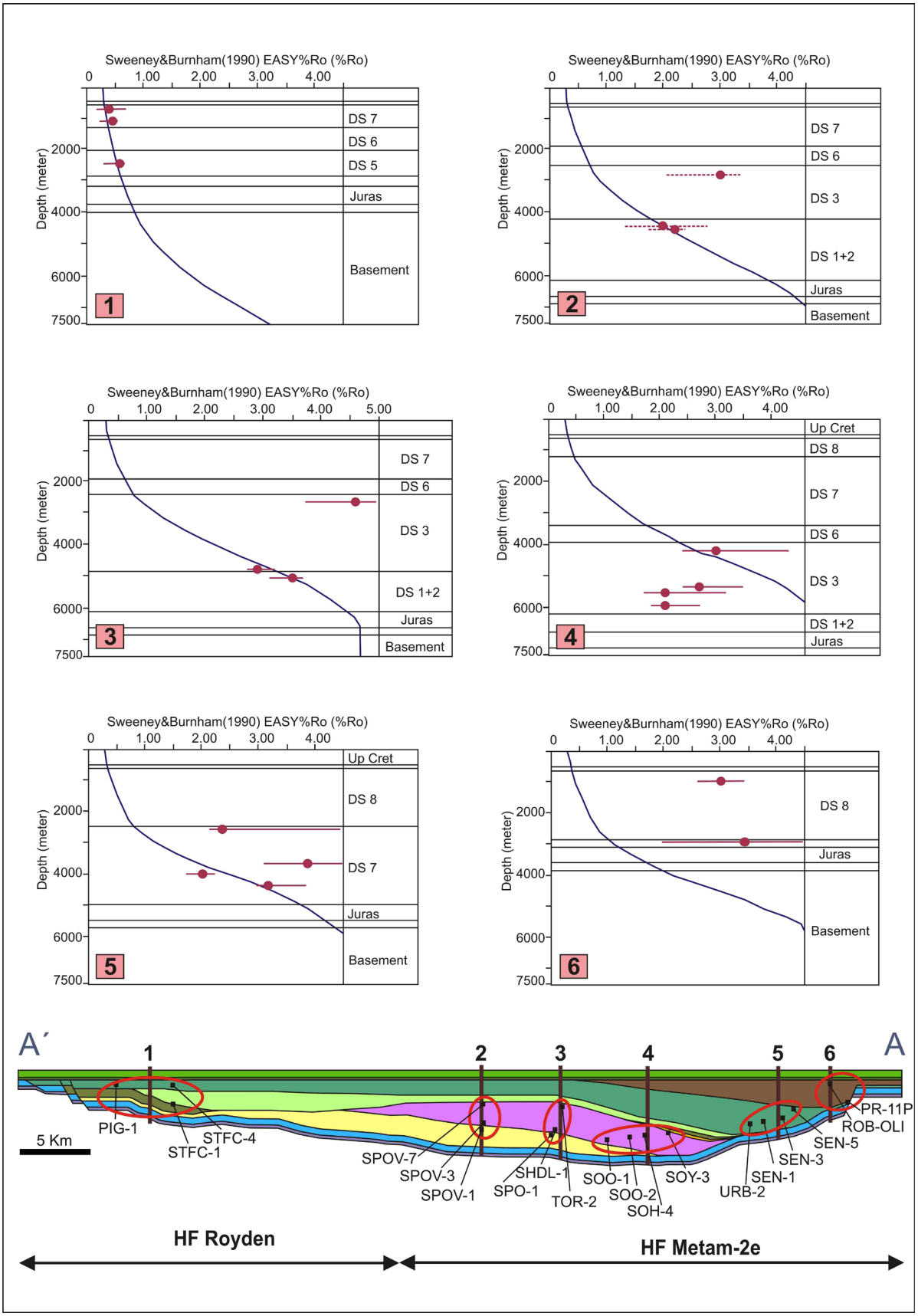

Fig. 9.15 - 2D Thermal model calibration using an additional heat flow of 200 mW/m² at 85 My and of 180 mW/m² at 45 My.in the northern and central sectors of the basin. Vitrinite reflectance data were used to calibrate the model. For the legend of the restored section see Fig. 9.2

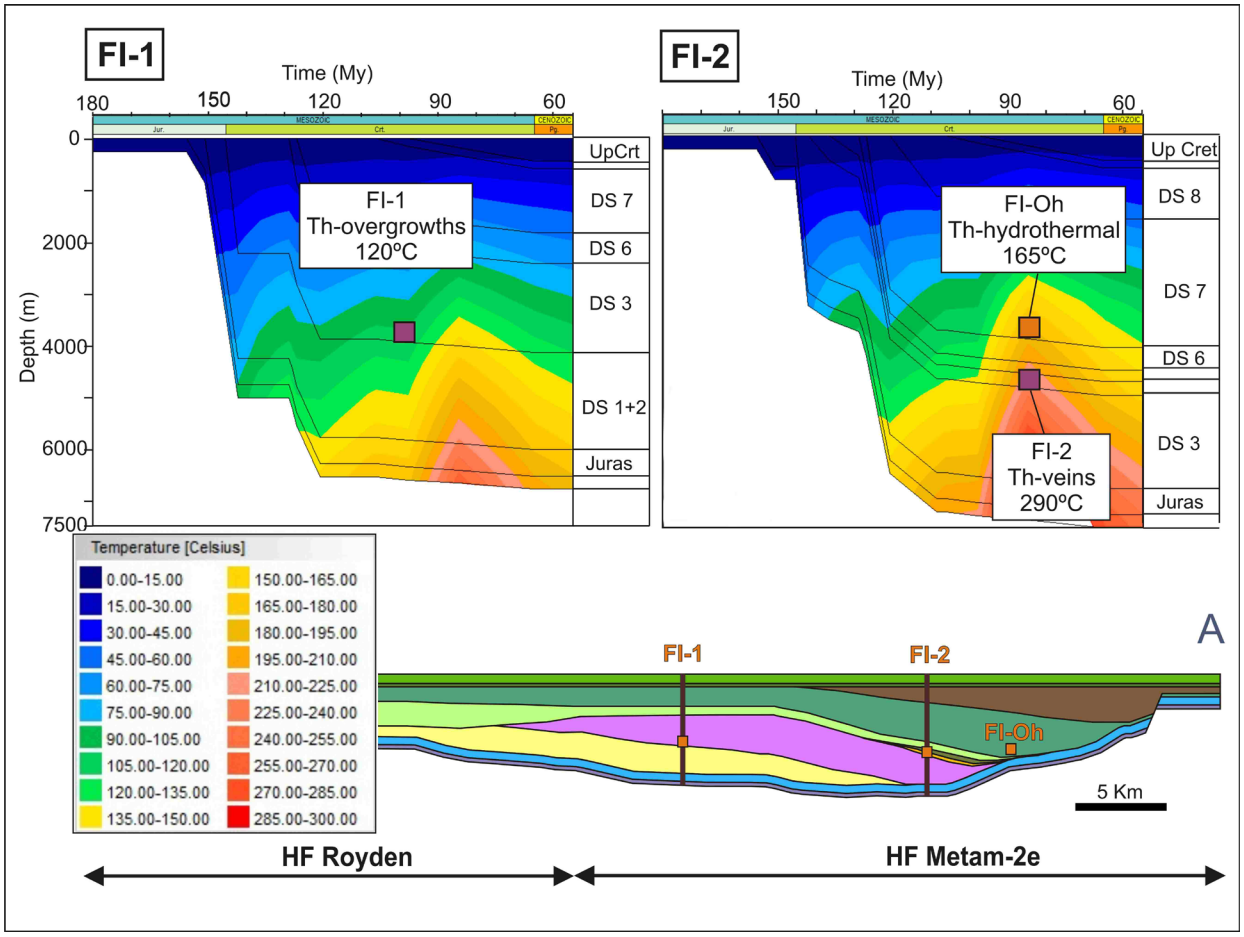

Fig. 9.16 - Burial diagram versus temperature plot extracted from the 2D thermal model at the site in the section where FI-1 and FI-2 fluid inclusion samples are located (Fig. 9.2 and Fig. 9.4). FI-Oh data is plotted on the same FI-2 virtual well, at the extrapolated stratigraphic depth. In this model the metamorphic events are reproduced, adding additional heat flow was considered at 85 and 45 My

simulation, basalt intrusions with a temperature of 300ºC were assigned at 85 My in the northern part of the section. It is important to clarify that the basalt intrusion assumption is used only to simulate in the model high temperatures in the uppermost stratigraphic layers, whereas it is known that any basalt intrusion occurred in this part of the basin.

As consequence of the intrusion, in an almost instantaneous time span, considerably higher temperatures were calculated by the model in the northern sector of the basin, even in the uppermost stratigraphic layers (Fig. 9.17). In this model a good calibration of the vitrinite

Fig. 9.17 - Output of the 2D thermal model that attempts to reproduce the circulation of hot fluids even in the uppermost stratigraphic layers affected by the metamorphism (northern sector), introducing an intrusion of hot temperature bodies in the stratigraphic record at 85 My. In an almost instantaneous time span considerably higher temperature were calculated by the model in the northern sector of the basin, even in the uppermost stratigraphic layers. For the legend of the restored section see Fig. 9.2

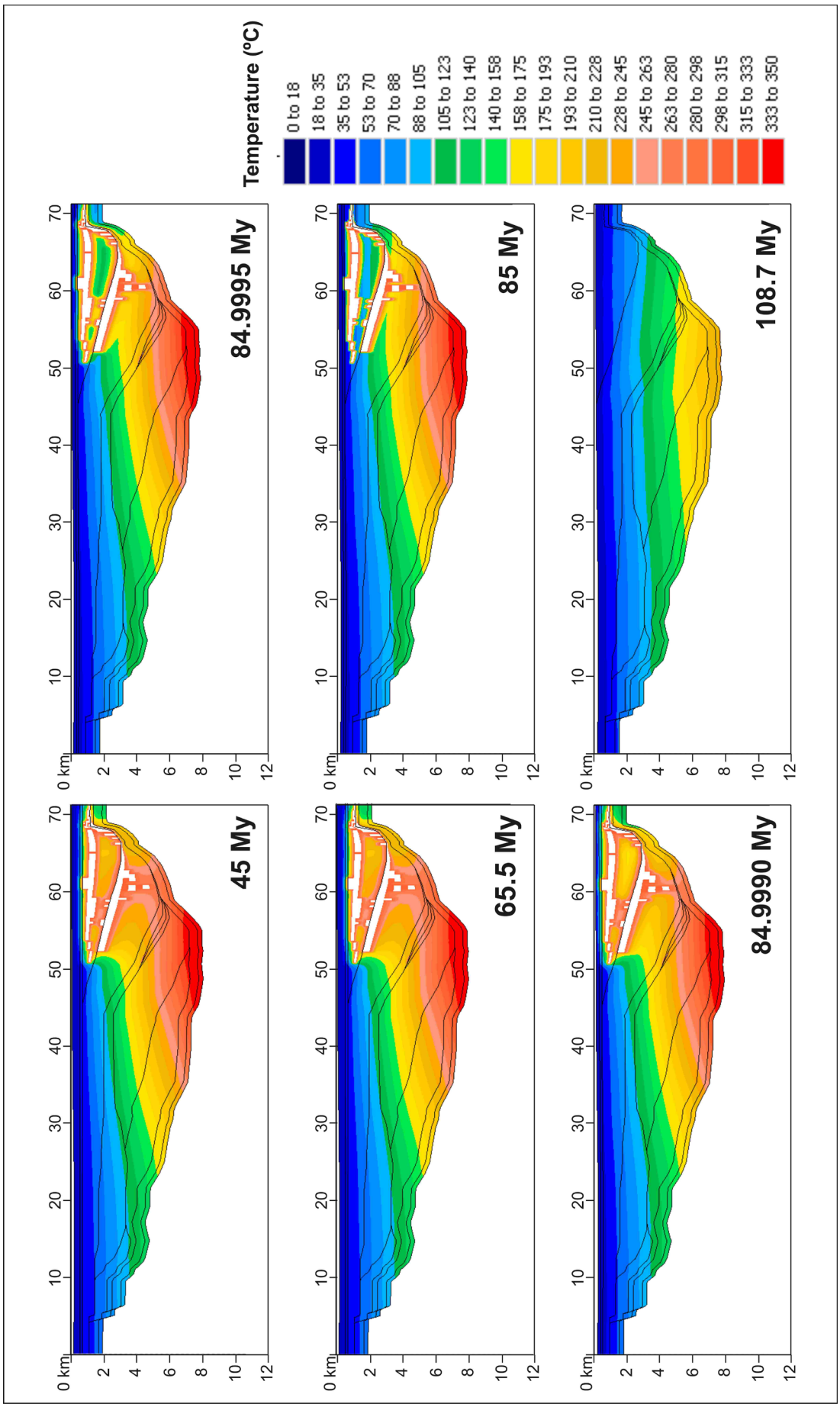
Temperature (°C)
0 to 18
18 to 35
35 to 53
53 to 70
70 to 88
88 to 105
105 to 123
123 to 140
140 to 158
158 to 175
175 to 193
193 to 210
210 to 228
228 to 245
245 to 263
263 to 280
280 to 298
298 to 315
315 to 333
333 to 350
84.9995 My
85 My
108.7 My
45 My
65.5 My
84.9990 My
0 km
2
4
6
8
10
12
70
60
50
40
30
20
10

reflectance data was performed for the calibration-wells 5 and 6, inverting the vitrinite reflectance increase-with-depth trend (Fig. 9.18).

The introduction of basalt intrusion facies at different stratigrafic levels can perform a better calibration of the model, as it can be reproduced high temperatures in the uppermost stratigraphic layers and the inversion of the vitrinite reflectance-increase-with-depth trend. On the other hand a drawback of this method is that basalt intrusions create impermeable layers in the basin infill, which could influence and limit fluid flows paths (e.g. hydrocarbons migration paths). Thus, despite of this method can be considered useful to reproduce correctly the thermal history of the basin, it cannot be used when the hydrocarbons generation, migration and accumulation have to be simulated.

9.6. CONCLUSIONS

1D and 2D thermal models reconstructs paleo-temperature over geologic time and its spatial variation in the basin. Results of the 1D and 2D thermal models, using a typical rift heat flow, show that the maximum temperature is attained in the central and northern sectors of the basin at the end of the extensional stage, whereas temperatures decreased towards the borders of the basin. Maximum temperatures correspond to the maximum heat flow peak recorded at the end of the extensional stage (108.7 My). 1D thermal models calculate lower temperature for the basin infill than the 2D thermal model, indicating that fluid flow and heat conduction occurred not only in a vertical direction but also in a lateral one.

Calibration with vitrinite reflectance data indicates that the 2D thermal model is correct only for the southern sector of the basin, where the maximum temperatures at the end of the extension (108.7 My) of 105-135 ^{o}C are calculated by the model. In the central and northern sectors, the %Ro values are markedly higher than the theoretical values of the model, and, in some cases, they invert the typical %Ro-increase-with the expected depth. On the other hand fluid inclusions data indicate that the model calculates correct burial diagenetic temperatures in the central sector of the basin, whereas in the northern sector of the basin indicate that higher temperatures need to be considered, as consequence of the circulation of hot fluids.

These results suggested that the anomalous temperatures recorded in the basin are consequence of hot fluid circulation during the evolution of the basin. Hot flow circulation can heat the sediments to anomalously high temperatures regardless of their stratigraphic position. Thus, permeability properties constitute a very important variable which determines heat transport in rocks. Furthermore, faults that favored the circulation of hot fluids can enhance heating of sediment layers. Fluid inclusions support the hypothesis of circulation of hot fluids in the basin, and they indicate that circulation may occur in a post-burial diagenetic stage of the

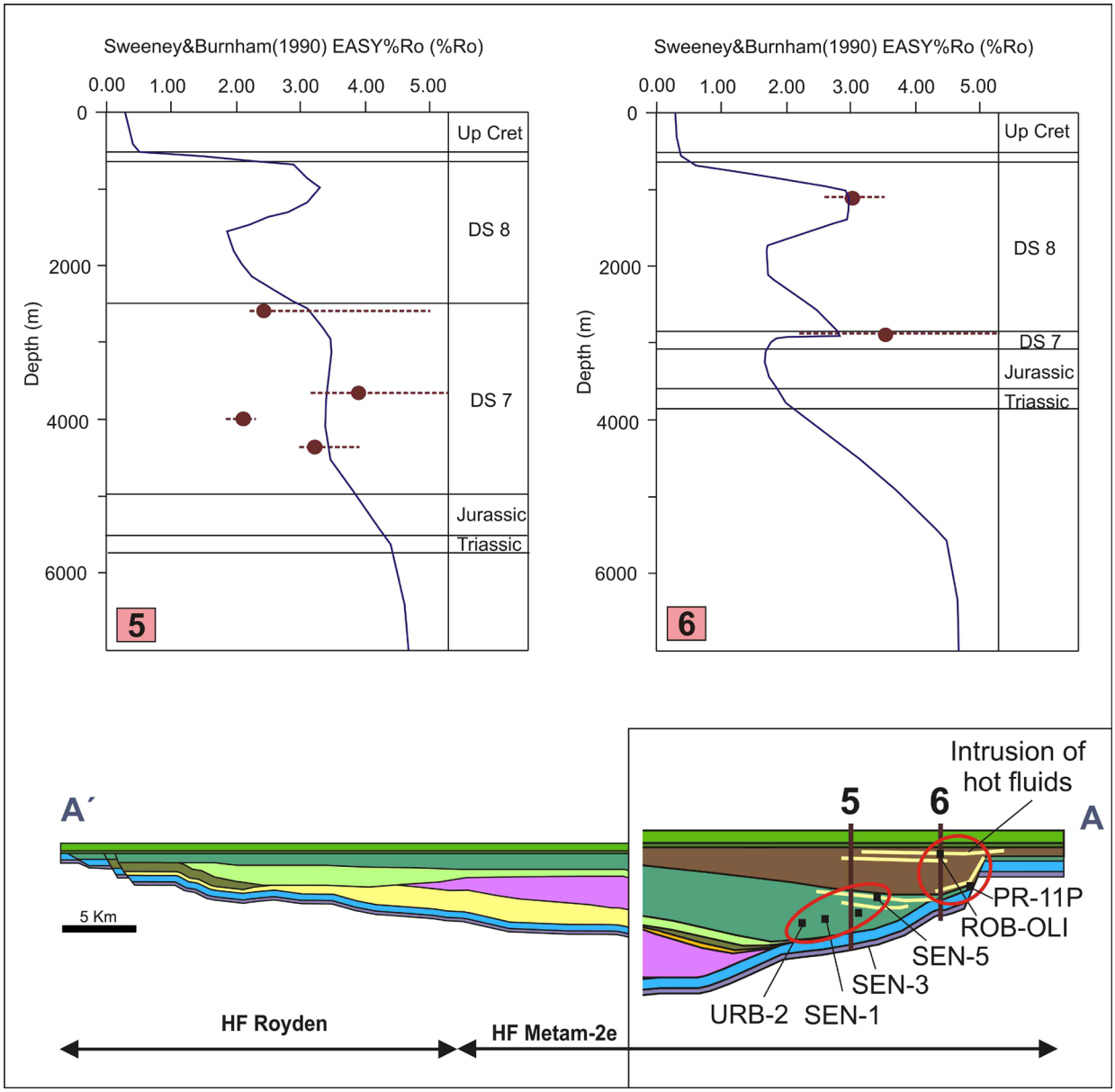

Fig. 9.18 - Introducing an intrusion of hot temperature bodies in the uppermost layers of the stratigraphic record, which simulate hydrothermal fluids circulation, an inversion of the vitrinite reflectance increase-with-depth trend was achieved. Calibration-wells 5 and 6 are now correctly calibrated. For the legend of the restored section see Fig. 9.2

basin infill evolution. Circulation of hot fluids was attributed to the metamorphic events that affected the central and northern sector of the basin during the post-extensional stage and the Alpine compressive phase.

The addition of two short-time heat flow peaks to the model only in the northern sector and in part of the central sector of the basin coeval with the metamorphic events improved the calibration of the models. Even so, the high temperatures recorded in the uppermost stratigraphic levels could not be calibrated satisfactorily because the modelling approach only allows the

conductive heat transport from the bottom towards the top of the basin.

An attempt to reproduce in the model high temperatures even in the uppermost stratigraphic layers, and to obtain the inversion of the vitrinite reflectance with depth trend, was done introducing in the model basalt intrusions in the uppermost stratigraphic layers. Intrusions reproduce the circulation of hot hydrothermal fluids in these levels and very good calibration results were performed by this model. Despite of the intrusion model can simulate a correct and reliable thermal history of the basin, it cannot be used when hydrocarbons migrations want to be modelled, as basalt intrusion would limit fluid flow circulation in the area.

The reconstruction of the thermal history of the Cameros Basin contributes significantly to the understanding of the most important parameters and conditions affecting the basin infill. It also provides a sound basis for future reconstructions of the thermal maturity of organic matter in the basin and for the possible generation, migration and accumulation timing of hydrocarbons.

Chapter 10

10. Organic Matter Characterisation

10.1. INTRODUCTION

10.1.1. Organic matter in sedimentary rocks

Characterisation of the organic matter in a sedimentary basin is a fundamental tool for coal and hydrocarbons exploration, as well as in the reconstruction of the paleoenvironmental conditions, in the calibration of the thermal history of the basin, and in sequence-stratigraphic analysis (Diessel, 2007).

"Organic matter has been defined as a solid substance containing organic carbon (Corg), which not includes carbonates of organic origin (Taylor et al., 1998). Most organic matter in a rock represents the solid, usually black or dark-coloured, remains of plants or animals, which lived at the time the rock was being deposited. Many sedimentary rocks contain minor amounts of organic matter, whereas comparatively few rocks – notably coal seams – are made up almost totally of organic matter. Organic matter preserved in other kinds of sedimentary rocks than coal, especially source rocks for oil and gas, is derived from a wide range of plant and animal organisms, preserved after varying, but commonly high degrees of biodegradation. As a result, much organic matter in sedimentary rocks other than coal is fine grained and widely dispersed" (Taylor et al., 1998)

"Two main requirements must be met for carbonaceous rocks to form: first, there must be a source of organic matter available at the time the sediment is being deposited and, second, some of that organic matter must be preserved during the processes of deposition, diagenesis and metamorphism. Most of the organic matter initially available is broken down soon after death of the organism to form carbon dioxide, water and other simple compounds. Partial preservation requires that processes of decay and oxidation do not remove all of the organic matter before some part can be preserved by burial beneath later deposits. In other words, the rate of generation of organic matter must exceed the rate of its destruction. Even in coal seams, the organic matter preserved represents only a small fraction of what was originally available" (Taylor et al., 1998).

10.1.2. Characterisation of the organic matter

10.1.2.1. Petrographic characterisation

"The basis of organic matter petrography is optical microscopy, that includes reflected and transmitted white light, fluorescence (UV and blue light excitation), and polarized light analysis of the organic matter in a broad sense. In some case palynological studies combined with organic petrography focused on the geological aspects are also taken into account Incident white light petrography allows the observation of images that are formed by reflectance contrast. Ultraviolet (UV), blue and blue-violet incident light allow imaging of organic material (mostly macerals of liptinite group) by autofluorescence emissions. Organic components observed using incident light are described as macerals, typically identified and described in coals" (Suárez-Ruiz et al., 2012).

"Macerals are identified on the basis of their physico-optical properties. Four macerals groups are identified, which nomenclature and classification has been regulated by International Committee for Coal and Organic Petrology (ICCP 1998, 2001) and Sýkorová et al., (2005). The huminite group is identified in low rank coals such as lignites and subbituminous coals (rock with a low degree of thermal maturity) and is the precursor of the vitrinite group found in medium and high rank coals (ICCP, 1998; Sýkorová et al., 2005). This group derives from botanical tissues mainly composed of lignin and cellulose. Huminite/vitrinite macerals are found in highest concentration in sediments of terrestrial origin (e.g., coals and carbonaceous shales) and are nearly absent in most carbonate rocks. The inertinite maceral group (ICCP, 2001) derives from plant material that has been affected by pre- or syn-sedimentary alteration processes such as oxidation, moldering and fungal attack. The liptinite maceral group (ICCP, 1971, 1975; Stach et al., 1982; Teichmüller, 1989; Taylor et al., 1998) is derived from the resistant lipoid part of the organisms such as spore and pollen, cuticles, and various types of vegetal secretions (plant waxes, fats, oils and resins), algal-derived materials, and some degradation

products and productsof secondary generation during the maturation processes. Macerals of the liptinite group are best characterised by their fluorescence properties at low rank/maturity and therefore observation with incident UV or blue light may be required. Liptinite macerals show the highest content in hydrogen and through thermal evolution they are a source of hydrocarbons (Tissot and Welte, 1984; Taylor et al., 1998)" (Suárez-Ruiz et al., 2012).

"In sedimentary rocks with dispersed organic matter (e.g., oil shales, source rocks) faunal relics, and microfossils of various compositions are found in addition to the huminite/vitrinite, inertinite, and liptinite groups. The zooclasts group includes: scolecodonts, chitinozoans, graptolites and conodonts, and other organic remains such as fish scales. Dinoflagellates and acritarchs are other forms of algal-derived materials in rocks which occur as resistant cysts. Moreover, non-structured organic matter, that is, amorphous organic matter (Bertrand, 1993) or an organo-mineral groundmass (organic matter intimately associated with the fine-grained minerals such as clays), commonly is identified in oil shales and source rocks. At low thermal maturity, the amorphous organic matter typically is fluorescent with spectra containing a strong green–yellow component at various intensities. Usually the amorphous organic matter constitutes an important fraction of the total organic matter in non-coaly organic rocks" (Suárez-Ruiz et al., 2012).

"Another component of the organic matter in sedimentary rocks is solid bitumens. Classifications of solids bitumens based on physico-optical properties have been reported by Jacob (1989, 1993) and Landis and Castaño (1995) among others. Solid bitumens appear in the macroporosity of the rocks, and as vein fillings, or dispersed in the mineralmatrix and their size is variable. They are secondary products of the coalification/maturation process and derive from the cracking of the macromolecular structure of kerogens into liquid hydrocarbons or from the cracking of oil to gas. Teichmüller (1973, 1974a, b) introduced the term exsudatinite for a solid bitumen generated (secondary maceral of the liptinite group) during the thermal evolution of the highly hydrogenated components of organic matter. Oil/hydrocarbons in the form of fluorescent droplets or absorbed by diagenetic minerals also are included as bitumens (Taylor et al., 1998)" (Suárez-Ruiz et al., 2012).

10.1.2.2. Geochemical characterisation

To completely characterise the organic matter organic petrography need to be implemented by geochemical analysis. One of the most applied whole rock geochemical technique is Rock-Eval pyrolysis (Barker (1974), Espitalié et al. (1977, 1985a, b, 1986) and Espitalié and Bordenave (1993). "In the Rock-Eval pyrolyzer, samples are combusted in the presence of an inert gas. The expelled products are measured as vaporized free hydrocarbons (S1), cracked kerogens (S2), and decomposed oxygen-containing compounds (S3). Other parameters also are provided

by this technique such as Tmax (°C), the temperature corresponding to the S2 peak; the total organic carbon (TOC); and indices such as the hydrogen and oxygen indices (HI; S2/TOC and OI; S3/TOC) and production index (PI; S1/[S1+S2]). Some of these indices are used as a proxy for elemental ratios in the pseudo-van Krevelen diagram for kerogen typing" (Suárez-Ruiz et al., 2012). Three main types of kerogens can be differentiated (Type I, Type II and Type III) in the order of decreasing HI and OI indexes (H/C and O/C ratios respectively in the original Van Krevelen diagram). The various types of kerogens can be associated to specific geological settings (Tissot andWelte, 1984). "Type I kerogen formed in lacustrine environments, where selective accumulation of algal material or severe biodegradation of the organic matter took place; Type II was related to open marine sediments where autochthonous organic matter derived from a mixture of phyto- and zooplankton was deposited in a reducing environment, with a Type II-S that was a high sulfur variety of Type II; and finally, Type III kerogen was essentially derived from terrestrial plants and deposited in proximal environments (Durand, 1993). A secondary type of kerogen (Type IV) composed of aromatic carbonized organic matter (pre-deposition, during deposition, or during oil cracking) with no potential for hydrocarbon generation also has been described" (Suárez-Ruiz et al., 2012).

10.1.2.3. Thermal maturity

"In addition to the identification of the organic matter components in sedimentary rocks, determination of its thermal maturation is essential to evaluate petroleum generation history, predict basin evolution, validate geological modeling, explore for hydrocarbons resources, and plan for resource utilization, among many other applications" (Suárez-Ruiz et al., 2012). Maturation depends mainly on the maximum rock temperature attained and in the way in which these temperatures varied over geological time (Taylor et al., 1998). Thus, to determine the thermal maturity, the reconstruction of the geothermal gradient of the area (which depend on heat flow and heat conductivity of the rocks) and of the burial time (subsidence rate, sedimentation rate, etc.,) need to be considered (Taylor et al., 1998). Maturation causes the loss of functional groups and of oxygen and an increase in carbon content of the organic matter components (coalification process) (Taylor et al., 1998).

"The evaluation of thermal maturity of the organic matter by optical microscopy is mostly based on direct measurement of optical properties (e.g., huminite/vitrinite reflectance measurement). Reflectance is the proportion of light reflected (expressed as a percentage) by a polished surface as measured by a photometer or other detector (digital cameras). This property is related to the aromaticity of the organic components and it increases (although not linearly) for all macerals as the level of coalification or maturation increases and the atomic O/C and H/C ratios decrease. Reflectance of solid bitumens has been used as well to evaluate thermal

maturity of a rock (Khavari-Khorasani and Michelsen, 1993; Kelemen et al., 2010), even if a direct relationship between solid bitumens and vitrinite reflectance has not been found yet (Suárez-Ruiz et al., 2012).

10.1.3. Exploration for hydrocarbons

"The search for hydrocarbons makes use of geophysics, field geologic interpretation, drilling and logging. All these expensive operation have increasingly benefited from a better understanding of the process of hydrocarbon generation, which helps in identifying the hydrocarbon-prone domains, in distinguishing between oil and gas occurrences and in reconstructing the migration paths, timing and filling of traps.

The formation of hydrocarbons requires the occurrence of organic source rocks and their thermal maturation. The characterisation and classification of the source rocks, as well as the definition of their thermal maturity, has become essential to obtain a complete understanding of the formation and occurrence of oil and gas" (Taylor et al., 1998).

10.1.3.1. Source Rocks

"Almost all sedimentary rocks contain at least some organic matter, 0.2 to 0.5% in most cases, sometimes more than 1% and very occasionally attaining 3 to 20%, or even more for lignite and coals. Thus, hydrocarbons are generated from almost all sedimentary rock when they reach maturity. However the amount of hydrocarbons generated varies over a wide range. The total amount of hydrocarbons which can be generated by a kerogen is function of its initial amount and elemental composition (especially to its initial H/C ratio). The amount of hydrocarbon generated by a source rock during its complete thermal evolution may represent 70 to 80% of its initial organic carbon content (TOC) for a Type I kerogen, 40 to 50% for a Type II and 10 to 20% for a type III" (Bordenave, 1993).

"The type of hydrocarbons formed by a source rock depends on the type of kerogen. The main petrological source components for oil are, in the lacustrine and marine sapropelic facies (Type I and Type II), algae, amorphous liptinite, and mineral bituminous groundmass, and, in the terrestrial facies (Type III kerogen), liptinite (sporinite, cutinite, fluorinate, resinite and derived from vascular plants) and secondarily vitrinite. The liquid hydrocarbons, formed from these organic constituents, may act as the source material for gaseous hydrocarbons, predominantly methane. Remaining organic matter, especially vitrinite and – within limits – also semi-inertinites, can relase methane in matured stage" (Taylor et al., 1998).

"According to Law (1999) source rocks can be divided into four major categories: 1) potential

source rocks, including rocks containing organic matter in sufficient quantity to generate and expel hydrocarbon if subjected to an increase in thermal maturation; 2) effective source rocks with organic matter that are generating and/or expelling hydrocarbons because a thermal cooling event such as uplift or erosion has occurred before exhaustion of its organic matter; 3) relic effective rocks, which are effective source rock that have ceased generating and expelling hydrocarbons because a thermal cooling event such as uplift or erosion has occurred before exhaustion of its organic matter; and, 4) spent source rock, which describes a source rock in an overmature state" (Suárez-Ruiz et al., 2012). Thus, to define the potential hydrocarbons that are and/or were generated in a basin it is necessary to determine for the organic matter of a source rock: 1) the type of organic matter that it contains (lacustrine, marine, continental) 2) the kind of hydrocarbons that can be generated 3) the hydrocarbons remaining potential, and 4) the thermal evolution of the rock. Combination of the petrographic and geochemical analyses is an excellent tool to obtain these information.

10.2. ORGANIC MATTER CHARACTERISATION IN THE CAMEROS BASIN

The Cameros Basin is characterised by a complex thermal history; during the post-extensional and inversion stages it was affected by a low to very low hydrothermal metamorphism that overheated some sectors of the basin (Casquet et al., 1992; Barrenechea et al., 1995; Alonso-Azcárate et al., 1999; Barrenechea et al., 2001; Mantilla-Figueroa et al., 2002; Mas et al., 2003; Ochoa et al., 2007; González-Acebrón et al., 2011; González-Acebrón et al., 2012; Omodeo-Salé, in rev.1). The differentiated subsidence trend recorded in the basin, which determines the differences in burial heating, increase the difference in the thermal conditions throughout the basin (**Chapter 9**).

Since the 30's, it has been known that the Cameros Basin is an active a petroleum system. As a result, a small amount of tar sandstone accumulation, located in the southern part of the basin, has been identified as the most important exploitable resource found in the area. Hydrocarbon generation, migration and accumulation have occurred at the end of the syn-extensional stage (Albian) in the most subsident area of the basin. Mas et al., (2003) and Ochoa et al., (2007) suggest that the hydrocarbons that accumulated in the reservoirs have been partially destroyed by hydrothermal metamorphism, which affected the basin during the post-extensional stage (Late Cretaceous).

Today, very little research has been performed to identify potential source rocks in the Cameros Basin petroleum system. In fact, due to the strong thermal alteration of the basin infill rocks, deduced by several inorganic proxies, such as mineral paragenesis, illite crystallinity,

fluid inclusions, etc. (Casquet et al., 1992; Barrenechea et al., 1995; Alonso-Azcárate et al., 1999; Barrenechea et al., 2001; Mata et al., 2001; Mantilla-Figueroa et al., 2002; Ochoa et al., 2007; Del Río et al., 2009a; González-Acebrón et al., 2011; González-Acebrón et al., 2012), it has been suggested that the original organic matter has been poorly preserved (Mas et al., 2003). Therefore, the potential source rocks have mainly been identified up to now based on sedimentary features (Mas et al., 2003), whereas no detailed petrographic nor geochemical study of the organic matter of the basin has been carried out.

Therefore, in this research a detailed study of the organic matter of the basin is performed, which aims to determine the following: 1) the thermal maturity of the basin infill; 2) the amount and type of organic matter presently preserved in the basin; 3) the effects of hydrothermalism on the preservation of organic matter; 4) the source rocks in the Cameros Basin petroleum system; and 5) the hydrocarbon potential, today and in the past, of the identified source rocks.

In this chapter a solid base for different types of research on the thermal evolution of the Cameros Basin and its petroleum system is provided. This work demonstrates how the interpretation of detailed petrographical and geochemical studies concerning the remaining organic matter may determine the potential and/or spent source rocks in a basin, even in the case of an over-mature organic matter that has been altered by hydrothermalism.

10.3. SAMPLING AND ANALYTICAL PROCEDURES

This work combines several disciplines to analyse Cameros Basin organic matter: 1) organic petrography, which involves a visual description of organic matter and vitrinite reflectance measurements; and 2) geochemistry, using total organic carbon measurements (TOC) and Rock-eval Pyrolysis.

10.3.1. Sampling

Seventy-six samples were collected from outcrops on the central-eastern section of the Cameros Basin (Fig. 10.1). The samples are representative of the entire basin infill record, including the pre-extensional deposits (substratum of the basin), and the syn-extensional and post-extensional deposits (Fig. 10.2 and Table 10.1). A synthesis of the lithological and sedimentary characteristics of the sampled units is reported in Table 10.2. The samples were grouped into six main sets, which correspond to the stratigraphic sections from which they were collected: the Soria, Casarejos, Montenegro, Torrecilla, Poveda, Yanguas, Enciso and Prejano sites (Fig. 10.1 and Fig. 10.2).

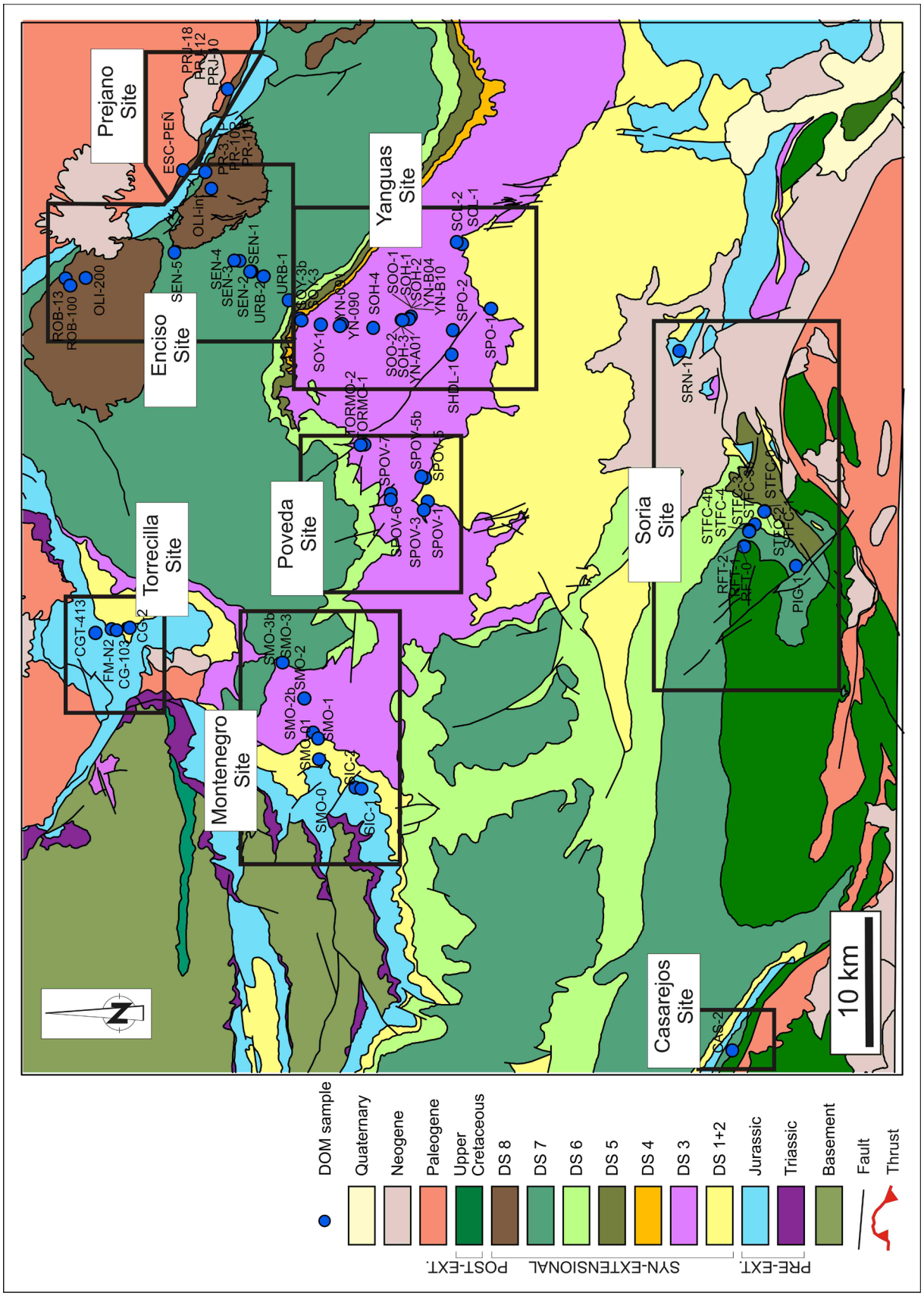

Fig. 10.1 - Geological setting of the study area and location of the analysed organic matter samples. The samples were grouped into eight sites on the map to facilitate the analysis

Most of the samples contained dispersed organic matter (DOM) and were taken primarily from dark fine-grained shale and, less frequently, from black limestone. Few samples are comprised of coal. The specific lithology of the deposits sampled from each unit is provided in Table 10.2. Samples were taken directly from outcrops and special caution was taken to avoid sampling levels affected by weathering and oxidation processes, which can compromise organic matter preservation. The total amount of collected material was variable, but was generally not less than 100 g of rock per sample.

10.3.2. Analytical procedures

10.3.2.1. Organic Petrography

The aim of the organic petrography analyses was 1) to identify the organic components contained in coal and in rocks containing dispersed organic matter (DOM) and 2) to determine the degree of organic matter maturity by measuring the huminite or vitrinite reflectance (Suárez-Ruiz et al., 2012). The microscopic organic remains of terrestrial, lacustrine and marine plants (macerals) were subdivided into three groups (ICCP, 1998; ICCP, 2001; Killops and Killops, 2009; Suárez-Ruiz et al., 2012): vitrinite, inertinite and liptinite. Solid bitumens, appearing as dispersed particles (Jacob, 1989; Suárez-Ruiz et al., 2012), were also considered.

The petrographic analyses were performed at the INCAR laboratory (Oviedo, Spain), using reflected white light and an oil immersion objective (50x) in an MPV-Combi-Leitz optical microscope. The petrographic pellets used for microscopic analysis were prepared using a modified procedure that is described in the ISO norm (ISO-7404-2, 2009). Those pellets are formed by 10-15 gr of rock, grounded until a particle size of about 1 mm, blended with a synthetic resin composed by styrene and phthalic anhydride. Rock particles stiffened in the resin in a random statistical orientation. The resulting block-rock samples were polished and put for minimum 24 hours in a silica-gel drier before the microscopic analysis. All of the samples were examined under reflected white light. The incident white light that was used to identify organic components helped to make observations in fluorescence mode, particularly in the case of immature samples. In this case, the organic matter was observed after excitation with UV and blue-violet light under a Leica DM 4500P microscope. For highly mature samples, the organic matter was examined under polarised light using the same microscpoe and incorporating a 1-λ-retarder plate in the microscope tube. This technique permits a better definition of the anisotropic properties of vitrinite and a precise differentiation from inertinite and/or solid bitumens. The recognition of irregular and rounded borders, particles that formed on the mineral borders and/or infilling in the mineral cavity, protruding rounded surfaces and the presence of degasification vacuoles, were used as a petrographic criteria to differentiate the solid bitumens from other macerals (Jacob, 1989; Taylor et al., 1998).

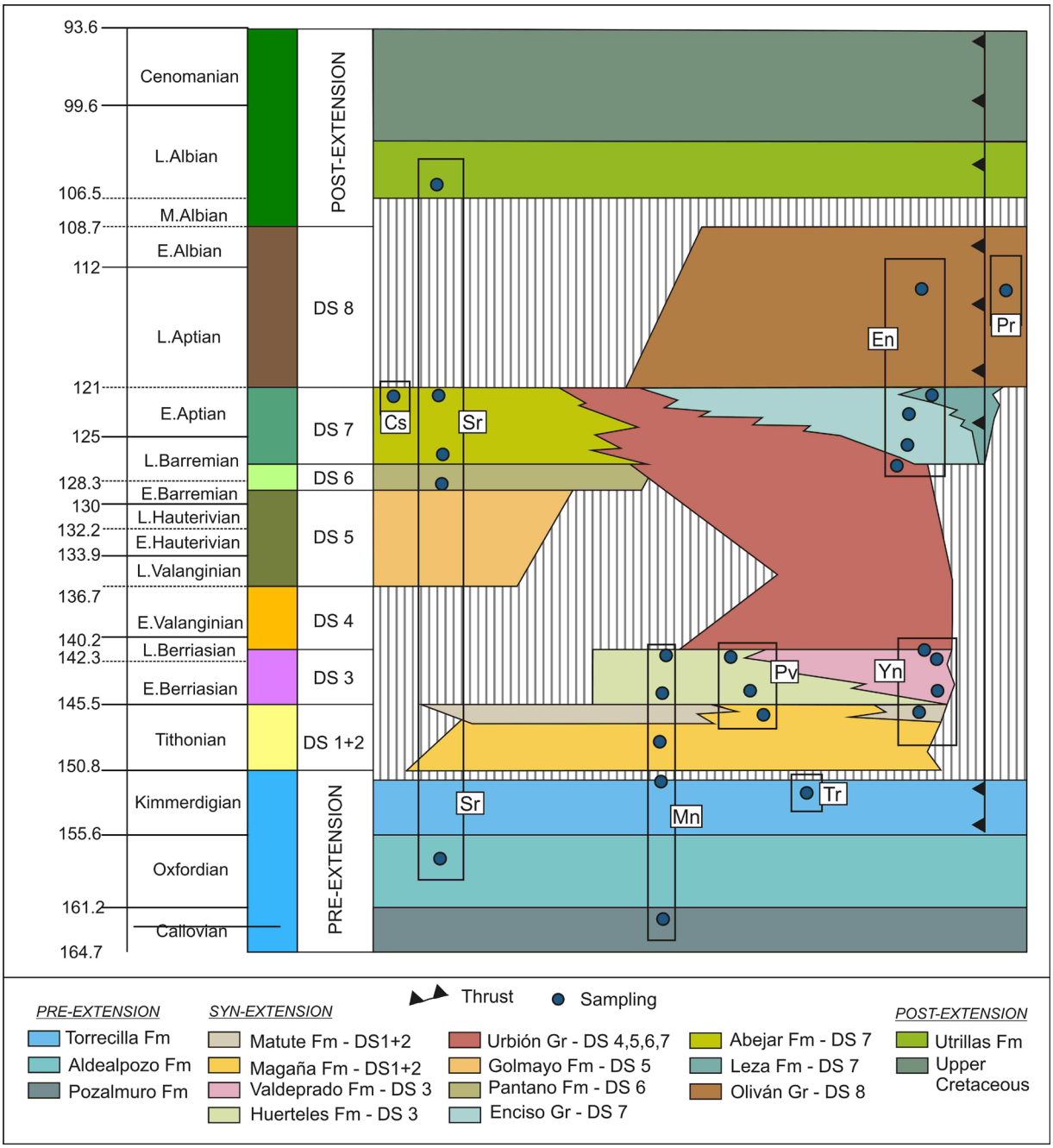

Fig. 10.2 - Stratigraphic chart of the basin. The sampling areas are identified as follows: (Cs) Casarejos site, (Sr) Soria site, (En) Enciso site, (Pr) Prejano site, (Pv) Poveda site, (Yn) Yanguas site, (Mn) Montenegro site and (Tr) Torrecilla site

On the huminite and vitrinite particles, the reflectance was measured in incident white light, following the ISO-7404-5 (2009) and ASTM-D7708-11, (2011) norms. In the case of altered/ oxidised samples, the vitrinite reflectance was not measured.

Site	Unit	ID-Sample	Site	Unit	ID-Sample
Torrecilla	Marine Jurassic - Torrecilla Fm	FM-N2 CGT-413 CG-103 CG-2	Yanguas	DS3 - Valdeprado Fm	SOO-1 SPO-2 SHDL-1
				DS1+2 - Matute Fm	SPO-1 SCL-2 SCL-1
Montenegro	DS3 Huerteles Fm	SMO-3b SMO-3 SMO-2 SMO-2b	Enciso	DS8 - Oliván Gr	ROB-100 ROB-13 OLI-200
	DS1+2 Magaña Fm	SMO-1 SMO-01		DS7 - Leza Fm	PR-11P PR-10P PR-3.1P
	Marine Jurassic - Torrecilla Fm	SMO-0			
	Marine Jurassic - Pozalmuro Fm	SIC-2 SIC-1		DS7 - Enciso Gr	SEN-5 SEN-4 SEN-3 SEN-2 SEN-1
Poveda	DS3 - Huerteles Fm	TORMO-2 TORMO-1 SPOV-7 SPOV-6 SPOV-5b SPOV-5		DS7 - Urbión Gr	URB-2 URB-1
	DS1+2 - Magaña Fm	SPOV-4 SPOV-3 SPOV-2 SPOV-1	Prejano	DS8 - Escucha Fm	PRJ 18 PRJ 12 PRJ 10 ESC-PEÑ
Yanguas	DS3 - Valdeprado Fm	SOY-3b SOY-3 SOY-1 YN-091 YN-090 SOH-4 YN-A01 SOH-3 SOO-2 YN-B10 YN-B04 SOH-2 SOH-1b SOH-1	Soria	Up. Cretaceous - Fm Utrillas	RFT-2 RFT-1 RFT-0
				DS7 - Abejar Fm	PIG-1 STFC-4b STFC-4 STFC-3b
				DS6 - Pantano Fm	STFC-3 STFC-2 STFC-1 STFC-0
				Marine Jurassic - Pozalmuro Fm	SRN-1
			Casarejos	DS7 - Abejar Fm	CAS-2

Table 10.1 - Sampling for site and unit. The order of the samples refers to their stratigraphic position (from bottom to top)

Unit	Age	Formation/Group	Whole unit lithology	Depositional environment	OM sample lithology
Utrillas	Late Albian	Utrillas Fm	Sandstone	Fluvial	Sandstones
DS8	Late Aptian-Early Albian	Oliván Gr	Sandstone bodies interbedded with shales and minor limestone beds	Fluvial and palustrine	Coal
		Escucha Fm	Sandstone and shale	Fluvio-deltaic	Coal and shales
DS7	Late Barremian-Early Aptian	Enciso Gr	Limestone alternated with sandstone and shale	Fluvio-lacustrine/palustrine	Dark shales
		Urbión Gr	Coarse grained sandstone and shales	Fluvial meandering	Dark shales
		Abejar Fm	Conglomerate and sandstone interbedded with thin shale levels	Fluvio-lacustrine-palustrine delta-plain	Grey shales
DS6	Late Barremian	Pantano Fm	Sanstone interbedded with conglomerate and shale	Alluvial-Fluvial braided	Shales
DS3	Berriasian	Valdeprado Fm	Carbonate-marls interbedded with gypsum levels	Shallow, perennial carbonate-sulfate coastal-lakes	Black-shales
		Huerteles Fm	Sandstone interbedded with shale and marls	Fluvial, tide-dominated deltaic and palustrine	Shales
DS1+2	Tithonian	Magaña Fm	Conglomerate and sandstone intercalated with shales	Fluvial-palustrine	Black limestones
		Matute Fm	Micritic limestone	Lacustrine	Dark shales
Jurassic	Kimmeridgian	Torrecilla Fm	Reefal and oolitic limestone	Shallow carbonate ramp	Dark limestones
	Oxfordian	Aldealpozo Fm	Limestone	Shallow carbonate ramp	Dark limestones
	Callovian	Pozalmuro Fm	Carbonate-Marls and shales	Mid-outer ramp	Black -shales

Table 10.2 - Lithologies and depositional environments of the stratigraphic units sampled for organic matter characterisation

10.3.2.2. TOC determination and Rock-Eval pyrolysis

Complementing the petrographic analyses, the chemical composition of the organic matter and its thermal maturity was obtained using Rock-Eval pyrolysis (Barker, 1974; Espitalié et al., 1977; Espitalié, 1985a, b; Espitalié et al., 1986; Peters, 1986; Espitalié and Bordenave, 1993; Behar

et al., 2001).

Rock-Eval pyrolysis analyses were carried out in a Rock-Eval 6 instrument (Université de Lausanne - Institute de Geoscience, Swisse). For the pyrolysis analysis, 1 gr of powder rock (40-50 micron in size), for each collected samples, was used. In a first step the powder sample was heated in an inert atmosphere to 300ºC, in order to determine the quantity of the thermovaporized free hydrocarbon present in the sample (S1 peak, expressed in mg HC/g of initial rock). Secondarily the programmed heating is carried out until 650º and the quantity of hydrocarbons released between 300º and 650ºC represent the hydrocarbons resulting from the artificial cracking of the organic matter (S2 peak, expressed in mg HC/g of initial rock). The temperature at which the S2 peak reach its maximum (maximum hydrocarbon generation) is defined as Tmax; this parameter can be used as maturity indicator of a source rock when reliable values are obtained (Tissot and Welte, 1984; Espitalié et al., 1986; Peters, 1986). The CO2 released during the pyrolysis, both organic and inorganic in origin, is trapped and measured (S3 peak, mg CO/g of initial rock). Finally the organic total carbon content in the sample (TOC, %) is determined. Pyrolisable and residual organic carbon (PC and RC, respectively) are discriminated with Pyrolisis Rock Eval 6, because two distinct signals are recorded, one during pyrolysis and one during oxidation phases (Behar et al., 2001). Hydrogen index (HI, S2/TOC*100) and Oxygen index (OI, S3/TOC*100) parameters are calculated from these measured values.

10.4. RESULTS

In this section, the results that were obtained from the petrographical and geochemical analyses of the pre-extensional, syn-extensional and post-extensional deposits are presented. These results are described for each stratigraphic unit in which the basin infill and its substratum has been subdivided. Vitrinite reflectance and Pyrolisis rock-eval analyses data are presented in Table 10.3 and Table 10.4. The vitrinite reflectance of samples containing only few and/or bad-preserved vitrinite particles are indicated as "uncertain data" (Table 10.3). In **Appendix 3** vitrinite reflectances measured for each sample, together with their statistical distribution, are indicated. In **Appendix 4** a collection of microscope photographs taken for each sample is reported. In Table 10.5, a synthesis of the most significant petrographic and geochemical data for every sample group is shown.

To visually analyse the spatial distribution of results ArcGIS software was used. Maps with distribution of the values of the measured vitrinite reflectance, TOC, HI and S2 parameters of the Rock-Eval were generated (Fig. 10.3, Fig. 10.4, Fig. 10.5 and Fig. 10.6). An Inverse Distance Weighted (IDW) methodology was applied to the resulting datasets for interpolation and contouring of the different variables. The HI and OI indexes were used as proxies of the elemental

ID_sample	%Ro_Mean	%Ro_Min	%Ro_Max	Unit	Area
RFT-2 **(B)**	0.034	0	0.034	Up. Cretaceous-Utrillas Fm	Soria
RFT-1 **(B)**	0.034	0	0.034		Soria
RFT-0 **(B)**	0.034	0	0.034		Soria
PRJ 18	0.63	0.57	0.70	DS8 Escucha Fm	Prejano
PRJ 12	Absence of vitrinite particles				Prejano
PRJ 10	0.56	0.45	0.78		Prejano
ESC-PEÑ	0.62	0.47	0.76		Prejano
ROB 100	3.20	3.03	3.52	DS8 Oliván Gr	Enciso
ROB 13	3.00	2.57	3.47		Enciso
OLI 200	2.86	2.45	3.30		Enciso
PR 11P **(B)**	4.35	1.94	5.6	DS7 Leza Fm	Enciso
PR 1OP	Absence of vitrinite particles				Enciso
PR 3.1	Absence of vitrinite particles				Enciso
SEN-5	2.40	2.20	5.10	DS7 Urbión Gr	Enciso
SEN-4	nada	nada	nada		Enciso
SEN-3	3.88	3.10	5.70		Enciso
SEN-2	Absence of vitrinite particles				Enciso
SEN-1*	2.09	1.80	2.30		Enciso
URB-2*	3.20	3.00	3.90		Enciso
URB-1	Absence of vitrinite particles				Enciso
CAS2	0.30	0.18	0.35	DS7 Abejar Fm	Casarejo
PIG-1	0.47	0.3	0.9		Soria
STFC-4b	0.38	0.22	0.47		Soria
STFC-4	0.5	0.4	0.6		Soria
STFC-3b*	0.7	0.4	0.8		Soria
STFC-3*	0.75	0.50	1.00		Soria
STFC-2*	0.75	0.50	1.00	DS6 Pantano Fm	Soria
STFC-1	0.57	0.40	0.65		Soria
STFC-0	0.55	0.3	0.6		Soria
SOY-3b	2.9	2.5	5.2	DS3 Valdeprado Fm	Yanguas
SOY-3	3	2.4	4.3		Yanguas
YN-091	Absence of vitrinite particles				Yanguas
YN-090	Absence of vitrinite particles				Yanguas
SOY-1	Absence of vitrinite particles				Yanguas
SOH-4	2.7	2.4	3.5		Yanguas
YN-A01	Absence of vitrinite particles				Yanguas
SOH-3	2.2	1.6	3.2		Yanguas
SOO-2	2.00	1.8	2.2		Yanguas
YN-B10	1.57	1.2	1.8		Yanguas
YN-B04	2.4	2.2	3.2		Yanguas
SOH-2	2.05	1.9	2.3		Yanguas
SOH-1b	1.9	1.77	2.1		Yanguas
SOH-1	2.1	1.7	2.7		Yanguas
SOO-1	1.9	1.55	2.8		Yanguas
SPO-2*	4.6	4.2	5.2		Yanguas
SHDL-1	2.9	2.7	3.2		Yanguas
SMO-3b **(B)**	3.9	1.7	5.16	DS3 Huerteles Fm	Montenegro
SMO-3	Absence of vitrinite particles				Montenegro
SMO-2	3.8	2.24	4.24		Montenegro

ID_sample	%Ro_Mean	%Ro_Min	%Ro_Max	Unit	Area
SMO-2b*	1.04	0.7	1.34	DS3 Huerteles Fm	Montenegro
TORMO-2	4.6	3.7	6	DS3 Huerteles Fm	Poveda
TORMO-1	3.7	3.09	4.1		Poveda
SPOV-7	3	2.07	3.47		Poveda
SPOV-6	Absence of vitrinite particles				Poveda
SPOV-5b	2.3	1.96	2.92		Poveda
SPOV-5	2.4	2.14	2.98		Poveda
SPO-1*	3.5	3.1	3.7	DS1+2 Matute Fm	Yanguas
SCL-2*	2.18	2.17	2.2		Yanguas
SCL-1	3.1	2.27	3.9		Yanguas
SMO-1	2.8	2	3.7	DS1+2 Magaña Fm	Montenegro
SMO-01	3.34	2.75	3.82		Montenegro
SPOV-4*	1.6	1.2	1.8		Poveda
SPOV-3	2	1.3	2.8		Poveda
SPOV-2*	Absence of vitrinite particles				Poveda
SPOV-1	2.2	1.7	2.4		Poveda
FM-N2	2.98	2.2	3.47	Marine Jurassic Torrecilla Fm	Torrecilla
CGT-413	2.5	2.2	2.8		Torrecilla
CG-103	3.3	2.2	3.6		Torrecilla
CG-2	3	2.8	3.3		Torrecilla
SMO-0	4.45	3.7	5		Montenegro
SRN-1	Absence of vitrinite particles			Marine Jurassic Aldealpozo Fm	Soria
SIC-1	4.2	3.3	4.5	Marine Jurassic Pozalmuro Fm	Montenegro
SIC-2	4.2	3.3	4.5		Montenegro
* uncertain data	(B) measurement on bytumen particles				

Table 10.3 (Part 1 on the left) - Vitrinite reflectance measured in all of the samples (Table 10.1). The order of the samples refers to their stratigraphic position (from bottom to top)

ratios in the pseudo-van Krevelen diagram for kerogen typing (Espitalié et al., 1986) (Fig. 10.7), whereas an HI vs. Tmax diagram (Espitalié, 1985a, b) was used to determine the rock maturity as well as to confirm the kerogen type (Fig. 10.8) as well as to confirm the kerogen type (Fig. 10.8).

10.4.1. Jurassic substratum (pre-extensional deposits)

Jurassic samples of the basin substratum were taken from the Montenegro, Torrecilla and Soria sites (Fig. 10.1, Fig. 10.2 and Table 10.1). In the Montenegro area Jurassic deposits analyzed belong to the mixed siliciclastic-carbonate Callovian age unit (Pozalmuro Fm) and samples correspond to shale layers of a black-shale sequence of alternated marls-carbonate and

ID_sample	TOC [%]	PC [%]	RC [%]	HI [mg HC/g TOC]	OI [mg CO2/g TOC]	Tmax [°C]	S1 [mg HC/g rock]	S2a [mg HC/g rock]	S2b [mg HC/g rock]	S3
FM-N2	0.24	0.03	0.22	44	238	450	0.03	0.11	0.00	0.58
CGT-413	0.19	0.02	0.16	52	223	423	0.05	0.10	0.00	0.42
CG-103	0.12	0.02	0.10	63	400	426	0.01	0.08	0.00	0.48
CG-2	0.20	0.03	0.17	60	281	293	0.05	0.12	0.00	0.55
SMO-0	0.28	0.02	0.27	23	101	441	0.02	0.07	0.00	0.29
SIC-1	0.68	0.02	0.65	10	52	381	0.11	0.07	0.00	0.35
SIC-2	0.75	0.03	0.73	9	55	375	0.10	0.07	0.00	0.41
SRN-1	0.17	0.01	0.15	33	174	495	0.02	0.05	0.00	0.29
SMO-01	1.91	0.00	1.91	2	4	336	0.02	0.04	0.00	0.08
SMO-1	0.20	0.02	0.18	20	117	381	0.09	0.04	0.00	0.23
SPOV-1	0.36	0.02	0.34	9	113	510	0.01	0.03	0.00	0.40
SPOV-2	0.43	0.02	0.42	15	94	496	0.02	0.07	0.00	0.41
SPOV-3	0.47	0.04	0.43	26	203	439	0.01	0.12	0.00	0.95
SPOV-4	0.33	0.01	0.31	27	56	495	0.02	0.09	0.00	0.18
SPO-1	0.27	0.02	0.25	16	185	437	0.01	0.04	0.00	0.50
SCL-1	0.20	0.02	0.18	32	228	336	0.02	0.06	0.00	0.46
SCL-2	0.45	0.02	0.43	10	126	413	0.02	0.04	0.00	0.57
SMO-2	0.41	0.01	0.40	5	62	493	0.01	0.02	0.00	0.25
SMO-2b	0.24	0.02	0.22	27	200	494	0.02	0.07	0.00	0.48
SMO-3	1.77	0.02	1.75	3	28	494	0.02	0.05	0.00	0.50
SMO-3b	1.83	0.02	1.81	4	29	303	0.03	0.08	0.00	0.54
SPOV-5	0.13	0.03	0.10	114	219	496	0.02	0.14	0.00	0.27
SPOV-5b	0.09	0.02	0.07	51	411	302	0.02	0.04	0.00	0.35
SPOV-6	0.10	0.02	0.08	101	179	390	0.02	0.10	0.00	0.17
SPOV-7	0.47	0.02	0.45	16	74	495	0.03	0.08	0.00	0.35
TORMO-1	1.18	0.01	1.17	3	38	454	0.02	0.03	0.00	0.45
TORMO-2	0.91	0.00	0.91	0	7	305	0.01	0.00	0.00	0.06
SPO-2	0.38	0.02	0.36	29	46	477	0.03	0.11	0.00	0.17
SHDL-1	1.37	0.03	1.34	4	56	303	0.03	0.05	0.00	0.77
SOO-1	0.18	0.02	0.16	43	136	365	0.13	0.08	0.00	0.25
SOH-1	0.50	0.02	0.48	6	114	336	0.01	0.03	0.00	0.57
SOH-1b	0.60	0.02	0.58	13	80	433	0.02	0.08	0.00	0.48
SOH-2	2.31	0.04	2.27	4	37	313	0.05	0.10	0.00	0.86
YN-B04	0.65	0.03	0.62	10	114	418	0.03	0.07	0.00	0.74
YN-B08	0.28	0.04	0.24	24	412	358	0.03	0.07	0.00	1.15
YN-B10	0.56	0.02	0.54	14	69	332	0.04	0.08	0.00	0.39
SOO-2	0.86	0.02	0.84	6	56	393	0.07	0.05	0.00	0.48
SOH-3	2.22	0.04	2.18	3	41	319	0.03	0.06	0.00	0.90
SOH-4	0.98	0.02	0.96	2	68	495	0.03	0.02	0.00	0.67
SOY-1	3.81	0.12	3.69	26	27	434	0.11	0.97	0.00	1.02
SOY-3	0.32	0.01	0.31	17	39	435	0.03	0.05	0.00	0.12
SOY-3b	0.37	0.01	0.36	21	17	345	0.02	0.08	0.00	0.06
YN-090	0.57	0.02	0.55	0	132	-	0.00	0.00	0.00	0.74
YN-091	0.50	0.02	0.48	0	119	-	0.02	0.00	0.00	0.59
SOY-1	3.81	0.12	3.69	26	27	434	0.11	0.97	0.00	1.02
YN-A01	0.48	0.03	0.45	13	147	495	0.02	0.06	0.00	0.71
STFC-2	2.67	0.13	2.54	12	135	477	0.02	0.33	0.00	3.62
STFC-1	5.44	0.16	5.28	12	73	434	0.03	0.63	0.00	3.97
STFC-0	1.46	0.07	1.39	46	31	438	0.04	0.68	0.00	0.45
URB-1	1.34	0.02	1.32	4	44	314	0.03	0.05	0.00	0.59
URB-2	0.13	0.01	0.12	57	207	347	0.02	0.07	0.00	0.27
SEN-1	0.27	0.02	0.25	32	70	379	0.17	0.09	0.00	0.19
SEN-2	1.68	0.02	1.66	4	21	367	0.03	0.06	0.00	0.36
SEN-3	1.45	0.02	1.43	6	39	333	0.03	0.09	0.00	0.57
SEN-4	1.50	0.03	1.47	6	60	495	0.02	0.09	0.00	0.90
SEN-5	1.11	0.00	1.11	1	8	326	0.02	0.01	0.00	0.09
SOTO 02P	0.11	0.01	0.10	0	401	-	0.00	0.00	0.00	0.45
PR 3.1	0.17	0.01	0.16	0	237	336	0.00	0.00	0.00	0.41

ID_sample	TOC [%]	PC [%]	RC [%]	HI [mg HC/g TOC]	OI [mg CO2/g TOC]	Tmax [°C]	S1 [mg HC/g rock]	S2a [mg HC/g rock]	S2b [mg HC/g rock]	S3
PR 1OP	0.27	0.03	0.24	38	296	429	0.06	0.10	0.00	0.81
PR 11P	0.11	0.01	0.10	0	394	-	0.01	0.00	0.00	0.44
CAS2	17.82	10.72	7.10	695	43	438	2.75	123.83	0.00	7.66
PIG-1	1.52	0.99	0.53	714	27	433	0.90	10.85	0.00	0.41
STFC-4	3.48	0.11	3.37	28	28	427	0.04	0.99	0.00	0.96
STFC-4b	3.95	0.34	3.61	81	70	431	0.04	3.19	0.00	2.78
STFC-3	2.21	0.07	2.14	7	88	480	0.04	0.16	0.00	1.94
STFC-3b	2.84	0.08	2.76	10	73	431	0.05	0.27	0.00	2.07
ROB 100	3.85	0.01	3.84	0	15	-	0.01	0.00	0.00	0.58
OLI 200	2.04	0.02	2.02	0	35	606	0.02	0.00	0.00	0.71
ROB 13	1.33	0.01	1.32	0	24	-	0.01	0.00	0.00	0.32
PRJ 10	41.35	16.70	24.65	476	19	416	1.95	196.64	0.00	7.73
PRJ 12	6.30	0.58	5.72	89	62	439	0.06	5.64	0.00	3.90
PRJ 18	3.21	0.31	2.9	99	45	435	0.06	3.17	0.00	1.43
ESC-PEÑ	15.09	1.08	14.01	71	43	423	0.18	10.69	0.00	6.54
RFT-0	6.31	4.70	1.61	757	14	436	8.60	47.74	0.00	0.85
RFT-1	0.67	0.03	0.64	24	43	403	0.14	0.16	0.00	0.29
RFT-2	2.79	1.92	0.88	747	26	437	1.98	20.86	0.00	0.72

Table 10.4 (Part 1 on the left) – Rock-Eval data measured for all of the samples (Table 10.1)

shale deposits, generated in an outer platform marine depositional environment under anoxic conditions (Mas et al., 2002, 2003). In the Torrecilla site samples were taken from dark limestone deposits belonging to a reefal and oolitic limestones kimmeridgian in age unit (Torrecilla Fm). These deposits were generated in a shallow carbonate ramp (Benito et al., 2005). In the Soria area, to the South part of the basin, samples from Jurassic substratum were taken from a dominantly carbonate reefal and oolitic Oxfordian unit (Aldealpozo Fm).

Petrographic observations indicate that in all the sites, Jurassic samples are characterised by very scarce dispersed organic matter content, formed by vitrinite and inertinite maceral group particles. However, in the Soria site, no rest of organic matter was found. A stressed optical anisotropy is commonly observed in vitrinite particles (Fig. 10.9a-a1). Solid bitumens are observed as dispersed particles in the mineral matrix (Fig. 10.9b) and according to the reflectance value (2.3-3.7 %) they can be classified as Meso to Cata-impsonite (Jacob, 1989).

Vitrinite reflectance measurements indicate a range of the mean %Ro values of 3.3-4.5% in the Montenegro site and of 2.5-4.45%in the Torrecilla site, which correspond to overmatured thermal conditions (Taylor et al., 1998) (Fig. 10.3 and Table 10.5). The measured high reflectance of the vitrinite (therefore high maturity) is in accordance with the optical anisotropy observed in the vitrinite particles.

Pyrolisis Rock-Eval analysis determines mean TOC values of 0.17%, 0.3% and 0.7% for the Soria, Torrecilla and Montenegro sites respectively (Fig. 10.4 and Table 10.5). HI and OI indices indicate the dominance of a Type III kerogen with very low hydrogen content (Fig. 10.5 and Fig.

Unit	Area	Formation/ Group	Number of samples	Macerals Abundance				%Ro range of mean	TOC (%) mean	HI (mgHC/g TOC) mean	OI (mgCO2/ gTOC) mean	S1 (mgHC/ g rock) mean	S2 (mgHC/ g rock) mean	Tmax (ºC) (mean)
				Vitrinite	Inertinite	Liptinite	Solid Bitumen							
Pre-extens	Torrecilla	Torrecilla	5	●	●	○	●	2.5-4.45	0.3	48	249	0.03	0.1	407
	Montenegro	Pozalmuro	2	●	●	○	●	3.3-4.5	0.7	10	53	0.1	0.07	379
	Soria	Aldealpozo	1	○	○	○	○	-	0.17	33	174	0.02	0.05	495
DS1+2	Montenegro	Magaña	2	•	•	○	○	2.7-3	1.06	11	61	0.06	0.04	359
	Poveda	Magaña	4	•	•	○	•	1.7-2.8	0.4	19	117	0.02	0.08	485
	Yanguas	Matute	3	•	•	○	•	2.2-3.5	0.31	19	179	0.02	0.05	395
DS3	Montenegro	Huerteles	4	•	○	○	●	3 (bitumen)	1.06	10	80	0.02	0.05	446
	Poveda	Huerteles	6	•	•	○	○	2.4-4	0.48	48	155	0.02	0.07	407
	Yanguas	Valdeprado	19	●	●	○	●	2-4.6	0.9	14	108	0.11	0.1	388
DS6	Soria	Pantano	3	●	●	●	○	0.56	3.19	23	80	0.03	0.54	449
DS7	Enciso	Enciso	6	•	•	○	●	2-3.88	1.02	7	100	0.05	0.07	380
	Enciso	Leza	3	○	○	○	●	4.35 (bitumen)	0.17	9	309	0.02	0.06	383
	Enciso	Urbión	2	•	•	○	○	3.2	0.74	32	107	0.03	0.06	330
	Soria	Abejar	5	●	●	●	•	0.38-0.6	2.8	168	57	0.22	3.09	445
	Casarejo	Abejar	1	•	•	●	○	0.3	17.82	695	43	2.75	123.83	438
DS8	Enciso	Olivan	3	●	•	○	○	3	2.41	0	0.01	25	0	606
	Prejano	Escucha	4	●	•	●	●	0.6	16.49	184	42	0.56	6.5	428
Post-extens	Soria	Utrillas	3	○	○	○	●	).033 (bitumen	4.55	752	28	3.57	34.3	437

Maceral abundance legend:

●	●	•	○
Very abundant	Abundant	Scarce	Very scarce

10.7).

In the Torrecilla and Montenegro sites Tmax values indicate an immature thermal stage of the organic matter (Fig. 10.8), in contrast with the very high values of vitrinite reflectance that indicate overmatured thermal conditions. This incongruence can be caused by the high degree of thermal maturity and by presence in the samples of numerous solid bitumen particles, which consistently lowered the Tmax values of the Rock-Eval (Éspitalié et al., 1985b, Bordenave, 1993). Thus, for these samples, pyrolisis Rock-Eval data cannot be used as a reliable maturity index. On the other hand the Tmax measured in the Soria area (495ºC) can be considered reliable. A correspondent virtrinite reflectance value of 1.7% was estimated for these deposits considering the %Ro-Tmax relationship proposed by Bordenave, (1993) (Fig. 10.3).

In all the areas S1 and S2 parameters are lower than 0.3 (mg HC/g rock) (Fig. 10.6 and Table 10.5), which indicate the presence of very reduced quantity of free hydrocarbon in the rock and a very reduced quantity of hydrocarbons formed from the artificial cracking of the organic matter (Espitalié et al., 1986).

10.4.2. Tithonian (DS1+2)

DS1+2 are constituted by a dominant siliciclastic unit (Magaña Fm), which locally passes upward to a carbonate unit (Matute Fm) (Fig. 10.2). In the Montenegro and Poveda sites (Fig. 10.1 and Table 10.1) samples were taken from dark-grey mudstone intervals, interbeded in sandstone fluvial channel bodies, deposited in a floodplain palustrine environment (Magaña Fm). In the Yanguas site few samples were taken from dark thick tabular lacustrine carbonate beds (Matute Fm) (Fig. 10.2). Several of the collected samples were altered/oxidized (Fig. 10.9c) and they were not used for vitrinite reflectance and neither for pyrolisis Rock-Eval. Thus only few data are available for this unit.

Petrographic analysis revealed very scarce organic matter content. Maceral particles belong to the vitrinite and inertinite group whereas macerals from liptinite group are not observed. In the Poveda site, several vitrinite particles with coke texture (Fig. 10.9d) and few particles of solid bitumens were observed (Fig. 10.9e). In all the areas vitrinite particles display a marked anisotropic optical properties. Due to the anisotropy and to the scarce amount of vitrinite particles results are markedly heterogeneous in the Poveda and Yanguas sites, with a mean range of 1.7-2.8% in the Poveda and 2.2-3.5% in the Yanguas sites (Table 10.5). More homogeneous values

Table 10.5 - Synthesis of the most significant petrographic and geochemical data for each group of samples

were obtained in the Montenegro site, with a mean range of 2.7-3.0% (Table 10.5). Dry-gas to overmatured thermal conditions can be considered in all the sites (Taylor et al., 1998) (Fig. 10.3), which explains the absence of the liptinite macerals in all the samples.

Pyrolisis Rock-Eval analysis determines mean TOC values of 1.06 % in the Montenegro site and lower than 0.5% in the Poveda and Yanguas sites (Fig. 10.4 and Table 10.5). Plot of the HI and OI indexes indicates the dominance of Type III kerogen with a very low hydrogen content (Fig. 10.7) in all the areas (Fig. 10.5). Due to the high degree of thermal maturity in most of the cases Tmax cannot be used as a reliable thermal index (Espitalié et al., 1985b). In fact data plotted in the HI vs. Tmax diagram (Fig. 10.8) indicate thermal conditions ranging from immature

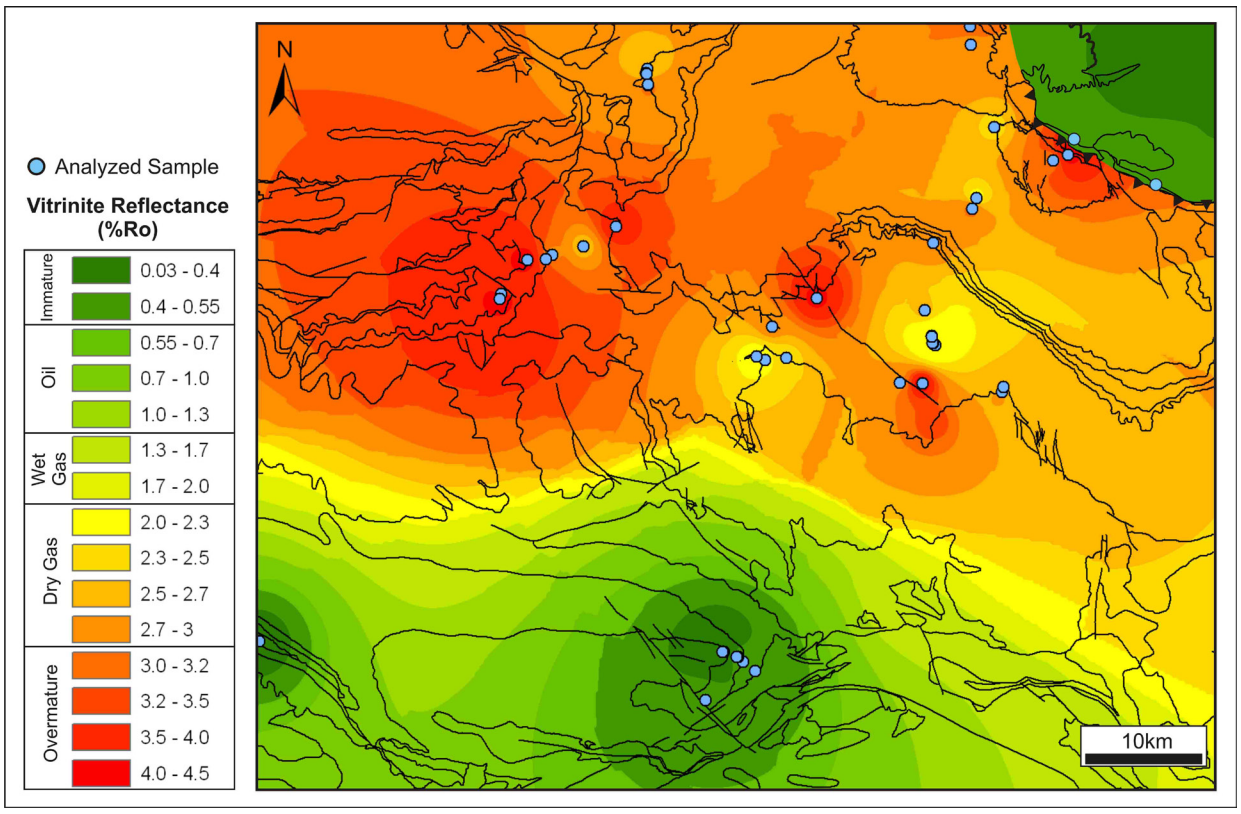

Fig. 10.3 - Interpolation of the vitrinite reflectance measured values (%Ro) in the study area

to overmatured, which is not consistent with the high vitrinite reflectance values. S1 and S2 parameters are lower than 0.1 (mg HC/g rock) (Fig. 10.6 and Table 10.5), which indicate the presence of very reduced quantity of free hydrocarbon in the rock and a very reduced quantity of hydrocarbons formed from the artificial cracking of the organic matter (Espitalié et al., 1986).

10.4.3. Berriasian (DS3)

DS3 is formed by siliciclastic deposits (Huerteles Fm) composed by alternation of thin laminated sandstone and shale beds, relative to a fluvial, tide-dominated deltaic and palustrine depositional system, that gradually evolves, laterally and vertically, to laminated carbonate-marls deposits (Valdeprado Fm) (Fig. 10.2). Valdeprado Fm deposits are frequently interbedded with thin gypsum levels, and thick black-shales intervals, generated in a shallow, perennial carbonate-sulfate coastal-lakes depositional environment and their peripheral mudflats with local marine influence (Quijada et al., 2010, 2013a,b). Analyzed samples were taken in the Yanguas, Poveda and Montenegro sites (Fig. 10.1, Fig. 10.2 and Table 10.1). In the Yanguas area samples belong to the Valdeprado Fm, whereas in the Poveda and Montenegro sites they belong to the Huerteles Fm.

Petrographic analysis indicates a very scarce amount of organic matter, formed by vitrinite and inertinite maceral group particles. Abundance in organic matter decreases from the Yanguas site to the Poveda and Montenegro sites. In the Yanguas and Poveda sites, in the samples located along the Oncala Fault were observed numerous vitrinite particles with coke texture. In the three areas frequently vitrinite shows anisotropic optical property. Very abundant solid bitumen

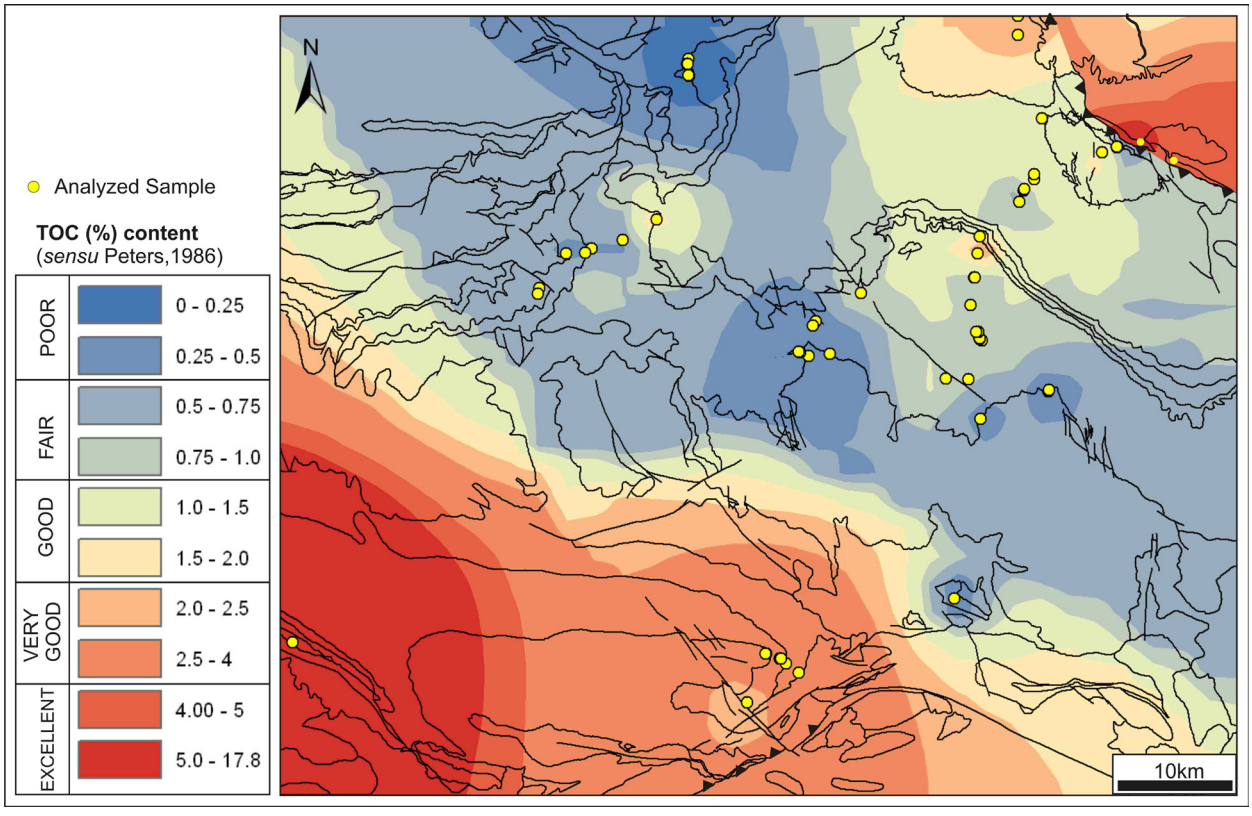

Fig. 10.4 - Interpolation of the TOC index values (%), recorded during Rock-eval pyrolysis in the study area

particles were found in the Yanguas and Montenegro sites (Fig. 10.9f and Fig. 10.9g). According to the reflectance values, 2%Ro in the Yanguas site and 3%Ro in the Montenegro site, solid bitumens are classified respectively as Meso-impsonite and Cata-impsonite (Jacob, 1989). In the Montenegro area bitumen particles have a coke mosaic texture with a marked anisotropy and they appear as inter-grown in the diagenetic carbonate crystal structure (Fig. 10.9g).

Vitrinite reflectance values indicate variable thermal conditions from dry-gas to overmature stages (Taylor et al., 1998) in the Yanguas and Poveda sites and overmature thermal conditions in the Montenegro site (Fig. 10.3). Generally vitrinite reflectance does not have a clear distribution

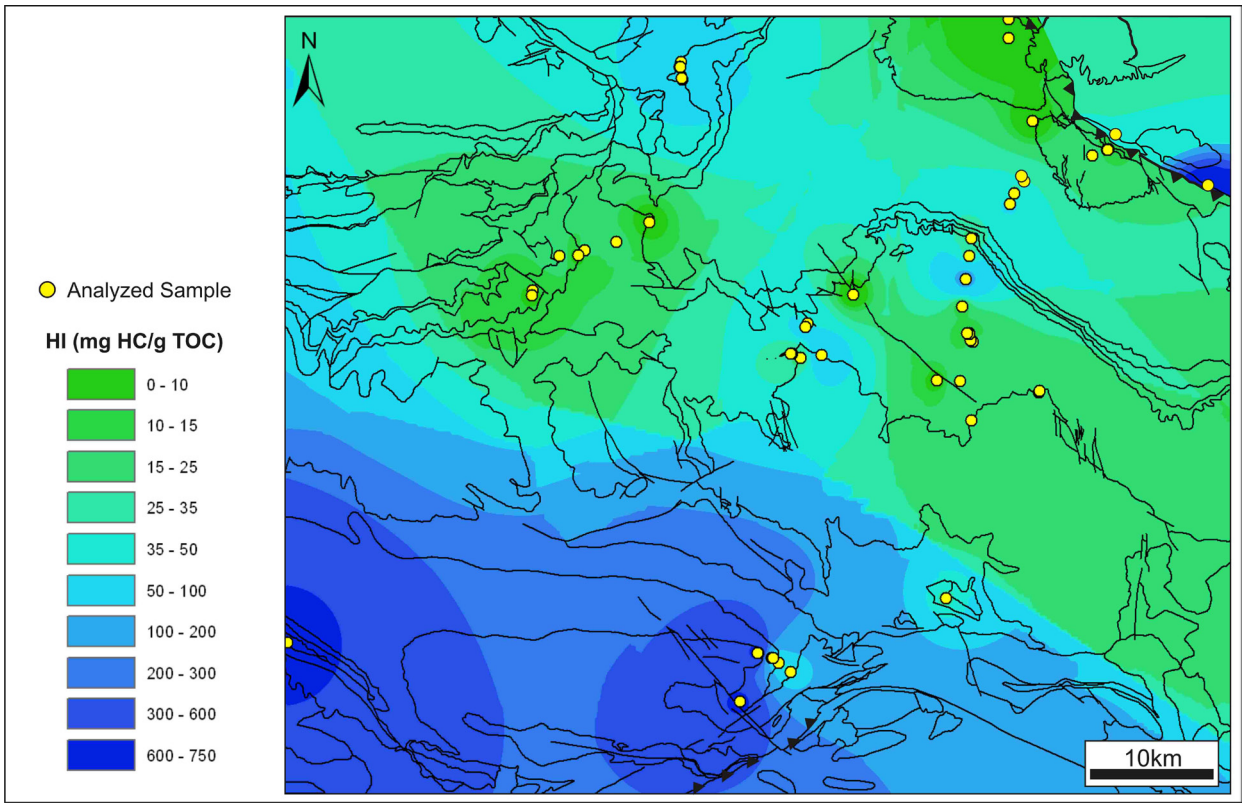

Fig. 10.5 - Interpolation of the HI parameters measured in the study area

trend along the stratigraphic series (Table 10.2). In the Yanguas site, and in correspondence of the Oncala Fault, lower stratigraphic levels show, %Ro values ranging from 3.0 to 4.6% (Fig. 10.1 and Table 10.2). In the upper stratigraphic levels, %Ro lowered to an average value of 2.0%. From this middle point of the stratigraphic succession to the top %Ro values gradually increase, reaching a maximum average of 3.0 %, in correspondence of the contact between the DS3 and the upper dominantly sandstone bodies (Urbión Gr) (Fig. 10.3 and Table 10.3), forming the DS4, DS5, DS6 and part of the DS7. In the Poveda site vitrinite reflectance measurements show an increasing trend of the maturity conditions from the bottom to the top of the section (Fig. 10.3 and Table

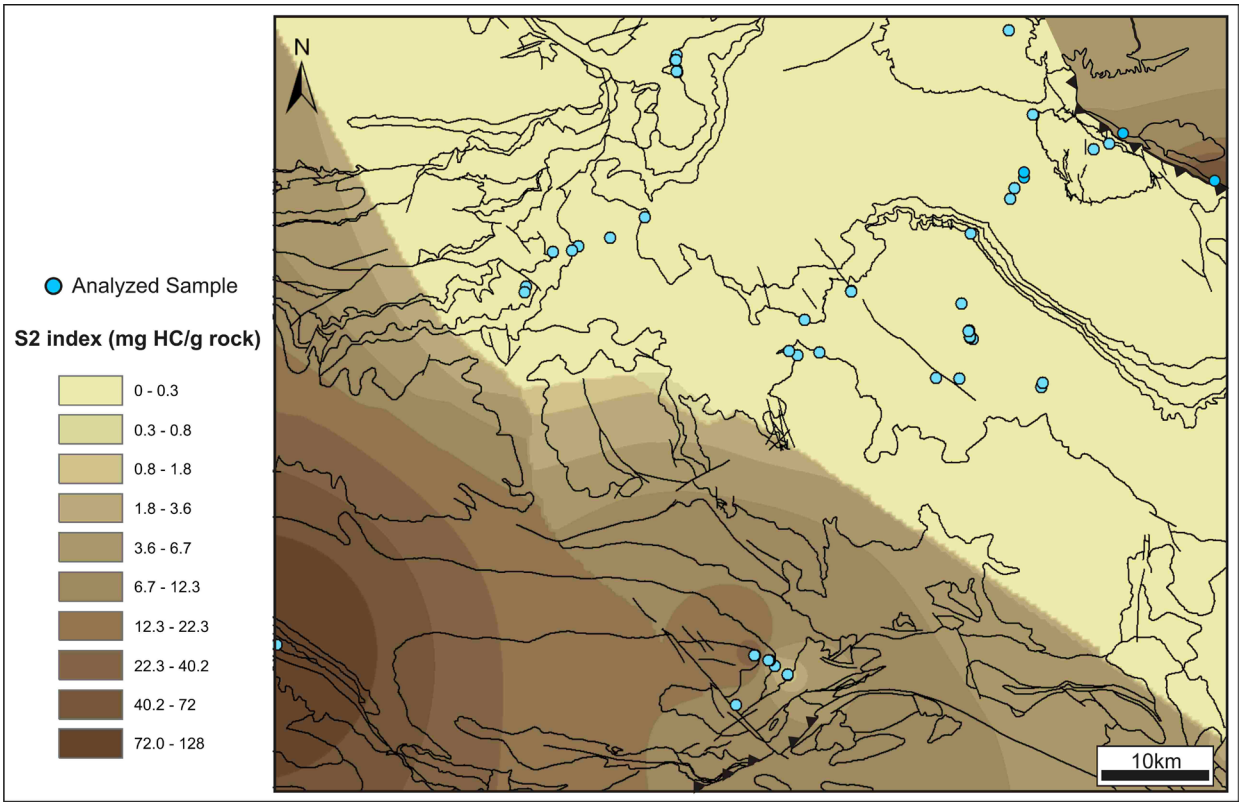

Fig. 10.6 - Interpolation of the S2 index values (mgHC/g rock) recorded from the Rock-eval pyrolysis in the study area

10.3). In fact an average of %Ro value of 2.4% is measured in the lowermost samples, of 2.5% in the intermediate samples and of 4.0% in the uppermost samples, in correspondence of the contact with the upper Urbión Gr sandstone bodies (DS6). In the Montenegro site measurements were performed only for a couple of samples, thus any vitrinite reflectance distribution trend can be extrapolated..

Pyrolisis rock-eval analysis determines mean TOC values of 1.06% and 0.9% in the Montenegro and Yanguas sites respectively and of 0.4% in the Poveda site (Fig. 10.4 and Table 10.5). In all the areas, the highest TOC were measured in the samples located in the uppermost stratigraphic layers of the DS3. HI and OI indexes indicate a Type III kerogen with very low content of hydrogen (Fig. 10.5 and Table 10.5). Due to the high degree of thermal maturity and the presence of solid bitumens, in most of the cases Tmax cannot be used as a reliable thermal index (Espitalié et al., 1985b, Bordenave, 1993). In fact Tmax values indicate very variable thermal conditions in all the areas (Fig. 10.8), despite of the general high vitrinite reflectance measured in most of the samples. S1 and S2 parameters are lower than 0.15 (mg HC/g rock) (Fig. 10.6 and Table 10.5), which indicate the presence of very reduced quantity of free hydrocarbon in the rock and a very reduced quantity of hydrocarbons formed from the artificial cracking of the organic matter (Espitalié et al., 1986).

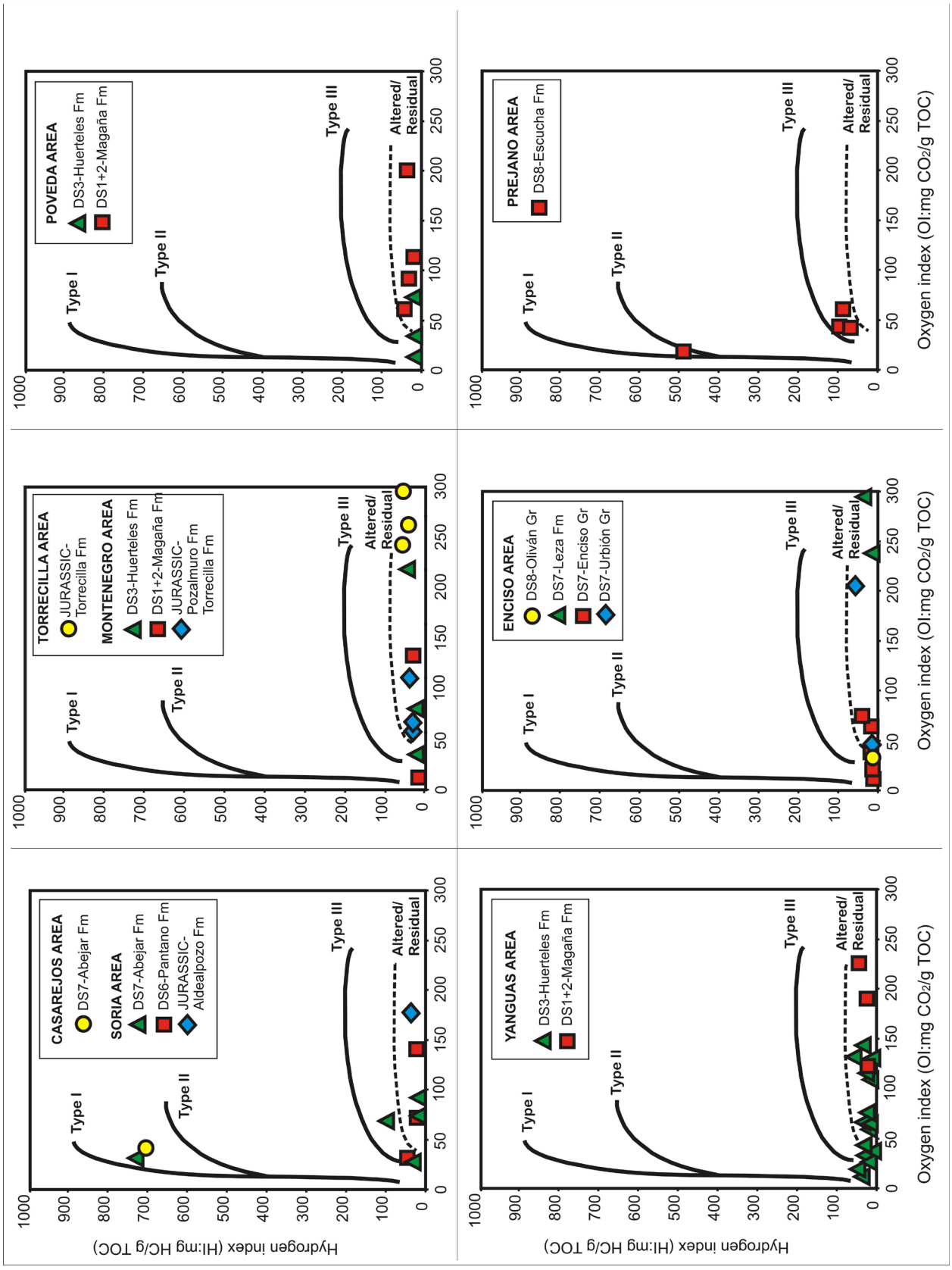

Fig. 10.7 - Hydrogen and oxygen index data plotted on a pseudo-Van Krevelen diagram (from Espitalié et al., 1986)

10.4.4. Late Barremian (DS6)

In the DS6 stratigraphic record, outcropping in the central and northern sectors of the basin scarce organic matter-rich layers can be found, because the predominance of coarse-grained fluvial facies. Differently, in the DS6 deposits outcropping in the south of the basin, in the Soria site (Fig. 10.1, Fig. 10.2 and Table 10.1), large amount of well preserved organic matter was found in fine-grained mudstone intervals, interbedded with the sandstone bodies (Pantano Fm).

Petrographic analysis reveals abundant and well preserved macerals from the huminite/ vitrinite, inertinite and liptinite maceral groups. Huminite group is formed by textinite (cell walls recognizable but compressed and gelified) (Fig. 10.10c) and ulminite (gelified tissues with not visible cell walls) in some case mixed with mineral material. Vitrinite particles are well preserved and they generally show an elongated shape. Inertinite maceral group is formed by well-preserved fusinite and semifusinite macerals. Liptinite macerals are observed in fluorescence mode and they are formed mostly by cuticles and in more scarce amounts by algae and spores.

Mean vitrinite reflectance is around 0.56 %Ro (Table 10.5). Fluorescence is dark-yellow to orange. Thus early oil-window thermal maturity conditions can be considered for this unit (Taylor et al., 1998) (Fig. 10.3).

Pyrolisis Rock-Eval analysis determines a mean TOC of 3.20 (Fig. 10.4 and Table 10.5). HI and OI values indicate a Type III kerogen (Fig. 10.5 and Fig. 10.7), which is consistent with the petrographic observations that indicate the dominance of terrestrial organic matter, characterised by very low hydrogen content. A mean Tmax value of 449 ^{o}C is recorded (Table 10.5), and data plotted on the HI vs Tmax diagram are located in the limit boundary of the diagenesis to catagenesis stages (Fig. 10.8). Thus, relatively Tmax index is in agreement with the vitrinite reflectance data, which indicate oil-window thermal conditions (Fig. 10.3). A mean S1 and S2 indexes of 0.03 and 0.54 mg HC/g rock respectively is recorded in the pyrolisis Rock Eval analysis (Fig. 10.6 and Table 10.5), which indicate the presence of very reduced quantity of free hydrocarbon in the rock and a scarce quantity of hydrocarbons formed from this type of organic matter (Espitalié et al., 1986).

10.4.5. Late Barremian-Early Aptian (DS7)

The deposits of this sequence are extended at basin-scale, although with a great variability of its lithological units (Fig. 10.1 and Fig. 10.2):

(1) Enciso Gr, extended in the northern sector of the basin, consisting of a mixed clastic-carbonate unit characterised by the cyclical alternation of limestone, sandstone and clay to

siltstone beds, deposited in a fluvio-lacustrine-palustrine depositional environment (Mas et al., 1993, 2003, 2011; Alonso-Azcárate, 1997). Organic matter characterisation was carried out on samples taken from the dark lutitic-marlstone intervals, intercalated between sandstone bodies. In addition, samples from limestone facies outcropping close to the northern border of the basin (Leza Fm), were analyzed. Samples of this unit were located in the Enciso site (Fig. 10.1, Fig. 10.2 and Table 10.1).

(2) The uppermost part of Urbión Gr, outcropping in the central-northern sector, is a dominant siliciclastic unit formed by coarse-grained sandstone bodies, deposited in a braided to meandering fluvial system dominated by oxic and high energy conditions (Mas et al., 1993, 2003, 2011, Ochoa et al., 2007). Analyzed samples of this unit were located in the Enciso site (Fig. 10.1, Fig. 10.2 and Table 10.1).

(3) Abejar Fm, outcropping in the southern and western sectors, is a siliciclastic unit formed by conglomerate and white sandstone bodies alternated with rich pedogenetic clay intervals. It has been interpreted as braided fluvial channels in a complex basin-transverse unconfined alluvial system where periodically developed lacustrine-palustrine systems (Mas et al., 1993, 2003, 2011, Arribas et al., 2003, Ochoa et al., 2007). Organic matter samples were taken from thedark-gray shale intervals of the unit, outcropping in the Soria and Casarejos sites (Fig. 10.1, Fig. 10.2 and Table 10.1).

Petrological properties are very different from one area to the other. In the Enciso site only few samples could be analyzed because several of them were oxidized. In the analyzed samples only few organic matter were found. In the case of the Urbión Gr the scarce organic matter content can be related to the oxidizing character of the depositional environment of this unit, which determines not favorable preservation conditions. In both Urbión Gr and Enciso Gr deposits the organic matter is mostly formed by particles of vitrinite and inertinite maceral groups. Vitrinite particle frequently show coke texture and optical anisotropy. Solid bitumen particles were also found in the rock matrix, coating the clastic minerals. In the limestone beds, outcropping in the northern border of the basin (Leza Fm), large dispersed of solid bitumen particles were found, showing mesophases spherules with anisotropic texture (Fig. 10.10a and Fig. 10.10b). The high reflectance (4.35%Ro) classified these bitumens as Cata-imposinite (Jacob, 1989).

A very different type of organic matter was observed in the Soria and Casarejos sites, where Abejar Fm unit was sampled. Here the organic matter is abundant and well preserved, formed by components of the three maceral groups (huminite, vitirnite, inertinite and liptinite) (Fig. 10.10e). In the Soria site huminite/vitrinite and inertinite groups are the most abundant. In the huminite macerals ulminite (cell walls are not visible) is dominant (Fig. 10.10e). Vitrinite macerals are well preserved, showing elongated and rounded shapes. Inertinite group is formed by very-well preserved fusinite and semifusinite particles. Liptinite group is mostly formed

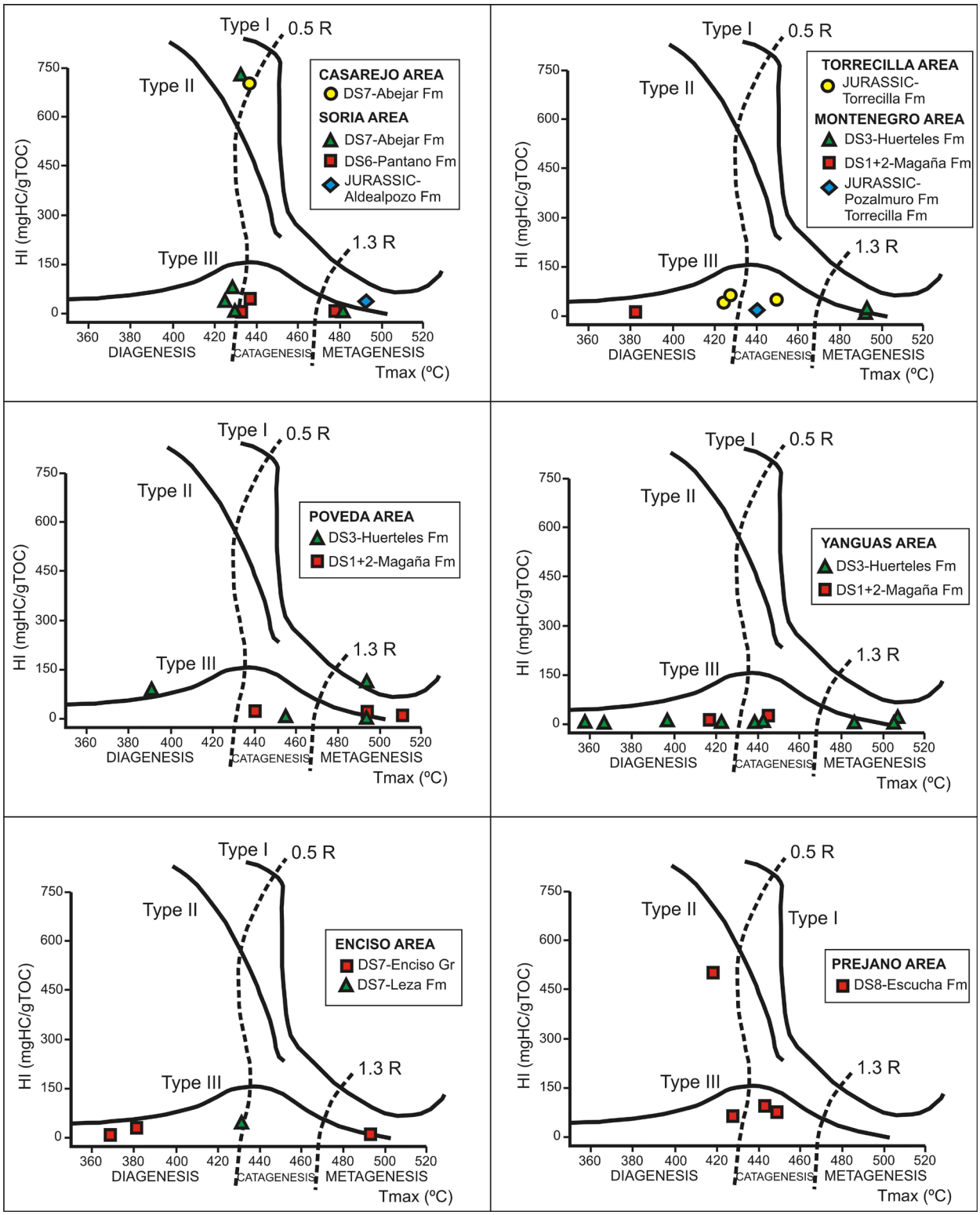

Fig. 10.8 - Hydrogen index vs. Tmax diagram for the studied samples, indicating the type of kerogen and thermal maturity (from Espitalié et al., 1985)

by cuticles (Fig. 10.10f), spores and algae, with a net predominance of the latter to the top of the depositional sequence. High reflectance solid bitumen particles were found dispersed in the mineral matrix and/or coating maceral particles (meso-impsonite to cata-impsonite, Jacob, 1989) (Fig. 10.10d). Occasionally, exsudatinite (also a bitumen but only visible in fluorescence mode), oil/hydrocarbons in form of green-yellow fluorescent droplets associated to liptinite macerals (Teichmuller, 1973; Teichmüller, 1974a, b), were observed (Fig. 10.10g). In the Casarejos site liptinite maceral group is the most abundant, which is formed by centimetric layers of thin algae oriented in laminae (lamalginites) and algal bodies (telalginites), such as Botryococcus (Fig. 10.10h). Lamalginite appear coating the few dispersed particles of huminite/vitrinite and fusinite/semifusinite.

In the Enciso site mean vitrinite reflectance values ranging from 2 to 3.88% (Table 5) determine overmatured thermal conditions (sensu Taylor et al., 1998) (Fig. 10.3). Any clear trend of the %Ro versus depth was observed along the stratigraphic section (Table 10.3). In the Soria site immature to oil-window thermal conditions were determined (Taylor et al., 1998), with a mean value of 0.5 %Ro (Fig. 10.3 and Table 10.5). Along the stratigraphic section vitrinite reflectance values range from a maximum value of 0.6% at the base to a minimum value of 0.38% at its top (Table 10.3). Finally, immature thermal conditions (Taylor et al., 1998) were considered for the Casarejos site (0.3%Ro) (Fig. 10.3 and Table 10.5).

Pyrolisis rock-eval data confirm the difference, in the organic matter content and preservation, observed from the northern to the southern areas of the basin by petrographic analyses. In the Enciso site pyrolisis rock-eval data indicate an average TOC of 0.74% (Fig. 10.4 and Table 10.5) and HI and OI indexes indicate the prevalence of a Type III kerogen with a very low content of hydrogen (Fig. 10.5 and Fig. 10.7). The presence in the rock of several solid bitumen particles, determines that Tmax index cannot be used as maturity index (Bordenave, 1993). In fact Tmax values generally indicate immature thermal conditions, which is not coherent with the high vitrinite reflectance measured (Fig. 10.8).

In the Soria and Casarejos sites pyrolisis Rock-eval data indicate the presence of abundant

Fig. 10.9 - Optical microscopy. Photomicrographs taken in reflected white light. Polarised light in photographs (b1). (a) A high reflectance vitrinite with stressed optical anisotropy (a1) (Marine Jurassic-Montenegro site). (b) High reflectance solid bitumen particles rounding mineral borders (Marine Jurassic-Montenegro site). (c) Vitrinite affected by meteoric alteration, and oxidation (DS1+2-Poveda site). (d) vitrinite particle with fine coke texture (DS1+2-Poveda site). (e) Solid bitumen particle rounded a mineral border (DS1+2, Poveda site). (f) Solid bitumen particle with degassing vacuolas (DS3-Yanguas site). (g) Very high reflectance solid bitumen filled mineral porosity, with coke mosaic texture (DS3-Montenegro site). (h) Fine-grained carbons remaining as a result of the liptinite thermal alteration. The width of the long dimension of the pictures: 200 µm

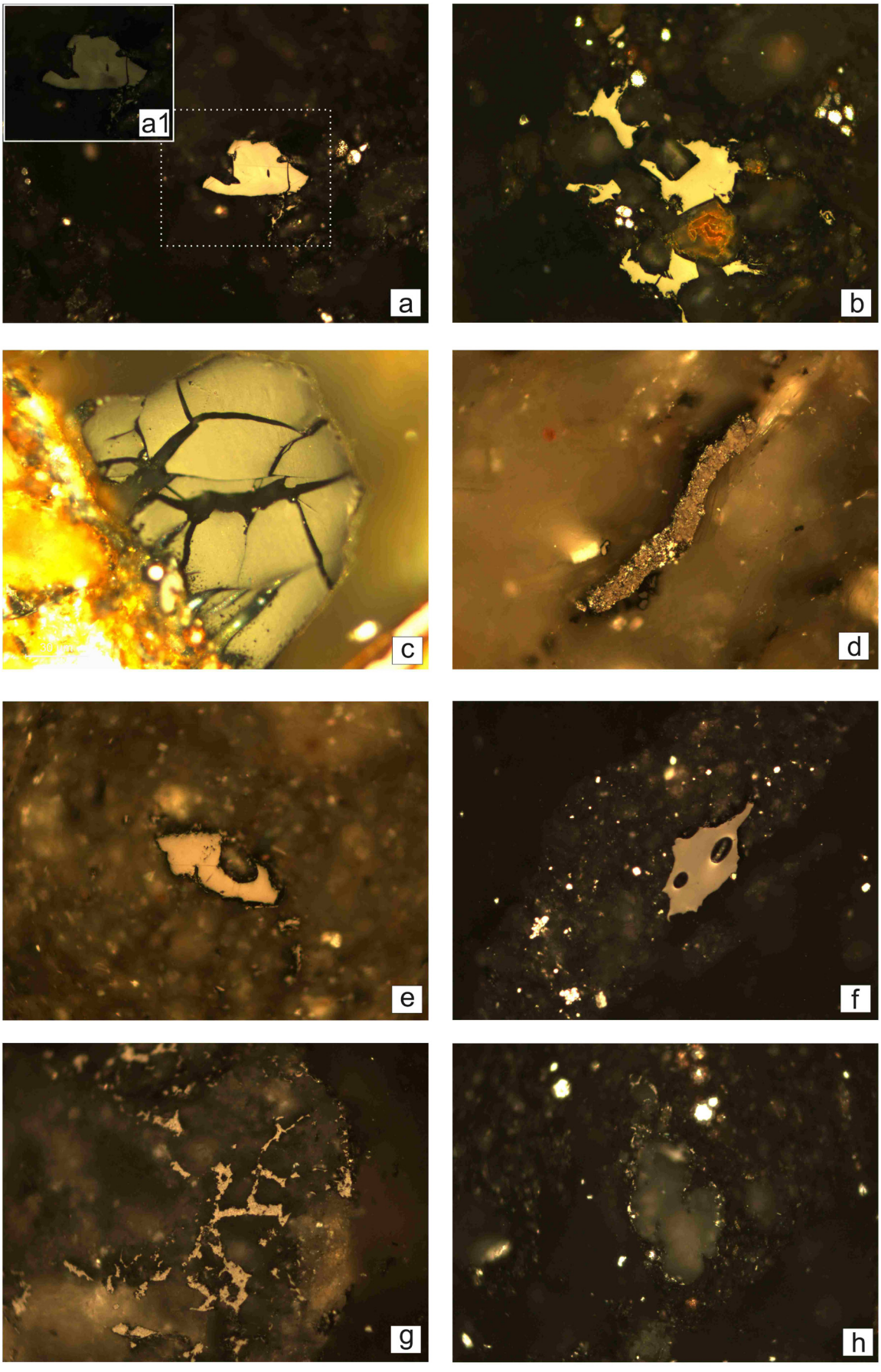
a1
a
b
c
d
e
f
g
h

organic matter (Fig. 10.4 and Table 10.5). In the Soria site variation in the geochemical properties can be observed along the sampled stratigraphic section (Table 10.1). The average TOC for all the sequence is 2.80 %. Pyrolized carbon (PC %) is only the 5% of the TOC for most of the samples, whereas, in sample of the uppermost stratigraphic layers, PC form the 65% of the TOC (Table 10.4). These data are confirmed by the dominance of vitrinite and inertinite macerals in the lowermost samples whereas liptinite macerals is most abundant in the uppermost samples. In the lower layers the average of HI and OI values are 32 mg HC/g and 259 mg CO2/g TOC respectively, S1 peak is irrelevant whereas a maximum S2 peak of 3.19 is registered (Table 10.5). In the upper stratigraphic layers the average values of HI and OI of 714 mg HC/g and 27 mg CO2/g TOC, S1 and S2 peaks of 0.90 and 10.85 mg HC/g. Tmax along the section has a nearly constant value of 440 ºC (Table 10.5), indicating immature to early-oil window conditions (Fig. 10.8). This is coherent with the vitrinite reflectance data measured (Fig. 10.3). Data plotted on the HI vs. OI diagram indicates a dominance of Kerogen Type III for the lower layers and of Type I for the upper layers (Fig. 10.7). The highest content in organic matter is recorded in the Casarejos site (TOC of 17.82%) (Fig. 10.4 and Table 10.5), with HI vs. OI of 695 mg HC/g and 43 mg CO2/g TOC respectively and S1 and S2 peaks of 2.75 and 123 mg HC/g respectively (Table 10.5). Tmax recorded is 438ºC. HI vs. OI diagram indicates Type I kerogen (Fig. 10.7), whereas HI vs. Tmax diagram indicates immature thermal conditions (Fig. 10.8), in agreement with the vitrinite reflectance measured (Fig. 10.3).

10.4.6. Late Aptian-Early Albian (DS8)

The deposits of the DS8, corresponding to the last syn-extensional unit, outcropping only in the northern border of the basin (Fig. 10.1) and they are formed by the Olivan Gr and the Escucha Fm.

The Olivan Gr is a prevalently siliciclastic unit, formed by sandstone bodies intercalated with lutite and scarce carbonate beds, deposited in a fluvial-palustrine depositional environment (Mas et al., 2009). The Olivan Gr topped the syn-extensional basin infill sequence (Fig. 10.2), and

Fig. 10.10 - Optical microscopy. Photomicrographs taken in reflected white light (fluorescence mode photograph f, g and h). (a) Mesophase spheres formed in bitumen/pitch particles as a consequence of heating to elevated temperatures. In (b) polarised light with evidence of the anisotropy of the mesophases (DS7-Enciso site). (c) Huminite (Textinite), mixed with mineral material (DS6-Soria area). (d) Vitrinite (collotelinite) with low reflectance, fusinite and solid bitumen rounding mineral borders (DS7-Soria area). (e) Huminite (Ulminite) rimmed by liptinite; on the right, a fusinite particle. In fluorescence mode (f) the liptinite appears as a cutinite (DS7-Soria area). (g) Oil/hydrocarbons (exsudatinite) in the form of green-yellow fluorescent droplets associated with liptinite material (DS7-Soria area) (h) Thin algae oriented in laminae (lamalginites) and algal bodies (telalginites) such as Botryococcus (DS7-Casarejos area).

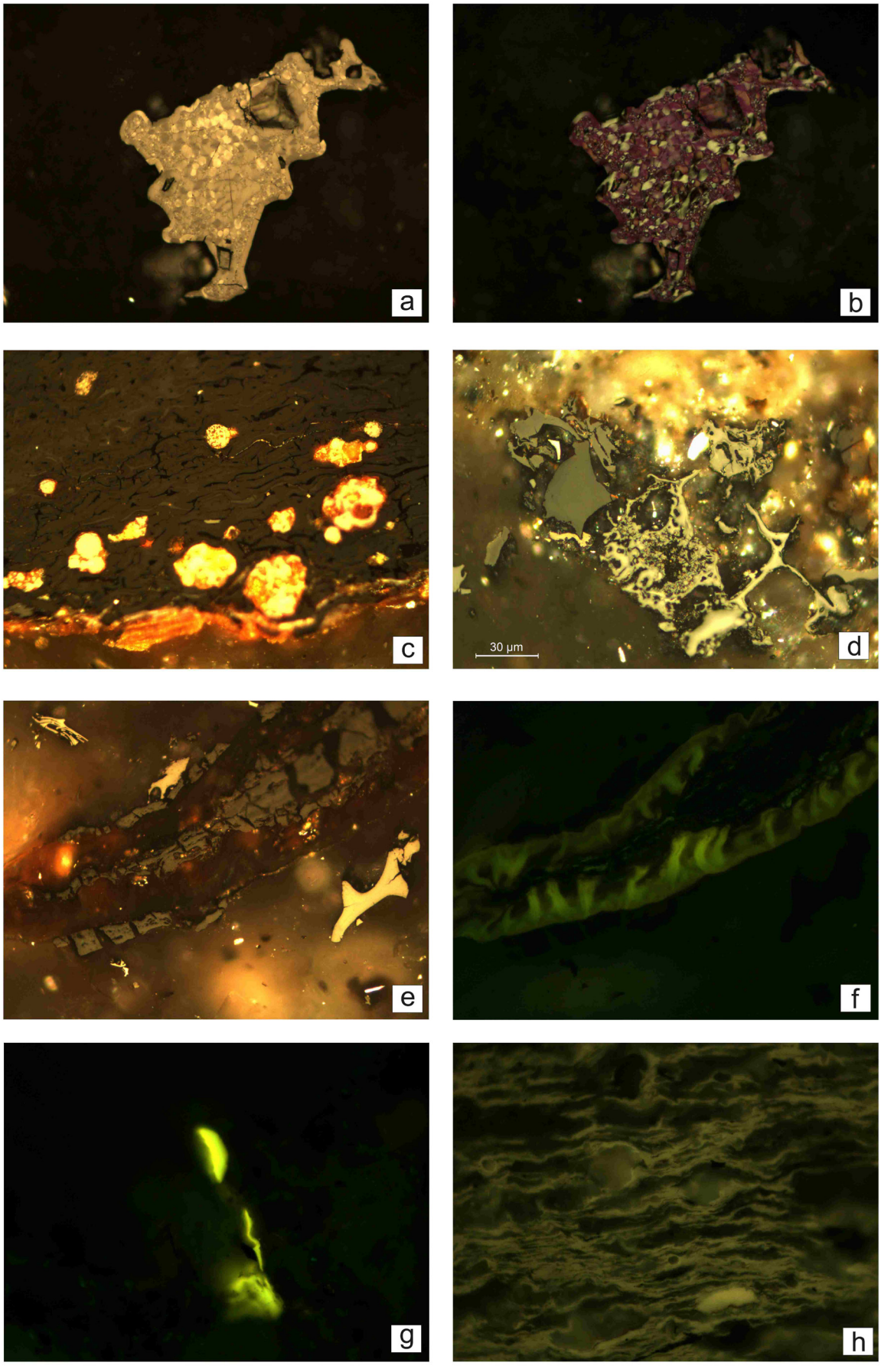
a
b
c
30 µm
d
e
f
g
h

it is located close to the thrust which inverted the basin during the Alpine contractional phase, in the hangingwall block (Fig. 10.1). Samples from Olivan Gr deposits were taken from shale to coal deposits, intercalated in fluvial sandstone bodies, outcropping in the Enciso area (Fig. 10.1, Fig. 10.2 and Table 10.1).

The Escucha Fm is mainly a siliciclastic unit, deposited in a fluvio-deltaic depositional system, where thick coal beds are frequently found (Mas et al., 2003, 2011). The Escucha Fm deposits, lies directly on the marine Jurassic substratum of the basin, in the footwall of the main thrust of the basin (Fig. 10.1 and Fig. 10.2). These deposits are considered a lateral equivalent of the uppermost part of the Oliván Gr., deposited in a less subsiding area, where more distal depositional environments were formed. Escucha Fm analyzed deposits are formed by coaly shale and they are located in the Prejano site.

Petrographic analysis of Oliván Gr samples determine the presence of abundant organic matter, formed by well-preserved vitrinite and inertinite macerals, whereas liptinite maceral is absent. Vitrinite macerals are composed by large size particles, characterised by homogeneous, structureless appeareance (collotelinite) (Fig. 10.11a). Frequently vitrinite particles show elongate and narrow cavities, filled with mineral matter (Fig. 10.11b). The cavities shape and size suggest that originally these cavities contained sporinite and/or resinite (liptinite) macerals, which were subsequently thermally transformed and replaced by mineral matter. In the inertinite macerals, fusinite particles with well-preserved intercellular pores, are dominant (Fig. 10.11c). In the Oliván Gr vitrinite particles are frequently fractured by veins, at the present-day filled by calcite cement (Fig. 10.11a and Fig. 10.11b). This suggests the circulation of fluids in the sediment after deposition and burial processes which could overmature the organic matter.

Different organic matter characteristics were observed in the Escucha Fm deposits, in the Prejano site. Organic petrography determines the presence of the vitrinite, liptinite and intertinite macerals, in order of abundance. Vitrinite is generally constituted by less uniform particle than in the Olivan Gr, where botanical cell structures are preserved, which may or may not be visible (telinite and collotelinite respectively) (Fig. 10.11d). Vitrinite fragments (vitrodetrinite) and

Fig. 10.11 - Optical microscopy. Photomicrographs taken in reflected white light (fluorescence mode photographs: e, f, and h). (a) High reflectance vitrinite with a homogeneous structure-less appearance (collotelinite). Vitrinite is fractured by veins filled with calcite cement (DS8-Enciso area). (b) Vitrinite particles include narrow cavities that retain their botanical structure, which most likely represent former sporinite, which was subsequently replaced by mineral cement. The vitrinite is fractured by veins (DS8-Enciso area). (c) Fusinite particles with well-preserved intercellular pores (DS8-Enciso area). (d) Coal vegetal tissue with a well-preserved botanical cell structure (telinite), including higher reflectance of vitrinite particles with cell structures not visible (DS8-Prejano). (e) Algae and Sporae (DS8-Prejano area). (f) Green to yellow fluorescence exsudatinite, associated with vitrinite cell cavities (DS8-Prejano area). (g) Dark-brown hydrocarbons impregnated in the mineral fracture and veins, with yellow fluorescence (h) (Utrillas Fm-Soria area). Width of the long dimension of the pictures: 200 µm

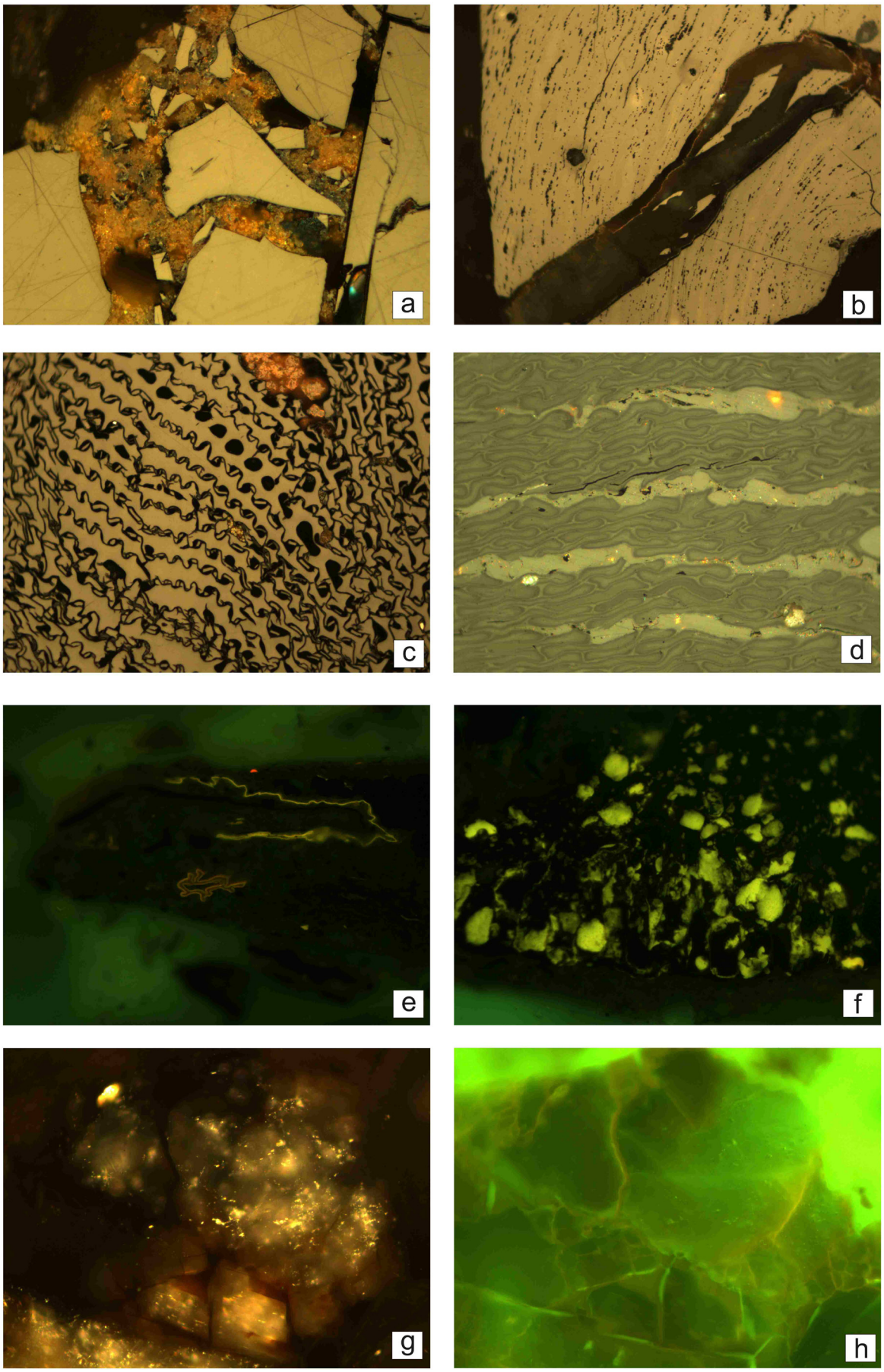
a
b
c
d
e
f
g
h

inertodetrinite are found dispersed in shaly sediment or contained in a mixture of amorphous vitrinitic matter and inorganic components (collodetrinite). Vitrinite macerals also appear in form of homogeneous and discrete bodies, representing cell infillings (corpogelinite). In the shale sediments, associated to the vitrinite macerals, elongated and rounded yellow to dark-yellow spores and algae particles are commonly observed (Fig. 10.11e). Associated to vitrinite cell cavities, probably some of them originally filled with liptinite macerals, green to yellow fluorescent exsudatinite (very immature oil-hydrocarbons) was observed (Fig. 10.11f).

Very uniform and constant vitrinite reflectance measurements indicate overmature thermal conditions (3%Ro), for the Oliván Gr in the Enciso site, and an oil-window thermal stage (0.60%Ro) for the Escucha Fm in the Prejano sites (Fig. 10.3 and Table 10.5).

Oliván Gr samples data record an average TOC of 2% (Fig. 10.4 and Table 10.5), mostly composed by inert residual carbon (Table 10.4), whereas the amount of pyrolized carbon (expressed by the IH, OI and S2 index) is irrelevant (Fig. 10.5, Fig. 10.6 and Table 10.5). Pyrolisis Rock-eval data plotted on a HI vs. OI diagram indicate the dominance of Type III kerogen with very low content of hydrogen (Fig. 10.7). The only realiable Tmax data (606ºC) confirms the overmature thermal conditions (Fig. 10.8) deduced from vitrinite reflectance data. A mean S1 and S2 parameters of 0.01 and 0.0 mg HC/g rock respectively were recorded in the Rock Eval analysis (Table 10.5), which indicate the presence of very reduced quantity of free hydrocarbon in the rock and the absence of hydrocarbons formed during the pyrolysis of the organic matter (Espitalié et al., 1984).

In the Escucha Fm pyrolis rock-eval data indicate an average TOC of 17% (Fig. 10.4 and Table 10.5) and HI and OI indexes determine the dominance of Type III kerogen, in some case with high content of hydrogen (Table 10.5). Average S1 and S2 parameters of respectively 0.56 and 6.50 mgHC/g were measured (Table 10.5). In a coal sample higher S1 and S2 parameters of 1.95 and 196.64 mg HC/g respectively were also measured Table 10.5).

The high content in yellow to dark-yellow fluorescent liptinite, mainly continental in origin, confirm the TOC and S2 values of these deposits, as well as the observation of free hydrocarbons in the sample (exsudatinite) justify the values obtained for the S1 index. Tmax indicate immature to oil-window thermal conditions (Fig. 10.8), which is coherent with the vitrinite reflectance measured (Fig. 10.3).

10.4.7. Post-extensional (Utrillas Fm)

Utrillas Fm is a dominant sandstone unit forming the base of the post-extensional deposits (Late Cretaceous Megacycle, Alonso et al., 1993), which unconformably overlies the syn-extensional basin infill in the south of the basin (Soria site) (Fig. 10.1, Fig. 10.2).

Petrographic observations indicate a complete infill of the sandstone porosity with light to dark brown bitumens and/or hydrocarbons. Hydrocarbons impregnated the mineral fractures and veins, from where pouring-out drops can be observed (Fig. 10.11g). Under fluorescence light bitumens appears from dark-yellow to brown in colour (Fig. 10.11h). Reflectance measurements determine a very low thermal maturity for these hydrocarbons (0.033%Ro) (Table 10.5), which can be classified as Asphalt (Jacob, 1989).

Pyrolisis rock-eval data indicate an average TOC of 4.55%, HI of 752 mgHC/gTOC, OI of 20 mgCO2/gTOC, S1 of 5.29 mgHC/g, S2 of 34.3 mgHC/g and Tmax of 437 ºC (Table 10.5). The abundance of hydrocarbons impregnating the rock justifies the high TOC value and the high HI index. Tmax value indicates immature thermal conditions (Fig. 10.8) which is coherent with the vitrinite reflectance measured (Fig. 10.3).

10.5. DISCUSSION

10.5.1. Thermal maturity of the organic matter

The thermal maturity of organic matter in the basin infill was deduced by primarily considering that the vitrinite reflectance data, due to the Tmax, could be used as a reliable maturity index only in few cases. In fact, only in the case of immature deposits, can the Tmax indicate coherent thermal maturity conditions with respect to the vitrinite reflectance measurements (Fig. 10.3 and Fig. 10.8), whereas in the rest of the Tmax cases, the thermal conditions determined are considerably more immature than those indicated by vitrinite reflectance. This incongruence may be caused by the following factors: 1) the insignificance product obtained from the Rock-Eval pyrolysis, which is due to the high degree of rock maturation (Espitalié, 1985a, b; Espitalié et al., 1986) and to the organically lean nature of some samples (with a TOC lower than 0.3 %). In these cases, the results are not as reliable because the order of magnitude is the same as the analytical error (Bordenave, 1993); 2) the presence of solid bitumens in the rock, which dramatically lowered the Tmax value (Bordenave, 1993; Espitalié, 1985a, b); 3) the presence of altered organic matter; and 4) the strong mineral effect in the samples containing dispersed organic matter (DOM) (Espitalié, 1985a).

The distribution of the vitrinite reflectance data (Fig. 10.3) showed a net maturity differentiation between the southern area (immature to early mature thermal conditions) and the north-central area (over-mature). An exception is the area located at the footwall of the main thrust (Prejano site), where early oil-window thermal conditions were recorded.

The causes of such different thermal history records can be attributed to a differentiated subsidence trend recorded throughout the basin and to differentiated hydrothermal fluid

circulation.

The northern and central sectors of the basin were affected by a considerably higher subsidence trend than the southern sector (**Chapter 8**); consequently, higher burial heating was recorded. The circulation of hot fluids in the basin is related to low-grade hydrothermal metamorphic events, affecting the Cameros basin during the post-extensional stage (Late Albian-Coniacian) and during the inversion of the basin (Eocene) (Casquet et al., 1992; Barrenechea et al., 1995; Alonso-Azcárate et al., 1999; Mas et al., 2003; Ochoa et al., 2007; González-Acebrón et al., 2011; Mas et al., 2011). A maximum temperature of over 350ºC has been estimated for the first event (Casquet et al., 1992; González-Acebrón et al., 2011) and of approximately 280-305ºC for the second event (González-Acebrón et al., 2011). The hot hydrothermal fluids extensively affected the northern sector of the basin and partially affected the central sector, whereas the southern sector was not affected. A vitrinite reflectance ranging from 2.5 to 4 % have been estimated by Kisch (1987) and Taylor et al. (1998) for the anchizone diagenetic grade, which was consistent with the values measured in the sectors of the Cameros Basin affected by metamorphism.

The differentiated hydrothermal fluid circulation throughout the basin can be related to the proximity of the northern areas to the main structures of the basin - ramp deep extensional detachment and to the main inversion thrust (Mas et al., 1993; Guimerà et al., 1995; Omodeo Salé, 2014) - along with preferentially circulated fluids.

The inversion of the expected increasing trend with the depth of the vitrinite reflectance data (Allen and Allen, 2009) at the Poveda, Yanguas and Enciso sites, can be explained by considering the circulation of hot fluids in these areas, which anomalously heated the sediments regardless of their stratigraphic position (**Chapter 8**). The highest %Ro was measured in the sediments located in proximity to the Oncala Fault and northern thrust (Fig. 10.3), along with hot fluids that could easily circulate. High thermal conditions were measured, even in the Urbión Gr (DS4, DS5, DS6 and DS7 units – Fig. 10.2) and Oliván Gr (DS8) deposits (Fig. 10.3), which corresponded to sandstone dominant units with high permeability that facilitated hot fluid circulation (**Chapter 8**). The effect of the anomalous heating gradually decreased with increasing distance from the faults and from the sandstone units, exhibiting an inversion of the typical %Ro-increase-with-depth trend (**Chapter 8**) (Fig. 10.3).

To the north of the basin, at the footwall of the thrust, the lateral equivalent of the Oliván Gr deposits, the Escucha Fm deposits, record oil-window thermal conditions (Fig. 10.3) and no evidence of fluid circulation in the veins was observed. These markedly different thermal conditions, which developed in these two neighbouring areas, suggests that the circulation of hot fluids along the northern border of the basin occurred after the basin inversion process, when the Oliván Gr and Escucha Fm deposits were separated by the thrust surface.

10.5.1.1. Organic matter textures resulting from thermal alteration

Anomalous textures in the organic matter formed as a consequence of hydrothermal metamorphism (Taylor et al., 1998). Alteration textures were found extensively in the samples, located in the central and northern parts of the basin, especially in the sediments close to faults or to permeable sediments, where hot fluid circulation occurred. The type and grade of alteration observed was variable because it depends on the original level of organic matter maturity at the time of metamorphism (Taylor et al., 1998).

Abundant vitrinite particles with a natural coke matrix (Fig. 10.9d) were found in the central-northern sector of the basin, especially in the samples located close to the Oncala Fault (DS1+2 at the Poveda and Yanguas sites) and in all of the units from the Enciso site (Urbión Gr, Enciso Gr and Oliván Gr). Natural coke is formed when the maturity of the organic matter before thermal alteration ranges from 0.6 to 2.0 %Ro (bituminous coalrank)(Taylor et al., 1998). In cases where the thermal maturity was above or below this range, the vitrinite and inertinite textures were preserved in a devolatilised form (Taylor et al., 1998). The result was that liptinite thermal alteration can be formed from the residues of fine-grained carbons (micrinite maceral) (Taylor et al., 1998), which were frequently found in the fine-laminated Valdeprado deposits at the Yanguas and Montenegro sites (Fig. 10.9h). In the DS8 (Oliván Gr – Enciso area), the coal deposits were strongly heat-altered. Numerous veins fracturing the vitrinite particles (Fig. 10.11a and Fig. 10.11b) indicated the circulation of hot fluids in the sediment. In some samples, the vitrinite was fused with pore development (Taylor et al., 1998). The botanical structure of sporinite, which was previously in the vitrinite particles, is occasionally retained (Hutton and Henstridge, 1985; Taylor et al., 1998) (Fig. 10.11b).

Solid bitumen particles with a mesophase and coke texture were observed at the Enciso and Montenegro sites (DS7 and DS3, respectively) (Fig. 10.9g and Fig. 10.10a and Fig. 10.10b) and can be explained as the result of intense thermal natural cracking of the primary organic matter. When the organic matter was heated to a temperature higher than 300ºC, hydrocarbons formed and solidified in the pores, cracks and fissures (Hutton and Henstridge, 1985; Taylor et al., 1998). Mesophase textures form as this material undergoes chemical and physical re-arrangement in the molecular structure in response to elevated temperatures (Rahimi et al., 1998; Taylor et al., 1998) (Fig. 10.10a and Fig. 10.10b). Coke with mosaic structures (Fig. 10.9g) is formed as consequence of further heating (Rahimi et al., 1998).

10.5.2. Amount of organic matter

The amount of organic matter contained in a rock depends on favourable conditions for

organic matter accumulation and preservation in the depositional environment and from the thermal history of the rock (Bordenave, 1993; Taylor et al., 1998; Tissot and Welte, 1984).

In the Cameros Basin, distribution of the TOC values (Fig. 10.4) in the central and northern areas of the basin generated poor to fair organic matter content (Peters, 1986), with the exception of a few samples that were located at the Montenegro, Yanguas and Enciso sites. On the other hand, good to excellent organic carbon content was identified in the southern areas of the basin (Soria and Casarejos) and at the footwall of the main thrust (Prejano site).

One of the most evident causes of the significantly reduced content of present-day organic matter in the central and northern sectors of the basin is the thermal history affecting these sectors. Areas characterised by a low content of kerogen correspond to dry-gas to over-mature stages (Fig. 10.3 and Fig. 10.4), suggesting that the original amount of kerogen has been thermally transformed by cracking. Furthermore, these sectors correspond to the parts of the basin that are highly affected by hydrothermal metamorphic events (Casquet et al., 1992; Alonso-Azcárate et al., 1999; Barrenechea et al., 2001; Mantilla-Figueroa et al., 2002; Mas et al., 2003; Ochoa et al., 2007; González-Acebrón et al., 2011; González-Acebrón et al., 2012). The circulation of high temperatures fluids, especially in presence of water, may be removed by organic matter reactions in the sediment, forming CO2 and other products (Taylor et al., 1998). On the other hand, the different thermal history in the southern sector of the basin, as well as at the footwall of the thrust, maintain here immature to early-oil window thermal conditions, making it possible to preserve the original amount of organic matter deposited in the depositional environment.

10.5.3. Type of organic matter

The type of kerogen generated in the basin was determined by interpreting the Rock-Eval pyrolysis data plotted on HI vs. OI diagrams (Fig. 10.7) in association with organic petrography data. HI vs. OI diagrams indicate that Type III kerogen constitutes deposits of the DS6 and DS7 units located at the Soria site and of the DS8 unit located at the Prejano site (Fig. 10.7). In the latter area highly hydrogenated Type III kerogen, corresponding to coal deposits, was also found (Fig. 10.7). These results are confirmed by petrographic observations, which determine that organic matter in these samples is continental in origin and consists mainly of vitrinite and inertinite macerals and less abundant liptinite (cuticles, pollen and spores) (Fig. 10.9, Fig. 10.10 and Fig. 10.11 and Table 10.5). Sedimentary features indicate that the deposits of these units are fluvio-palustrine (Table 10.1), where most of the terrestrial organic matter accumulated. On the other hand, Type I kerogen is the dominant kerogen in the DS7 deposits of the Casarejos area and in the uppermost stratigraphic layers of the DS7 at the Soria site. Petrographic observations confirm that these samples are constituted of highly hydrogenated organic matter, lacustrine in origin and are mostly comprised of liptinite macerals (algae) (Fig. 10.10 and Table 10.5).

Accordingly, the sedimentary features suggest that the deposits of these units are lacustrine-palustrine facies (Table 10.1), where mostly accumulated lacustrine organic matter.

In the case of mature to over-mature rocks, interpreting the type of kerogen is more complex. The HI vs. OI diagrams (Fig. 10.7) indicate the net predominance of very poorly hydrogenated Type III kerogen (HI<50 mg HC/g TOC). Kerogen with this geochemical composition has been defined by several authors (Bordenave, 1993; Espitalié et al., 1986; Tissot and Welte, 1984) as essentially inert, with no hydrocarbon-generating potential, and as being a result of repeated organic matter alteration/oxidation processes in the depositional environment. On the other hand, petrographic observations of very poorly hydrogenated organic matter do not indicate any evidence of alterations and/or oxidation, whereas few well-preserved organic matter particles, mostly formed by small vitrinite and solid bitumen particles, were observed. Therefore, the kerogen forming into these samples is residual kerogen, instead of an altered/inert kerogen, formed as a consequence of the thermal maturity of the original kerogen, which was depleted in hydrogen and enriched in carbon (Bordenave, 1993; Taylor et al., 1998). The over-mature thermal conditions of these deposits (Fig. 10.3) and the very low content of organic carbon (TOC) (Fig. 10.4) confirms this assumption, especially in the case of abundant solid bitumen particles (Jurassic deposits, DS3 deposits at the Yanguas and Montenegro sites and DS7 deposits at the Enciso site, see Table 10.5).

The original nature and richness of the kerogen accumulated in these rocks, before it has thermally matured and transformed into oil and gas, can be deduced based on the original depositional setting of the related deposits.

The marine depositional environment can be deduced for pre-extensional deposits: the Pozalmuro Fm formed in an outer platform depositional environment (Alonso and Mas, 1990; Benito et al., 2005) and the Torrecilla Fm and Aldealpozo Fm formed on a shallow carbonate ramp (Alonso and Mas, 1990; Benito et al., 2005). The depositional anoxic conditions of the black-shale deposits forming the Pozalmuro Fm facilitated good preservation of the original organic matter (Pedersen and Calvert, 1990), whereas the oxidised and high energy conditions of a shallow carbonate ramp were not favourable (Bordenave, 1993). Therefore, the large amount of highly hydrogenated Type II kerogen, formed from a mixture of phyto- and zooplankton deposits and a minor amount of terrestrially sourced material, could be originally accumulated in the Pozalmuro Fm. In the Torrecilla Fm and Aldealpozo Fm, scarce organic matter could be preserved.

The thinly laminated black-shales forming in the Valdeprado Fm (DS3) deposits developed in saline shallow environments, as coastal sabkhas lakes (Quijada et al., 2013a, b). The high salinities that characterised these water bodies most likely caused stratification of the water column, and consequently anoxic conditions, which, accompanied by high rates of organic matter production

(typical in saline water bodies), may have favoured the accumulation and preservation of large amounts of organic matter (Durand, 1980; Tissot and Welte, 1984; Berger et al., 1989; Pedersen and Calvert, 1990; Bordenave, 1993; Einsele, 2000). In these environments, hydrogen-rich lipid-derived organic matter could accumulate (Bornhold, 1973; Pelet and Debyser, 1977; Palacas et al., 1984). A Type I or IS kerogen, mainly formed by algae, is very similar to the lamalginite found in the DS7 deposits from the Casarejos site (Fig. 10.10h), and could originally constitute the organic matter of the Valdeprado Fm (DS3) deposits. A considerable amount of residual carbon found in the DS3 deposits of the Yanguas area (Valdeprado Fm) (mean value of 0.9 %, with a maximum of 3.81 % on the top of the stratigraphic section) can identify the original petroleum potential of these rocks (Bordenave, 1993).

At the Enciso Gr (DS7), the dark marls and shale intervals, intercalated in sandstone and limestone bodies, formed in the palustrine, marsh and flood plain of a complex fluvio-lacustrine depositional system (Mas et al., 1993, 2003; Alonso-Azcárate, 1997). In these environments, favourable conditions for organic matter accumulation could develop (Durand, 1980; Tissot and Welte, 1984; Berger et al., 1989; Taylor et al., 1998; Einsele, 2000). The accumulation and decomposition of large amounts of organic matter in these depositional environments could determine the formation of anoxic conditions, which favoured organic matter preservation (Pedersen and Calvert, 1990). In any case, it is necessary to consider the limited areal extension and the frequent aerial exposure of these depositional environments could limit the preservation of the organic matter (Kenig et al., 1990). Therefore, a fair to good amount of Type III kerogen mixed with a Type I kerogen, similar to the organic facies of the Abejar Fm (DS7) deposits at the Soria site, as well as of the Escucha Fm (DS8) deposits at the Prejano site, could originally constitute the organic matter of the Enciso Gr (DS7).

The shale intervals of the Magaña Fm (DS1+2), Huerteles Fm (DS3), the Urbión Gr (DS7) and the Oliván Gr (DS8) units were deposited in a fluvial depositional setting, where marsh and floodplain frequently developed. Because high-energy and frequent sub-aerial exposition characterised these depositional environments, the organic matter could not be easily accumulated and preserved (Durand, 1980; Tissot and Welte, 1984; Berger et al., 1989; Taylor et al., 1998; Einsele, 2000). In the fine-grained deposits, organic matter that accumulates is mostly formed by humic low-hydrogen organic matter (Pelet and Debyser, 1977). In these environments, coal deposits, as with the Oliván Gr (DS8) deposits, can form (Pedersen and Calvert, 1990). Therefore, low Type III and/or oxidised/altered inert kerogen content may have originally constituted the Magaña Fm (DS1+2), Huerteles Fm (DS3), the Urbión Gr (DS7) and the Oliván Gr (DS8).

In summary, with the exception of the pre-extensional deposits (marine organic matter, Type II kerogen), organic matter accumulated in the Cameros Basin, was mostly continental in origin, varying from terrestrial (Type III) to lacustrine (Type I). Favourable conditions for the accumulation and preservation of abundant organic matter were reached during the deposition

of the Pozalmuro Fm in the pre-extensional deposits and in the Valdeprado Fm (DS3), Enciso Gr (DS7), Abejar Fm (DS7) and Escucha Fm (DS8) in the syn-extensional deposits.

10.5.4. Hydrocarbon potential

To perform a reliable estimation of the hydrocarbon potential of the analysed rocks, the TOC and S2 indices were related (Bordenave, 1993; Peters and Cassa, 1994; Dembicki, 2009). The S2 index is an excellent indirect indicator of the amount of hydrogen present in the organic matter and it is a more realistic measure of the source rock potential than the TOC by itself (Peters, 1986; Bordenave, 1993; Dembicki, 2009).

The distribution map of the S2 in the basin study area (Fig. 10.4) and the S2 versus TOC graphs (Fig. 10.12) indicate that the deposits at the Casarejos site, in the uppermost stratigraphic layers of the DS7 at the Soria site and the Prejano site have good to excellent hydrocarbon potential (S2>5 mg HC/g TOC) (Peters and Cassa, 1994). These data are consistent with the immature to early-oil-window thermal conditions of these deposits (Fig. 10.3), the high hydrogen index (Fig. 10.5) and the abundance of organic matter in high-hydrogenated macerals (liptinite) (Table 10.5). From these data, the deposits can be considered potential source rocks (Law, 1999). Considering the petrographic and geochemical features, oil production from the DS7 deposits from the Casarejos site show potential, whereas oil and gas could be extracted from both the DS7 deposits at the Soria site and the DS8 deposits at the Prejano site (Peters, 1986). The characteristics of these potential source rocks are summarised in Table 10.6. However, it is important to consider that the organic-rich levels characterised in these deposits are diluted in thick successions of conglomerate and sandstone bodies, which constitute the majority of the stratigraphic thickness of these units. Therefore, it is doubtful that large amounts of hydrocarbons could be generated from these rocks, despite the excellent kerogen properties.

In the rest of the basin, a distribution map of the S2 (Fig. 10.6) and the S2 versus TOC graphs (Fig. 10.12) indicate poor hydrocarbon potential (S2<2.5 mg HC/g TOC) (Peters and Cassa, 1994). Therefore, the deposits located at these sites are characterised by a high TOC content (Fig. 10.4) and cannot be considered as having high petroleum potential (Peters, 1986) because very low S2 values were measured (Fig. 10.6). The organic carbon contained in these samples was not pyrolysed and has to be considered residual carbon (fixed carbon) (Bordenave, 1993), which formed as a consequence of the complete thermal evolution of these deposits (Fig. 10.3).

In the case of the Jurassic deposits at the Torrecilla and Montenegro sites, of the DS3 deposits at the Yanguas site and of the DS7 deposits at the Enciso site, there is evidence that organic matter could accumulate and be preserved in the related depositional environments (see previous section); the presence of solid bitumen particles, the over-mature thermal conditions and the

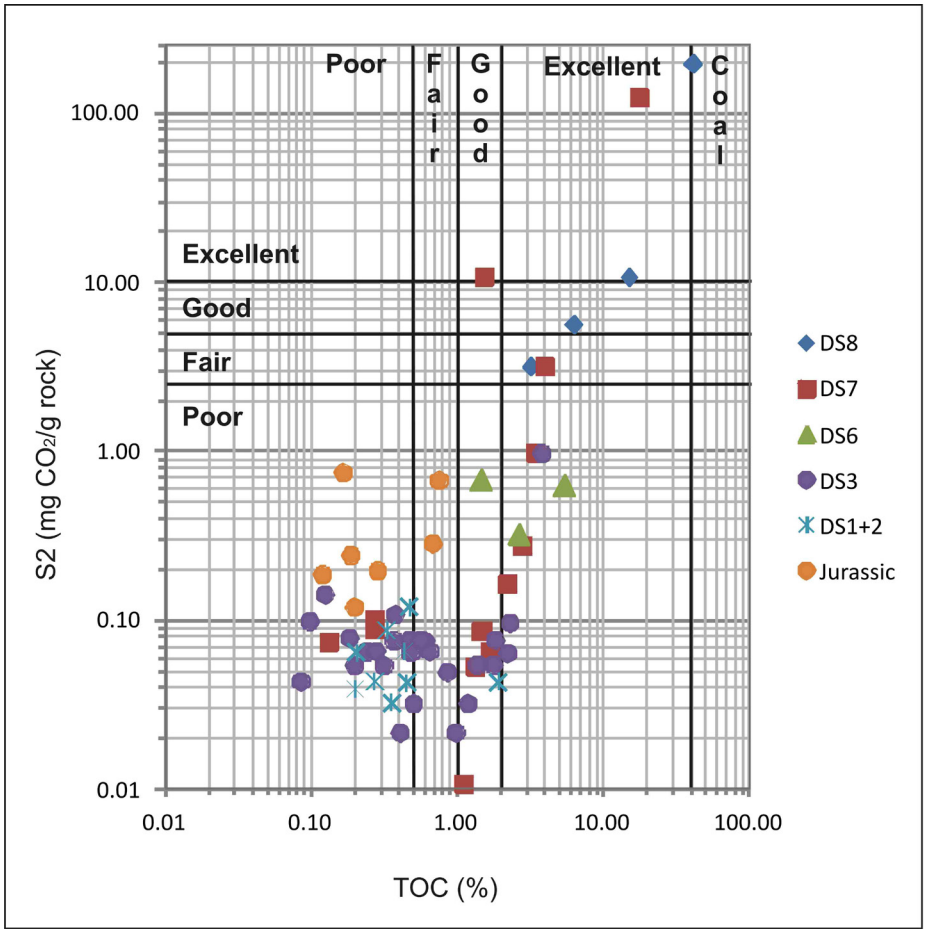

Fig. 10.12 - S2 index vs. TOC index diagram, which allows for the determination of the hydrocarbon potential of a source roc, not only by considering the organic carbon content but also by the amount of hydrocarbon formed during the thermal decomposition of the kerogen (S2) (from Dimbicky, (2009)

residual kerogen types, make these rocks potential spent source rocks rock (Law, 1999). From the type of kerogen deduced from the sedimentary evidence, the Jurassic and DS3 deposits could generate the most oil, whereas the DS7 (Enciso Gr) deposits could generate mostly gas (Peters, 1986). A synthesis of the characteristics of the spent source rocks recognised in the basin is shown in Table 10.7. Because these spent source rocks are located in sectors of the basin that are more affected by hydrothermal metamorphic events, these deposits may lose their potential as petroleum source rocks as a consequence of rapid heating of the organic matter above the ideal temperature (Taylor et al., 1998). To determine if the metamorphism could cause the source rocks to lose their petroleum potential, the timing of organic matter maturation needs to be determined using thermal modelling and needs to be compared with the timing of metamorphic events.

Potential source rock	TOC (%) mean	HI (mgHC/g TOC) mean	S2 (mgHC/g rock) mean	Type of Kerogen	Type of hydrocarbon generated
DS7-Abejar - Casarejos Area	17.82	695	123.83	Type I	Oil
DS7- Abejar - Soria Area	2.8	168	3.09	Type III-I	Gas and Oil
DS8-Escucha - Prejano area	16.49	184	6.5	Type III	Gas and Oil

Table 10.6 - A synthesis of potential source rocks characteristics in the basin and of the possible types hydrocarbons that could be generated (Peters, 1986)

10.5.5. Hydrocarbon generation

In the Cameros Basin, abundant evidence of hydrocarbons and bitumen were found, representing different stages of hydrocarbon generation, accumulation and thermal maturation.

Tar sandstones (Fig. 10.11g and Fig. 10.11h), constituting part of the Utrillas Fm post-extensional deposits are the most relevant hydrocarbon accumulation that is preserved in the Cameros Basin petroleum system. Sandstone pores are mostly filled by bitumen, suggesting that these deposits represent an important reservoir in the basin (Ochoa et al., 2007). The very low maturity (0.033 % Ro) of these asphaltic bitumens (Table 10.5) suggests that, after accumulation, the reservoir was not affected by relevant burials or by additional thermal events.

A very early hydrocarbon formation stage was identified in the DS7 deposits at the Soria site, as well as in the DS8 deposits at the Prejano site, where fluorescent exsudatinite was associated with liptinite macerals (Fig. 10.10g and Fig. 10.11f). The occurrence of primary cracking is consistent by early oil-window thermal conditions in these areas (Fig. 10.3).

In the over-mature deposits, proof of hydrocarbon generation and migration were often found in the mineral matrix in the form of evolved solid bitumen particles (Meso to Cata-impsonite). These particles are very abundant in Jurassic deposits (Fig. 10.9b), in DS3 deposits at the Yanguas site (Fig. 10.9f) and in the DS7 deposits at the Enciso site (Fig. 10.10a). Sporadic solid bitumen particles are found in the DS1+2 at the Poveda site (Fig. 10.9e) , in the DS3 deposits at the Montenegro site (Fig. 10.9g) and in the DS7 at the Soria site (Fig. 10.10d) (Table 10.5). The presence of bitumen traces in the over-mature deposits suggests that the original kerogen was already completely transformed in hydrocarbon during the thermal evolution of the rock, as well as that these areas were involved in hydrocarbon migration (Bordenave, 1993; Taylor et al., 1998).

Evidence of thermal physio-chemical transformation in the generated bitumens was found

Spent source rock	TOC (%) mean	HI (mgHC/g TOC) mean	S2 (mgHC/g rock) mean	Type of original keorogen	Type of hydrocarbon generated
Jurassic - all Sites	0.39	30.5	0.07	Type II	Oil and Gas
DS3-Valdeprado - Yanguas Site	0.9	14	0.1	Type I	Oil
DS7-Enciso - Enciso Site	1.21	10	0.07	Type III-I	Gas

Table 10.7 - A synthesis of the spent source rock characteristics in the basin and of the possible type of hydrocarbon that could be generated (Peters, 1986). Types of original kerogens that were deduced primarily by considering the sedimentological features of the deposits

in the DS3 uppermost stratigraphic level at the Montenegro site and in the DS7 limestone bed (Leza Fm) outcropping in the northernmost part of the Enciso site. In the first case, solid bitumen particles with high-reflectance coke-texture were found (Fig. 10.9g); however, in the second case, mesophase with different sizes was recognised in the solid bitumen particles (Fig. 10.10a and Fig. 10.10b). These textures indicate that the hydrocarbons that were generated in or migrated to these areas were affected by very high temperatures, which caused a thermal transformation (Rahimi et al., 1998; Taylor et al., 1998).

10.6. CONCLUSIONS

The integration of petrographical and geochemical analysis enables detailed characterisation of the organic matter in the Cameros Basin. These results determine the reconstruction of the basin infill maturity and the potential source rocks in the basin.

Clear differentiation of the thermal maturity in the basin was identified. The northern and central sectors of the basin are characterised by over-mature to dry-gas thermal conditions, whereas the southern sector is characterised by immature to early-oil-window thermal conditions. The different thermal histories recorded in the basin can be related to different tectonic evolution in the basin sectors, which determine different subsidence rates and burial. The circulation of hot fluids in the central-northern sectors of the basin, related to hydrothermal metamorphic events, occurred during basin evolution, emphasised thermal maturity differences and caused anomalous thermal maturity distribution.

The deposits with more abundant organic matter content were located in the southern sector of the basin and to the north, at the footwall of the main thrust, whereas in the rest, low organic matter content was preserved.

In the over-mature deposits, residual kerogen is dominant as a result of the thermal transformation of the original kerogen. Sedimentological data indicate the possible nature of the original kerogen in these deposits: Type II for the pre-extensional Jurassic deposits, Type I for the DS3 Valdeprado Fm deposits, Type III-I for the Enciso Gr deposits and Type III for the rest of the basin deposits. In the immature deposits, Type III kerogen dominates (Prejano site and most of the Soria site), and less frequently Type I kerogen dominates (Casarejos site and some samples from the Soria site).

The immature deposits have very high hydrocarbon potential, especially at the Casarejos and Prejano sites, and they were considered to be potential source rocks. Despite of that, the high dilution of these latter fine-grained organic-rich deposits, in the coarse-grained siliciclastic interval forming these units, provides dual benefits if a large amount of hydrocarbons could be generated from these rocks.

The over-mature deposits have poor hydrocarbon potential. The petrographic, geochemical and sedimentological data indicate that the pre-extensional (Pozalmuro Fm) deposits, the DS3 (Valdeprado Fm) and the DS7 (Enciso Gr) deposits are defined as spent source rocks, where kerogen was already transformed into oil and gas due to thermal maturity. Abundant rests of hydrocarbons and bitumen were found, representing different stages of hydrocarbon generation, accumulation and thermal maturation. The most important hydrocarbons accumulation is located at the Utrillas Fm post-extensional sandstone unit.

The analysis of the organic matter performed herein represents significant progress in understanding the petroleum system in the Cameros Basin, especially related to the identification of source rocks in the system. Furthermore, it provides the keys to understanding failed petroleum systems, providing descriptions of the effect of hot fluid circulation (hydrothermal metamorphism) on organic matter preservation in a basin.

Chapter 11

11. Kinetic Calculation and Definition

11.1. INTRODUCTION

11.1.1. Kerogen in sedimentary rocks

Sedimentary organic matter (SOM) largely consists carbon (C) and hydrogen (H), with some additional heteroatoms, mainly oxygen, nitrogen and sulphur (O, N and S). Produced oil and gas comprise the same elements, arranged primarily into hydrocarbons (pure C and H) and N, S and O compounds that are arranged into more complex molecules (Tissot and Welte, 1987; Pepper and Corvi, 1995) (Fig. 11.1). Petroleum is present in all organic matter from the time of deposition. This initial petroleum, often called 'immature oil' or 'bitumen' represents that portion of SOM that escaped condensation into kerogen during a very early diagenesis (Pepper and Corvi, 1995). Historically, the petroleum content of source rocks has been measured by extraction with mild organic solvents such as dichloromethane. By contrast, kerogen is the insoluble (non-petroleum) component of SOM, defined as the unextractable organic residue (Durand, 1980) (Fig. 11.1).

Bitumen contains free hydrocarbons ranging from C1 to C40, heavy hydrocarbons and NSOs grouped into resins and asphaltenes. Hydrocarbons ranging from C1 to C33 form the S1 peak of the Rock-Eval, whereas heavier hydrocarbons, resins and asphaltenes are minor contributors to the

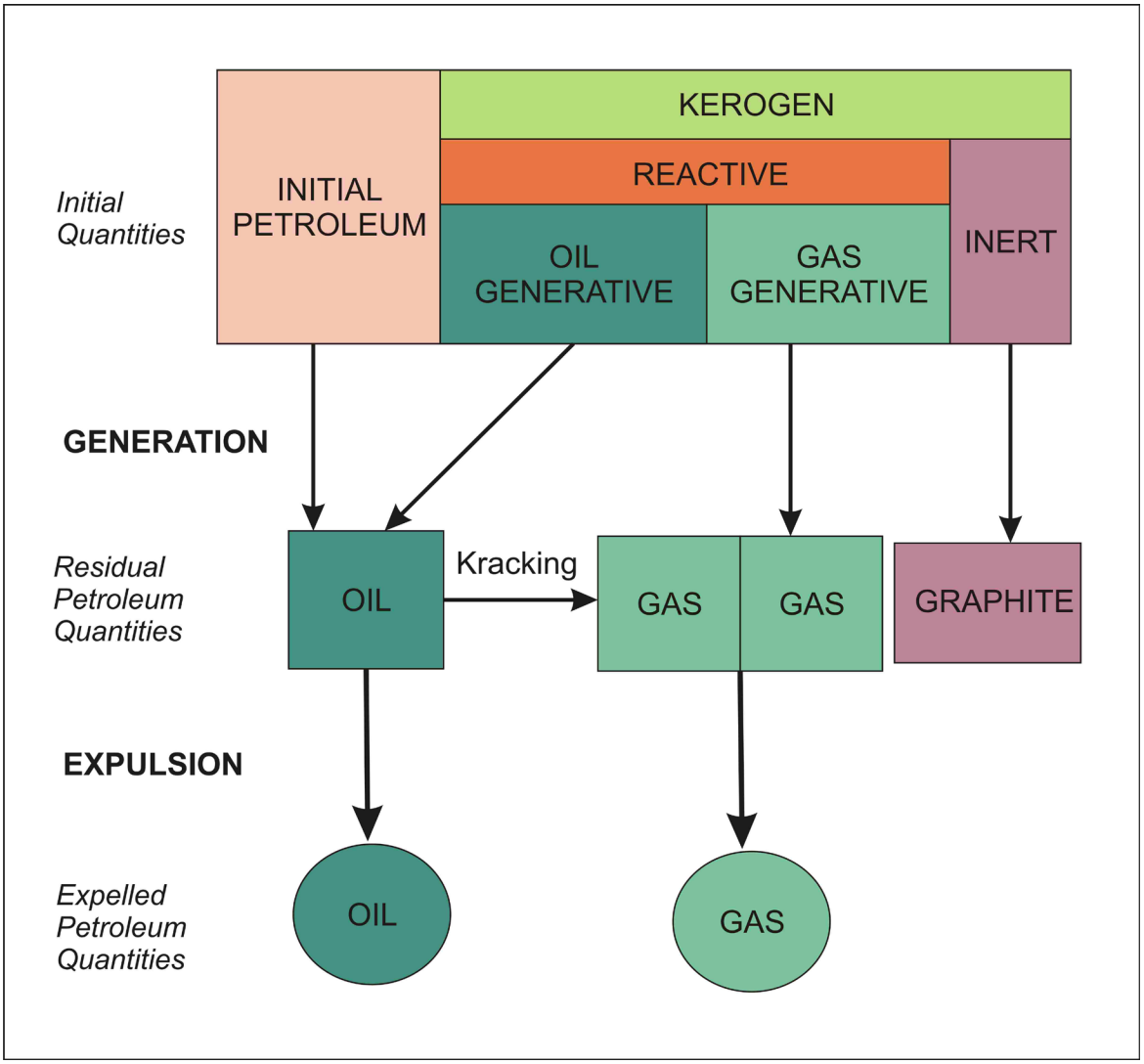

Fig. 11.1 - Scheme of petroleum generation, cracking and expulsion (from Pepper and Corvi, 1995)

S2 peak (Bordenave et al., 1993). The free hydrocarbons include oil and gas components: gas hydrocarbons have one to five carbon atoms, whereas oil hydrocarbons with six or more carbon atoms form oil molecules (England et al., 1987). The S1 peak is lower than the extractable fraction for immature sediments (Snowdon and Powell, 1982), as the latter is mostly formed by resins and asphaltenes. In the mature sediments the S1 peak corresponds to the extractable fraction (Bordenave et al., 1993) (Fig. 11.2).

The S2 peak represents the reactive kerogen, which does not yield a thermal volatility and is thermally degradable (Pepper and Corvi, 1995). Thus, the HI index (S2 yield normalised to the TOC) provides an indication of the reactive to inert kerogen proportions in the SOM (Espitalié et al., 1977; Bordenave et al., 1993; Pepper and Corvi, 1995). The "S2 peak gives a reasonable evaluation of the current potential of a rock sample, indicating the amount of oil and gas that

can be generated from its present stage of thermal maturation to the graphite stage" (Bordenave et al., 1993).

11.1.2. Kerogen degradation: cracking

To evaluate the timing of kerogen thermal degradation and hydrocarbon formation, as a consequence of the progressive temperature increase for the burial of the source rock, it is fundamental to determine the synchrony in the basin between the generation of petroleum and the formation of traps and seals (Tissot and Welte, 1984). To estimate the timing of kerogen transformation, two main factors need to be considered: the thermal history of the source rock and the kinetic behaviour of the kerogen contained within the source rock (Tegelaar and Noble, 1994, Tissot and Welte, 1984). Basin modelling is generally used to solve the first factor, providing thermal profiles of source rock maturation throughout geological time (Welte and Yukler, 1981a; Tissot et al., 1987; Lerche, 1988; Welte and Yalçin, 1988; Welte et al., 1997; Littke, 2008) (**Chapter 9**). By contrast, kerogen kinetic modelling determines the influence of time and temperature in the process of kerogen maturation (Tissot and Espitalié, 1975; Quigley et al., 1987; Tissot et al., 1987; Braun et al., 1991).

"Kerogen is a macromolecule composed of polycondensate nuclei bearing alkyl and functional groups linked with heteroatomic bonds or carbon chains. As the burial depth and temperature increase, the bonds are gradually broken in order to increase the rupture bond energies. The first products generated are heavy heteroatomic compounds, carbon dioxide and

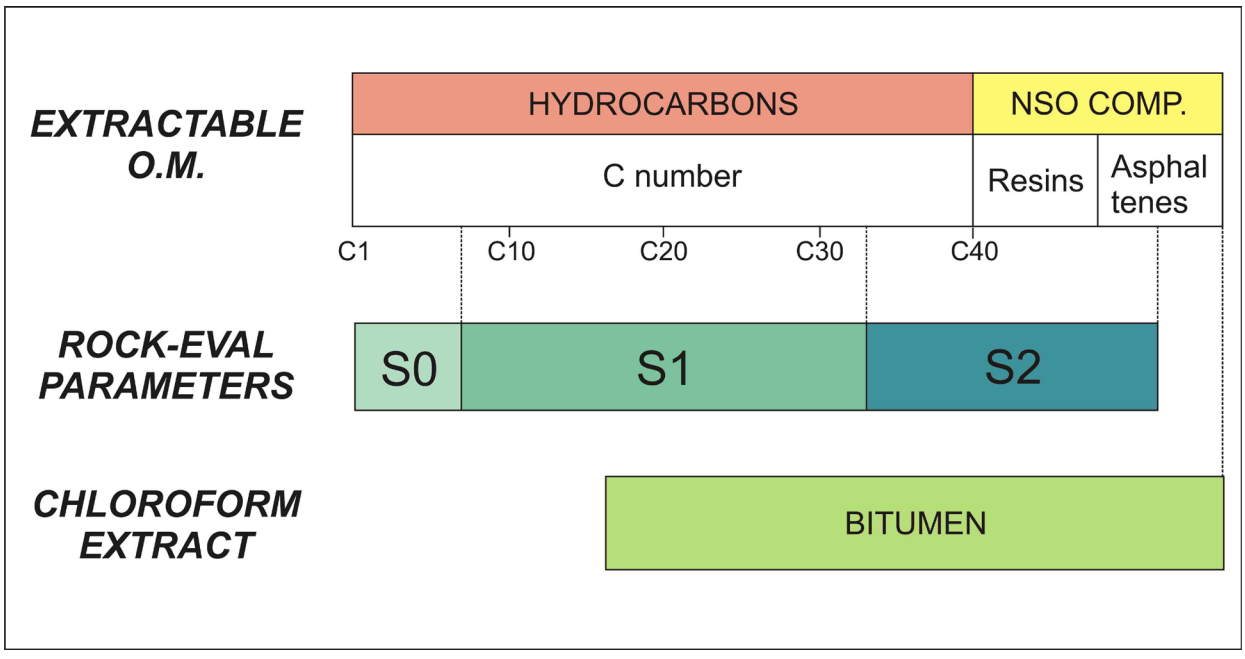

Fig. 11.2 - Relationship between bitumen composition and Rock-Eval peaks (from Bordenave, 1993)

water, and then progressively smaller molecules and finally hydrocarbons are generated. At the same time, kerogen becomes more aromatic and evolves toward a carbon residue" (Tissot and Welte, 1984) (Fig. 11.1). These processes have been defined as cracking (Tissot and Espitalié, 1975).

Kerogen degradation has been represented by a series of first-order, parallel, irreversible and independent reactions, resulting in a discrete distribution of activation energies (Quigley et al., 1987; Tissot et al., 1987; Ungerer and Pelet, 1987; Braun et al., 1991). These sets of reactions represent the successive steps of the kerogen transformation in oil and gas as temperature and time increase (Tissot and Welte, 1984). The first-order reaction of kerogen degradation indicates that the rate of degradation (dc/dt) is proportional to the concentration (c) of kerogen at any time (t):

$$dc/dt = -kc$$

The rate constant (k) is a function of temperature, as reproduced by the classical Arrhenius law verified experimentally as early as 1889 (Jüntgen and Klein, 1975; Tissot and Espitalié, 1975; Ungerer, 1993):

$$K = Ao \exp(-E/RT)$$

where Ao is the pre-exponential frequency factor (in s-1), E is the activation energy (in J/mol), R is the gas constant (8.31441 Jmol/K-1), and T is the absolute temperature (in K).

A and E are intrinsic properties of the reactant (i.e., oil or gas generating kerogen), and they represent the molecule's vibrational frequency and the strength of the molecular bonds that need to be broken to allow the reaction to occur (Tissot and Espitalié, 1975, Pepper and Corvi, 1995).

Early models used single activation energies to describe organic maturation and the associated processes (Huck and Karweil, 1955; Karweil, 1955; Tissot and Espitalié, 1975). "However, it is now widely appreciated that such models are unsuitable for describing kerogen breakdown, as they do not explain the experimentally observed increase in activation energy with reaction progression" (Pepper and Corvi, 1995). A reaction suite governed by a range of activation energies has been considered to be more realistic (Pepper and Corvi, 1995).

The activation energies of each reaction series correspond to the energy necessary to break the bonds of the different kerogen compounds. Each transformation reaction corresponds to a percentage of the generation potential of the rock, and it is expressed by the S2 peak of the pyrolysis Rock-Eval analysis and by the related HI index. The Tmax measured in the pyrolysis Rock-Eval analysis depends on the activation energies and it can be used to calibrate the kinetic modelling (Ungerer et al., 1986).

Compositional kinetics representing the primary and secondary cracking have been modelled, subdividing the products generated from the kerogen transformation into different classes of components (e.g., C1, C2, C3, C5, C6 and C15), each one characterised by a generation potential and by a characteristic distribution of activation energies (Espitalié et al., 1988; Ungerer et al., 1990; Behar et al., 1997). This compositional kinetics model allows for the determination of the composition and physical properties of the hydrocarbons formed during cracking.

11.1.3. Traditional kinetic parameters calculation

In most laboratories, determination of the kinetic parameters for hydrocarbon generation is generally realised in two steps, consisting of artificial maturation experiments followed by a fitting of kinetic parameters to the laboratory data (Tegelaar and Noble, 1994). An open system pyrolysis using multiple constant heating rates is the artificial maturation technique most commonly used (Ungerer and Pelet, 1987; Braun et al., 1991; Tegelaar and Noble, 1994). Samples are pyrolyzed in Rock-Eval equipment (Espitalié et al., 1977) operating at multiple constant heating rates (e.g., 1, 5, 15 and 50^{o}C/min). If the modelled S2 pyrolysis peak is not in agreement with the S2 peak measured in the pyrolysis, additional runs at the problematic heating rates are performed to establish the most appropriate set of kinetic (Ungerer, 1984; Ungerer et al., 1986; Burnham et al., 1987; Tissot et al., 1987; Ungerer and Pelet, 1987; Ungerer, 1993; Tegelaar and Noble, 1994). Some models determine a discrete distribution of the activation energies, performing the linear combination of several first-order parallel and independent reactions (Tissot and Espitalié, 1975; Ungerer, 1984; Ungerer et al., 1986; Braun and Burnham, 1987; Burnham et al., 1987; Burnham et al., 1988; Sundararaman et al., 1988; Okui and Waples, 1992). By contrast, other models propose an infinite number of unknown reactions, assigning a Gaussian or normal distribution to the activation energies (e.g., Anthony and Howard, 1976; Braun and Burnham, 1987; Burnham et al., 1987; Quigley et al., 1987; Mackenzie and Quigley, 1988; Quigley and Mackenzie, 1988).

Kinetics parameters have to be calculated on immature to early mature kerogen (immediately above the top of the oil window) (Tissot et al., 1987). Very immature samples, which have not entered the diagenesis yet, may indeed cause artefacts, and mature samples will lose part of their initial potential (Tissot et al., 1987, Ungerer, 1993, Tegelaar and Noble, 1994).

11.1.4. Kerogen kinetic behaviour

Kinetic parameters are a function of the chemical composition and type of molecular bonds of the kerogen (Tegelaar and Noble, 1994). Thus, the activation energy's (AE) distribution and the frequency factors (Ao) describing the thermal cracking of the kerogen can be used to

characterise a kerogen (Ungerer and Pelet, 1987, Tissot et al., 1987, Espitalié et al., 1988, Behar et al., 1997).

Kerogen composition can be represented as a histogram of activation energies versus the genetic potential of the kerogen (Tissot and Welte, 1984), corresponding to the HI (mgHC/g TOC) of the pyrolysis Rock-Eval. The genetic potential represents the total amount of hydrocarbons that can be produced by a certain kerogen (Tissot and Welte, 1984). With increasing burial and temperature the various bonds corresponding to the successive activation energies are progressively broken, in order of increasing activation energies, as suggested by the temperature dependence of the reaction parameters (Tissot and Welte, 1984). The distribution of the activation energies results from the chemical composition of the kerogen (Tissot et al., 1987). In the pyrolysis Rock-Eval the temperature recorded when at the maximum chemical transformation velocity is the Tmax (Espitalié et al., 1987; Bordenave et al., 1993). The Tmax is measured in the 25°/min heating rate run. At any time the stage of the kerogen evolution can be determined by calculating the transformation ratio, which is the ratio between the kerogen already transformed and the initial genetic potential (Tissot and Welte, 1984). The distribution of the activation energies of a kerogen can be represented even as cumulative curves of the transformation ratio percentages versus temperatures (Tegelaar and Noble, 1994).

The relationship between the chemical composition of the kerogen and the kinetic behaviour has been demonstrated for the classical type of kerogens (Tissot and Espitalié, 1975; Tissot et al., 1987). The Type I kerogen contains a large portion of labile organic material, and thus it has a high genetic potential (Tissot and Welte, 1984). It generally exhibits a unimodal activation energies distribution (AE 54/70 kcal/mol with an Ao of 1.026*1014s-1), which reflects the homogeneity of the chemical bonds (carbon-carbon) (Tissot and Espitalié, 1975; Tissot et al., 1987) (Fig. 11.3). The Type II kerogen contains slightly less of the labile organic material, resulting in a genetic potential slightly lower than in Type I (Tissot and Welte, 1984). Type II kerogens contain a larger variety of chemical bonds because they contains more heteroatoms (N, O and S). The distribution of the activation energies is wider than that if Type I molecules (AE 44–60 kcal/mol with an Ao of 1.11*1015s-1) (Tissot and Espitalié, 1975; Tissot et al., 1987) (Fig. 11.3). Type III kerogen contains even less of the labile organic material than the other types, and its genetic potential is low (Tissot and Welte, 1984). The presence of different types of chemical bonds, with the dominance of bonds that are thermally stable, results in a wide distribution of activation energies with dominantly high values (AE 50–74 kcal/mol, with an Ao of 5.4*1016 s-1) (Tissot and Espitalié, 1975; Tissot et al., 1987) (Fig. 11.3).

The difference in the kerogen kinetic behaviour has an effect on the synchronism of the hydrocarbon generation with the formation of traps and seals, as different kerogens in the same basin can be transformed at different temperatures and times. A Type II kerogen is transformed earlier than the others and for a longer time than Type I, whose transformation

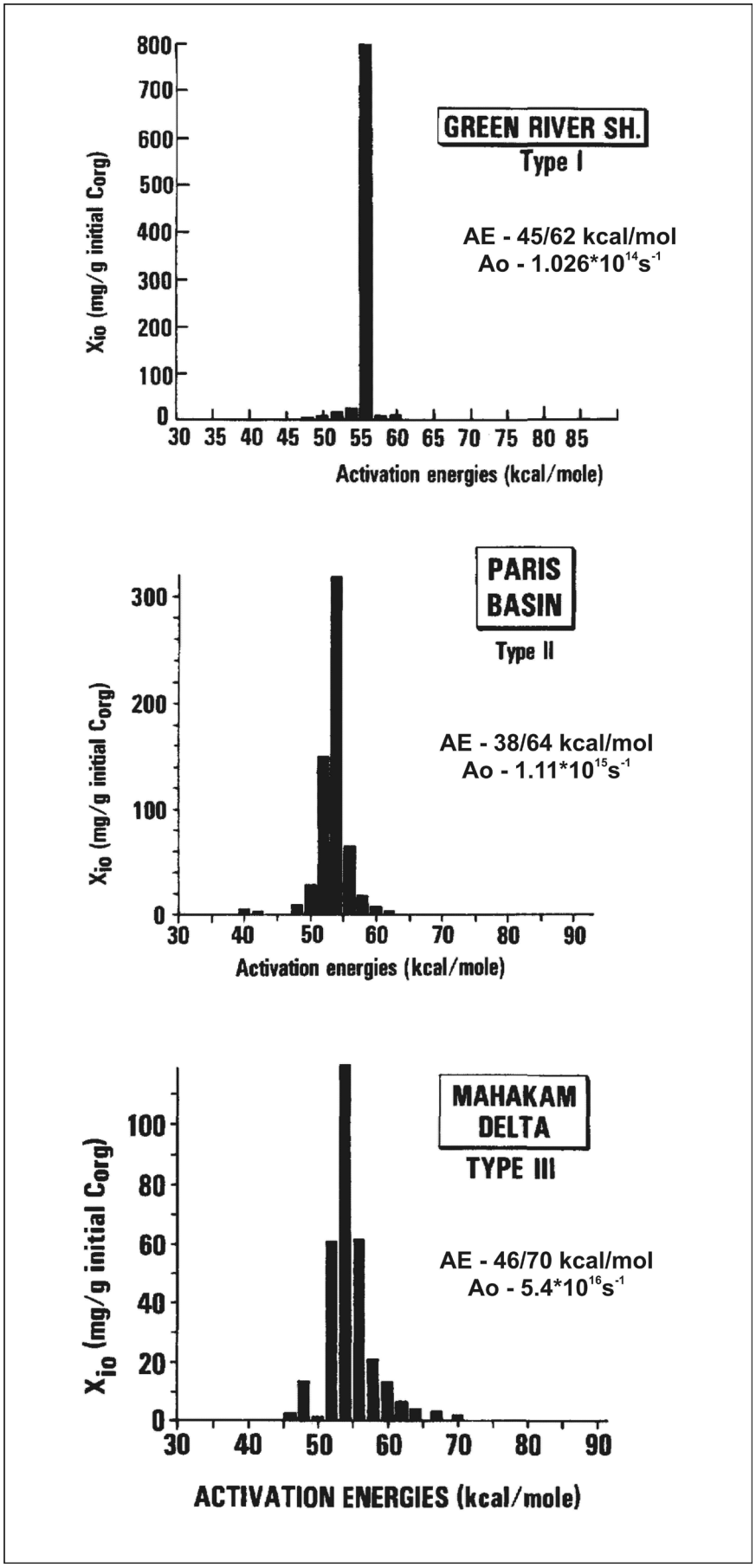

Fig. 11.3 - Activation energies (AE) distribution of the classical kerogen types versus petroleum potential (X_{io}) (Tissot et al., 1987). Frequency factor (A) for each type of kerogen is indicated

is quite instantaneous. Type III kerogen is transformed at a higher temperature than the other types (Tissot and Welte, 1984).

Commonly, these types of kinetics are applied in the hydrocarbon generation model once the specific kerogen type is known (I, II or III) from an optical examination or the geochemical data (HI index) (Tissot and Welte, 1984; Gonçavales et al., 2001). However, it has been observed that kerogens belonging to the same type can have different kinetic behaviours (Jarvie, 1991; Burwood et al., 1992; Sundararaman et al., 1992; Gonçavales et al., 1994; Tegelaar and Noble, 1994). Tegelaar and Noble (1994) demonstrate that kerogen typing based on the hydrogen index is insufficient to predict the kinetic parameters of a kerogen (Tegelaar and Noble, 1994). Hence, a typical Type I, Type II and Type III kerogen kinetic behaviour does not exist and the hydrogen index cannot provide a good discriminator for predicting the kinetic behaviour of a kerogen. Waples et al. (1992) stressed how errors are made in determining the type of kerogen of a source rock (e.g., type, mixed or pure kerogen and S content) and, consequently, the assignment of an incorrect kinetic can lead to important errors in calculating the timing and amount of hydrocarbon generation. Tegelaar and Noble (1994) asserted that kerogen parameters depend primarily on the molecular structure of the kerogens. A pyrolysis gas chromatography mass spectrometry (Py-GC) signature can be used to reveal the kerogen molecular structure (Tegelaar and Noble, 1994). The organic sulphur content affects the magnitude of the kinetic parameters, determining lower temperatures for kerogen decomposition, as a consequence of the C-S bond being weaker than the C-C bond (Tissot et al., 1987; Baskin and Peters, 1992; Tegelaar and Noble, 1994; Tomić et al., 1995).

11.2. KINETIC PARAMETERS OF THE KEROGEN OF THE CAMEROS BASIN

To model the generation, migration and accumulation of hydrocarbons in the Cameros Basin it is fundamental 1) to reconstruct the thermal history of the basin (**Chapter 9**), and 2) to determine the kinetic parameters of the kerogen forming the original source rocks of the petroleum system. Difficulties calculating the kinetic parameters in the Cameros Basin occur because most of the potential source rocks of the system are presently overmature and are, therefore, consequently constituted by a very poor content of organic matter (spent source rocks, sensu Law, 1999) (**Chapter 10**). Thus, these rocks cannot be used for kinetic calculations. Kinetics obtained from the literature can be assigned to the spent source rocks, considering the type of the original kerogen. The kerogen type is deducible from the depositional environment of the related deposits (**Chapter 10**). Alternatively, kinetic parameters for the Cameros Basin kerogen can be calculated on the immature deposits, cropping out in the southern sector of the basin. At a later stage, geochemical and kinetic parameters of these immature deposits can be assigned to

the spent source rocks in the case that they have been deposited in an equivalent depositional environment (lacustrine-palustrine coastal wetlands of a fluvial-deltaic system).

In this work a calculation of the bulk kinetic parameters of the immature Cameros Basin kerogen was proposed. To interpret the thermal alteration behaviour of the kerogen of the Cameros Basin, the results are compared with the parameters of kinetics proposed for classical Type I, Type II and Type III kerogens (Tissot in Weples et al., 1992; Behar et al., 1997), as well as for other types (Burnham and Sweeney, 1989; Ungerer, 1990; Tegelaar and Noble, 1994; Pepper and Corvi, 1995). Due to the reduced number of samples analysed, the results presented here provide only an indicative and generalised characterisation of the kinetic behaviour of the basin's kerogen. In a future, to confirm the proposed data, more detailed and extended analyses would be necessary.

11.3. METHODS AND SAMPLES

11.3.1. Methods

The method used here to determine the kinetic parameters is based on a mathematical computational modelling of the S2 peak from the pyrolysis Rock-Eval. This method was developed and calibrated at the University of Strasbourg, Nancy (Chaduli, 2013), and will be published and patented in the near future. Thus, in this work, only a synthetic explication of the method is reported.

The kinetic mechanism used in the new proposed method refers to the classical method described by Ungerer (1993), which proposed that the kerogen transformation reaction in the bulk hydrocarbons follows the Arrhenius equation in a geological context as well as in the laboratory. To model the kinetic behaviour of the kerogen, Ungerer (1993) determined the activation energies and pre-exponential frequency factor corresponding with the interval measured in the laboratory during the kerogen reaction (expressed by the S2 peak of the Rock-Eval), at a heating rate of 25ºC/min (corresponding to the heating rate used to measure the Tmax in the Rock-Eval). In the classical method (Ungerer and Pelet, 1987; Ungerer, 1993; Braun et al., 1991 and Burnham et al., 1987) three heating rates were used to verify that the calculations determine the same activation energies and frequency factor for three different heating rates. Because the frequency factor can be considered constant with the temperature (Martínez et al., 1993, Ungerer, 1993) (Fig. 11.4), the new method presented here proposed the use of only one heating rate (25º/min), which is the heating rate used in the pyrolysis Rock-Eval. Thus, the kinetic calculations can be performed directly on the S2 peak of the Rock-Eval without having to repeat them for three different heating rates. The pre-exponential frequency factor depends on the S2 peak and on the related Tmax (Martínez et al., 1993). The calibration of the frequency factor

can be performed based on the Tmax variation with depth (Fig. 11.5). Because in the Cameros Basin it was not possible to reconstruct a clear Tmax variation with depth, the calibration of the calculated pre-exponential frequency factor was performed with respect to the S2 peak of the Rock-Eval.

A detailed explanation of the method proposed was presented by Chaduli (2013), where all of the singular steps of the method are described, and is synthesised as follows:

1) First, the temperature measured in the Rock-Eval has to be corrected in the thermocouple with respect to the real temperature that reaches the sample during the analysis. Thus, the Tmax performed by the Rock-Eval analysis needs to be corrected to be the real Tmax. In correcting the Tmax, the S2 peak is shifted to the real measured temperatures.

2) Second, taking into account the heating rate of the Rock-Eval analysis (25ºC/min), the activation energy that better approximates the S2 peak (Tmax) of the analysed sample is chosen (between a range of 40 to 70 kcal/mol) (Fig. 11.6a).

3) A frequency factor is determined, which can be calculated directly from the Tmax of the S2 peak of the Rock-Eval, when possible (Fig. 11.5).

4) Finally, the intensity of the activation energies are adjusted using mathematical software

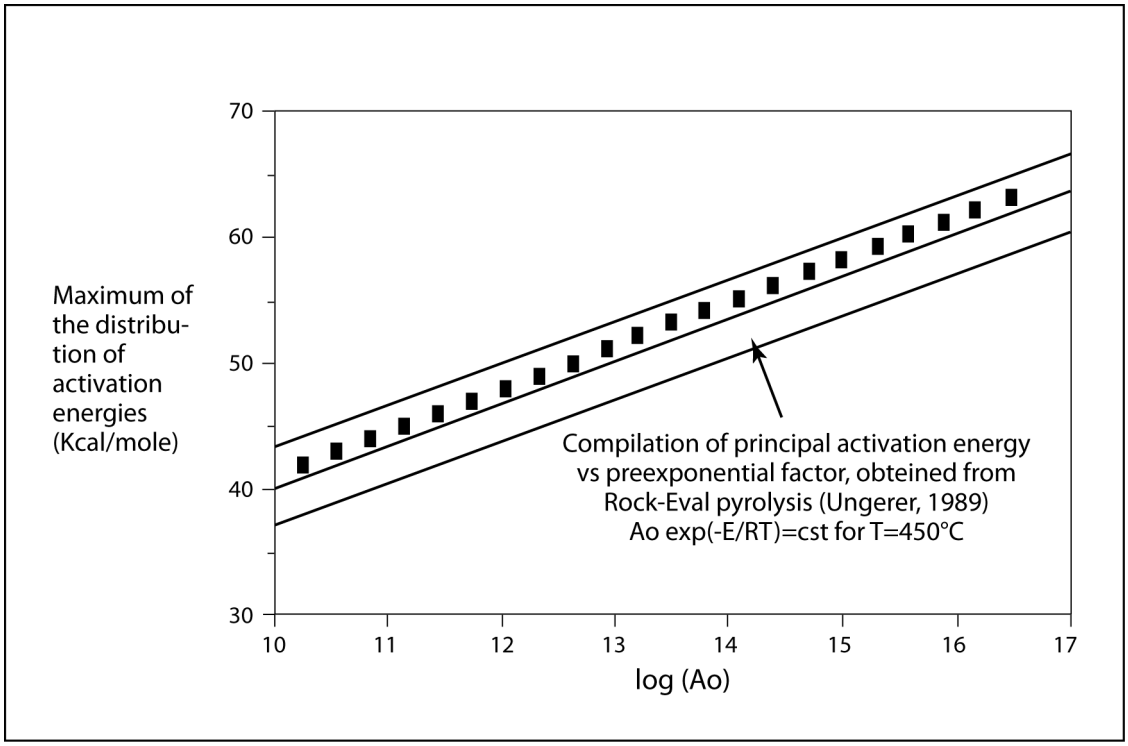

Fig. 11.4 - Evolution of the pre-exponential frequency factor with respect to the activation energy for a Tmax of 450°C (from Martínez et al., 1993)

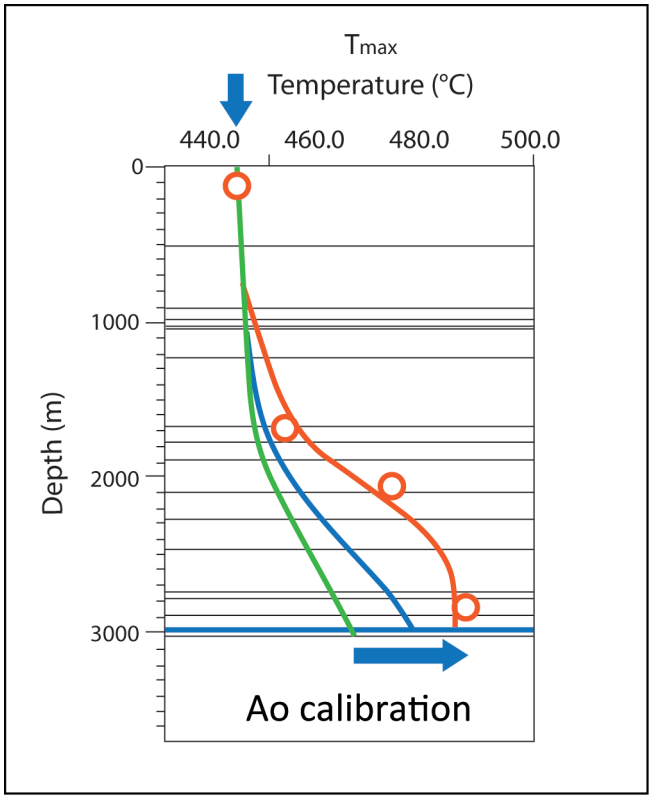

Fig. 11.5 - Example of a calibration of the pre-exponential frequency factor (Ao) for the Tmax variation with depth (sample from an Iranian basin, Chadouli, 2013)

until the activation energies and proposed frequency factor perform a perfect calibration between the S2 peak modelled and measured in the Rock-Eval (Fig. 11.6b).

To verify the method presented, the Chaduli (2013) calculation of the kinetic parameters was performed on a number of samples from an Iranian basin, which were previously analysed with a classical kinetic model that used three different heating rates (Ungerer and Pelet, 1987, Ungerer, 1993; Braun et al., 1991; Burnham et al., 1987). The equivalence of the kinetic parameters results performed by the two methods allows one to consider the newly proposed method reliable (Chaduli, 2013).

To analyse the kinetic behaviour of the Cameros Basin kerogen, the kinetic parameters calculated were introduced in the PetroMod software, obtaining the cumulative yield curves, which indicate the total mass of hydrocarbons formed per gram of organic carbon (transformation ratio, %) as a function of temperature. These curves can be compared with the cumulative yield curves of other kinetics presented in the PetroMod library, as the later equally refers to a heating rate of 25ºC/min.

11.3.2. Samples

As only immature to early-mature samples can be considered for obtaining the kinetic parameters (Tissot et al., 1987, Ungerer, 1993, Tegelaar and Noble, 1994), only a few samples could be analysed as a large part of the Cameros Basin is presently overmature (**Chapter 10**). Appropriate samples for this analysis are reduced if considering only samples with sufficient and well-preserved organic matter content with a TOC >1% (Bordenave et al., 1993).

In the set of immature samples collected in the Cameros Basin, three representative samples were selected (Fig. 11.7). The samples were taken from the dark-grey shale intervals of the dominant siliciclastic syn-extensional AbejarFm unit (DS7; Fig. 11.7), which corresponds to the

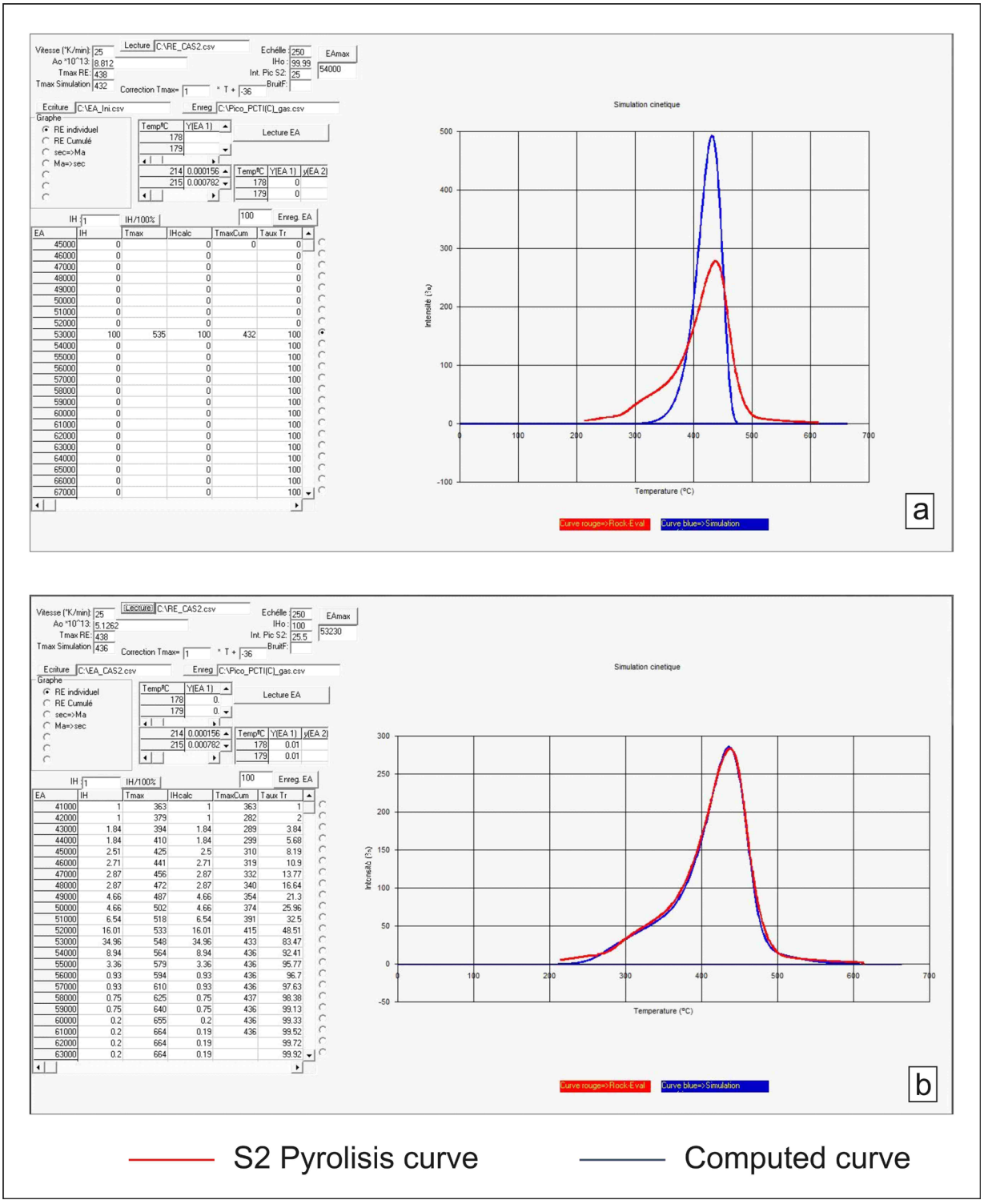

Fig. 11.6 – (a) Estimation of the activation energy that better approximates the S2 peak of the Rock-Eval (sample CAS-2). (b) In a second step, the intensity of the other activation energies were changed until a correct reproduction of the S2 peak was achieved

intervals of lacustrine-palustrine deposits related with coastal wetland plains of a fluvial-deltaic system (Mas et al., 1993, 2003, 2011, Arribas et al., 2003, Ochoa et al., 2007, **Chapter 10**). The

difference in the organo-facies and in the organic carbon content among the three samples is due to the paleo-environment fluctuation (lacustrine to palustrine) and the degree of marine influences. Variations in the physic-chemical depositional conditions determine differences in the type of organic matter accumulated as well as on the occurrence of favourable preservation conditions.

The first sample (CAS-2) was collected in the dark fine-grained deposits of the Abejar Fm (DS7) outcropping in the western sector of the basin (Fig. 11.7). Organic matter is very abundant (TOC 17.82%), formed mostly by liptinite and in minor amounts by vitrinite and inertinite maceral groups. Liptinite is constituted by algae oriented in laminae (lamalginites), algal bodies (telalginites), such as Botryococcus, and amorphous dispersed organic matter (Fig. 11.8a and Fig. 11.8b). The HI index indicates a Type I kerogen (695 mgHC/gTOC). An S2 peak (123.83 mg/HCg) indicates excellent petroleum potential (Peters, 1986, Bordenave et al., 1993). Vitrinite reflectance measurements determine immature thermal conditions (Taylor et al., 1998), with a mean value of 0.3% Ro (Table 11.1).

The second sample (PIG-1) was collected in the stratigraphically uppermost dark fine-grained deposits of the Abejar Fm (DS7) outcropping in the southern sector of the basin. Organic matter is rather scarce (TOC 1.52%), formed by liptinite, vitrinite and inertinite, in order of abundance. Liptinite is primarily formed by algae (Fig. 11.8c and Fig. 11.8d). The HI index is typical of a Type I kerogen (714 mgHC/gTOC). The S2 peak (10.85 mg/HCg) indicates good petroleum potential (Peters, 1986, Bordenave et al., 1993). Vitrinite reflectance measurements determine immature thermal conditions (Taylor et al., 1998) with a mean value of 0.47% Ro (Table 11.1).

The third sample (STFC-4b) was collected in the stratigraphically lowermost dark fine-grained deposits of the Abejar Fm (DS7) outcropping in the southern sector of the basin. Organic matter is rather abundant (TOC 3.95%), formed by vitrinite, liptinite and inertinite in order of abundance. Liptinite is primarily constituted by cuticles (Fig. 11.8e) and less frequently by algae (Fig. 11.8f). The HI index indicates a Type III kerogen (81 mgHC/gTOC). The S2 peak (3.19 mg/HCg) indicates fair petroleum potential (Peters, 1986, Bordenave et al., 1993). Vitrinite reflectance measurements determine immature to early oil window thermal conditions (Taylor et al., 1998) with a mean value of 0.38% Ro (Table 11.1).

11.4. RESULTS

The results of the mathematical computational modelling were very satisfactory for the three samples, as a correct reproduction of the S2 peak measured in the pyrolysis was performed by the model (Fig. 11.9i). De-convolution of the obtained peaks shows the activation energies distribution (for 1 kcal/mol) (Fig. 11.9ii). The results are represented in histograms of activation

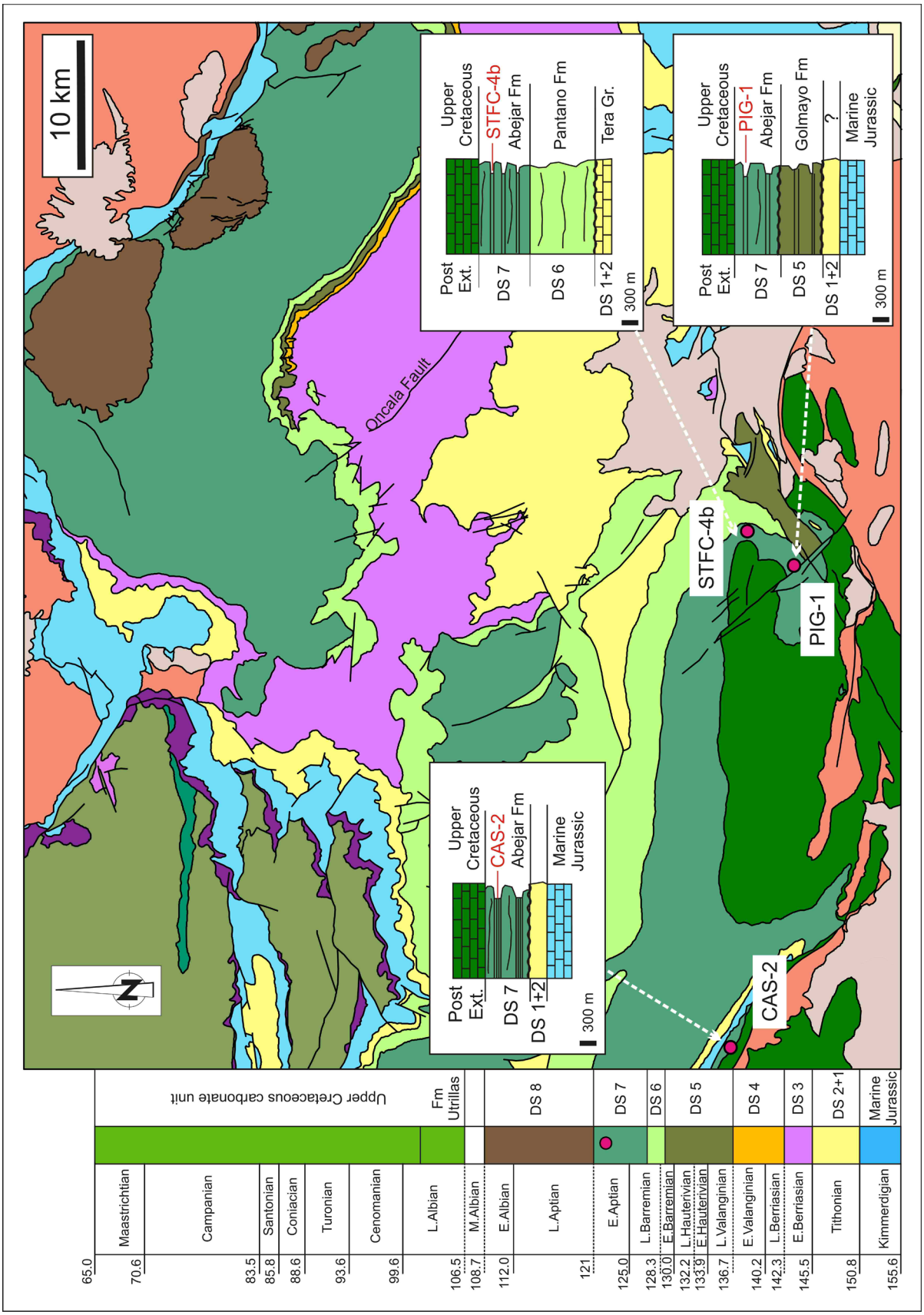

Fig. 11.7 - Geological and stratigraphical setting of the kerogen samples used for the kinetics calculation

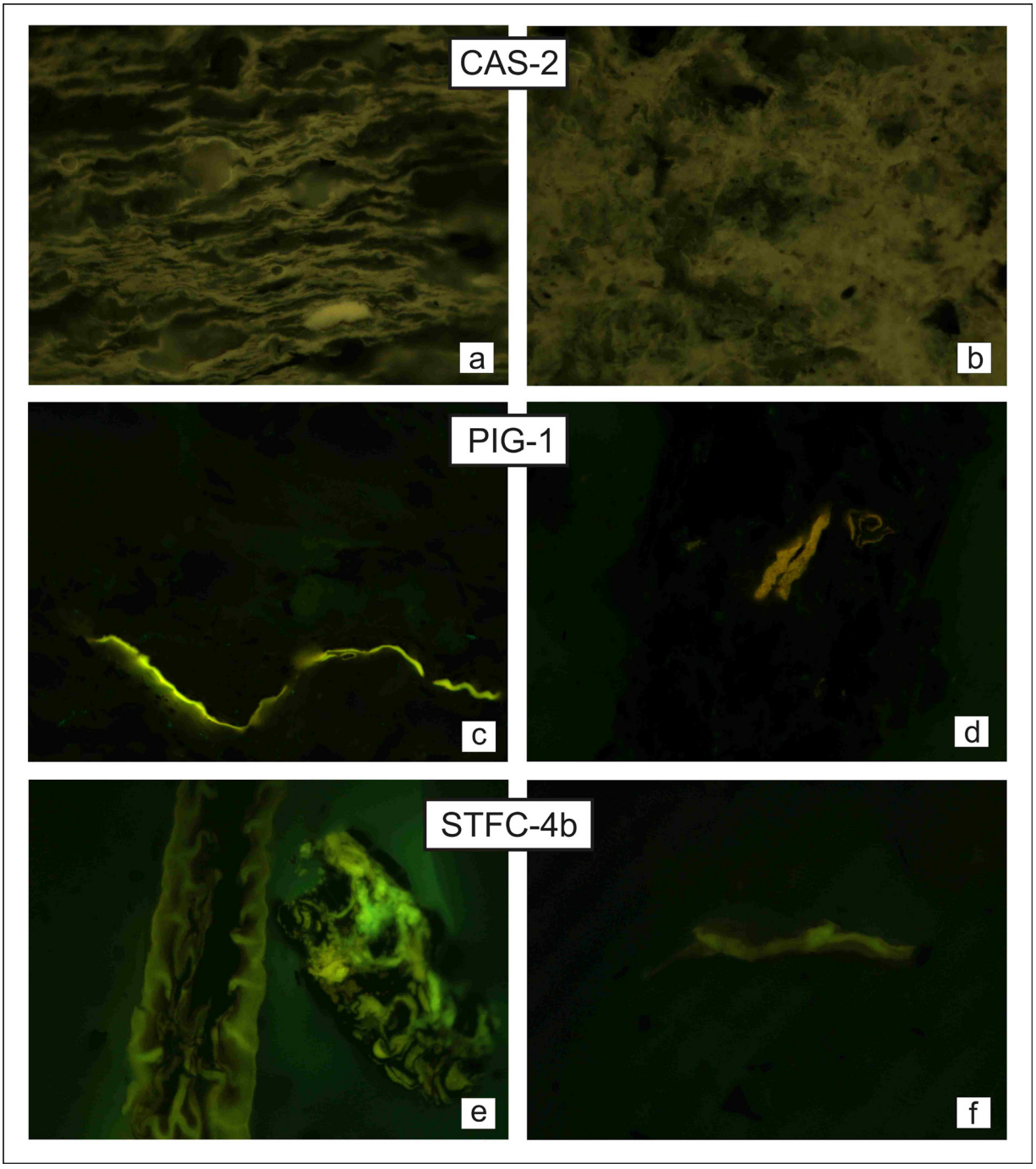

Fig. 11.8 - Organofacies of the analysed samples: (a) and (b) CAS-2, (c) and (d) PIG-1; (e) and (f) STFC-4b. (a) Thin algae oriented in laminae (lamalginites) and algal bodies (telalginites) such as Botryococcus; (b) Amorphous organic matter; (c), (d) and (f) algae; (e) cuticule. Optical microscopy. Photomicrographs taken in fluorescence mode. Width of the long dimension of the pictures: 200 µm

energies versus the fraction (%) of the genetic potential of kerogen (Tissot et al., 1987) (Fig. 11.10) and versus the hydrogen index (mgHC/gTOC) (Fig. 11.11). To compare the kinetic behaviour of the three samples, data were represented in cumulative yields curves, indicating the total mass of hydrocarbons formed per gram of organic carbon (transformation ratio) as a function of

Sample	TOC [%]	HI [mg HC/g TOC]	OI [mg CO2/g TOC]	Tmax [°C]	S1 [mg HC/g]	S2a [mg HC/g]	S3	%Ro
CAS-2	17.82	695	43	438	2.75	123.83	7.66	0.30
PIG-1	1.52	714	27	433	0.90	10.85	0.41	0.47
STFC-4b	3.95	81	70	431	0.04	3.19	2.78	0.38

Table 11.1 - Pyrolysis Rock-Eval data and vitrinite reflectance measured in the samples analysed for the kinetic calculation

temperature (Fig. 11.12). These curves were created introducing the calculated kinetic parameters in the PetroMod software, the kinetic module.

The calculation determines for the three samples the same frequency factor (2.9*1013/s-1) and a very similar activation energies mode (the activation energy measured when the maximum genetic potential of the kerogen is reached), ranging from 50 to 52 kcal/mol. However, differences exist in the amount of hydrocarbons generated when the maximum genetic potential is reached. This fact is manifested by the different HI index measured in the pyrolysis (Table 11.1). Furthermore, the difference in the distribution of the activation energies is observed.

In the CAS-2 sample the activation energies distribute on a large interval ranging from 40 to 56 kcal/mol (Fig. 11.10). The maximum genetic potential is recorded to be approximately 51 to 53 kcal/mol, with a maximum peak at 52 kcal/mol, corresponding to 27% of the genetic potential initial ratio and to 695 mgHC/gTOC (HI) (Fig. 11.10 and Fig. 11.11). The AE distribution is asymmetrical due to the frequent record of low activation energies (from 40 to 50 kcal/mol), whereas an AE higher than 53 kcal/mol was rarely recorded. The transformation ratio (%) versus temperature curve indicates that the transformation of 50% and 98% of the initial kerogen was achieved at 129ºC and 163ºC, respectively (Table 11.1).

The PIG-1 sample is characterised by a nearly unimodal and symmetric activation energy distribution (Fig. 11.10). A maximum genetic potential of 50 kcal/mol is markedly defined, which corresponds to 57% of the genetic potential initial ratio and to 714 mgHC/gTOC (HI) (Fig. 11.10 and Fig. 11.11). Less frequently, an AE ranging from 48 to 53 kcal/mol was measured. The transformation ratio (%) versus temperature curve indicates that a transformation of 50% and 98% of the initial kerogen was achieved at 118ºC and 149ºC, respectively (Table 11.1).

In the STFC-4b sample the activation energy distribution proceeds on a large interval ranging from 51 to 61 kcal/mol (Fig. 11.12). Two maximum genetic potentials are recorded at 51 and 52 kcal/mol, which corresponds to 33% of the genetic potential initial ratio and to 81 mgHC/gTOC (HI) (Fig. 11.10 and Fig. 11.11). The AE distribution is asymmetrical due to the frequent record of activation energies higher than 52 kcal/mol. However, an AE lower than 51 kcal/mol was rarely

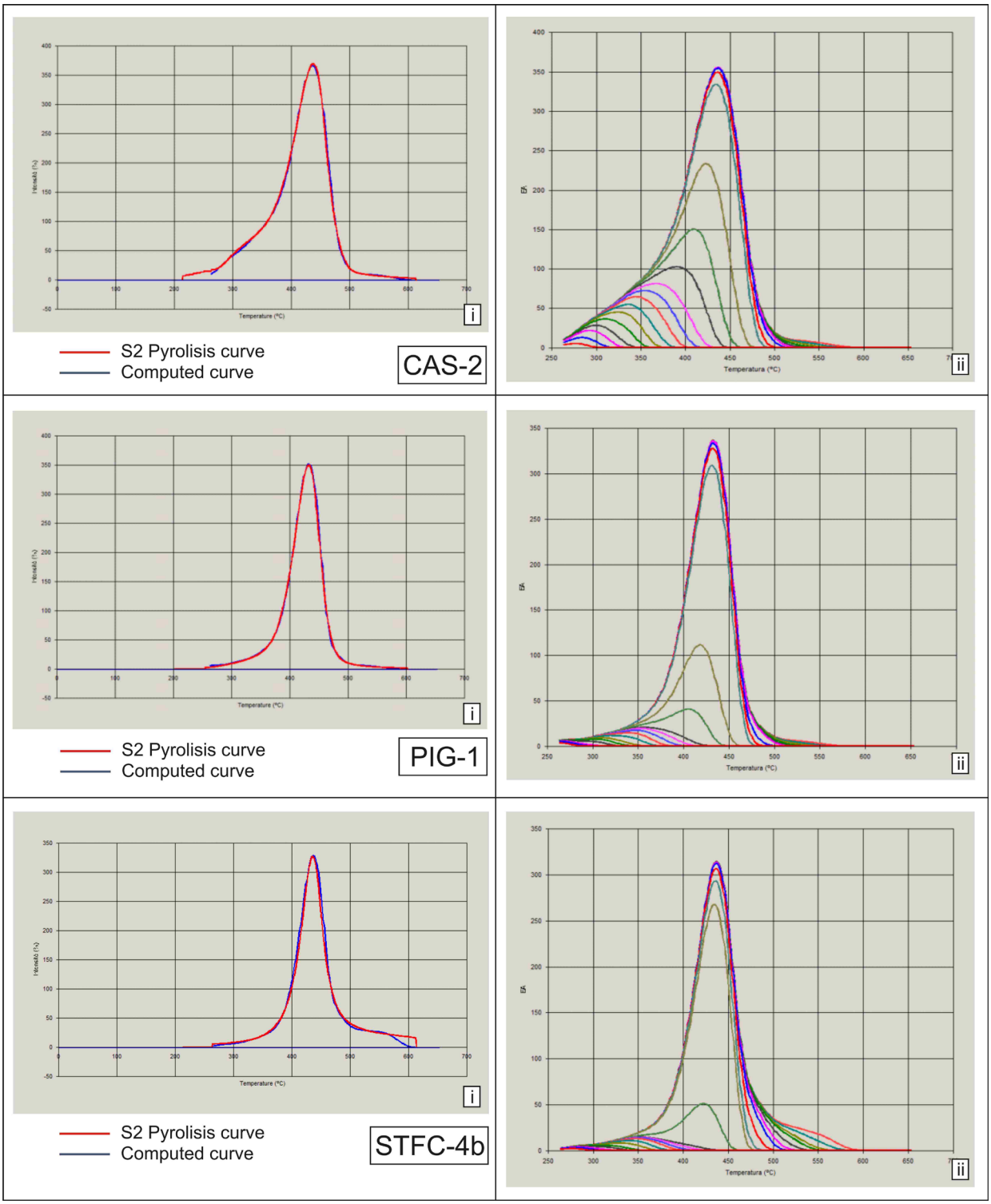

Fig. 11.9 - Results of the mathematical computational modelling of the S2 peak of the Rock-Eval for the three samples. (i) A correct reproduction of the S2 peak measured in the pyrolysis was achieved using the model; (ii) De-convolution of the obtained peak

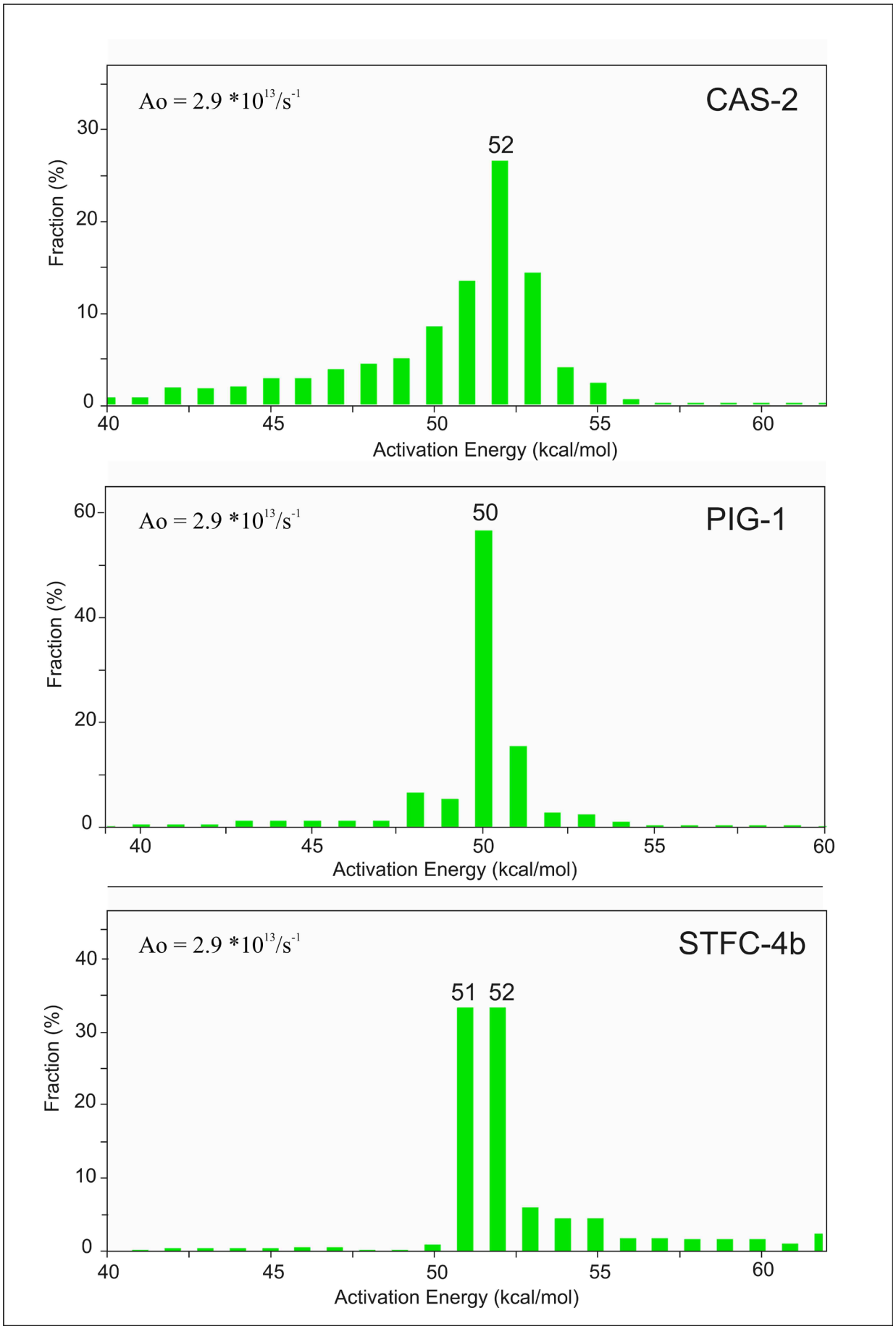
Ao = 2.9 *10^13/s^-1
CAS-2
52
Fraction (%)
Activation Energy (kcal/mol)
Ao = 2.9 *10^13/s^-1
PIG-1
50
Fraction (%)
Activation Energy (kcal/mol)
Ao = 2.9 *10^13/s^-1
STFC-4b
51 52
Fraction (%)
Activation Energy (kcal/mol)

recorded. The transformation ratio (%) versus temperature curve indicates that a transformation of 50% and 98% of the initial kerogen was achieved at 133ºC and 202ºC, respectively (Table 11.2).

A comparison of the activation energy distribution of the three kinetics is illustrated in Fig. 11.12, where the three cumulative percentages of the transformation rate (TR %) versus the temperature curves are plotted together. A synthesis of the data represented in these curves is proposed in Table 11.2 and Table 11.3. From 0ºC to 100ºC the kerogen of the CAS-2 sample is transformed faster than the kerogen of the other two samples (at 100ºC the CAS-2 records a TR of 20.11%, whereas PIG-1 and STFC-4b are only 11.54% and 4.47%, respectively) (Table 11.1). By contrast, from 100ºC the transformation rate of PIG-1 increases considerably if compared with the other samples (at 135ºC the TR of PIG-1 is 93.09%, whereas the TR of CAS-2 and STFC-4b are 66.28% and 54%, respectively) (Table 11.1). Over 180ºC the CAS-2 and PIG-1 are nearly transformed completely, whereas the STFC-b continues to be transformed until over 200ºC (Table 11.1). In the three samples the temperatures needed to reach a given transformation rate are markedly different at the beginning of the transformation process (TR of 10%) and at the end (TR of 98%). Temperatures in the middle of the process are more uniform (TR of 25%, 50% and 75%) (Table 11.2). In the CAS-2 the process of transformation of the original kerogen occurred in the longest interval of temperature (117ºC, from 10% to 98% TR), followed by the STFC-4b sample (89ºC) and by PIG-1 (61ºC) (Table 11.2).

11.4.1. Comparison of the Cameros Basin kinetics with literature kinetics

Kinetics parameters calculated for the kerogen formed in the Cameros Basin were compared to the kinetics in other basins and described in the literature. The TR versus temperature curves presented in the PetroMod software were used to illustrate the main differences in the activation energy distribution (Fig. 11.13 and Fig. 11.14).

In Fig. 11.13 the three kinetics calculated for the Cameros Basin are compared with classical Type I, Type II and Type III kinetics proposed by Tissot (in Waples et al., 1992) and Behar et al. (1997). From this graph it can be appreciated that the CAS-2 curve has a very similar shape to the curves proposed for a Type II kerogen by Behar et al. (1997) and Tissot (in Waples et al., 1992), the PIG-1 curve has a very similar shape to the curve proposed for a Type I kerogen in Behar et al. (1997) and Tegelaar and Noble (1994) and, finally, the STFC-4b curve has a very similar

Fig. 11.10 - For the three samples, histograms representing the activation energy distribution versus the fraction of genetic potential kerogen. The mode of the histogram represents the maximum genetic potential

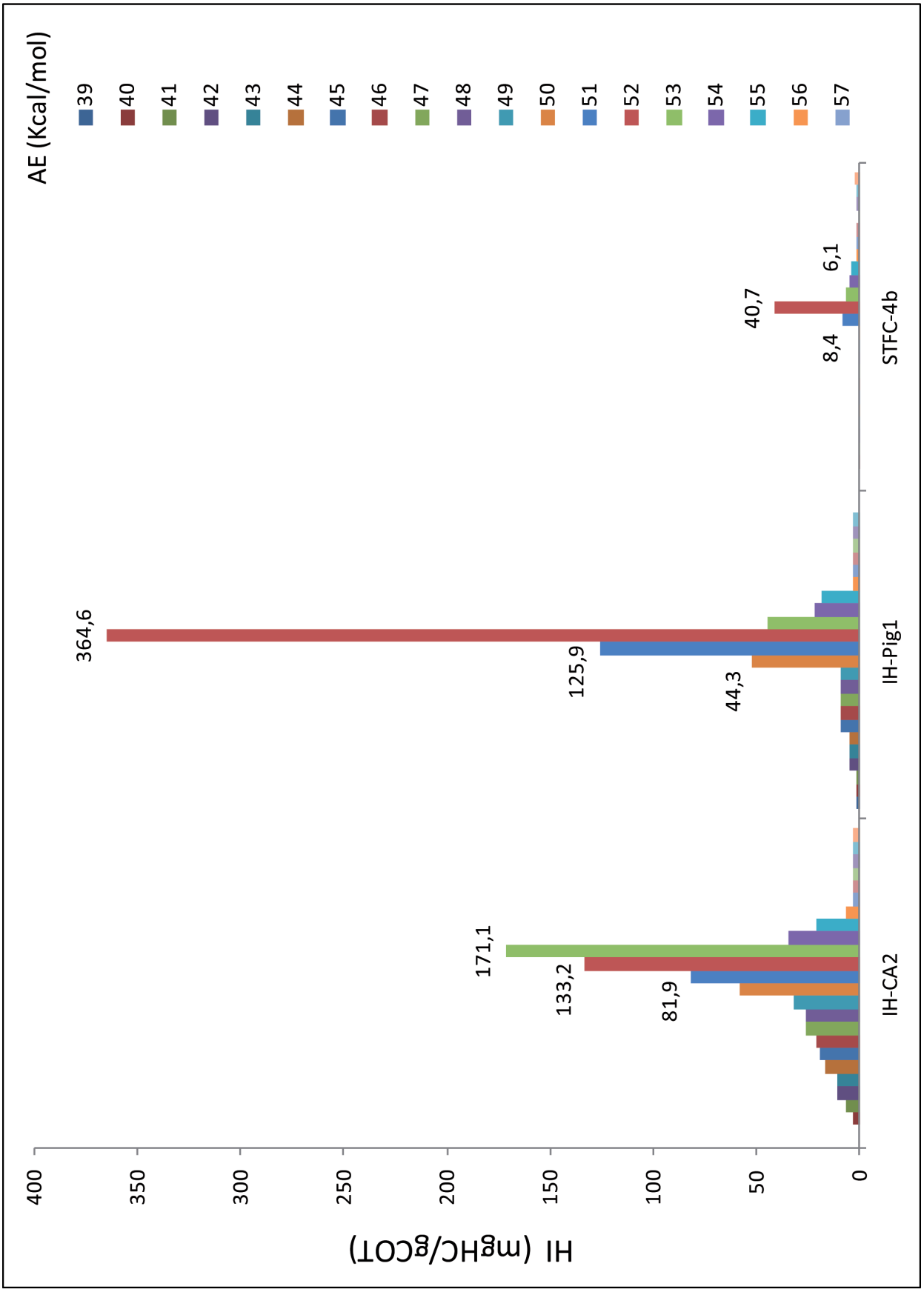
AE (Kcal/mol)
39
40
41
42
43
44
45
46
47
48
49
50
51
52
53
54
55
56
57
HI (mgHC/gCOT)
400
350
300
250
200
150
100
50
0
364,6
125,9
44,3
171,1
133,2
81,9
40,7
8,4
6,1
IH-Pig1
IH-CA2
STFC-4b

shape to the curve proposed for a Type III kerogen by Tissot (in Waples et al., 1992) and Behar et al. (1997). Despite the similar shape, the curves of the three Cameros Basin kerogens are shifted 30–40ºC to the left, towards lower temperatures, with respect to the kinetic curves proposed for classical Type I, II and III kerogens.

Comparisons of the Cameros Basin kinetic with other bulk and compositional kinetics (Burnham and Sweeney, 1989; Ungerer, 1990; Tegelaar and Noble, 1994; Pepper and Corvi, 1995; Behar et al., 1997) are presented in Fig. 11.14. The kerogen with a more similar TR versus temperature curve than the CAS-2 sample curve is a Type IIS kerogen proposed by Pepper and Corvi (1995). The PIG-1 curve has a similar shape with respect to the curves proposed for a Type I kerogen by Pepper and Corvi (1995), Tegelaar and Noble (1994) and Behar et al. (1997), but it is always shifted towards lower temperature values. The STFC-4b has a typical Type III kerogen curve shape, but with respect to those curves it is shifted towards lower temperatures, typical of Type I or Type II kerogens (e.g., the Type I-Mae Sot proposed by Tegelaar and Noble, 1994) (Fig. 11.14). Thus, no single curve in the literature fits well with the STFC-4b curve.

11.5. DISCUSSION

11.5.1. Kinetic behaviour of the three kerogens

Using the mathematical method proposed here, the calculation determines that the three samples of immature organic matter are of the same frequency factor (2.9*1013/s-1) and a similar activation energy mode (50–52 kcal/mol) (Fig. 11.10). By contrast, it is determined that there is a marked difference in the activation energy distributions and in the amount of the hydrocarbon genetic potential (HI-mgHC/gTOC) (Fig. 11.11 and Table 11.1). The same frequency factor may indicate that the organic matter is formed by similar molecules that respond with the same vibrational frequency when heated (Tissot and Welte, 1984). A similar activation energy distribution mode suggests that the maximum amount of hydrocarbons in the three samples is formed as a consequence of the rupture of a molecular bond with a similar activation energy (similar activation energy mode). The activation energy mode has quite a low value, if contrasted with the classical kerogens of hydrocarbon source rocks (40–80 kcal/mol, Tissot and Welte, 1984). This fact suggests that the kerogen of the Cameros Basin, which forms the maximum amount of hydrocarbons, is mostly constituted by labile organic material that is characterised by weak chemical bonds. Labile organic matter can be represented by liptinite

Fig. 11.11 - Activation energy distribution of the three samples versus the hydrogen index

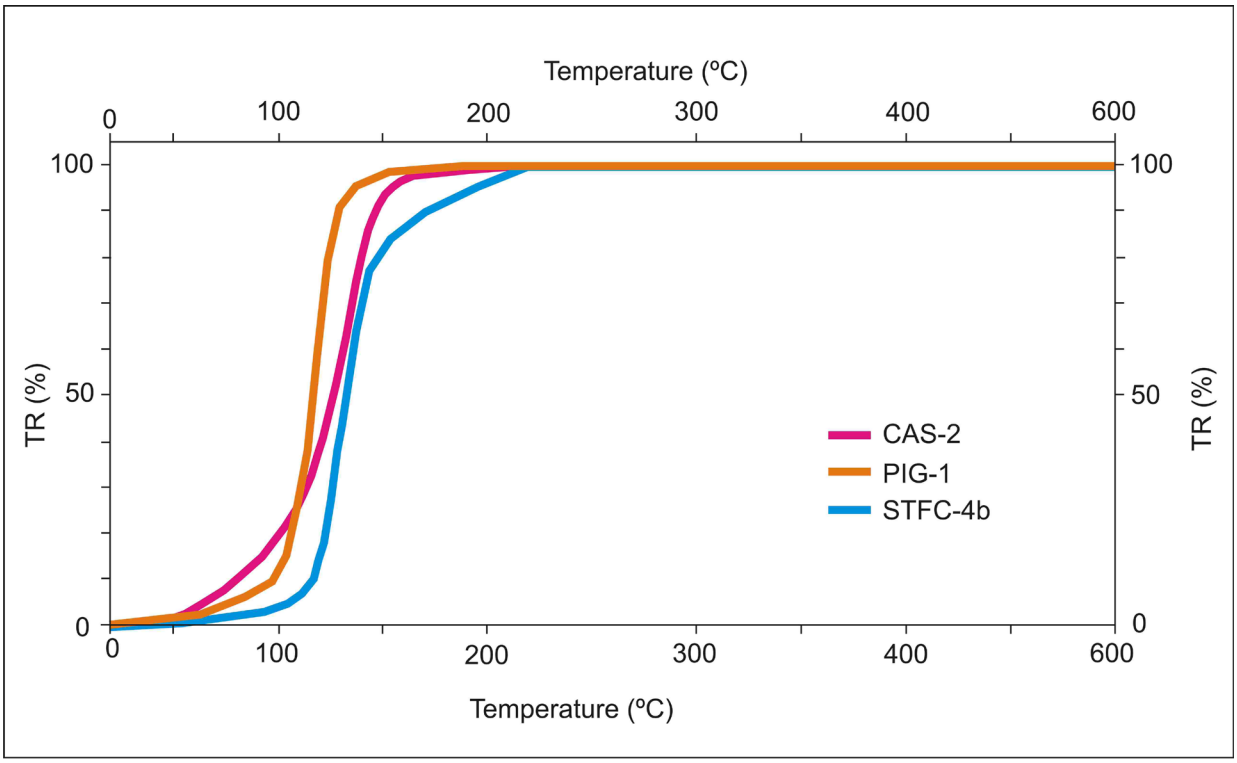

Fig. 11.12 - Cumulative yield curves of the three samples, indicating the transformation ratio TR % (mass of hydrocarbon formed per gram of organic carbon) as a function of temperature

macerals, which is the first organic matter component that it is transformed in hydrocarbons when the temperature increases (Tissot and Welte, 1984; Taylor et al., 1998). As liptinite has a very high productivity (Taylor et al., 1998), the difference in the genetic potential among the three samples can be strongly influenced by differences in the content and type of liptinite. The CAS-2 and PIG-1 samples are formed by abundant and mostly autochthonous liptinite, formed in the lacustrine aquatic environment, whereas by contrast the STFC-4b sample is formed by scarce and mostly allochthonous liptinite, derived from the terrestrial sub-aerial environment and re-deposited in lacustrine waters.

Variation in the activation energy distribution may be related to the more or less homogeneous composition of kerogens – formed by few types of components or by numerous types – and consequently to the presence of structural entities of the kerogen characterised by different bond strengths (Tissot and Welte, 1984; Tissot et al., 1987). Petrographic observation of the CAS-2 sample indicates the presence of different types of algae, such as lamaliginites and Botryococcus, and amorphous fluorescent organic matter (dispersed organic matter) (Fig. 11.8a and Fig. 11.8b). This heterogeneous composition is reflected in the large activation energies distribution. This sample is nearly completely formed by liptinite material (causing a very high TOC, 17.82%), whose labile bonds explain the dominance of very low activation energies. By contrast, petrographic

ID sample	Temperature (ºC)							
	50ºC	75ºC	100ºC	120ºC	135ºC	150ºC	180ºC	200ºC
CAS-2	1.86	8.56	20.11	38	66.28	93	98.67	99
PIG-1	1.12	4.47	11.54	56.22	93.09	97.18	99.04	100
STFC-4b	0.4	1.86	4.47	12.66	54	81.91	92.34	96.81

Table 11.2 - Transformation ratio values (%) at different temperatures, as estimated for the kerogen of the three samples from the kinetics calculated data (yields curves in Fig. 11.12)

ID sample	Transformation Ratio				
	10%	25%	50%	75%	98%
CAS-2	80	125	127	137	197
PIG-1	99	109	118	125	160
STFC-4b	116	124	133	142	205

Table 11.3 - Temperatures (°C) necessary to reach a given transformation ratio (%), as estimated for the kerogen of the three samples from the kinetics calculated data (yields curves of Fig. 11.12)

observations of the PIG-1 sample indicate that liptinite is formed by a homogenous type of algae, characterised by a very high fluorescence (Fig. 11.8c and Fig. 11.8d). Such is the unimodal activation energy distribution explained. The high hydrocarbon productivity of the sample (HI of 714 mgHC/gTOC) suggests a high productivity by this alga. However, in the sample the liptinite maceral forms only a reduced portion of the total organic matter amount, which is formed by vitrinite and inertinite macerals, explaining the lower TOC (1.52%) (Table 11.1). The STFC-4b petrographic observation indicates the presence of heterogeneous organic matter formed by vitrinite, inertinite and liptinite macerals groups, where liptinite is primarily formed by terrestrial material such as cuticles (Fig. 11.8e). Terrestrial organic matter is characterised by stronger bonds than is lacustrine organic matter, thus the activation energies shifted to higher values than in the CAS-2 and PIG-1 samples (Fig. 11.10). Additionally, the terrestrial organic matter has lower hydrocarbon productivity (HI of 81 mgHC/gTOC) than does lacustrine organic matter. The presence of even a small amount of algae (Fig. 11.8f) can be the cause of a record of a maximum genetic potential at activation energies similar to the other two samples (51–52 kcal/mol). The high content of organic carbon (TOC of 3.95%) is due to the abundance in the sample of vitrinite and inertinite maceral.

In summary, as the three kerogens analysed are deposited in a common lacustrine-palustrine terrestrial depositional setting, they are formed by a similar organic matter, which determines

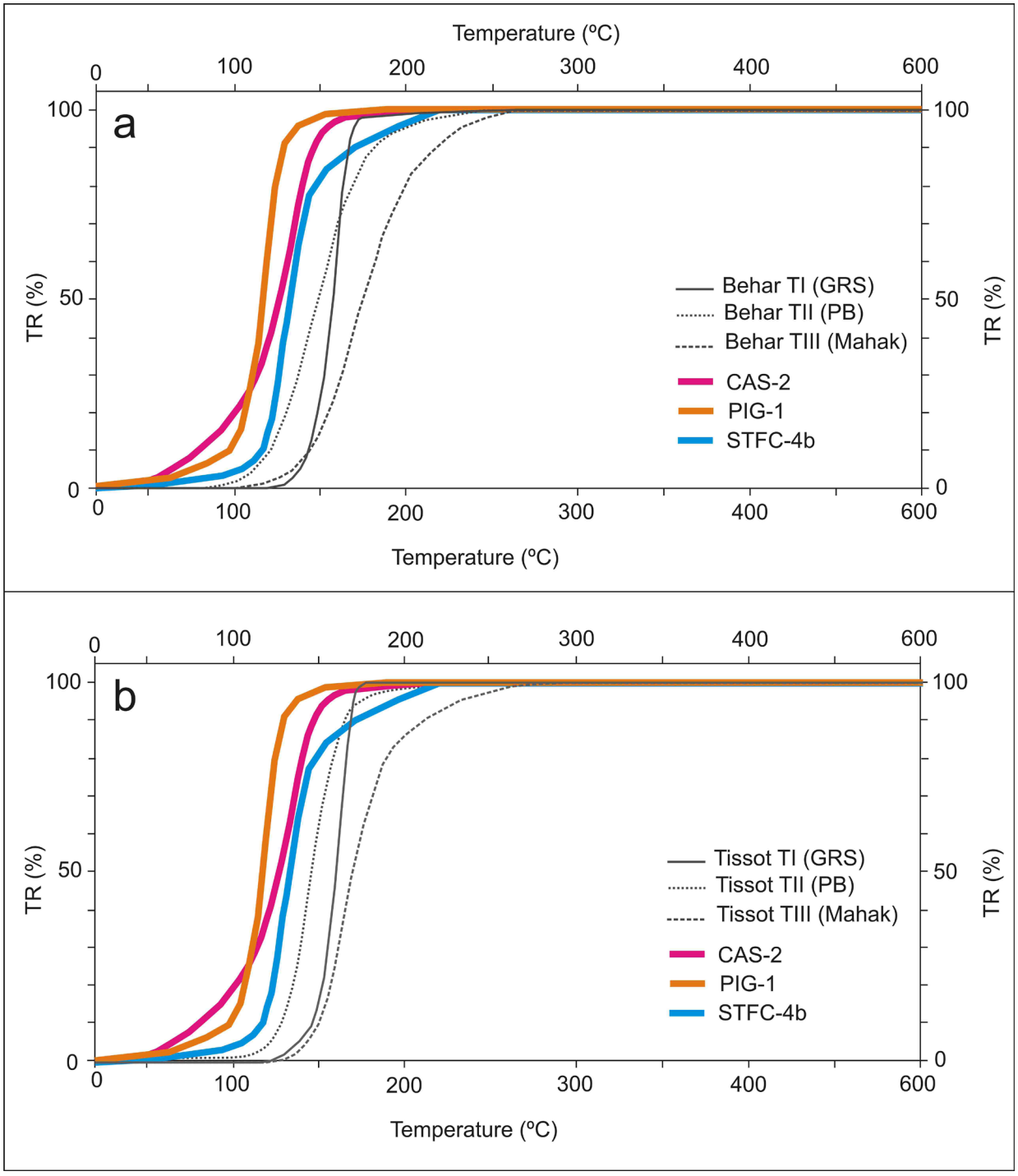

Fig. 11.13 - Comparison between the kinetics calculated for the Cameros Basin and the classical Type I, Type II and Type III kinetics proposed by Tissot et al. (1987) (a) and Behar et al. (1997) (b)

a similar frequency factor and AE mode. Variation in the abundance and type of organo-facies, related to different environmental conditions (aquatic/sub-aereal), determines a different distribution of the activation energies and of the maximum genetic potential.

Comparison of the kinetics calculated for the Cameros Basin with the kinetics calculated

for different types of kerogens (Tissot et al., 1987; Burnham and Sweeney, 1989; Ungerer, 1990; Tegelaar and Noble, 1994; Pepper and Corvi, 1995; Behar et al., 1997) (Fig. 11.13 and Fig. 11.14) provides interesting information on the behaviour of the analysed kerogens. The first unexpected data are that the CAS-2 sample has a kinetic behaviour similar to a Type II kerogen (Fig. 11.13), and particularly to a Type IIS kerogen (Pepper and Corvi, 1994, and partially to those proposed by Behar et al., 1997) (Fig. 11.14), despite the hydrogen index and the petrographic observations clearly indicating that the sample is a Type I kerogen (sensu Tissot and Welte, 1984, Peters, 1986, Taylor et al., 1998). Secondly, the activation energy distribution of PIG-1 is typical of a Type I kerogen, according to the HI index and petrographic observations (sensu Tissot and Welte, 1984, Peters, 1986, Taylor et al., 1998). However, the activation energies values are considerably lower than a typical Type I (Fig. 11.13 and Fig. 11.14). Thirdly, the STFC-4b has an activation energy distribution similar to a Type III kerogen according to the HI index and petrographic observations (sensu Tissot and Welte, 1984, Peters, 1986, Taylor et al., 1998). However, the STFC-4b records activation energy values markedly lower with respect to what it is expected by a Type III kerogen (Fig. 11.13 and Fig. 11.14).

The lack of correspondence between the kerogen type, indicated by petrography and the HI index, and the kerogen behaviour during thermal alteration determined by the kinetic calculation confirms that within the same kerogen group different kinetic behaviours can be observed (Tegelaar and Noble, 1994). As stated by these authors, the kinetic parameters depend primarily on the molecular structure of the kerogen, which can be independent to the amount of hydrocarbons produced during the pyrolysis (HI index). The two main factors controlling the molecular structure of kerogen is the mixture of different biomacromolecules and the organic sulphur content (Tegelaar and Noble, 1994). Thus, the shift of the calculated kinetics curves of the Cameros Basin towards a lower temperature, with respect to the classic kerogen curves, suggests a relevant presence of sulphur molecules in the kerogen structure, decreasing the strength of the molecular bonds (Tissot et al., 1987; Klomp and Wright, 1990; Hunt et al., 1991; Baskin and Peters, 1992; Tegelaar and Noble, 1994). Additionally, the behaviour of the STFC-4b kerogen can be interpreted as being a consequence of a mixed kerogen assemblage of Type I and Type III kerogens, both characterised by high sulphur content.

11.5.2. Kinetic behaviour versus temperature and time

To model the evolution of the petroleum system of the Cameros Basin, the calculated kinetic parameters can be applied to the overmature spent source rock of the basin when similar depositional settings are suggested (**Chapter 10**). The choice of the type of kerogen kinetic behaviour can have important consequences on the timing of hydrocarbon production, generation and accumulation. Kinetic kerogen behaviour can determine the synchrony between

cracking and the formation of traps and seals (Tissot and Welte, 1984).

A comparison between the transformation ratio versus temperature curves (Fig. 11.12) clearly illustrates the different kerogen behaviours of the three samples as the effect of the temperature increases. A CAS-2 kinetic determines the production of hydrocarbons because the record low temperatures, as formed by a kerogen constituted by a molecule with low activation energies (mostly liptinite). A wider distribution of the activation energies (a heterogeneous composition of the kerogen) determines that the hydrocarbons are produced during a long temperature interval (117°C from 10 to 98% TR) (Table 11.2). A PIG-1 kinetic determines that hydrocarbon production starts later than CAS-2 (approximately 20°C higher as determined at a TR of 10%) (Table 11.2). The nearly unimodal distribution of the activation energies (a homogeneous composition of the kerogen) determines that the kerogen transformation in hydrocarbons occurred over a very short temperature interval (61°C, from 10 to 98% TR) (Table 11.2). Transformation of 98% of the original kerogen in the hydrocarbons occurred at 160°C, 37°C less than in the case of the CAS-2 kerogen (Table 11.2). A STFC-4b kinetic determines the beginning of hydrocarbon production at a higher temperature than CAS-2 and PIG-1 kerogens (36°C higher than CAS-2 and 17°C than PIG-1, determined at a transformation ratio of 10%) (Table 11.2); this fact is due to the higher activation energies (higher proportion of vitrinite macerals than liptinite). The complete transformation of the STFC-4b original kerogen in hydrocarbons occurred in a shorter temperature interval than the CAS-2 kerogen but in a longer temperature interval than the PIG-1 kerogen (Table 11.3).

The results performed here allow for the determination of the differences in the timing of hydrocarbon generation, migration and accumulation by a source rock as a consequence of different kinetic assignation. A source rock formed by a kerogen similar to the CAS-2 sample begins producing at a lower burial depth than source rocks formed by a kerogen similar to the PIG-1 and STFC-4b samples and for a longer time span. Thus, it could be highly possible that during hydrocarbon generation traps and/or seals form, as the process lasts a longer time than in the case of the other kerogens, even if the risk of hydrocarbon losses and alteration during migration might be high. By contrast, the transformation of the PIG-1 kerogen in hydrocarbons is quite instantaneous, which reduces the possibility of synchronism with the formation of traps and seals, but at the same time decreases the risk of hydrocarbon losses or degradation by migration. The STFC-4b kerogen begins producing hydrocarbons later than the other two kerogens and it continues production later than the others. Thus, a source rock with a STFC-4b kerogen needs a higher burial rate than the other kerogens to be completely transformed. The generation of the maximum amount of hydrocarbons (critical moment, sensu Magoon and Dow, 1994) is reached earlier by the PIG-1 sample and later by the CAS-2 and STFC-4b samples; however, there is not a consistent difference that is congruent with a similar mode of the activation energy distribution. Furthermore, a difference in the amount of hydrocarbons produced from the three samples is

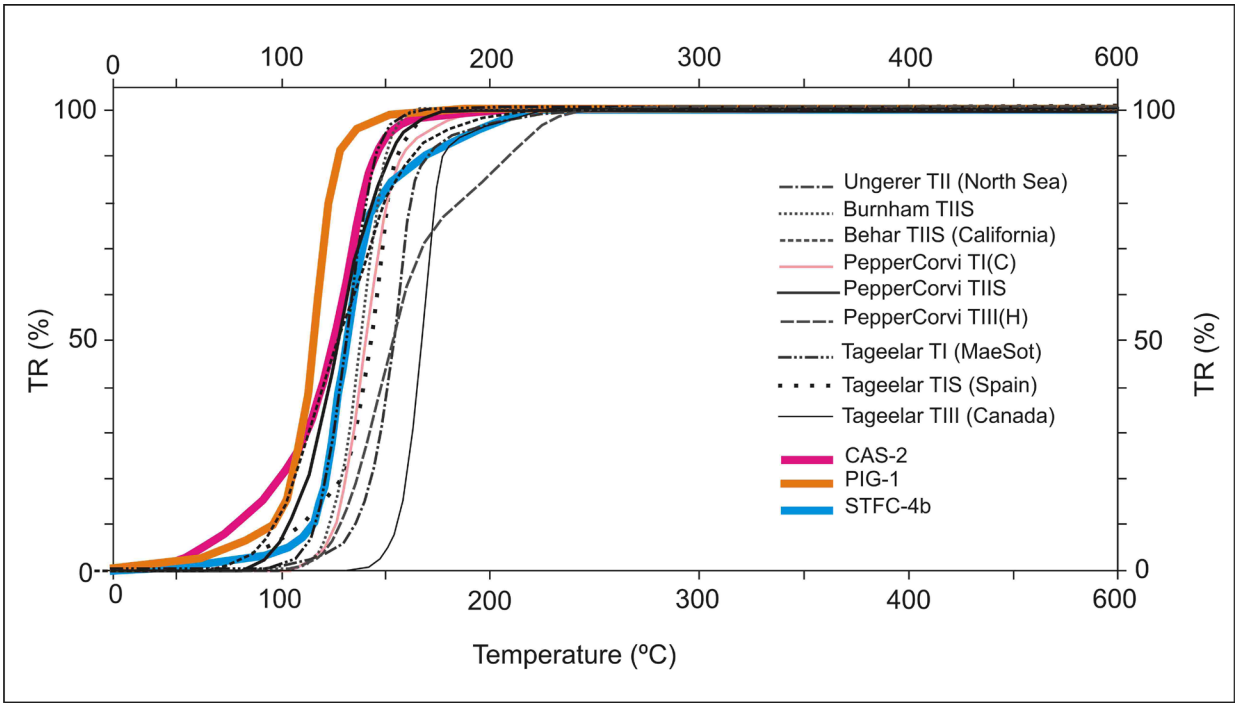

Fig. 11.14 - Comparison of the kinetics calculated for the Cameros Basin with other bulk and compositional kinetics of different types of kerogens proposed by Burnham and Sweeney (1989), Ungerer (1990), Pepper and Corvi (1995), Tegelaar and Noble (1995) and Behar et al. (1997)

observed, which is expressed by different HI indices (Table 11.1).

The data presented in this work provide a first approach to the analysis of the influence of the kinetics of the three kerogens on the generation, migration and accumulation processes in the Cameros Basin. However, a thermal model that integrates the geological, structural and geochemical data would be necessary to complete and verify these results (Tissot et al., 1987). In modelling the petroleum system the results performed here can be extremely helpful in deciding which compositional kinetic in the literature could be assigned to the spent source rocks of the basin.

11.6. CONCLUSIONS

This work determines the kinetic parameters of three immature kerogens deposited in a terrestrial-transitional depositional environment, forming part of a Lower Cretaceous (Barremian) syn-extensional unit of the Cameros Basin. Due to the small number of samples that have optimal geochemical characteristics for kinetic calculation, analysis was performed on a reduced number of samples.

The kinetic parameters calculation was based on a mathematical computational modelling of the S2 peak of the pyrolysis Rock-Eval. The mathematical computational modelling was satisfactory, as a correct reproduction of the S2 peak measured in the pyrolysis was performed by the model. A calculation of the kinetic parameters determined the same frequency factor (2.9*1013/s-1) and the recording of a similar activation energy for the three analysed samples when the maximum hydrocarbon genetic potential is reached. A similar organic matter among the three samples is considered, as the related deposits have been sedimented in similar lacustrine-palustrine environments, characterised by coastal wetland plains of a fluvial-deltaic system. The difference in the maceral composition and proportion, due to the greater or lesser presence of autochthonous or allochthonous components (i.e., from the terrestrial sub-aerial environment and re-deposited in lacustrine waters or formed in the lacustrine aquatic environment itself), determines the difference in the activation energies distribution and in the amount of hydrocarbons generated.

A comparison of the calculated kinetic parameters with the parameters of classical Type I, Type II and Type III kerogens indicates a different kerogen behaviour with respect to what it was expected if considering only pyrolysis data. The CAS-2 sample, which HI indicates as being a Type I kerogen, has a kinetic behaviour similar to that of a Type IIS kerogen; the PIG-1 sample, which HI indicates as being a Type I kerogen, has a kinetic behaviour similar to that of a Type I kerogen but with lower activation energies; the STFC-4b sample, which HI indicates as being a Type III kerogen, has a kinetic behaviour similar to that of a Type III kerogen but with activation energies typical of a Type I. These differences were explained, in the case of the CAS-2 and PIG-1 samples, as being a consequence of the presence of sulphur in the structure of the kerogens and, in the case of the STFC-4b sample, due to a mixture of different types of kerogens. These results confirm that in determining the kinetic behaviour of the kerogen by only considering the pyrolysis index can result in significant errors.

Differences in the distribution energies can have significant consequences on the timing of hydrocarbon generation, migration and accumulation. A source rock constituted by a CAS-2 kerogen would produce hydrocarbons earlier and for a longer time than source rocks formed by a PIG-1 and STFC-4b kerogen. A source rock constituted by a PIG-1 kerogen would produce hydrocarbons quite instantaneously and the maximum hydrocarbon generation would be reached at a lower temperature/burial than the other two kerogen types. A source rock constituted by a STFC-4b kerogen would reach the maximum hydrocarbon generation at a similar temperature/time as a CAS-2 kerogen, and later than a PIG-1 kerogen, even if it would need a higher temperature/time to be completely transformed than the other two kerogens.

Due to the small number of samples analysed, the results presented in this chapter have to be considered only as a possible representative scenario of the kinetic behaviour of the immature kerogen of the Cameros Basin. In future research a detailed and exhaustive analyses would be

necessary to confirm the proposed data. However, this work represents advancement in the knowledge of the kinetic behaviour of the continental organic matter formed in an extensional basin.

Chapter 12

12. Modelling of the Petroleum System

12.1. INTRODUCTION

"Since the 50s numerous efforts have been done to develop a predictive methodology to connect the past – a basin, the sediments and fluids that fill it and the dynamic processes acting on them – to the present, the hydrocarbons discoveries. Early endeavors try to describe how basins form, fill and deform, focusing mainly on compacting sediments, burial and the resulting rock structure" (Al-Hajeri et al., 2009). The developing of basin modelling discipline allowed to reconstruct these geological basin processes quantitatively (Weeks, 1952). In a second phase, sedimentary basin models started to be used as structural framework for geochemical genetic correlation between hydrocarbons and source rocks (Dow, 1974). This new approach was defined as modelling of the petroleum system (Magoon and Dow, 1994).

"A petroleum system is defined as a natural system that encompasses a pod of active source rock and all related oil and gas and which includes all the geologic elements and processes that are essential to allow hydrocarbons accumulation formation. The term system describes the interdependent elements and processes that form the functional unit that creates hydrocarbons accumulations. The essential elements include a petroleum source rock, reservoir rock, seal rock and overburdern rock. Source rocks can be active or inactive/spent. The processes are trap formation and the generation-

migration-accumulation of petroleum. These essential elements and processes must occur in time and space so that organic matter included in a source rock can be converted to a petroleum accumulation. A petroleum system exists wherever the essential elements and processes occur" (Magoon and Dow, 1994).

The purpose of modelling the evaluation of a sedimentary basin in terms of petroleum exploration is to know the amount of oil and gas generated and accumulated in the basin (Tissot and Welte, 1984). The following points must be determined: 1) Timing of thermal maturity of the source rocks in the basin, 2) The amount of oil and gas generated in each source rock; 3) Timing of hydrocarbons generation and migration to compare it with the time of seals and traps formation; 4) Evaluation of the ultimate oil and gas reserve of a sedimentary basin and of the potential at the present-day of its source rocks.

To characterise the quality and thermal stage of the organic matter several indexes have been proposed (e.g. vitrinite reflectance, pyrolysis Rock-Eval parameters) (**Chapter 10**). However, petrographic and geochemical analyses by themselves do not allow a quantitative evaluation of hydrocarbon generation as function of time (Tissot and Welte, 1984). On the other hand, computational mathematical models allow a quantitative approach (Poelchau et al., 1997). The computer simulation requires the quantification of all defining parameters that can influence the evolution of the petroleum system (Poelchau et al., 1997). It is necessary to reconstruct a conceptual model, defining the temporal framework that structures the input data (Wygrala, 1988, Poelchau et al., 1997). The conceptual model is a condensed description of the geologic evolution of the basin (Welte and Yalçin, 1987) and it includes the concept of the petroleum system (sensu Magoon and Dow, 1994 and Poelchau et al., 1997). It contains the definition of the source rocks, reservoir rocks, seals, underburden and overburden units (Poelchau et al., 1997).

12.1.1. Building of the Petroleum System model

As the evolution of the petroleum system in a sedimentary basin is linked to several variables, basin and petroleum system modelling is an iterative process with many interrelated steps, each of which is a scientific discipline in itself. In the model these steps need to be assembled in a single work-flow.

"The first step is to create a depth-based structural model of the area of interest, which may encompass a single or multiple petroleum systems in one basin or in many basins across a region. This model of present-day architecture represents the final result of all the processes acting on the basin throughout geologic time (Poelchau et al., 1997). The second step is to subdivide the basin history into an uninterrupted series of stratigraphic events of specified age and duration (Poelchau et al., 1997). These events can be summarized in a petroleum system events chart.

Each event represents a span of time during which deposition, nondeposition or erosion occurred. This summary describes the chronology of the geologic elements in a petroleum system. The absolute age of each layer in the basin and petroleum system model is an important parameter for determining the timing of the processes that generate, move and trap petroleum. Age information may be available from paleontologic data, radiometric dating, fission-track dates and magnetic-reversal tracking (Peters et al., 2005). Syn- and postdepositional episodes of folding, faulting, salt tectonics, igneous intrusion, diagenetic alteration and hydrothermal activity can be included to explain the model. Determining the timing of trap formation is a fundamental key in the hydrocarbons generation, migration and accumulation modelling" (Al-Hajeri et al., 2009).

"Identification of the lithology and depositional environment of each stratigraphic unit is crucial. In fact classifying the depositional environment, and thus properties, such as porosity and permeability, of coarse-grained sediments helps identify their potential as reservoir or carrier rocks that facilitate migration of petroleum from source rock to reservoir. Source-rock properties are needed as inputs. Characterising the source-rock depositional environment helps predict the probable petroleum product generated through kerogen maturation. Fine-grained sediments deposited in deep marine basins, on continental shelves and in anoxic lakes all contain different types of kerogen, leading to different petroleum outputs (Peters et al., 2005). Several other physical properties must also be specified for each layer. Porosity and permeability in reservoir and carrier layers are important for fluid-flow computations and reservoir volumetric estimates. Permeability of source rocks affects the efficiency with which generated hydrocarbons can be expelled. Heat capacity and thermal conductivity, usually inferred from lithology and mineralogy, are needed for the thermal calculations that model kerogen maturation and petroleum generation. In addition, density and compressibility data are required inputs to model compaction and burial" (Al-Hajeri et al., 2009).

"Modeling the petroleum potential of a basin requires reconstruction of the temperature over geologic time and across the basin (see **Chapter 9**). The thermal history of a basin is linked to the history of the crust in which it formed (Allen and Allen, 2009). Crustal behavior determines basin subsidence, uplift and heat flow. Therefore, in addition to model properties, some specific past conditions must be evaluated. These conditions, treated as boundary conditions by the modeling software and which include paleobathymetry, sediment/water interface temperatures throughout geologic time and paleoheat-flow estimates, are required to calculate the temperature history of the basin" (Al-Hajeri et al., 2009) (see **Chapter 9**).

Temperature is the primary variable in conversion of kerogen to petroleum. The conversion of the kerogen of a source rocks in petroleum is described by a sequence of first-order reactions that obey the Arrhenius equation (Tissot and Welte, 1984; Tissot et al., 1987). The application of a kinetic approach to hydrocarbons generation, other than determine appropriate kinetic

parameters (**Chapter 11**), needs to reconstruct an accurate thermal history (Yalçin et al., 1997).

12.1.2. Forward modelling

"After the boundary conditions and ages and properties of all layers have been defined, the simulation can run forward, starting with the sedimentation of the oldest layer and progressing to the present. The software follows a series of sequential steps which can be summarized as follow (Hantschel and Kaurearuf, 2009) (Fig. 12.1): 1) Deposition – Layers are created on the upper surface during sedimentation and/or are removed during erosion. Depositional thickness is calculated by porosity-controlled backstripping, starting with present-day thickness. 2) Pressure calculation and compaction. The pressure calculation treats dewatering as a one phase flow problem driven by changes in overburden weight caused by sedimentation. Compaction causes changes in many rock properties, including porosity, and to a lesser extent, density, elastic moduli, conductivity and heat capacity. Pressure and compaction calculations are performed before heat-flow analysis in each time step. 3) Heat flow analysis – The main purpose of heat flow analysis is temperature calculation, a prerequisite for determining geochemical reaction rates. Heat conduction and convection from below as well as heat generation by emissions from naturally occurring radioactive minerals must be considered. In the heat flow analysis, boundary conditions defined in the previous step are considered. 4) Petroleum generation - The generation of petroleum from kerogen in source rocks, called primary cracking, and the subsequent breakdown of oil to gas in source or reservoir rocks, called secondary cracking, can be described by the decomposition kinetics of sets of parallel reactions (Tissot and Welte, 1984; Tissot et al., 1987). The software introduces the reaction kinetics parameters to predict the phases and properties of hydrocarbons generated from source rocks of various types. 5) Fluid analysis - The generated hydrocarbons are mixtures of chemical components. Fluid-flow models deal with fluid phases that are typically liquid, vapor and supercritical or undersaturated phases. The fluid-analysis step examines temperature- and pressure-dependent dissolution of hydrocarbon components in the fluid phases to determine fluid properties, such as density and viscosity, for input to fluid-flow calculations. These properties are also essential for subsequent migration modeling and calculation of reservoir volumetrics. Fluids may be modeled using a black-oil bulk model, two components or phases (oil and gas) model or a multicomponent model. 6) Fluid-flow calculations - There are several fluid-flow approaches to model migration of generated hydrocarbons from source rock to trap. Darcy flow describes multicomponent three-phase flow based on the relative-permeability and capillary pressure concept. With this method, migration velocities and accumulation saturations are calculated in one step. Describing fluid migration across faults requires special algorithms. A simplified fluid-flow calculation is made by flowpath analysis. In high-permeability layers, known as carriers, lateral petroleum flow occurs instantaneously on geologic time scales. It can be modeled with geometrically

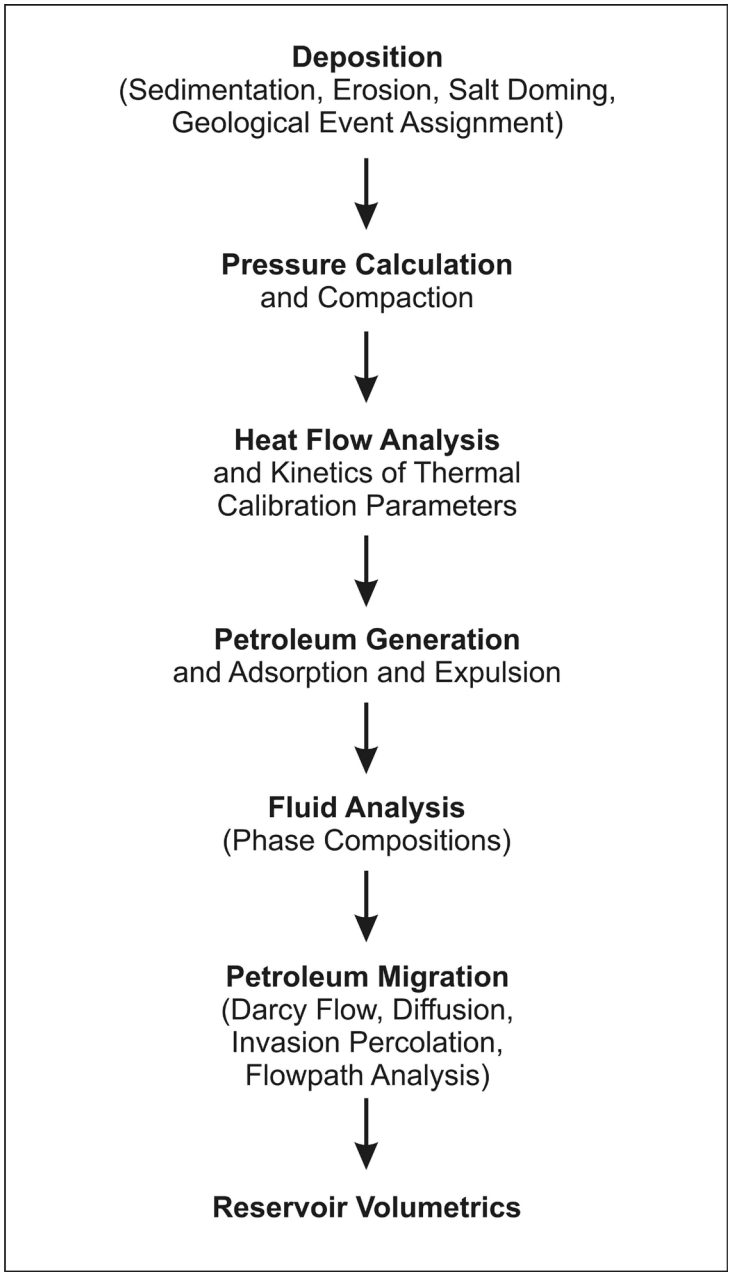

Fig. 12.1 Sequential steps followed by the basin modelling software, which reproduces the major geological processes (modified from Hantschel and Kauerauf, 2009)

constructed flowpaths to predict the locations and compositions of accumulations. In a hybrid method, flowpath analysis in highpermeability zones may be combined with Darcy flow in low-permeability regions. 7) Reservoir volumetrics. The height of a petroleum accumulation is limited by the capillary entry pressure of the overlying seal and the spill point at the base of the structure. Loss at the spill point and leakage through the seal reduce the trapped volume. Other processes, such as secondary cracking or biodegradation, can also impact the quality and quantity of accumulated petroleum. 8) Calibration parameters. It is possible to predict

rock temperature, vitrinite reflectance values and concentration ratios of molecular fossils (biomarkers) using models based on Arrhenius-type reaction rates and simple conversion equations. These temperature-sensitive predictions can be compared with measured data to calibrate uncertain thermal input data, such as paleoheat-flow values. 8) Risk. Numerical models, including basin and petroleum system models, provide scenarios for what might happen given various constraints on the input data (Peters, 2009). The impact of uncertain data can be studied by multiple simulation runs with varying model parameters. These simulations do not provide a unique answer, but rather a range of possible outcomes with estimates of uncertainty. Increased computing power combined with multiple simulations allows to compare the effects of various scenarios and to identify which variables exert the most control on the computed results. Final outcomes are mainly scenario probabilities and confidence intervals" (Al-Hajeri et al., 2009).

Historically, modelling has been applied to basin-scale studies of petroleum system active to the present-day to assess uncertainties in hydrocarbon charge, migration and trap formation. However modelling can be used even in case of paleopetroleum systems, to reconstruct the main processes and elements in basin where geological evidences indicate that hydrocarbons generation, migration and accumulations processes occurred despite of any relevant accumulation is exploitable in the present-day.

12.2. MODELLING OF THE CAMEROS BASIN PETROLEUM SYSTEM

Knowledge of an active petroleum system in the Cameros Basin has existed since the 1930s. Because of the setting of this petroleum system the most important exploitable resources found in the area correspond to a few small tar sandstone accumulations in the Utrillas Fm (first post-extensional unit), cropping out in the southern sector of the Cameros Basin (Fig. 12.2), and in the Escucha Fm (last syn-extensional unit), located in a small satellite half-graben basin south of the main basin of Cameros (Mas et al., 2002, 2003). Petrographic studies of the basin's infill deposits (Mantilla-Figueroa et al., 1998; Ochoa et al., 2007, **Chapter 10**) reveal numerous remainders of bitumen, testifying to the occurrence of hydrocarbon generation and migration throughout the entire basin. Presently, very few hypotheses have been suggested to determine the main elements of the basin's petroleum system or to explain the processes responsible for its evolution (Mas et al., 2002, 2003, Ochoa et al., 2007).

In this chapter, the evolution of the petroleum system of the Cameros Basin was reconstructed by means of a 2D thermal model of the basin's petroleum system. In the model, a synthesis of the geological history of the basin, which includes the structural deformation history, physical stratigraphy, chronostratigraphy, burial history, paleogeography, paleotemperature, paleoheat flow, petrophysical properties of the sediments, kinetics parameters, organic petrology and

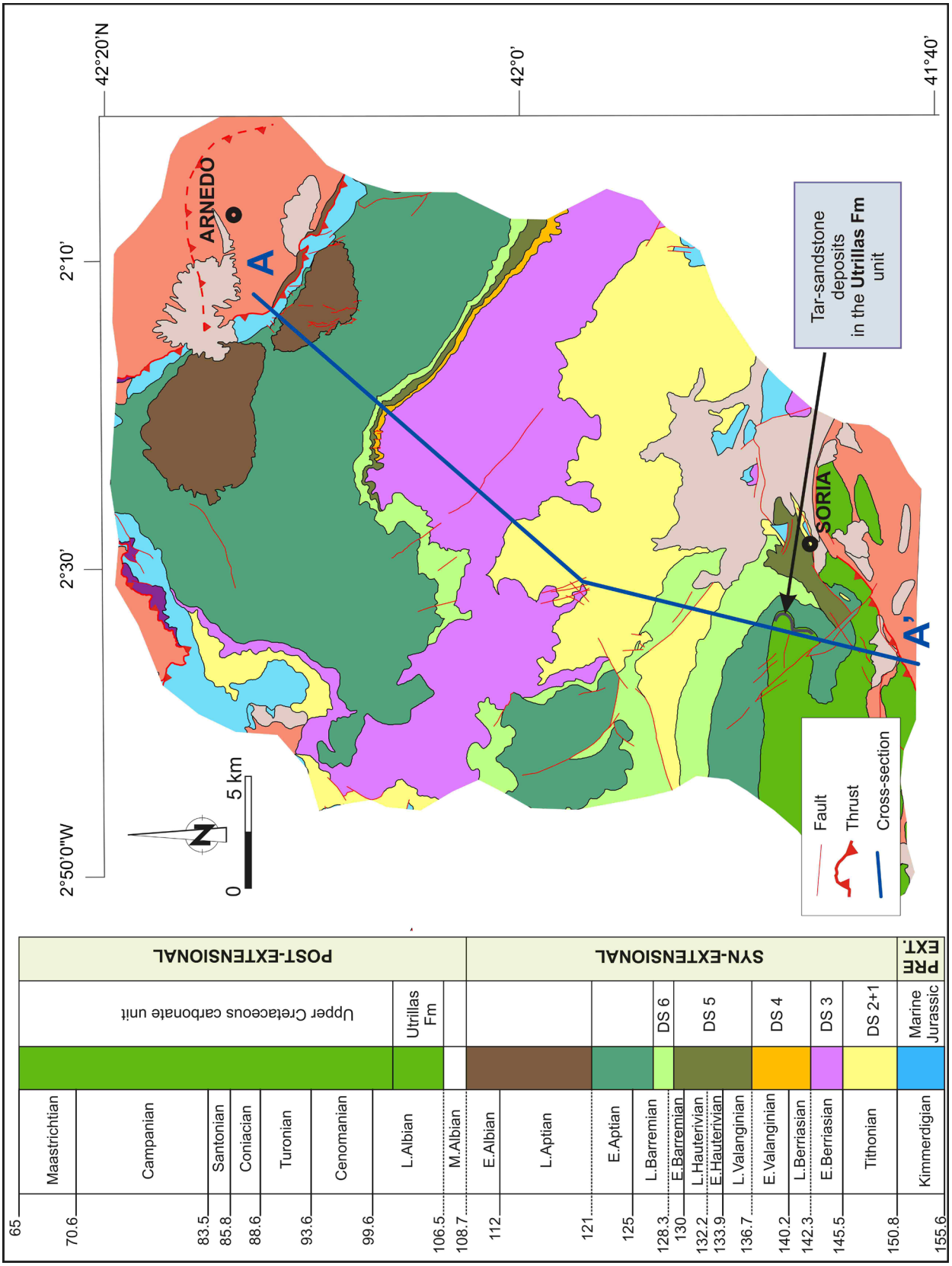

Fig. 12.2 - Geological setting of the Cameros Basin modelled area

geochemistry data, was performed. For this purpose, all of the data and results collected and determined in the previous chapters were used to reconstruct a reliable and complete model.

A complex geologic conceptual model was reconstructed, from the extensional and post-extensional stages, when the basin was formed and the basin infill was deposited, to the inversion stage, when the basin was uplifted and the basin infill was gradually eroded. The structure and geometry of the basin necessary to reconstruct the geologic conceptual model, as well as sedimentological and chronostratigraphical data, were defined considering the data and results performed in **Chapter 7.** Boundary conditions were defined similar to the thermal models reconstructed in **Chapter 9**. The heat flow trend, which performs the best calibration of the thermal model, was used (**Chapter 9**).

Potential source rocks of the system were defined, considering the results determined in **Chapter 10**. Interpreting the latter data, the geochemical data of the potential source rocks were introduced in the model. Bulk kinetics, previously calculated for the Cameros Basin kerogen (**Chapter 11**), were assigned to the source rocks. Furthermore, to model the generation of the oil and gas components, compositional kinetics, which are characterised by kinetic parameters similar to the calculated bulk kinetics, were also considered.

Interpreting model results, as well as the whole multidisciplinary geological data collected on the basin in the previous chapters, the elements and process of the petroleum system (sensu Magoon and Down, 1994) were determined, as were the timing and amount of hydrocarbon generation, migration and accumulation. Finally, causes of the absence of the accumulation of relevant commercial quantities of hydrocarbons in the area were analyzed.

To model the basin's petroleum system, data and information of the basin history are used. Thus, to help with the comprehension of the methodologies, results and discussion of the modelling in this chapter, a short resume of the main relevant points of the tectonic evolution, structure and stratigraphy of the Cameros Basin is reported below. Afterwards, a synthesis is presented of the petroleum system's elements and processes that have been identified through the preceding chapters, as well as in other studies.

12.3. GEOLOGICAL FRAMEWORK

12.3.1. Geo-tectonic evolution

The evolution of the Cameros Basin can be subdivided into three important geotectonic phases (Fig. 12.3). The first one corresponds to the extensional phase that formed the basin during the

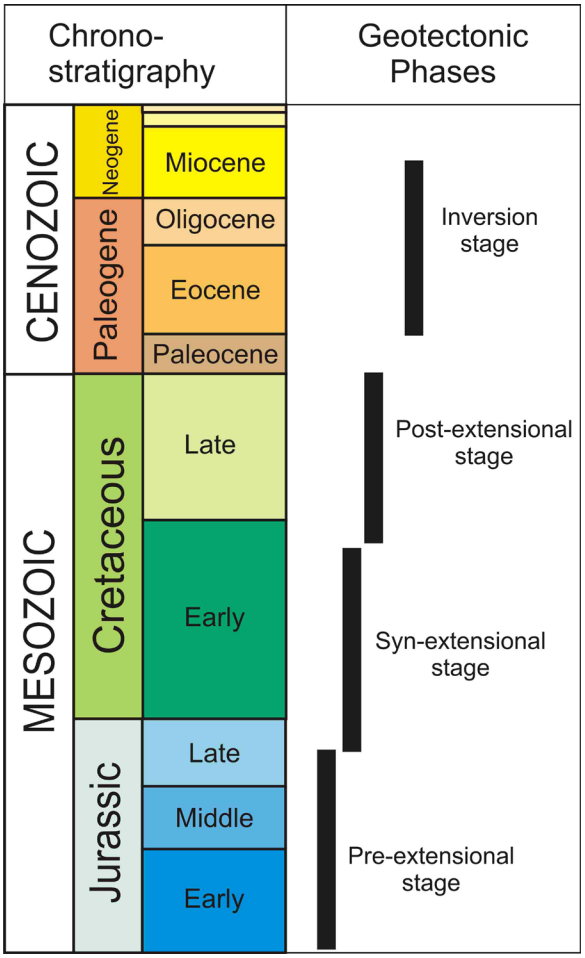

Fig. 12.3 - Geotectonic phases of the Cameros Basin

Mesozoic Iberian Rift System (Tithonian to Early Albian) (Salas et al., 2001). The onset of this extension was due to the opening of the Western Tethys and North Atlantic domain and it completely affected the Iberian plate with two main extensional/ post-extensional phases (Arche and López-Gómez, 1996; Salas et al., 2001; Vera, 2001; Vergés and García-Senz 2001; Mas et al., 2003).

The second geotectonic phase is represented by the post-extensional phase (Late Albian to the end of the Cretaceous period). At that time, the entire Iberian Basin underwent thermal relaxation of the lithosphere, with the deposition of a sedimentary succession characterised by a uniform thickness and facies in the whole area.

The third geotectonic phase was recorded during the Cenozoic (Eocene to Early Miocene) when the Cameros Basin, together with all the Mesozoic Iberian Basin, was completely inverted, creating the Iberian and Catalan Coastal Chains (Casas and Salas 1992; Salas and Casas 1993; Salas et al., 2001).

During its evolution the Cameros Basin was affected by low to very-low grade metamorphism events (Casquet et al. 1992; Alonso-Azcárate et al. 1995; Barrenechea et al. 1995, 2001; Mantilla-Figueroa et al. 1998, 1999; Alonso-Azcárate et al. 1999; Mata et al., 2001; Mas et al. 2003, Ochoa et al., 2007; Del Río et al., 2009; González-Acebrón et al., 2011, 2012; Casas et al., 2012); the first event occurred during the post-extensional stage (Late Albian to Coniacian period), with a maximum temperature greater than 350 ºC (Casquet et al., 1992, González-Acebrón et al., 2011), whereas the second event occurred in the Eocene, which recorded maximum temperatures of approximately 280–305ºC in the sediment (González-Acebrón et al., 2011).

12.3.2. Structure

The Cameros Basin is contained within the Cameros thrust-sheet (Guimerà et al., 1995), including the extensional and post-extensional sedimentary infill of the Cameros Basin and its Jurassic and Triassic substratum, as well as the Variscan Basement (cropping out primarily in the Sierra de la Demanda in the Northwest sector of the basin) (Fig. 12.2 and Fig. 12.4).

The Cameros thrust-sheet thrusts northward onto the Ebro Basin foreland, with nearly 28 km of horizontal displacement, and southward, with a back-thrust system, onto the local Almazán Basin foreland, with a smaller displacement of nearly 5 km (Guimerà et al., 1995) (Fig. 12.2).

The most relevant structural features of the Cameros Basin are the thrusts that bounded the Cameros Structural Unit to the north and to the south (Guimerà et al., 1995). The main thrust can be recognised all along the northern border of the Cameros unit. Nevertheless, in the study area the main thrust is blind and covered by Cenozoic deposits (Fig. 12.2). Thus, the thrust surface cropping out in this area has been interpreted as a secondary splay of the main thrust (Omodeo Salé 2014, **Chapter 7**).

12.3.3. Stratigraphy

The sedimentary succession of the Cameros Basin can be subdivided into pre-extensional, syn-extensional and post-extensional deposits (Fig. 12.2 and Fig. 12.5). Callovian to Kimmeridgian pre-extensional deposits represent the substratum of the basin. Presently, they outcrop only in the basin borders, especially in the northern border, where they are bounded by and overlie the main northern thrust. Geophysical data demonstrate that these units constitute the substratum of the syn-extensional deposits all along the basin (Mas et al., 1993; Guimerà et al., 1995; Omodeo Salé et al., 2014). The sedimentary record of these pre-extensional deposits is largely made up of marine deposits, which are primarily carbonates and shales (Alonso and Mas 1990; Aurell and Meléndez 1993; Leinfelder 1994; Bádenas and Aurell 2001; Benito et al., 2005).

The syn-extensional deposits form the largest part of the basin infill. They outcrop extensively throughout the entire basin, with a total vertical thickness in the depocentral area of 6500 m. Continental deposits mainly formed the syn-extensional sedimentary, predominantly fluvial and lacustrine, with episodic marine incursions (Mas et al., 1993, 2003, 2011). The syn-extensional deposits have been divided into eight depositional sequences (DS) (Mas et al., 1993; Martín i Closas and Alonso Millán, 1998; Arribas et al., 2003; Mas et al., 2003), composed of several lithological units (Fig. 12.5).

The post-extensional deposits form part of the Cretaceous Upper Megacycle (Alonso et al.,

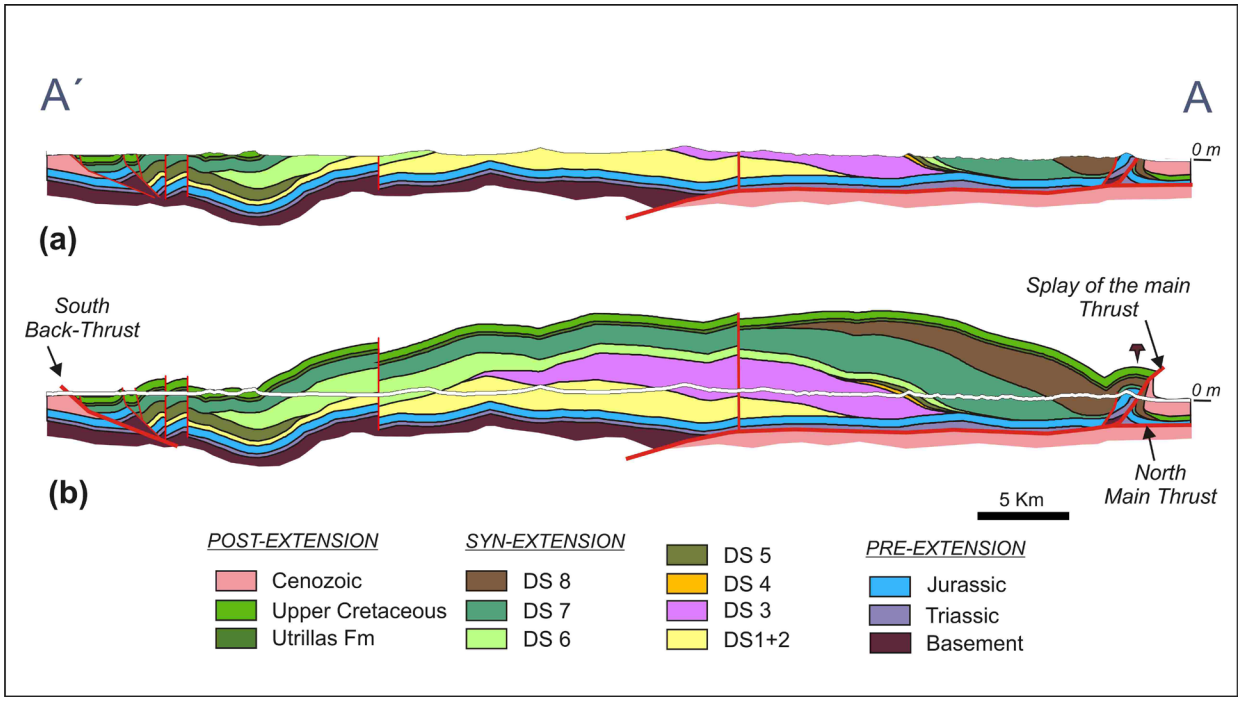

Fig. 12.4 - (a) Geological cross-section of the Cameros Basin at the present topographic profile. (b) Balanced geological cross-section used for modelling. In the geologic conceptual model, the planes of the splay of the main thrust to the north and the back-thrust to the south were used as the limiting boundary of the basin. To simplify, faults along the section and the syn-extensional stratigraphic sequence cropping out in the footwall of the north thrust-splay were not represented in the model

1993), which represents the post-extensional phase of the Lower Cretaceous syn-extensional stage (Salas et al., 2001). At present, the post-extensional deposits outcrop only in the southern area of the basin, unconformably overlying the earlier syn-extensional deposits (Alonso et al., 1993; Salas et al., 2001).

A synthesis of the age, lithological Group/Formation, lithology and depositional setting of each unit constituting the basin infill is shown in Table 12.1.

12.4. PETROLEUM SYSTEM

As previously mentioned, numerous data indicate that during the evolution of the Cameros Basin a petroleum system (sensu Magoon and Beaumont, 1999) was activated (Lanaja, 1987; Mantilla-Figueroa et al., 1998; Mas et al., 2002, 2003, 2011; Ochoa et al., 2007 and **Chapter 10**). A synthesis of the elements and processes for this petroleum system is discussed below.

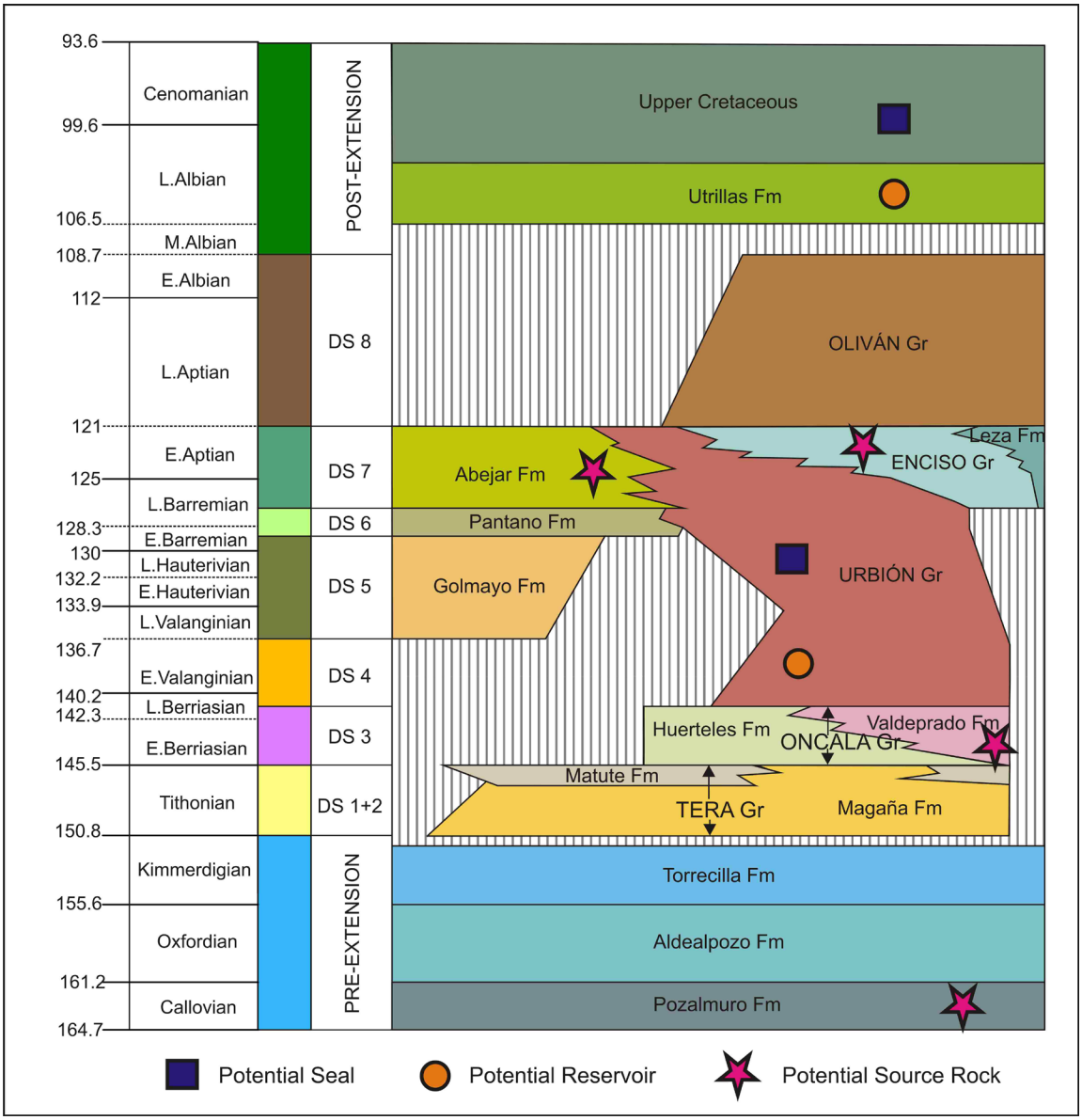

Fig. 12.5 - Stratigraphic chart of the Cameros Basin. Formations and Groups lithological units that form the pre-extensional, syn-extensional (depositional sequences) and post-extensional units are represented. The possible petroleum system elements are indicated in the chart

12.4.1. Petroleum system elements

12.4.1.1. Source rocks

From previous sedimentologic, petrographic and geochemical data (Mantilla-Figueroa et al., 1998; Mas et al., 2003, 2011; Ochoa et al., 2007, **Chapter 10**) four potential source rocks are identified in the Cameros Basin.

1) Marine Jurassic source rock (MJSR): These deposits formed in the pre-extensional stage and

they constituted the substratum of the basin (Mas et al., 1993; Guimerà et al., 1995; Omodeo Salé et al., 2014). The potential source rock is represented by the Pozalmuro Fm, a sequence of alternated marls-carbonate and black-shale deposits, which were generated in an outer platform marine depositional environment under anoxic conditions (Mas et al., 2002, 2003). In the study area, it outcrops in the north-west border of the basin. Presently the MJSR deposits are characterised by very scarce organic matter content, mostly constituted by vitrinite, inertinite macerals and solid bytumens particles (Table 12.2). Pyrolisis Rock-Eval data indicate the dominance of a residual kerogen and a very poor hydrocarbon potential (sensu Peter and Cassa, 1994 and Dembicky, 2009) (Table 12.2). Vitrinite reflectance indicates overmatured thermal conditions (sensu Taylor et al., 1998) (Table 12.2).

2) Valdeprado source rock (VSR): The syn-extensional Valdeprado Fm deposits forms part of this source rock. It is the uppermost facies (dominantly carbonate-evaporite) of the DS3 (Berriasian), which outcrops in the northern sector of the basin. Valdeprado Fm is composed by laminated carbonate-marls and relatively thick black-shale intervals, deposited in shallow carbonate-sulfate coastal-shallow lakes, coastal-salt flats and their peripheral mudflats (Mas et al., 1993; Gómez Fernández and Meléndez, 1994; Quijada et al., 2013a, b). Presently, the organic matter content of this potential source rock is very scarce, mostly constituted by vitrinite and inertinite macerals and solid bitumen particles. Pyrolisis Rock-Eval data indicate the dominance of a residual kerogen and a very poor hydrocarbon potential (sensu Peter and Cassa, 1994 and Dembicky, 2009) (Table 12.2). Vitrinite reflectance indicates thermal maturity ranging from the dry gas stage to the overmatured stage (sensu Taylor et al., 1998).

3) Enciso source rock (ESR): This potential source rock is constituted by the dark lutitic intervals of the Enciso Gr (DS7) syn-extensional unit (Late Barremian-Early Aptian), formed in broad and flat lacustrine-palustrine areas, with carbonate deposition and strong siliciclastic supplies (Mas et al., 1993; Alonso-Azcárate, 1997; Alonso-Azcárate et al., 1999; Suárez-González et al., 2013). Presently, the organic matter content of this potential source rock is very scarce, mostly constituted by vitrinite and inertinite macerals and solid bitumen particles. Pyrolisis Rock-Eval data indicate the dominance of a residual kerogen and a very poor hydrocarbon potential (sensu Peter and Cassa, 1994 and Dembicky, 2009) (Table 12.2). Vitrinite reflectance indicates thermal maturity ranging from the dry gas stage to the overmatured stage (sensu Taylor et al., 1998) (Table 12.2).

4) Abejar source rock (ASRs and ASRw): This potential source rock forms part of the dark fine siliciclastic deposits, which correspond to intervals of lacustrine-palustrine deposits that are related to coastal wet land plains of a fluvial-deltaic system (Mas et al., 1993, 2002, 2003, 2011; Arribas et al., 2003; Ochoa et al., 2007 and **Chapter 10**), being intercalated in the conglomerates and white sandstone bodies that constitute the Abejar Fm (DS7, Late Barremian-Early Aptian) (Table 12.1). The deposits outcropping in the southern sector of the basin (ASRs) contain

Age (My)		Unit	Group/Formation	Lythology	Depositional System	Facies assigned in
From	To					
50	17	Cenozoic	Cenozoic	Sandstone, clay poor	Fluvial-alluvial	Cenozoic
65.5	98	Post-rift	Upper Cretaceous	Limestone	Inner-Outer marine platforms	UpCretac
98	106.5		Utrillas Fm	Sandstone, clay rich	Fluvial	Utrillas
121	108.7	DS8	Olivan Gr	Sandstone bodies interbedded with shales and minor limestone beds	Fluvial + minor lacustrine	Oliván
127	121	DS7	Leza Fm	Micritic limestone	Lacustrine-coastal	Enciso
			Enciso Gr	Limestone alternated with sandstone and shale	Fluvio-lacustrine/palustrine	
			Urbión Gr	Coarse grained sandstone and shales	Fluvial meandering	Urbión
			Abejar Fm	Conglomerate and sandstone interbedded with thin shale levels	Fluvial-alluvial/palustrine	Abejar
129	127	DS6	Urbión Gr	Coarse grained sandstone and shales	Fluvial meandering	Urbión
			Pantano Fm	Sanstone interbedded with conglomerate and shale	Alluvial-Fluvial braided	Pantano
136.7	129	DS5	Urbión Gr	Coarse grained sandstone and shales	Fluvial meandering	Urbión
			Golmayo Fm	Sandstone interbedded with shale and limestone	Fluvial+minor lacustrine	Golmayo
142.3	136.7	DS4	Urbión Gr	Coarse grained sandstone and shales	Fluvial meandering	Urbión
145.5	142.3	DS3	Valdeprado Fm	Carbonate-marls interbedded with gypsum levels	Lacustrine-sabkha and playa-lake	Valdeprado

abundant organic matter, which is formed by the three vitrinite, liptinite and inertinite maceral groups, in order of abundance. Liptinite is constituted by cuticles, spore, pollen and algae. Pyrolisis Rock-Eval data indicate the dominance of Type III kerogen, whereas Type I kerogen is less abundant. A fair to good hydrocarbon potential has been deduced (sensu Peters and Cassa, 1994 and Dembicky, 2009) (Table 12.2). Vitrinite reflectance values indicate thermal maturity ranging from immature to early oil window stages (sensu Taylor et al., 1998) (Table 12.2). The deposits of the Abejar Fm outcropping in the western sector of the basin (ASRw) contain very abundant organic matter, which is formed mostly by liptinite and a minor amount by vitrinite and inertinite maceral groups. Liptinite is constituted by algae oriented in laminae (lamalginites) and algal bodies (telalginites) such as Botryococcus. Pyrolysis Rock-Eval analysis indicates the predominance of Type I kerogen and an excellent hydrocarbon potential (sensu Peters and Cassa, 1994 and Dembicky, 2009) (Table 12.2). Vitrinite reflectance indicates immature thermal conditions (sensu Taylor et al., 1998) (Table 12.2).

The MJSR, VSR and ESR were defined as spent source rocks (sensu Law, 1999) (**Chapter 10**). In fact sedimentological, petrographic and geochemical evidences indicate that the original abundant organic matter has already been completely transformed into hydrocarbons for thermal alteration (**Chapter 10**). A type II kerogen has been deduced for the MJSR deposits, type I for the VSR deposits and a mixture of Type III and Type I for the ESR deposits. Additionally, due to the high content and good quality of the organic matter contained in the ASRs and ASRw deposits, these source rocks have been defined as good potential source rock (sensu Law, 1999) (**Chapter 10**).

12.4.1.2. Reservoir

The most relevant hydrocarbon accumulation found in the Cameros Basin areas is constituted by the tar sandstone deposits outcropping in the south of the basin (Mas et al., 2002, 2003, 2011, Permanyer et al., 2011), forming part of the post-extensional Utrillas Fm unit. Tar sandstones were even found in the Escucha Fm deposits cropping out in the satellite half-graben basin located to the south of the Cameros Basin. However, because this work focuses on modelling the petroleum system only in the area of the Cameros Basin s.s. the latter accumulation was not considered. Petrographic observations of the Utrillas Fm sandstones indicate a complete infill of the sandstone porosity with light to dark-brown bitumens, which have been classified (sensu Jacob, 1989) as asphalt (**Chapter 10**).

Table 12.1 - Ages, lithology and sedimentological features of the units forming the basin infill

Source Rock	OM compo-nents	%Ro (mean range)	mean TOC [%]	mean HI [mg HC/g TOC]	mean OI [mg CO2/g TOC]	S1 [mg HC/g]	S2 [mg HC/g]	mean T_{max} [°C]	Kerogen Type
MJSR	sB, V, I	3-4.5	0.5	37	193	0.05	0.09	398	Residual
VSR	sB, V, I	2-4.6	0.9	14	108	0.04	0.1	388	Residual
ESR	V, I, sB	2-4	1.21	10	170	0.04	0.07	380	Residual
ASRs	V, L, I	0.38-0.6	2.8	168	57	0.22	3.09	445	Type III-I
ASRw	L, V, I	0.3	17.82	695	43	2.75	128.83	138	Type I

Table 12.2 - Petrographic and geochemical proprieties of the potential source rocks considered in the basin. Data refer to Chapter 10. Organic matter (OM) components are indicated in order of abundance: V – vitrinite, I – inertinite, L – liptinite and sB – solid bitumen

The Urbión Gr fluvial sandstone bodies (DS4, DS5 DS6, and DS7) have been suggested to be another important reservoir of the system (Mas et al., 2002, 2003, 2011; Ochoa et al., 2007), for which petrological characteristics have indicated an excellent rigid grain framework, suggesting the preservation of high primary porosity during burial (Arribas et al., 2003, 2013; Ochoa et al., 2007).

12.4.1.3. Seal

The mudstone levels interbedded in the Enciso Gr (DS7) have been suggested to be the seal of the reservoir formed in the Urbión Gr sandstone bodies (Mas et al., 2002, 2003, 2011; Ochoa et al., 2007), whereas the post-extensional dominant marl-limestone upper Cretaceous unit has been suggested to be the seal of the reservoir formed in the Utrillas sandstone unit (Mas et al., 2002, 2003 and 2011).

12.4.2. Petroleum system processes

Mas et al., (2002, 2003 and 2011) have suggested a first hydrocarbon generation at the end of the syn-extensional stage (Albian) in the central sector of the Cameros Basin, a consequence of the organic matter maturation during burial (Mas et al., 2003 and Ochoa et al., 2007). An early-migration is indicated by the hydrocarbons fibres found in the Urbión Gr sandstone deposits as they predate the diagenetic quartz overgrowths (Ochoa et al., 2007). A second hydrocarbon generation was suggested during the post-extensional stage (Late Cretaceous), induced by "abnormal heat flow" related with the first hydrothermal event that affected the basin (Mas et al., 2002, 2003; Ochoa et al., 2007). The occurrence of this second event was induced by the

circulation of hydrothermal fluids, which matured the organic matter levels located within the basin borders (Mas et al., 2003). The tar sandstone deposits outcropping in the south of the basin could be a possible accumulation of this second hydrocarbons generation and migration event (Mas et al., 2002, 2003).

The occurrence in the central-northern sector of the basin of two metamorphic hydrothermal events has been considered the possible cause of the destruction of the reservoir formed in the Urbión Gr deposits (Mas et al., 2003). By contrast, the reservoir formed in the Utrillas Fm sandstone unit lost its integrity when the basin infill was inverted and eroded (Mas et al., 2002, 2003).

12.5. METHODS

To reconstruct with detail the elements and processes of the petroleum system of the Cameros Basin, a thermal model of the basin is herein proposed, which takes into account all of the geological, physical and geochemical variables. With the model the source rocks thermal maturation causes and timing are determined, together with the hydrocarbon migration paths and timing of hydrocarbon accumulation. The 2D model was built using PetroMod 2D software (Schlumberger). To provide the essential physical and temporal input necessary for modelling a conceptual model of the basin, the basin's history was reconstructed (Welte and Yükler, 1981; Tissot et al., 1987; Welte et al., 1997; Littke et al., 2008).

The model reconstructed herein was based on the balanced geological cross-section of the basin (Fig. 12.4), determined in **Chapter 7**. The cross-section provides the geometry of the basin infill, the main structures of the basin and the sequence of deposition and deposition/erosion events along the traced cross-section. A series of sections, representing the intermediate steps of the thrust process, were included in the model (Fig. 12.6). Intermediate sections were obtained using Move software, considering as input end-members the balanced geological cross-section and the related pre-inversion restored section (**Chapter 7**). The PetroMod TecLink module was used to combine the sections and to reconstruct a model of the entire tectonic basin evolution.

Ages and facies assigned in the model refer to data presented in previous works (Mas et al., 1993, 2003, 2011 and cited authors). Data on boundary conditions, heat flow, paleowater depth correction and sea-level fluctuations are determined considering previously published data (**Chapters 8 and 9**). A calibration of the heat flow trend assigned to the model was obtained by vitrinite reflectance data (**Chapter 9**).

To model the hydrocarbon generation and accumulation in the basin geochemical and kinetic parameters were assigned to the potential source rocks. Geochemical and kinetic parameters

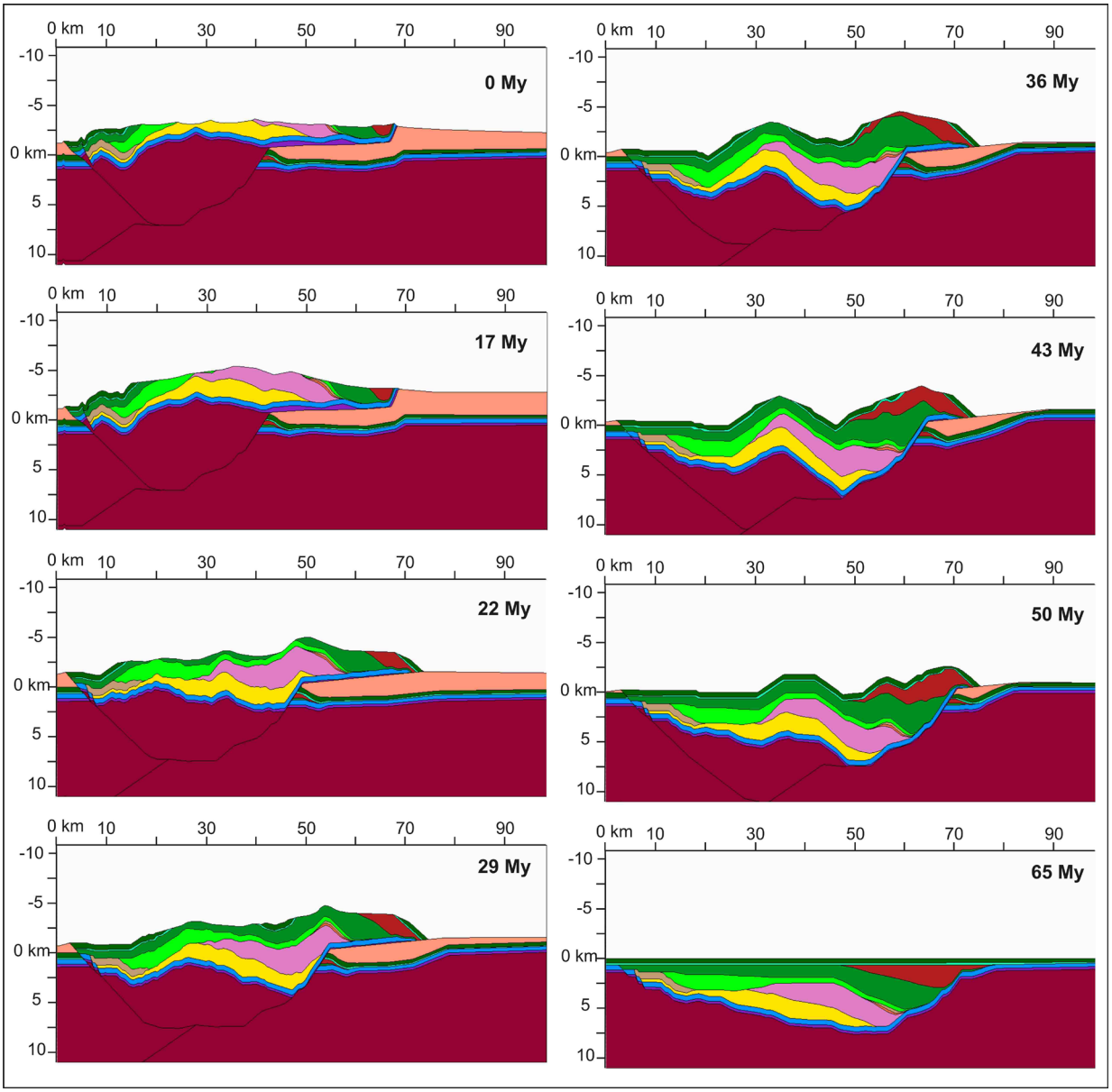

Fig. 12.6 - Intermediate steps of the thrust process, between the undeformed basin structure (65 My section) and the present-day inverted structure (0 My section), introduced in the model. Sections were formerly introduced in the model partially eroded, considering a constant erosional rate between the beginning of the uplift and the present day

can be directly determined from the immature kerogen forming the ASR. Contrary to the other spent source rocks (MJSR, VSR and ESR), the chemical properties of the original kerogen need to be hypothesised. In this work we propose to assign data on the immature organic matter of the basin to the overmature source rock when similar organo-facies can be suggested.

The geochemical parameters considered for the immature source rocks (ASRs and ASRw) refer to data presented in **Chapter 10**. To determine the kerogen behaviour of the immature deposits, possible bulk kinetics have been calculated on two end-member palustrine-lacustrine

types of organic matter, forming part of the Abejar Fm unit (DS7): a Type I kerogen, forming part of the ASRw, and a mixture of Type III and Type I kerogen, forming part of the ASRs, are considered (**Chapter 11**). The calculation of the kinetic parameters was based on a mathematical computational modelling of the S2 peak of the pyrolysis Rock-Eval (Ungerer, 1993) (**Chapter 11**). A set of first-order parallel and independent reactions is reproduced, considering the temperature dependence of the rate constants governed by the Arrhenius equation. To determine the activation energies and the frequency factor that better reproduces the S2 peak measured in the pyrolysis analysis (Ungerer, 1993), mathematical results were adjusted until a perfect calibration between the modelled and measured S2 peak was obtained (**Chapter 11**).

A first hydrocarbon generation, migration and accumulation model (Model-A) was reconstructed, assigning the calculated bulk kinetics to the original potential source rocks of the basin. In a second model (Model-B), to determine the products generated from kerogen transformation (oil and gas) and the relative timing of the generation, migration and accumulation, compositional kinetics taken from the PetroMod kinetic library were assigned. Compositional kinetics were chosen based on the most similar activation energy distribution with respect to the kinetics calculated for Cameros Basin kerogen. To model the fluid-flow circulation a hybrid approach (flow-path analysis combined with Darcy analysis) was used (see Introduction section) in both models.

12.6. MODELLING INPUT

12.6.1. Geologic conceptual model

The balanced section, used as a model profile, represents the structure and geometry of the basin after the inversion and reconstructs the amount of erosion that occurred during and after the Alpine compressive phase (Fig. 12.4b). To simplify the reconstruction of the geologic conceptual model, simplifications of the balanced geological cross-section in Fig. 12.4 were performed. In the northern extremity of the modelled section the main thrust surface, here covered by Cenozoic deposits, is not used in the model. However, the splay of the main thrust of the basin was used as a limiting boundary of the basin. Thus the thin syn-extensional stratigraphic sequence, cropping out in the footwall of the thrust-splay, was not considered. To simplify none of the post-sedimentary vertical faults along the section were considered in the model. In the southern extremity of the modelled section, the southern back-thrust of the basin was used as a limitary boundary.

In the conceptual model, the basin history was subdivided into an interrupted sequence of events (deposition, no-deposition and/or erosion) of a specified age (Table 12.3). Ages and units representing the subsequent depositional events of the basin are reported in Table 12.1. For

the syn-extensional deposits a unique "Jurassic" unit was considered (Table 12.1). In the syn-extensional deposits eight units were defined, corresponding with the depositional sequences defined by Mas et al., (2002, 2003). Finally the post-extensional deposits were subdivided in two units: the "Utrillas" and the "Upper Cretaceous" units.

For each unit specific lithological facies were assigned (Table 12.1). The facies defined refer to the Formation's and Group's lithological units in which the basin infill has been subdivided (Fig. 12.5). Because the limited thickness along the modeled section area of the Matute Fm and Leza Fm units, these units were not considered in the model, whereas included in the Tera Gr and Enciso Gr respectively. Facies were built in terms of the percentage of lithological composition (Table 12.4). Petrophysical properties of the defined facies were provided by the modelling package (Table 12.5). Facies were assigned to the cross-section, considering the areal distribution of the formations and groups (Mas et al., 1993, 2002, 2003 and 2011) (Fig. 12.7)

Age at the base (My)	Event no.	Event Type	Layer
0	24	Erosion	Paleo-Section 0My
17	23	Tectonic/Erosion	Paleo-Section 17My
22	22	Tectonic/Erosion	Paleo-Section 22My
29	21	Tectonic/Erosion	Paleo-Section 29My
36	20	Tectonic/Erosion	Paleo-Section 36My
43	19	Tectonic/Erosion	Paleo-Section 43My
50	18	Deposition	Cenozoic
50	17	Tectonic	Paleo-Section 50My
65.5	16	Hiatus	Hiatus 65.5_0
98	15	Deposition	Upp_Cretaceous
106.5	14	Deposition	Utrillas
108.7	13	Hiatus	Hiatus 108.7_106.5
121	12	Deposition	DS8
127	11	Deposition	DS7
129	10	Deposition	DS6
136.7	9	Deposition	DS5
142.3	8	Deposition	DS4
145.5	7	Deposition	DS3
150.8	6	Deposition	DS1+2
164.7	5	Deposition	Jurassic
205	4	Hiatus	Hiatus 205_164.7
245	3	Deposition	Triassic
380	2	Hiatus	Hiatus 380_245
500	1	Deposition	Basement

Table 12.3 - Events defined in the geological concept of the model

Unit	Group/Formation	Lithology		
		Limestone	Sandstone	Shale
Cenozoic	Various	0	95	5
Up.Cretaceous	Various	60	20	20
Utrillas	Utrillas Fm	0	80	20
DS8	Olivan Gr	5	70	25
DS7	Enciso Gr	45	20	35
	Urbión Gr	0	60	40
DS6	Abejar Fm	0	70	30
	Urbión Gr	0	60	40
	Pantano Fm	0	80	20
DS5	Urbión Gr	0	60	40
	Golmayo Fm	40	40	20
DS4	Urbión Gr	0	60	40
DS3	Valdeprado Fm	60	4	36
	Huerteles Fm	15	35	50
DS1+2	Tera Gr	5	60	35
Jurassic	Torrecilla Fm	100	0	0
	Aldealpozo Fm	100	0	0
	Pozalmuro Fm	50	0	50

Table 12.4 - Facies assigned to the units defined in the model, in terms of percentage of lithological composition

12.6.1.1 Tec-Link model

To model the entire tectonic evolution of the Cameros Basin, the inversion stage is included, and to avoid the problems of erosion assignment, eight sections were introduced in the model. Sections represent the intermediate steps of the thrust from the undeformed state to the present-day structure (Fig. 12.6).

In the basic PetroBuilder PetroMod module the same horizon/layer cannot be defined by multiple z-values on one vertical grid line (IES, 2007). This can be a limitation in case of complex tectonic settings, especially in the overthrusting areas, where horizons/layers, representing the same time-line, are superimposed in the vertical. The PetroMod TecLink module is able to handle multiple definitions, introducing the block concept (IES, 2007). TecLink is based on the "Paleo-Stepping approach" which means that for every paleo section introduced in the model the geometry of each step is defined (IES, 2007). The paleo sections together with their geological age are the basis for forward modelling. The 2D sections are split into several blocks that retain their structural integrity during the model's tectonic evolution and are calculated separately by the simulator (IES, 2007). A block is defined by a characteristic layer stack and by its boundaries

Facies	Initial Porosity (%)	Density (Kg m^{-3})	Permeability at porosity of (log		Heat Capacity (Kcal kg^{-1} K^{-1})		Thermal Conductivity	
			25%	45%	20ºC	100ºC	20ºC	100ºC
Cenozoic	42	2700	3	4.84	0.2	0.23	5.95	4.85
Up Cretac	51	2710	1	1.52	0.2	0.23	3	2.69
Utrillas Fm	40	2760	2	3.62	0.21	0.24	3.35	2.95
Oliván	49	2667	1.4	3.55	0.21	0.24	3.75	3.24
Enciso	51	2704	-0.36	1.10	0.21	0.24	2.13	2.05
Abejar	46	2700	1.7	4.37	0.2	0.23	4.21	3.58
Pantano	47	2684	1.8	3.88	0.21	0.24	3.74	3.23
Golmayo	51	2700	0.89	2.09	0.2	0.24	2.54	2.35
Urbión	53	2664	0.6	2.93	0.21	0.24	3.73	3.22
Valdeprado	55	2670	-0.81	0.28	0.21	0.24	2.01	1.96
Huerteles	50	2714	1.2	2.97	0.2	0.24	3.03	2.71
Tera	51	2673	0.76	3.48	0.21	0.24	3.37	2.96
Jurassic	51	2680	0.73	1.00	0.2	0.23	2	1.96
Triassic	10	2540	-	-	0.19	0.21	4.69	3.91
Basement	5	2750	-	-	0.19	0.22	2.72	2.35

Table 12.5 - Petrophysical properties of the facies used in the model

with no z-values within its boundaries (IES, 2007).

To build a model with TecLink three different levels need to be considered: paleo sections, blocks and layers. Eight paleo sections, representing the intermediate steps of the thrust from the undeformed state to the present-day structure were introduced in the model (Fig. 12.5). Ages were assigned to the paleo sections as indicated in Table 12.3. Next the depositional ages for the individual layers of the model were set (Table 12.3). The next step was building blocks in the sections. Each paleo section was cut into individual blocks, where each block represents an individual little 2D model (Fig. 12.8). Block boundaries correspond with the section top and bottom layers and with the fault lines that correspond with the main northern thrust and the southern back-thrust. In a secondary step, the blocks names were defined and assigned on the paleo sections. The purpose to assigning names to the blocks is to provide information to the simulator on how to handle all the historical aspects of the model (IES, 2007). The order in which the section is rebuilt by the simulator was defined by enumerating the blocks in a sequential order. The block with the lowest number is the first in the sequence and the one with the highest number is the last in the sequence. Additionally, in each section, parent blocks were defined in case different blocks were formed from a unique block of a previous stage (Fig. 12.8). A list of the blocks and parents blocks defined in all the paleo sections and their sequential order is shown in Table 12.6. Finally, facies were assigned to each layer in each block of all the paleo sections

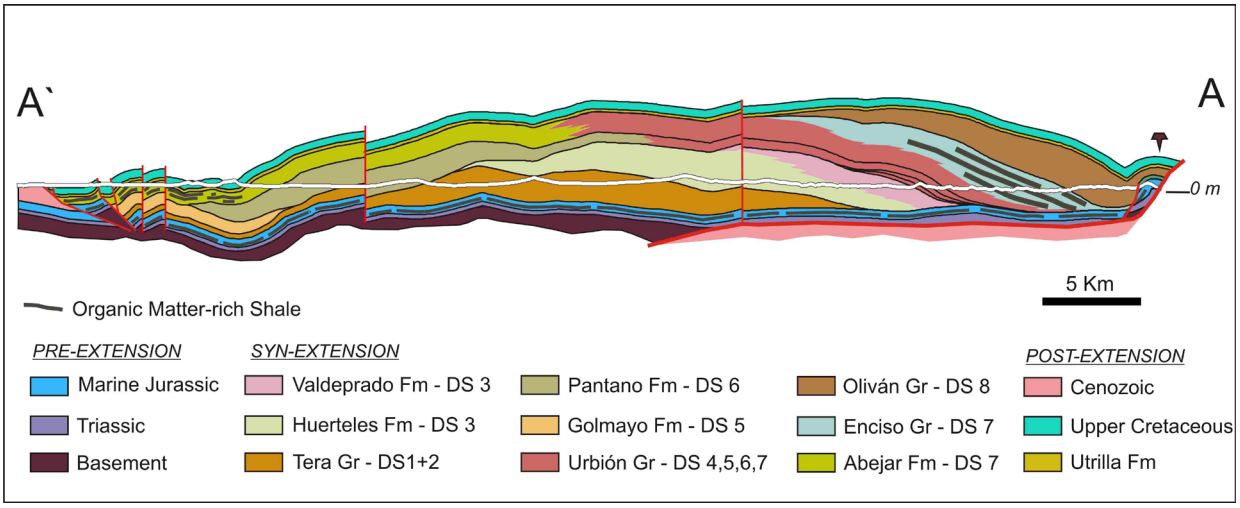

Fig. 12.7 - Along the cross-section specific lithological facies were assigned. The facies defined refer to the Formation's and Group's lithological units in which the basin infill has been subdivided (Fig. 12.5). Facies were assigned to the cross-section, considering the areal distribution of the formations and groups

12.6.2. Erosion

The most relevant erosion event that occurred in the basin was a consequence of the uplift of the basin during the inversion stage (Eocene to Early Miocene). During the basin infill phase, corresponding to the pre-extensional, syn-extensional and post-extensional stages (Fig. 12.3), any relevant erosion event was considered. The amount of the erosion that occurred in the inversion stage was estimated by considering the data provided by the balanced geological cross-section (**Chapter 7**) (Fig. 12.4). A maximum vertical thickness erosion of 5500 m has been calculated in the central part of the section, which gradually decreases toward the southern section extremity (Omodeo Salé et al., 2014) (Fig. 12.4).

To assign the erosion we introduced to the model the inversion step sections that were already partially eroded (Fig. 12.6). This solution allows us to simulate the erosion at the same time as the units with different ages, avoiding conflict with the model layer-oriented-concept on which PetroMod modelling is based (each layer is deposited sequentially after the other and in the same way they have to be removed sequentially, Poelchau et al., 1997). The amount of erosion defined for each section was determined considering a constant erosional rate between the beginning of the uplift and the present day (Fig. 12.6). This assumption is most likely not totally correct but, because there are no available data regarding the uplift and erosional rate during the inversion of the basin, we consider this assumption the one that introduces the lower error in the model. The last section introduced in the model represents the present-day geometry of the basin, resulting from the combination of the compressive deformation tectonic and the

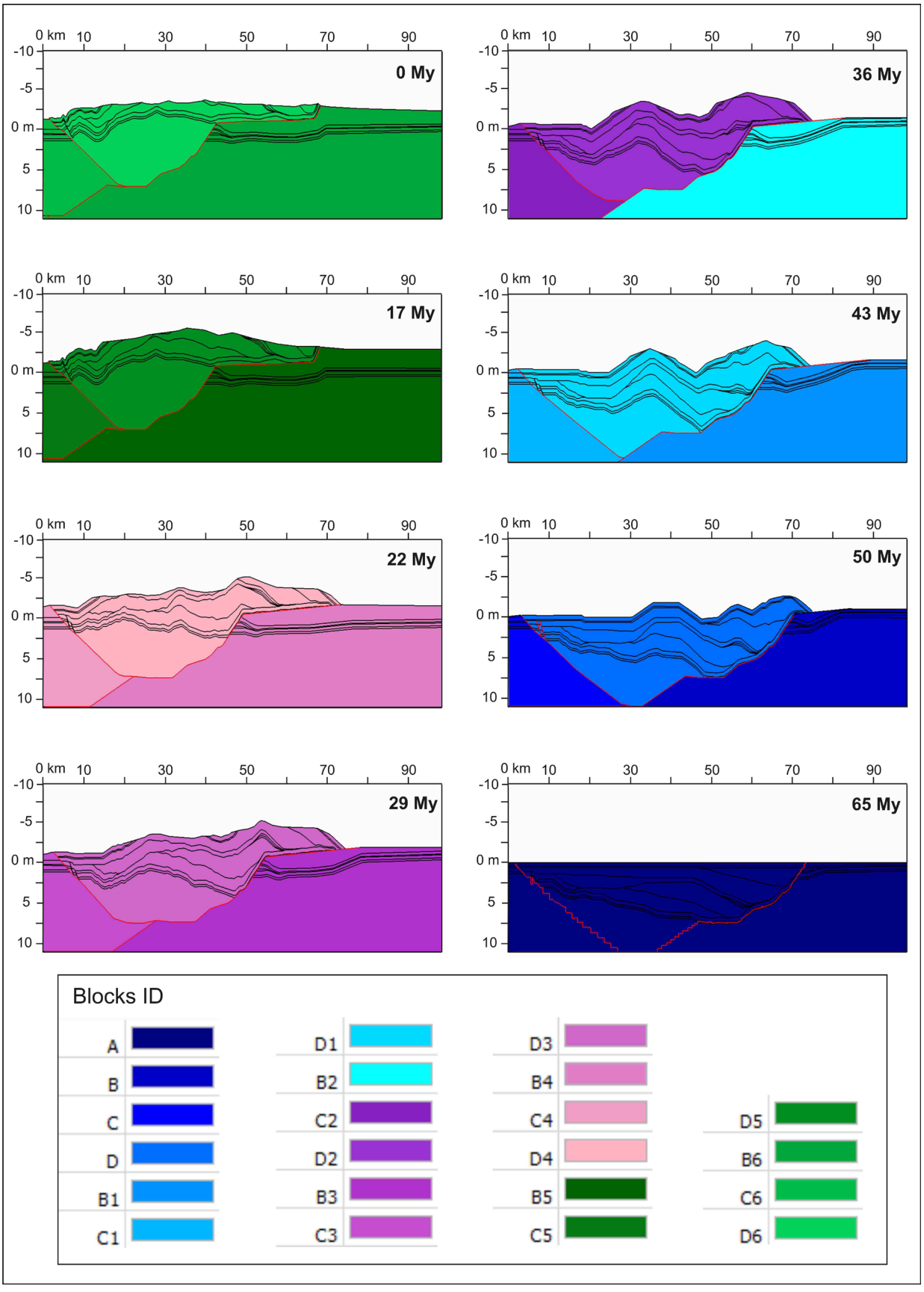
0 km 10 30 50 70 90
-10
-5
0 m
5
10
0 My
36 My
17 My
43 My
22 My
50 My
29 My
65 My
Blocks ID
A
B
C
D
B1
C1
D1
B2
C2
D2
B3
C3
D3
B4
C4
D4
B5
C5
D5
B6
C6
D6

Block_ID	Parent Block	Block Order
A		10
B	A	20
C	A	30
D	A	40
B1	B	50
C1	C	60
D1	D	70
B2	B1	80
C2	C1	90
D2	D1	100
B3	B2	110
C3	C2	120
D3	D2	130
B4	B3	140
C4	C3	150
D4	D3	160
B5	B4	170
C5	C4	180
D5	D4	190
B6	B5	200
C6	C5	210
D6	D5	220

Table 12.6 - List of the blocks and parent blocks defined in the paleosections (Fig. 12.8) and the related sequential order used to reconstruct the section using the simulator

erosion processes.

12.6.3. Heat flow

The most important boundary condition introduced in the model is the heat flow trend recorded during the evolution of the basin. However, the paleowater depth correction is not considered because of the continental nature of most of the deposits, and sea-level fluctuations were ignored.

The heat flow trend recorded in the basin was calculated and calibrated in **Chapter 8**. The heat flow was calculated by distinguishing the initial and thermal subsidence phases and by determining the relative magnitudes (Royden, 1986). The calculated heat flow was calibrated with vitrinite reflectance data (%Ro) (**Chapter 9**).

In the southern sector of the basin a maximum peak of 64 mW/m^2 was calculated for the end of the syn-extensional stage (108.7 My), corresponding with the maximum lithosphere stretching. In the post-extensional stage a value of 50-55 mW/m^2 was assumed, in accordance with Allen and Allen (2009) (Fig. 12.9). Under present-day conditions, a heat flow of 60 mW/m^2 was adopted taking into account the commercial exploration of oil-well heat flow data located in the area (Fernández et al. 1998) (Fig. 12.9). By contrast, in the central and northern sector of the basin two extra heat flow peaks of short duration (1 My) of 200 mW/m^2 and 180 mW/m^2 at 85 My and 45 My respectively were added to this trend (Fig. 12.9). The extra heat flow peaks attempt to reproduce the effect of the hydrothermal metamorphic events affecting these

Fig. 12.8 - In the conceptual model paleosections were split into several blocks, where each block represents an individual miniature 2D model. Blocks were ordered and related to provide information to the simulator on how to handle the historical aspect of the model

sectors of the basin in the post-extensional stage and in the Alpine compressive phase (Casquet et al. 1992; Alonso-Azcárate et al. 1995; Barrenechea et al. 1995, 2001; Mantilla-Figueroa et al. 1998, 1999; Alonso-Azcárate et al. 1999; Mas et al. 2003, Ochoa et al., 2007; González-Acebrón et al., 2011, 2012). However, in the sectors affected by metamorphism a complete calibration of the model cannot be performed because of advective heat transport; generating high temperatures into the uppermost stratigraphic layers of the model, cannot be simulated by the traditional basin modelling software. Due to software limitations, the heat flow trend determined (Fig. 12.9) may be considered the most reliable for modelling the petroleum system of the basin.

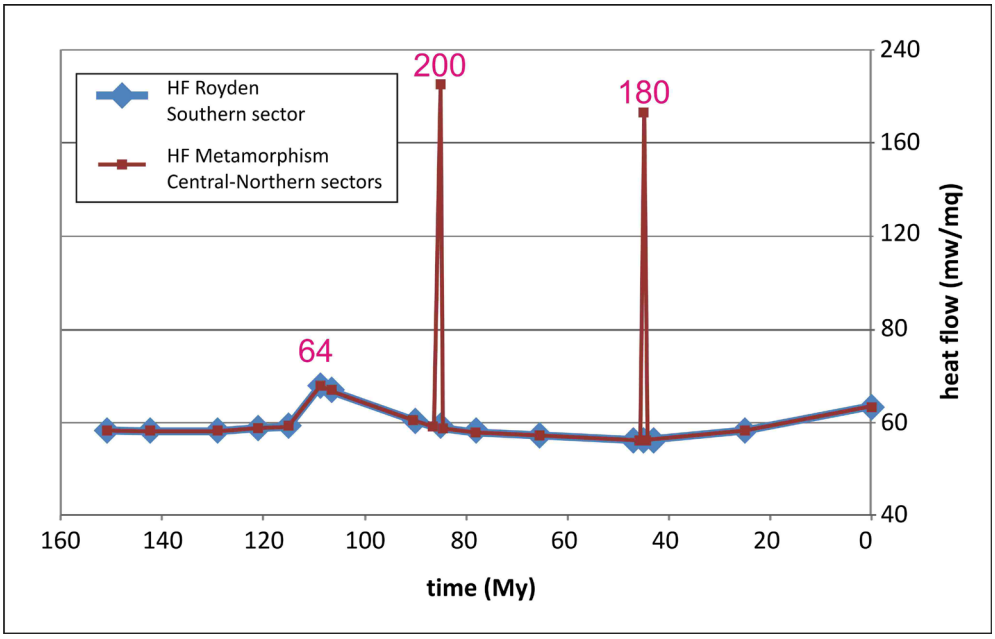

Fig. 12.9 - Heat flow trend introduced in the model. In the central and northern sector of the basin's two peaks, 200 and 180 mW/m2 were considered at 85 and 45 My, respectively

12.6.4. Source rocks and geochemical parameters

To model the generation and migration of petroleum in the basin the four source rocks previously characterised were considered in the model: MJSR, VSR, ESR and ASR. The source rocks' organic matter richness and type were defined in the model according to the data presented in Chapter 10.

To characterise the ASR source rock in the model, the geochemical parameters of the organic matter levels for the outcropping in the southern sector of the basin (ASRs) were used, as they are located closest to the section modelled: a Type III-Type I kerogen, TOC of 2.8% and HI of 168 mg HC/g TOC (Table 12.7)

To characterise the syn-extensional spent source rocks (VSR and ESR) in the model the geochemical parameters of the immature rocks of the basin, whose depositional setting suggests the deposition of similar organo-facies (Chapter 10), were assigned. In the case of the ESR, data of the ASRs were assigned: TOC of 2.8%, HI of 168 mg HC/g TOC and a kinetic of a mixed Type III-I kerogen. For the VSR data of the ASRw were assigned: TOC of 17%, HI of 695 mg HC/g TOC and a kinetic for a Type I kerogen (Table 12.7).

The absence of any immature analogue in the basin associated with the pre-extensional source rock (MJSR) forced to assign data from the Lower Jurassic source rocks of the adjacent petroleum field (Ayoluengo field, Burgos, N Spain). These deposits were generated in a similar marine depositional environment (organic rich marls and black shales) (Sanz, 1967; Abeger et al., 2003; Permanyer et al., 2013): TOC of 8% , HI of 730 mg HC/g TOC and a kinetic for Type II kerogen (Table 12.7).

Source Rock	TOC [%]	HI [mg HC/g TOC]	Kerogen Type	Bulk kinetic (Model-A)	Compositional Kinetic (Model-B)
MJSR	8	730	Type II	Tageelar TII (NS)	Ungerer TII (NS)
VSR	17	695	Type I	CAS-2 (CB)	Pepper and Corvi TIIS
ESR	2.8	168	Type III-I	STFC-4b (CB)	Pepper and Corvi TI
ASR	2.8	168	Type III-I	STFC-4b (CB)	Pepper and Corvi TI

Table 12.7 - Geochemical and kinetic parameters assigned to the source rocks defined in the model

12.6.5. Kinetics assignement

To the MJSR source rock we assigned kinetics calculated for a Type II Jurassic source rock characterised in the North Sea Basin, Kimmeridgian in age; the bulk kinetic was proposed by Tegelaar and Noble (1994) and the compositional kinetic was proposed by Ungerer (1990) (Table 12.6). Cumulative yield curves of the assigned kinetics are shown in Fig. 12.10.

For the syn-extensional deposits, a calculation performed for the immature kerogen of the basin determined two type of kinetics. The first type (CAS-2 kinetic) represents a Type I kerogen mostly formed by liptinite, constituted by lamalginites and secondarily by telalginite and amorphous organic matter. A frequency factor of 2.9*1013/s-1 was calculated for this kerogen (**Chapter 11**). The activation energies are distributed on an asymmetric large interval ranging from 40 to 56 kcal/mol, recording a maximum genetic potential at 52 kcal/mol. The kinetic parameters calculated indicate that the kerogen of this sample when it is thermally altered has a behaviour similar to a Type IIS kerogen. A Type IIS kinetic proposed by Pepper and Corvi (1995) is the compositional kinetic of the PetroMod kinetics library, which is more similar to the CAS-2

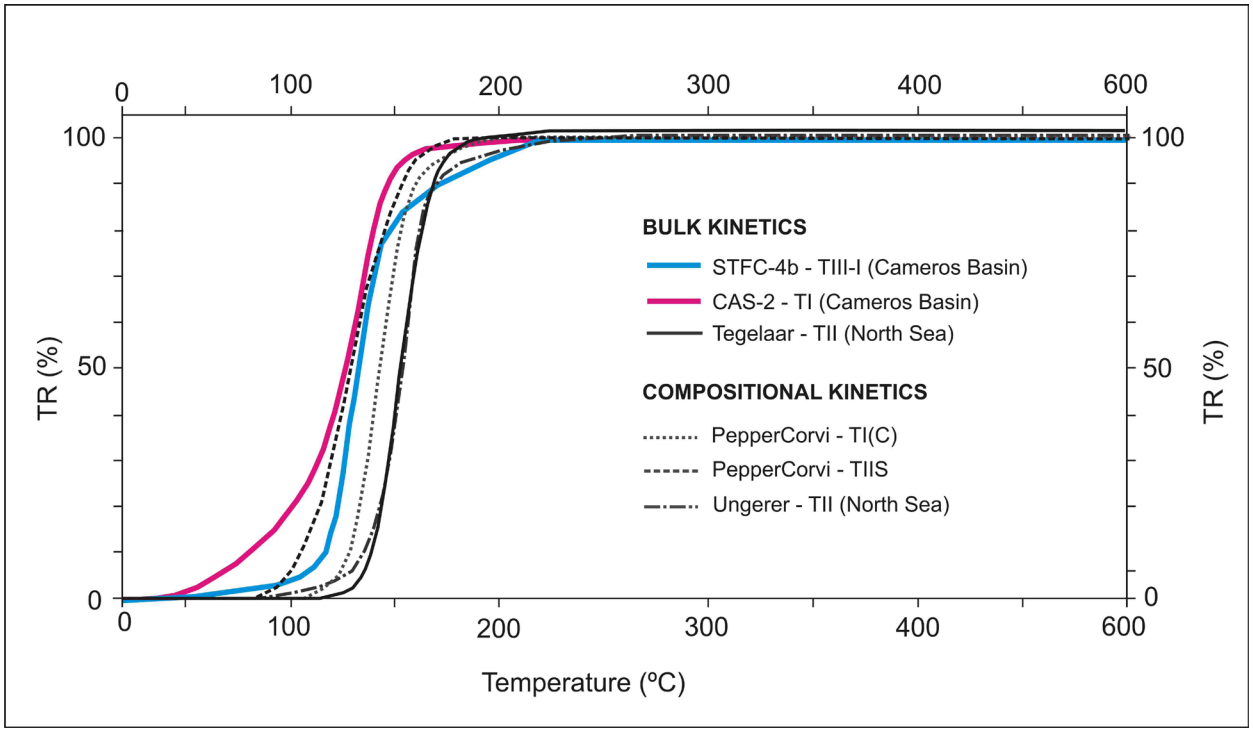

Fig. 12.10 - Transformation ratio (TR%) versus temperature (°C) of the compositional and bulk kinetics assigned to Model-A and Model-B, respectively

kinetic (Fig. 12.10). The second type (STFC-4b kinetic) represents a Type III-I kerogen, formed mostly by vitrinite, liptinite and inertinite in order of abundance; where liptinite is mostly constituted by cuticles and less frequently by algae. The frequency factor calculated for this kerogen is 2.9*1013/s-1 (**Chapter 11**). The activation energies are distributed on an asymmetric large interval ranging from 51 to 61 kcal/mol, recording a maximum genetic potential at 51–52 kcal/mol. The kinetic parameters indicate that the kerogen of this sample has a behaviour similar to a Type III kerogen when it is thermally altered, even if activation energies are more similar to a Type I. A Type I kinetic proposed by Pepper and Corvi (1995) is the compositional kinetic of the PetroMod kinetics library, which is more similar to the STFC-4b kinetic (Fig. 12.10).

Assignation of the calculated kinetics in Model-A, and of the related similar compositional kinetics in Model-B, to the spent source rock was performed considering the possible original type of kerogen that could form these deposits. Sedimentological features were considered (**Chapter 10**). The CAS-2 kinetic was assigned to the VSR source rock (Table 6), as these deposits formed in saline carbonate-sulfate coastal wetlands and their peripheral mudflats, where hydrogen-rich, lipid derived organic matter, such as alginate, can accumulate (Bornhold, 1973; Pelet and Debyser, 1977; Palacas et al., 1984; Horsfield et al., 1994). The STFC-4b kinetic was assigned to the ESR source rock (Table 12.7), as these deposits formed in fresh-water palustrine-lacustrine environments that mostly accumulate terrestrial organic matter such as cuticles, spore pollen

and ligneous material (Durand, 1980a; Tissot and Welte, 1984; Berger et al., 1989; Horsfield et al., 1994; Einsele, 2000).

12.7. RESULTS

The evolution of the petroleum system of the Cameros Basin was reconstructed in Model-A using the bulk kinetics calculated for the kerogen of the Cameros Basin, whereas in Model-B literature compositional kinetics were used. The modelling results determined 1) the thermal maturity of the source rocks throughout time; 2) the transformation ratio of the original kerogen; 3) the timing of hydrocarbon generation, migration and accumulation; 4) the migration paths of the hydrocarbons; and 5) the preservation of the accumulated hydrocarbons.

12.7.1. Source rock thermal maturity

The thermal maturity of the four source rocks was calculated using the Sweeney and Burnham (1990) algorithm of the PetroMod software. The evolution of the source rocks' thermal maturity through time depends mostly on the thermal history of the basin, thus results calculated by Model-A and Model-B are similar.

In the earlier phase of the extensional stage (from 142.3 to 136.7 My) the model calculated oil-window thermal conditions for the MJSR located in the most subsiding area (central-northern sector of the basin) and for the deepest layers of the VSR. In this earlier phase the other source rocks are immature (Fig. 12.11).

In an intermediate phase of the extensional stage (from 136.7 to 121 My) the VSR enters into the oil window, whereas the MJSR starts entering the wet-gas window in the central part of the section and into the oil window toward the borders. The ASR and ESR during this phase remain immature (Fig. 12.11).

In the latest phase of the extensional stage (from 121 My to 108.7 My) the MJSR is completely in the gas window in the central part of the section, whereas it is in the oil-window stage in the remainder of the section. In the northern and southern extremities of the section the MJSR is still immature. In this latest phase most of the VSR is in the gas window, the ESR enters into the oil window and the ASR is still immature (Fig. 12.11).

In the post-extensional stage (from 108.7 to 65.6 My) the thermal maturity of the deposits located in the central and northern part of the section increases abruptly as a consequence of the metamorphic thermal event affecting this area at 85 My. Thus, the source rocks located in this part of the section (part of the MJSR, VSR and ESR) rapidly reach the gas-window to

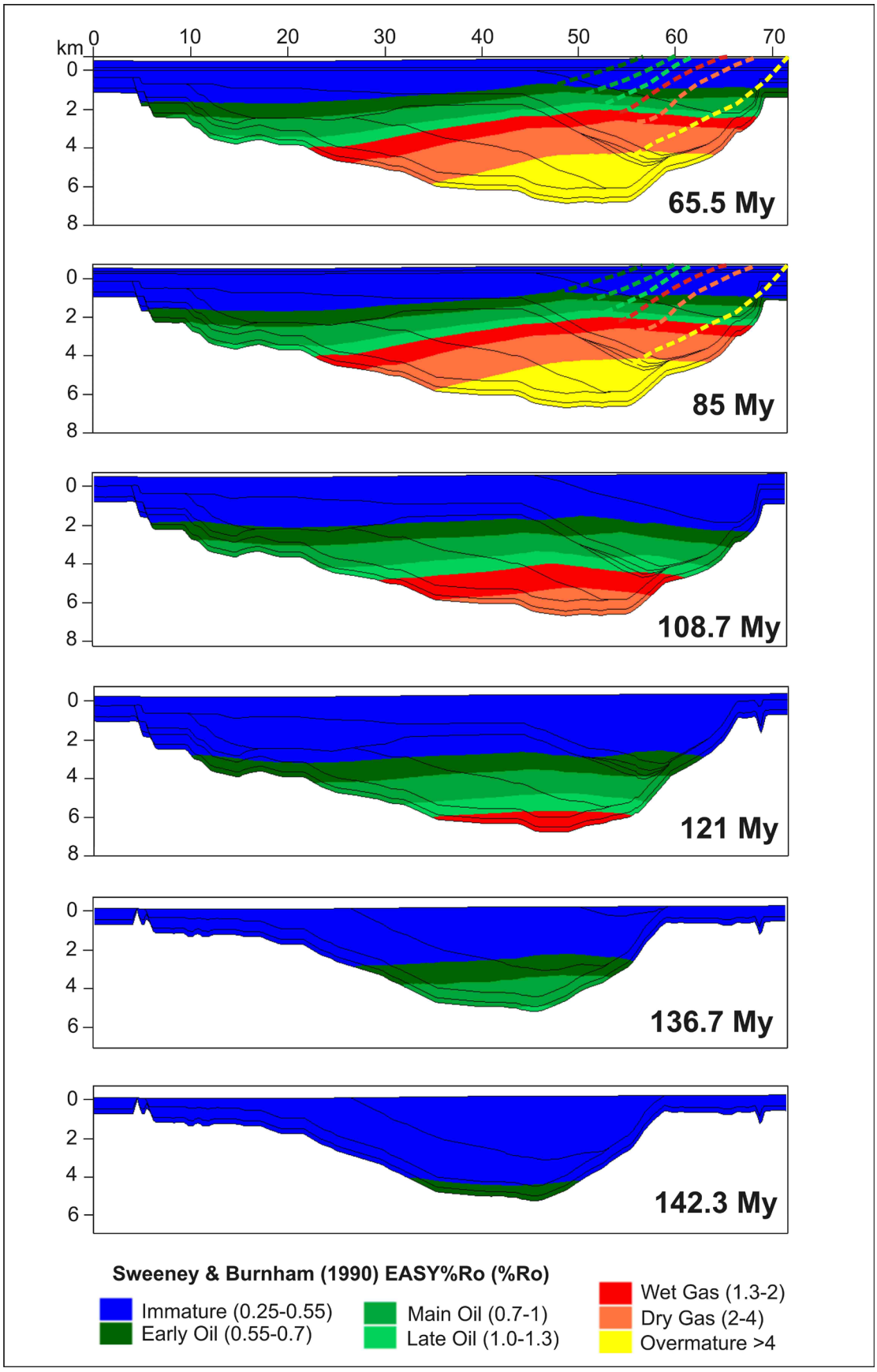
km
0
10
20
30
40
50
60
70
65.5 My
85 My
108.7 My
121 My
136.7 My
142.3 My
Sweeney & Burnham (1990) EASY%Ro (%Ro)
Immature (0.25-0.55)
Early Oil (0.55-0.7)
Main Oil (0.7-1)
Late Oil (1.0-1.3)
Wet Gas (1.3-2)
Dry Gas (2-4)
Overmature >4

overmatured thermal conditions (Fig. 12.11). Because of the difficulty in correctly reproducing the model effects of the circulation of hydrothermal hot fluids in the sediments (see section 5.3), slightly higher thermal conditions need to be considered in the uppermost stratigraphic layers with respect to those calculated by the model (Fig. 12.11, see lines drawn in the 85 and 65.5 My sections). Toward the south of the section no relevant change is recorded concerning thermal conditions, as the southern sector of the basin was not affected by the metamorphism. The MJSR remains in the oil-window to immature conditions and the ASR remains immature (Fig. 12.11).

In the inversion stage (from 50 My to 17 My) Model-B indicates that the thermal maturity of the basin infill is not modified, as the basin was uplifted to colder thermal conditions (Fig. 12.12). The increase of the heat flow at 45 My, due to the Cenozoic metamorphic event, does not cause relevant changes in the maturity of thermal conditions of the basin infill (Fig. 12.12).

12.7.2. Kerogen transformation ratio

Model-A calculated that in the earlier phase of the extensional stage (from 142.3 to 136.7 My) kerogen of the deepest MJSR deposits (central part of the section) records a transformation ratio (TR) ranging from 25 to 100%, whereas kerogen located in the VSR ranged from 5 to 30%. In the other source rocks kerogen has not yet been transformed in this phase (Fig. 12.13).

In the intermediate phase of the extensional stage (from 136.7 to 121 My) the kerogen of the MJSR located in the central-northern part of the section is completely transformed (TR of 100%), whereas in the VSR the TR of the kerogen ranges from 15% in the shallower layer to 98% in the deepest layers. Kerogen of the ASR and ESR is not transformed in this second phase either (Fig. 12.13).

In the latest phase of the extensional stage (from 121 My to 108.7 My) even the ESR kerogen begins to be transformed, with a maximum TR of 75%. In this phase the kerogen of the VSR is almost completely transformed (TR from 90 to 100%), with the exception of the shallower layers. In the southern part of the section the TR of the kerogen of the MJSR reaches 45%, whereas in the ASR the kerogen has not yet been transformed (Fig. 12.13).

In the early phase of the post-extensional stage (from 108.7 to 98 My) the transformation ratio does not record relevant change with respect to the previous phase. At 85 My the occurrence of the metamorphic event completely transforms (TR 100%) most of the kerogen of the source

Fig. 12.11 - Thermal maturity calculated for the basin infill by both Model-A and Model-B. To correctly reproduce the effects of the circulation of hydrothermal hot fluids in the northern sector of the basin, higher thermal conditions need to be considered in the uppermost stratigraphic layers in the northern part of the section

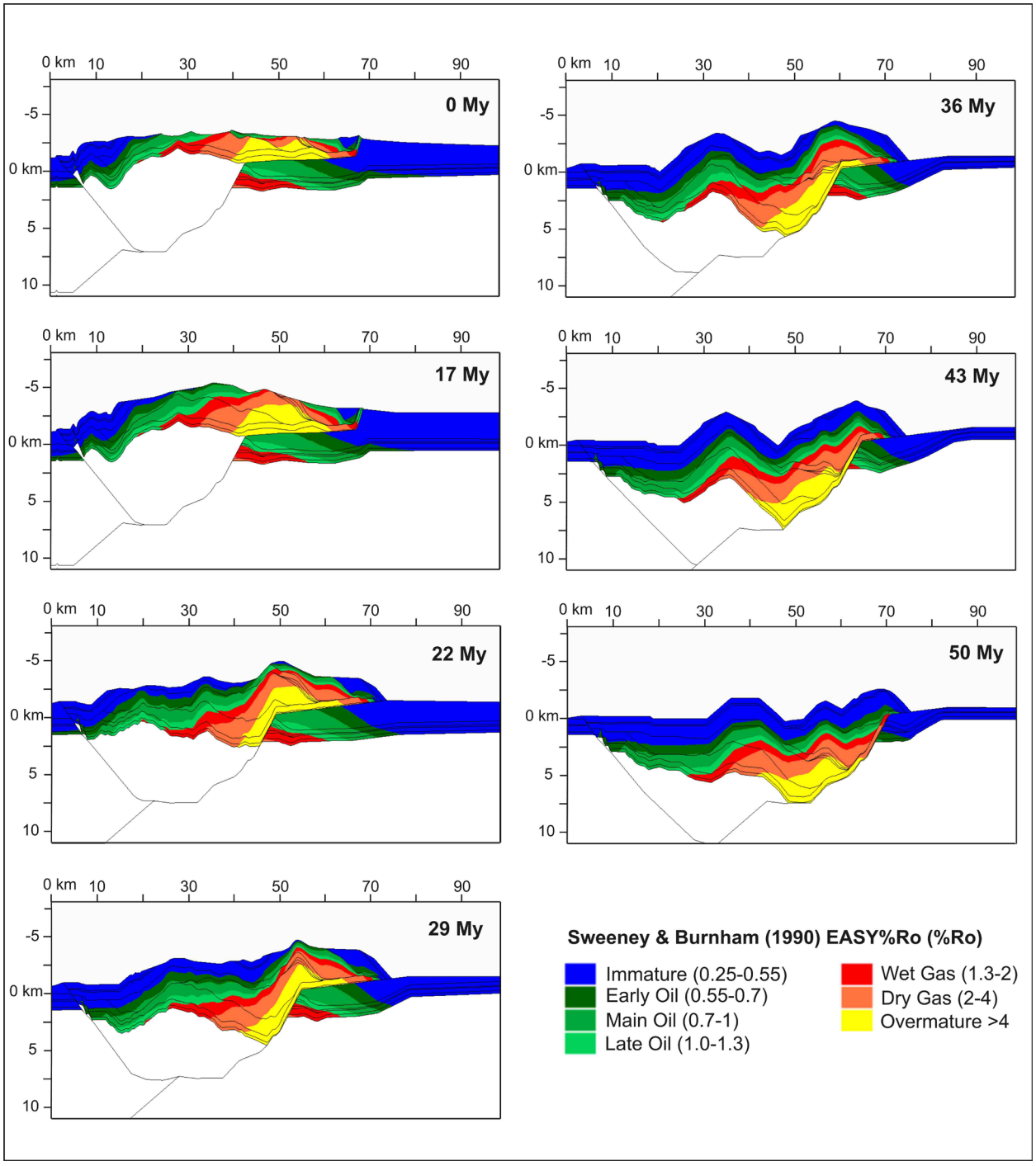

Fig. 12.12 - Thermal maturity calculated by the model for the basin infill and for the northern foreland during the inversion stage

rocks located in the northern sector, with the exception of the shallow layers of the ESR. In the post-extensional stage, in the southern part of the section, the MJSR is transformed at 50% and the kerogen of the ASR is not transformed in the least.

In Model-B some differences in the calculated transformation ratio can be observed (Fig.

12.14). In the early-intermediate phase of the extensional stage (from 142.3 to 121 My) in Model-B (Fig. 12.14) only the kerogen of the deepest layers of the VSR begins to transform, with a TR of 21%, whereas in Model-A (Fig. 12.13) the entire VSR kerogen begins to be transformed at the same time, with slightly higher TR values (30%). By contrast, in the last phase of the extensional stage and in the post-extensional stage (from 108.7 to 85 My) the TR calculated in Model-B (Fig. 12.14) is slightly higher than in Model-A (Fig. 12.13).

In the inversion stage any relevant change in the transformation ratio was determined with respect to the previous stages, as any significant variation in the thermal conditions occurred in this period (Fig. 12.15). Thus, in the inversion stage a similar TR evolution was calculated by the two models.

12.7.3 Migration paths

Model-1 calculated that in the earliest phase of the extensional stage (from 142.3 to 136.7 My) hydrocarbons migration occurred mostly in a vertical direction, throughout the permeable Magaña Fm facies (DS1+2) (Fig. 12.16).

In the intermediate phase of the extensional stage (from 136.7 to 121 My) hydrocarbons generated from the MJSR continued migrating to the top throughout the uppermost units, as well as laterally to the south throughout the sandstone bodies of the DS1+2 (Fig. 12.16). By contrast hydrocarbons generated by the VSR migrated laterally to the north and south, flowing along the stratigraphic contact of the upper and lower units (Fig. 12.16). A reduced migration occurs in the vertical direction, throughout the DS3 unit, due to the low permeability of this unit (Fig. 12.16). A relevant hydrocarbon flow path forms throughout the sandstone dominant Urbión Gr facies, forming the DS4, DS5, DS6 and DS7 units in the central-northern sector of the basin, as consequence of the high permeability and the dip geometry of these units during this phase (Fig. 12.16).

In the latest phase of the extensional stage (from 121 My to 108.7 My) the hydrocarbons generated by the VSR gradually reach the surface throughout the Urbión Gr, whereas the hydrocarbons generated by the ESR migrate to the top along the stratigraphic contact with the DS8 unit (Fig. 12.16). In the northern border of the basin, the hydrocarbons migrate along syn-sedimentary faults (Fig. 12.16), which were active during the deposition of the uppermost depositional sequences (DS7 and DS8) (Suárez-González et al., 2013; Omodeo Salé et al., 2014). In this phase migration begins in the southern part of the section. In the south migration occurs primarily in the vertical direction, throughout the Magaña Fm facies (DS1+2) (Fig. 12.16).

In the post-extensional phase (from 108.7 to 65.5 My) in the central and northern parts of the section the hydrocarbons generated by the VSR, ESR and partially by the MJSR migrate to

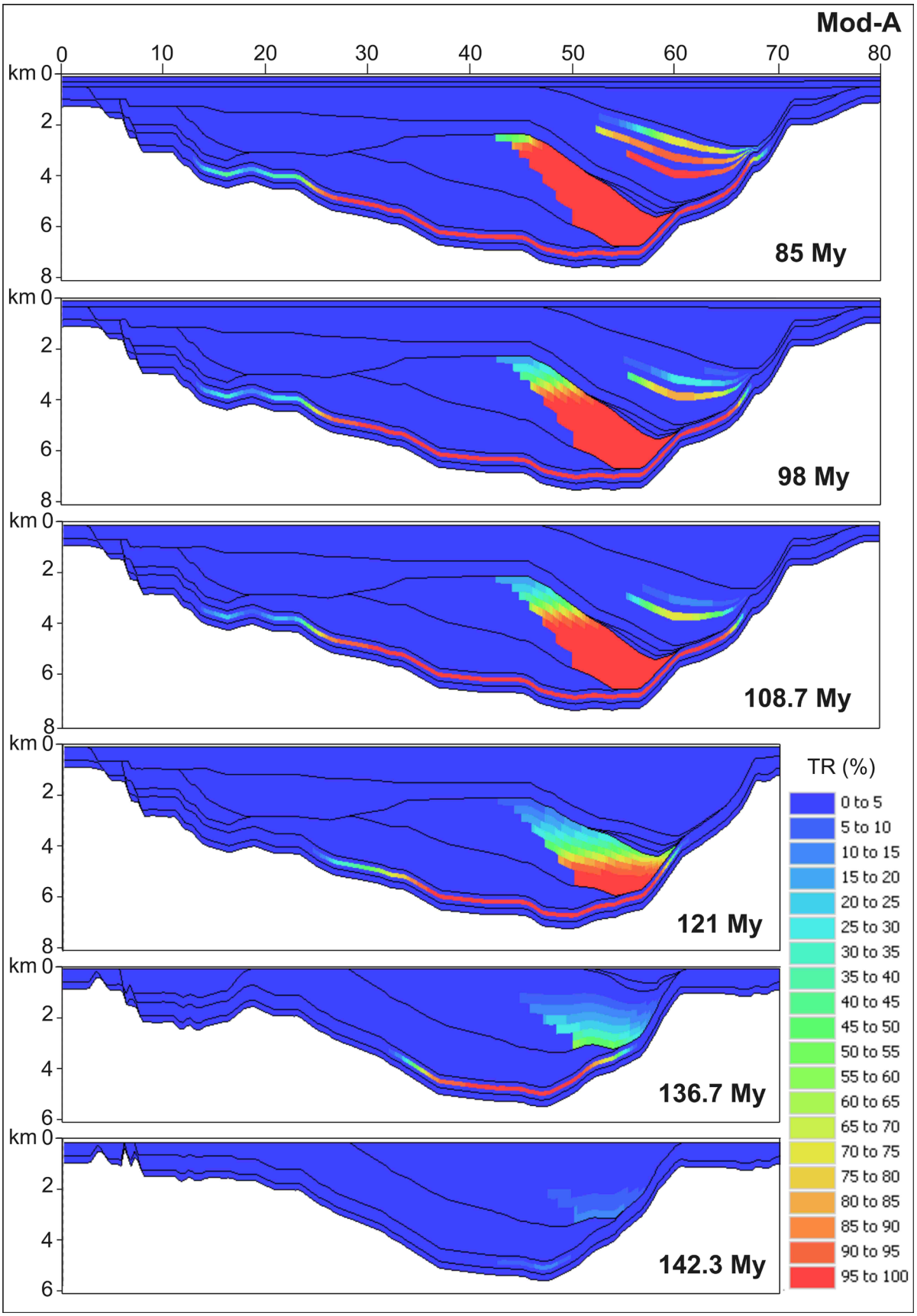

Fig. 12.13 - Transformation ratio (TR%) versus time of the initial kerogen contained in the source rocks of the basin, calculated using Model-A for the syn-extensional and post-extensional stages

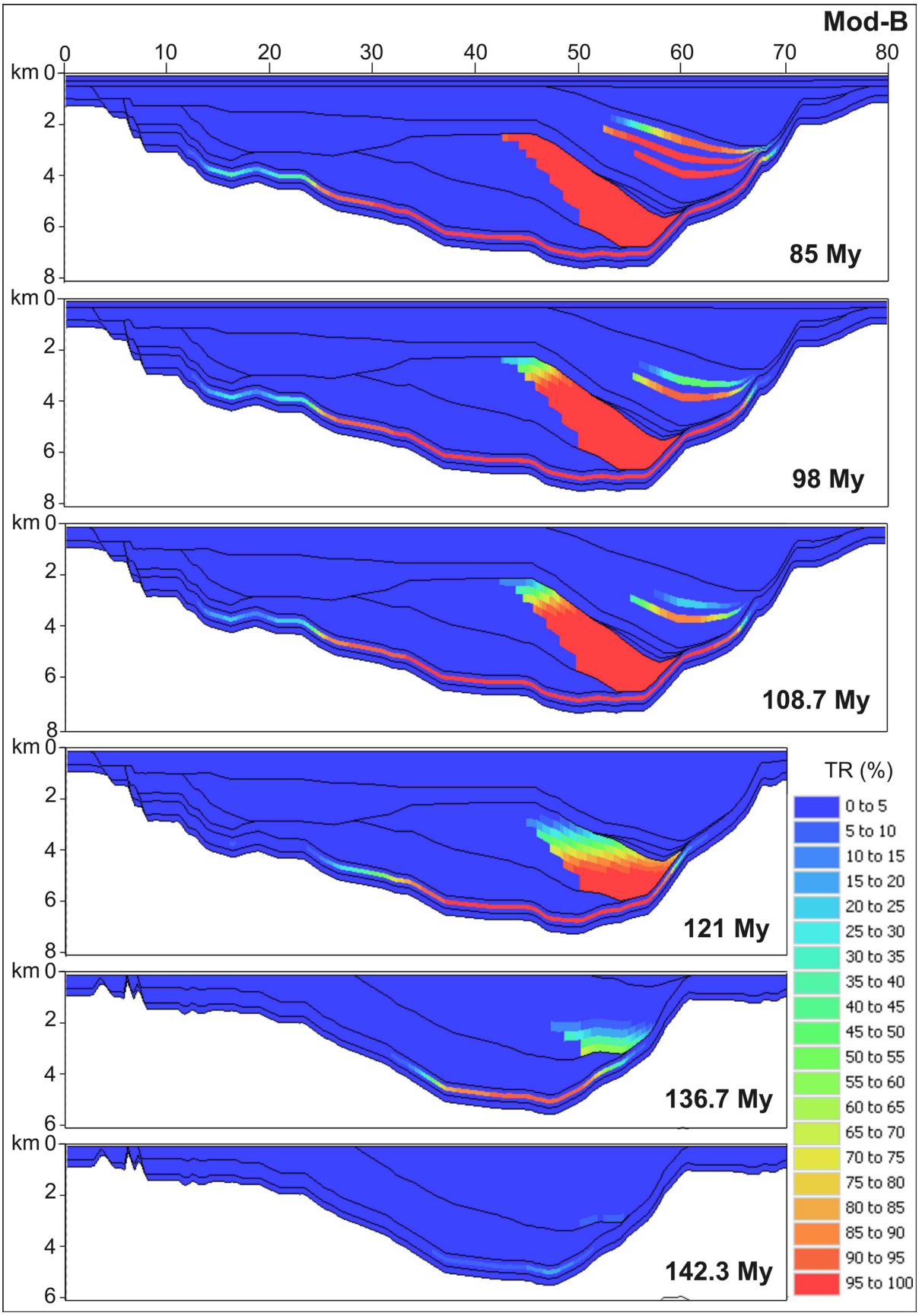

Fig. 12.14 - Transformation ratio (%) versus time of the initial kerogen contained in the source rocks of the basin, calculated using Model-B for the syn-extensional and post-extensional stages

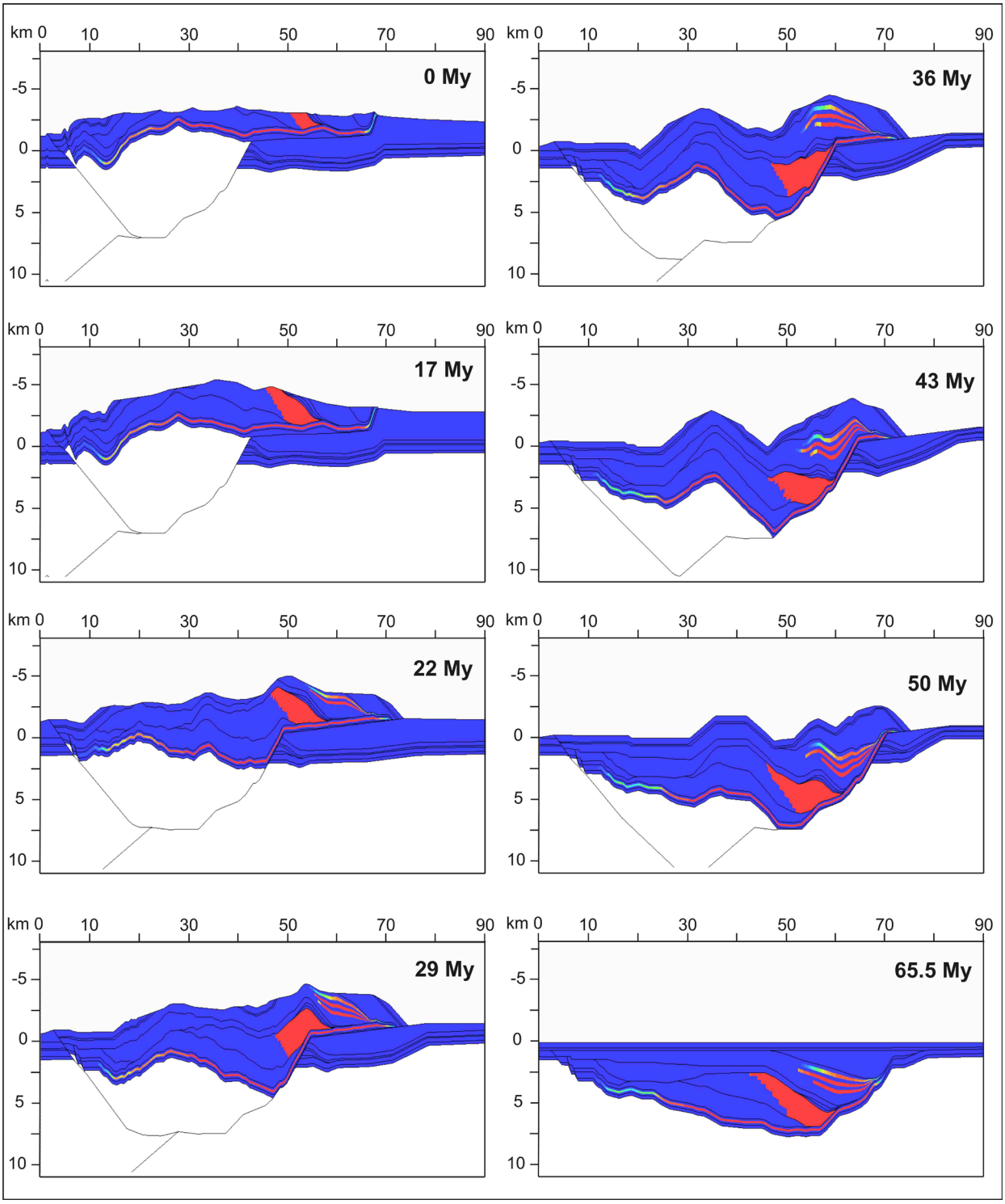

Fig. 12.15 - Transformation ratio (%) versus time of the initial kerogen during the inversion stage calculated using Model-B. For legend, see Fig. 12.12 and Fig. 12.13

the surface throughout the dominant Urbión Gr (DS7) and Oliván Gr (DS8) sandstone facies (Fig. 12.16). In the southern part of the section the hydrocarbons generated by the MJSR migrate to the top throughout the DS1+2, DS5, DS6 and DS7 units, which are formed in this part of the

basin respectively by the Tera Gr, Golmayo Fm, Pantano Fm and Abejar Fm facies (Fig. 12.16).

Until 98 My the hydrocarbons generated in the entire basin were discharged and lost to the surface due to the absence of a seal or trap (Fig. 12.16). At this time, the deposition of the marls-carbonatic Upper Cretaceous unit sealed the system (Mas et al., 1993; Salas et al., 2001). A reservoir formed in the underlying Utrillas Fm sandstone unit, which extends along the whole section (Fig. 12.16). Hydrocarbons continued to migrate in the formed reservoir, especially in the southern sector, where source rocks were still in the oil-window stage.

Model-B calculated the same migration paths as Model-A (Fig. 12.17). However in the initial and intermediate phase of the extensional stage (from 142.3 to 121 My) a slight difference in the timing of hydrocarbon migration between the two models was observed. In fact, the Model-B migration occurred earlier and faster than that in Model-A (Fig. 12.16 and Fig. 12.17). Thus, in Model-B the generated hydrocarbons reached the top surface were discharged earlier than in Model-A.

In Model-B, as compositional kinetics were assigned, the oil and gas migration paths are differentiated (Fig. 12.17). In the central and northern part of the section the hydrocarbons are composed of both oil and gas components, whereas in the southern part of the section the hydrocarbons are mostly oil (Fig. 12.17).

During the inversion stage (from 50 My to 17 My) the generated hydrocarbons continued to migrate to the top. In this phase new migration paths developed, following the new geometries formed as a consequence of the inversion of the basin (Fig. 12.18). In this phase new accumulations developed in structural traps that formed during the inversion of the basin. Small accumulations form even in the northern foreland of the basin (Fig. 12.18). The continuous deformation, uplift and erosion processes that occurred during the inversion, determined that most of the structural traps and related accumulations could not be preserved.

12.7.4 Hydrocarbon generation, accumulation and preservation

The total balance of the hydrocarbons generated, accumulated and lost in the entire evolution of the basin, including the inversion stage, was determined (Fig. 12.19). A similar evolution trend of the petroleum system was determined from the two models. The maximum generation peak is recorded during the syn-extensional phase (145.5 to 108.7 My), whereas in the post-extensional and inversion stages the generation of hydrocarbons continues at a lower and more constant rate (Fig. 12.19). The most relevant accumulations form initially in the post-extensional stage and secondarily in the inversion stage. Accumulations disappear at the end of the inversion (approximately 17 My) (Fig. 12.19). Hydrocarbons were lost during the entire evolution of the basin, with maximum loss peaks occurring initially during the syn-

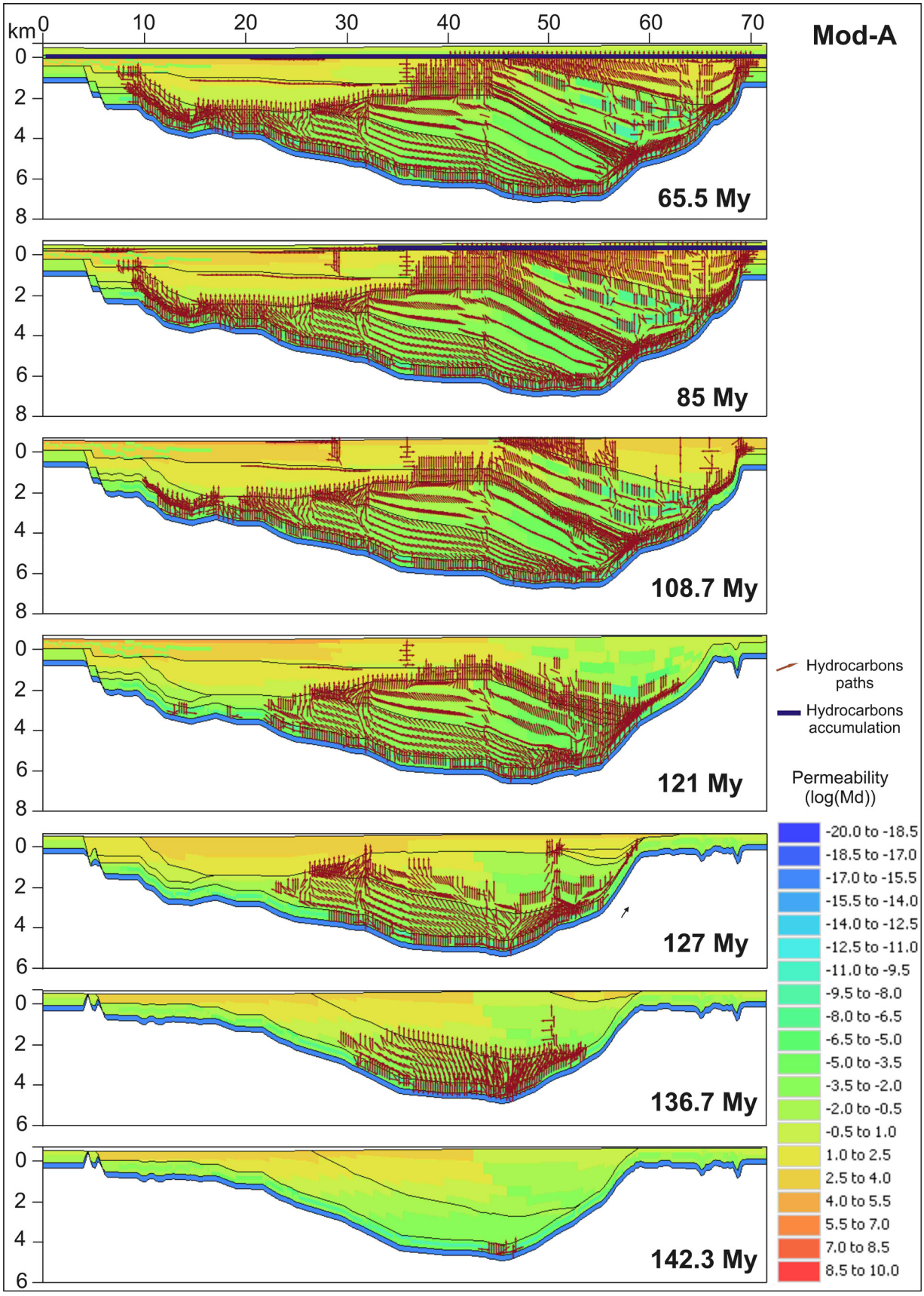

Fig. 12.16 - Hydrocarbon migration paths calculated by Model-A in the syn-extensional and post-extensional stages. Hydrocarbon accumulations formed in these stages are indicated

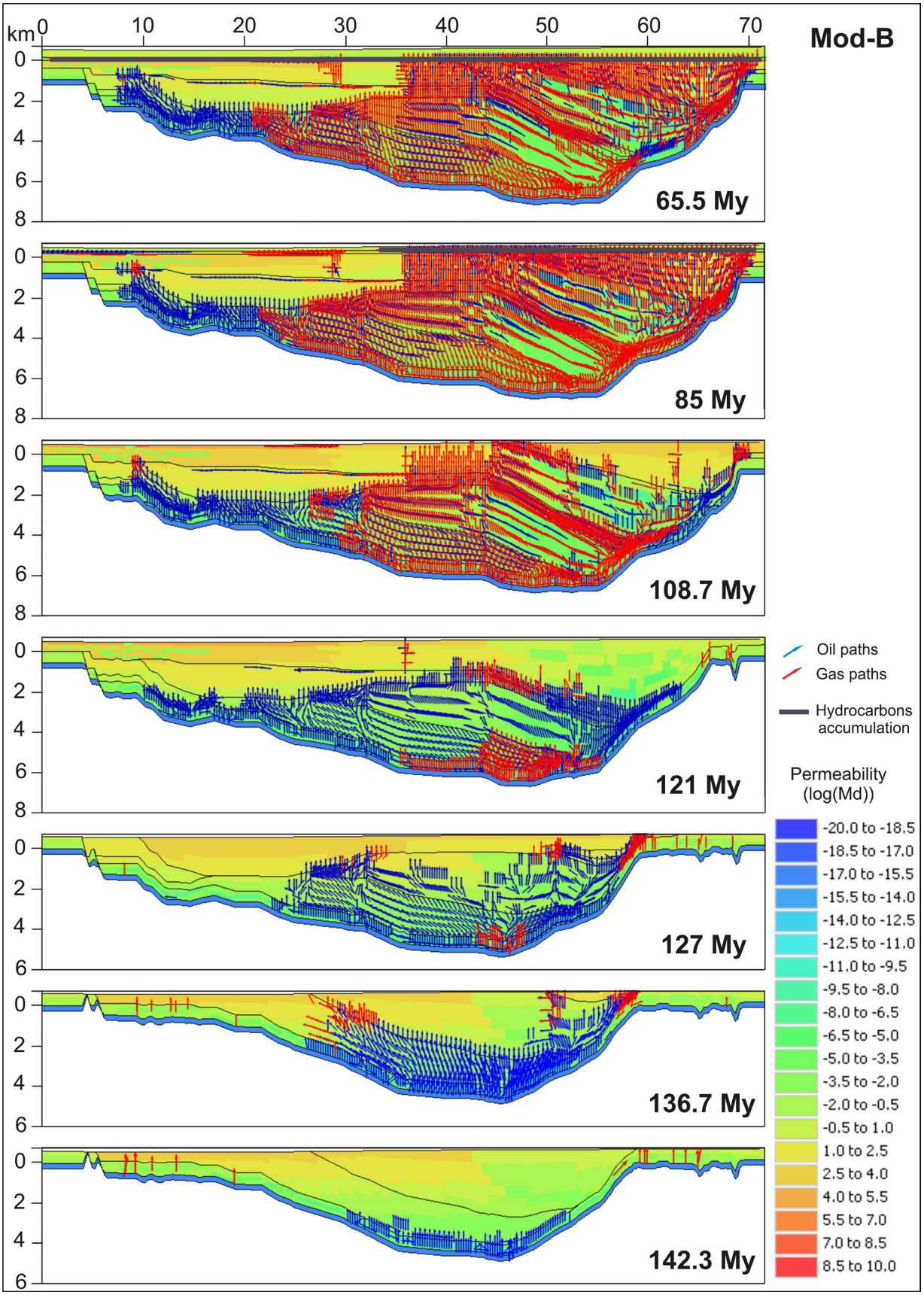

Fig. 12.17 - Hydrocarbon migration paths calculated by Model-B in the syn-extensional and post-extensional stages. Hydrocarbon accumulations formed in these stages are indicated

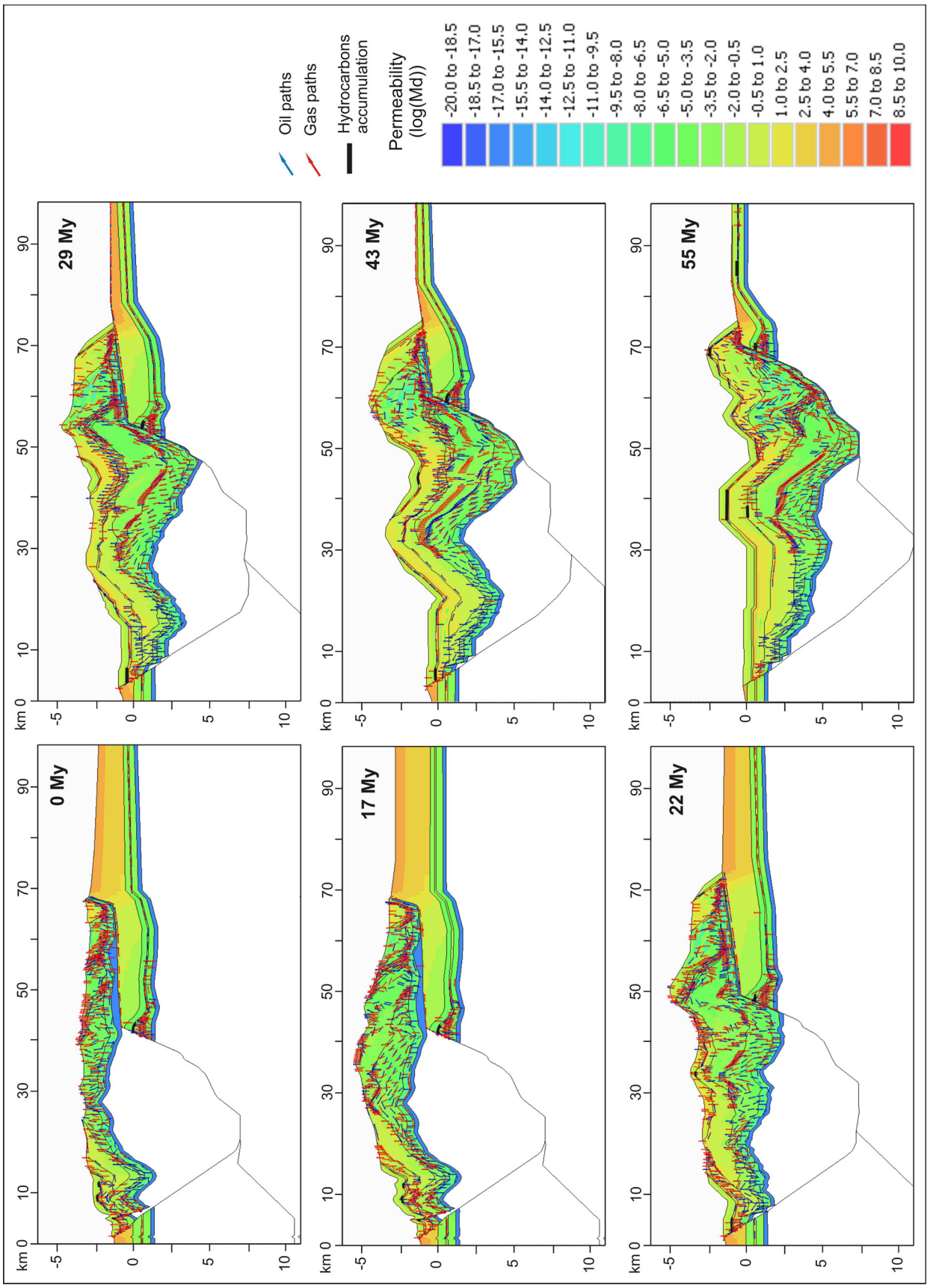
Oil paths
Gas paths
Hydrocarbons accumulation
Permeability (log(Md))
-20.0 to -18.5
-18.5 to -17.0
-17.0 to -15.5
-15.5 to -14.0
-14.0 to -12.5
-12.5 to -11.0
-11.0 to -9.5
-9.5 to -8.0
-8.0 to -6.5
-6.5 to -5.0
-5.0 to -3.5
-3.5 to -2.0
-2.0 to -0.5
-0.5 to 1.0
1.0 to 2.5
2.5 to 4.0
4.0 to 5.5
5.5 to 7.0
7.0 to 8.5
8.5 to 10.0
0 My
17 My
22 My
29 My
43 My
55 My
km 0
10
30
50
70
90
-5
0
5
10

extensional stage and secondarily during the inversion stage (Fig. 12.19). The slight differences in the balance of hydrocarbons generated lost and accumulated versus time were determined by the two models. In Model-A the hydrocarbons begin to be generated earlier than in Model-B (145.5 and 142.3 My respectively) (Fig. 12.19). In Model A, during the syn-extensional and post-extensional stages, a lower amount of hydrocarbons were lost than in Model-B, which signifies that higher accumulations formed in Model-A at these stages (Fig. 12.19). By contrast, during the inversion stage, higher losses are calculated in Mod-A than in the Model-B. Thus, the total balance of hydrocarbons lost and accumulated throughout the entire evolution of the basin is similarly calculated by the two models (Fig. 12.19).

Model-B calculated the timing and amount of oil and gas components generated, accumulated and lost. During the entire period the amount of oil components generated is considerably more relevant that of gas components (Fig. 12.20). The generation of oil components begins at 142.3 My, with a maximum peak from 127 to 121 My (Fig. 12.20). A secondary peak is recorded between 121 and 108.7 My. The generation of oil components decreases from 108.7 to 85 My, whereas it becomes constant from 85 to 22 My. In the last phase of the basin evolution (from 22 My to 0 My) a new low peak of oil component generation is recorded (Fig. 12.20). Gas components are generated from 127 My until 85 My (Fig. 12.20). Two gas generation peaks are considered, the first from 127 to 108.7 My and the second from 98 to 85 My (Fig. 12.20).

The hydrocarbon generation balance for each of the source rocks is reconstructed in Fig. 12.21. From this graph is evident that the VSR is the source rock that primarily contributes to the generation of hydrocarbons in the basin, followed by the MJSR and finally by the ESR. The ASR does not generate hydrocarbons during the entire evolution of the basin. The hydrocarbon generation trend of the VSR is very similar to the total generation trend previously described (with a maximum generation peak between 127 and 108.7 My). By contrast, the MJSR and ESR generated hydrocarbons at a constant rate during the entire evolution of the basin. In the inversion stage a slight increase in the generation of hydrocarbons for the MJSR is determined. The ASR does not generate any amount of hydrocarbons during the entire evolution of the basin.

The first small accumulations, of oil components, are formed from 121 to 108.7 My (Fig. 12.22), in stratigraphic traps formed in the Urbión Gr (DS6 and DS7). From 98 to 85 My, in the Utrillas Fm unit, the most relevant hydrocarbon accumulation of the basin is formed (Fig. 12.22a), comprised mostly of gas components (Fig. 12.22b and Fig. 12.23).

Accumulations are preserved until 50 My, when the inversion process begins and

Fig. 12.18 - Hydrocarbon migration paths formed during the inversion stage, calculated by Model-B. Accumulations formed during the inversion are indicated

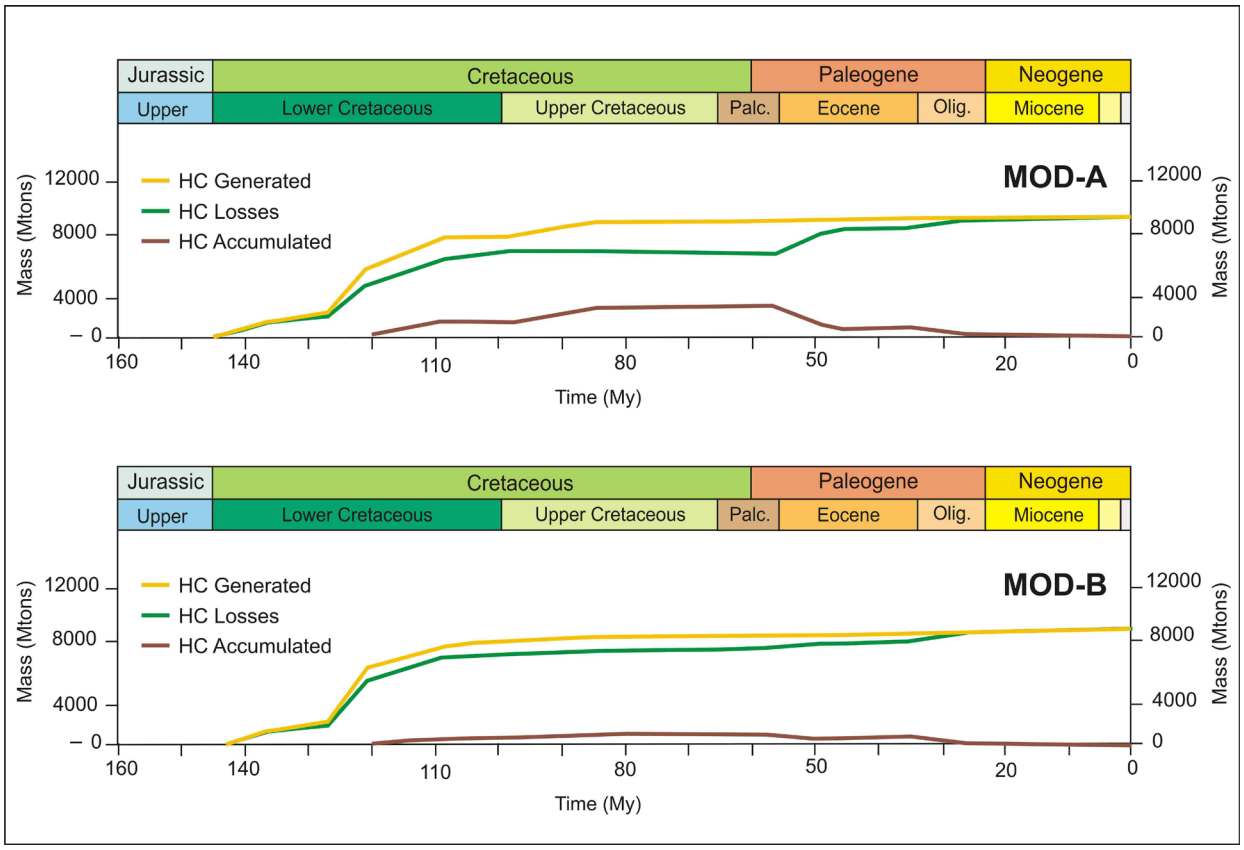

Fig. 12.19 - Balance of the hydrocarbons generated, accumulated and lost versus time, as calculated by Model-A and Model-B, for the entire basin's evolution

hydrocarbon accumulations are gradually lost. During the inversion, especially from 50 to 36 My, new hydrocarbon accumulations formed in the Utrillas Fm as well as in the Urbión Gr (DS7). The accumulations formed during the inversion are mostly formed by gas, with the exception of the last inversion stages in which they are mostly formed by oil (Fig. 12.23).

Hydrocarbons are lost from the very beginning of the generation process (Fig. 12.19 and Fig. 12.24), due to the absence of relevant seals or traps. The loss of oil components is considerably more relevant than that of gas components during the whole petroleum system evolution (Fig. 12.24). The first peak of hydrocarbon losses peak (from 127 to 108.7 My) is primarily of oil components, whereas the second peak (from 55 to 29 My) is mostly represented by gas component losses (Fig. 12.24). From 108.7 My the loss rate of oil components remains constant, whereas the losses of gas components increases at a constant rate over the entire evolution of the basin (Fig. 12.24). Hydrocarbons are primarily lost throughout the DS3 unit in the first phase of the syn-extensional stage, throughout the DS7 in the remainder of the syn-extensional stage and partially during the inversion and throughout most of the Utrillas Fm during the inversion stage (Fig. 12.25).

A synthetic quantitative balance of the amount of hydrocarbons generated, accumulated and lost before the inversion stage is presented in Table 12.8. Despite the slight differences calculated by the two models for hydrocarbons lost and accumulated, observable in Fig. 12.19, the total balance of hydrocarbons generated, accumulated and lost as calculated by the two models is considered to be similar (Table 12.8). In Model-A the report calculated that:

1) the VSR generates 83% of the total amount of hydrocarbons generated in the basin, whereas

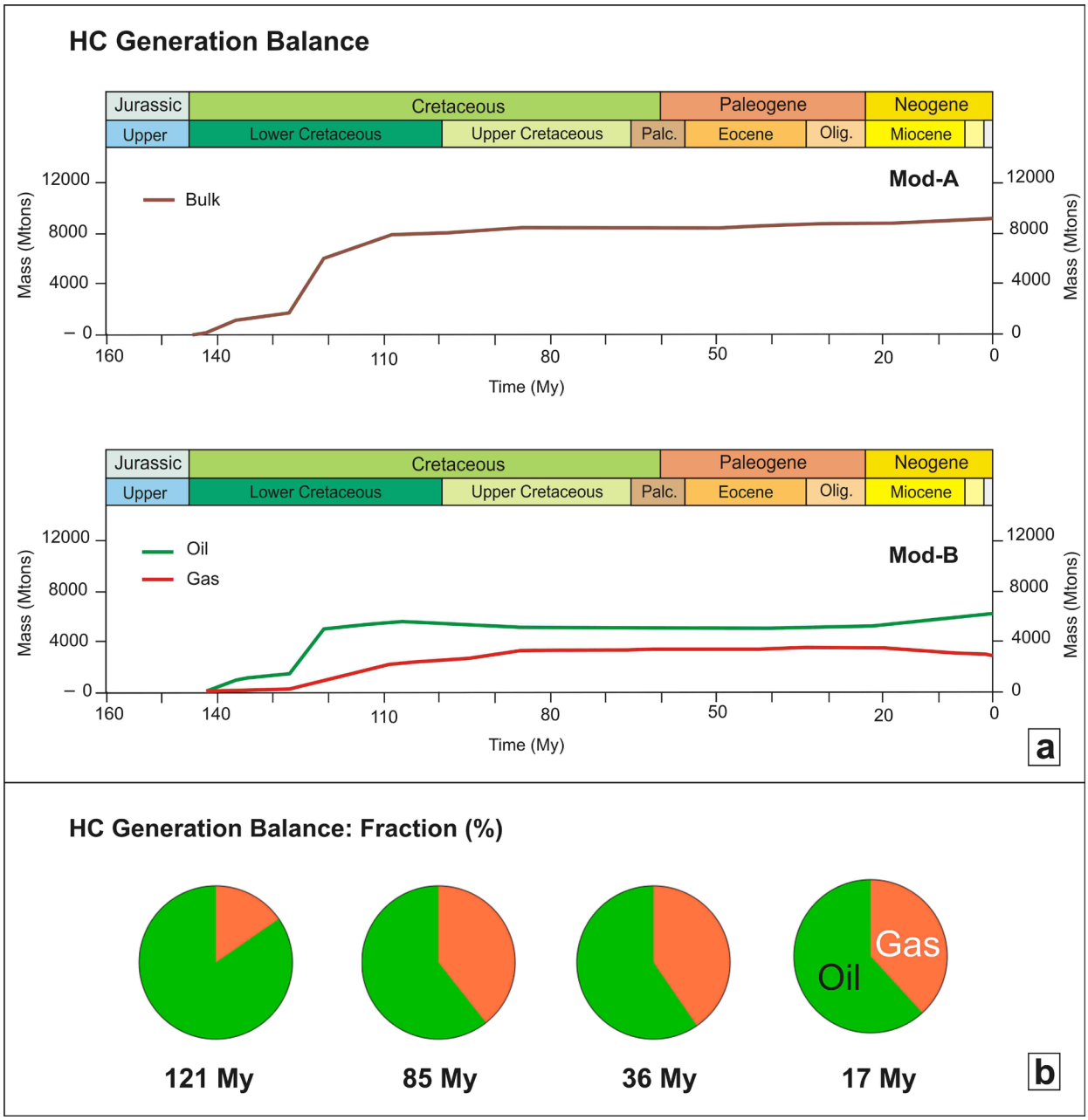

Fig. 12.20 - (a) Hydrocarbon generation balance versus time calculated by Model-A and Model-B. In Model-B the balance of the oil and gas component generated is determined. (b) Proportion of oil and gas components generated in four instants of the petroleum system evolution, calculated by Model-B

the MJSR generates 14% and the ESR generates 3%;

2) 99.9% of the hydrocarbons generated are expelled, whereas only 0.1% accumulate in the source rock;

3) only 0.22% of the expelled hydrocarbons accumulated in the reservoir, whereas the remainder are lost;

4) most of the hydrocarbon losses are expelled on the surface throughout the DS7, Utrillas Fm and DS3 units (respectively 51%, 2% and 10% of the total hydrocarbons losses);

5) for the present day, the model reconstructs the accumulation of 20.71 Mtons of hydrocarbons, which are primarily located in the Utrillas Fm unit.

In Model-B very similar results were calculated:

1) the VSR generates 83% of the total amount of hydrocarbons generated in the basin, whereas the MJSR generates 14% and the ESR generates 3%;

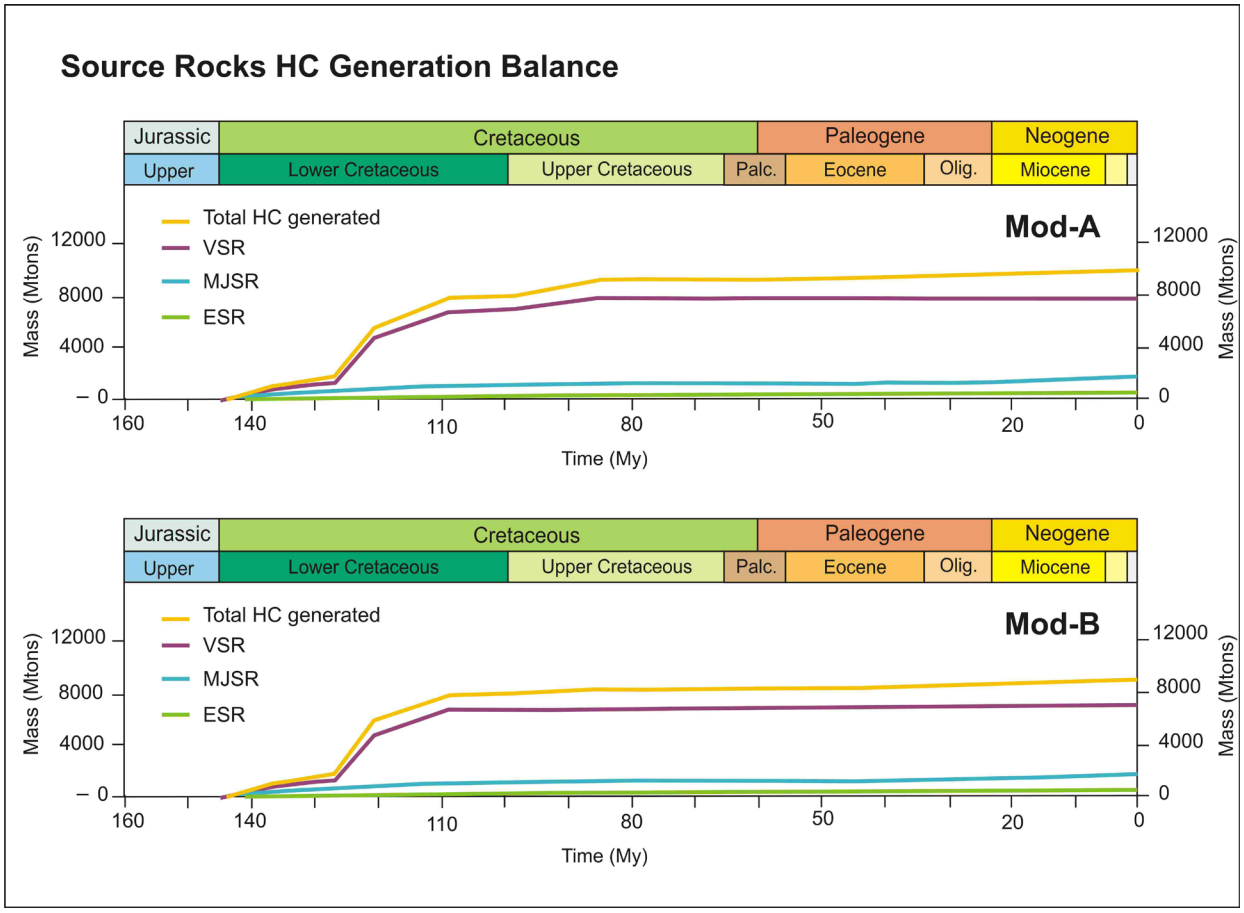

Fig. 12.21 - Hydrocarbon oil and gas components generation balance, calculated by Model-A and Model-B for the ESR, VSR and MJSR source rocks

2) 99.9% of the hydrocarbons generated are expelled, whereas only 0.1% accumulate in the source rock;

3) only 0.01% of the expelled hydrocarbons accumulate in the reservoir, whereas the remainder are lost;

4) most of the hydrocarbon losses are expelled on the top surface throughout the DS7, DS3, Utrillas Fm and Upper Cretaceous units (respectively 72%, 7%, 7% and 4% of the total

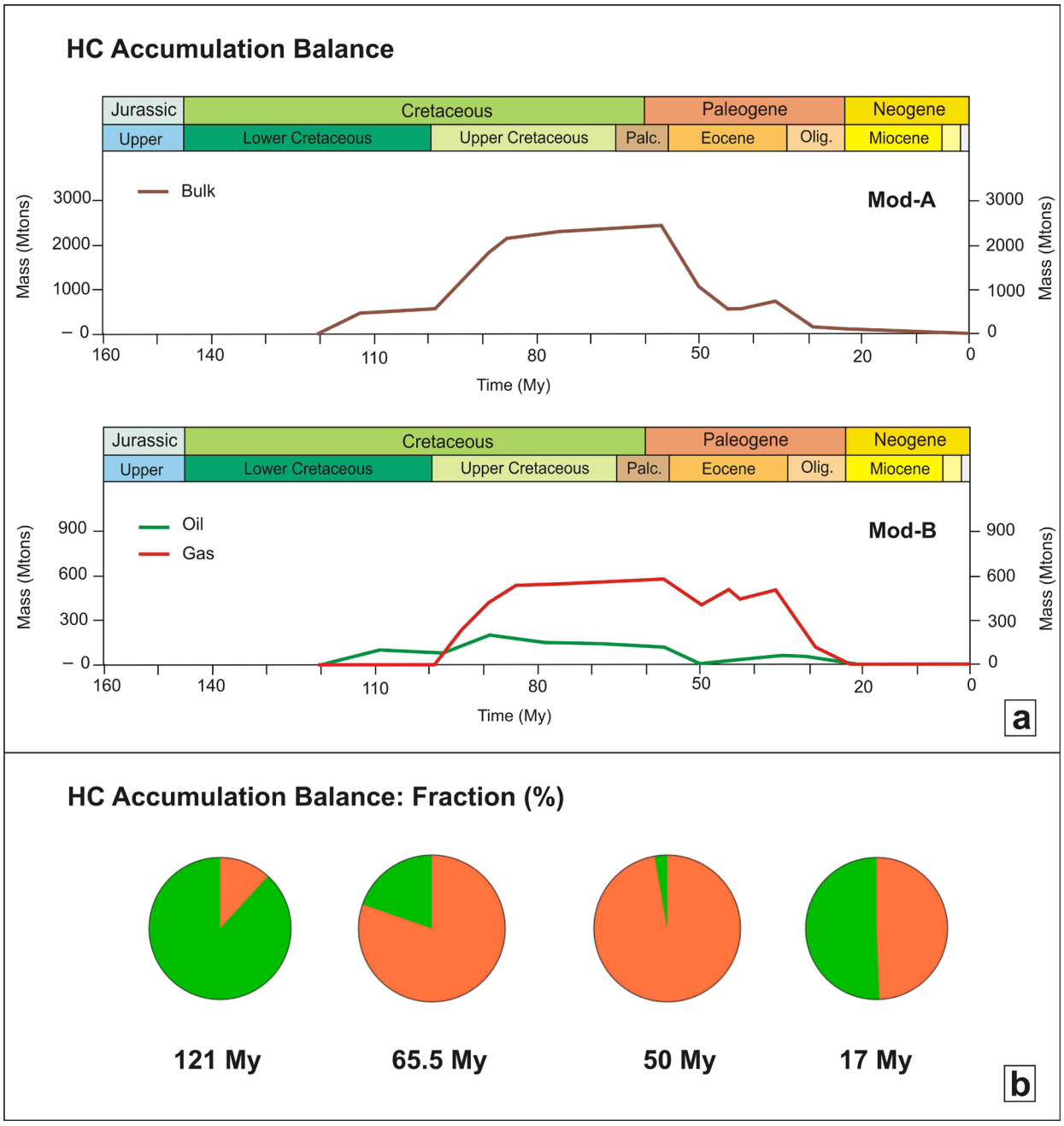

Fig. 12.22 - (a) Hydrocarbons accumulated during the evolution of the basin reconstructed by Model-A and Model-B. In Model-B the amount of oil and gas components accumulated is indicated. (b) Proportion of oil and gas components accumulated in four instants of the petroleum system evolution

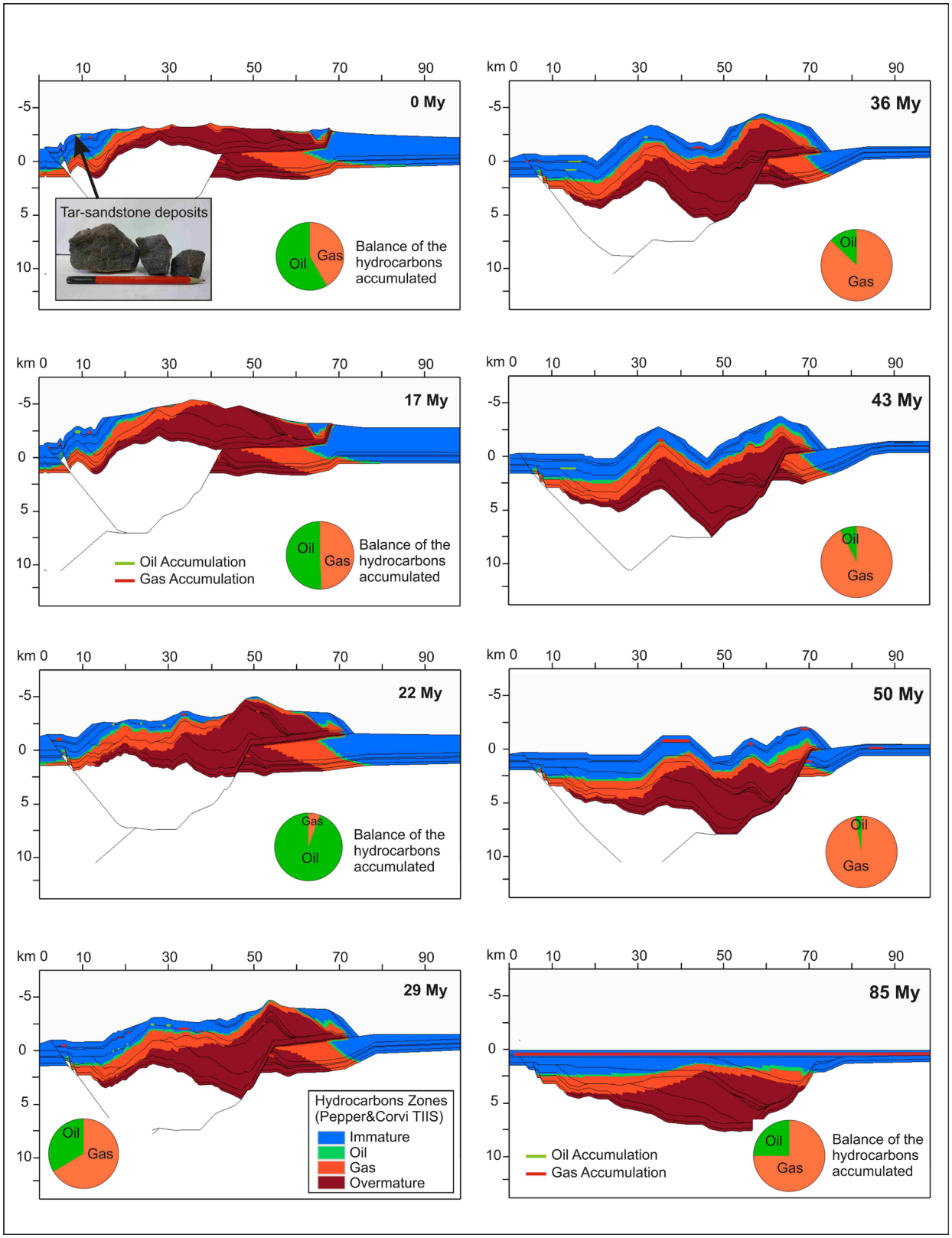

Fig. 12.23 - Hydrocarbon accumulations formed during the inversion stage and balance of the oil and gas components accumulated in each step (Model-B). The hydrocarbon zones determined by the Pepper and Corvi TII-S kinetic are indicated

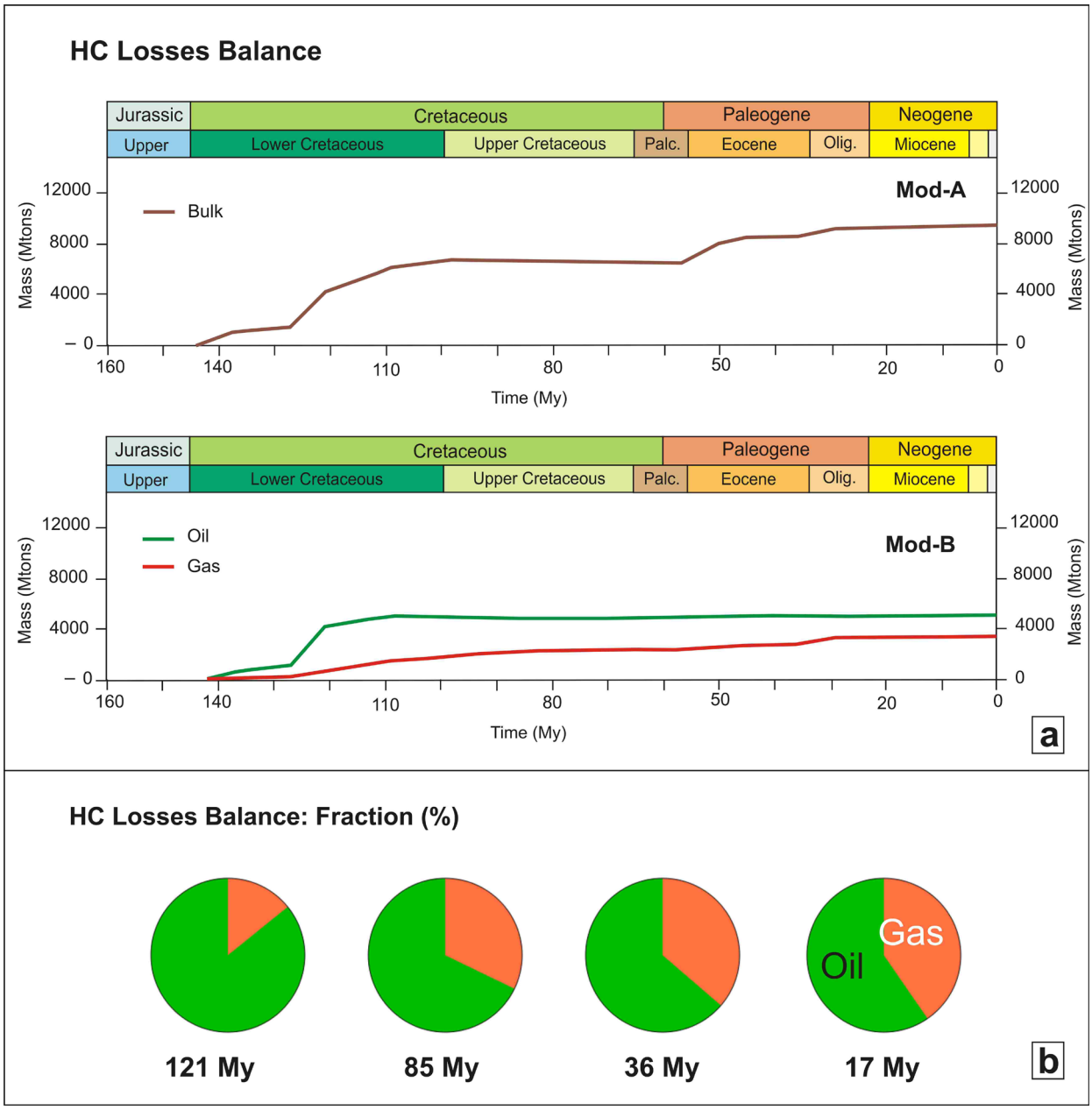

Fig. 12.24 - (a) Hydrocarbon losses during the evolution of the basin, reconstructed by Model-A and Model-B. In Model-B the balance of oil and gas component losses is determined. (b) Proportion of oil and gas component losses in four instants of the petroleum system evolution

hydrocarbon losses);

5) for the present day, the model reconstructs the accumulation of 1.61 Mtons of hydrocarbons.

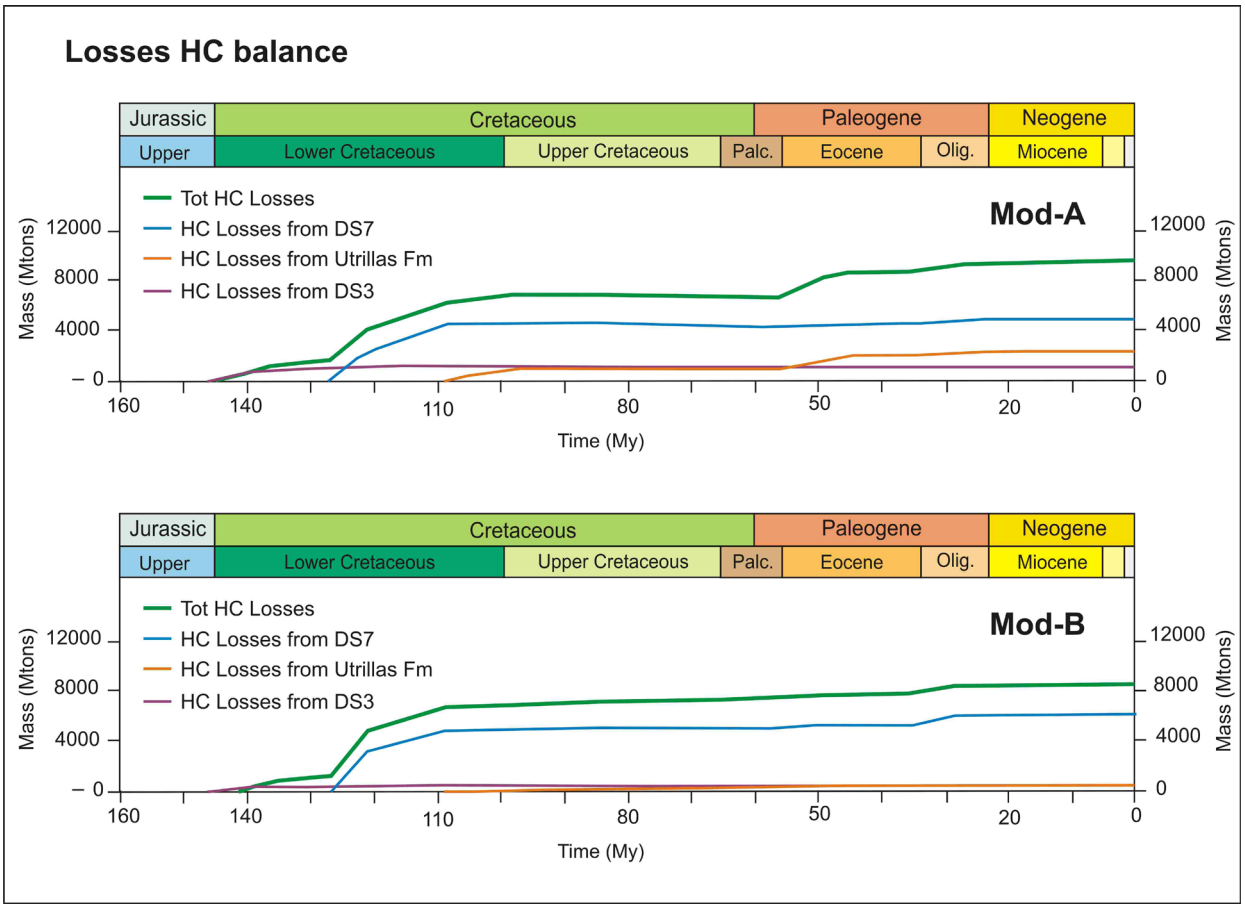

Fig. 12.25 - Balance of the hydrocarbon losses during the entire evolution of the basin. The most relevant units from which hydrocarbons flowed out are reported

12.8. DISCUSSION

12.8.1. Comparison between the two kinetic models

The source rocks' thermal maturity, transformation ratio and the amount and timing of the hydrocarbon generation, accumulation and losses are very similar as calculated by the two models (Table 12.8). However, slight differences were observed for the pre-extensional and post-extensional stages in 1) the TR timing of the VSR and ESR in the early phase of the extensional stage and in the latest phase (Fig. 12.13 and Fig. 12.14); 2) the migration velocity in the first phases of the extensional stage (Fig. 12.16 and Fig. 12.17); 3) the starting time of the hydrocarbon generation (Fig. 12.19); and 4) the balance of the hydrocarbons lost and accumulated (Fig. 12.19).

Differences in the timing of TR between the two models can be explained by the difference in the distribution of activation energies between the bulk and compositional kinetics that were assigned (Fig. 12.10). For the lower transformation ratio of the kerogen (TR<50%) the activation

Mod-A	Remaining Potential	Generation Balance	Accumulated in Source	Expulsion Balance	Accumulated in Reservoir	HC Losses Balance	Migration Balance
	882.97	9370.07	2.99	9367.08	20.71	9346.37	-9174.55
Cenozoic	0	0	0	0	0	250.11	0.75
Upper Cret.	0	0	0	0	0	210.46	0.91
Utrillas	0	0	0	0	20.15	2240.28	20.15
DS8	0	0	0	0	0	199.05	29.18
DS7	67.02	270.49	0.57	269.91	0.55	4811.94	-236.81
DS6	0	0	0	0	0.01	113.64	0.16
DS5	0	0	0	0	0	115.18	5.14
DS4	0	0	0	0	0	345.72	0.35
DS3	491.4	7822.17	0.77	7821.4	0	912.19	-7819.78
DS1+2	0	0	0	0	0	39.26	7.95
Jurassic	324.56	1277.42	1.64	1275.77	0	108.53	-1182.55

Mod-B	Remaining Potential	Generation Balance	Accumulated in Source	Expulsion Balance	Accumulated in Reservoir	HC Losses Balance	Migration Balance
	883.48	9097.24	2.16	9095.08	1.61	8698.72	-8625.38
Cenozoic	0	0	0	0	0	18.44	0
Upper Cret.	0	0	0	0	0	350.41	0
Utrillas	0	-0.01	0	-0.01	0.98	596.52	0.99
DS8	0	-0.2	0	-0.2	0	42.86	0.36
DS7	66.91	275.86	0.54	275.32	0.59	6259.83	-198.5
DS6	0	-7.55	0	-7.55	0.05	136.81	67.51
DS5	0	-5.84	0	-5.84	0	165.15	23.43
DS4	0	-3.88	0	-3.88	0	389.68	13.54
DS3	503.18	7598.73	0.23	7598.5	0	639.49	-7331.49
DS1+2	0	-9.26	0	-9.26	0	49.45	14.35
Jurassic	313.39	1249.38	1.4	1247.99	0	50.07	-1215.57

Table 12.8 - Report of the hydrocarbons generated, migrated and accumulated as calculated by Model-A and Model-B at 0 My

energies of both the CAS-2 and STFC-4b bulk kinetics, which were assigned in Model-A to the VSR and ESR, respectively, are lower than the correspondent compositional kinetics assigned in Model-B (Type IIS and Type I of Pepper and Corvi, 1994). Thus, it is reasoned that at lower temperatures in Model-A the kerogen began to transform earlier than in Model-B (Fig. 12.10) and consequently, in Model-A the hydrocarbons were generated earlier (145.5 My) than in Model-B (142.3 My) (Fig. 12.13 and Fig. 12.14). By contrast, for the higher transformation ratio (TR>80%) the activation energies of the bulk kinetics (Model-A) are higher than the activation energies of the correspondent compositional kinetics (Model-B). Thus, it is reasoned that in Model-A the kerogen needs a higher temperature than in Model-B to be completely transformed.

In the first phase of the extensional stage a higher amount of hydrocarbon loss is calculated

in Model-B than in Model-A (Fig. 12.19). This difference may be related to the different types of hydrocarbon components generated by the two models, which can have different migration velocities. In fact, comparing Fig. 12.16 with Fig. 12.17 it is clear that in the first phases of the extensional stage the hydrocarbons generated in Model-B migrate more quickly to the top than in Model-A. Thus, in Model-B a higher amount of hydrocarbons flowed out to the surface and were lost than was the case in Model-A. As a consequence of this different trend, in Model-A, during the syn-extensional and post-extensional stage, a higher amount of hydrocarbons accumulated than in Model-B (Fig. 12.19). By contrast, when the basin is uplifted and eroded (inversion stage) the hydrocarbon losses are more relevant in Model-A than in Model-B, as a lower amount of hydrocarbons in the latter model were accumulated in the previous stages (Fig. 12.19).

It can be summarised that despite these differences a similar reconstruction of the evolution of the Cameros Basin petroleum system was performed by the two models (Fig. 12.19 and Table 12.8). Thus, the chosen compositional kinetics results in an appropriate simulation of the thermal kerogen behaviour of the Cameros Basin's kerogen. The hydrocarbons' oil and gas components generation, accumulation and preservation timing and trends, as determined by the Model-B, may be considered reliable for the Cameros Basin petroleum system.

12.8.2. Source rocks thermal maturity and kerogen transformation

A different thermal history was recorded in the northern and southern areas of the basin due to a different burial rate (higher in the north and lower in the south). Differences in the thermal conditions recorded in the in the northern sector and in part of the central sector of the basin were stressed by the circulation of hydrothermal hot fluids during the post-extensional and inversion stages (Casquet et al. 1992; Alonso-Azcárate et al. 1995; Barrenechea et al. 1995, 2001; Mantilla-Figueroa et al. 1998, 1999; Alonso-Azcárate et al. 1999; Mas et al. 2003, Ochoa et al., 2007; González-Acebrón et al., 2011, 2012) (**Chapter 9 and Chapter 10**). Thus, the timing and rate of the source rocks maturity change along the modelled section.

In the central and northern part of the section the source rocks (MJSR, VSR and ESR) reach dry gas-window to overmatured thermal conditions, whereas the source rocks located in the southern part (MJSR and ASR) reach oil-window to immature thermal conditions (Fig. 12.11). These results are confirmed by the vitrinite reflectance measured for these deposits (Table 12.2). The different thermal history is reflected in the TR of the source rocks' kerogen. At the end of the post-extensional stage most of the kerogen of the source rocks located in the northern sector was completely transformed (Fig. 12.13 and Fig. 12.14) as a consequence of both burial and hot fluid circulation processes. The model is constructed such that at the end of the syn-extensional stage the kerogen of the MJSR, part of the VSR and the deepest layers of the ESR were already partially transformed, as a consequence of burial. Subsequently, in the post-extensional stage, the most

relevant hydrothermal metamorphic event, which affected the northern sector of the basin at 85 My, completely transformed all the kerogen of the source rocks located in this sector (Fig. 12.13 and Fig. 12.14). These results are confirmed by the petrographical and geochemical analyses of the MJSR, VSR and ESR, which determine for these source rocks a very scarce amount of organic matter, mostly formed by residual kerogen (Fig. 12.26d) and solid bitumen particles (Fig. 12.26e and Fig. 12.26f), which in some cases is altered by the hydrothermalism (Fig. 12.26f). The model did not reconstruct a complete transformation of the kerogen in the uppermost layers of the ESR, as it cannot completely simulate high temperatures at a shallow depth (see **Chapter 9**). However, the high vitrinite reflectance measured in these layers and the very limited organic matter content suggests that even most of the kerogen of the ESR was completely transformed as a consequence of the circulation of the hot hydrothermal fluids. In the southern sector of the basin, at the end of the post-extensional stage, only 50% of the kerogen of the MJSR was transformed, whereas the kerogen of the ASR was not transformed (Fig. 12.13 and Fig. 12.14). Coherently, petrographical and geochemical analyses indicate in the ASR the presence of very abundant and immature organic matter.

Summarising, in the entire basin burial was the first cause of kerogen maturation, whereas the occurrence of metamorphism determines the transformation of the kerogen primarily for the shallowest source rock layers located in the northern sector of the basin. No evidence was found to support the hypothesis that the occurrence of the hydrothermal metamorphic events determines a relevant hydrocarbon generation event in the Cameros Basin during the post-extensional stage (Mas et al., 2003). The thermal maturity and, consequently, even the transformation ratio of the basin infill deposits was completely recorded during the basin formation (syn-extensional and post-extensional stages), whereas it was not relevantly affected by the basin inversion process (Fig. 12.15).

12.8.3. Hydrocarbon generation

The models determined that the maximum generation peak was recorded during the syn-extensional stage, whereas only a small amount of hydrocarbons were generated during the inversion (Fig. 12.19 and Fig. 12.20). Hydrocarbons were generated in the basin by the MJSR, VSR and ESR, whereas the ASR did not generate any hydrocarbons. Hydrocarbon generation in the MJSR, VSR and ESR is confirmed by petrography, as numerous rests of solid bitumen particles were found in their deposits (Fig.12.26c, e and f). During the syn-extensional and post-extensional stage the VSR is the source rock of the basin that mostly contributes to the generation of hydrocarbons (83%), followed by the MJSR (14%) and lastly by the ESR (3%) (Fig. 12.21 and Table 12.8). These results can be explained considering the type of organic matter and total thickness of the deposits forming these source rocks. The VSR was originally formed by a very high content

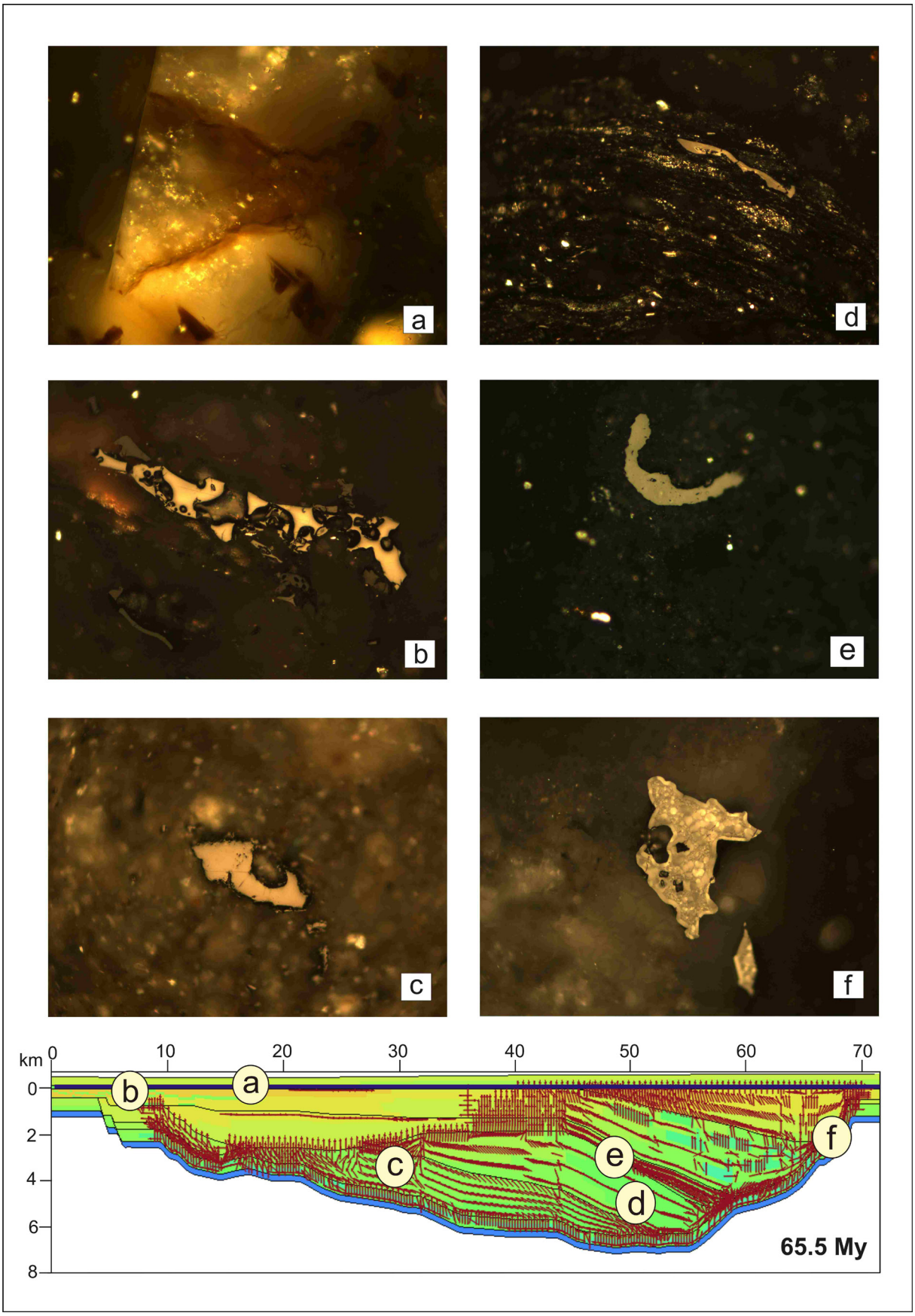
a
d
b
e
c
f
km
0
10
20
30
40
50
60
70
0
2
4
6
8
b
a
c
e
d
f
65.5 My

of organic matter (estimated TOC of 17%), constituted by high-hydrogenated lacustrine kerogen (estimated HI of 695 mg/g TOC), such as algae (Table 12.7). Thus, considering the excellent type of organic matter and the relevant thickness of the VSR deposits (more than 1500 m) (**Chapter 7**), it is reasonable to assume that a large amount of hydrocarbons were produced by this source rock. The irrelevant amount of hydrocarbons produced by the ESR (Fig. 12.21) is coherent with the original low organic carbon content estimated for these deposits (estimated TOC of 2.8%) and with their original type of organic matter - low-hydrogenated, mostly terrestrial kerogen (estimated HI of 168 mgHC/g TOC) (Table 12.7). By contrast, in the case of the MJSR, despite the high content of organic carbon (estimated TOC of 10%) and the high-hydrogenated organic matter (estimated IH of 710 mgHC/g TOC) (Table 12.7), the thickness of the related deposits was much reduced (maximum 150 m). Thus, the low amount of hydrocarbons was produced by this source rock. However, the MJSR located in the southern sector of the basin continued to generate hydrocarbons even in the inversion stage (Fig. 12.21). In fact, at the end of the post extensional stage the kerogen of the MJSR located in the south of the basin was not completely transformed (Fig. 12.15); thus, it could continue to generate hydrocarbons even during the inversion. By contrast, the kerogens of the VSR and ESR source rocks and of the MJSR, located in the northern part of the basin, were already completely transformed at the end of the post-extensional stage, (Fig. 12.13 and Fig. 12.14); thus, the very limited amount of hydrocarbons may have been generated by these source rocks during the inversion.

The prevalence of the generation of oil components over gas components (Fig. 12.20) can be explained by the type of kerogen forming the source rocks. In fact, both the Type II kerogen forming the MJSR and the Type I kerogen forming the VSR can be considered primarily oil-prone (Peters and Cassa, 1994). By contrast, the Type III-I kerogen forming the ESR can be considered primarily gas-prone (Peters and Cassa, 1994). Taking into account the scarce amount of hydrocarbons generated by this source rock (3% of the total), no relevant change in the total oil/gas balance was determined by these data.

The generation of hydrocarbons began in the Early Berriasian (from 145.5 to 142.3 My) when the MJSR and VSR entered the oil-window by burial, a consequence of the deposition of the

Fig. 12.26 - Petrographic observations confirm model results. (a) Tar sandstone reservoir (Utrillas Fm). Hydrocarbons are impregnated in the mineral fractures and veins; (b) Solid bitumens (high reflectance particles), rounding vitrinite particles, found in the DS7 (Abejar Fm) deposits; (c) Solid bitumen particles, rounding mineral borders, found in the DS1+2 (Tera Gr) deposits; (d) Remainder of the organic matter found in the deposits where the original kerogen was completely thermally transformed (DS3 - Valdeprado Fm deposits); (e) Solid bitumens particles found in the DS3 (Valdeprado Fm) deposits; (f) Mesophases formed in bitumen particles as a consequence of heating to elevated temperatures, found in the DS7 (Enciso Gr - Leza Fm) deposits

DS1+2 and DS3 units (Fig. 12.11, Fig. 12.13, Fig. 12.14 and Fig. 12.20). The maximum generation peak was reached in the Late Barremian – Early Aptian (from127 to 121 My), a consequence of the deposition of the very thick DS7 unit, which considerably increases the burial depth and thermal maturation of the VSR and MJSR (Fig. 12.11 and Fig. 12.20). At this time even gas begins to be generated from the VSR (Fig. 12.21). The deposition of the thick DS8 unit in the Late Aptian – Early Albian (from 121 to 108.7 My) caused the maturation of the ESR to oil-window thermal conditions and another important generation peak from the VSR (Fig. 12.11 and Fig. 12.21). From 108.7 My, in Model-B and from 85 My, in Model-A, the production of hydrocarbons became nearly constant (Fig. 12.21), as at this time the kerogen of these source rocks was completely transformed (Fig. 12.13 and Fig. 12.14). At 85 My the occurrence of the metamorphic events determines a reduction of the generation of hydrocarbons from all the source rocks located in the northern area of the basin (Fig. 12.21).

In the south of the basin the hydrocarbon generation (oil components) began at 121 My (Fig. 12.13 and Fig. 12.14). In this part of the basin the hydrocarbons were generated from the MJSR, which entered the oil-window thermal conditions when they were deposited in the DS7 and Upper Cretaceous units (Fig. 12.11). As this area was not affected by metamorphism, the oil-window thermal conditions remain steady during the inversion stage, allowing for the generation of hydrocarbons from the MJSR in this stage (Fig. 12.15, Fig. 12.19 and Fig. 12.20).

12.8.4. Hydrocarbons migration

The reconstructed models show that the hydrocarbons generated in the basin migrated throughout those units with a sandstone-dominant lithology and along the stratigraphic contacts and faults. Before the inversion few syn-sedimentary faults were active in the basin, mostly those located in the northern and southern margins of the basin (**Chapter 7**). Thus, the permeability and geometry of the stratigraphic units were the most relevant variables influencing migration paths during the syn-extensional and post-extensional stages.

Hydrocarbons generated by the MJSR migrate to the top throughout the sandstone facies of the DS1+2 unit (Magaña Fm) in the central part of the basin, whereas toward the south even throughout the Golmayo Fm and Abejar Fm units (DS5 and DS7, respectively) (Fig. 12.16 and Fig. 12.17). By petrography solid bitumen particles have been found in the Magaña Fm deposits outcropping in the central part of the basin (Fig. 12.26c) and in the Abejar Fm deposits outcropping in the south (Fig. 12.26b).

Hydrocarbons generated by the VSR and ESR migrated upwards, mostly along the surface of the stratigraphic contacts of the units located in the area, facilitated by their dip geometries. Important migration paths formed throughout the Urbión Gr unit (Fig. 12.16 and Fig. 12.17).

Petrological and diagenetical studies of the Urbión Gr deposits (Ochoa et al., 2007; Arribas et al., 2013) define excellent properties for fluid circulation and/or accumulation during burial diagenesis, as they were characterised by a rigid framework that could maintain high porosity values. Hydrocarbon fibres, laying between quartz grains, have been found in the Urbión Gr sandstone deposits of the DS4 (Ochoa et al., 2007), testifying to the occurrence of migration throughout these deposits.

Other migration paths formed in the northern basin border of the basin, along the contact surface of the syn-extensional units with the Jurassic substratum, as well as along the numerous syn-sedimentary faults affecting this area (Suárez-González et al., 2013) (Fig. 12.16 and Fig. 12.17). In the northern border of the basin, solid bitumen particles have been found in the Enciso Gr - Leza Fm (DS7) (**Chapter 10**) (Fig. 12.26f), demonstrating that the migration of hydrocarbons occurred even in this area. The anisotropic mesophase texture that characterises these solid bitumen particles (**Chapter 10**) suggests that the same paths were used for the circulation of hot fluids related with the hydrothermal metamorphism.

During the inversion process numerous new migration paths formed, as a consequence of the formation of new geometries in the basin. Hydrocarbons migrated and were expelled to the surface or in some cases accumulated in structural traps formed by anticlines (Fig. 12.18).

12.8.5. Hydrocarbon accumulation and preservation

During the syn-extensional stage (from 121 My to 98 My), small hydrocarbon accumulations formed in the Urbión Gr (DS6 and DS7) unit, due to the formation of stratigraphic traps. A result of the inconsistency of the traps was that a very scarce amount of hydrocarbons could accumulate (Fig. 12.22). In Mas et al. (2002, 2003), the Urbión Gr bodies, forming the DS4 unit in the northern sector of the basin, are proposed as a possible relevant reservoir of the basin, which formed during the syn-extensional and post-extensional stages because of the stratigraphic trap created by the onlap of the DS4 on the lower DS3 unit and by the dominant shale layers deposited at the top (base of the DS5). In this work, neither the modelling results nor the petrographic analyses of these deposits (**Chapter 10**) suggest the formation of relevant hydrocarbon accumulation in this unit. However, considering that the hydrothermal metamorphic event, affecting the northern sector of the basin, could have altered/transformed/removed proof of the hydrocarbon accumulation formed in these syn-extensional deposits, herein the formation of the reservoir is not completely excluded, even in the Urbión Group (DS4) bodies.

Accumulations formed in the post-extensional Utrillas Fm sandstone bodies are considered herein the most relevant reservoir formed in the basin. Accumulations formed when the marly-carbonate Upper Cretaceous unit was deposited on the whole basin (from 98 to 65.5 My) (Fig.

12.19), sealing the petroleum system (Fig. 12.16 and Fig. 12.17). Hydrocarbons continued to be accumulated even during the inversion stage, mostly in the Utrillas Fm and Urbión Gr (DS7) units (Fig. 12.23), because of the formation of structural traps. The accumulations formed during the post-extensional stage were mostly constituted by gas (Fig. 12.22b and Fig. 12.23), as at this time gas components were prevalently generated from the most relevant source rock of the basin (VSR). Even accumulations formed at the beginning of the inversion stages were mostly formed by gas, as at this time primarily gas was migrating in the basin (Fig. 12.23). By contrast, in the latest inversion stages primarily oil was accumulated, as at this time most of area where gas was generated and migrating was uplifted and eroded (Fig. 12.23); whereas the southern part of the basin, which remained in the oil-window conditions during the entire evolution of the basin, was not uplifted and oil generation, migration and accumulation could continue (Fig. 12.23). The model determines that at 0 My only a few oil and gas accumulations in the anticlines located in the south of the basin were preserved (Fig. 12.23), which corresponds exactly with the position where tar-sandstones crop out at the present-day (Fig. 12.2 and Fig. 12.23). These accumulations could be formed during the inversion stages (as reconstructed by the model) or to be remainder of the accumulations formed in the post-extensional stage. The proximity of the reservoir with the aerial surface supports the formation of tar sands, as a consequence of the degradation of the hydrocarbon accumulation for water washing (Tissot and Welte, 1984). The long migration paths from source rocks to the reservoir can equally have caused the alteration of the original hydrocarbons (Tissot and Welte, 1984; Mann et al., 1997).

The accumulations formed in the Utrillas Fm represent only a small portion of the total amount of hydrocarbons generated in the Cameros Basin (0.22% in Model-A and 0.01% in Model-B). From the graphs in Fig. 12.19 it is evident that, during the entire evolution of the basin, at the same time most of the hydrocarbons were being generated they were also being lost. Thus, very small accumulations could form. During the maximum generation peak (from 127 to 108.7 My) the hydrocarbons flowed out to the surface, due to the absence of a seal on the system. Outflow occurred mostly throughout the DS3 unit in the early syn-extensional phase and throughout the DS7 in the last syn-extensional phase. During the inversion the hydrocarbons continued to be lost, as a consequence of the hydrocarbon outflow to the surface, as well as for the erosion of the formed accumulations. The continued deformation of the basin infill during the inversion process determined that most of the structural traps, and the related hydrocarbon accumulations, were continuously destroyed and/or eroded (Fig. 12.19). However, the amount of hydrocarbons that were lost as a consequence of the erosion of the reservoirs during the inversion stage was small compared with the amount of hydrocarbons that flowed out to the surface during the syn-extensional stage (Fig.12. 24). Thus, it can be concluded that the first cause of the lack of hydrocarbon accumulation in the Cameros Basin was the absence of a seal or trap when the most important generation and migration processes were occurring (during the syn-extensional and part of the post-extensional stages), whereas the erosion of the reservoir

during the inversion of the basin can be considered a secondary cause. However, the occurrence of the hydrothermal metamorphism in the northern sector of the basin needs to be considered as it could in some cases influence the preservation of the hydrocarbon accumulations forming in this area during the syn-extensional and post-extensional stages (Mas et al., 2002, 2003, Ochoa et al., 2007).

12.8.6. Petroleum systems of the basin

Summarising the previous data, in the Cameros Basin two petroleum systems (sensu, Magoon and Dow, 1994) are considered to be active (Fig.12. 27). The first petroleum system was working primarily in the northern-central sector of the basin (Fig. 12.27). The most relevant source rock was the syn-extensional VSR (Berriasian) and in a minor way the MJSR (Callovian); the reservoir was initially the Utrillas Fm unit and secondarily the Urbión Gr unit, and the seal was the Upper Cretaceous unit. The generation of hydrocarbons started in the first phase of the syn-extensional stage (from 145.5 to 142.3 My), it then reduced during the post-extensional stage and stopped during the inversion. The preservation of this system was limited to the post-extensional stage and part of the inversion stage, as at this time most of the system was uplifted and eroded. Furthermore, the hydrothermal metamorphism could have partially influenced the preservation of the hydrocarbon accumulations. The critical moment of this system was considered to be at 85 My, when most of the hydrocarbons were accumulated.

The second petroleum system was working in the central-southern sector of the basin (Fig. 12.27). The most relevant source rock was the MJSR (Callovian), the reservoirs were the Utrillas Fm and the Urbión Gr units, the seal was the Upper Cretaceous unit and the traps were the anticlines formed during the inversion. The generation of hydrocarbons began from the last phase of the syn-extensional stage (121 My) and it continued until the end of the inversion stage. The preservation of this system was variable from one point to the other, as it depends on the rate of uplift and erosion of the formed reservoirs. Several critical moments can be considered for this system: one at 85 My, when the hydrocarbon accumulations formed as a consequence of the deposition of the Upper Cretaceous seal, and the others being during the inversion stage, when the formation of the structural traps allowed the constitution of new hydrocarbon accumulations.

12.9. CONCLUSIONS

This work reconstructs the evolution of the petroleum system of the Cameros Basin, integrating geological, structural, thermal, petrographical and geochemical data. The primary

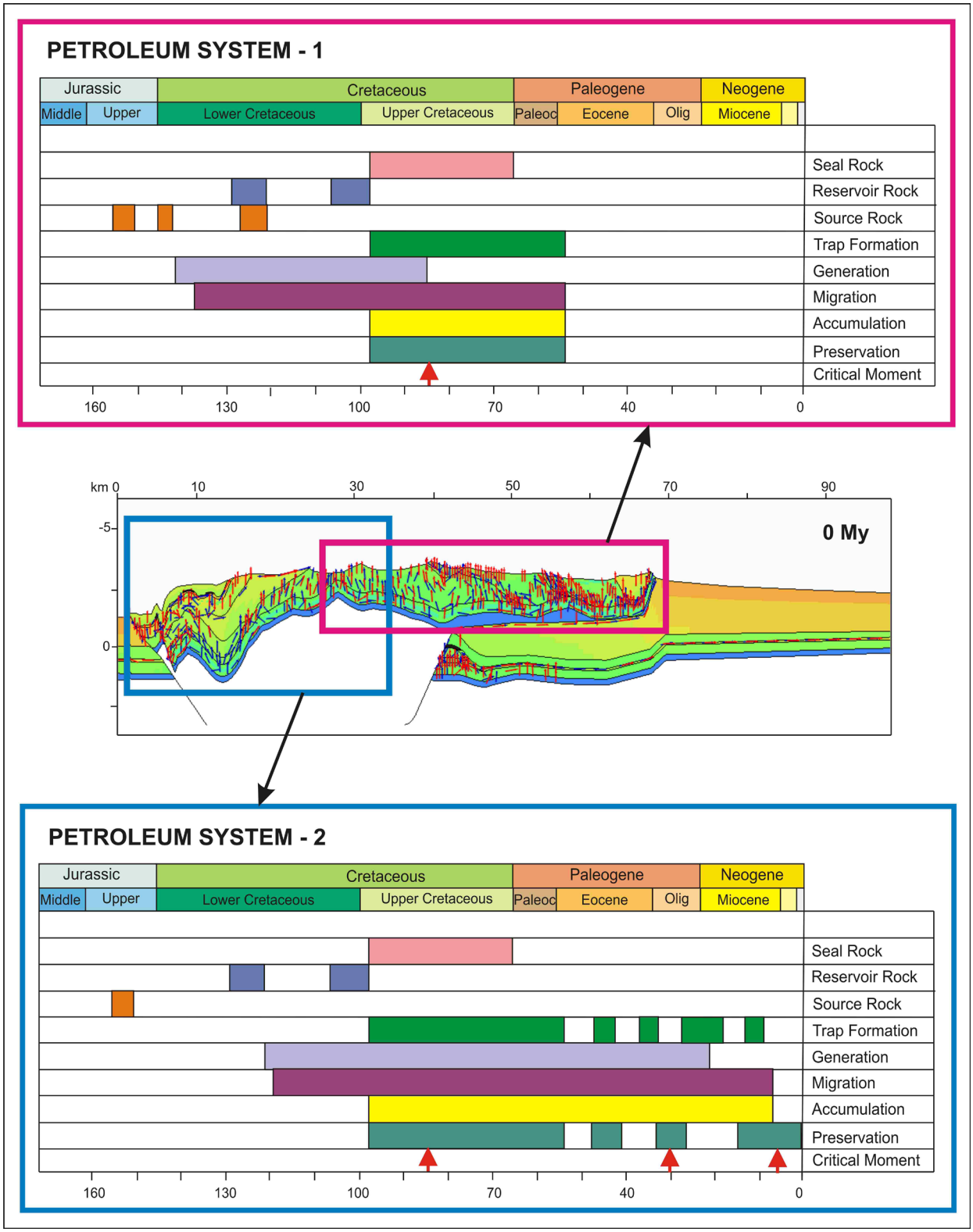

Fig. 12.27 - Chart of petroleum systems of the Cameros Basin

elements and processes of the petroleum system were determined.

To compare the results performed by assigning the bulk kinetics calculated for the Cameros Basin kerogen with the results from literature compositional kinetics, two different models were reconstructed. A very similar reconstruction of the evolution of the Cameros Basin's petroleum system was performed with the two models. Thus, the hydrocarbon oil and gas components' generation, accumulation and preservation timing and trend, reconstructed herein by the compositional kinetic model, can be considered reliable for the Cameros Basin petroleum system.

Different thermal histories were recorded in the northern and central areas of the basin with respect to the areas located in the south. In the central and northern part of the basin, the source rocks reached dry gas-window to overmature thermal conditions, whereas the source rocks located in the southern part reached oil-window to immature thermal conditions. At the end of the post-extensional stage, the kerogen of the source rocks located in the northern sector was completely transformed. The complete transformation of the kerogen of these source rocks primarily occurred before the sediments were affected by the metamorphic event. In the southern sector of the basin, at the end of the post-extensional stage, only 50% of the kerogen of the pre-extensional Jurassic source rocks was transformed, whereas the kerogen of the syn-extensional Late Barremian – Early Aptian source rock was not transformed in the least. During the inversion stage no relevant change in the thermal maturity conditions and, consequently, in the transformation ratio of the source rocks was determined.

The generation of hydrocarbons started in the Early Berriasian (145.5 to 142.3 My) and continued until the inversion stage. The maximum generation peak was reached in the Late Barremian – Early Aptian (from 127 to 121 My). During the syn-extensional and the post-extensional stages the source rock of the basin, which mostly contributes to the generation of hydrocarbons, was the syn-extensional black-shales Berriasian facies (Valdeprado Fm) and followed by the pre-extensional black-shales marine Jurassic facies (Pozalmuro Fm). Due to the type of kerogen that formed these source rocks, Type I for the Valdeprado Fm and Type II for the Pozalmuro Fm, oil components were prevalently generated. In the inversion stage the Jurassic facies located in the south of the basin continued to generate hydrocarbons, as this area remained in the oil-window thermal condition during the entire inversion process.

From the very beginning of the generation process, hydrocarbons were lost, flowing out to the surface. Thus, a majority of the hydrocarbons generated in the basin were lost due to the absence of a seal or trap. The most important accumulations formed when the marls-carbonate Upper Cretaceous unit was deposited on the whole basin (from 98 to 65.5 My), sealing the petroleum system. The most relevant accumulation of the basin formed in the sandstone bodies (Utrillas Fm) at the end of the post-extensional stage. A secondary hydrocarbon accumulation formed in the inversion stage, as a result of the formation of structural traps during the inversion process

in the Utrillas Fm and in the Urbión Gr. Presently, only few accumulations have been preserved in the Utrillas Fm cropping out in the south of the basin, as the uplift of the basin during the inversion stage (from 55 My) caused the erosion of most of the reservoirs.

Accumulations that formed in the Utrillas Fm in the post-extensional stage were primarily constituted by gas, because when the Upper Cretaceous seal deposited, it was produced mostly of gas by the more active source rocks in this stage (Valdeprado Fm and marine Jurassic facies located in the north of the basin). By contrast, in the south of the basin, the accumulations formed in the Utrillas Fm were mostly constituted by oil (presently, tar-sandstone cropping out in this area), as they were charged, during both the post-extensional and inversion stages, by the marine Jurassic facies located in this area of the basin, which were maintained in the oil-window thermal condition until the present day.

Two petroleum systems can be considered in the basin. The first petroleum system was active in the northern sector of the basin. Generation occurred mostly in the syn-extensional stage, whereas accumulation occurred in the post-extensional stage. The most relevant source rock of this system was a lacustrine black-shale syn-extensional unit (DS3, Berriasian). The second petroleum system was more active in the central-southern sector of the basin. Generation occurred in the latest syn-extensional stage and during the inversion of the basin. Accumulations formed in both the post-extensional and inversion stages. The most relevant source rock of this system was the pre-extensional marine black-shales unit (Pozalmuro Fm, Callovian), forming part of the substratum of the basin.

Chapter 13

13. Conclusions

This thesis represents a multidisciplinary characterisation of the geological evolution of the Cameros Basin, which makes a clear and coherent synthesis of all the structural, sedimentological, petrological, geochemical and thermal issues of the basin. Herein, it is performed the reconstruction of the tectono-stratigraphic and thermal evolution of the Cameros Basin, as well as of the petroleum system from the basin.The most relevant conclusions obtained in this work are summarized, grouped into the different multidisciplinary areas in which this work has been subdivided.

1) Geometry and Structure

A combination of field work, geophysical and subsurface data with sedimentological information allowed to establish the evolution of the basin during the extensional stage and the original thickness of the syn-extensional units. During the extensional stage, a northward lateral migration of the depocentres occurred. This trend was inverted during Late Valanginian-Early Barremian times, when the depocentres were located in the southern sector of the basin. The deposits of the syn-extensional phase were dominantly siliciclastic, generated in fluvio-deltaic and alluvial-palustrine systems. The thickest carbonate successions were deposited during Berriasian (DS3) and in Late Barremian to Early Aptian (DS7) times, when lacustrine to playa-lake depositional systems were

formed. The maximum thickness is recorded in Early Berriasian time (DS3), with deposition, in the depocentral area, of 2445 m of sediments. BetweenLate Barremian to Early Aptian times (DS7), the deposition in the depocentral area attained a thickness of 2900 m , whereas in the Late Aptian to Early Albian (DS8), the succession reached a thickness of 2200 m. The overall stratigraphic architecture of the syn-extensional units displays an onlap geometry towards the north onto the underlying Jurassic marine substratum, caused by the lateral migration of the depocentres instead of being vertically superimposed.

In the basin boundaries, there is no evidence of major normal faults that could have been active during the extensional stage. The extensional substratum (Jurassic marine deposits) appears to be continuous throughout the whole basin and consequently it was not affected by any major stretching. The Cameros Basin is interpreted as an extensional ramp syncline basin, which formed over a south-dipping ramp joining two flats of a blind extensional fault located deep in the basement. The inversion of the basin was produced by a main thrust generated and located in the weakness zone, the Upper Triassic (Keuper) beds, which branched in depth with the Mesozoic extensional fault flat.

2) Subsidence analysis and heat flow estimation

Subsidence analysis was made in order to reconstruct the burial evolution of the basin over time together with its essential basin forming mechanisms. The maximum depth in the basin was attained in the central-northern sector of the basin. The tectonic subsidence curves are characterised by a succession of steep and smooth slopes that vary in age from 150.8 to 106.5.7 My. This trend is interpreted as caused by cycles of rapid and decelerated subsidence phases that occurred during the mechanical subsidence of a syn-extensional stage. Two main cycles of rapid/decelerated subsidence phases are identified. The first cycle ranges from Tithonian to Early Berriasian in age (from 150.8 to 142.3 My), whereas the second one ranges in age from Early Barremian to Early Albian (from 129 to 108.7 My). These two rapid/decelerated cycles were recorded diachronously in the basin, as a consequence of the lateral migration of the areas where new accommodation space was generated (depocentre area) instead of a vertical stacking of the depocentres.

A maximum heat flow peak at the end of the syn-extensional stage (108.7 My) was calculated by distinguishing the initial and thermal subsidence phases and by determining their relative magnitudes. The maximum heat flow peak ranges from 60 to 65 mW/m2, which is related to the maximum heat flow attained in the basin, recorded as a consequence of the thinning of the lithosphere and the upwelling of the hot asthenosphere. The resultant relatively low heat flow value obtained for the Cameros Basin compared to the heat flow estimated for a typical extensional area, can be explained by considering a reduced lithosphere extension in the basin

area, which determines a reduced asthenosphere uprising.

3) Thermal Modelling

1D and 2D thermal models reconstruct paleo-temperatures over geologic time intervals and its spatial variations in the basin. The results of the 1D and 2D thermal models, using a typical rift heat flow, show that the maximum temperature was attained in the central and northern sectors of the basin at the end of the syn-extensional stage, whereas temperatures decreased towards the borders of the basin. The 1D thermal model has calculated lower temperatures for the basin infill than the 2D thermal model, indicating that fluid flow and heat conduction occurred not only in a vertical direction but also in a lateral one.

Calibration with vitrinite reflectance data indicates that the 2D thermal model is correct only for the southern sector of the basin. In the central and northern sectors, the %Ro values are markedly higher than the theoretical values of the model, and, in some cases, they invert the typical %Ro-increase-with the expected depth. The anomalous temperatures recorded in the basin are explained considering the circulation of hot fluid during the evolution of the basin. Hot fluids circulation heats the sediments to anomalously high temperatures regardless of their stratigraphic position. Thus, permeability properties constitute a very important variable that determines heat transport within rocks. Furthermore, faults that favored the circulation of hot fluids can enhance heating of sediment layers. Fluid inclusions support the hypothesis of circulation of hot fluids in the basin, and they indicate that circulation may occur in a post-diagenetic stage of the basin infill evolution. Hydrothermal metamorphic events that affected the northern and central part of the basin were attributed to the circulation of these hot fluids during the post-extensional stage and the Alpine compressive phase.

4) Organic matter characterisation

The integration of petrographical and geochemical analysis has lead to a detailed characterisation of the organic matter in the Cameros Basin. As a result, it was established that the northern and central sectors of the basin are characterised by over-mature to dry-gas thermal conditions, whereas the southern sector is characterised by immature to early-oil-window thermal conditions. The different thermal histories recorded can be related to different tectonic evolution in the basin sectors. In the same manner it can be related as well to the circulation of hot fluids in the central-northern sectors of the basin, caused by hydrothermal metamorphic events, which emphasised thermal maturity differences and produced an anomalous thermal maturity distribution.

The over-mature deposits are characterised by a low to very low content of organic matter, which is interpreted as residual kerogen. A poor hydrocarbon potential is considered for these deposits. Sedimentological data indicate the possible nature of the original kerogen in these deposits: Type II for the pre-extensional Jurassic deposits, Type I for the DS3 Valdeprado Fm deposits, Type III-I for the Enciso Gr deposits and Type III for the rest of the basin deposits. In the pre-extensional (Pozalmuro Fm) deposits, in the syn-extensional DS3 (Valdeprado Fm) and the DS7 (Enciso Gr) deposits, abundant hydrocarbons and bitumen rests were found, representing different stages of hydrocarbon generation, accumulation and thermal maturation. Thus, these units are defined as spent source rocks, where kerogen was already transformed into oil and gas due to thermal maturation.

In the immature deposits, Type III kerogen dominates (Prejano site and most of the Soria site), and Type I kerogen appears less frequently (Casarejos site and some samples from the Soria site). These deposits have a very high hydrocarbon potential, especially at the Casarejos and Prejano sites, and they were considered to be potential source rocks. Despite of that, the high dilution of these latter fine-grained organic-rich deposits in the coarse-grained siliciclastic beds would make it doubtful that these rocks could generate a large amount of hydrocarbons.

5) Kinetic calculation and definition

Kinetic parameters were calculated of three immature kerogens forming part of the DS7 unit from the south of the basin.. They were deposited in a continental-transitional depositional environment. Kinetic parameters calculation was based on mathematical computational modelling of the S2 peak of the pyrolysis Rock-Eval. Mathematical computational modelling was satisfactory, as a correct reproduction of the S2 peak measured in the pyrolysis was as well obtained by the model. Frequency factor and the set of activation energies describing the thermal cracking of the analyzed kerogens were determined.

Calculation of kinetic parameters determined the same frequency factor and the record of similar activation energies for the three analyzed samples, as the three samples have been deposited in similar lacustrine-palustrine environments related with coastal wet lands plains of a fluvio-deltaic system. Differences in the maceral composition and proportion, determine a contrast in the activation energies distribution and in the amount of hydrocarbons generated.

Comparison of the calculated kinetic parameters with the parameters of classical Type I, Type II and Type III kerogens indicate a different kerogen behavior in respect to what was expected, considering only pyrolysis data. These differences are explained as a consequence of the presence of sulfur in the structure of the kerogens, caused by a mixture of different types of kerogen. In order to model the petroleum system evolution of the basin the calculated kinetic

parameters can be applied to the overmatured spent source rock of the basin, which have been deposited in a similar lacustrine-palustrine to transitional depositional setting. Differences in the distribution energies have important consequences on the timing of hydrocarbons generation, migration and accumulation.

6) Modelling of the petroleum system

The main elements and processes that characterise the petroleum system were determined by modelling its evolution in the Cameros Basin, integrating geological, structural, thermal, petrographical and geochemical data . Very similar results were obtained by modelling with bulk kinetics calculated for the Cameros Basin and with those obtained from literature compositional kinetics. . Therefore, base on the similar results, the compositional kinetics appear to be the correct ones to characterise the kerogen behaviour of the Cameros Basin kerogen.

Different thermal histories were recorded in the northern and central areas of the basin relatively to areas located in the south. In the central and northern part of the basin, source rocks have reached dry gas-window to overmature thermal conditions, whereas source rocks located in the southern part have reached oil-window to immature thermal conditions. At the end of the post-extensional stage, the kerogen of the source rocks from the northern sector was completely transformed, mostly as a consequence of burial. In the southern sector of the basin, at the end of the post-extensional stage, only 50% of the kerogen of the pre-extensional Jurassic source rocks was transformed, whereas the kerogen of syn-extensional Late Barremian-Early Aptian source rock was not transformed at all. During the inversion stage, there was no relevant change in thermal maturity conditions, and consequently in the transformation ratio of the source rocks. The maximum generation peak was reached in Late Barremian-Early Aptian times (from127 to 121 My). During the syn-extensional and the post-extensional stages, the source rock of the basin that mostly contributes to the generation of hydrocarbons, were the syn-extensional Berriasian black-shales facies (Valdeprado Fm), followed by the pre-extensional Jurassic black-shales marine facies (Pozalmuro Fm). During the inversion stage, only the Jurassic facies located in the south of the basin, continued to generate hydrocarbons. Thisarea remained in the oil-window thermal condition during the entire inversion process.

The major amount of generated hydrocarbons was lost by outflowing to the surface due to the absence of a seal or trap. The most important accumulations formed when the Upper Cretaceous marls-carbonate unit was deposited on the whole basin (from 98 to 65.5 My), sealing the petroleum system. The most relevant hydrocarbons accumulation of the basin appears in sandstone bodies of the Utrillas Fm, deposited at the end of the post-extensional stage. A secondary hydrocarbons accumulation was produced in the inversion stage as well, caused by the formation of structural traps in the Utrillas Fm and Urbión Gr. At present-day, only few

accumulations are preserved in the Utrillas Fm cropping out in the south of the basin, as the uplift of the basin during the inversion stage (approx. from 50 My to 17 My) caused the erosion of most of the reservoirs. Accumulations formed in the post-extensional stage and in the early inversion stage were mostly composed of gas, although most gas components were migrating at this time. In the late inversion stage, hydrocarbons continued to be generated, migrated and accumulated only in the south of the basin, as this part was not uplifted and eroded and the source rocks (Jurassic marine units) were still in the oil-window conditions.

Therefore, two petroleum systems can be considered in the basin. The first petroleum system was active in the northern sector of the basin. Generation occurred mostly in the syn-extensional stage, whereas accumulation took place in the post-extensional stage. The most relevant source rock of this system was a lacustrine black-shale syn-extensional unit (DS3, Berriasian). The second petroleum system was active mainly in the central-southern sector of the basin. Generation occurred in latest syn-extensional stage and during the inversion of the basin. Accumulations formed in both post-extensional and inversion stages. The most relevant source rock of this system was the pre-extensional marine black-shales unit (Pozalmuro Fm, Callovian), which formed part of the substratum of the basin.

13.1. PROPOSED FUTURE RESEARCH LINES

The results obtained in this thesis represent a solid base for future research on the basin and contributes to a better understanding of the geodynamic evolution of the study area. Furthermore, these results may be applied in the analysis of potential petroleum systems in other inverted extensional basins. The research lines proposed herein, which could be carried out in the future, can be summarized as follow:

- To perform a detailed structural study of the basin area, increasing this new data set with already available geophysical, stratigraphical and sedimentological information of the basin . This would permit to develop a complete tectonic model of the basin.

- Reconstruction of a 3D thermal model of the basin, taking into account the structure and geometry of the entire basin. The definition of a 3D thermal model would determine a more detailed variation of the thermal conditions in the basin area, and would define the hydrocarbon migration paths and locate the accumulation areas throughout the entire basin.

- To implement the thermal model calibration performed in this thesis with vitrinite reflectance data, with other inorganic paleothermometers such as illite crystallinity and fluid inclusions analysis. Illite crystallinity could permit to obtain thermal data of the rocks where organic matter is not accumulated and/or preserved, whereas fluid inclusions would provide new data of the temperature of fluids circulating in the basin.

- To characterize with more detail the tar bitumen accumulated in the southern sector of the basin by means of geochemical analysis such as pyrolysis gas chromatography mass spectrometry (Py-GC). The PyGC signature could be used to find a correlation between these hydrocarbons accumulations with their possible source rocks.

- To extend the petroleum system modelling performed in this thesis to the half-graben satellite basins located to the north and south of the Cameros Basin (Rioja and Bigornia sub-basins respectively). In these sub-basins, elements and processes of theirs petroleum systems would be determined by means of petrological and geochemical studies and by modelling their thermal evolutions. A correlation of their thermal histories with the Cameros Basin evolution would be of great interest.

- To apply the methodology implemented in this thesis to the analysis of petroleum systems in inverted extensional basins.

Chapter 14

14. References

Abeger, G., A. J. Fernandez, A. Serrano, S. Quesada, T. Vallaure, J. Varela, and W. M. del Olmo, 2003, Petroleum Geology of the Oil and Gas Commercial Discoveries in Spanish Basins: Onshore Cantabrian basin: 2003 AAPG International Conference & Exhibition Technical Program.

Aitken, R., 1942, The Sierra of the Demanda (Burgos, Spain). Note of the tectonics of the northern margin: Gological Magazine, v. 79, p. 33-48.

Aitken, R., 1946, La Sierra de la Demanda (Burgos, España). Nota sobre la tectónica del Borde Norte.: Notas y Comunicaciones del Instituto Geologico y Minero de Espana, v. 15, p. 181-205.

Al-Hajeri, M. M., M. Al Saeed, J. Derks, T. Fuchs, T. Hantschel, A. Kauerauf, M. Neumaier, O. Schenk, O. Swientek, and N. Tessen, 2009, Basin and petroleum system modeling: Oilfield Review, v. 21, p. 14-29.

Alonso-Azcárate, J., 1997, Evolución de los filosilicatos y génesis de los yacimientos de pirita: su relación con las facies sedimentarias y el metamorfismo en la Cuenca de Cameros. Cretácico inferior. La Rioja-Soria, Universidad Complutense de Madrid, 544 p.

Alonso-Azcárate, J., J. F. Barrenechea, M. Rodas, and J. R. Mas, 1995, Comparative study of the transition between very low-grade and low-grade metamorphism in siliciclastic and carbonate sediments: Early Cretaceous, Cameros Basin (northern Spain): Clay Minerals, v. 30, p. 407-419.

Alonso-Azcárate, J., M. I. Benito, R. Mas, and M. Rodas, 1997, Evolución desde la diagénesis temprana

al metamorfismo de los nódulos edáficos del grupo Urbión. Cretácico inferior. Cuenca de Cameros. La Rioja: Geogaceta, v. 21, p. 9-12.

Alonso-Azcárate, J., M. Rodas, J. F. Barrenechea, and J. R. Mas, 1999, Factores que controlan la evolución de los parámetros cristaloquímicos y las asociaciones minerales en los sedimentos del Grupo Enciso (Cretacico Inferior). Cuenca de Cameros. La Rioja (norte de Espana): Boletín de la Sociedad Española de Mineralogía, v. 22A, p. 7-8.

Alonso, Á., M. Floquet, R. Mas, and A. Meléndez, 1993, Late Cretaceous Carbonate Platforms: Origin and Evolution, Iberian Range, Spain, in R. W. Scott, J. A. T. Simo, and J. P. Masse, eds., Cretaceous Carbonate Platforms: American Association of Petroleum Geologists, Memoir, v. 56: Oklahoma, p. 297-313.

Alonso, A., M. Floquet, A. Meléndez, and J. Salomon, 1982, Cameros-Castilla, in A. García, ed., El Cretácico de España: Madrid, Universidad Complutense de Madrid, p. 345-456.

Alonso, A., and J. R. Mas, 1988, La transgresión aptiense al sur del Moncayo (límite de las provincias de Soria y Zaragoza), in Sociedad Geológica de España, ed., II Congreso Geológico de España, Granada (España), Universidad de Granada, p. 11-14.

Alonso, A., and J. R. Mas, 1993, Control tectónico e influencia del eustatismo en la sedimentación del Cretácico inferior de la Cuenca de Los Cameros: Cuadernos de Geología Ibérica, v. 17, p. 285-310.

Alonso, A., J. R. Mas, and N. Meléndez, 1986-1987, Los arrecifes coralinos del Malm en la Sierra de los Cameros (La Rioja, España): Acta Geològica Hispànica, v. 21-22, p. 293-306.

Alonso, A., and R. Mas, 1990, El Jurásico superior marino en el sector Demanda-Cameros (La Rioja-Soria): Cuadernos de Geología Ibérica, v. 14, p. 173-198.

Álvaro, M., R. Capote, and R. Vegas, 1979, Un modelo de evolución geotectónica para la Cadena Celtibérica: Acta Geològica Hispànica, v. 14, p. 172-177.

Allen, P. A., and J. R. Allen, 2009, Basin analysis: principles and applications, Blackwell, 549 p.

Anthony, D. B., and J. B. Howard, 1976, Coal devolatilization and hydrogastification: AIChE Journal, v. 22, p. 625-656.

Aránzazu, M., 1877, Apuntes para una descripción físico-geológica de las províncias de Logroño, Soria y Guadalajara: Bol. Com. Mapa Geol. Esp. IV, Madrid.

Arche, A., and J. López-Gómez, 1996, Origin of the Permian-Triassic Iberian Basin, central-eastern Spain: Tectonophysics, v. 266, p. 443-464.

Arribas, J., 1985, Base litoestratigráfica de las facies Buntsandstein y Muschelkalk en la rama aragonesa de la Cordillera Ibérica (Zona Norte): Estudios Geológicos, v. 41, p. 47-58.

Arribas, J., L. Gonzáez-Acebrón, S. Omodeo-Salé, and R. Mas, 2013, The influence of the provenance of arenite on its diagenesis in the Cameros Rift Basin (Spain): Geological Society, London, Special Publications, v. 386.

Arribas, J., R. Mas, Á. Alonso, and M. Ochoa, 2003, Diagenetic Processes Controlling the Quality of Potential Clastic Reservoirs in a Continental Rift Basin: Western Cameros Basin, Spain, AAPG International Conference, Barcelona (Spain).

Arribas, J., R. Mas, M. E. Arribas, L. González-Acebrón, and M. Ochoa, 2007, Sandstone petrofacies in the northwestern sector of the Iberian Basin: Journal of Iberian Geology, v. 33, p. 191-206.

Arribas, J., R. Mas, M. Ochoa, and Á. Alonso, 2002, Composición y diagénesis del registro detrítico en el borde suroccidental de la Cuenca de Cameros: Zubía Monográfico, v. 14, p. 99-119.

ASTM-D7708-11, 2011, Standard test method for microscopical determination of the reflectance of vitrinite dispersed in sedimentary rocks. : Annual book of ASTM standards: petroleum products, lubricants and fossil fuels; gaseous fuels; coal and coke, sec. 5, v. 506., v. ASTM Internation, West Conshohocken, PA, p. 823-830.

Aurell, M., and A. Meléndez, 1993, Sedimentary evolution and sequence stratigraphy of the Upper Jurassic in central Iberian Chain, northeast Spain,, in H. W. Posamentier, Summerhayes, C.P., Haq, B.U. and Allen, G.P., ed., Sequence stratigraphy and Facies Associations, v. 18, International Association of Sedimentologists, Special Publication, p. 343-368.

Bádenas, B., and M. Aurell, 2001, Kimmeridgian palaeogeography and basin evolution of northeastern Iberia: Palaeogeography,Palaeoclimatology,Palaeoecology, v. 168, p. 291-310.

Bally, A., and S. Snelson, eds., 1980, Realms of subsidence, 9-94 p.

Barker, C., 1974, Pyrolysis techniques for source-rock evaluation: AAPG Bulletin, v. 58, p. 2349-2361.

Barrenechea, J. F., M. Rodas, M. Frey, J. Alonso-Azcárate, and J. R. Mas, 2001, Clay diagenesis and low-grade metamorphism of Tithonian and Berriasian sediments in the Cameros Basin (Spain): Clay Minerals, v. 36, p. 325-333.

Barrenechea, J. F., M. Rodas, and J. R. Mas, 1995, Clay mineral variations associated with diagenesis and low-grade metamorphism of Early Cretaceous sediments in the Cameros Basin, Spain: Clay Minerals, v. 30, p. 119-133.

Barrenechea, J. M., 1993, Evolución de la mineralogía de arcillas en el tránsito diagénesis-metamorfismo de bajo grado en el Grupo Urbión (Cretácico Inferior) de la Cuenca de los Cameros (Soria-La Rioja). Tesis Doctoral, Universidad Complutense de Madrid, 297 p.

Baskin, D. K., and K. E. Peters, 1992, Early Generation Characteristics of a Sulfur-Rich Monterey Kerogen {1}: AAPG Bulletin, v. 76, p. 1-13.

Behar, F., V. Beaumont, and H. D. B. Penteado, 2001, Rock-Eval 6 technology: performances and developments: Oil & Gas Science and Technology, v. 56, p. 111-134.

Behar, F., M. Vandenbroucke, Y. Tang, F. Marquis, and J. Espitalié, 1997, Thermal cracking of kerogen in open and closed systems: determination of kinetic parameters and stoichiometric coefficients for oil and gas generation: Organic geochemistry, v. 26, p. 321-339.

Beltrán-Cabrera, F. J., J. M. Ríos-Mitchell, and L. M. Ríos-Aragües, 1980, Hoja geológica 349 (Cabrejas del Pinar). Mapa Geológico de España 1:50.000. Segunda Serie: Instituto Geológico y Minero de España.

Benito-Moreno, M. I., 2001, Estudio comparativo de la evolución sedimentaria y diagenética de los litosomas carbonatados arrecifales (pre-rifting) de la Cuenca de Cameros. Kimmeridgiense. La Rioja-Soria, Universidad Complutense de Madrid, Madrid, 410 p.

Benito, M. I., K. C. Lohmann, and R. Mas, 2005, Late Jurassic Paleogeography and Paleoclimate in the Northern Iberian Basin of Spain: Constraints from Diagenetic Records in Reefal and Continental Carbonates: Journal of Sedimentary Research, v. 75, p. 82-96.

Benito, M. I., K. C. Lohmann, and R. Mas, 2006, Micro-Sized Dolomite Inclusions in Ferroan Calcite Cements Developed During Burial Diagenesis of Kimmeridgian Reefs, Northern Iberian Basin, Spain: Journal of Sedimentary Research, v. 76, p. 472-482.

Benito, M. I., and R. Mas, 2001, Diagenesis temprana meteorica de la formacion Torrecilla en Cameros (kimmeridgiense inferior; prerift) y de los carbonatos de la base del grupo tera (tithonico; sinrift) en el sector de Soria; Cuenca de Cameros, en Espana: Geotemas, v. 3, p. 82-88.

Benito, M. I., and R. Mas, 2006, Sedimentary evolution of the Torrecilla Reef Complex in response to tectonically forced regression (Early Kimmeridgian, Northern Spain): Sedimentary Geology, v. 183, p. 31-49.

Benito, M. I., R. Mas, and K. C. Lohmann, 2003, Eustatic and Tectonic Controls on Coral Reef Morphology and Porosity: The Torrecilla en Cameros Fm. Early Kimmeridgian, Northern Spain, AAPG International Conference, Barcelona (Spain).

Berger, W., V. Smetacek, and G. Wefer, 1989, Ocean productivity and paleoproductivity-an overview: Productivity of the Oceans present and past: Report of the Dahlem Workshop on Productivity of the Ocean, Berlin, 1988 (WH Berger, VS Smetacek, G Wefer, eds) Life sciences research reports 44, Wiley & Sons, Chichester, p. 1-34.

Bertrand, R., 1993, Standardization of solid bitumen reflectance to vitrinite in some Paleozoic sequences of Canada: Energy sources, v. 15, p. 269-287.

Beuther, A., 1966, Geologische Untersuchungen in Wealden und Utrillas-Schichten im Westteil der Sierra de los Cameros (Nordwestliche Iberische Ketten): Beitr Geol Jb v. 44, p. 103-121.

Boquera-Fillol, J., G. Gil-Serrano, and J. M. Zubieta-Freire, 1978a, Hoja geológica 239 (Pradoluengo). Mapa Geológico de España 1:50.000. Segunda Serie: Instituto Tecnológico GeoMinero de España.

Boquera-Fillol, J., G. Gil-Serrano, and J. M. Zubieta-Freire, 1978b, Hoja geológica 240 (Ezcaray). Mapa Geológico de España 1:50.000. Segunda Serie: Instituto Tecnológico GeoMinero de España.

Bordenave, M., J. Espitalié, L. P., and M. Vandenbrouke, 1993, Screening techniques for source rock evaluation: Applied Petroleum Geochemistry. Editions Technip, Paris, p. 217.

Bordenave, M. L., 1993, Applied petroleum geochemistry, Editions OPHRYS.

Bornhold, B. D., 1973, Late Quarternary Sedimentation in the Eastern Angola Basin, DTIC Document.

Bott, M., 1992, Passive margins and their subsidence: Journal of the Geological Society, v. 149,

p. 805-812.

Braun, R., and A. Burnham, 1987, Analysis of chemical reaction kinetics using a distribution of activation energies and simpler models: Energy & fuels, v. 1, p. 153-161.

Braun, R. L., A. K. Burnham, J. G. Reynolds, and J. E. Clarkson, 1991, Pyrolysis kinetics for lacustrine and marine source rocks by programmed micropyrolysis: Energy & fuels, v. 5, p. 192-204.

Brenner, P., 1976, Ostracoden und Charophyten des spanischen Wealden (Systematik, Ökologie, Stratigraphie, Paläogeographie): Palaeontographica Abteilung A: Palaeozoologie-Stratigraphie, v. 152, p. 113-201.

Büker, C., R. Littke, and D. H. Welte, 1995, 2D-modelling of the thermal evolution of Carboniferous and Devonian sedimentary rocks of the eastern Ruhr basin and northern Rhenish Massif, Germany: Zeitschrift der Deutschen Geologischen Gesellschaft, v. 146, p. 321-339.

Burnham, A., and J. Sweeney, 1989, Modeling the maturation and migration of petroleum: Lawrence Livermore National Laboratory Report UCRL 102602, Preprint.

Burnham, A. K., R. L. Braun, H. R. Gregg, and A. M. Samoun, 1987, Comparison of methods for measuring kerogen pyrolysis rates and fitting kinetic parameters: Energy & fuels, v. 1, p. 452-458.

Burnham, A. K., R. L. Braun, and A. M. Samoun, 1988, Further comparison of methods for measuring kerogen pyrolysis rates and fitting kinetic parameters: Organic geochemistry, v. 13, p. 839-845.

Burrus, J., and F. Bessis, 1986, Thermal modelling in the Provençal Basin (NW-Mediterranean): Thermal Modeling in Sedimentary Basins, Editions Technip, Paris, p. 393-416.

Burton, R., C. G. S. C. Kendall, and I. Lerche, 1987, Out of our depth: on the impossibility of fathoming eustasy from the stratigraphic record: Earth-Science Reviews, v. 24, p. 237-277.

Burwood, R., P. Leplat, B. Mycke, and J. Paulet, 1992, Rifted margin source rock deposition: a carbon isotope and biomarker study of a west African Lower Cretaceous “lacustrine” section: Organic geochemistry, v. 19, p. 41-52.

Busby, C., and R. V. Ingersoll, 1995, Tectonics of sedimentary basins.

Cámara-Rupelo, P., and O. Durántez-Romero, 1982, Hoja geológica 279 (Villoslada de Cameros). Mapa Geológico de España 1:50.000. Segunda serie: Instituto Geológico y Minero de España.

Cámara-Rupelo, P. L., and O. Durántez-Romero, 1981, Hoja geológica 280 (Enciso). Mapa Geológico de España 1:50.000. Segunda Serie: Instituto Geológico y Minero de España,.

Carter, K., and I. Lerche, 1991, Basin evolution, thermal history and hydrocarbon potential of the St. George Basin, Bering Sea, Alaska: a comparative study using one-and two-dimensional models: Marine and Petroleum Geology, v. 8, p. 392-409.

Casas-Sainz, A. M., 1993, Oblique tectonic inversion and basement thrusting in the Cameros Massif (northern Spain): Geodinamica Acta, v. 6, p. 202-216.

Casas-Sainz, A. M., Á. L. Cortés-Gracia, and A. Maestro-González, 2000, Intraplate deformation

and basin formation during the Tertiary within the northern Iberian plate: origin and evolution of the Almazán Basin: Tectonics, v. 19, p. 258-289.

Casas-Sainz, A. M., and A. Gil-Imaz, 1994, Evolución tectonosedimentaria de una cuenca extensional intraplaca: la cuenca finijurásica-eocretácica de Los Cameros (La Rioja-Soria): Discusión: Revista de la Sociedad Geológica de España, v. 7, p. 337-345.

Casas-Sainz, A. M., and A. Gil-Imaz, 1998, Extensional subsidence, contractional folding and thrust inversion of the eastern Cameros basin, northern Spain: Geologische Rundschau, v. 86, p. 802-818.

Casas-Sainz, A. M., and J. L. Simón-Gómez, 1992, Stress field and thrust kinematics: a model for the tectonic inversion of the cameros massif (Spain): Journal of Structural Geology, v. 14, p. 521-530.

Casas, A., P. Río, P. Mata, J. Villalaìn, and L. Barbero, 2012, Comment on González-Acebrón et al. Criteria for the recognition of localization and timing of multiple events of hydrothermal alteration in sandstones illustrated by petrographic, fluid inclusion, and isotopic analysis of the Tera Group, Northern Spain Int J Earth Sciences (2011) 100:1811-1826: International Journal of Earth Sciences, v. 101, p. 2043-2048.

Casas, A., and R. Salas, 1992, Historia de la subsistencia, anomalías gravimétricas y evolución mesozoica de las Cuencas del margen oriental de Iberia: Actas de las sesiones científicas: III Congreso Geológico de España, p. 112-116.

Casas, A. M., J. J. Villalaín, R. Soto, A. Gil-Imaz, P. del Río, and G. Fernández, 2009, Multidisciplinary approach to an extensional syncline model for the Mesozoic Cameros Basin (N Spain): Tectonophysics, v. 470, p. 3-20.

Casquet, C., C. Galindo, J. M. González-Casado, A. Alonso, R. Mas, M. Rodas, E. García, and J. F. Barrenechea, 1992, El metamorfismo en la Cuenca de los Cameros. Geocronología e implicaciones tectónicas: Geogaceta, v. 11, p. 22-25.

Castiella-Muruzábal, J., J. Solé-Sedó, and L. Villalobos-Vilches, 1977, Hoja geológica 243 (Calahorra). Mapa Geológico de España 1:50.000. Segunda Serie: Instituto Geológico y Minero de España.

Clemente, P., 2010, Review of the Upper Jurassic-Lower Cretaceous stratigraphy in Western Cameros Basin, Northern Spain: Sociedad Geologica de Espana. Revista, v. 23, p. 101-143.

Clemente, P., and A. Alonso, 1990a, Estratigrafía y sedimentología de las facies continentales del Cretácico Inferior en el borde meridional de la Cuenca de los Cameros: Estudios Geológicos, v. 46, p. 257-276.

Clemente, P., and Á. Alonso, 1990b, Sedimentary evolution of a fluvio-lacustrine sequence in relation with an active fault (Lower Cretaceous. Cameros Basin, central Spain), 13th International Sedimentological Congress, Nottingham (UK), p. 50.

Clemente, P., and M. Pérez-Arlucea, 1993, Depositional architecture of the Cuerda del Pozo Formation, Lower Cretaceous of the extensional Cameros Basin, north-central Spain: Journal of Sedimentary Petrology, v. 63, p. 437-452.

Colchen, M., 1974, Geologie de la sierra de la Demanda: Burgos-Logroño (Espagne), v. 1, IGME.

Chadouli, K., 2013, Caractérisation pétrographique des systèmes pétroliers conventionnels et non conventionnels appliquée à la modélisation d'un play, Université de Lorraine, Nancy.

Chudeau, 1896, Contribution a l'étude géologique de la vieille-Castille, Universidad de Paris, 92 p.

del Río-Bermejo, P., 2009, Historia termal del sector oriental de la Sierra de Cameros: restricciones a partir del análisis de huellas de fisión y otras herramientas geocronológicas (U-Pb SHRIMP y (U-Th)/He), Universidad de Zaragoza, Zaragoza, 239 p.

Del Río, P., L. Barbero, P. Mata, and C. M. Fanning, 2009a, Timing of diagenesis and very low-grade metamorphism in the eastern sector of the Sierra de Cameros (Iberian Range, Spain): a U-Pb SHRIMP study on monazite: Terra Nova, v. 21, p. 438-445.

del Río, P., L. Barbero, and F. M. Stuart, 2009b, Exhumation of the Sierra de Cameros (Iberian Range, Spain): constraints from low-temperature thermochronology, in F. Lisker, B. Ventura, and U. A. Glasmacher, eds., Thermochronological Methods: From Palaeotemperature Constraints to Landscape Evolution Models: Geological Society, London, Special Publications, v. 324, p. 153-166.

Del Río, P., A. Casas, J. J. Villalaín, T. Mochales, R. Soto, and B. Oliva-Urcia, 2013, Interpretation of gravimetric and magnetic anomalies in the Cameros Basin (North Spain): combination of deep and shallow sources: Studia Geophysica et Geodaetica, v. 57, p. 442-459.

Dembicki, J., Harry, 2009, Three common source rock evaluation errors made by geologists during prospect or play appraisals: AAPG Bulletin, v. 93, p. 341-356.

Derreims, A., 1898, Recherches géologiques dans le sud de l'Aragon. Tesis doctoral, Universidad de Paris, 199 p.

Díaz-Martínez, E., 1988, El Cretácico Inferior del sector de Jubera (norte de la sierra de los Cameros, La Rioja): relación entre tectónica y sedimentación, II Congreso Geológico de España, Granada, p. 67-70.

Diessel, C. F., 2007, Utility of coal petrology for sequence-stratigraphic analysis: International Journal of Coal Geology, v. 70, p. 3-34.

Dow, W. G., 1974, Application of oil-correlation and source-rock data to exploration in Williston Basin: AAPG Bulletin, v. 58, p. 1253-1262.

Durand, B., 1980a, Kerogen: Insoluble organic matter from sedimentary rocks, Editions technip.

Durand, B., 1980b, Sedimentary organic matter and kerogen. Definition and quantitative importance of kerogen: Kerogen: insoluble organic matter from sedimentary rocks, p. 13-34.

Durand, B., 1993, Composition and structure of organic matter in immature sediments: Applied Petroleum Geochemistry. Paris, Editions Technip, p. 77-100.

Durántez, O., J. Solé, J. Castiella, and L. Villalobos, 1982, Hoja geológica 281 (Cervera del Río Alhama). Mapa Geológico de España 1:50.000. Segunda Serie: Instituto Geológico y Minero de España.

Ebinger, C., and M. Casey, 2001, Continental breakup in magmatic provinces: An Ethiopian example: Geology, v. 29, p. 527-530.

Einsele, G., 2000, Sedimentary basins: evolution, facies, and sediment budget, Springer.

England, W., A. Mackenzie, D. Mann, and T. Quigley, 1987, The movement and entrapment of petroleum fluids in the subsurface: Journal of the Geological Society, v. 144, p. 327-347.

Esnaola-Gómez, J. M., and M. Martín-Fernández, 1973, Hoja geológica 351 (Olvega). Mapa Geológico de España 1:50.000. Segunda Serie: Instituto Geológico y Minero de España.

Espitalié, J., and M. Bordenave, 1993, Source rock parameters: Bordenave, v. 35, p. 237-272.

Espitalié, J., G. Deroo, and F. Marquis, 1986, La pyrolyse Rock-Eval et ses applications. Troisième partie: Oil & Gas Science and Technology, v. 41, p. 73-89.

Espitalié, J., G. Deroo, and F. Marquis, 1985a, La pyrolisis Rock-Eval et ses applications: Deuxième partie: Oil & Gas Science and Technology v. 40, p. 755-784.

Espitalié, J., G. Deroo, and F. Marquis, 1985b, La pyrolyse Rock-Eval et ses applications: Première Partie: Oil & Gas Science and Technology v. 40, p. 563-580.

Espitalié, J., J. L. Laporte, M. Madec, F. Marquis, P. Leplat, J. Paulet, and A. Boutefeu, 1977, Méthode rapide de caractérisation des roches mètres, de leur potentiel pétrolier et de leur degré d'évolution: Oil & Gas Science and Technology, v. 32, p. 23-42.

Espitalié, J., J. Maxwell, Y. Chenet, and F. Marquis, 1987, Aspects of hydrocarbon migration in the Mesozoic in the Paris Basin as deduced from an organic geochemical survey: Organic geochemistry, v. 13, p. 467-481.

Espitalié, J., P. Ungerer, I. Irwin, and F. Marquis, 1988, Primary cracking of kerogens. Experimenting and modeling C1, C2− C5, C6C15+ classes of hydrocarbons formed: Organic geochemistry, v. 13, p. 893-899.

Ezquerra, A., L., 1841, Observaciones geognósticas y mineras sobre la Sierra del Moncayo: Anales de Minas, v. II, p. 71-93.

Fernández, M., I. Marzán, A. Correia, and E. Ramalho, 1998, Heat flow, heat production, and lithospheric thermal regime in the Iberian Peninsula: Tectonophysics, v. 291, p. 29-53.

García-Mondéjar, J., L. M. Agirrezabala, A. Aranburu, P. A. Fernández-Mendiola, I. Gómez-Pérez, M. López-Horgue, and I. Rosales, 1996, Aptian— Albian tectonic pattern of the Basque— Cantabrian Basin (Northern Spain): Geological Journal, v. 31, p. 13-45.

García-Mondéjar, J., P. A. Fernàndez-Mendiola, L. M. Agirrezabala, A. Aranburu, M. A. López-Horgue, E. Iriarte, and S. Martínez de Rituerto, 2004, Extensón del Aptiense-Albiense en la Cuenca Vasco-Cantábrica, SGEIGME, Madrid, p. 340-343.

García, A., and R. Mas, 2004, Segunda fase de post-rifting:Cretácico Superior, in e. V. J. (ed), ed., Geología de España: Madrid, Sociedad Geológica de España; Instituto Geológico y Minero de España, p. 510-522.

Gawthorpe, R., and M. Leeder, 2000, Tectono-sedimentary evolution of active extensional basins: Basin Research, v. 12, p. 195-218.

Gibbs, A., 1987, Development of extension and mixed-mode sedimentary basins: Geological Society, London, Special Publications, v. 28, p. 19-33.

Gibson, J., J. Walsh, and J. Watterson, 1989, Modelling of bed contours and cross-sections adjacent to planar normal faults: Journal of Structural Geology, v. 11, p. 317-328.

Gil-Imaz, A., P. Mata, A. Canals, and A. M. Casa-Sainz, 1995, Tectono-thermal evolution of a Mesozoic extensional basin; Cameros Massif, N. Spain: Journal of the Czech Geological Society (Casopis Ceske Geologicke Spolecnosti), v. 40, p. 131-132.

Gil-Serrano, G., S. Jiménez-Beneyas, and J. M. Zubieta-Freire, 1978, Hoja geológica 278 (Canales de La Sierra), in Instituto Geológico y Minero de España, ed., Mapa Geológico de España E. 1:50.000 - Segunda serie, Madrid, Ministerio de Industria y Energía.

Gil-Serrano, G., and J. M. Zubieta-Freire, 1978, Hoja geólogica 277 (Salas de los Infantes). Mapa Geológico de España 1:50.000. Segunda Serie. Instituto Geológico y Minero de España, Madrid.

Goldstein, R. H., and T. J. Reynolds, 1994, Systematics of fluid inclusions in diagenetic minerals: SEPM (Society for Sedimentary Geology) Short Course, v. 31, p. 199.

Gómez-Fernández, J. C., 1992, Análisis de la cuenca sedimentaria de los Cameros durante sus etapas iniciales de relleno en relación con su evolución paleogeográfica, Universidad Complutense de Madrid, Madrid, 343 p.

Gómez-Fernández, J. C., and N. Meléndez, 1994, Climatic control on Lower Cretaceous sedimentation in a playa-lake system of a tectonically active basin (Huérteles Alloformation, Eastern Cameros Basin, North-Central Spain): Journal of Paleolimnology, v. 11, p. 91-107.

Gonçavales, F. T. T., D. G. García, H. D. B. Penteado, B. N. Giraldo, R. P. Bedregal, and P. Gómez, 2001, Cinética de la generación del petróleo: principios y aplicación en las cuencas colombianas: Ciencia, Tecnología y Futuro, v. 2, p. 27-41.

Gonçavales, F. T. T., J. A. Trigüis, F. G. Gonzaga, and L. F. C. Coutinho, 1994, Kerogen composition vs. kinetic variability in marine source rocks from Amazonas Basin, Brazil, IV Latin American on Organic Geochemestry, Bucaramanga, Colombia.

González-Acebrón, L., 2009, El Grupo Tera en el sector oriental de la Cuenca de Cameros: ambientes sedimentarios, procedencia y evolución diagenética, Universidad Complutense de Madrid, Madrid, 405 p.

González-Acebrón, L., J. Arribas, and R. Mas, 2007, Provenance of fluvial sandstones at the start of late Jurassic-Early Cretaceous rifting in the Cameros Basin (N. Spain): Sedimentary Geology, v. 202, p. 138-157.

González-Acebrón, L., R. Goldstein, R. Mas, and J. Arribas, 2012, Answer to the comment of Casas et al. about González Acebrón et al.'s (2011) paper: International Journal of Earth Sciences, p. 1-5.

González-Acebrón, L., R. H. Goldstein, J. Arribas, R. Mas, and M. I. Benito, 2009, Thermal evolution of the first stages of a rift record: petrography and fluid inclusions, in V. Pascucci, and S. Andreucci, eds., Sedimentary environments of Mediterranean Island(s)-27th IAS Meeting, Alghero (Italy), p. 188.

González-Acebrón, L., R. H. Goldstein, R. Mas, and J. Arribas, 2011, Criteria for recognition of localization and timing of multiple events of hydrothermal alteration in sandstones

illustrated by petrographic, fluid inclusion, and isotopic analysis of the Tera Group, Northern Spain: International Journal of Earth Sciences, v. 100, p. 1811-1826.

González-Acebrón, L., J. R. Mas, and J. Arribas, 2005, Provenance of fluvial sandstones at the beginning of the latest Jurassic-early Cretaceous rift stage of the north Iberian Basin, 8th International Conference on Fluvial Sedimentology: Abstract Book, Delft (Holland), p. 27-28.

González-Acebrón, L., Omodeo-Salé, S., López-Elorza, M., Mas, R., Arribas, J., Goldstein, R.H., 2013, Comparison between a Basin Thermal Model Based on Vitrinite Reflectance with Fluid Inclusion Microthermometry: Cameros Basin, N Spain, ECROFI XXII, Instanbul, Turkey, p. 55-56.

Gradstein, F. M., J. G. Ogg, and A. G. Smith, 2004, A geologic time scale 2004, v. 86, Cambridge University Press.

Guimerà , J., 1984, Paleogene evolution of deformation in the northeastern Iberian Peninsula, Cambridge Univ Press, p. 413-420.

Guimerà, J., Á. Alonso, and J. R. Mas, 1995, Inversion of an extensional-ramp basin by a newly formed thrust: the Cameros Basin (N. Spain), in J. G. Buchanan, and P. G. Buchanan, eds., Basin Inversion: Geological Society, London, Special Publications, v. 88, p. 433-453.

Guimerà, J., and M. Alvaro, 1990, Structure et Evolution de la compression alpine dans la Chaîne Ibérique et la chaîne côtière catalane (Espagne), SGF, p. 339-348.

Guimerà, J., R. Mas, and Á. Alonso, 2004, Intraplate deformation in the NW Iberian Chain: Mesozoic extension and Tertiary contractional inversion: Journal of the Geological Society, London, v. 161, p. 291-303.

Guiraud, M., 1983, Evolution tectono-sédimentaire du bassin wealdien (Crétacé inferieur) en relais de décrochements de Logroño-Soria (N-W Espagne), Université des Sciences et Techniques du Languedoc, Montpellier, 183 p.

Guiraud, M., and M. Séguret, 1985, A releasing solitary overstep model for the late Jurassic-early Cretaceous (Wealdian) Soria strike-slip basin (Northern Spain), in K. T. Biddle, and N. Christie-Blick, eds., Strike Slip Deformation, Basin Formation and Sedimentation: SEPM Special Publication, v. 37: Tulsa, Society of Economic Paleontologists and Mineralogists, p. 159-175.

Hantschel, T., and A. I. Kauerauf, 2009, Fundamentals of basin and petroleum systems modeling, Springer.

Haq, B. U., J. Hardenbol, and P. R. Vail, 1988, Mesozoic and Cenozoic chronostratigraphy and cycles of sea-level change: Sea-level changes: an integrated approach SEPM Spec. Publ, v. 42, p. 72-108.

Hernández-Samaniego, A., J. I. Ramírez-Merino, and A. Olivé-Davó, 1990, Hoja geológica 242 (Munilla). Mapa Geológico de España 1:50.000. Segunda Serie: Instituto Tecnológico GeoMinero de España.

Horsfield, B., D. Curry, K. Bohacs, R. Littke, J. Rullkötter, H. Schenk, M. Radke, R. Schaefer, A. Carroll, and G. Isaksen, 1994, Organic geochemistry of freshwater and alkaline lacustrine sediments in the Green River Formation of the Washakie Basin, Wyoming, USA: Organic

geochemistry, v. 22, p. 415-440.

Huck, G., and J. Karweil, 1955, Physikalisch-chemische probleme der inkohlung: Brennstoff-Chemie, v. 36, p. 2.

Hunt, J. M., M. Lewan, and R. J. Hennet, 1991, Modeling Oil Generation with Time-Temperature Index Graphs Based on the Arrhenius Equation (1): AAPG Bulletin, v. 75, p. 795-807.

Hutton, A. C., and D. A. Henstridge, 1985, Pyrolysis of Tertiary oil shale by a dolerite intrusion, Stuart Deposit, Queensland, Australia: Fuel, v. 64, p. 546-552.

I.G.M.E., 1971a, Mapa de sínteis geológica, E.: 1.200000. Hoja n.31. Soria.

I.G.M.E., 1971b, Mapa de síntesis geológica, E.: 1:200000. Hoja n. 21. Logroño.

ICCP, 1971, Internation Handbook of Coal Petrology: 1st Supplement to 2nd Edition, v. CNRS, Paris.

ICCP, 1975, International Handbook of Coal Petrography: 2nd Supplement to 2nd Edition, v. CNRS, Paris.

ICCP, 1998, The new vitrinite classification (ICCP System 1994): Fuel, v. 77, p. 349-358.

ICCP, 2001, The new inertinite classification (ICCP System 1994): Fuel, v. 80, p. 459-471.

IES, ed., 2007, PetroMod 2D Advanced, Tutorial Software Version 10, IES, GmbH Integrated Exploration System, Aachen.

ISO-7404-2, 2009, Methods for the Petrographic Analysis of Coals — Part 2: Methods of Preparing Coal Samples, International Organization for Standardization Geneva, Switzerland., p. 12 pp.

ISO-7404-5, 2009, Methods for the Petrographic Analysis of Coal—Part 5: Methods of Determining Microscopically the Reflectance of Vitrinite, International Organization for Standardization. Geneva, switzerland, p. 14 pp.

Jackson, C., and E. Larsen, 2008, Temporal constraints on basin inversion provided by 3D seismic and well data: a case study from the South Viking Graben, offshore Norway: Basin Research, v. 20, p. 397-417.

Jacob, H., 1989, Classification, structure, genesis and practical importance of natural solid oil bitumen ("migrabitumen"): International Journal of Coal Geology, v. 11, p. 65-79.

Jacob, H., 1993, Nomenclature, classification, characterization, and genesis of natural solid bitumen (migrabitumen), Bitumens in ore deposits, Springer, p. 11-27.

Jarvie, D. M., 1991, Factors affecting Rock-Eval derived kinetic parameters: Chemical Geology, v. 93, p. 79-99.

Jüntgen, H., and J. Klein, 1975, Entstehung von Erdgas aus kohligen Sedimenten: Erdöl und Kohle-Erdgas-Petrochemie, v. 28, p. 65-73.

Karweil, J., 1955, Die Metamorphose der Kohlen vom Standpunkt der physikalischen Chemie: Zeitschrift der Deutschen Geologischen Gesellschaft, p. 132-139.

Keen, C., 1979, Thermal history and subsidence of rifted continental margins-evidence from wells on the Nova Scotian and Labrador Shelves: Canadian journal of earth sciences, v. 16, p. 505-522.

Kelemen, S. R., C. C. Walters, P. J. Kwiatek, H. Freund, M. Afeworki, M. Sansone, W. A. Lamberti, R. J. Pottorf, H. G. Machel, and K. E. Peters, 2010, Characterization of solid bitumens originating from thermal chemical alteration and thermochemical sulfate reduction: Geochimica et Cosmochimica Acta, v. 74, p. 5305-5332.

Kendall, J.-M., S. Pilidou, D. Keir, I. Bastow, G. Stuart, and A. Ayele, 2006, Mantle upwellings, melt migration and the rifting of Africa: Insights from seismic anisotropy: Geological Society, London, Special Publications, v. 259, p. 55-72.

Kenig, F., A. Y. Huc, B. H. Purser, and J.-L. Oudin, 1990, Sedimentation, distribution and diagenesis of organic matter in a recent carbonate environment, Abu Dhabi, UAE: Organic geochemistry, v. 16, p. 735-747.

Khavari-Khorasani, G., and J. k. Michelsen, 1993, The thermal evolution of solid bitumens, bitumen reflectance, and kinetic modeling of reflectance: application in petroleum and ore prospecting: Energy sources, v. 15, p. 181-204.

Killops, S. D., and V. J. Killops, 2009, Introduction to organic geochemistry, John Wiley & Sons.

Kisch, H., 1987, Correlation between indicators of very low-grade metamorphism: Low temperature metamorphism, p. 227-300.

Klomp, U., and P. Wright, 1990, A new method for the measurement of kinetic parameters of hydrocarbon generation from source rocks: Organic geochemistry, v. 16, p. 49-60.

Kneuper-Haack, F., 1966, Ostrakoden aus dem Wealden der Sierra de los Cameros (Nordwestliche Iberische Ketten): Beihefte zum Geologischen Jahrbuch, v. 44, p. 165-209.

Kurz, T., R. Gloaguen, C. Ebinger, M. Casey, and B. Abebe, 2007, Deformation distribution and type in the Main Ethiopian Rift (MER): a remote sensing study: Journal of African Earth Sciences, v. 48, p. 100-114.

Lanaja, J. M., 1987, Contribución de la exploración petrolífera al conocimiento de la geología de España: Madrid, Instituto Geológico y Minero de España, 465 p.

Landis, C. R., and J. R. Castaño, 1995, Maturation and bulk chemical properties of a suite of solid hydrocarbons: Organic geochemistry, v. 22, p. 137-149.

Larrazet, M., 1896, Recherches géologiques sur la región orientale de la province de Burgos et sur quelques points des provincess d'Alava et de Logroño. These doctoral, Universidad de Paris, 310 p.

Law, C. A., 1999, Evaluating source rocks: Exploring for Oil and Gas Traps, American Association of Petroleum Geologists, Treatise of Petroleum Geology, Handbook of Petroleum Geology, p. 6-1.

Leeder, M., and R. Gawthorpe, 1987, Sedimentary models for extensional tilt-block/half-graben basins: Geological Society, London, Special Publications, v. 28, p. 139-152.

Leinfelder, R. R., 1994, Distribution of Jurassic reef types: a mirror of structural and environmental changes during breakup of Pangea: Global environment and resources: Canadian Society

of Petroleum Geologists, v. Memoir 17, p. 677-700.

Leischner, K., Welte, D.H., Littke, R., 1993, Fluid inclusions and organic maturity parameters as calibration tools in basin modelling, in A. G. Dore, Augustson, J.H., Hermanrud, C., Stewart, D.J., Sylta, Q., ed., Basin modelling: advances and applications, v. 3: Amsterdam, NPF Spec Publ. Elsevier, p. 161-172.

Lerche, I., 1988, Inversion of multiple thermal indicators: quantitative methods of determining paleoheat flux and geological parameters. I. Theoretical development for paleoheat flux: Mathematical Geology, v. 20, p. 1-36.

Littke, R., 2008, Dynamics of Complex Intracontinental Basins: The Central European Basin System, Springer.

Lotze, F., 1929, Stratigraphie und Tektonik des Keltiberischen Grundgebirges (Spanien). : Abh. Ges. Wiss. G6ttingen math. phys. K.N.F., v. 14, p. 320. Traduc. San Miguel de la Cámara, M.: Estratigrafia y tectónica de las cadenas paleozoicas celtibéricas. Publ. Extr. Geol. Esp., 8, 313, 1955.

Lotze, F., 1961, Das Kambrium Spanien. Teil 1: Stratigraphie: Wiss. Lit. Abh. Math. Naturwiss Kl, v. 6, p. 283-498. Traduc. Gómez de Liarena, J.: El cámbrico de España. Memorias LG.ME., 70, 356 p., 1970.

Mackenzie, A. S., and T. M. Quigley, 1988, Principles of geochemical prospect appraisal: AAPG Bulletin, v. 72, p. 399-415.

Magoon, L. B., and E. A. Beaumont, 1999, Treatise of Petroleum Geology/Handbook of Petroleum Geology: Exploring for Oil and Gas Traps. Chapter 3: Petroleum Systems.

Magoon, L. B., and W. G. Dow, 1994, The petroleum system: The petroleum system—From source to trap: AAPG Memoir, v. 60, p. 3-24.

Mallada, L., 1904, Explicación del Mapa Geológico de España: Sistemas Infracretáceo y Cretáceo, v. 5: Madrid, Est. Tip. Viuda e Hijos de M. Tello, 519 p.

Mallada, L., 1984, Sinopsis de las especies fósiles que se han encontrado en España: Bol. Com. Mapa Geol. Esp. XI, Madrid, p. 209-358.

Mallada, L., 1985, Índice alfabético de los géneros y especies de los sistemas triásico y jurásico que se resñan en el Tomo II de la sinopsis paleontológica de España: Bol. Com. Mapa Geol. Esp. XIII, Madrid, p. 631-640.

Mallada, L., 1987, Sinopsis de las especies fósiles que se han encontrado en España. Sistema Cuenca de Cameros: Revista de la Sociedad Geológica de España, v. 11, p. 253-269.

Mann, U., T. Hantschel, R. Schaefer, B. Krooss, D. Leythaeuser, R. Littke, and R. Sachsenhofer, 1997, Petroleum migration: mechanisms, pathways, efficiencies and numerical simulations, Petroleum and basin evolution, Springer, p. 403-520.

Mantilla-Figueroa, L. C., 1999, El metamorfismo hidrotermal de la Sierra de Cameros (La Rioja, España): petrología, geoquímica, geocronología y contexto estructural de los procesos de interacción fluido-roca. Doctoral Thesis, Universidad Complutense de Madrid, Madrid, 361 p.

Mantilla-Figueroa, L. C., C. Casquet, C. Galindo, and R. Mas, 2002, El metamorfismo hidrotermal

cretácico y paléogeno en la Cuenca de Cameros (Cordillera ibérica, España): Zubía Monográfico, v. 14, p. 143-154.

Mantilla-Figueroa, L. C., C. Casquet, and J. R. Mas, 1998, Los paleofluidos en el Grupo Oncala, Cuenca de Cameros (la Rioja, España): Datos de inclusiones fluidas, isótopos de oxígeno y SEM: Geogaceta, v. 24, p. 207-210.

Mantilla-Figueroa, L. C., C. Casquet, and J. R. Mas, 1999, Comparación entre el metamorfismo de la Cuenca de Cameros y el de la Cuenca Aurífera de Witwatersrand (Suráfrica). Implicaciones Metalogenéticas: Geogaceta, p. 131-134.

Martín-Closas, C., and Á. Alonso-Millán, 1998, Estratigrafía y bioestratigrafía (Charophyta) del Cretácico inferior en el sector occidental de la cuenca de Cameros (Cordillera Ibérica): Revista de la Sociedad Geológica de España, v. 11, p. 253-269.

Martínez, L., J. Connan, B. O., B. Sahuquet, and R. Martínez-Ortegon, 1993, Etude de la migration primaire des hydrocarbures en laboratoire: Le modèle Expoil: Bull. Centres Rech. Explor.-Prod. Société Nationale Elf-Aquitaine, v. 18, Pub. Spec., p. 37-59.

Mas, J. R., Á. Alonso, and M. I. Benito, 1997, Depositional and diagenetic evolution of late Jurassic coral reefs in Northern Iberian Ranges (North Spain). Boletín de la Real Sociedad Española de Historia Natural (Sección Geológica), v. 92, p. 143-160.

Mas, J. R., A. Alonso, A. García, C. Arias, L. Vilas, N. Meléndez, and R. Rincón, 1982, Les grandes étapes dans l'evolution du Crétacé de la zone sudoccidental de la Chaîne Ibérique (Espagne): 9 Reunion Annuelle des Sciences de la Terre, Soc. Géol. de France, Paris, p. 417.

Mas R, A. J., Miranda J, Najarro M, Benito MI, Arribas ME, Le Pera E 2009, Fluvial architecture and provenance evolution at the ending sedimentary record of a rift basin (Early Cretaceous, Cameros Basin, N Spain): 27th IAS Meeting p. 598.

Mas, R., Á. Alonso, and J. Guimerà, 1993, Evolución tectonosedimentaria de una cuenca extensional intraplaca: La cuenca finijurásica-eocretácica de Los Cameros (La Rioja-Soria): Revista de la Sociedad Geológica de España, v. 6, p. 129-144.

Mas, R., J. Arribas, J. Miranda, M. Najarro, M. I. Benito, M. E. Arribas, and E. le Pera, 2009, Fluvial architecture and provenance evolution at the ending sedimentary record of a rift basin (Early Cretaceous, Cameros Basin, N Spain), in V. Pascucci, and S. Andreucci, eds., Sedimentary environments of Mediterranean Island(s)-27th IAS Meeting, Alghero (Italy), p. 598.

Mas, R., M. I. Benito, J. Arribas, A. Alonso, M. E. Arribas, L. González-Acebrón, J. Hernán, E. Quijada, P. Suárez, and S. Omodeo-Salé, 2011, Evolution of an intra-plate rift basin: the Latest Jurassic-Early Cretaceous Cameros Basin (Northwest Iberian Ranges, North Spain), in L. P. a. F. C. C. Arenas, ed., Post-Meeting field trips 28th IAS Meeting, Zaragoza (Spain), p. 117-154.

Mas, R., M. I. Benito, J. Arribas, A. Serrano, J. Guimerà, Á. Alonso, and J. Alonso-Azcárate, 2002, La Cuenca de Cameros: desde la extensión finijurásica-eocretácica a la inversión Terciaria - Implicaciones en la exploración de hidrocarburos: Zubía Monográfico, v. 14, p. 9-64.

Mas, R., M. I. Benito, J. Arribas, A. Serrano, J. Guimerà, Á. Alonso, and J. Alonso-Azcárate, 2003, Geological Field Trip 11-The Cameros Basin: From Late Jurassic-Early Cretaceous

Extension to Tertiary Contractional Inversion-Implications of Hydrocarbon Exploration, AAPG International Conference and Exhibition, Barcelona (Spain), Total, p. 1-52.

Mata-Campo, M. P., 1997, Caracterización y evolución mineralógicas de la cuenca mesozoica de Cameros (Soria-La Rioja), Universidad de Zaragoza, Zaragoza, 349 p.

Mata, M. P., A. M. Casas, A. Canals, A. Gil, and A. Pocoví, 2001, Thermal history during Mesozoic extension and Tertiary uplift in the Cameros Basin, northern Spain: Basin Research, v. 13, p. 91-111.

McClay, K., 1992, Glossary of thrust tectonics terms: Thrust tectonics, v. 419-433.

McClay, K. R., 1990, Extensional fault systems in sedimentary basins: a review of analogue model studies: Marine and Petroleum Geology, v. 7, p. 206-233.

McKenzie, D., 1978, Some remarks on the development of sedimentary basins: Earth and Planetary Science Letters, v. 40, p. 25-32.

Meléndez, N., and L. Vilas, 1980, Las facies detríticas de la región de Picofrentes (Soria): Boletín de la Real Sociedad Española de Historia Natural (Sección Geológica), v. 78, p. 157-174.

Miegebielle, V., Y. Hervouet, and J. P. Xavier, 1993, Analyse structurale de la partie méridionale du bassin de Soria (Espagne): Bulletin des Centres de Recherches Exploration-Production Elf-Aquitaine, v. 17, p. 19-37.

Mitchum, R. J., P. Vail, and J. Sangree, 1977, Seismic stratigraphy and global changes of sea level, part 7: seismic stratigraphic interpretation procedure. Seismic Stratigr: Appl Hydrocarb Explor: AAPG Memoir, v. 26, p. 135-143.

Mitra, S., and J. S. Namson, 1989, Equal-area balancing: American Journal of Science, v. 289, p. 563-599.

Mora, A., T. Gaona, J. Kley, D. Montoya, M. Parra, L. I. Quiroz, G. Reyes, and M. R. Strecker, 2009, The role of inherited extensional fault segmentation and linkage in contractional orogenesis: a reconstruction of Lower Cretaceous inverted rift basins in the Eastern Cordillera of Colombia: Basin Research, v. 21, p. 111-137.

Muñoz-Recio, A., 1993, Análisis del Pérmico y Triásico en el subsuelo del tercio noroccidental de la Cordillera Ibérica y áreas adyacentes, Universidad Complutense de Madrid, Madrid, 367 p.

Muñoz, A., A. Soria, J. I. Canudo, A. M. Casas, A. Gil, and M. P. Mata, 1997, Caracterización estratigráfica y sedimentológica del Albiense marino del borde Norte de la Sierra de Cameros. Implicaciones paleogeográficas: Cuadernos de Geología Ibérica, v. 22, p. 139-163.

Najarro de la Parra, M., 2005, Sedimentología y diagénesis del Grupo Oliván: la secuencia Aptiense superior-Albiense inferior de la Cuenca de Cameros (La Rioja), Universidad Complutense de Madrid, Madrid, 117 p.

Navarro-Vázquez, D., 1991, Hoja geológica 350 (Soria). Mapa Geológico de España 1:50.000. Segunda Serie: Instituto Tecnológico GeoMinero de España.

Navarro Vázquez, D., Gabaldón López, V. and Martín Serrano, A., 1991, Mapa Geológico de España. E: 1:50000. Hoja 350, Soria.

Navás, L., 1931, El Moncayo: Revista de la Academia de Ciencias Exactas Físico-Químicas y Naturales, v. XV, p. 49-90.

Ochoa-Rodríguez, M., 2006, Procedencia y diagénesis del registro arenoso del Grupo Urbión (Cretácico inferior) de la Cuenca de Cameros (Cordillera Ibérica septentrional), Universidad Complutense de Madrid, Madrid, 240 p.

Ochoa, M., J. Arribas, and R. Mas, 2004, Changes in sandstone composition during Lower Cretaceous syn-rift fluvial sedimentation (Cameros Basin, Spain) 32nd International Geological Congress: Abstract CD - Session 242-34, Florence (Italia).

Ochoa, M., M. E. Arribas, J. Arribas, and R. Mas, 2007, Significance of geochemical signatures on provenance in intracratonic rift basins: Examples from the Iberian plate, in J. Arribas, M. J. Johnsson, and S. Critelli, eds., Sedimentary Provenance and Petrogenesis: Perspectives from Petrography and Geochemistry: Geological Society of America Special Papers, v. 420, p. 199-219.

Ogg, J. G., G. Ogg, and F. M. Gradstein, 2008, The concise geologic time scale, v. 1.

Okui, A., and D. Waples, 1992, The influence of oil expulsion efficiency on the type of hydrocarbons accumulating in traps: Proceedings, Offshore SE Asia, 9th Conference and Exhibition, l-2 December 1992, 685.

Omodeo Salé, S., J. Guimerà, R. Mas, and J. Arribas, 2014, Tecono-Stratigraphic Evolution of an Inverted Extensional Basin: The Cameros Basin (North of Spain). : International Journal of Earth Sciences, v. 103, (6), p. 1597-1620, DOI: 10.1007/s00531-014-1026-5

Omodeo-Salé, S., Salas, R., Ondrak, R. , Suárez-Ruiz, I., Martínez, L., Mas, R., Arribas, J., Guimerà, J., in rev.1, Subsidence analysis and 2D thermal modelling of an inverted extensional basin (Cameros Basin, North of Spain): Basin Research.

Palacas, J. G., D. E. Anders, and J. D. King, 1984, South Florida basin--a prime example of carbonate source rocks of petroleum, in J. G. Palacas, ed., Petroleum Geochemestry and source rock potential of carbonate rocks, v. 18, American Association Petroleum Geology Studies in Geology, p. 71-96.

Palacios-Sáenz, P., 1890, Descripción física, geológica y agrológica de la provincia de Soria: Memorias de la Comisión del Mapa Geológico de España, Imp. y Fund. de Manuel Tello, 558 p.

Palacios, P., and R. Sánchez Lozano, 1885, La formación wealdense en las provincias de Soria y Logroño: Boletín de la Comisión del Mapa Geológico de España, v. 12, p. 109-140.

Pedersen, T., and S. Calvert, 1990, Anoxia vs. Productivity: What Controls the Formation of Organic-Carbon-Rich Sediments and Sedimentary Rocks?(1): AAPG Bulletin, v. 74, p. 454-466.

Pelet, R., and Y. Debyser, 1977, Organic geochemistry of Black Sea cores: Geochimica et Cosmochimica Acta, v. 41, p. 1575-1586.

Pepper, A. S., and P. J. Corvi, 1995, Simple kinetic models of petroleum formation. Part I: oil and gas generation from kerogen: Marine and Petroleum Geology, v. 12, p. 291-319.

Pérez-Estaún, A., F. Bastida, J. Martínez Catalán, J. Gutiérrez-Marco, A. Marcos, and J. Pulgar,

1990, West Asturian-Leonese Zone: Stratigraphy. RD Dallmeyer, E.Martinez García (Eds.), Pre-Mesozoic Geology of Iberia, Springer, Berlin (1990), pp. 92–102.

Permanyer, A., G. Márquez, and J. Gallego, 2013, Compositional variability in oils and formation waters from the Ayoluengo and Hontomín fields (Burgos, Spain). Implications for assessing biodegradation and reservoir compartmentalization: Organic geochemistry, v. 54, p. 125-139.

Permanyer, A., R. Salas, R. Mas, and J. Arribas, 2011, Geochemical characterization of tar sands in southern Cameros Basin: implications for source rocks derivation, 28th IAS, Meeting of Sedimentology, Zaragoza, Spain, p. 572.

Peters, K., 1986, Guidelines for evaluating petroleum source rock using programmed pyrolysis: AAPG Bulletin, v. 70, p. 318-329.

Peters, K., 2009, Basin and petroleum system modeling: AAPG Getting Started Series, v. 16.

Peters, K. E., and M. R. Cassa, 1994, Applied source rock geochemistry: MEMOIRS-AMERICAN ASSOCIATION OF PETROLEUM GEOLOGISTS, p. 93-93.

Peters, K. E., C. C. Walters, and J. M. Moldowan, 2005, The biomarker guide: biomarkers and isotopes in the environment and human history, v. 1, Cambridge University Press Ed.

Platt, N. H., 1989a, Climatic and tectonic controls on sedimentation of a Mesozoic lacustrine sequence: the Purbeck of the Western Cameros Basin, Northern Spain: Palaeogeography, Palaeoclimatology, Palaeoecology, v. 70, p. 187-197.

Platt, N. H., 1989b, Continental sedimentation in an evolving rift basin: the Lower Cretaceous of the western Cameros Basin (northern Spain): Sedimentary Geology, v. 64, p. 91-109.

Platt, N. H., 1990, Basin evolution and fault reactivation in the western Cameros Basin, Northern Spain: Journal of the Geological Society, London, v. 147, p. 165-175.

Platt, N. H., 1995, Sedimentation and tectonics of a synrift succession: Upper Jurassic alluvial fans and palaeokarst at the late Cimmerian unconformity, western Cameros Basin, northern Spain, in A. G. Plint, ed., Sedimentary facies analysis: a tribute to the research and teaching of Harold G. Reading: Special Publication of the International Association of Sedimentologists, v. 22, Blackwell, p. 219-236.

Poelchau, H., D. Baker, T. Hantschel, B. Horsfield, and B. Wygrala, 1997, Basin simulation and the design of the conceptual basin model, Petroleum and basin evolution, Springer, p. 3-70.

Pujalte, V., S. Robles, J. García-Ramos, and J. Hernández, 2004, El Malm-Barremiense no marinos de la Cordillera Cantábrica, in J. A. Vera, ed., Geología de España: , Instituto Geológico y Minero de España Sociedad Geologica de España, Madrid, p. 288-291.

Quigley, T., and A. Mackenzie, 1988, The temperatures of oil and gas formation in the sub-surface: Nature, v. 333, p. 549-552.

Quigley, T., A. Mackenzie, and J. Gray, 1987, Kinetic theory of petroleum generation: Collection colloques et séminaires-Institut français du pétrole, p. 649-665.

Quijada, I. E., P. Suárez-González, M. I. Benito, and R. Mas, 2013a, Depositional Depth of Laminated Carbonate Deposits: Insights From the Lower Cretaceous Valdeprado

Formation (Cameros Basin, Northern Spain): Journal of Sedimentary Research, v. 83, p. 241-257.

Quijada, I. E., P. Suárez González, B. Moreno, M. Isabel, and J. Mas, 2013b, New insights on stratigraphy and sedimentology of the Oncala Group (eastern Cameros Basin): implications for the paleogeographic reconstruction of NE Iberia at Berriasian times: Journal of Iberian Geology, v. 39, p. 313-334.

Quijada, I. E., P. Suárez González, B. Moreno, M. Isabel, J. R. Mas, and Á. Alonso Millán, 2010, Un ejemplo de llanura fluvio-deltaica influenciada por las mareas: el yacimiento de icnitas de Serrantes (Grupo Oncala, Berriasiense, Cuenca de Cameros, N. de EspaÃ±a): Geogaceta, v. 49, p. 15-18.

Quintero-Amador, I., and H. Mansilla-Izquierdo, 1981, Hoja geológica 348 (San Leonardo de Yagüe). Mapa Geológico de España 1:50.000. Segunda Serie: Instituto Geológico y Minero de España.

Quintero-Amador, I., and H. Mansilla-Izquierdo, 1982, Hoja geológica 315 (Santo Domingo de Silos). Mapa Geológico de España 1:50.000. Segunda Serie: Instituto Geológico y Minero de España.

Quintero-Amador, I., and H. Mansilla-Izquierdo, 1986, Hoja geológica 316 (Quintanar de la Sierra). Mapa Geológico de España 1:50.000. Segunda Serie: Instituto Geológico y Minero de España.

Quintero-Amador, I., and H. Mansilla-Izquierdo, 1988, Hoja geológica 317 (Vinuesa). Mapa Geológico de España 1:50.000. Segunda Serie: Instituto Geológico y Minero de España.

Rahimi, P., T. Gentzis, W. H. Dawson, C. Fairbridge, C. Khulbe, K. Chung, V. Nowlan, and A. DelBianco, 1998, Investigation of coking propensity of narrow cut fractions from Athabasca bitumen using hot-stage microscopy: Energy & fuels, v. 12, p. 1020-1030.

Ramírez-Merino, J. I., A. Olivé-Davó, M. Álvaro-López, and A. Hernández-Samaniego, 1990, Hoja geológica 241 (Anguiano). Mapa Geológico de España 1:50.000. Segunda Serie: Instituto Geológico y Minero de España.

Rat, P., 1988, The Basque-Cantabrian basin between the Iberian and European plates: Some facts but still many problems: Rev. Soc. Geol. Esp, v. 1, p. 327-348.

Rey, D., and A. Ramos, 1991, Estratigrafía y sedimentología del Pérmico y Triásico del sector Deza-Castejón (Soria): Revista Sociedad Geológica Española, v. 4, p. 105-126.

Rey de la Rosa, J., and S. Rivera-Navarro, 1981a, Hoja geológica 318 (Almarza). Mapa Geológico de España 1:50.000. Segunda serie: Instituto Geológico y Minero de España.

Rey de la Rosa, J., and S. Rivera-Navarro, 1981b, Hoja geológica 319 (Agreda). Mapa Geológico de España 1:50.000. Segunda Serie: Instituto Geológico y Minero de España, p. 24.

Rey, J., and Rivera, S., 1981, Hoja Geológica nº 319, Ágreda. S: 1:50000: Mapa geológico de España, v. Serie M.A.G.N.A. I.G.M.E.

Richter, G., 1930, Las Cadenas Celtibéircas entre el Valle del Jalón y la Sierra de la Demanda: Publicación Extra de Geología de España, v. 9, p. 62-142.

Richter, G. T., R., 1933, Die Entwicklung der Keltiberischen Ketten: Abh. Ges. Wiss. Göttingen,

v. III, 7, p. 1-118.

Rosales, I., K. Gräfe, S. Robles, S. Quesada, and M. Floquet, 2002, The Basque–Cantabrian Basin: Gibbons W, Mo-In: Gibbons W, Moreno T (eds) The Geology of Spain. The Geological Society, London, p. 272-284.

Rouby, D., H. Fossen, and P. R. Cobbold, 1996, Extension, displacement, and block rotation in the larger Gullfaks area, northern North Sea: determined from map view restoration: AAPG Bulletin-American Association of Petroleum Geologists, v. 80, p. 875.

Roure, F., J.-P. Brun, B. Colletta, and J. Van Den Driessche, 1992, Geometry and kinematics of extensional structures in the Alpine foreland basin of southeastern France: Journal of Structural Geology, v. 14, p. 503-519.

Royden, L., 1986, A simple method for analyzing subsidence and heat flow in extensional basins: Thermal Modeling in Sedimentary Basins (ed. Burrus-Jean), Paris: Technip, p. 49-73.

Royden, L., and C. Keen, 1980, Rifting process and thermal evolution of the continental margin of eastern Canada determined from subsidence curves: Earth and Planetary Science Letters, v. 51, p. 343-361.

Sáenz García, C., 1942, Notala para el estudio de la facies Weáldica española: Asociación Española para el progreso de las Ciencias, p. 59-76.

Salas, R., and A. Casas, 1993, Mesozoic extensional tectonics, stratigraphy and crustal evolution during the Alpine cycle of the eastern Iberian basin: Tectonophysics, v. 228, p. 33-55.

Salas, R., J. Guimerà, R. Mas, C. Martín-Closas, A. Meléndez, and Á. Alonso, 2001, Evolution of the Mesozoic Central Iberian Rift System and its Cainozoic inversion (Iberian chain), in P. A. Ziegler, W. Cavazza, R. A. H. F., and S. Crasquin-Soleau, eds., Peri-Tethys Memoir 6: Peri-Tethyan Rift/Wrench Basins and Passive Margins: Mémoires du Museum National d'Histoire Naturelle, v. 186: Paris, p. 145-186.

Salomon, J., 1982a, Les formations continentales du bassin de Soria (NW Chaînes ibériques) au Jurassique Supérier-Crétacé Inferieur. Relations entre tectonique et sedimentation: Cuadernos de Geología Ibérica, v. 8, p. 167-185.

Salomon, J., 1982b, Les formations continentales du Jurassique Supérieur-Crétacé Inférieur (Espagne du Nord-Chaînes Cantabrique et NW Ibérique): stratigraphie, sédimentologie, cartographie, relations entre tectonique et sédimentation: Mémoires Géologiques de l'Université de Dijon, v. 6: Dijon, Institut des Sciences de la Terre, 228 p.

Salomon, J., 1983a, Le Crétacé inférieur continental. Le Fosse de Soria, Vue Sur le Crétacé Basco-Cantabrique et Nord-Ibérique: Mémoires Géologiques de l'Université de Dijon, v. 9: Dijon, Institut des Sciences de la Terre, p. 25-43.

Salomon, J., 1983b, Les phases "fossé" dans l'histoire du bassin de Soria (Espagne du Nord) au Jurassique supérieur-Crétacé inférieur: Bulletin des Centres de Recherches Exploration-Production Elf-Aquitaine, v. 7, p. 399-407.

Sánchez-Lozano, R., 1894, Descripción física, geológica y minera de la provincia de Logroño: Memorias de la Comisión del Mapa Geológico de España, Madrid Comisión del Mapa Geológico de España Est. Tip. Vda. e Hijos de M. Tello 548 p.

Sanz, R. n., 1967, Ayoluengo Field. Southwest Cantabrian Basin North-Central Spain: 7th World Petroleum Congress.

Sclater, J. G., and P. Christie, 1980, Continental stretching: An explanation of the post-Mid-Cretaceous subsidence of the central North Sea Basin: Journal of Geophysical Research: Solid Earth (1978-2012), v. 85, p. 3711-3739.

Schlische, R. W., 1991, Half-graben basin filling models: new constraints on continental extensional basin development: Basin Research, v. 3, p. 123-141.

Schlische, R. W., and P. E. Olsen, 1990, Quantitative filling model for continental extensional basins with applications to early Mesozoic rifts of eastern North America: The Journal of Geology, p. 135-155.

Schmoker, J. W., and R. B. Halley, 1982, Carbonate porosity versus depth; a predictable relation for South Florida: AAPG Bulletin, v. 66, p. 2561-2570.

Schudack, M., 1987, Charophytenflora und fazielle Entwicklung der Grenzschichten mariner Jura/Wealden in den Nordwestlichen Iberischen Ketten (mit Vergleichen zu Asturien und Kantabrien): Palaeontographica Beiträde zur Naturgeschichte der Vorzeit Abteilung B, v. 204, p. 1-180.

Schudack, M., and U. Schudack, 1989, Late Kimmeridgian to Berriasian paleogeography of the northwestern Iberian Ranges (Spain): Berliner Geowissenschaftliche Abhandlungen, p. 445-457.

Simancas, J., R. Carbonell, F. González Lodeiro, A. Pérez Estaún, C. Juhlin, P. Ayarza, A. Kashubin, A. Azor, D. Martínez Poyatos, and G. R. Almodóvar, 2003, Crustal structure of the transpressional Variscan orogen of SW Iberia: SW Iberia deep seismic reflection profile (IBERSEIS): Tectonics, v. 22.

Sleep, N. H., 1971, Thermal effects of the formation of Atlantic continental margins by continental break up: Geophysical Journal International, v. 24, p. 325-350.

Snowdon, L., and T. Powell, 1982, Immature oil and condensate--modification of hydrocarbon generation model for terrestrial organic matter: AAPG Bulletin, v. 66, p. 775-788.

Soto, R., A. Casas-Sainz, M., and P. del Río, 2007, Geometry of half-grabens containing a mid-level viscous décollement: Basin Research, v. 19, p. 437-450.

Stach, E., M.-T. Mackowsky, M. Teichmüller, G. Taylor, D. Chandra, and R. Teichmüller, 1982, Coal petrology: Gebrüder Borntraeger, Berlin, p. 535.

Suárez-González, P., I. E. Quijada, M. I. Benito, and R. Mas, 2013, Eustatic versus tectonic control in an intraplate rift basin (Leza Fm, Cameros Basin). Chronostratigraphic and paleogeographic implications for the Aptian of Iberia: Journal of Iberian Geology, v. 39, p. 285-312.

Suárez-Ruiz, I., D. Flores, J. G. Mendonça Filho, and P. C. Hackley, 2012, Review and update of the applications of organic petrology: Part 1, geological applications: International Journal of Coal Geology, v. 99, p. 54-112.

Suárez González, P., I. E. Quijada, J. Mas, and M. I. Benito, 2010, Nuevas aportaciones sobre la influencia marina y la edad de los carbonatos de la Fm Leza en el sector de Préjano (SE

de La Rioja). Cretácico Inferior, Cuenca de Cameros: Geogaceta, p. 7-10.

Sundararaman, P., P. H. Merz, and R. G. Mann, 1992, Determination of kerogen activation energy distribution: Energy & fuels, v. 6, p. 793-803.

Sundararaman, P., S. C. Teerman, R. G. Mann, and B. Mertani, 1988, Activation energy distribution: A key parameter in basin modeling and a geochemical technique for studying maturation and organic facies: Proceedings, Indonesian Petroleum Association, 17th Annual Convention, October 1988, p. 169-185.

Suppe, J., 1983, Geometry and kinematics of fault-bend folding: American Journal of Science, v. 283, p. 684-721.

Sweeney, J. J., and A. K. Burnham, 1990, Evaluation of a Simple Model of Vitrinite Reflectance Based on Chemical Kinetics (1): AAPG Bulletin, v. 74, p. 1559-1570.

Sýkorová, I., W. Pickel, K. Christanis, M. Wolf, G. Taylor, and D. Flores, 2005, Classification of huminite—ICCP System 1994: International Journal of Coal Geology, v. 62, p. 85-106.

Taylor, G., M. Teichmüler, A. Davis, C. Diessel, R. Littke, and P. Robert, 1998, Organic petrology: Berlin: Gebrüder Borntraeger.

Tegelaar, E. W., and R. A. Noble, 1994, Kinetics of hydrocarbon generation as a function of the molecular structure of kerogen as revealed by pyrolysis-gas chromatography: Organic geochemistry, v. 22, p. 543-574.

Teichmuller, M., 1973, Generation of petroleum-like substances in coal seams as seen under the microscope: Advances in organic geochemistry, v. 1974, p. 321-348.

Teichmüller, M., 1974a, Entstehung und Veränderung bituminöser Substanzen in Kohlen in Beziehung zur Entstehung und Umwandlung des Erdöls: Fortschr. Geol. Rheinl. Westfalen, v. 24, p. 65-112.

Teichmüller, M., 1974b, Über neue Macerale der Liptinit-Gruppe und die Entstehung von Micrinit: Fortschr. Geol. Rheinl. Westfalen, v. 24, p. 37-64.

Teichmüller, M., 1989, The genesis of coal from the viewpoint of coal petrology: International Journal of Coal Geology, v. 12, p. 1-87.

Teichmüller, M., and R. Teichmüller, 1982, Fundamentals of coal petrology: Stach, E., Mackowsky, M.-Th., Teichmüller, M., Taylor, GH, Chandra, D., and Techmüller, R., Stach's Textbook of Coal Petrology, 3rd revised and enlarged edition: Berlin, Stuttgart, Gebrüder Borntraeger, p. 5-86.

Tischer, G., 1965, Über die Wealden-Ablagerung und die Tektonik der östlichen Sierra de los Cameros in den nordwestlichen Iberischen Ketten (Spanien): Beihefte zum Geologischen Jahrbuch, v. 44, p. 123-164.

Tischer, G., 1966a, Datos geomorfológicos sobre la cuenca superior del río Alhama: Notas y Comunicaciones del Instituto Geológico y Minero de España, v. 84, p. 55-92.

Tischer, G., 1966b, El delta weáldico de las Montañas Ibéricas Occidentales y sus enlaces tectónicos: Notas y Comunicaciones del Instituto Geológico y Minero de España, v. 81, p. 53-78.

Tissot, B., and J. Espitalié, 1975, L'evolution thermique de la matière organique des sédiments: applications d'une simulation mathématique. Potentiel pétrolier des bassins sédimentaires de reconstitution de l'histoire thermique des sédiments: Oil & Gas Science and Technology, v. 30, p. 743-778.

Tissot, B., R. Pelet, and P. Ungerer, 1987, Thermal history of sedimentary basins, maturation indices, and kinetics of oil and gas generation: AAPG Bull.;(United States), v. 71.

Tissot, B., and D. Welte, 1984, Petroleum Formation and Occurrence, Springer Verlag, Berlin.

Tomić, J., F. Behar, M. Vandenbroucke, and Y. Tang, 1995, Artificial maturation of Monterey kerogen (Type II-S) in a closed system and comparison with Type II kerogen: implications on the fate of sulfur: Organic geochemistry, v. 23, p. 647-660.

Ungerer, P., 1984, Models of petroleum formation: how to take into account geology and chemical kinetics: Thermal Phenomena in Sedimentary Basins, p. 235-246.

Ungerer, P., 1990, State of the art of research in kinetic modelling of oil formation and expulsion: Organic geochemistry, v. 16, p. 1-25.

Ungerer, P., 1993, Modeling of petroleum generation and migration: Applied Petroleum Geochemistry, p. 395-442.

Ungerer, P., J. Burrus, B. Doligez, P. Chenet, and F. Bessis, 1990, Basin Evaluation by Integrated Two-Dimensional Modeling of Heat Transfer, Fluid Flow, Hydrocarbon Generation, and Migration (1): AAPG Bulletin, v. 74, p. 309-335.

Ungerer, P., J. Espitalié, F. Marquis, and B. Durand, 1986, Use of kinetic models of organic matter evolution for the reconstruction of paleotemperatures: application to the case of the Gironville well (France), in J. Burrus, ed., Thermal modelling in sedimentary basins: Paris, Technip, Paris, p. 531-546.

Ungerer, P., and R. Pelet, 1987, Extrapolation of the kinetics of oil and gas formation from laboratory experiments to sedimentary basins.

Urrutia, P. L., 1878, Datos geológico-mineros de la provincia de Logroño: Boletín de la Comisión del Mapa Geológico de España, v. 5, p. 315-320.

Vail, P., J. Hardenbol, and R. Todd, 1984, Jurassic unconformities, chronostratigraphy, and sea-level changes from seismic stratigraphy and biostratigraphy.

Vail, P. R., 1977, Seismic stratigraphy and global changes of sea level, Part 5: Chronostratigraphic significance of seismic reflections, Seismic stratigraphy-applications to hydrocarbon exploration: Mem. Amer. Assoc. Petrol. Geol., p. 99-116.

Vail, P. R., 1987, Seismic stratigraphy interpretation using sequence stratigraphy: Part 1: Seismic stratigraphy interpretation procedure, in A. Bally, ed., Atlas of Seismic Stratigraphy, v. AAPG Studies in Geology, p. 1-10.

Vera, J.-A., 2001, Evolution of the South Iberian continental margin: Mémoires du Muséum national d'histoire naturelle, v. 186, p. 109-143.

Verges, J., and J. Garcia-Senz, 2001, Mesozoic evolution and Cainozoic inversion of the Pyrenean rift: Mémoires du Muséum national d'histoire naturelle, v. 186, p. 187-212.

Viallard, P., 1989, Decollement de couverture et decollement medio-crustal dans une chaine intraplaque; variations verticales du style tectonique des Iberides (Espagne): Bulletin de la Societe Geologique de France, p. 913-918.

Villalaín, J. J., G. Fernández-González, A. M. Casas, and A. Gil-Imaz, 2003, Evidence of a Cretaceous remagnetization in the Cameros Basin (North Spain): implications for basin geometry: Tectonophysics, v. 377, p. 101-117.

Waltham, D., 2001, Decompact: Royal Holloway (UK).

Waples, D. W., H. Kamata, and M. Suizu, 1992, The Art of Maturity Modeling, Part 1: Finding a Satisfactory Geologic Model (1): AAPG Bulletin, v. 76, p. 31-46.

Watts, A., and W. Ryan, 1976, Flexure of the lithosphere and continental margin basins: Tectonophysics, v. 36, p. 25-44.

Watts, A., and M. Steckler, 1981, Subsidence and tectonics of Atlantic-type continental margins: Oceanol. Acta, v. 4, p. 143-153.

Weeks, L. G., 1952, Factors of sedimentary basin development that control oil occurrence: AAPG Bulletin, v. 36, p. 2071-2124.

Welte, D., and M. Yalçin, 1987, Formation and occurrence of petroleum in sedimentary basins as deduced from computer-aided basin modelling: Petroleum geochemistry and exploration in the Afro-Asian region. Balkema, Rotterdam, p. 17-23.

Welte, D., and M. Yalçin, 1988, Basin modelling—a new comprehensive method in petroleum geology: Organic geochemistry, v. 13, p. 141-151.

Welte, D., and M. Yukler, 1981a, Petroleum origin and accumulation in basin evolution--a quantitative model: AAPG Bulletin, v. 65, p. 1387-1396.

Welte, D., and M. Yukler, 1981b, Petroleum origin and accumulation in basin evolution: A quantitative model: Am. Assoc. Pet. Geol., Bull.;(United States), v. 65.

Welte, D. H., B. Horsfield, and D. R. Baker, 1997, Petroleum and basin evolution: insights from petroleum geochemistry, geology and basin modeling.

Wernicke, B., 1985, Uniform-sense normal simple shear of the continental lithosphere: Canadian journal of earth sciences, v. 22, p. 108-125.

Wygrala, B., 1988, Integrated computer-aided basin modeling applied to analysis of hydrocarbon generation history in a Northern Italian oil field: Organic geochemistry, v. 13, p. 187-197.

Yalçin, M., R. Littke, and R. Sachsenhofer, 1997, Thermal history of sedimentary basins, Petroleum and basin evolution, Springer, p. 71-167.

Yalçin, M. N., 1991, Basin modeling and hydrocarbon exploration: Journal of Petroleum Science and Engineering, v. 5, p. 379-398.

Yalçin, M. N., and D. Welte, 1988, The thermal evolution of sedimentary basins and significance for hydrocarbon generation: Bulletin Turkish Petroleum Geology, v. Ankara, 1, p. 12-26.

Ziegler, P., 1978, North Sea rift and basin development, Tectonics and geophysics of continental rifts, Springer, p. 249-277.

Appendix 1

Appendix 1

THICKNESS DATA OF THE STRATIGRAPHIC SECTIONS MEASURED IN THE CAMEROS BASIN IN PREVIOUS STUDIES

ID Sectio	1º stratigraphic Unit	Thickness (m)	2º stratigraphic Unit	Thickness (m)	3º stratigraphic Unit	Thickness (m)	4º stratigraphic unit	Thickness (m)	5º stratigraphic unit	Thicknes s (m)	6º stratigraphic unit	Thickness (m)	7º stratigraphic unit	Thicknes s (m)	8º stratigraphic unit	Thicknes s (m)
RUP	Brezales Fm	86	Boleras Fm	40	Jaramillo Fm	17	Campolara Fm	34	Salcedal Fm	42	San Marcos Fm	47	Pinilla de los Moros I	60	-	-
CML	Boleras Fm	19	Jaramillo Fm	33	Campolara Fm	21	Salcedal Fm	9	San Marcos Fm	33	Pinilla de los Moros Fr	98	Hortiguela Fm	109	Pantano Fm	0.4
TRR	Jaramillo Fm	37	Brezales fm	61	-	-	-	-	-	-	-	-	-	-	-	-
TRZ	Brezales Fm	72	Boleras Fm	3	Jaramillo Fm	213	Campolara Fm	8	Pinilla-Salcedal Fm	5	-	-	-	-	-	-
CTV	Campolara Fm	6	Salcedal Fm	205	San Marcos Fm	33	Pinilla de los Moros Fm	609	Castrillo de la Reina Fm	94	-	-	-	-	-	-
CON	Peñacoba Fm	24	Hortiguela Fm	167	Castrillo de la Reina Fm	743	-	-	-	-	-	-	-	-	-	-
MON2	Jaramillo Fm	30	Pinilla de los Moros Fm	21	Pantano/Pinilla Fm	50	Pantano-Pinilla Fm	248	Castrillo de la Reina Fm	202	-	-	-	-	-	-
GAN	Pinilla de los Moros Fm	50	Abejar Fm	94	Castrillo de la Reina Fm	97	-	-	-	-	-	-	-	-	-	-
GAS1	Brezales-Boleras Fm	23	Peñacoba Fm	6	Pinilla de los Moros Fm	62	-	-	-	-	-	-	-	-	-	-
PEÐ3	Abejar Fm	92	Castrillo Fm	64	-	-	-	-	-	-	-	-	-	-	-	-
HIN	Pinilla de los Moros Fm	8	-		-	-	-	-	-	-	-	-	-	-	-	-
TAL	Brezales-Boleras Fm	23	Pinilla de los Moros Fm	88	-	-	-	-	-	-	-	-	-	-	-	-
CID	Jaramillo Fm (Magaña Fm)	442	Campolara Fm (Matute Fm)	96	Pantano Fm	1188	-	-	-	-	-	-	-	-	-	-
ABJ	Abejar Fm	934	Pantano Fm	529	-	-	-	-	-	-	-	-	-	-	-	-
HYM	Brezales-Boleras Fm	338	-	-	-	-	-	-	-	-	-	-	-	-	-	-
MUR	Abejar Fm	800	-	-	-	-	-	-	-	-	-	-	-	-	-	-
CUB	Hortiguela Fm	75	Castrillo de la Reina Fm	121	-	-	-	-	-	-	-	-	-	-	-	-
ALMA_ ARZA	Agreda Fm	10	Magaña Fm	500	Matute Fm	227	-	-	-	-	-	-	-	-	-	-
PRA	Agreda Fm	10	Magaña Fm	260	-	-	-	-	-	-	-	-	-	-	-	-
MOV	Magaña Fm	133	-	-	-	-	-	-	-	-	-	-	-	-	-	-
POV	Agreda Fm	160	-	-	-	-	-	-	-	-	-	-	-	-	-	-
POR	Agreda Fm	90	Magaña Fm	30	Matute Fm	96	-	-	-	-	-	-	-	-	-	-
CAS	Agreda Fm	90	Magaña Fm	320	Matute Fm	96	-	-	-	-	-	-	-	-	-	-
ALM	Agreda Fm	100	Magaña Fm	143	Matute Fm	100	-	-	-	-	-	-	-	-	-	-
ESP	Agreda Fm	60	Magaña Fm	260	Matute Fm	213	-	-	-	-	-	-	-	-	-	-
MAG	Magaña Fm	110	Matute Fm	302	-	-	-	-	-	-	-	-	-	-	-	-
CSP	Matute Fm	410	-	-	-	-	-	-	-	-	-	-	-	-	-	-
AGE	Agreda Fm	140	Magaña Fm	255	Matute Fm	81	-	-	-	-	-	-	-	-	-	-
AGO	Matute Fm	519	-		-	-	-	-	-	-	-	-	-	-	-	-
BLA	Agreda Fm	255	-	-	-	-	-	-	-	-	-	-	-	-	-	-
1SAN	Agreda Fm	80	-	-	-	-	-	-	-	-	-	-	-	-	-	-
2SAN	Magaña Fm	418	-	-	-	-	-	-	-	-	-	-	-	-	-	-
3SAN	Magaña Fm	290	Matute Fm	655	-	-	-	-	-	-	-	-	-	-	-	-
VUR	Agreda Fm	45	Magaña Fm	71	Matute Fm	41	-	-	-	-	-	-	-	-	-	-
EN	Enciso Gr	1069	-	-	-	-	-	-	-	-	-	-	-	-	-	-
MU	Enciso Gr	1025	-	-	-	-	-	-	-	-	-	-	-	-	-	-
AM	Enciso Gr	474	-	-	-	-	-	-	-	-	-	-	-	-	-	-
GR	Enciso Gr	583	-	-	-	-	-	-	-	-	-	-	-	-	-	-
AR	Enciso Gr	469	Leza Fm	200	-	-	-	-	-	-	-	-	-	-	-	-
PR	Enciso Gr	80	Leza Fm	95	-	-	-	-	-	-	-	-	-	-	-	-
LE	Leza Fm	202	-	-	-	-	-	-	-	-	-	-	-	-	-	-
SA	Urbión Gr (D)	176	-	-	-	-	-	-	-	-	-	-	-	-	-	-
YA	Urbión Gr (A)	130	Urbión Gr (B)	140	Urbión Gr (C)	540	Urbión Gr (D)	137			-	-	-	-	-	-
SP	Urbión Gr (A)	98	Urbión Gr (B)	160	Urbión Gr (C)	342	Urbión Gr (D)	390			-	-	-	-	-	-
VM	Urbión Gr (A)	100	Urbión Gr (B)	130	Urbión Gr (C)	390	Urbión Gr (D)	197			-	-	-	-	-	-
1	Agreda Fm	70	Magaña Fm	20	-	-	-	-	-		-	-	-	-	-	-
2	Agreda Fm	5	Magaña Fm	235	Matute Fm	378	Valdeprado Fm	176	-		-	-	-	-	-	-
3	Agreda Fm	5	Magaña Fm	140	-	-	-	-	-		-	-	-	-	-	-
4	Agreda Fm	8	Magaña Fm	152	Matute Fm	220	Valdeprado Fm	667	-		-	-	-	-	-	-
5	Magaña Fm	126	Matute Fm	140	Valdeprado Fm	290	-	-	-		-	-	-	-	-	-
6	Magaña Fm	584	Matute Fm	83	-	-	-	-	-		-	-	-	-	-	-
7	Magaña Fm	435	Matute Fm	170	Huerteles Fm	18	-	-	-		-	-	-	-	-	-
8	Magaña Fm	90	Matute Fm	185	Huerteles Fm	90	Valdeprado Fm	153	-		-	-	-	-	-	-
9	Huerteles Fm	282	Valdeprado Fm	352	-	-	-	-	-	-	-	-	-	-	-	-

Appendix 1 - Thickness of each stratigraphic unit forming the stratigraphic sections measured in the Cameros Basin in previous studies. See Chapter 6 for more deatils on the complete section name, Location, Basal and Top contact and Author

ID Sectio	1º stratigraphic Unit	Thickness (m)	2º stratigraphic Unit	Thickness (m)	3º stratigraphic Unit	Thickness (m)	4º stratigraphic unit	Thickness (m)	5º stratigraphic unit	Thicknes s (m)	6º stratigraphic unit	Thickness (m)	7º stratigraphic unit	Thicknes s (m)	8º stratigraphic unit	Thicknes s (m)
10	Magaña Fm	270	Matute Fm	448	-	-	-	-	-	-	-	-	-	-	-	-
11	Huerteles Fm	136	-	-	-	-	-	-	-	-	-	-	-	-	-	-
12	Huerteles Fm	100	Valdeprado Fm	661	-	-	-	-	-	-	-	-	-	-	-	-
13	Magaña Fm	204	-	-	-	-	-	-	-	-	-	-	-	-	-	-
14	Magaña Fm	190	Matute Fm	352	-	-	-	-	-	-	-	-	-	-	-	-
15	Agreda Fm	25	Magaña Fm	85	Matute Fm	77	_		-		-	-	-	-	-	-
16	Agreda Fm	85	Magaña Fm	157	Matute Fm	96	_		-		-	-	-	-	-	-
17	Magaña Fm	520	-	-	-	-	-	-	-	-	-	-	-	-	-	-
18	Huerteles Fm	314	-	-	-	-	-	-	-	-	-	-	-	-	-	-
19	Matute Fm	260	Huerteles Fm	680	Valdeprado Fm	206	_		-		-	-	-	-	-	-
20	Magaña Fm	90	Matute Fm	133	-	-	-	-	-	-	-	-	-	-	-	-
21	Agreda Fm	69	-	-	-	-	-	-	-	-	-	-	-	-	-	-
22	Agreda Fm	55	Magaña Fm	155	Matute Fm	325	-		-		-	-	-	-	-	-
23	Matute Fm	460	Valdeprado Fm	15	-	-	-	-	-	-	-	-	-	-	-	-
24	Magaña Fm	65	Matute Fm	405	Huerteles Fm	618	-	-	-	-	-	-	-	-	-	-
25	Huerteles Fm	460	Valdeprado Fm	9	-	-	-	-	-	-	-	-	-	-	-	-
26	Matute Fm	100	Huerteles Fm	1010	-	-	-	-	-	-	-	-	-	-	-	-
27	Valdeprado Fm	1164	-	-	-	-	-	-	-	-	-	-	-	-	-	-
28	Matute Fm	25	Huerteles Fm	395	Valdeprado Fm	248	-	-	-	-	-	-	-	-	-	-
29	Huerteles Fm	114	-	-	-	-	-	-	-	-	-	-	-	-	-	-
30	Agreda Fm	78	-	-	-	-	-	-	-	-	-	-	-	-	-	-
31	Agreda Fm	114	-	-	-	-	-	-	-	-	-	-	-	-	-	-
32	Agreda Fm	140	Magaña Fm	198	-	-	-	-	-	-	-	-	-	-	-	-
33	Agreda Fm	95	Magaña Fm	55	Matute Fm	30	Huerteles Fm	10	-	-	-	-	-	-	-	-
34	Agreda Fm	255	-	-	-	-	-	-	-	-	-	-	-	-	-	-
35	Agreda Fm	155	Magaña Fm	534	Matute Fm	2	-		-	-	-	-	-	-	-	-
36	Agreda Fm	8	Magaña Fm	427	-	-	-	-	-	-	-	-	-	-	-	-
37	Matute Fm	244	-	-	-	-	-	-	-	-	-	-	-	-	-	-
TRE	Jubera Fm	265	-	-	-	-	-	-	-	-	-	-	-	-	-	-
JUR	Jubera Fm	120	-	-	-	-	-	-	-	-	-	-	-	-	-	-
ARN	Jubera Fm	170	-	-	-	-	-	-	-	-	-	-	-	-	-	-
PRE	Jubera Fm	100	-	-	-	-	-	-	-	-	-	-	-	-	-	-
SAN	Urbión Gr (D)	155	-	-	-	-	-	-	-	-	-	-	-	-	-	-
YNG	Urbión Gr (A)	147	Urbión Gr (B)	143	Urbión Gr (C)	565	Urbión Gr (D)	1705	-	-	-	-	-	-	-	-
SPM	Urbión Gr (A)	115	Urbión Gr (B)	155	Urbión Gr (C)	324	Urbión Gr (D)	266	-	-	-	-	-	-	-	-
VLM	Urbión Gr (A)	109	Urbión Gr (B)	136	Urbión Gr (C)	352	Urbión Gr (D)	183	-	-	-	-	-	-	-	-
TFC	Pantano Fm	1089	Abejar Fm	714	-	-	-	-	-	-	-	-	-	-	-	-

Appendix 1 - Continued

Appendix 2

Appendix 2

STRIKE -AND-DIP MEASUREMENTS

Data ID	x (longW)	y (latN)	z (m slm)	Unit	Facies	Strike (ºN)	Dip (ºN)	Type of Data	Dip Domain
C1	564463	4670804	1060	DS7	Jubera Fm	225	75	Field data	
C17	563090	4668577	1005	DS8	Olivan Gr	70	45	Field data	
C19	564279	4670788	990	DS7	Leza Fm	220	40	Field data	
C28	561867	4667452	840	DS7	Enciso Gr	45	30	Field data	
C502	564271	4670638	965	DS8	Olivan Gr	195	40	Field data	
C503	564251	4670588	958	DS8	Olivan Gr	210	50	Field data	
C504	564160	4670524	940	DS8	Olivan Gr	200	40	Field data	
C505	564081	4670494	925	DS8	Olivan Gr	200	50	Field data	
C507	563950	4670558	900	DS8	Olivan Gr	135	30	Field data	
C506	563993	4670500	908	DS8	Olivan Gr	150	20	Field data	
C510	563892	4670386	955	DS8	Olivan Gr	150	30	Field data	
C511	563883	4670329	970	DS8	Olivan Gr	150	30	Field data	01
C1int	563667	4670317	940	DS8	Olivan Gr	105	40	Field data	
C2int	563582	4669995	910	DS8	Olivan Gr	100	45	Field data	
C3int	563460	4669740	895	DS8	Olivan Gr	80	35	Field data	
C4int	563167	4669633	985	DS8	Olivan Gr	75	35	Field data	
C5int	563055	4669479	1000	DS8	Olivan Gr	63	35	Field data	
C6int	562811	4669174	1025	DS8	Olivan Gr	64	40	Field data	
C7int	562717	4668825	1044	DS8	Olivan Gr	55	45	Field data	
C8int	562372	4668526	1042	DS8	Olivan Gr	65	35	Field data	
C9int	562229	4668181	950	DS8	Olivan Gr	40	30	Field data	
C10int	562101	4667898	900	DS8	Olivan Gr	44	25	Field data	
C11int	562678	4668571	1062	DS8	Olivan Gr	62	40	Field data	
C23	560808	4666966	775	DS7	Enciso Gr	50	25	Field data	
C24	560959	4667001	795	DS7	Enciso Gr	50	30	Field data	
C25	561068	4667196	805	DS7	Enciso Gr	50	20	Field data	
C26	561100	4667440	795	DS7	Enciso Gr	50	25	Field data	
C40	560799	4666900	785	DS7	Enciso Gr	55	30	Field data	
C41	560659	4666748	770	DS7	Enciso Gr	80	20	Field data	
C44	560269	4666442	790	DS7	Enciso Gr	50	20	Field data	
C45	560129	4666527	800	DS7	Enciso Gr	50	25	Field data	
C46	559876	4666382	800	DS7	Enciso Gr	50	15	Field data	
C47	559714	4666220	845	DS7	Enciso Gr	30	27	Field data	
C48	559234	4665962	870	DS7	Enciso Gr	60	25	Field data	
C49	558898	4665751	840	DS7	Enciso Gr	55	23	Field data	
C50	558806	4665291	910	DS7	Enciso Gr	55	23	Field data	02
C51	558516	4665056	890	DS7	Enciso Gr	60	22	Field data	
C52	558496	4664419	905	DS7	Enciso Gr	60	30	Field data	
C53	558142	4664143	905	DS7	Enciso Gr	75	22	Field data	
C54	558274	4663907	890	DS7	Enciso Gr	60	33	Field data	
C55	557890	4663714	890	DS7	Urbión Gr	75	30	Field data	
C56	557884	4663400	885	DS7	Urbión Gr	55	35	Field data	
C57	557617	4663400	1000	DS7	Urbión Gr	68	35	Field data	
C58	557751	4662880	905	DS7	Urbión Gr	75	35	Field data	
C59	557224	4663046	920	DS7	Urbión Gr	73	30	Field data	
C60	556910	4662653	920	DS6	Urbión Gr	75	30	Field data	
C61	556674	4662721	940	DS6	Urbión Gr	70	28	Field data	
C62	556455	4662467	940	DS6	Urbión Gr	35	30	Field data	
C63	556310	4662122	940	DS5	Urbión Gr	50	42	Field data	
C64	555981	4662086	1010	DS5	Urbión Gr	50	35	Field data	
C65	555530	4661987	960	DS5	Urbión Gr	60	35	Field data	
C66	555362	4661866	960	DS4	Urbión Gr	50	40	Field data	02
C67	555140	4661588	975	DS4	Urbión Gr	30	30	Field data	
C69	555008	4661490	970	DS3	Valdeprado Fm	45	30	Field data	
C70	554800	4660956	970	DS3	Valdeprado Fm	45	27	Field data	

Data ID	x (longW)	y (latN)	z (m slm)	Unit	Facies	Strike (ºN)	Dip (ºN)	Type of Data	Dip Domain
C71	554937	4660455	990	DS3	Valdeprado Fm	45	27	Field data	02
C72	554961	4659931	990	DS3	Valdeprado Fm	45	27	Field data	
C74	554327	4659122	1060	DS3	Valdeprado Fm	350	30	Field data	
C75	554585	4659436	1050	DS3	Valdeprado Fm	5	30	Field data	
C76	554604	4659489	1055	DS3	Valdeprado Fm	30	15	Field data	
C77	554622	4659547	1065	DS3	Valdeprado Fm	30	27	Field data	
C78	554663	4659607	1060	DS3	Valdeprado Fm	35	27	Field data	
C79	554701	4659663	1050	DS3	Valdeprado Fm	30	18	Field data	
C80	553885	4659162	1055	DS3	Valdeprado Fm	5	20	Field data	
C81	554226	4658698	1020	DS3	Valdeprado Fm	5	15	Field data	
C82	553803	4658510	1025	DS3	Valdeprado Fm	5	18	Field data	
C83	553409	4658391	1025	DS3	Valdeprado Fm	5	12	Field data	
C84	553144	4658394	1035	DS3	Valdeprado Fm	13	15	Field data	
C85	553101	4658275	1030	DS3	Valdeprado Fm	5	10	Field data	
C86	552790	4657987	1030	DS3	Huerteles Fm	15	20	Field data	03
C87	552605	4657765	1040	DS3	Huerteles Fm	20	15	Field data	
C88	552112	4657421	1050	DS3	Huerteles Fm	15	15	Field data	
C89	552128	4657073	1070	DS3	Huerteles Fm	10	25	Field data	
C90	551857	4656680	1100	DS3	Huerteles Fm	360	20	Field data	
C91	551188	4656620	1100	DS3	Huerteles Fm	23	13	Field data	
C93	551122	4656362	1170	DS3	Huerteles Fm	15	10	Field data	
C95	551162	4656120	1135	DS3	Huerteles Fm	10	10	Field data	
C96	551135	4655948	1110	DS3	Huerteles Fm	10	10	Field data	
Or1	550613	4655718	1166	DS3	Huerteles Fm	6	9	Orthophoto data	
Or2	550782	4655885	1096	DS3	Huerteles Fm	12	7	Orthophoto data	
Or3	550667	4655871	1124	DS3	Huerteles Fm	12	10	Orthophoto data	
Or4	550586	4655719	1174	DS3	Huerteles Fm	7	8	Orthophoto data	
C97	549550	4654628	1360	DS3	Huerteles Fm	25	10	Field data	
C100	550037	4655167	1260	DS3	Huerteles Fm	360	10	Field data	
C99	549898	4655144	1280	DS3	Huerteles Fm	360	10	Field data	
C108	547453	4653114	1330	DS3	Huerteles Fm	225	15	Field data	
C109	547317	4653085	1330	DS3	Huerteles Fm	220	10	Field data	
C110	547372	4652916	1345	DS3	Huerteles Fm	235	10	Field data	
C111	547166	4652623	1370	DS3	Huerteles Fm	260	15	Field data	
C113	546759	4652110	1365	DS3	Huerteles Fm	330	7	Field data	04
C116	546769	4651845	1400	DS3	Huerteles Fm	0	0	Field data	
C122	545498	4651276	1659	DS3	Huerteles Fm	50	10	Field data	
C513	548795	4652850	1212	DS3	Huerteles Fm	220	35	Field data	
C514	548695	4652999	1240	DS3	Huerteles Fm	215	26	Field data	
C515	548748	4653068	1260	DS3	Huerteles Fm	170	25	Field data	
C516	548792	4653170	1280	DS3	Huerteles Fm	155	15	Field data	
C517	548814	4653270	1290	DS3	Huerteles Fm	105	7	Field data	
C518	548789	4653479	1290	DS3	Huerteles Fm	30	12	Field data	
C519	548868	4653711	1280	DS3	Huerteles Fm	45	9	Field data	
Or5	550032	4655312	1248	DS3	Huerteles Fm	354	8	Orthophoto data	
Or6	549730	4654603	1339	DS3	Huerteles Fm	359	8	Orthophoto data	
Or7	548709	4654199	1365	DS3	Huerteles Fm	16	7	Orthophoto data	
Or8	550586	4655414	1135	DS3	Huerteles Fm	352	9	Orthophoto data	
Or9	550772	4655546	1077	DS3	Huerteles Fm	350	8	Orthophoto data	04
Or10	549931	4655349	1249	DS3	Huerteles Fm	358	9	Orthophoto data	
Or11	545946	4651891	1504	DS3	Huerteles Fm	39	5	Orthophoto data	
Or12	546117	4650943	1668	DS3	Huerteles Fm	38	6	Orthophoto data	
Or13	546426	4651164	1558	DS3	Huerteles Fm	33	5	Orthophoto data	
Or14	548803	4654433	1360	DS3	Huerteles Fm	9	5	Orthophoto data	
Or15	548348	4652531	1275	DS3	Huerteles Fm	220	30	Orthophoto data	

Data ID	x (longW)	y (latN)	z (m slm)	Unit	Facies	Strike (ºN)	Dip (ºN)	Type of Data	Dip Domain
Or16	547334	4652063	1356	DS3	Huerteles Fm	320	8	Orthophoto data	04
Or17	546732	4651550	1460	DS3	Huerteles Fm	35	5	Orthophoto data	
C148	542824	4647481	1203	DS1+2	Magaña Fm	75	5	Field data	
C151	543010	4647727	1225	DS1+2	Magaña Fm	65	5	Field data	
C155	543115	4647637	1220	DS1+2	Magaña Fm	75	5	Field data	
C157	542757	4647143	1202	DS1+2	Magaña Fm	70	10	Field data	
C159	542346	4646517	1202	DS1+2	Magaña Fm	220	10	Field data	
C164	541785	4646126	1212	DS1+2	Magaña Fm	280	5	Field data	
C165	541713	4646049	1212	DS1+2	Magaña Fm	280	5	Field data	
C167	541394	4645679	1225	DS1+2	Magaña Fm	285	14	Field data	
C168	541373	4645652	1226	DS1+2	Magaña Fm	280	10	Field data	
C169	541355	4645594	1228	DS1+2	Magaña Fm	300	19	Field data	
C170	541306	4645509	1235	DS1+2	Magaña Fm	300	15	Field data	
C195	540531	4644327	1420	DS1+2	Magaña Fm	230	20	Field data	
C196	540452	4644293	1435	DS1+2	Magaña Fm	280	15	Field data	
C197	540363	4644264	1450	DS1+2	Magaña Fm	270	15	Field data	
C198	540275	4644201	1472	DS1+2	Magaña Fm	280	10	Field data	
C199	540173	4644151	1510	DS1+2	Magaña Fm	280	15	Field data	
C160	542589	4646600	1202	DS1+2	Magaña Fm	60	5	Field data	
C161	542495	4646447	1204	DS1+2	Magaña Fm	72	5	Field data	05
C162	542466	4646424	1202	DS1+2	Magaña Fm	240	7	Field data	
C163	542052	4646557	1211	DS1+2	Magaña Fm	285	12	Field data	
C166	541351	4645775	1235	DS1+2	Magaña Fm	280	16	Field data	
C171	541087	4645393	1245	DS1+2	Magaña Fm	310	25	Field data	
C173	541923	4645173	1210	DS1+2	Magaña Fm	280	15	Field data	
C172	541869	4645097	1210	DS1+2	Magaña Fm	310	12	Field data	
C174	542050	4645217	1205	DS1+2	Magaña Fm	290	5	Field data	
C175	542334	4645531	1194	DS1+2	Magaña Fm	210	10	Field data	
C176	542517	4645594	1182	DS1+2	Magaña Fm	235	10	Field data	
C177	542449	4645756	1183	DS1+2	Magaña Fm	240	10	Field data	
C178	540946	4644738	1300	DS1+2	Magaña Fm	310	15	Field data	
C179	540935	4644519	1325	DS1+2	Magaña Fm	235	17	Field data	
C180	540871	4644429	1345	DS1+2	Magaña Fm	255	25	Field data	
C181	540838	4644347	1353	DS1+2	Magaña Fm	275	12	Field data	
C182	540847	4644314	1353	DS1+2	Magaña Fm	260	20	Field data	
C183	540790	4644288	1367	DS1+2	Magaña Fm	270	15	Field data	
C184	540770	4644220	1375	DS1+2	Magaña Fm	285	14	Field data	
C186	540614	4644224	1415	DS1+2	Magaña Fm	230	15	Field data	
C185	540605	4644018	1415	DS1+2	Magaña Fm	265	5	Field data	
C201	540093	4643919	1448	DS1+2	Magaña Fm	285	15	Field data	05
C202	540022	4643887	1492	DS1+2	Magaña Fm	280	10	Field data	
C203	540022	4643844	1475	DS1+2	Magaña Fm	280	10	Field data	
C200	540097	4644058	1539	DS1+2	Magaña Fm	280	10	Field data	
C204	539998	4643772	1455	DS1+2	Matute Fm	320	15	Field data	
C205	539955	4643644	1422	DS1+2	Magaña Fm	330	17	Field data	
C206	539933	4643567	1405	DS1+2	Magaña Fm	300	10	Field data	
C207	539912	4643464	1360	DS1+2	Magaña Fm	315	20	Field data	
C208	539917	4643361	1356	DS1+2	Magaña Fm	300	10	Field data	
C213	539879	4642595	1252	DS1+2	Magaña Fm	320	10	Field data	06
C216	539793	4642181	1192	DS1+2	Magaña Fm	330	20	Field data	
C217	539751	4642056	1180	DS1+2	Magaña Fm	340	10	Field data	
C218	539728	4642009	1177	DS1+2	Magaña Fm	320	10	Field data	
C219	539445	4641717	1150	DS1+2	Magaña Fm	340	10	Field data	
C220	539484	4641632	1150	DS1+2	Magaña Fm	320	17	Field data	
C221	539429	4642072	1180	DS1+2	Magaña Fm	320	17	Field data	

Data ID	x (longW)	y (latN)	z (m slm)	Unit	Facies	Strike (ºN)	Dip (ºN)	Type of Data	Dip Domain
C209	540075	4643191	1320	DS1+2	Magaña Fm	320	10	Field data	
C210	540065	4643067	1298	DS1+2	Magaña Fm	290	7	Field data	
C211	540074	4643021	1288	DS1+2	Magaña Fm	305	10	Field data	
C212	540061	4642981	1270	DS1+2	Magaña Fm	315	15	Field data	
C215	539900	4642328	1210	DS1+2	Magaña Fm	330	10	Field data	
C214	539942	4642490	1235	DS1+2	Magaña Fm	360	10	Field data	
C222	539262	4640759	1128	DS1+2	Magaña Fm	220	25	Field data	
C223	539697	4640822	1145	DS1+2	Magaña Fm	210	25	Field data	
C224	539303	4640651	1128	DS1+2	Magaña Fm	240	20	Field data	
C225	539185	4640463	1122	DS1+2	Magaña Fm	220	25	Field data	
C226	539224	4640340	1121	DS1+2	Magaña Fm	210	20	Field data	
C227	539053	4640124	1120	DS1+2	Magaña Fm	210	18	Field data	06
C228	538967	4639920	1091	DS1+2	Magaña Fm	190	20	Field data	
C229	538867	4639934	1090	DS1+2	Magaña Fm	185	20	Field data	
C230	538935	4639709	1085	DS1+2	Magaña Fm	185	25	Field data	
C231	538873	4639645	1070	DS1+2	Magaña Fm	200	25	Field data	
C250	539289	4638302	1121	DS1+2	Magaña Fm	200	25	Field data	
C251	539163	4638356	1130	DS1+2	Magaña Fm	205	15	Field data	
C252	538682	4638342	1160	DS1+2	Magaña Fm	205	25	Field data	
C255	538655	4638149	1172	DS1+2	Magaña Fm	205	20	Field data	
C253	538696	4638089	1180	DS1+2	Magaña Fm	190	25	Field data	
C1IN	538974	4639148	1120	DS1+2	Magaña Fm	200	25	Field data	
C2IN	538812	4638727	1120	DS1+2	Magaña Fm	205	25	Field data	
C254	538713	4637948	1200	DS1+2	Matute Fm	200	15	Field data	
C235	538179	4637614	1340	DS6	Pantano Fm	200	15	Field data	
C236	538050	4637614	1360	DS6	Pantano Fm	205	15	Field data	
C237	537948	4637410	1385	DS6	Pantano Fm	200	20	Field data	07
C238	537853	4637248	1375	DS6	Pantano Fm	240	10	Field data	
C239	537827	4637176	1360	DS6	Pantano Fm	210	20	Field data	
C240	537744	4636888	1340	DS6	Pantano Fm	215	20	Field data	
C241	537737	4636793	1341	DS6	Pantano Fm	215	10	Field data	
C242	537674	4636504	1340	DS6	Pantano Fm	215	11	Field data	
C243	537665	4636376	1325	DS6	Pantano Fm	205	12	Field data	
C244	537570	4636311	1305	DS6	Pantano Fm	210	12	Field data	
C245	537363	4636126	1265	DS6	Pantano Fm	215	15	Field data	
C246	537294	4636059	1252	DS6	Pantano Fm	210	20	Field data	
C247	537285	4636005	1245	DS6	Pantano Fm	220	11	Field data	
C249	537234	4635963	1235	DS6	Pantano Fm	210	10	Field data	
C248	537238	4635878	1222	DS6	Pantano Fm	208	8	Field data	
C256	538234	4634897	1082	DS6	Pantano Fm	200	15	Field data	
C257	538320	4635122	1105	DS6	Pantano Fm	210	20	Field data	
C270	537193	4634628	1065	DS12	Matute Fm	200	9	Field data	
C260	537225	4634950	1070	DS6	Pantano Fm	217	16	Field data	07
C261	537221	4635018	1080	DS6	Pantano Fm	205	15	Field data	
C265	537207	4635622	1178	DS6	Pantano Fm	200	15	Field data	
C266	537263	4635800	1210	DS6	Pantano Fm	200	8	Field data	
C272	537274	4634372	1062	DS12	Matute Fm	210	5	Field data	
C273	537281	4634150	1048	DS12	Matute Fm	210	14	Field data	
C275	537260	4634062	1048	DS12	Matute Fm	215	10	Field data	
C276	537258	4633855	1042	DS12	Matute Fm	225	10	Field data	
C295	537172	4633728	1040	DS12	Matute Fm	240	15	Field data	
C277	536759	4633156	1030	DS12	Matute Fm	210	15	Field data	
C280	536791	4632938	1035	DS12	Matute Fm	210	15	Field data	
C283	536944	4632985	1030	DS12	Matute Fm	210	15	Field data	
C282	537130	4632829	1030	DS12	Matute Fm	220	15	Field data	

Data ID	x (longW)	y (latN)	z (m slm)	Unit	Facies	Strike (ºN)	Dip (ºN)	Type of Data	Dip Domain
C297	536371	4630624	1105	DS6	Pantano Fm	215	40	Field data	
C298	536504	4630768	1082	DS6	Pantano Fm	215	45	Field data	
C299	536620	4631119	1075	DS6	Pantano Fm	200	30	Field data	
C300	536701	4631135	1075	DS6	Pantano Fm	220	20	Field data	
C301	536762	4631324	1069	DS6	Pantano Fm	210	20	Field data	
C303	536915	4631609	1063	DS6	Pantano Fm	220	17	Field data	
C304	537034	4631632	1062	DS6	Pantano Fm	220	20	Field data	
C305	537131	4631692	1062	DS6	Pantano Fm	225	12	Field data	
C308	537220	4631624	1062	DS6	Pantano Fm	230	10	Field data	
C306	537420	4631969	1045	DS6	Pantano Fm	220	30	Field data	
C307	537502	4632033	1040	DS6	Pantano Fm	210	12	Field data	
C309	536518	4630653	1090	DS6	Pantano Fm	210	40	Field data	08
C310	536298	4630547	1100	DS6	Pantano Fm	210	40	Field data	
C311	536169	4630460	1090	DS6	Pantano Fm	210	30	Field data	
C312	536399	4630234	1082	DS6	Pantano Fm	220	25	Field data	
C314	536810	4629757	1078	DS6	Pantano Fm	210	30	Field data	
C315	536733	4629700	1085	DS6	Pantano Fm	200	25	Field data	
C317	536721	4629141	1040	DS6	Pantano Fm	206	30	Field data	
C318	536438	4629399	1045	DS6	Pantano Fm	212	25	Field data	
C319	536962	4628581	1035	DS6	Pantano Fm	215	20	Field data	
C320	536955	4628196	1048	DS7	Abejar Fm	210	35	Field data	
C321	536605	4628180	1048	DS7	Abejar Fm	215	25	Field data	
C322	536037	4628344	1048	DS7	Abejar Fm	210	27	Field data	
C425	535994	4625742	1135	Upp-Cretac	Limestone	5	45	Field data	
C427	536175	4626952	1170	Upp-Cretac	Limestone	203	65	Field data	
C428	536159	4626994	1160	Upp-Cretac	Limestone	200	62	Field data	
C429	536124	4627099	1128	Upp-Cretac	Utrillas Fm	203	60	Field data	
C324	536106	4627818	1065	DS7	Abejar Fm	190	45	Field data	
C325	536125	4627725	1072	DS7	Abejar Fm	190	50	Field data	
C323	536065	4627874	1060	DS7	Abejar Fm	190	45	Field data	
C326	536415	4627222	1095	DS7	Abejar Fm	210	40	Field data	
C433	535365	4625779	1125	DS7	Abejar Fm	35	42	Field data	09
C434	535377	4625816	1140	DS7	Abejar Fm	28	30	Field data	
C435	535461	4625851	1160	Upp-Cretac	Utrillas Fm	30	40	Field data	
C441	536406	4627300	1088	DS7	Abejar Fm	190	32	Field data	
C442	536410	4627130	1105	Upp-Cretac	Utrillas Fm	205	30	Field data	
C443	536051	4627716	1075	DS7	Abejar Fm	205	30	Field data	
C447	536093	4627833	1065	DS7	Abejar Fm	200	50	Field data	
C445	535973	4627878	1060	DS7	Abejar Fm	200	48	Field data	
C446	536006	4627919	1059	DS7	Abejar Fm	185	50	Field data	
Or18	536362	4626073	1230	Upp-Cretac	Utrillas Fm	312	13	Field data	
C415	534799	4623309	1125	Upp-Cretac	Limestone	310	20	Field data	
C416	535132	4623672	1165	Upp-Cretac	Limestone	355	50	Field data	
C417	535233	4623734	1165	Upp-Cretac	Limestone	345	50	Field data	
C418	535277	4623811	1175	Upp-Cretac	Limestone	270	60	Field data	
C419	535363	4623921	1159	Upp-Cretac	Limestone	270	50	Field data	
C420	535440	4624251	1150	Upp-Cretac	Limestone	290	42	Field data	
C421	535442	4624449	1164	Upp-Cretac	Limestone	280	33	Field data	10
C422	535484	4624651	1150	Upp-Cretac	Limestone	280	38	Field data	
C423	535394	4624889	1157	Upp-Cretac	Limestone	240	23	Field data	
C436	535387	4625619	1115	Upp-Cretac	Utrillas Fm	260	10	Field data	
C437	535346	4625578	1110	Upp-Cretac	Utrillas Fm	260	15	Field data	
C438	535162	4625206	1142	Upp-Cretac	Limestone	265	10	Field data	
C439	535165	4625109	1143	Upp-Cretac	Limestone	232	25	Field data	
C440	535318	4624981	1150	Upp-Cretac	Limestone	235	25	Field data	

Data ID	x (longW)	y (latN)	z (m slm)	Unit	Facies	Strike (ºN)	Dip (ºN)	Type of Data	Dip Domain
C402	535104	4620962	1145	DS7	Abejar Fm	220	30	Field data	10
C411	534378	4622147	1155	DS7	Abejar Fm	215	30	Field data	
C408	534838	4621879	1140	DS7	Abejar Fm	225	35	Field data	
C409	534881	4621863	1140	DS7	Abejar Fm	225	35	Field data	
C410	534797	4621714	1140	DS7	Abejar Fm	225	42	Field data	
C448	534931	4619946	1123	DS7	Abejar Fm	205	35	Field data	
C449	535001	4620531	1120	DS7	Abejar Fm	215	12	Field data	
C450	534252	4619781	1120	Upp-Cretac	Limestone	190	57	Field data	11
C451	533928	4619656	1155	Upp-Cretac	Limestone	200	70	Field data	
C452	533956	4619596	1162	Upp-Cretac	Limestone	205	70	Field data	
C453	533916	4619506	1165	Upp-Cretac	Limestone	185	45	Field data	
C459	533817	4618870	1129	Upp-Cretac	Limestone	205	62	Field data	
C460	533855	4618921	1143	Upp-Cretac	Limestone	215	67	Field data	
C464	533855	4619620	1168	Upp-Cretac	Limestone	210	70	Field data	
C450	534252	4619781	1120	Upp-Cretac	Limestone	190	57	Field data	
C451	533928	4619656	1155	Upp-Cretac	Limestone	200	70	Field data	
C452	533956	4619596	1162	Upp-Cretac	Limestone	205	70	Field data	
C453	533916	4619506	1165	Upp-Cretac	Limestone	185	45	Field data	
C459	533817	4618870	1129	Upp-Cretac	Limestone	205	62	Field data	
C460	533855	4618921	1143	Upp-Cretac	Limestone	215	67	Field data	12
C464	533855	4619620	1168	Upp-Cretac	Limestone	210	70	Field data	
C465	533673	4618448	1120	Upp-Cretac	Limestone	235	70	Field data	
C466	533833	4618579	1115	Upp-Cretac	Limestone	225	71	Field data	
C470	532901	4615925	1097	Upp-Cretac	Limestone	175	50	Field data	
C471	532884	4615797	1099	Upp-Cretac	Limestone	185	59	Field data	
C472	532800	4615583	1115	Cenozoic	Conglomerate	150	45	Field data	

Appendix 2 - Strike and dip data measured along the cross-section trace, from field and orthophoto data (Chapter 7)

Appendix 3

Appendix 3

VITRINITE REFLECTANCE MEASUREMENTS

ID_Sample	Unit	Vitrinite Measurement	Estimated (%Ro)	Min (%Ro)	Max (%Ro)
RFT-2	Upp.Cret. - Utrillas Fm	Bitumen	0.034	0	0.034
RFT-1	Upp.Cret. - Utrillas Fm	Bitumen	0.034	0	0.034
RFT-0	Upp.Cret. - Utrillas Fm	Bitumen	0.034	0	0.034
PRJ-18	DS8 - Escucha Fm	Yes	0.63	0.57	0.7
PRJ-10	DS8 - Escucha Fm	Yes	0.56	0.45	0.78
ESC-Peñ	DS8 - Escucha Fm	Yes	0.62	0.47	0.76
ROB-13	DS8 - Oliván Gr	Yes	3	2.57	3.47
ROB-100	DS8 - Oliván Gr	Yes	3.2	3.03	3.52
OLI-200	DS8 - Oliván Gr	Yes	2.86	2.45	3.3
PR-3.1P	DS7 - Leza Fm	No	-	-	-
PR-11P	DS7 - Leza Fm	Bitumen	4.35	1.94	5.6
SEN-5	DS7 - Enciso Gr	Yes	2.4	2.2	5.1
SEN-4	DS7 - Enciso Gr	No	-	-	-
SEN-3	DS7 - Enciso Gr	Yes	3.88	3.1	5.7
SEN-2	DS7 - Enciso Gr	No	-	-	-
SEN-1	DS7 - Enciso Gr	Scarce	2.09	1.8	2.3
URB-2	DS7 - Urbion Gr	Scarce	3.2	3	3.9
URB-1	DS7 - Urbion Gr	No	-	-	-
CAS-2	DS7 - Abejar Fm	Yes	0.3	0.18	0.35
PIG-1	DS7 - Abejar Fm	Yes	0.55	0.4	0.7
STFC-4b	DS7 - Abejar Fm	Yes	0.4	0.22	0.7
STFC-4	DS7 - Abejar Fm	Yes	0.55	0.4	0.6
STFC-3b	DS7 - Abejar Fm	Altered	0.7	0.4	1
STFC-3	DS7 - Abejar Fm	Altered	0.75	0.5	1.3
STFC-2	DS6 - Pantano Fm	Oxidized	0.75	0.5	1
STFC-1	DS6 - Pantano Fm	Yes	0.4	0.4	0.6
STFC-0	DS6 - Pantano Fm	Yes	0.5	0.3	1.3
SOY-3b	DS3 - Valdeprado Fm	Yes	2.9	2.5	5.2
SOY-3	DS3 - Valdeprado Fm	Yes	3	2.4	4.3
SOY-1	DS3 - Valdeprado Fm	No	-	-	-
SOY-2	DS3 - Valdeprado Fm	No	-	-	-
SOH-4	DS3 - Valdeprado Fm	Yes	2.7	2.4	3.5
YN-A01E	DS3 - Valdeprado Fm	No	-	-	-
SOH-3	DS3 - Valdeprado Fm	Yes	2.2	1.6	3.2
SOO-2	DS3 - Valdeprado Fm	Yes	2	1.8	2.2
YN-B10	DS3 - Valdeprado Fm	Yes	1.57	1.2	1.8
YN-B04	DS3 - Valdeprado Fm	Yes	2.4	2.2	3.2
SOH-2	DS3 - Valdeprado Fm	Yes	2.05	1.9	2.3
SOH-1b	DS3 - Valdeprado Fm	Yes	1.9	1.77	2.1
SOH-1	DS3 - Valdeprado Fm	Yes	2.1	1.7	2.7
SOO-1	DS3 - Valdeprado Fm	Yes	1.9	1.55	2.8
SHDL-1	DS3 - Huerteles Fm	Yes	2.9	2.7	3.2
SPO-2	DS3 - Huerteles Fm	Scarce	4.6	4.2	5.2
TORMO-1	DS3 - Huerteles Fm	Yes	3.7	3.09	4.1
TORMO-2	DS3 - Huerteles Fm	Yes	4.6	3.7	6
SPOV-7	DS3 - Huerteles Fm	Yes	3	2.07	3.47
SPOV-6	DS3 - Huerteles Fm	Scarce	-	-	-
SPOV-5b	DS3 - Huerteles Fm	Yes	2.35	1.96	2.9

ID_Sample	Unit	Vitrinite Measurement	Estimated (%Ro)	Min (%Ro)	Max (%Ro)
SPOV-5	DS3 - Huerteles Fm	Yes	2.4	2.14	2.98
SMO-3b	DS3 - Huerteles Fm	Bitumen	3.9	1.7	5.16
SMO-3	DS3 - Huerteles Fm	No	-	-	-
SMO-2b	DS3 - Huerteles Fm	Altered	1.04	0.7	1.34
SMO-2	DS3 - Huerteles Fm	Yes	3.8	2.24	4.24
SPO-1	DS2 - Matute Fm	Scarce	3.5	3.1	3.7
SCL-1	DS2 - Matute Fm	yes	3.1	2.27	3.9
SCL-2	DS2 - Matute Fm	Scarce	2	2.17	2.2
SPOV-4	DS2 - Magaña Fm	No	-	-	-
SPOV-3t	DS2 - Magaña Fm	Oxidized	3.5	2	4.5
SPOV-3	DS2 - Magaña Fm	Yes	2	1.3	2.8
SPOV-2	DS2 - Magaña Fm	Altered	3.8	2.74	4.7
SPOV-1	DS2 - Magaña Fm	Yes	2.2	1.7	2.4
SMO-1	DS2 - Magaña Fm	Yes	2.8	2	3.7
SMO-01	DS2 - Magaña Fm	Yes	3.34	2.75	3.82
SMO-0	Jurassic - Torrecilla Fm	Yes	4.45	3.7	5
SIC-1	Jurassic - Pozalmuro Fm	Yes	4.2	3.3	4.4
SIC-2	Jurassic - Pozalmuro Fm	Yes	4.2	3.3	4.5
CCGT 413	Jurassic - Torrecilla Fm	Yes	2.5	2.2	2.8
CG-2	Jurassic - Torrecilla Fm	Yes	3	2.8	3.3
CG-103	Jurassic - Torrecilla Fm	Yes	3.3	2.2	3.6
FM-N2	Jurassic - Aldealpozo Fm	Yes	2.98	2.2	3.47

Appendix 3 - List of the samples analysed for vitrinite reflectance measurement. Estimated, minimum and maximum reflectance values are indicated. Singular reflectance measured in each sample and statistical disribution of the measured data are reported in the next pages

Analysis realized in: **MPV-1 Combi-Leitz**

Sample: **RFT-2**
Objective: **50x**
Pattern: **274**

Singular Reflectances:

0.03	0.00	0.00	0.00	0.00
0.03	0.00	0.03	0.00	0.00
0.03	0.03	0.03	0.03	0.03
0.03	0.03	0.00	0.03	0.00

Class	n	n%	Sn	Sn%
0.0	11	55.00	11	55.00

Re = 0.02 **s = 0.02** **R< = 0.00** **R> = 0.03** **N = 20** **MVR = 52.3**

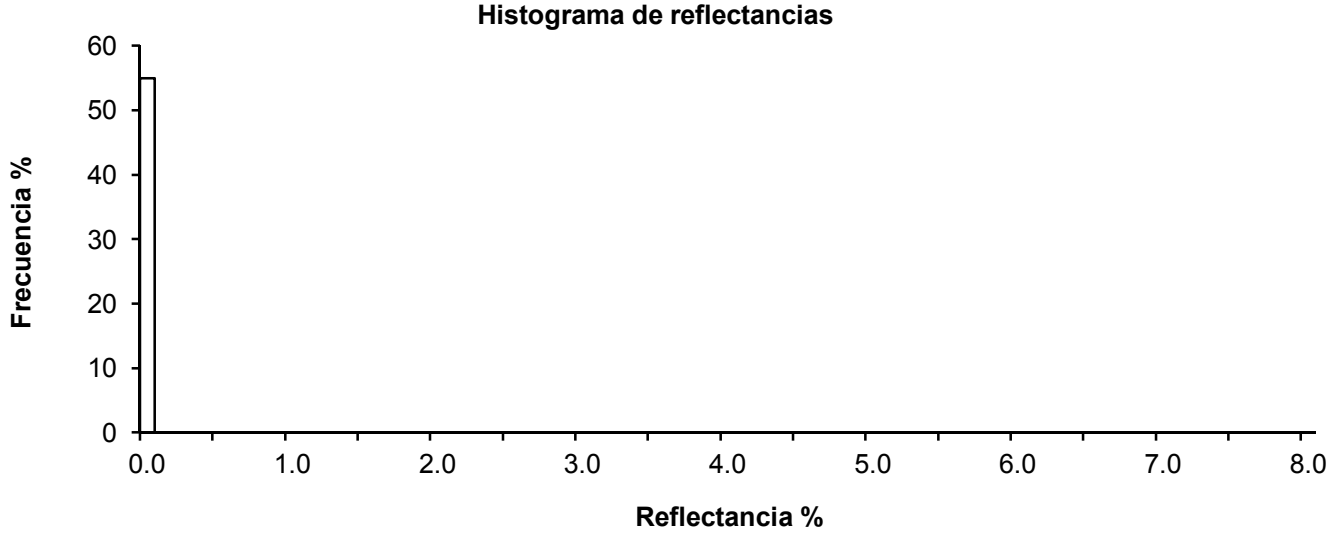

Analysis realized in: **MPV-1 Combi-Leitz**

Sample:
Objective: **50x**
Pattern: **274**

Singular Reflectances:

0.07	0.03	0.03	0.03	0.00
0.20	0.03	0.00	0.00	0.00
0.00	0.03	0.03	0.00	0.00
0.00	0.03	0.03	0.03	0.03

Class	n	n%	Sn	Sn%
0.0	11	55.00	11	55.00
0.2	1	5.00	12	60.00

Re = 0.03 **s = 0.04** **R< = 0.00** **R> = 0.14** **N = 20** **MVR = 55.6**

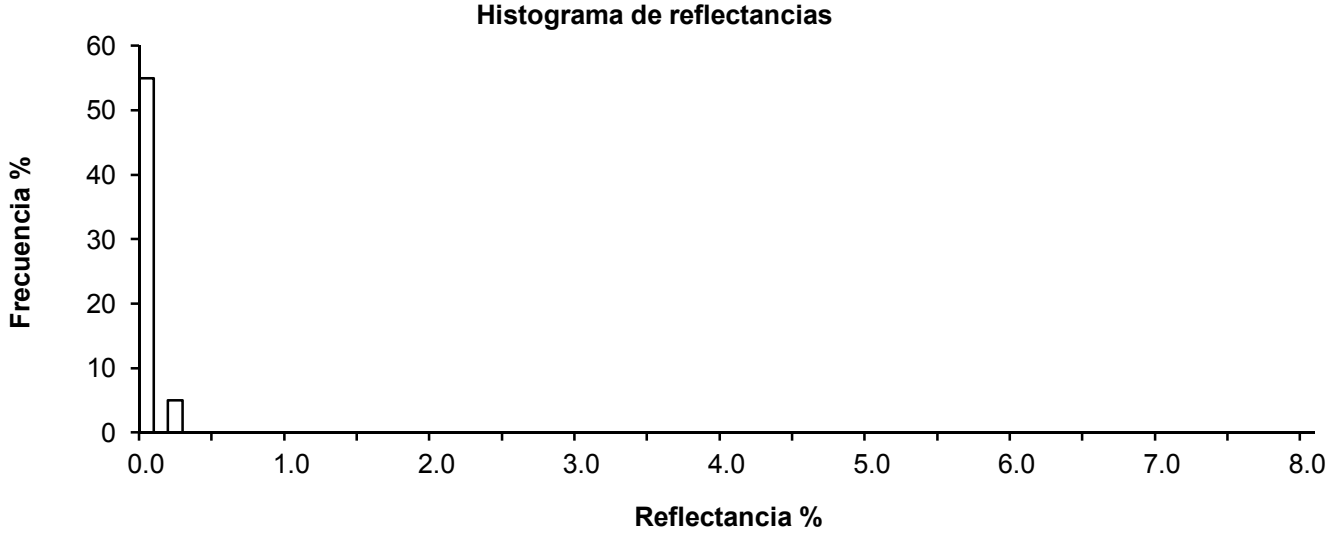

Analysis realized in: **MPV-1 Combi-Leitz**

Sample: RFT-0
Objective: 50x
Pattern: 274

Singular Reflectances:

0.03	0.00	0.03	0.03	0.00
0.00	0.03	0.00	0.00	0.00
0.03	0.03	0.00	0.00	0.00
0.00	0.03	0.03	0.03	0.03
0.00	0.00	0.03	0.00	0.00
0.00	0.00	0.00	0.00	0.00
0.00	0.00	0.00	0.00	0.00
0.00	0.00	0.00	0.00	0.00

Class	n	n%	Sn	Sn%
0.0	11	27.50	11	27.50

Re = 0.01 **s = 0.02** **R< = 0.00** **R> = 0.03** **N = 40** **MVR = 26.1**

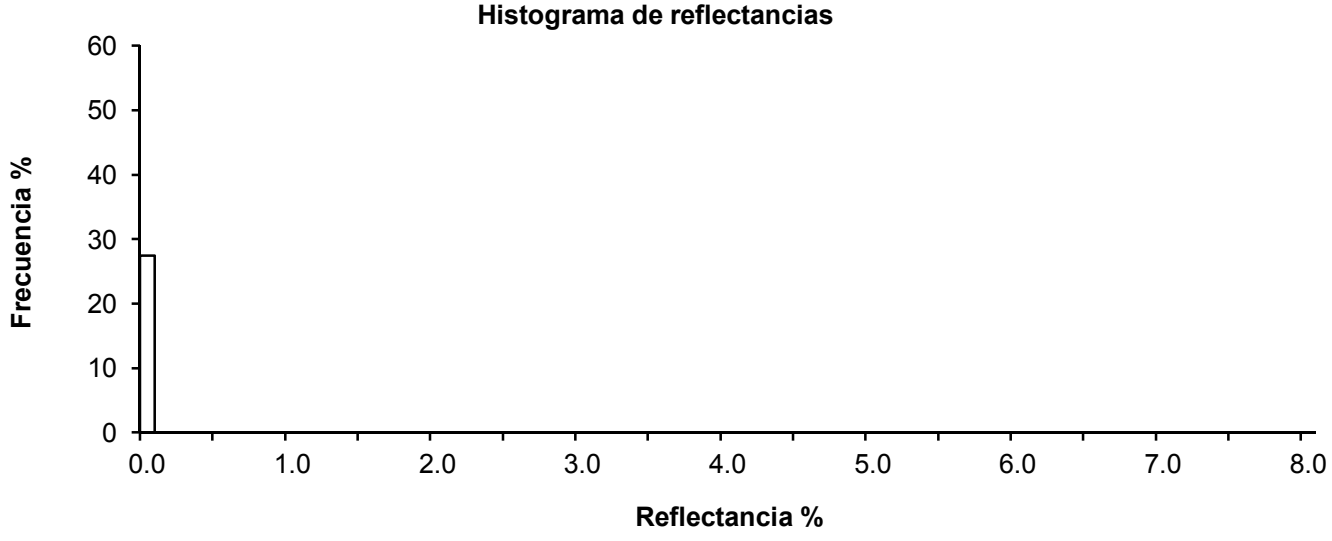

Analysis realized in: **MPV-1 Combi-Leitz**

Sample: PRJ-18
Objective: 50x
Pattern: 274

Singular Reflectances:

0.48	0.57	0.57	0.57	0.57
0.60	0.60	0.60	0.60	0.60
0.60	0.60	0.60	0.60	0.60
0.60	0.60	0.64	0.64	0.64
0.64	0.64	0.64	0.64	0.64
0.64	0.64	0.64	0.64	0.64
0.64	0.64	0.64	0.64	0.64
0.64	0.64	0.64	0.67	0.67
0.67	0.67	0.67	0.67	0.67
0.67	0.67	0.67	0.70	0.70

Class	n	n%	Sn	Sn%
0.4	1	2.00	1	2.00
0.5	4	8.00	5	10.00
0.6	43	86.00	48	96.00
0.7	2	4.00	50	100.00

Re = 0.63 **s = 0.04** **R< = 0.57** **R> = 0.69** **N = 50** **MVR = 43.5**

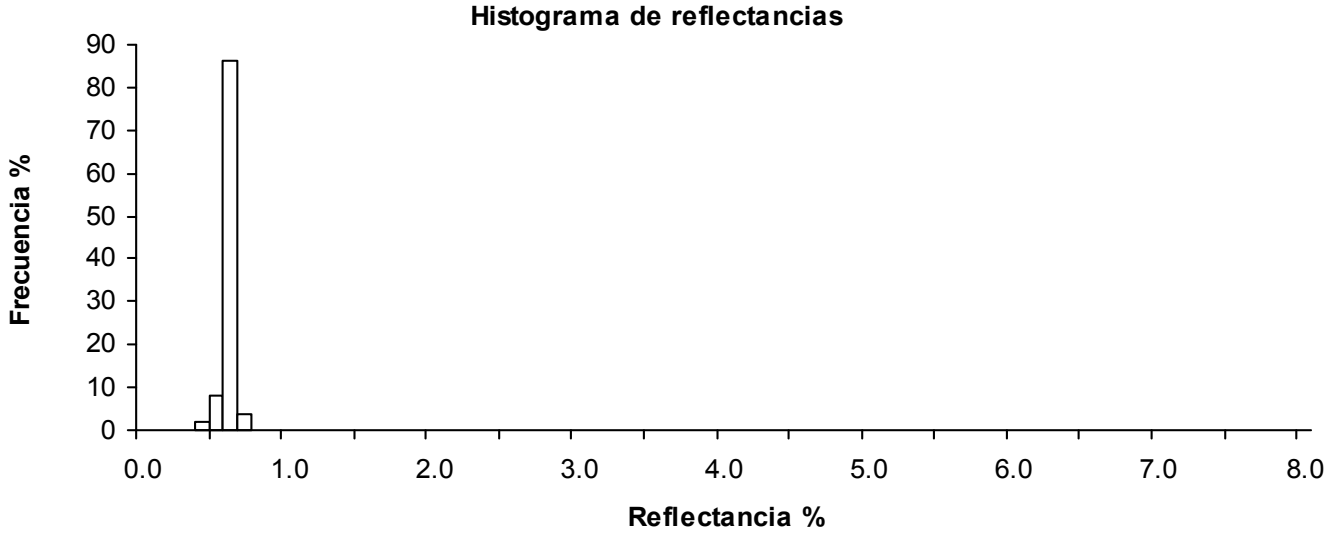

Analysis realized in: **MPV-1 Combi-Leitz**

Sample: **PRJ-10**
Objective: **50x**
Pattern: **274**

Singular Reflectances:

0.31	0.34	0.34	0.37	0.40
0.40	0.40	0.40	0.40	0.43
0.43	0.43	0.43	0.43	0.43
0.47	0.47	0.47	0.47	0.47
0.50	0.50	0.50	0.50	0.50
0.50	0.50	0.50	0.50	0.53
0.53	0.53	0.53	0.53	0.56
0.56	0.56	0.56	0.56	0.59
0.59	0.59	0.59	0.59	0.59
0.59	0.59	0.59	0.59	0.62
0.62	0.62	0.62	0.62	0.62
0.62	0.65	0.65	0.65	0.65
0.65	0.65	0.65	0.65	0.65
0.65	0.65	0.68	0.68	0.68
0.68	0.71	0.71	0.71	0.71
0.71	0.71	0.74	0.78	0.78

Class	n	n%	Sn	Sn%
0.3	4	5.00	4	5.00
0.4	16	20.00	20	25.00
0.5	29	36.25	49	61.25
0.6	22	27.50	71	88.75
0.7	9	11.25	80	100.00

Re = 0.56 **s = 0.11** **R< = 0.34** **R> = 0.74** **N = 80** **MVR = 46.2**

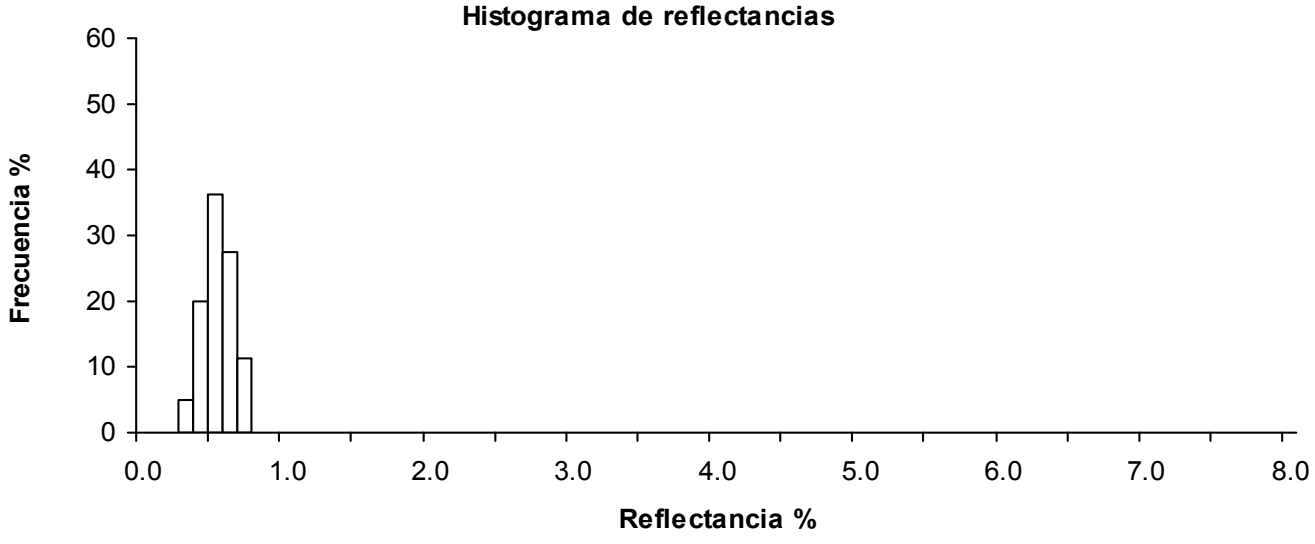

Analysis realized in: **MPV-1 Combi-Leitz**

Sample: **ESC-PEÑ**
Objective: **50x**
Pattern: **274**

Singular Reflectances:

0.56	0.48	0.59	0.67	0.59
0.68	0.51	0.52	0.54	0.51
0.49	0.38	0.48	0.52	0.54
0.56	0.60	0.76	0.67	0.54
0.64	0.59	0.65	0.60	0.56
0.67	0.64	0.68	0.67	0.65
0.59	0.64	0.65	0.59	0.60

Class	n	n%	Sn	Sn%
0.3	1	2.86	1	2.86
0.4	3	8.57	4	11.43
0.5	15	42.86	19	54.29
0.6	15	42.86	34	97.14
0.7	1	2.86	35	100.00

Re = 0.59 **s = 0.08** **R< = 0.46** **R> = 0.70** **N = 35** **MVR = 45.7**

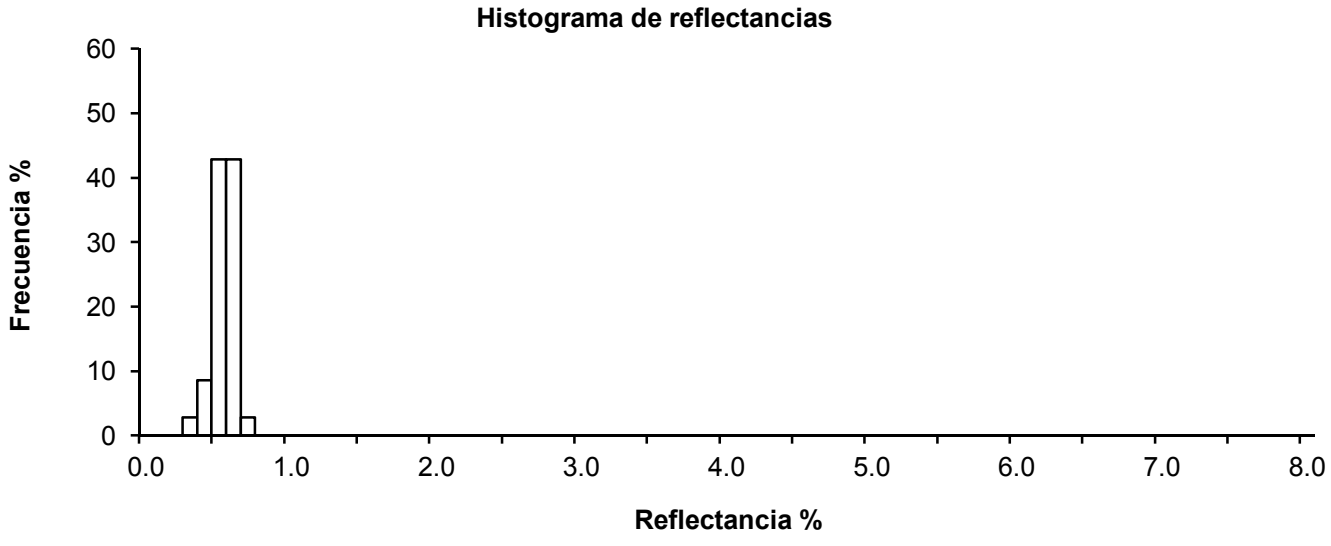

Analysis realized in: **MPV-1 Combi-Leitz**

Sample: ROB-13
Objective: 50x
Pattern: 274

Singular Reflectances:

2.48	2.56	2.60	2.64	2.67
2.67	2.71	2.71	2.75	2.75
2.79	2.83	2.87	2.87	2.87
2.87	2.87	2.91	2.91	2.91
2.95	2.95	2.98	2.98	3.02
3.02	3.02	3.02	3.02	3.02
3.02	3.06	3.06	3.06	3.10
3.14	3.14	3.18	3.18	3.18
3.26	3.26	3.26	3.29	3.33
3.37	3.41	3.41	3.49	3.57

Class	n	n%	Sn	Sn%
2.4	1	2.00	1	2.00
2.5	1	2.00	2	4.00
2.6	4	8.00	6	12.00
2.7	5	10.00	11	22.00
2.8	6	12.00	17	34.00
2.9	7	14.00	24	48.00
3.0	10	20.00	34	68.00
3.1	6	12.00	40	80.00
3.2	4	8.00	44	88.00
3.3	2	4.00	46	92.00
3.4	3	6.00	49	98.00
3.5	1	2.00	50	100.00

Re = 3.00 **s = 0.25** **R< = 2.57** **R> = 3.47** **N = 50** **MVR = 7.9**

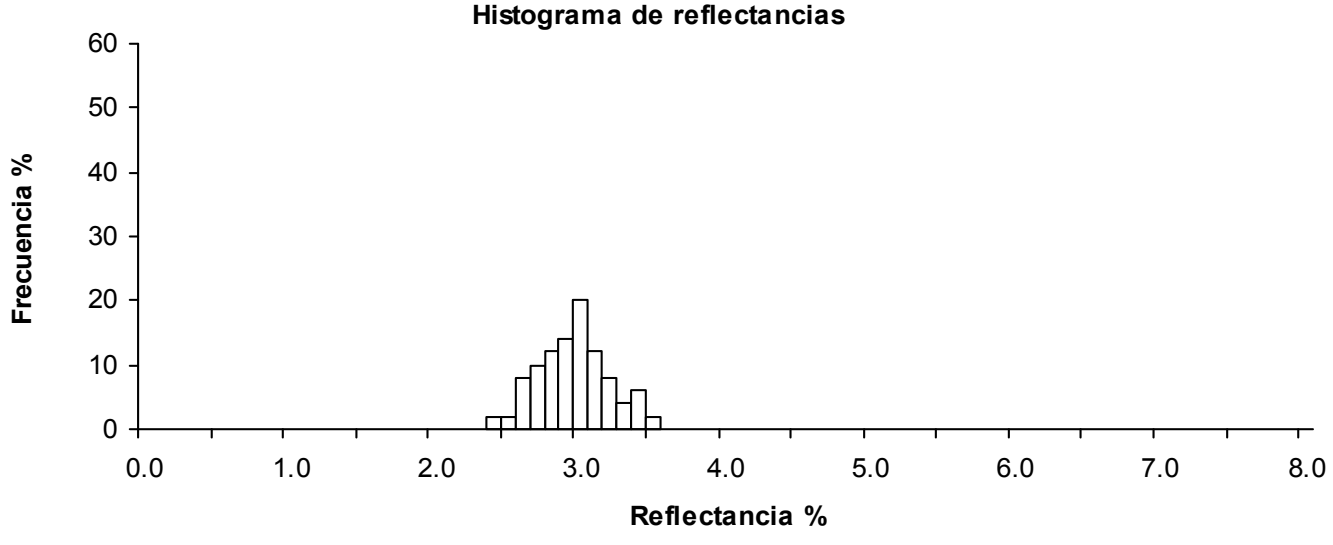

Analysis realized in: **MPV-1 Combi-Leitz**

Sample: ROB-100
Objective: 50x
Pattern: 274

Singular Reflectances:

2.98	3.02	3.06	3.06	3.10
3.10	3.10	3.10	3.14	3.14
3.14	3.18	3.18	3.18	3.22
3.22	3.22	3.22	3.22	3.22
3.22	3.22	3.22	3.26	3.26
3.26	3.26	3.29	3.29	3.29
3.29	3.29	3.29	3.33	3.33
3.33	3.33	3.33	3.33	3.37
3.41	3.41	3.41	3.41	3.41
3.45	3.49	3.49	3.53	3.57

Class	n	n%	Sn	Sn%
2.9	1	2.00	1	2.00
3.0	3	6.00	4	8.00
3.1	10	20.00	14	28.00
3.2	19	38.00	33	66.00
3.3	7	14.00	40	80.00
3.4	8	16.00	48	96.00
3.5	2	4.00	50	100.00

Re = 3.26 **s = 0.13** **R< = 3.03** **R> = 3.52** **N = 50** **MVR = 7.0**

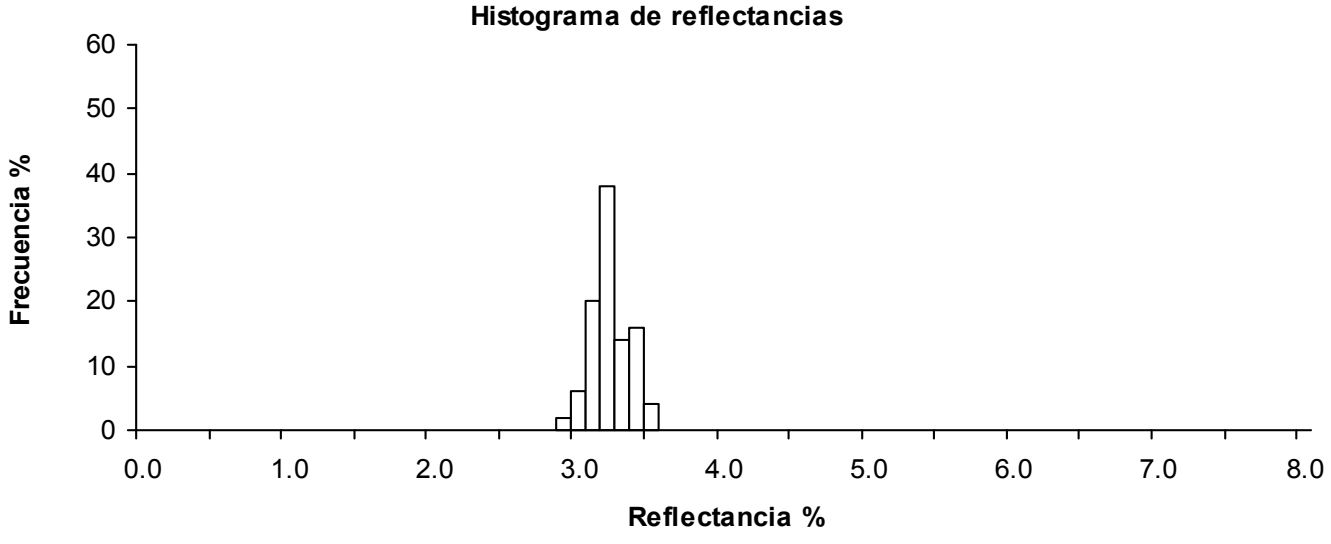

Analysis realized in: **MPV-1 Combi-Leitz**

Sample: **OLI-200**
Objective: **50x**
Pattern: **274**

Singular Reflectances:

2.44	2.48	2.60	2.71	2.71
2.75	2.79	2.79	2.83	2.91
3.02	3.06	3.06	3.10	3.22
3.33				

Class	n	n%	Sn	Sn%
2.4	2	12.50	2	12.50
2.6	1	6.25	3	18.75
2.7	5	31.25	8	50.00
2.8	1	6.25	9	56.25
2.9	1	6.25	10	62.50
3.0	3	18.75	13	81.25
3.1	1	6.25	14	87.50
3.2	1	6.25	15	93.75
3.3	1	6.25	16	100.00

Re = 2.86 **s = 0.25** **R< = 2.46** **R> = 3.29** **N = 16** **MVR = 8.4**

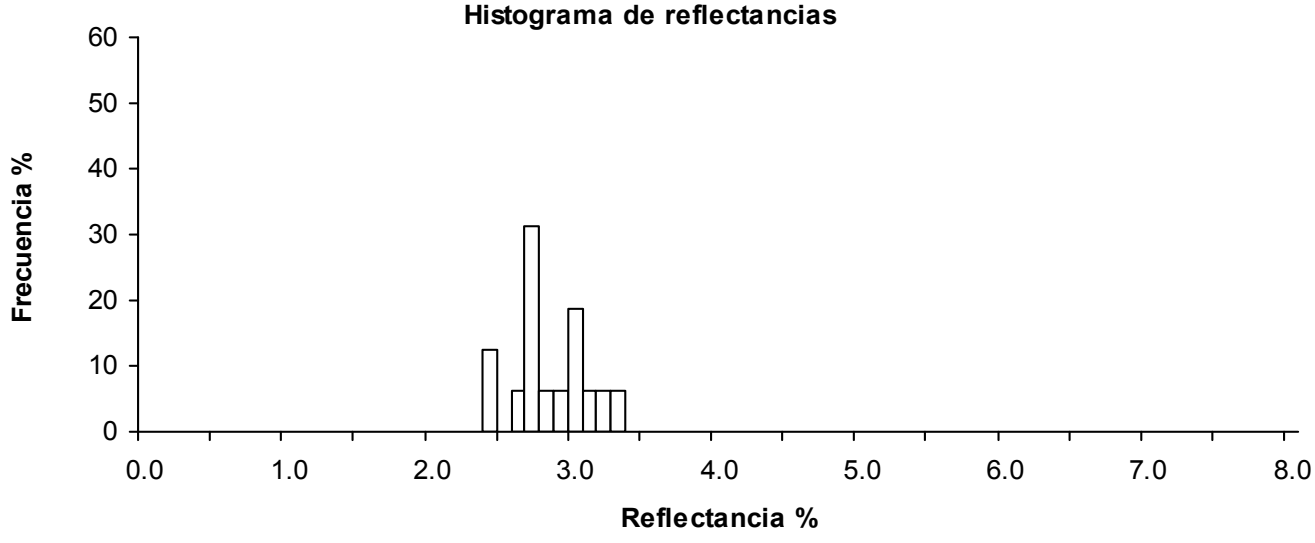

Analysis realized in: **MPV-1 Combi-Leitz**

Sample: **PR-11P**
Objective: **50x**
Pattern: **274**

Singular Reflectances:

4.79	4.49	5.63	4.39	4.76
4.06	4.42	2.75	1.94	4.52
2.85	4.09	3.92	4.36	4.62
3.62	3.92	4.59	4.39	4.83
4.26				

Class	n	n%	Sn	Sn%
1.9	1	4.76	1	4.76
2.7	1	4.76	2	9.52
2.8	1	4.76	3	14.29
3.6	1	4.76	4	19.05
3.9	2	9.52	6	28.57
4.0	2	9.52	8	38.10
4.2	1	4.76	9	42.86
4.3	3	14.29	12	57.14
4.4	2	9.52	14	66.67
4.5	2	9.52	16	76.19
4.6	1	4.76	17	80.95
4.7	2	9.52	19	90.48
4.8	1	4.76	20	95.24
5.6	1	4.76	21	100.00

Re = 4.15 **s = 0.81** **R< = 2.35** **R> = 5.23** **N = 21** **MVR = 5.2**

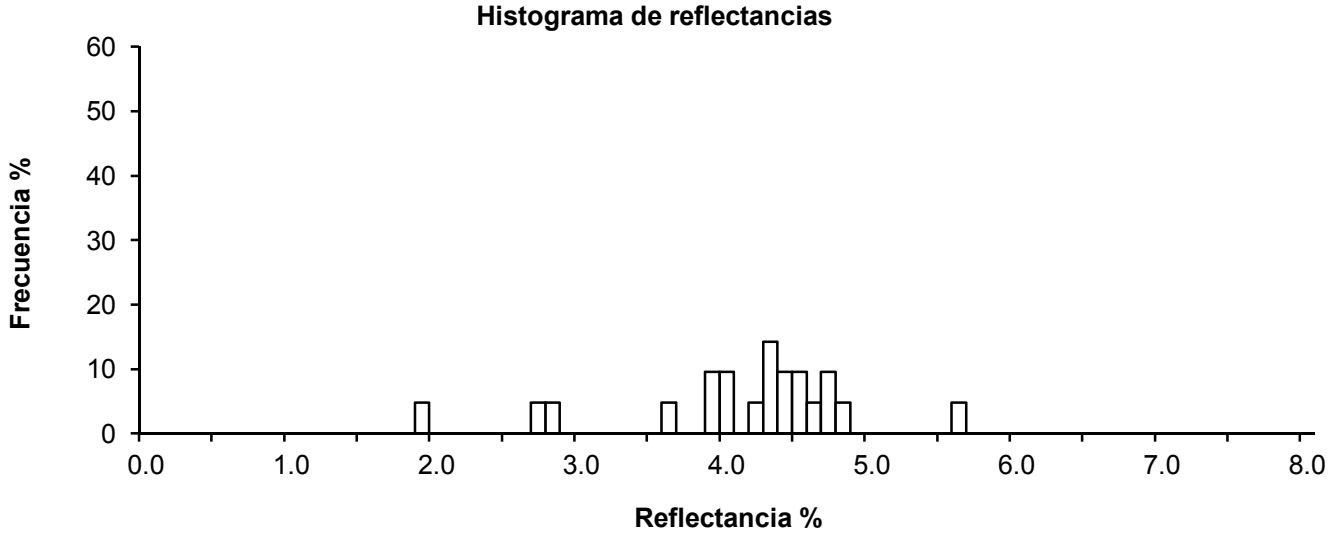

Analysis realized in: **MPV-1 Combi-Leitz**

Sample: **SEN-5**
Objective: **50x**
Pattern: **274**

Singular Reflectances:

1.72	1.82	1.86	1.92	2.03
2.03	2.03	2.07	2.19	2.19
2.25	2.29	2.42	2.62	2.66
2.67	2.85	2.89	3.06	3.93
4.39	5.08			

Class	n	n%	Sn	Sn%
1.7	1	4.55	1	4.55
1.8	2	9.09	3	13.64
1.9	1	4.55	4	18.18
2.0	4	18.18	8	36.36
2.1	2	9.09	10	45.45
2.2	2	9.09	12	54.55
2.4	1	4.55	13	59.09
2.6	3	13.64	16	72.73
2.8	2	9.09	18	81.82
3.0	1	4.55	19	86.36
3.9	1	4.55	20	90.91
4.3	1	4.55	21	95.45
5.0	1	4.55	22	100.00

Re = 2.59 **s = 0.87** **R< = 1.78** **R> = 4.72** **N = 22** **MVR = 10.5**

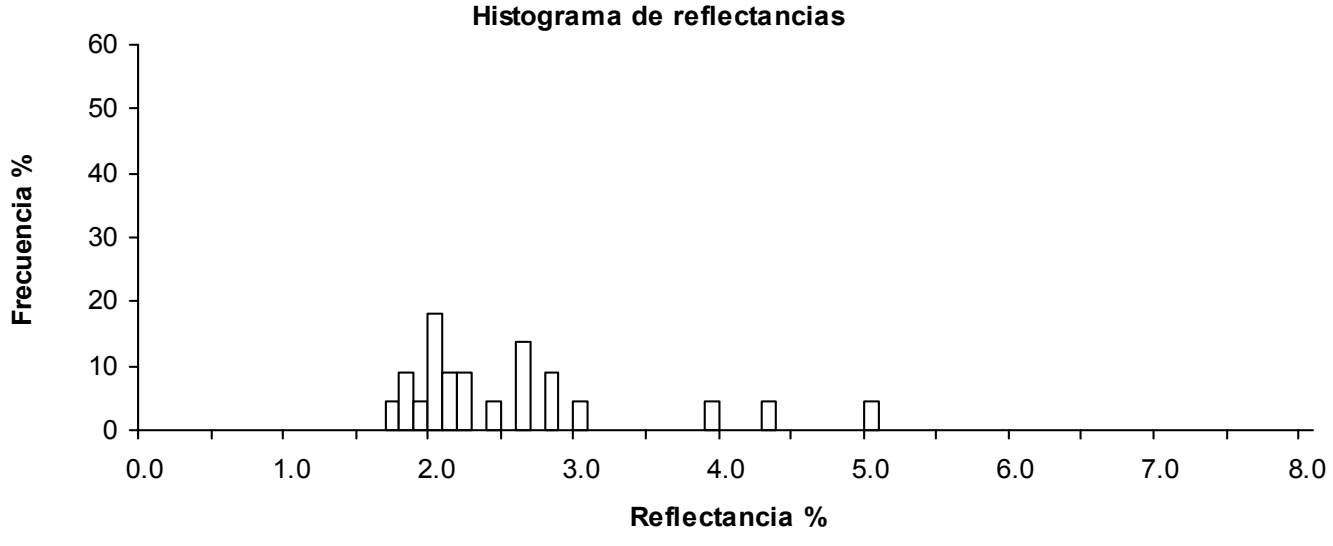

Analysis realized in: **MPV-1 Combi-Leitz**

Sample: SEN-3
Objective: 50x
Pattern: 274

Singular Reflectances:

2.65	2.89	3.08	3.20	3.29
3.29	3.29	3.40	3.47	3.50
3.58	3.72	4.09	4.10	4.17
4.24	4.40	4.55	4.69	4.74
5.28	5.75			

Class	n	n%	Sn	Sn%
2.6	1	4.55	1	4.55
2.8	1	4.55	2	9.09
3.0	1	4.55	3	13.64
3.2	4	18.18	7	31.82
3.4	2	9.09	9	40.91
3.5	2	9.09	11	50.00
3.7	1	4.55	12	54.55
4.0	1	4.55	13	59.09
4.1	2	9.09	15	68.18
4.2	1	4.55	16	72.73
4.4	1	4.55	17	77.27
4.5	1	4.55	18	81.82
4.6	1	4.55	19	86.36
4.7	1	4.55	20	90.91
5.2	1	4.55	21	95.45
5.7	1	4.55	22	100.00

Re = 3.88 **s = 0.79** **R< = 2.78** **R> = 5.50** **N = 22** **MVR = 5.7**

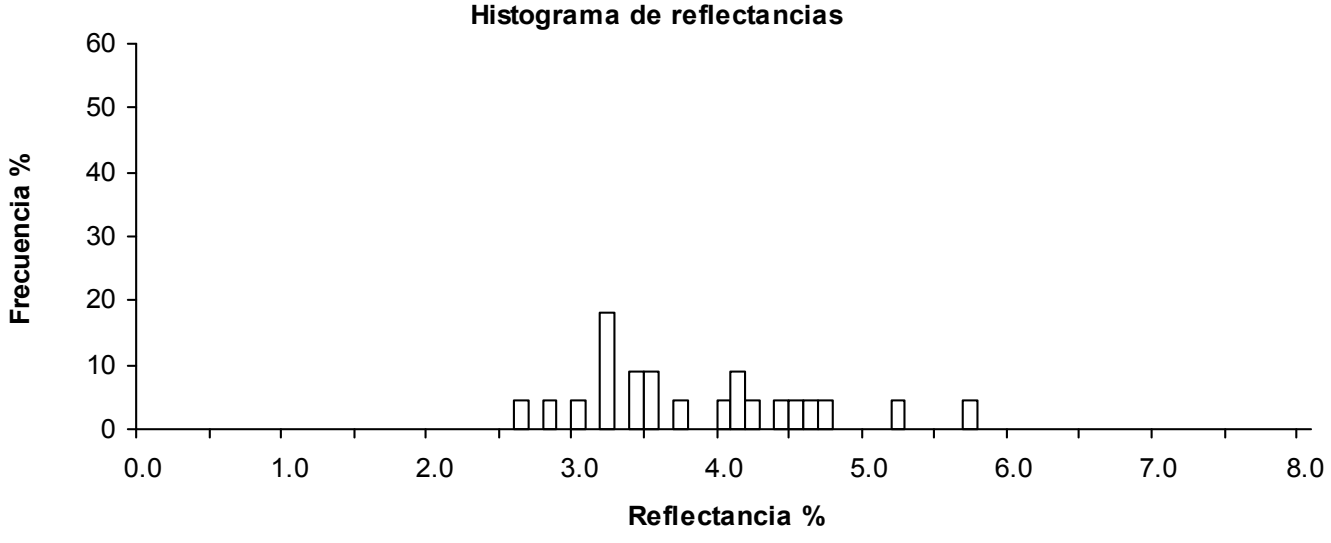

Analysis realized in: **MPV-1 Combi-Leitz**

Sample: SEN-1
Objective: 50x
Pattern: 274

Singular Reflectances:

1.82 1.98 2.25 2.33

Class	n	n%	Sn	Sn%
1.8	1	25.00	1	25.00
1.9	1	25.00	2	50.00
2.2	1	25.00	3	75.00
2.3	1	25.00	4	100.00

Re = 2.09 **s = 0.23** **R< = 1.83** **R> = 2.32** **N = 4** **MVR = 12.5**

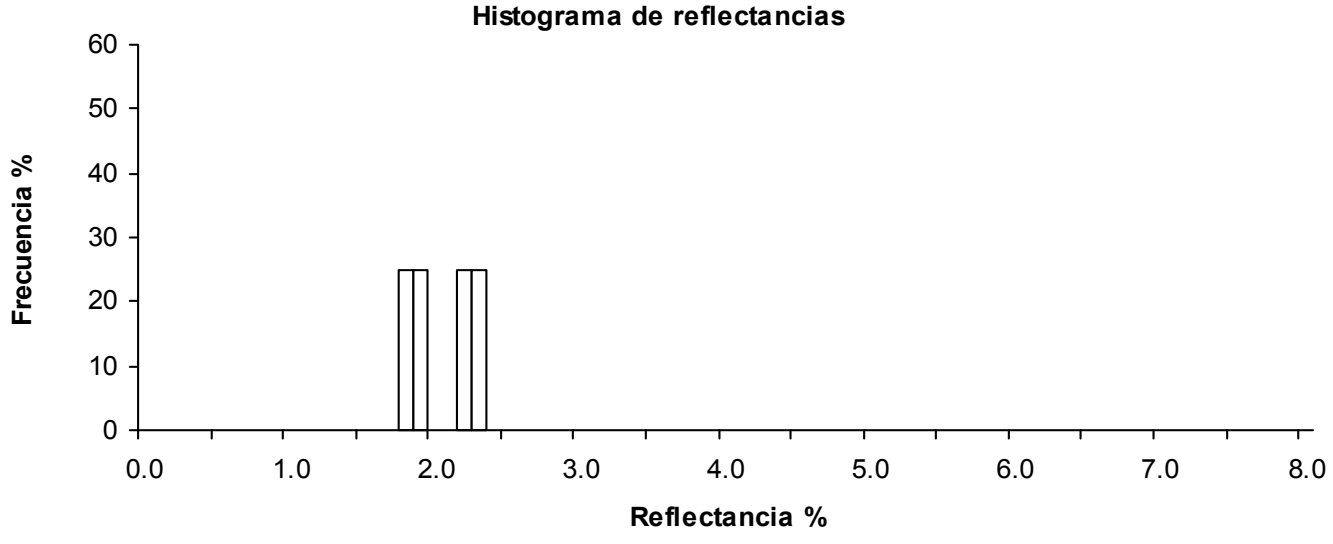

Analysis realized in: **MPV-1 Combi-Leitz**

Sample: URB-2
Objective: 50x
Pattern: 274

Singular Reflectances:

1.40	2.90	2.95	3.00	3.02
3.05	3.16	3.18	3.22	3.22
3.29	3.35	3.39	3.41	3.43
3.49	3.77	3.91		

Class	n	n%	Sn	Sn%
1.4	1	5.56	1	5.56
2.9	2	11.11	3	16.67
3.0	3	16.67	6	33.33
3.1	2	11.11	8	44.44
3.2	3	16.67	11	61.11
3.3	2	11.11	13	72.22
3.4	3	16.67	16	88.89
3.7	1	5.56	17	94.44
3.9	1	5.56	18	100.00

Re = 3.17 **s = 0.52** **R< = 2.03** **R> = 3.85** **N = 18** **MVR = 7.7**

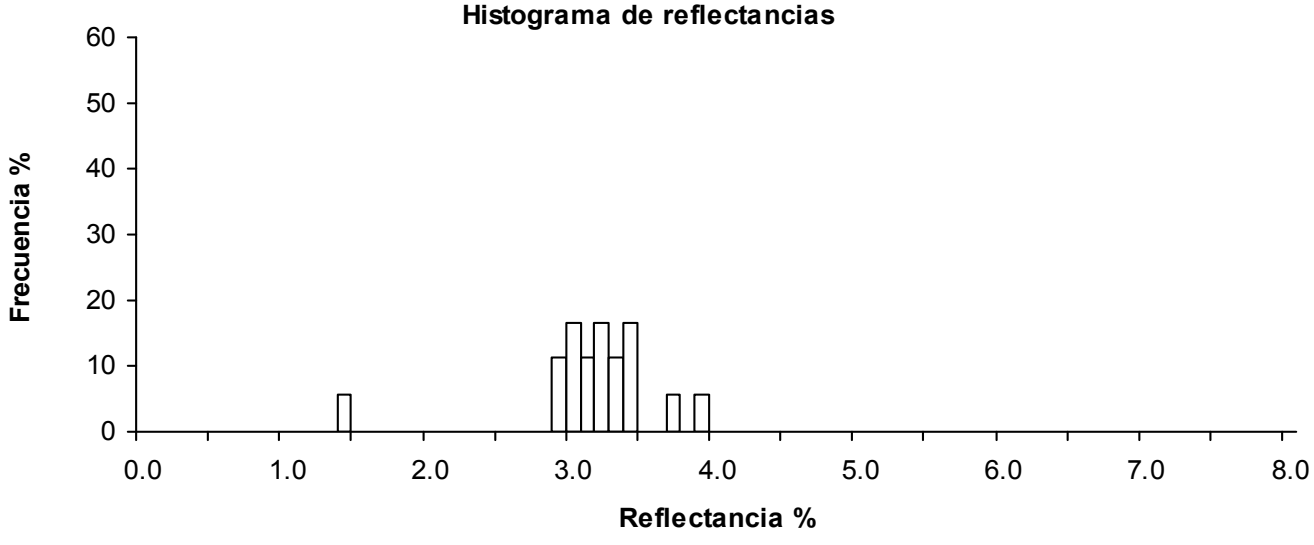

Analysis realized in: **MPV-1 Combi-Leitz**

Sample: **CAS-2**
Objective: **50x**
Pattern: **274**

Singular Reflectances:

0.28	0.29	0.24	0.29	0.29
0.21	0.28	0.35	0.23	0.31
0.31	0.31	0.32	0.26	0.34
0.29	0.34	0.26	0.18	0.29
0.31	0.26			

Class	n	n%	Sn	Sn%
0.1	1	4.55	1	4.55
0.2	13	59.09	14	63.64
0.3	8	36.36	22	100.00

Re = 0.28 **s = 0.04** **R< = 0.20** **R> = 0.34** **N = 22** **MVR = 63.1**

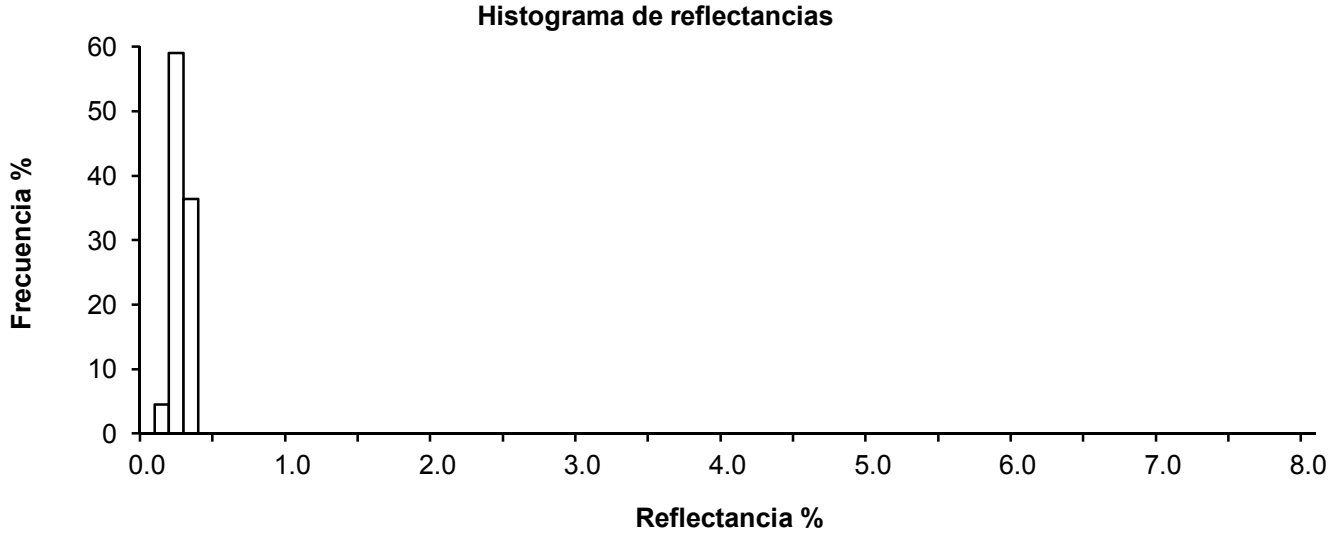

Analysis realized in: **MPV-1 Combi-Leitz**

Sample: PIG-1
Objective: 50x
Pattern: 274

Singular Reflectances:

0.37	0.37	0.40	0.43	0.43
0.43	0.47	0.47	0.47	0.47
0.47	0.50	0.50	0.50	0.50
0.50	0.50	0.50	0.53	0.53
0.53	0.56	0.56	0.56	0.56
0.59	0.59	0.65	0.65	0.65
0.65	0.68	0.68	0.71	0.74
0.78	0.78	0.81	0.84	0.90
0.90	0.93	1.02	1.12	1.21
1.30				

Class	n	n%	Sn	Sn%
0.3	2	4.35	2	4.35
0.4	9	19.57	11	23.91
0.5	16	34.78	27	58.70
0.6	6	13.04	33	71.74
0.7	4	8.70	37	80.43
0.8	2	4.35	39	84.78
0.9	3	6.52	42	91.30
1.0	1	2.17	43	93.48
1.1	1	2.17	44	95.65
1.2	1	2.17	45	97.83
1.3	1	2.17	46	100.00

Re = 0.64 **s = 0.22** **R< = 0.38** **R> = 1.20** **N = 46** **MVR = 43.6**

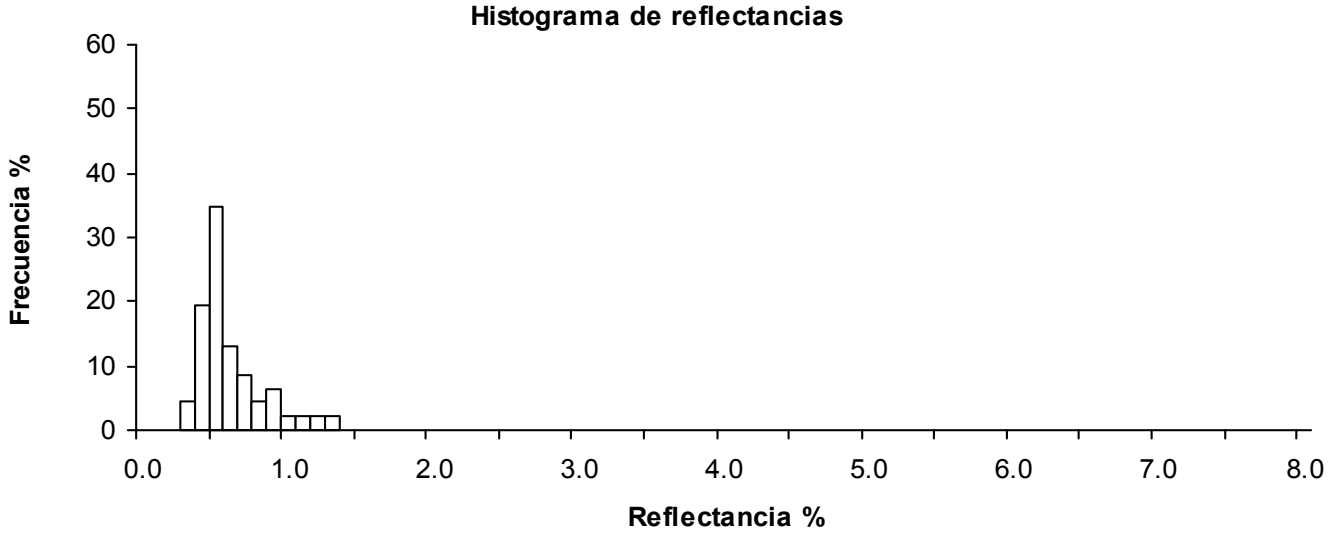

Analysis realized in: **MPV-1 Combi-Leitz**

Sample: STFC-4b
Objective: 50x
Pattern: 274

Singular Reflectances:

0.28	0.30	0.39	0.39	0.41
0.41	0.42	0.44	0.44	0.44
0.47	0.47	0.50	0.50	0.50
0.50	0.50	0.50	0.50	0.55
0.55	0.55	0.55	0.58	0.58
0.58	0.58	0.61	0.63	0.63
0.63	0.63	0.63	0.66	0.66
0.69	0.72	0.72	0.74	0.77
0.77				

Class	n	n%	Sn	Sn%
0.2	1	2.44	1	2.44
0.3	3	7.32	4	9.76
0.4	8	19.51	12	29.27
0.5	15	36.59	27	65.85
0.6	9	21.95	36	87.80
0.7	5	12.20	41	100.00

Re = 0.55 **s = 0.12** **R< = 0.30** **R> = 0.77** **N = 41** **MVR = 47.0**

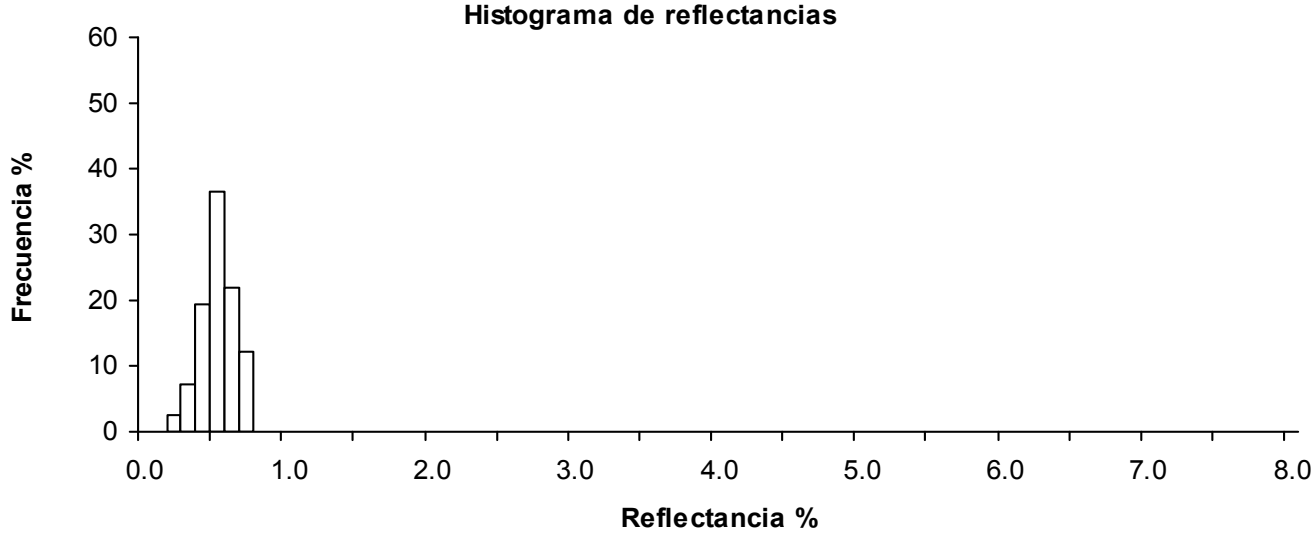

Analysis realized in: **MPV-1 Combi-Leitz**

Sample: STFC-4
Objective: 50x
Pattern: 274

Singular Reflectances:

0.27	0.29	0.32	0.34	0.36
0.38	0.38	0.38	0.38	0.38
0.38	0.41	0.41	0.45	0.45
0.50	0.52	0.52	0.61	0.63
0.63	0.65	0.68	0.68	0.68
0.68	0.72	0.92	0.95	0.95
1.06				

Class	n	n%	Sn	Sn%
0.2	2	6.45	2	6.45
0.3	9	29.03	11	35.48
0.4	4	12.90	15	48.39
0.5	3	9.68	18	58.06
0.6	8	25.81	26	83.87
0.7	1	3.23	27	87.10
0.9	3	9.68	30	96.77
1.0	1	3.23	31	100.00

Re = 0.55 **s = 0.21** **R< = 0.29** **R> = 0.98** **N = 31** **MVR = 48.1**

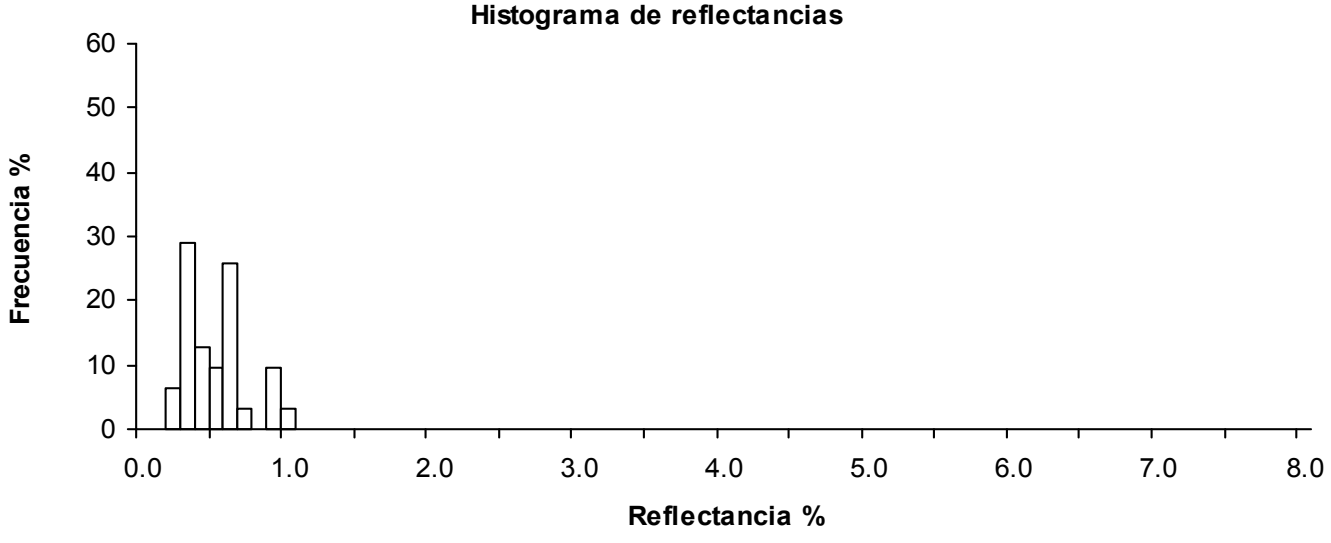

Analysis realized in: **MPV-1 Combi-Leitz**

Sample: **STFC-3b**
Objective: **50x**
Pattern: **274**

Singular Reflectances:

0.77	0.84	0.70	1.11	0.74
0.84	0.77	0.57	0.97	0.74
0.80	0.64	0.54	0.60	1.11
0.67	0.87	0.67	0.77	0.40
0.74	0.40	0.67		

Class	n	n%	Sn	Sn%
0.4	2	8.70	2	8.70
0.5	2	8.70	4	17.39
0.6	5	21.74	9	39.13
0.7	7	30.43	16	69.57
0.8	4	17.39	20	86.96
0.9	1	4.35	21	91.30
1.1	2	8.70	23	100.00

Re = 0.74 **s = 0.18** **R< = 0.40** **R> = 1.11** **N = 23** **MVR = 40.0**

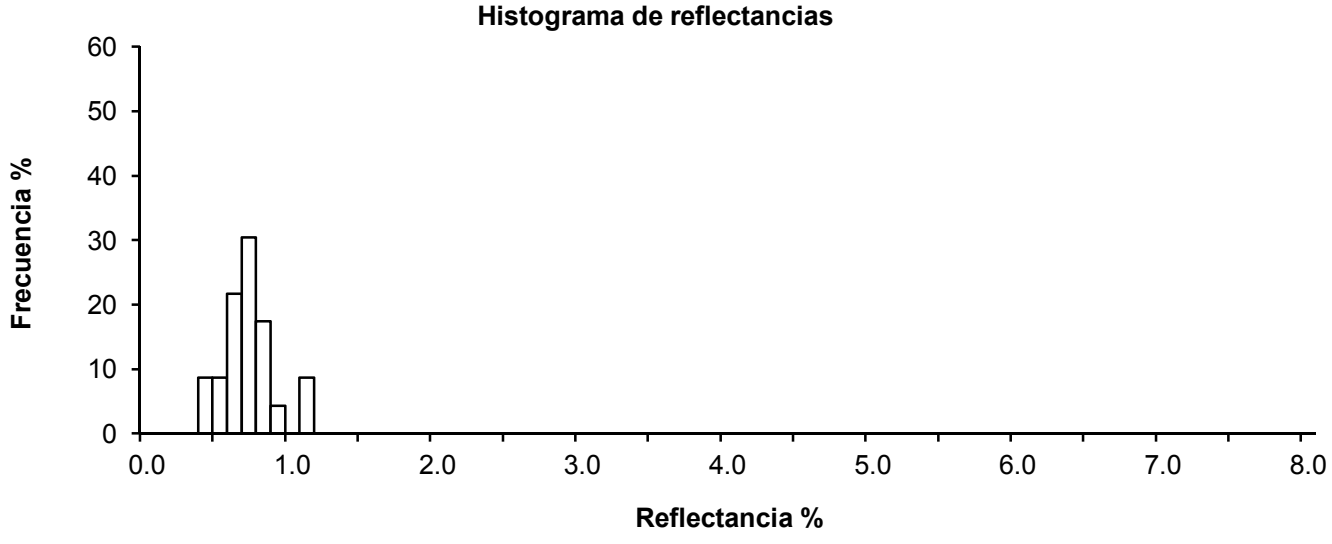

Analysis realized in: **MPV-1 Combi-Leitz**

Sample: **STFC-3**
Objective: **50x**
Pattern: **274**

Singular Reflectances:

0.69	0.71	0.63	0.82	1.30
0.69	0.79	0.74	0.93	0.64
0.81	1.00	1.00	0.74	1.01
0.63	0.77	1.03	0.87	0.64
0.72	0.87	1.21	0.72	0.85
0.69	0.85	0.60	0.97	0.69
0.72	0.81	0.97	1.32	0.72
0.81	0.60	1.10	1.13	0.64
0.82	0.69	0.81	0.72	0.84
0.68	1.01	0.72	1.05	0.95
1.10	0.82	0.72	1.01	

Class	n	n%	Sn	Sn%
0.6	13	24.07	13	24.07
0.7	12	22.22	25	46.30
0.8	12	22.22	37	68.52
0.9	4	7.41	41	75.93
1.0	7	12.96	48	88.89
1.1	3	5.56	51	94.44
1.2	1	1.85	52	96.30
1.3	2	3.70	54	100.00

Re = 0.84 **s = 0.18** **R< = 0.61** **R> = 1.27** **N = 54** **MVR = 36.4**

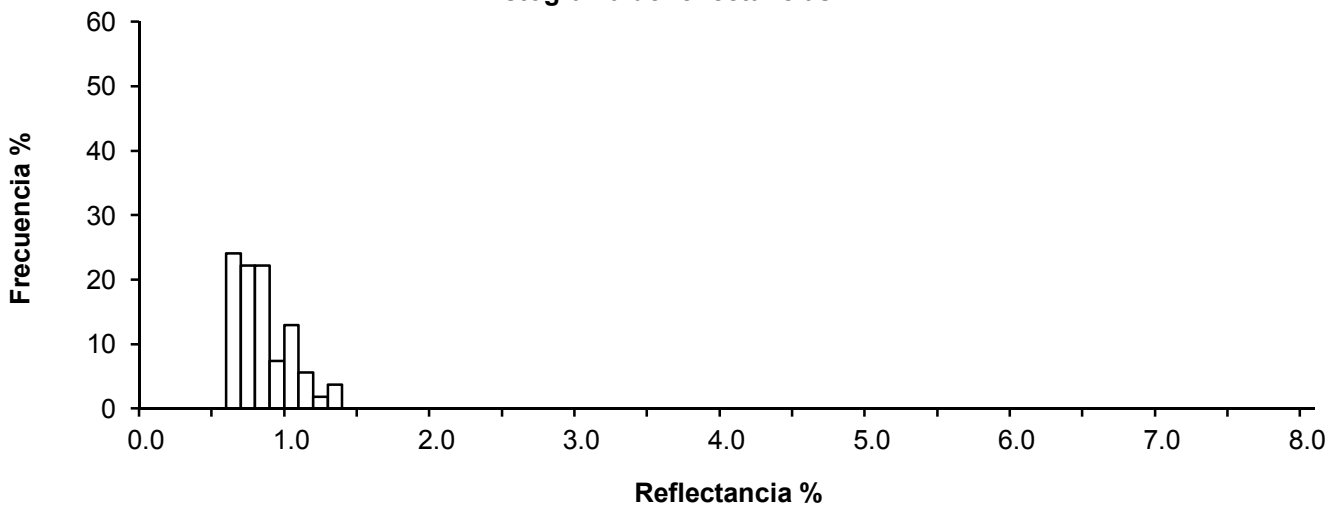

Analysis realized in: **MPV-1 Combi-Leitz**

Sample: **STFC-2**
Objective: **50x**
Pattern: **274**

Singular Reflectances:

0.41	0.44	0.44	0.44	0.44
0.47	0.47	0.47	0.50	0.52
0.52	0.52	0.52	0.52	0.55
0.55	0.55	0.58	0.58	0.61
0.61	0.61	0.61	0.63	0.63
0.63	0.63	0.66	0.66	0.66
0.66	0.69	0.69	0.69	0.69
0.72	0.74			

Class	n	n%	Sn	Sn%
0.4	8	21.62	8	21.62
0.5	11	29.73	19	51.35
0.6	16	43.24	35	94.59
0.7	2	5.41	37	100.00

Re = 0.58 **s = 0.09** **R< = 0.44** **R> = 0.72** **N = 37** **MVR = 45.6**

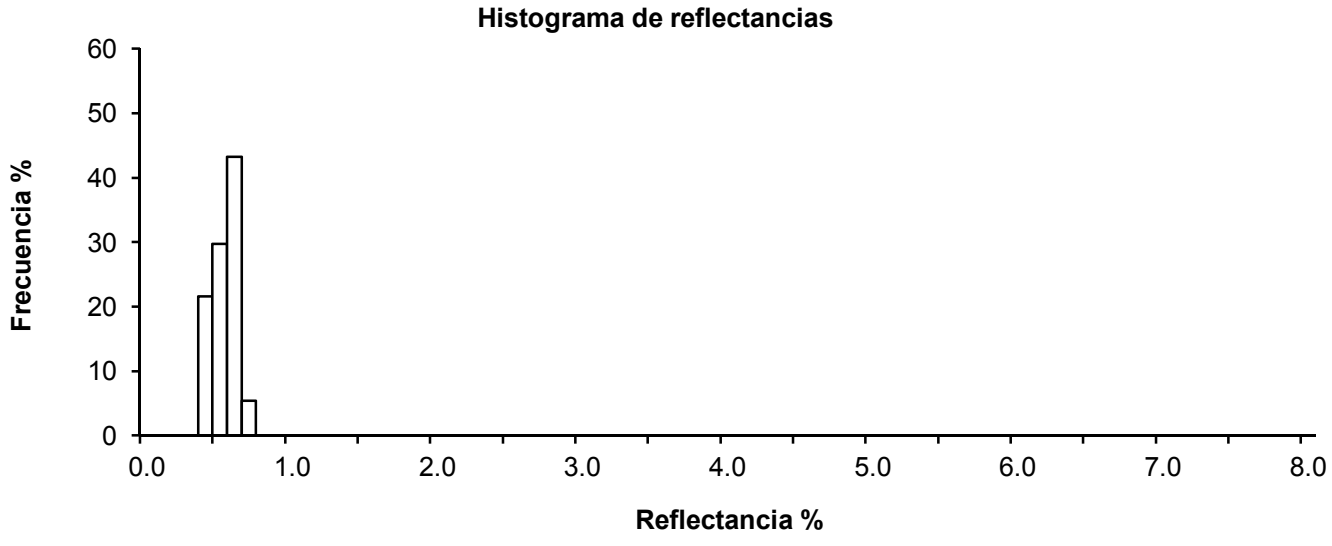

Analysis realized in: **MPV-1 Combi-Leitz**

Sample: STFC-1
Objective: 50x
Pattern: 274

Singular Reflectances:

0.28	0.33	0.33	0.34	0.34
0.35	0.36	0.36	0.37	0.37
0.37	0.38	0.38	0.39	0.40
0.40	0.41	0.42	0.43	0.45
0.47	0.47	0.48	0.49	0.49
0.50	0.50	0.51	0.52	0.53
0.53	0.53	0.54	0.54	0.54
0.54	0.55	0.55	0.55	0.55
0.56	0.56	0.57	0.58	0.58
0.59	0.59	0.61	0.61	0.63
0.66	0.72	0.74	0.78	0.91
1.01	1.03	1.07		

Class	n	n%	Sn	Sn%
0.2	1	1.72	1	1.72
0.3	13	22.41	14	24.14
0.4	11	18.97	25	43.10
0.5	22	37.93	47	81.03
0.6	4	6.90	51	87.93
0.7	3	5.17	54	93.10
0.9	1	1.72	55	94.83
1.0	3	5.17	58	100.00

Re = 0.53 **s = 0.17** **R< = 0.33** **R> = 1.02** **N = 58** **MVR = 48.2**

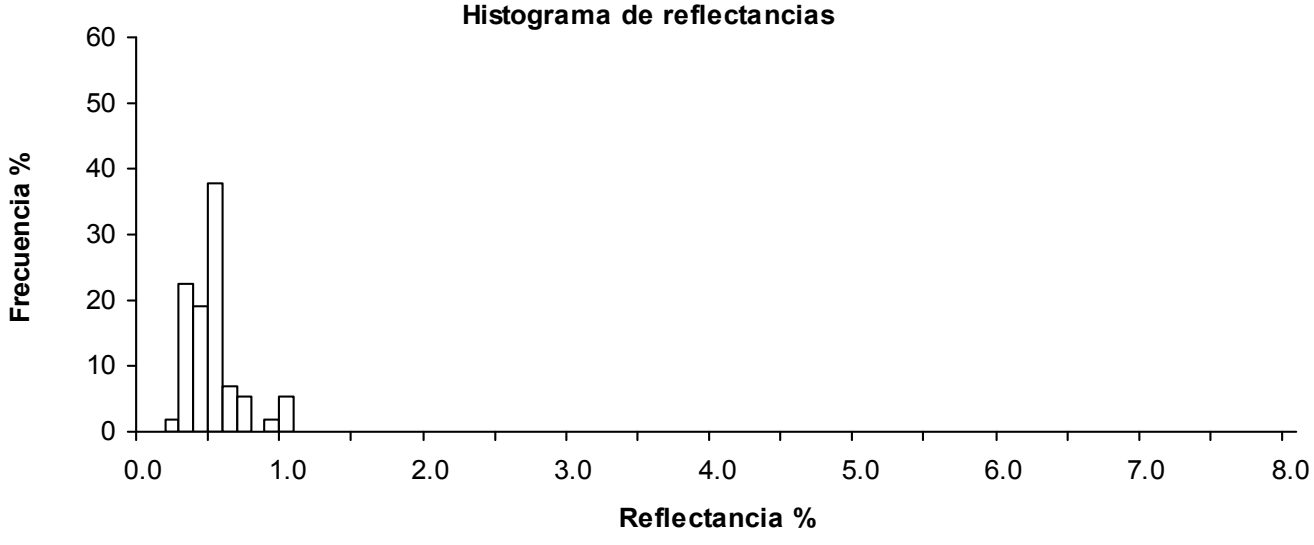

Analysis realized in: **MPV-1 Combi-Leitz**

Sample: **STFC-0**
Objective: **50x**
Pattern: **274**

Singular Reflectances:

0.44	0.59	0.49	0.44	0.54
0.54	0.39	0.62	0.54	0.44
0.47	0.49	0.52	0.57	0.52
0.41	1.32	1.24	0.39	0.41
0.49	0.54	0.49	0.75	0.57
0.44	0.36	0.44	0.70	0.39
0.34	0.49	0.54	0.39	0.41
0.36	0.39	0.59	0.52	0.52
0.62	1.06	0.80	0.65	0.67
0.41	0.44	0.39	0.59	0.41
0.52	1.21	0.41	0.39	0.62
0.36	0.36			

Class	n	n%	Sn	Sn%
0.3	12	21.05	12	21.05
0.4	18	31.58	30	52.63
0.5	15	26.32	45	78.95
0.6	5	8.77	50	87.72
0.7	2	3.51	52	91.23
0.8	1	1.75	53	92.98
1.0	1	1.75	54	94.74
1.2	2	3.51	56	98.25
1.3	1	1.75	57	100.00

Re = 0.54 **s = 0.21** **R< = 0.36** **R> = 1.23** **N = 57** **MVR = 47.5**

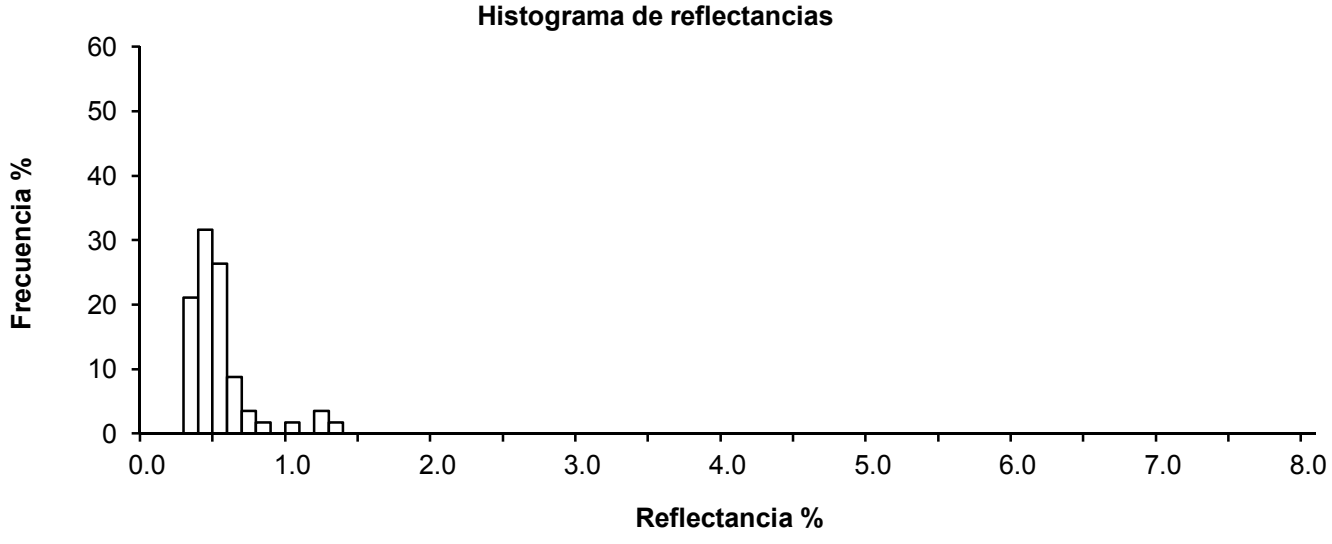

Analysis realized in: **MPV-1 Combi-Leitz**

Sample: SOY-3b
Objective: 50x
Pattern: 274

Singular Reflectances:

2.51	3.08	5.23	2.31	2.95
2.58	2.71	1.68	3.15	2.85
3.08	2.88	2.88	4.02	3.72
3.89	4.83	3.45	4.49	2.88

Class	n	n%	Sn	Sn%
1.6	1	5.00	1	5.00
2.3	1	5.00	2	10.00
2.5	2	10.00	4	20.00
2.7	1	5.00	5	25.00
2.8	4	20.00	9	45.00
2.9	1	5.00	10	50.00
3.0	2	10.00	12	60.00
3.1	1	5.00	13	65.00
3.4	1	5.00	14	70.00
3.7	1	5.00	15	75.00
3.8	1	5.00	16	80.00
4.0	1	5.00	17	85.00
4.4	1	5.00	18	90.00
4.8	1	5.00	19	95.00
5.2	1	5.00	20	100.00

Re = 3.26 **s = 0.88** **R< = 1.98** **R> = 5.04** **N = 20** **MVR = 7.7**

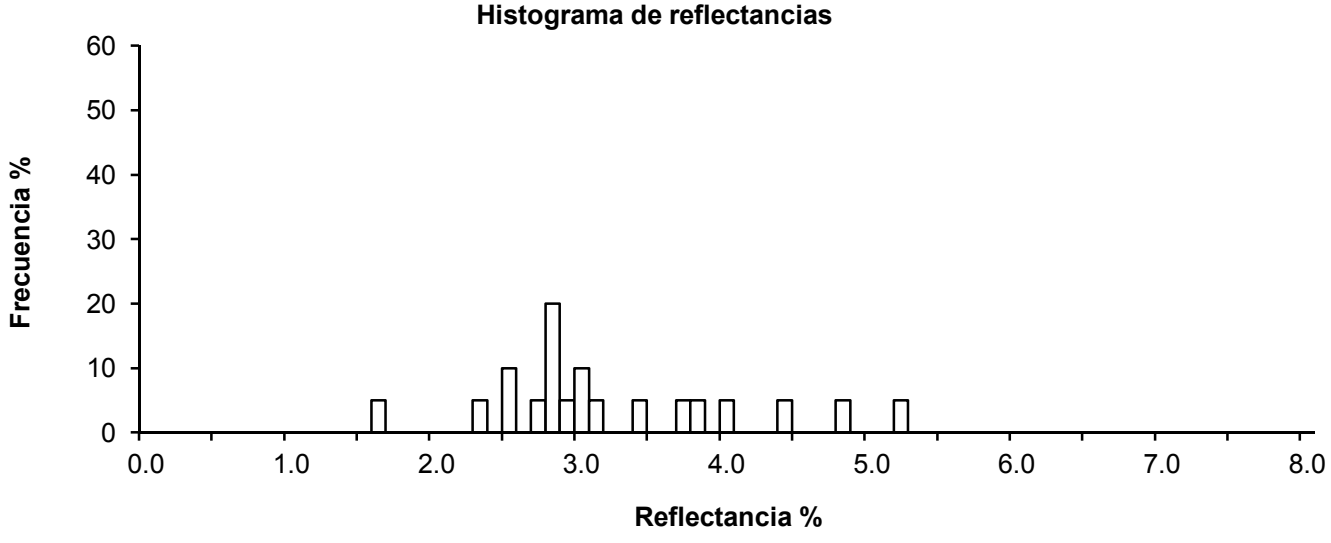

Analysis realized in: **MPV-1 Combi-Leitz**

Sample: SOY-3
Objective: 50x
Pattern: 274

Singular Reflectances:

1.41	1.62	1.91	1.96	1.96
2.03	2.18	2.21	2.21	2.26
2.26	2.28	2.36	2.41	2.41
2.43	2.45	2.53	2.55	2.65
2.65	2.70	2.78	2.80	2.80
2.80	2.86	2.89	2.93	2.95
3.08	3.09	3.10	3.12	3.14
3.19	3.20	3.34	3.40	3.42
3.44	3.52	3.64	3.69	3.70
4.08	4.19	4.24	4.35	4.51
4.51	5.11	5.70		

Class	n	n%	Sn	Sn%
1.4	1	1.89	1	1.89
1.6	1	1.89	2	3.77
1.9	3	5.66	5	9.43
2.0	1	1.89	6	11.32
2.1	1	1.89	7	13.21
2.2	5	9.43	12	22.64
2.3	1	1.89	13	24.53
2.4	4	7.55	17	32.08
2.5	2	3.77	19	35.85
2.6	2	3.77	21	39.62
2.7	2	3.77	23	43.40
2.8	5	9.43	28	52.83
2.9	2	3.77	30	56.60
3.0	2	3.77	32	60.38
3.1	4	7.55	36	67.92
3.2	1	1.89	37	69.81
3.3	1	1.89	38	71.70
3.4	3	5.66	41	77.36
3.5	1	1.89	42	79.25
3.6	2	3.77	44	83.02
3.7	1	1.89	45	84.91
4.0	1	1.89	46	86.79
4.1	1	1.89	47	88.68
4.2	1	1.89	48	90.57
4.3	1	1.89	49	92.45
4.5	2	3.77	51	96.23
5.1	1	1.89	52	98.11
5.7	1	1.89	53	100.00

Re = 3.00 **s = 0.87** **R< = 1.70** **R> = 4.93** **N = 53** **MVR = 8.7**

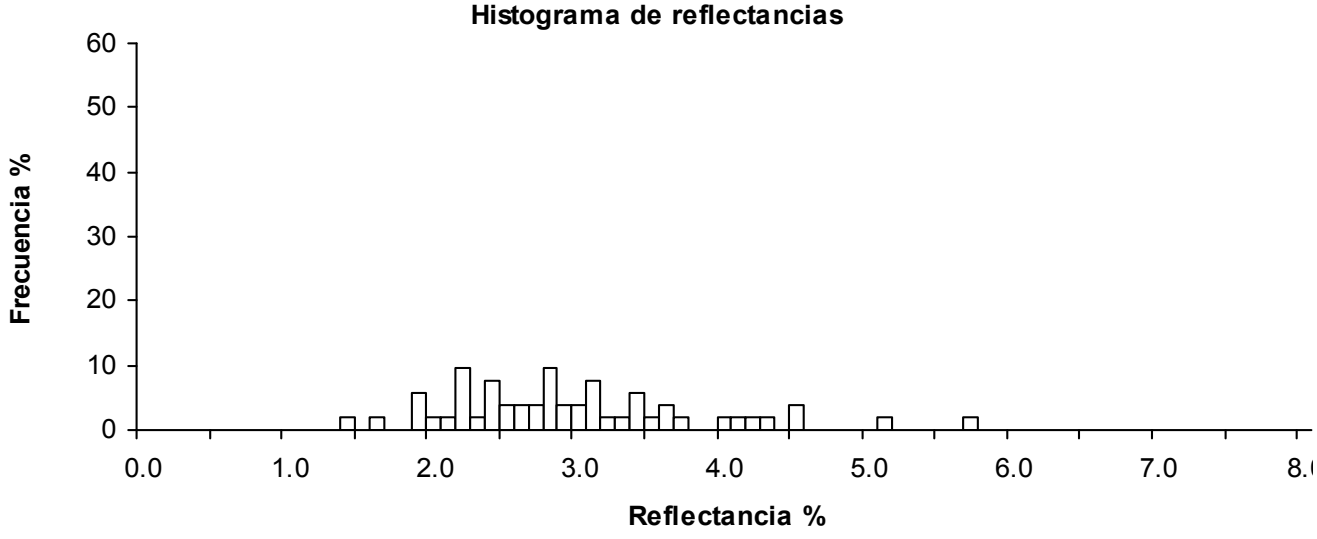

Analysis realized in: **MPV-1 Combi-Leitz**

Sample: SOH-4
Objective: 50x
Pattern: 274

Singular Reflectances:

2.44	2.48	2.52	2.56	2.66
2.66	2.76	2.78	2.79	3.01
3.17	3.50			

Class	n	n%	Sn	Sn%
2.4	2	16.67	2	16.67
2.5	2	16.67	4	33.33
2.6	2	16.67	6	50.00
2.7	3	25.00	9	75.00
3.0	1	8.33	10	83.33
3.1	1	8.33	11	91.67
3.5	1	8.33	12	100.00

Re = 2.78 **s = 0.31** **R< = 2.45** **R> = 3.41** **N = 12** **MVR = 8.8**

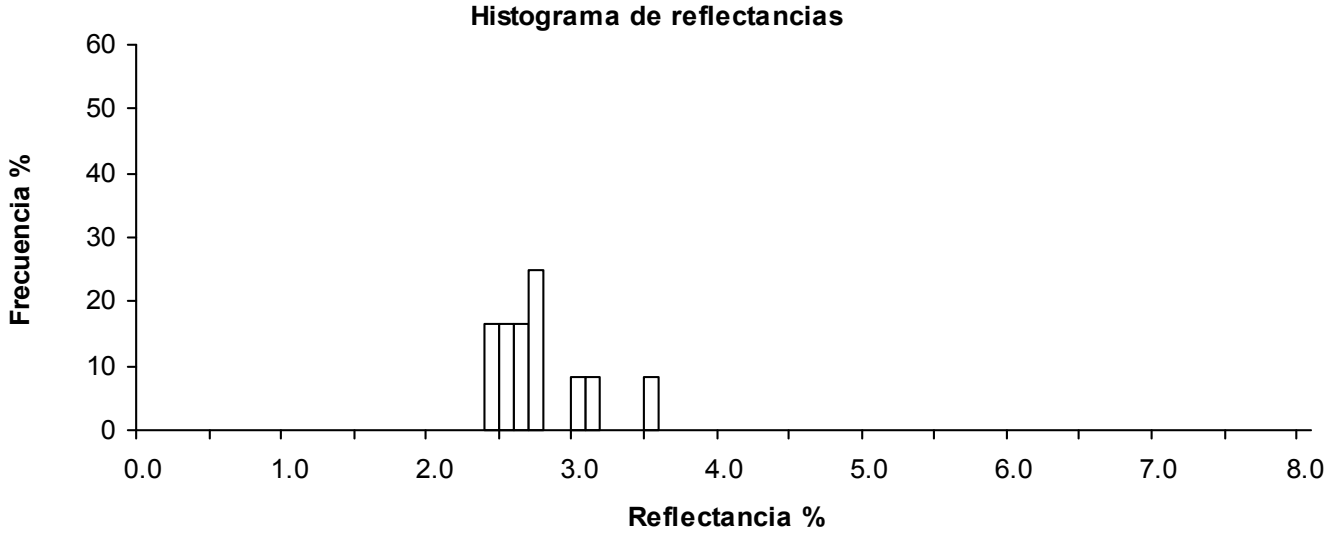

Analysis realized in: **MPV-1 Combi-Leitz**

Sample: SOH-3
Objective: 50x
Pattern: 274

Singular Reflectances:

1.35	1.58	1.61	1.66	1.75
1.75	1.80	1.83	1.83	1.83
1.83	1.83	1.83	1.89	1.89
1.92	1.92	1.92	1.97	2.00
2.03	2.03	2.03	2.11	2.17
2.20	2.34	2.62	2.82	2.82
2.82	3.24			

Class	n	n%	Sn	Sn%
1.3	1	3.13	1	3.13
1.5	1	3.13	2	6.25
1.6	2	6.25	4	12.50
1.7	2	6.25	6	18.75
1.8	9	28.13	15	46.88
1.9	4	12.50	19	59.38
2.0	4	12.50	23	71.88
2.1	2	6.25	25	78.13
2.2	1	3.13	26	81.25
2.3	1	3.13	27	84.38
2.6	1	3.13	28	87.50
2.8	3	9.38	31	96.88
3.2	1	3.13	32	100.00

Re = 2.04 **s = 0.41** **R< = 1.53** **R> = 2.91** **N = 32** **MVR = 13.4**

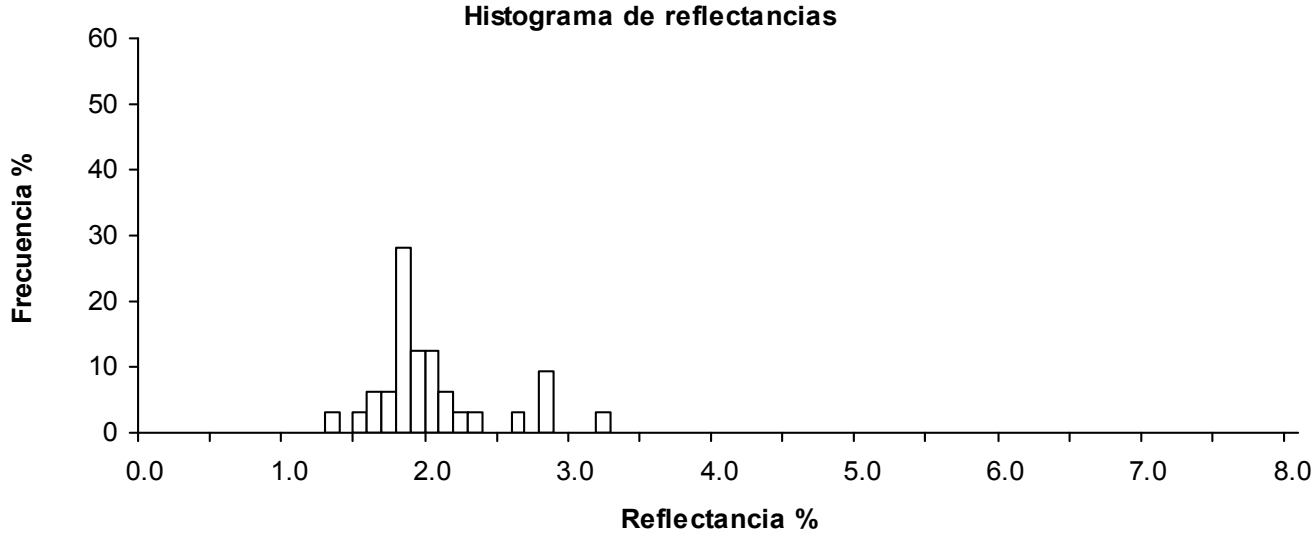

Analysis realized in: **MPV-1 Combi-Leitz**

Sample: SOO-2
Objective: 50x
Pattern: 274

Singular Reflectances:

1.49	1.56	1.58	1.58	1.67
1.74	1.83	1.85	1.85	1.87
1.87	1.89	1.89	1.92	1.94
1.98	2.05	2.05	2.05	2.10
2.10	2.12	2.14	2.19	2.21
2.28	2.37			

Class	n	n%	Sn	Sn%
1.4	1	3.70	1	3.70
1.5	3	11.11	4	14.81
1.6	1	3.70	5	18.52
1.7	1	3.70	6	22.22
1.8	7	25.93	13	48.15
1.9	3	11.11	16	59.26
2.0	3	11.11	19	70.37
2.1	5	18.52	24	88.89
2.2	2	7.41	26	96.30
2.3	1	3.70	27	100.00

Re = 1.93 **s = 0.23** **R< = 1.53** **R> = 2.31** **N = 27** **MVR = 14.1**

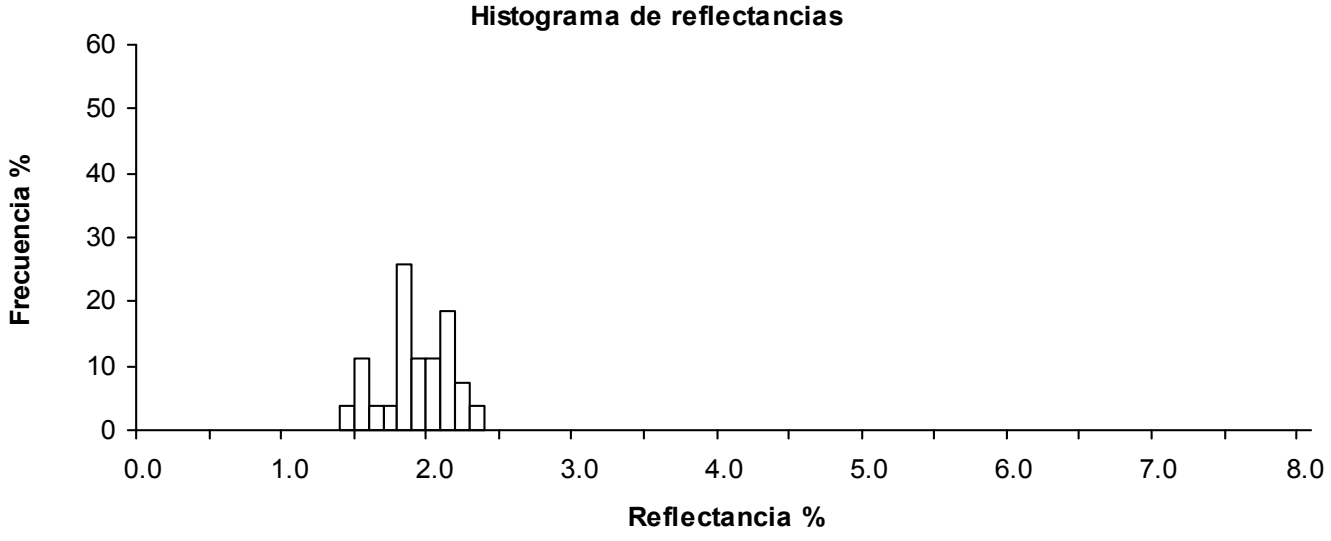

Analysis realized in: **MPV-1 Combi-Leitz**

Sample: YN-B04
Objective: 50x
Pattern: 274

Singular Reflectances:

1.53	1.57	1.79	2.02	2.06
2.17	2.21	2.21	2.28	2.30
2.33	2.35	2.35	2.41	2.41
2.41	2.44	2.55	2.57	2.59
2.59	2.64	2.68	2.68	2.70
2.75	2.79	2.79	2.83	2.92
2.95	2.97	2.99	3.06	3.06
3.06	3.21	3.23	3.28	3.32

Class	n	n%	Sn	Sn%
1.5	2	5.00	2	5.00
1.7	1	2.50	3	7.50
2.0	2	5.00	5	12.50
2.1	1	2.50	6	15.00
2.2	3	7.50	9	22.50
2.3	4	10.00	13	32.50
2.4	4	10.00	17	42.50
2.5	4	10.00	21	52.50
2.6	3	7.50	24	60.00
2.7	4	10.00	28	70.00
2.8	1	2.50	29	72.50
2.9	4	10.00	33	82.50
3.0	3	7.50	36	90.00
3.2	3	7.50	39	97.50
3.3	1	2.50	40	100.00

Re = 2.58 **s = 0.44** **R< = 1.57** **R> = 3.28** **N = 40** **MVR = 10.0**

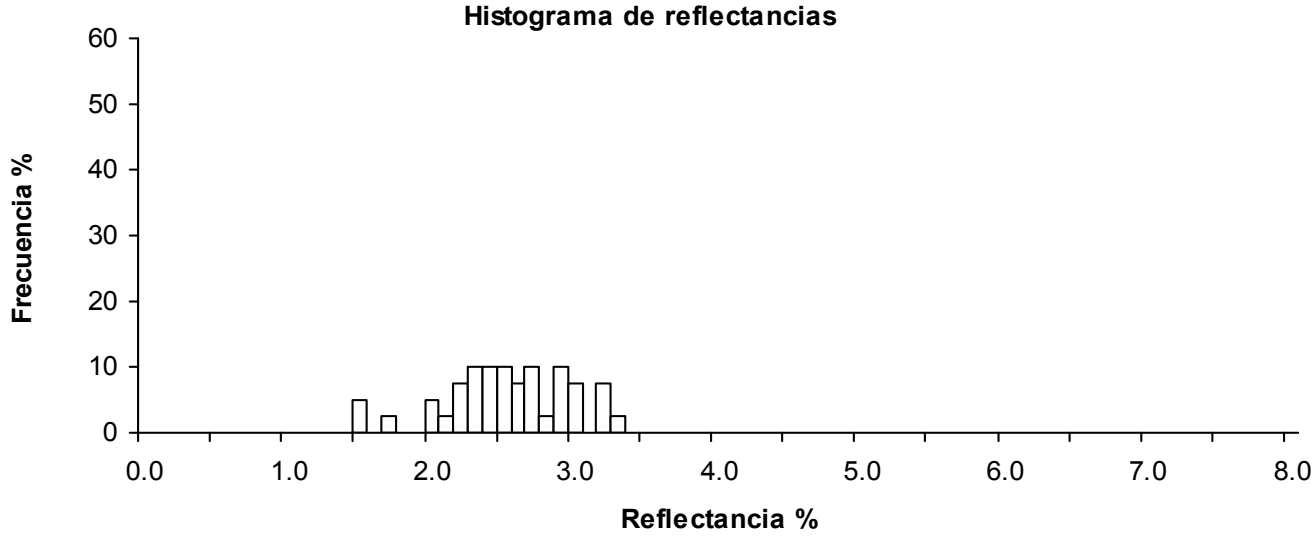

Analysis realized in: **MPV-1 Combi-Leitz**

Sample: **YN-B10**
Objective: **50x**
Pattern: **274**

Singular Reflectances:

1.57	1.54	1.62	1.26	1.84
1.45	1.66	1.62		

Class	n	n%	Sn	Sn%
1.2	1	12.50	1	12.50
1.4	1	12.50	2	25.00
1.5	2	25.00	4	50.00
1.6	3	37.50	7	87.50
1.8	1	12.50	8	100.00

Re = 1.57 **s = 0.17** **R< = 1.29** **R> = 1.81** **N = 8** **MVR = 18.2**

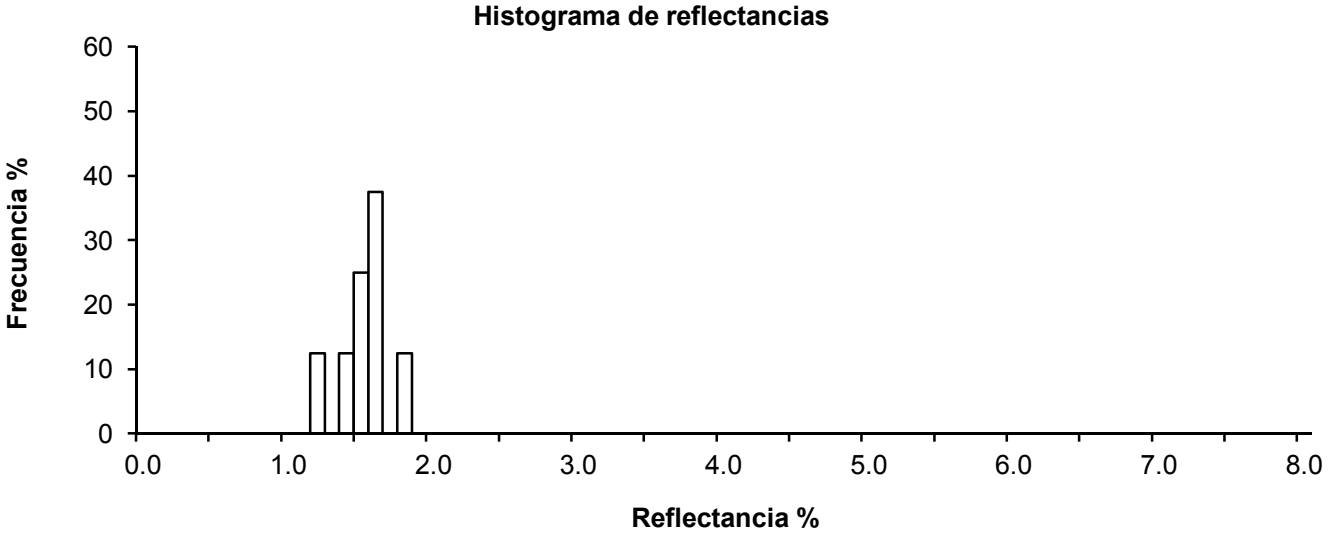

Analysis realized in: **MPV-1 Combi-Leitz**

Sample: SOH-2
Objective: 50x
Pattern: 274

Singular Reflectances:

1.47	1.72	1.78	1.83	1.83
1.89	1.97	2.00	2.03	2.03
2.03	2.09	2.11	2.11	2.14
2.17	2.28	2.31	2.48	2.62

Class	n	n%	Sn	Sn%
1.4	1	5.00	1	5.00
1.7	2	10.00	3	15.00
1.8	3	15.00	6	30.00
1.9	1	5.00	7	35.00
2.0	5	25.00	12	60.00
2.1	4	20.00	16	80.00
2.2	1	5.00	17	85.00
2.3	1	5.00	18	90.00
2.4	1	5.00	19	95.00
2.6	1	5.00	20	100.00

Re = 2.04 **s = 0.26** **R< = 1.59** **R> = 2.55** **N = 20** **MVR = 13.1**

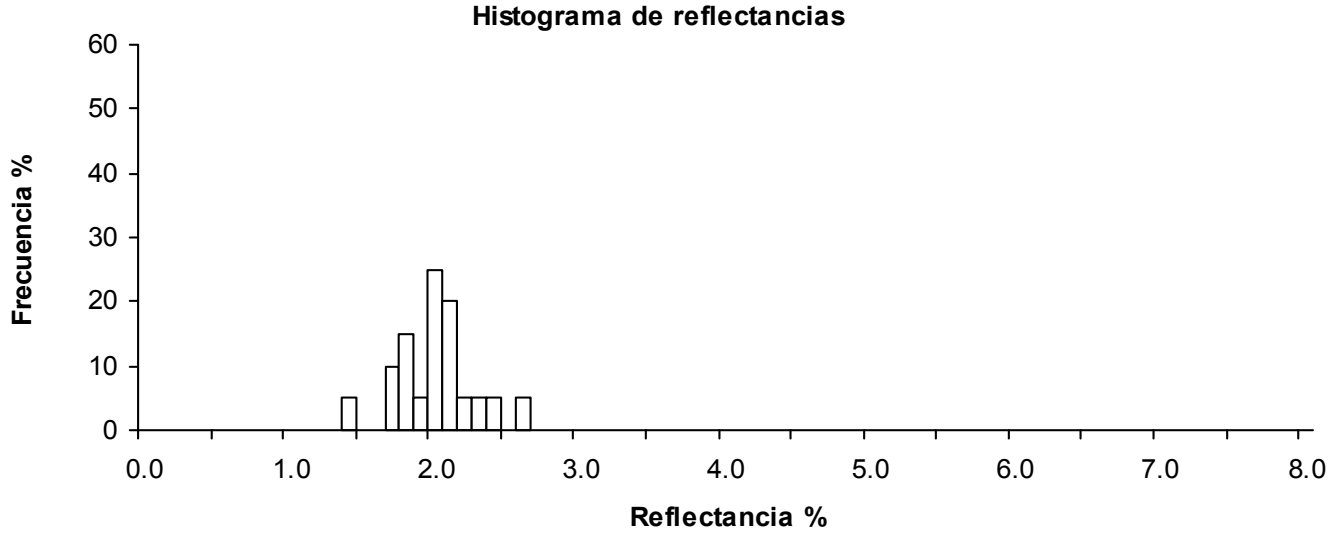

Analysis realized in: **MPV-1 Combi-Leitz**

Sample: **SOH-1b**
Objective: **50x**
Pattern: **274**

Singular Reflectances:

1.94	2.11	2.14	2.41	1.91
1.94	2.21	1.74	1.94	1.88

Class	n	n%	Sn	Sn%
1.7	1	10.00	1	10.00
1.8	1	10.00	2	20.00
1.9	4	40.00	6	60.00
2.1	2	20.00	8	80.00
2.2	1	10.00	9	90.00
2.4	1	10.00	10	100.00

Re = 2.02 **s = 0.19** **R< = 1.77** **R> = 2.37** **N = 10** **MVR = 13.0**

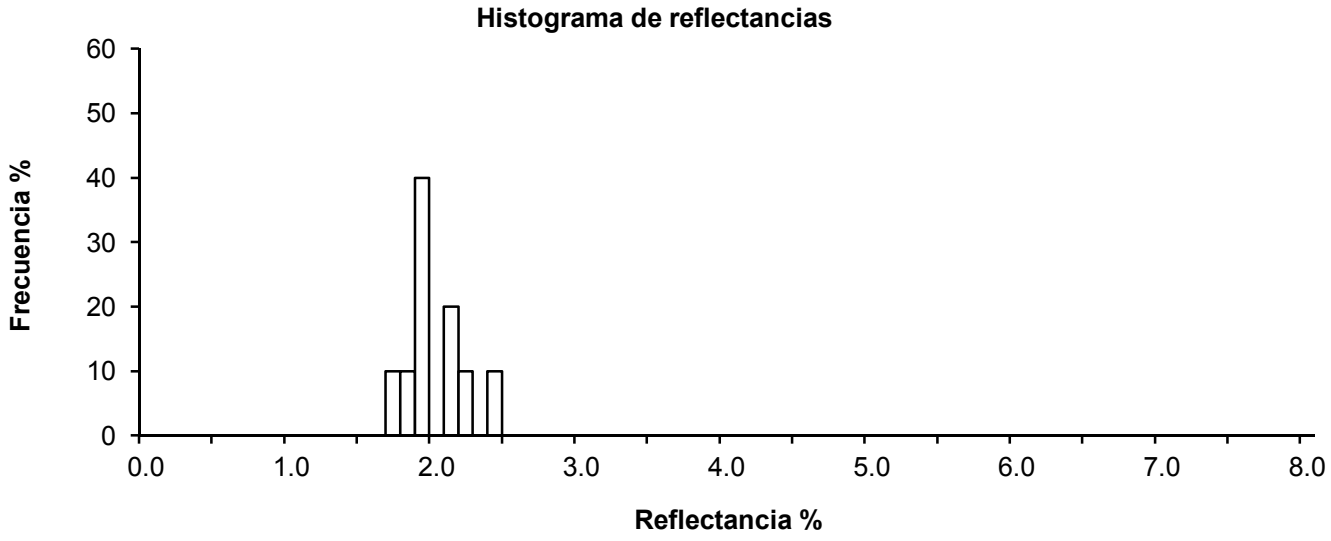

Analysis realized in: **MPV-1 Combi-Leitz**

Sample: SOH-1
Objective: 50x
Pattern: 274

Singular Reflectances:

2.38	2.61	2.75	2.28	1.78
2.38	2.68	2.04	2.35	2.18
2.71	2.75	2.28	2.28	2.61
2.51				

Class	n	n%	Sn	Sn%
1.7	1	6.25	1	6.25
2.0	1	6.25	2	12.50
2.1	1	6.25	3	18.75
2.2	3	18.75	6	37.50
2.3	3	18.75	9	56.25
2.5	1	6.25	10	62.50
2.6	3	18.75	13	81.25
2.7	3	18.75	16	100.00

Re = 2.41 **s = 0.28** **R< = 1.88** **R> = 2.75** **N = 16** **MVR = 10.6**

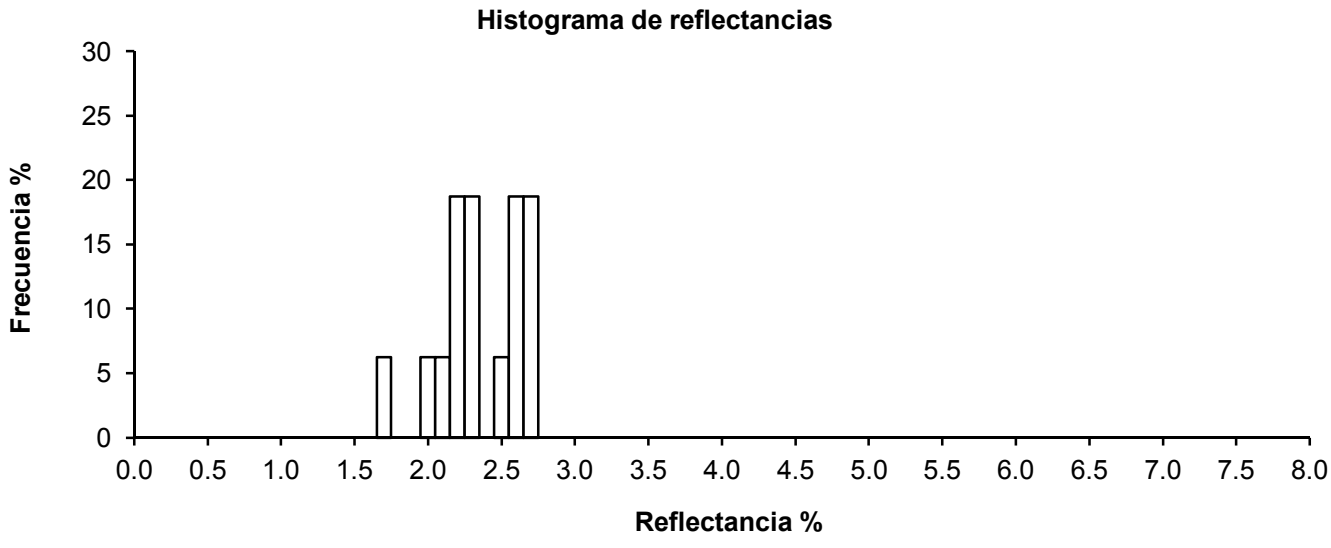

Analysis realized in: **MPV-1 Combi-Leitz**

Sample: **SOO-1**
Objective: **50x**
Pattern: **274**

Singular Reflectances:

1.53	1.56	1.62	1.62	1.74
1.76	1.80	1.83	1.89	1.89
1.92	1.94	1.94	2.10	2.12
2.23	2.25	2.39	2.41	2.64
2.80	2.86	2.91		

Class	n	n%	Sn	Sn%
1.5	2	8.70	2	8.70
1.6	2	8.70	4	17.39
1.7	2	8.70	6	26.09
1.8	4	17.39	10	43.48
1.9	3	13.04	13	56.52
2.1	2	8.70	15	65.22
2.2	2	8.70	17	73.91
2.3	1	4.35	18	78.26
2.4	1	4.35	19	82.61
2.6	1	4.35	20	86.96
2.8	2	8.70	22	95.65
2.9	1	4.35	23	100.00

Re = 2.08 **s = 0.42** **R< = 1.55** **R> = 2.88** **N = 23** **MVR = 13.1**

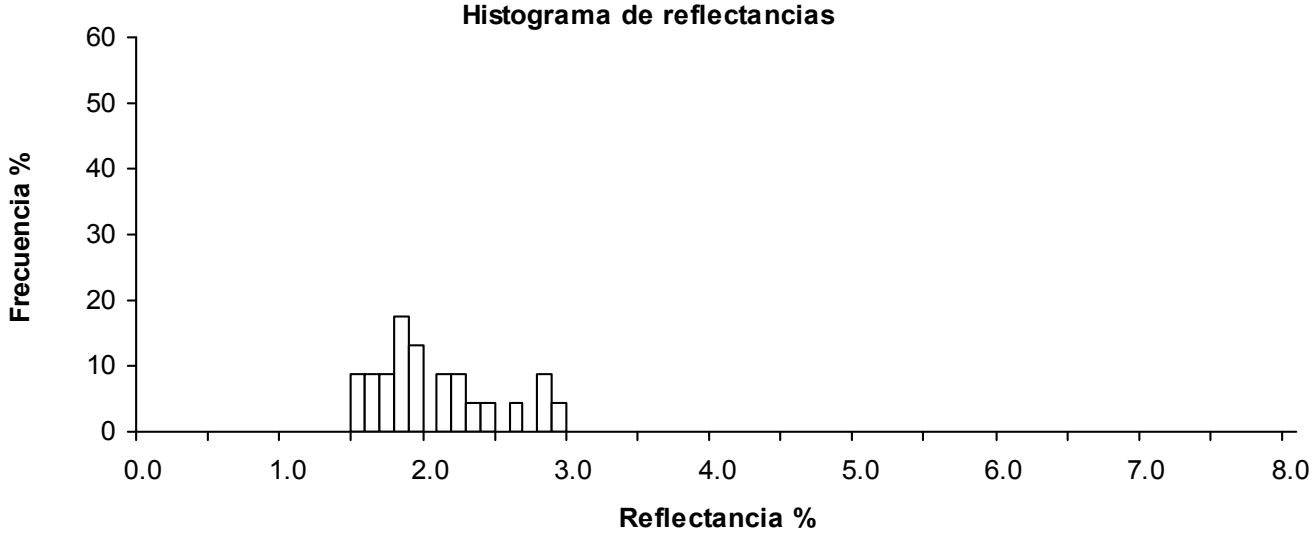

Analysis realized in: **MPV-1 Combi-Leitz**

Sample: SHDL-1
Objective: 50x
Pattern: 274

Singular Reflectances:

2.65	2.77	2.85	2.93	2.93
3.02	3.02	3.06	3.06	3.10
3.14	3.18	3.18	3.18	3.22
3.27	3.31	3.31	3.31	3.39
3.39	3.39	3.43	3.43	3.43
3.43	3.47	3.47	3.51	3.55
3.68	3.68	3.68	3.68	3.72

Class	n	n%	Sn	Sn%
2.6	1	2.86	1	2.86
2.7	1	2.86	2	5.71
2.8	1	2.86	3	8.57
2.9	2	5.71	5	14.29
3.0	4	11.43	9	25.71
3.1	5	14.29	14	40.00
3.2	2	5.71	16	45.71
3.3	6	17.14	22	62.86
3.4	6	17.14	28	80.00
3.5	2	5.71	30	85.71
3.6	4	11.43	34	97.14
3.7	1	2.86	35	100.00

Re = 3.28 **s = 0.27** **R< = 2.75** **R> = 3.68** **N = 35** **MVR = 7.0**

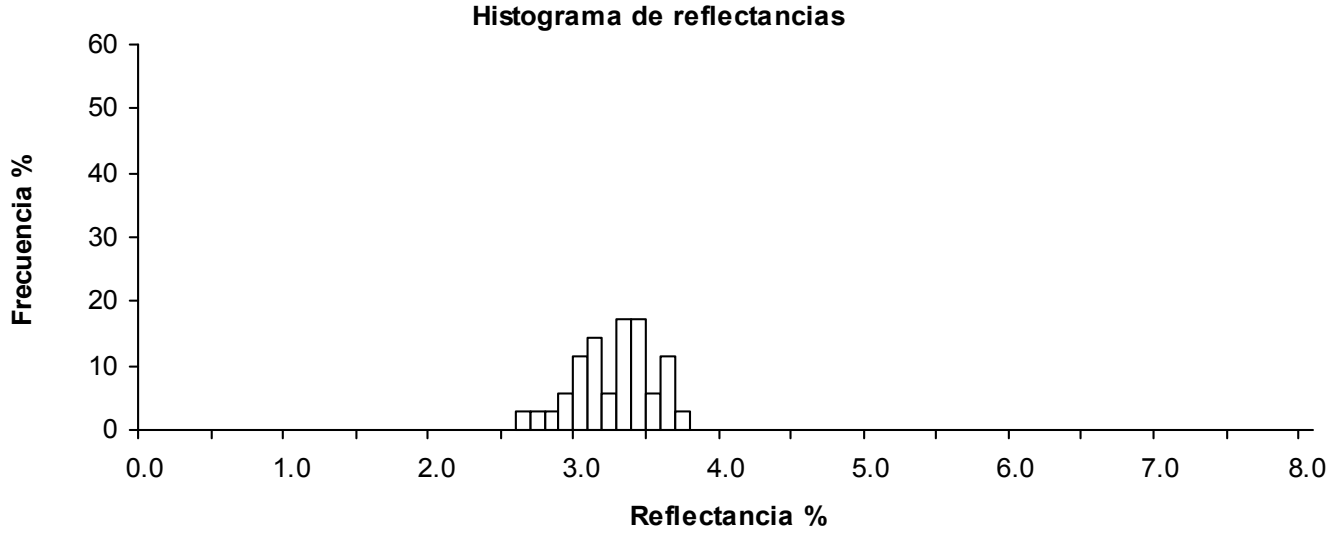

Analysis realized in: **MPV-1 Combi-Leitz**

Sample: SPO-2
Objective: 50x
Pattern: 274

Singular Reflectances:

3.37	3.50	3.85	3.85	3.88
3.91	3.94	3.94	4.01	4.07
4.10	4.13	4.13	4.13	4.15
4.20	4.20	4.26	4.26	4.29
4.34	4.36	4.36	4.37	4.42
4.45	4.48	4.55	4.61	4.61
4.63	4.64	4.67	4.67	4.74
4.77	4.81	4.86	5.09	5.15
5.18	5.29	5.34	5.37	5.41
5.82				

Class	n	n%	Sn	Sn%
3.3	1	2.17	1	2.17
3.5	1	2.17	2	4.35
3.8	3	6.52	5	10.87
3.9	3	6.52	8	17.39
4.0	2	4.35	10	21.74
4.1	5	10.87	15	32.61
4.2	5	10.87	20	43.48
4.3	4	8.70	24	52.17
4.4	3	6.52	27	58.70
4.5	1	2.17	28	60.87
4.6	6	13.04	34	73.91
4.7	2	4.35	36	78.26
4.8	2	4.35	38	82.61
5.0	1	2.17	39	84.78
5.1	2	4.35	41	89.13
5.2	1	2.17	42	91.30
5.3	2	4.35	44	95.65
5.4	1	2.17	45	97.83
5.8	1	2.17	46	100.00

Re = 4.46 **s = 0.52** **R< = 3.54** **R> = 5.40** **N = 46** **MVR = 4.4**

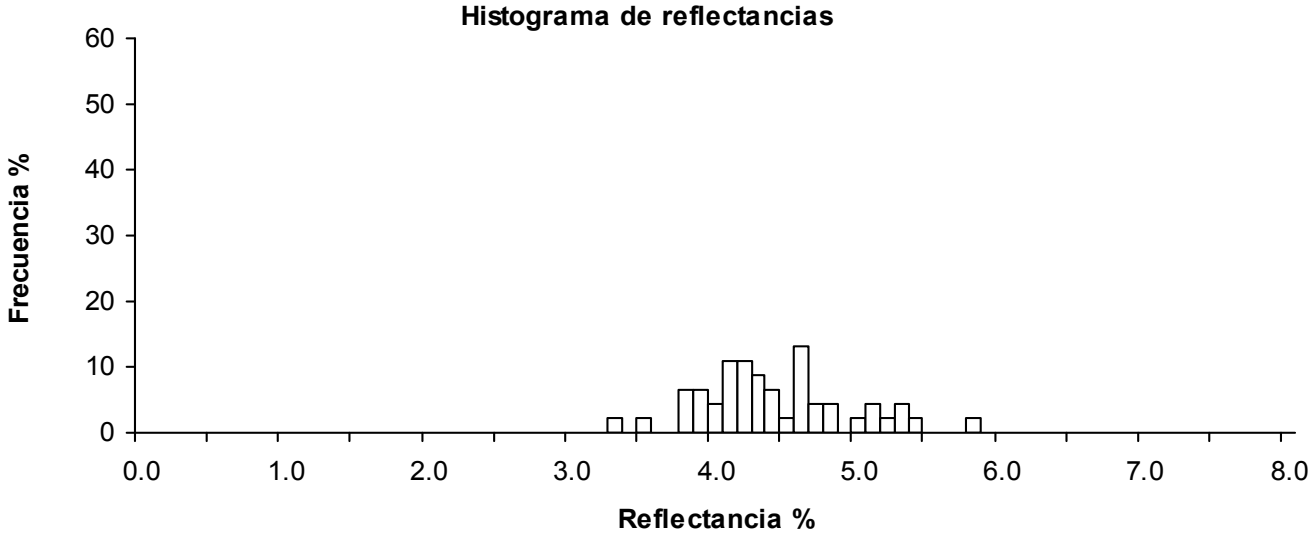

Analysis realized in: **MPV-1 Combi-Leitz**

Sample: **TORMO-1**
Objective: **50x**
Pattern: **274**

Singular Reflectances:

4.11	4.07	3.66	3.01	4.01

Class	n	n%	Sn	Sn%
3.0	1	20.00	1	20.00
3.6	1	20.00	2	40.00
4.0	2	40.00	4	80.00
4.1	1	20.00	5	100.00

Re = 3.77 **s = 0.46** **R< = 3.07** **R> = 4.11** **N = 5** **MVR = 5.7**

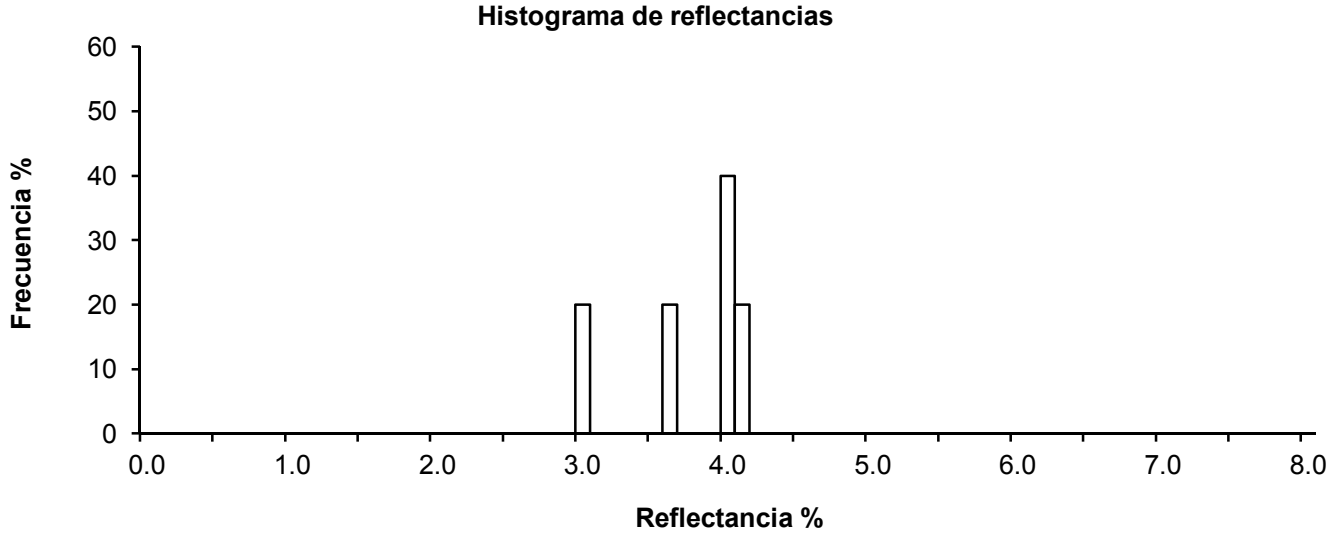

Analysis realized in: **MPV-1 Combi-Leitz**

Sample: **TORMO-2**
Objective: **50x**
Pattern: **274**

Singular Reflectances:

4.19	4.56	4.39	4.22	4.49
5.03	4.69	3.72	4.39	6.07
4.39	4.39	4.59	4.62	4.49
4.32	5.23	4.79	4.42	4.66

Class	n	n%	Sn	Sn%
3.7	1	5.00	1	5.00
4.1	1	5.00	2	10.00
4.2	1	5.00	3	15.00
4.3	5	25.00	8	40.00
4.4	3	15.00	11	55.00
4.5	2	10.00	13	65.00
4.6	3	15.00	16	80.00
4.7	1	5.00	17	85.00
5.0	1	5.00	18	90.00
5.2	1	5.00	19	95.00
6.0	1	5.00	20	100.00

Re = 4.58 **s = 0.47** **R< = 3.94** **R> = 5.67** **N = 20** **MVR = 4.1**

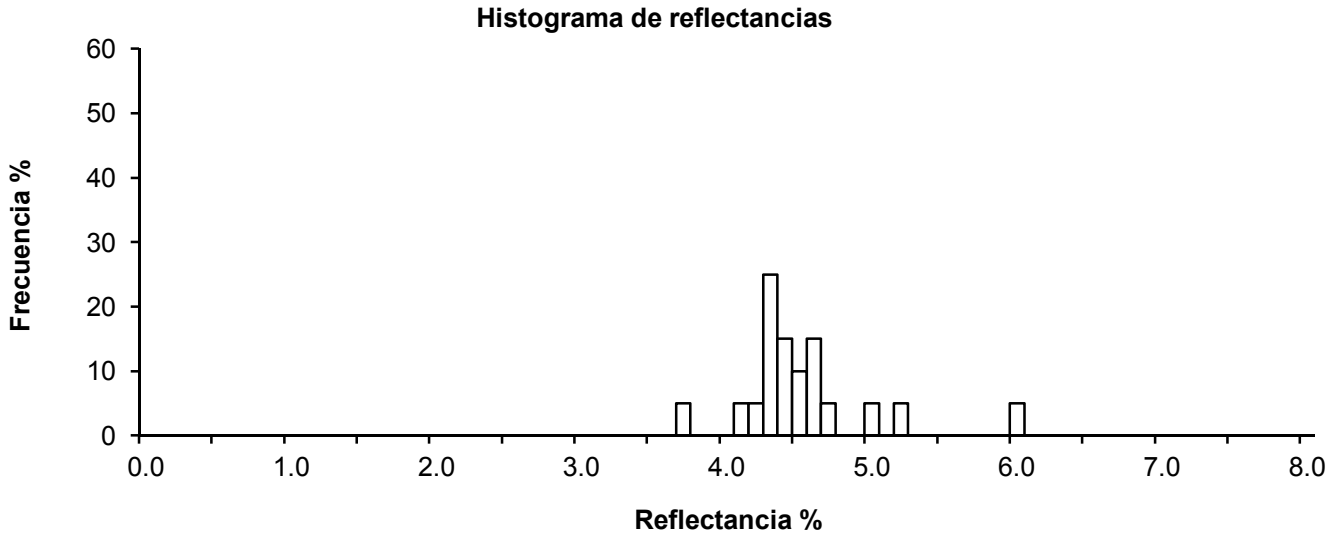

Analysis realized in: **MPV-1 Combi-Leitz**

Sample: SPOV-7
Objective: 50x
Pattern: 274

Singular Reflectances:

3.32	2.08	3.42	2.85	2.28
3.05	3.45	3.28	3.15	3.99
3.08	3.02	3.15	2.85	2.85
3.45	2.85	3.32	3.52	3.45
2.82				

Class	n	n%	Sn	Sn%
2.0	1	4.76	1	4.76
2.2	1	4.76	2	9.52
2.8	5	23.81	7	33.33
3.0	3	14.29	10	47.62
3.1	2	9.52	12	57.14
3.2	1	4.76	13	61.90
3.3	2	9.52	15	71.43
3.4	4	19.05	19	90.48
3.5	1	4.76	20	95.24
3.9	1	4.76	21	100.00

Re = 3.11 **s = 0.43** **R< = 2.18** **R> = 3.75** **N = 21** **MVR = 7.7**

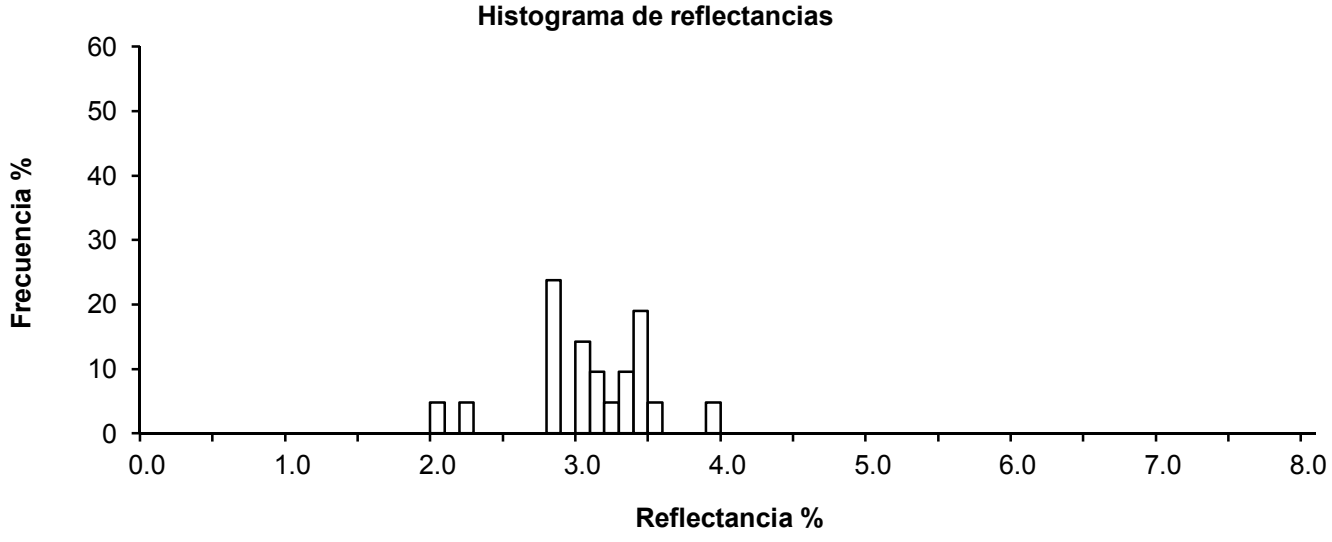

Analysis realized in: **MPV-1 Combi-Leitz**

Sample: **SPOV-5b**
Objective: **50x**
Pattern: **274**

Singular Reflectances:

2.17	2.93	2.17	2.62	2.45
1.96	2.76			

Class	n	n%	Sn	Sn%
1.9	1	14.29	1	14.29
2.1	2	28.57	3	42.86
2.4	1	14.29	4	57.14
2.6	1	14.29	5	71.43
2.7	1	14.29	6	85.71
2.9	1	14.29	7	100.00

Re = 2.44 **s = 0.35** **R< = 1.99** **R> = 2.90** **N = 7** **MVR = 10.5**

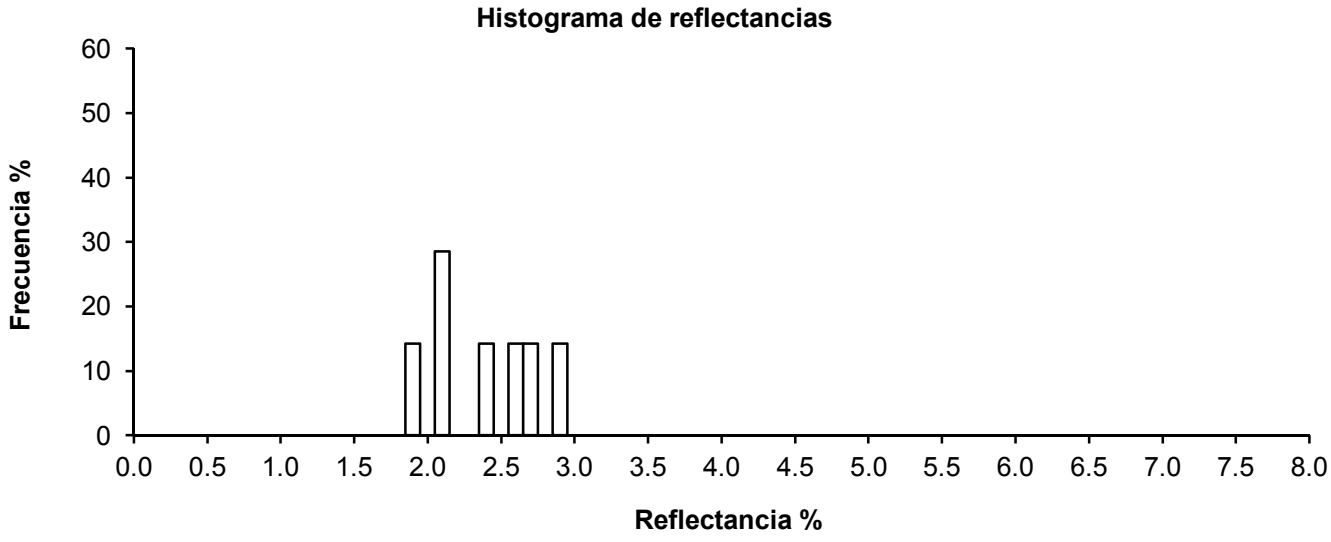

Analysis realized in: **MPV-1 Combi-Leitz**

Sample: **SPOV-5**
Objective: **50x**
Pattern: **274**

Singular Reflectances:

2.18	2.21	2.45	2.18	2.31
2.98	2.58	2.61	2.14	

Class	n	n%	Sn	Sn%
2.1	3	33.33	3	33.33
2.2	1	11.11	4	44.44
2.3	1	11.11	5	55.56
2.4	1	11.11	6	66.67
2.5	1	11.11	7	77.78
2.6	1	11.11	8	88.89
2.9	1	11.11	9	100.00

Re = 2.41 **s = 0.28** **R< = 2.15** **R> = 2.91** **N = 9** **MVR = 10.6**

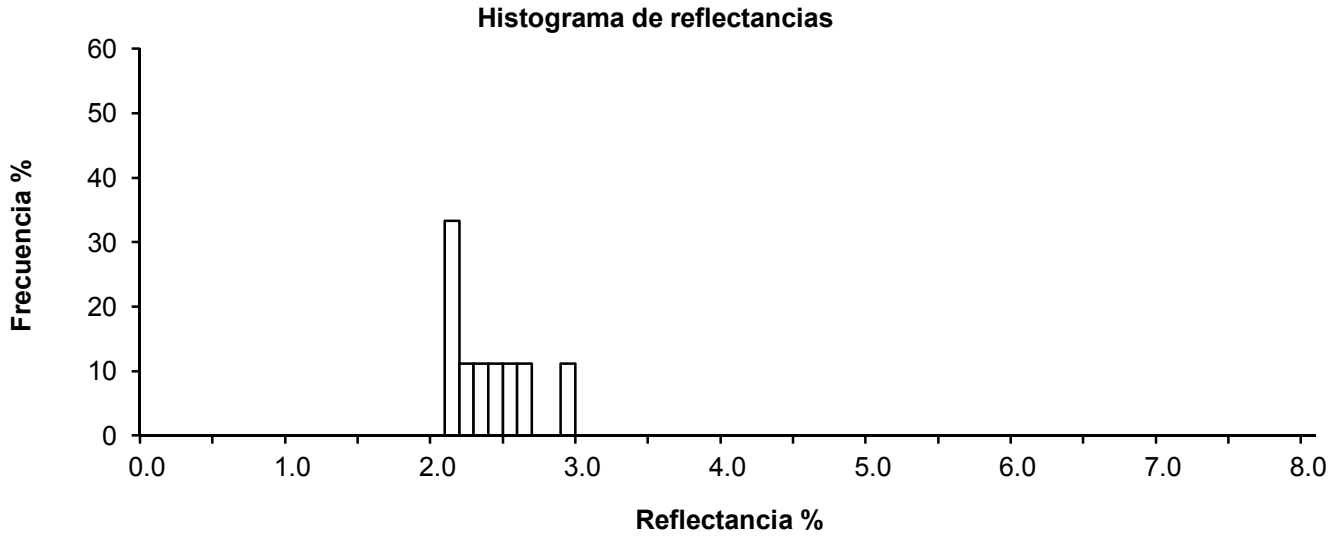

Analysis realized in: **MPV-1 Combi-Leitz**

Sample: SMO-3b
Objective: 50x
Pattern: 274

Singular Reflectances:

2.68	1.78	4.06	4.83	4.36
4.16	3.45	3.99	2.71	4.06
4.02	4.46	4.02	3.55	5.16
4.59				

Class	n	n%	Sn	Sn%
1.7	1	6.25	1	6.25
2.6	1	6.25	2	12.50
2.7	1	6.25	3	18.75
3.4	1	6.25	4	25.00
3.5	1	6.25	5	31.25
3.9	1	6.25	6	37.50
4.0	4	25.00	10	62.50
4.1	1	6.25	11	68.75
4.3	1	6.25	12	75.00
4.4	1	6.25	13	81.25
4.5	1	6.25	14	87.50
4.8	1	6.25	15	93.75
5.1	1	6.25	16	100.00

Re = 3.87 **s = 0.87** **R< = 2.12** **R> = 5.04** **N = 16** **MVR = 6.0**

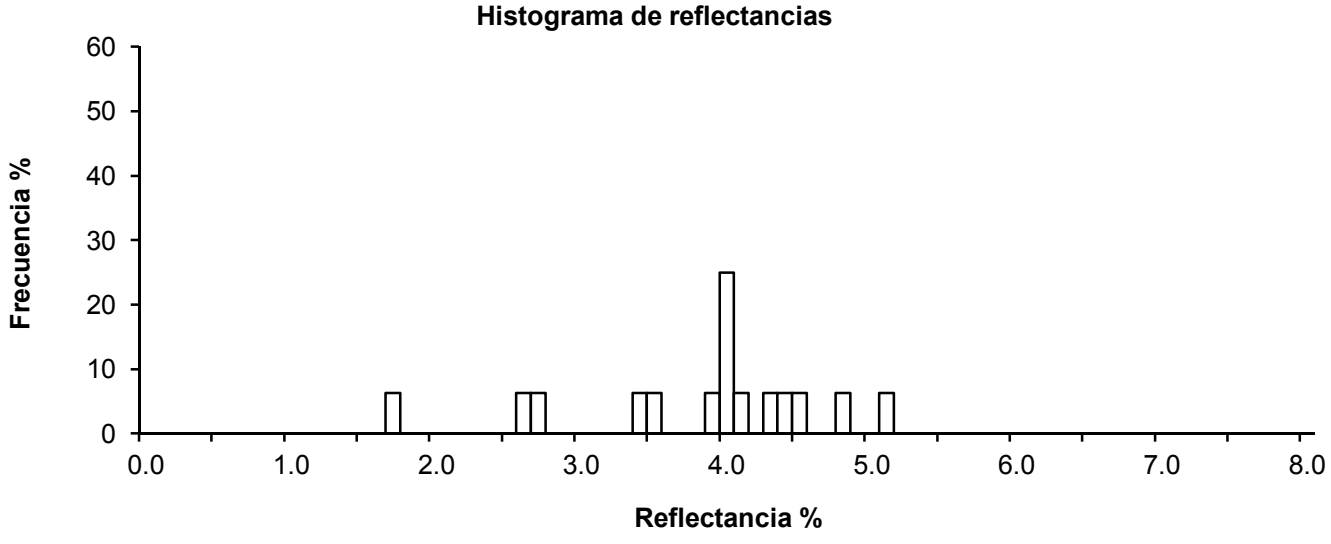

Analysis realized in: **MPV-1 Combi-Leitz**

Sample: **SMO-2b**
Objective: **50x**
Pattern: **274**

Singular Reflectances:

1.11	1.18	0.92	1.16	0.97
1.24	1.24	0.99	0.94	1.08
0.89	0.92	0.95	1.16	1.10
0.91	1.07	1.37	0.95	0.75
1.00	0.81	1.13	1.32	1.11
0.75				

Class	n	n%	Sn	Sn%
0.7	2	7.69	2	7.69
0.8	2	7.69	4	15.38
0.9	8	30.77	12	46.15
1.0	3	11.54	15	57.69
1.1	7	26.92	22	84.62
1.2	2	7.69	24	92.31
1.3	2	7.69	26	100.00

Re = 1.04 **s = 0.16** **R< = 0.75** **R> = 1.34** **N = 26** **MVR = 30.4**

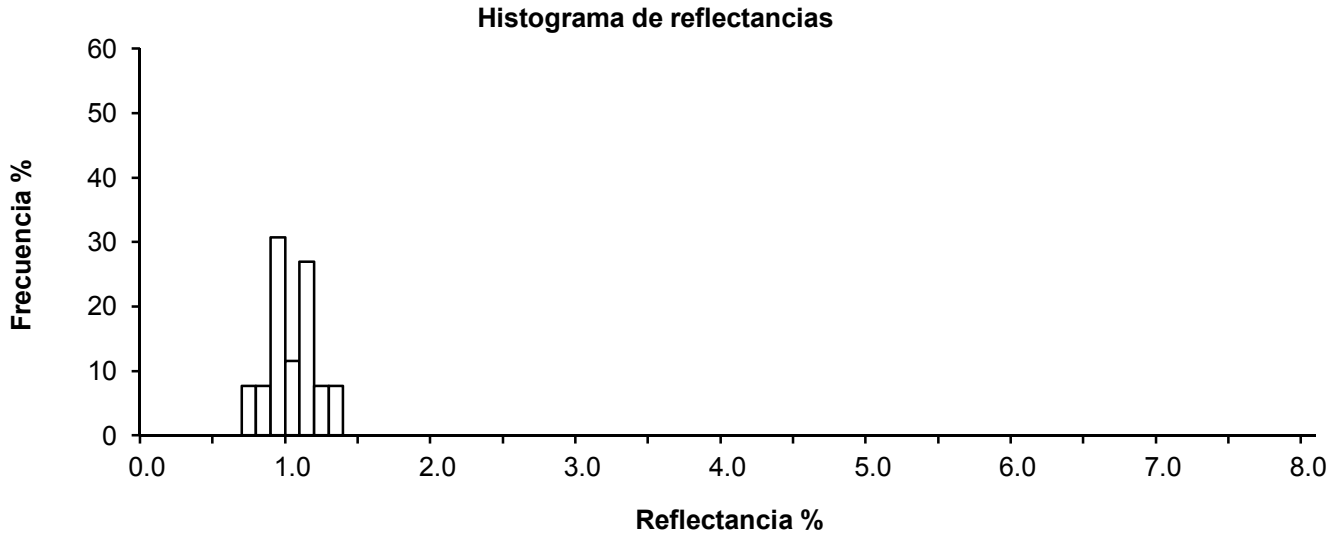

Analysis realized in: **MPV-1 Combi-Leitz**

Sample: **SMO-2**
Objective: **50x**
Pattern: **274**

Singular Reflectances:

3.41	4.01	3.89	3.36	4.08
4.16	2.25	3.16	3.56	3.79

Class	n	n%	Sn	Sn%
2.2	1	10.00	1	10.00
3.1	1	10.00	2	20.00
3.3	1	10.00	3	30.00
3.4	1	10.00	4	40.00
3.5	1	10.00	5	50.00
3.7	1	10.00	6	60.00
3.8	1	10.00	7	70.00
4.0	2	20.00	9	90.00
4.1	1	10.00	10	100.00

Re = 3.57 **s = 0.57** **R< = 2.45** **R> = 4.14** **N = 10** **MVR = 6.4**

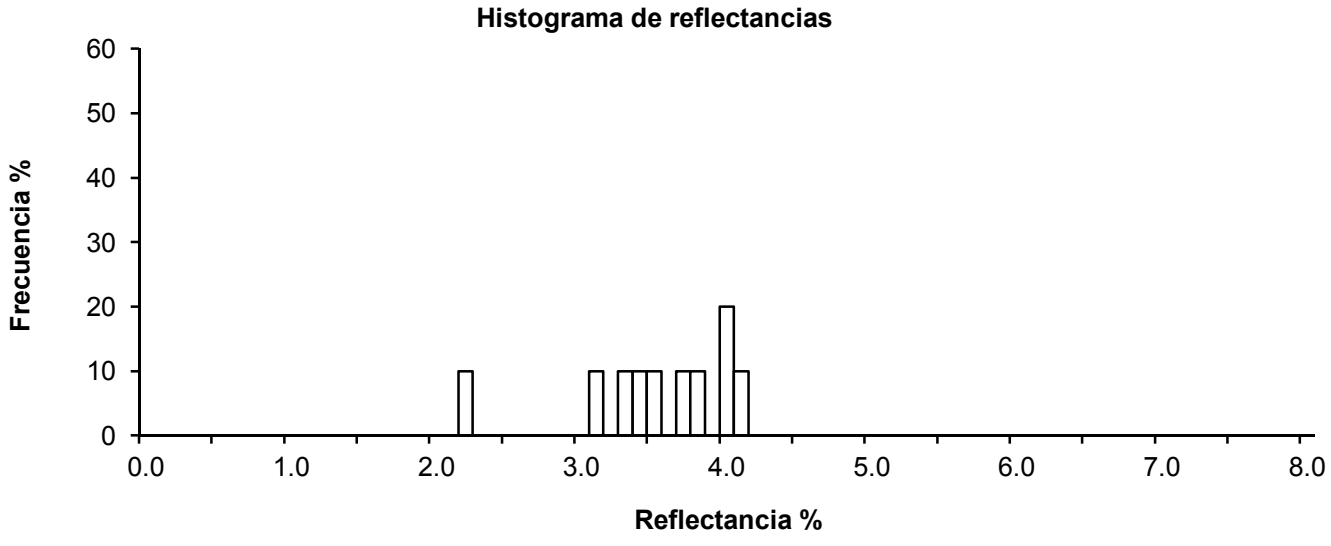

Analysis realized in: **MPV-1 Combi-Leitz**

Sample: SPO-1
Objective: 50x
Pattern: 274

Singular Reflectances:

3.18 3.60 3.75

Class	n	n%	Sn	Sn%
3.1	1	33.33	1	33.33
3.6	1	33.33	2	66.67
3.7	1	33.33	3	100.00

Re = 3.51 **s = 0.30** **R< = 3.20** **R> = 3.74** **N = 3** **MVR = 6.4**

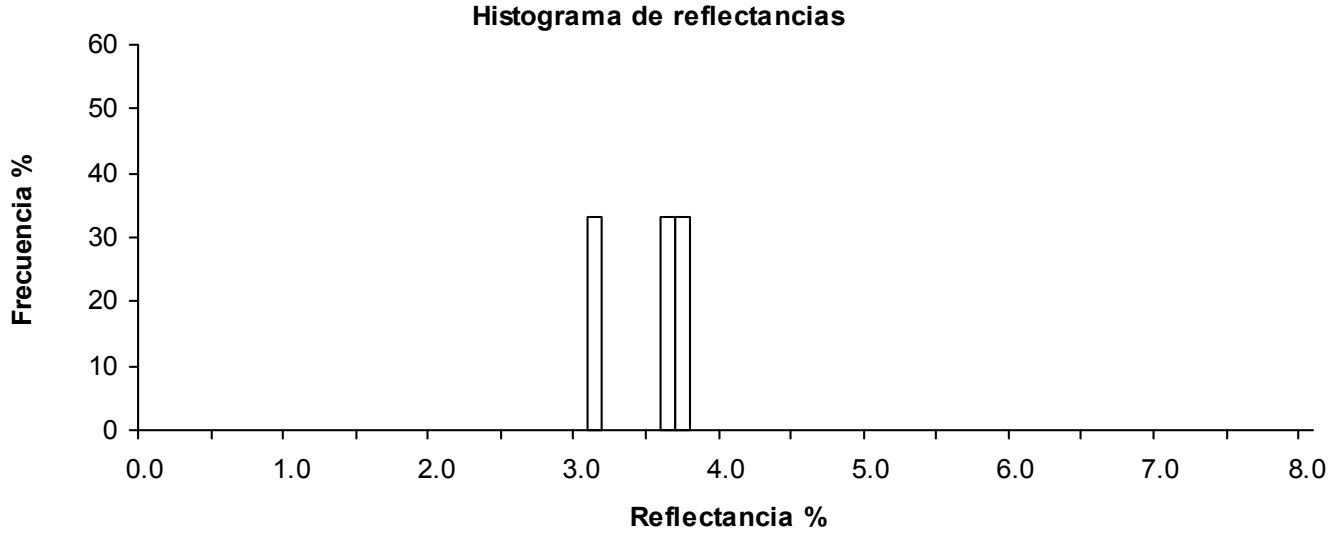

Analysis realized in: **MPV-1 Combi-Leitz**

Sample: SCL-1
Objective: 50x
Pattern: 274

Singular Reflectances:

1.37	1.88	2.26	2.29	2.35
2.48	2.61	2.61	2.64	2.64
2.73	2.77	3.05	3.15	3.16
3.18	3.24	3.27	3.27	3.32
3.46	3.56	3.56	3.70	3.78
3.78	3.97			

Class	n	n%	Sn	Sn%
1.3	1	3.70	1	3.70
1.8	1	3.70	2	7.41
2.2	2	7.41	4	14.81
2.3	1	3.70	5	18.52
2.4	1	3.70	6	22.22
2.6	4	14.81	10	37.04
2.7	2	7.41	12	44.44
3.0	1	3.70	13	48.15
3.1	3	11.11	16	59.26
3.2	3	11.11	19	70.37
3.3	1	3.70	20	74.07
3.4	1	3.70	21	77.78
3.5	2	7.41	23	85.19
3.7	3	11.11	26	96.30
3.9	1	3.70	27	100.00

Re = 2.97 **s = 0.63** **R< = 1.70** **R> = 3.85** **N = 27** **MVR = 8.6**

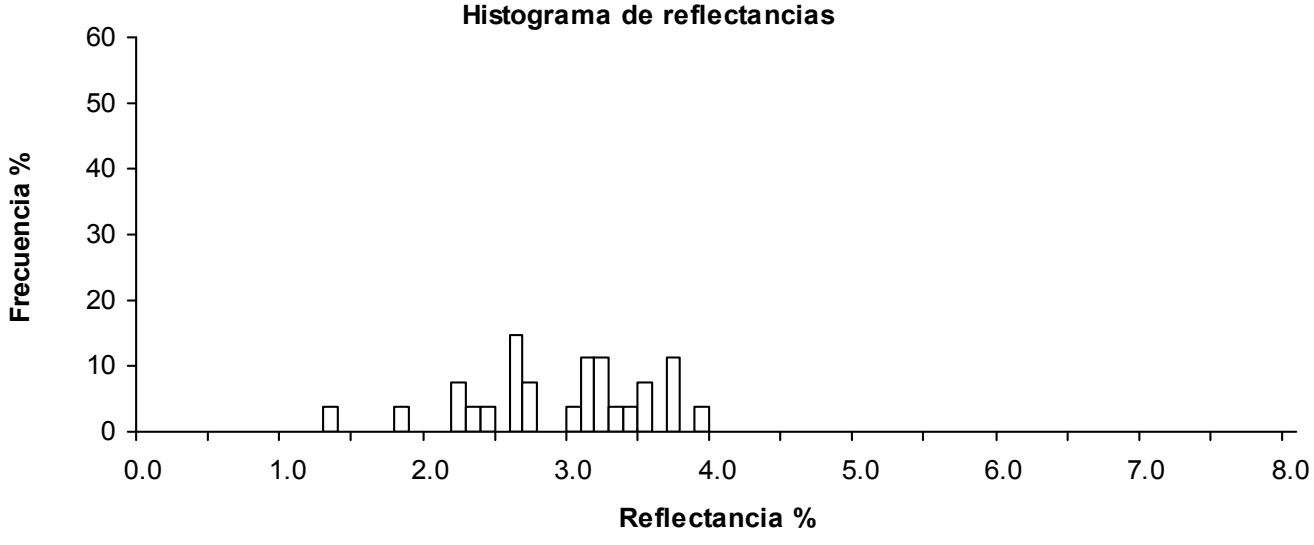

Analysis realized in: **MPV-1 Combi-Leitz**

Sample: **SCL-2**
Objective: **50x**
Pattern: **274**

Singular Reflectances:
2.17 2.20

Class	n	n%	Sn	Sn%
2.1	1	50.00	1	50.00
2.2	1	50.00	2	100.00

Re = 2.19 **s = 0.02** **R< = 2.17** **R> = 2.20** **N = 2** **MVR = 11.7**

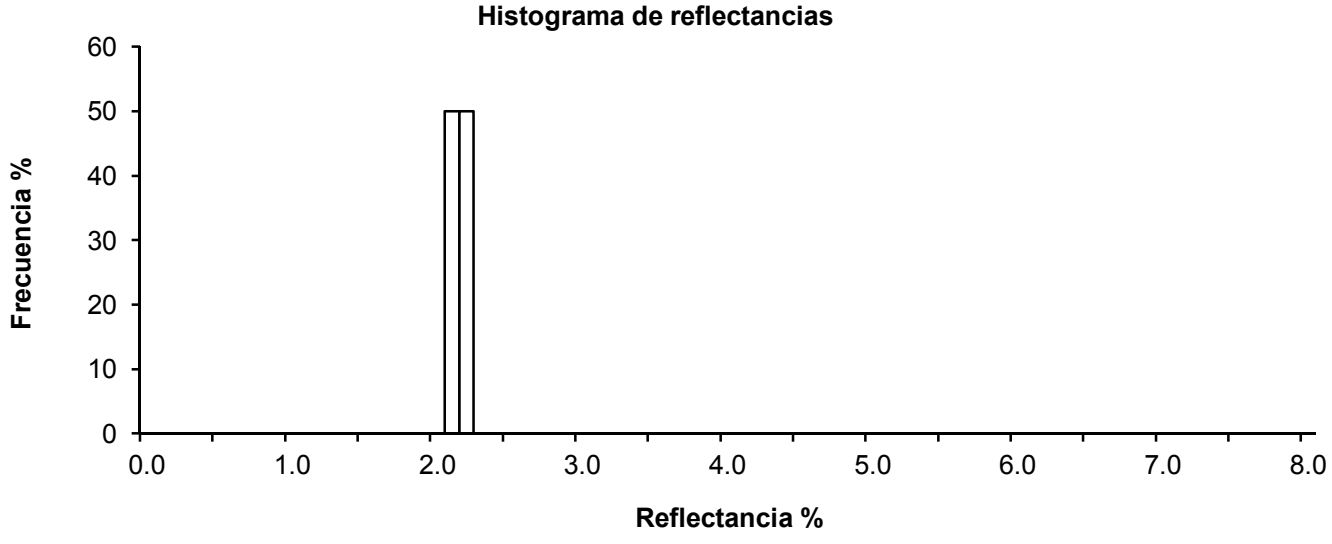

Analysis realized in: **MPV-1 Combi-Leitz**

Sample: SPOV-3t
Objective: 50x
Pattern: 274

Singular Reflectances:

2.04	2.16	2.74	3.51	3.61
3.93	4.29	4.48	4.51	5.17

Class	n	n%	Sn	Sn%
2.0	1	10.00	1	10.00
2.1	1	10.00	2	20.00
2.7	1	10.00	3	30.00
3.5	1	10.00	4	40.00
3.6	1	10.00	5	50.00
3.9	1	10.00	6	60.00
4.2	1	10.00	7	70.00
4.4	1	10.00	8	80.00
4.5	1	10.00	9	90.00
5.1	1	10.00	10	100.00

Re = 3.64 **s = 1.05** **R< = 2.07** **R> = 5.02** **N = 10** **MVR = 6.7**

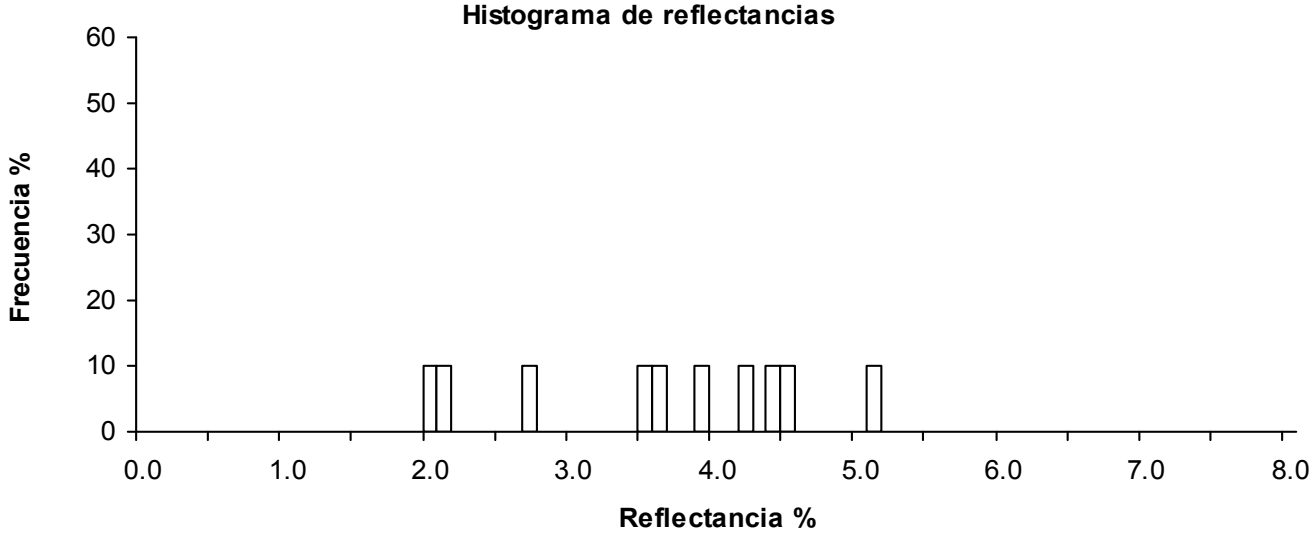

Analysis realized in: **MPV-1 Combi-Leitz**

Sample: **SPOV-3**
Objective: **50x**
Pattern: **274**

Singular Reflectances:

2.82	1.68	1.61	2.48	2.82
1.31	2.04	1.78	2.85	1.78
2.41	2.55	1.74	1.27	1.31
1.91	1.58			

Class	n	n%	Sn	Sn%
1.2	1	5.88	1	5.88
1.3	2	11.76	3	17.65
1.5	1	5.88	4	23.53
1.6	2	11.76	6	35.29
1.7	3	17.65	9	52.94
1.9	1	5.88	10	58.82
2.0	1	5.88	11	64.71
2.4	2	11.76	13	76.47
2.5	1	5.88	14	82.35
2.8	3	17.65	17	100.00

Re = 2.00 **s = 0.55** **R< = 1.29** **R> = 2.84** **N = 17** **MVR = 14.6**

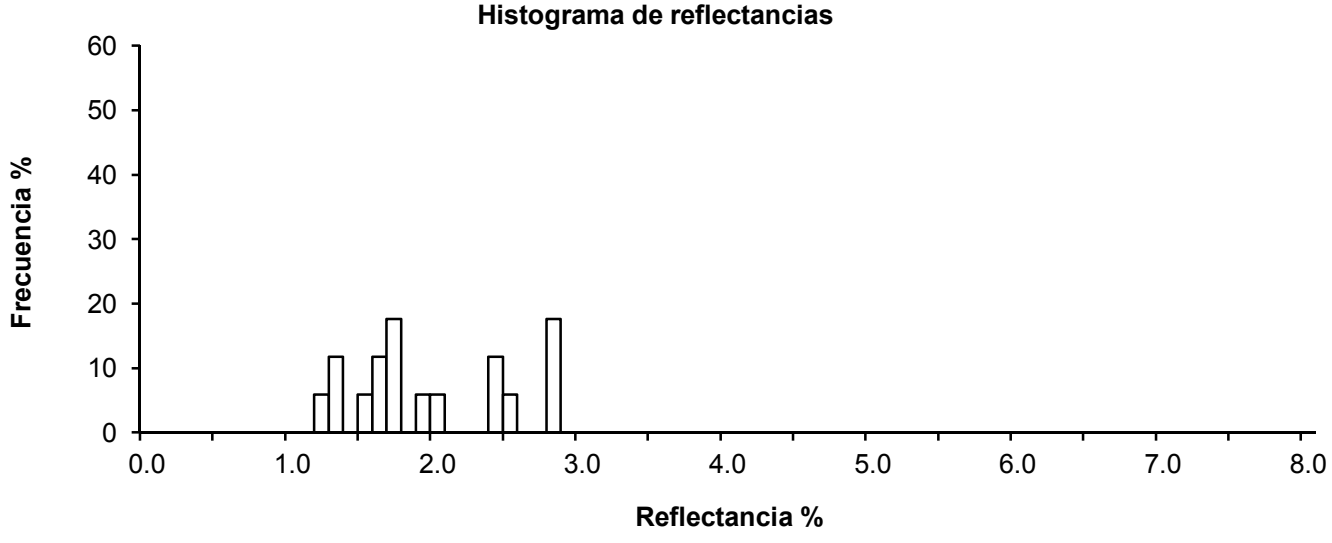

Analysis realized in: **MPV-1 Combi-Leitz**

Sample: **SPOV-2**
Objective: **50x**
Pattern: **274**

Singular Reflectances:

3.89	2.75	3.92	4.52	3.38
3.45	4.09	4.19	3.62	3.49
4.09	4.22	4.73	3.25	

Class	n	n%	Sn	Sn%
2.7	1	7.14	1	7.14
3.2	1	7.14	2	14.29
3.3	1	7.14	3	21.43
3.4	2	14.29	5	35.71
3.6	1	7.14	6	42.86
3.8	1	7.14	7	50.00
3.9	1	7.14	8	57.14
4.0	2	14.29	10	71.43
4.1	1	7.14	11	78.57
4.2	1	7.14	12	85.71
4.5	1	7.14	13	92.86
4.7	1	7.14	14	100.00

Re = 3.83 **s = 0.54** **R< = 2.91** **R> = 4.66** **N = 14** **MVR = 5.7**

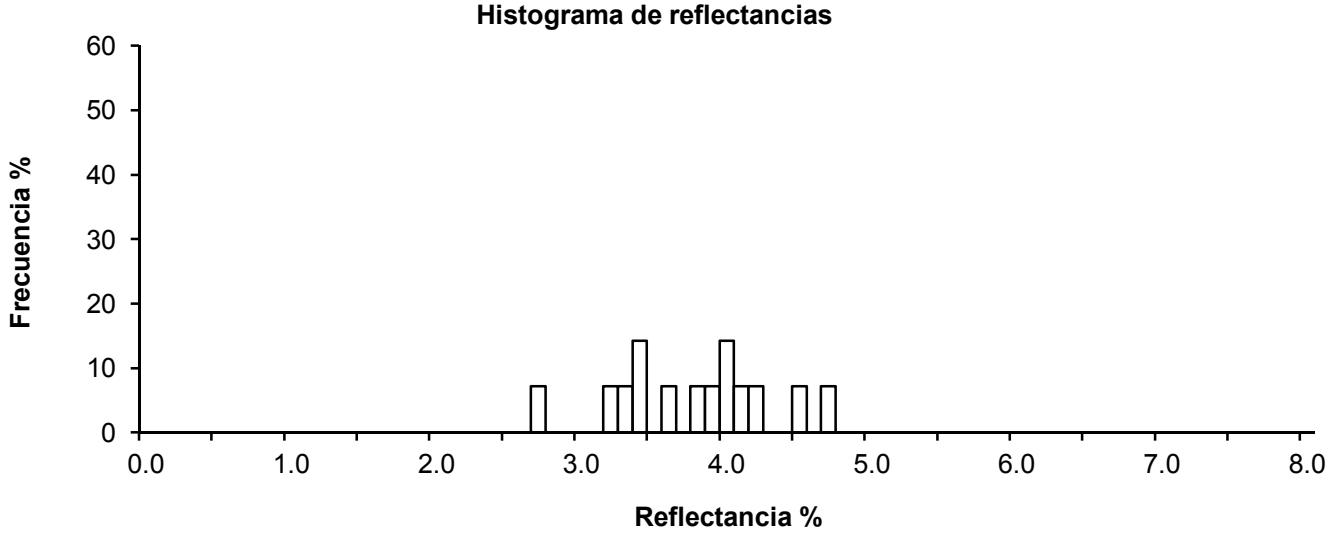

Analysis realized in: **MPV-1 Combi-Leitz**

Sample: SPOV-1
Objective: 50x
Pattern: 274

Singular Reflectances:

2.21	2.38	3.89	1.78	1.74
2.31	2.25	2.41	2.48	2.08
1.91	2.21	1.68	1.47	2.08
2.45	1.94	2.21		

Class	n	n%	Sn	Sn%
1.4	1	5.56	1	5.56
1.6	1	5.56	2	11.11
1.7	2	11.11	4	22.22
1.9	2	11.11	6	33.33
2.0	2	11.11	8	44.44
2.2	4	22.22	12	66.67
2.3	2	11.11	14	77.78
2.4	3	16.67	17	94.44
3.8	1	5.56	18	100.00

Re = 2.19 **s = 0.51** **R< = 1.56** **R> = 3.29** **N = 18** **MVR = 12.4**

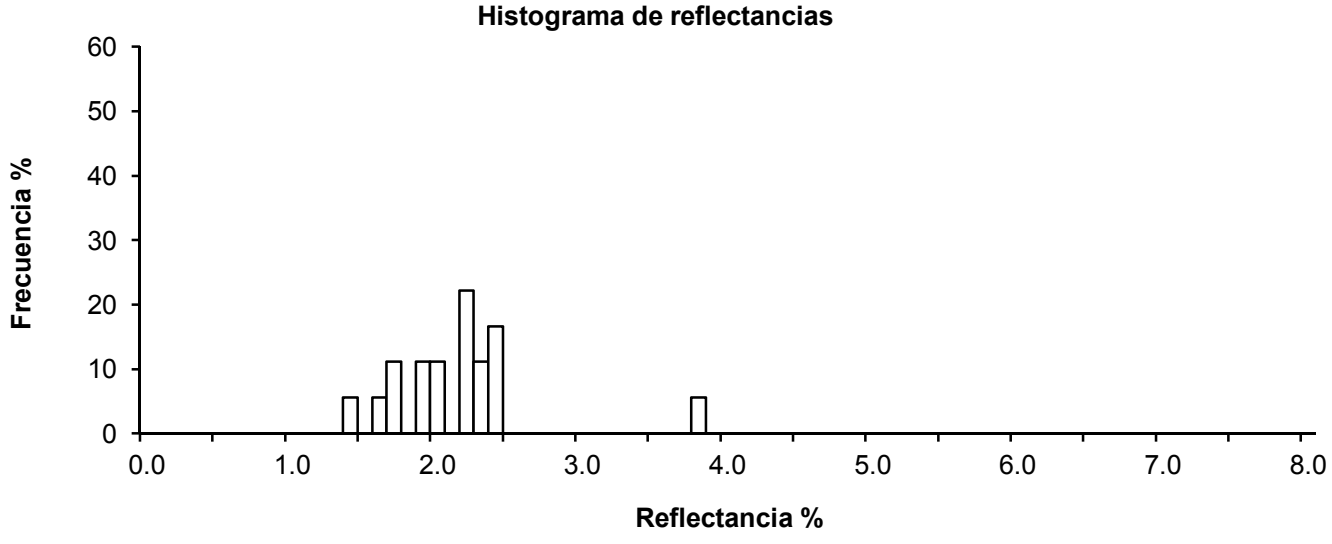

Analysis realized in: **MPV-1 Combi-Leitz**

Sample: **SMO-1**
Objective: **50x**
Pattern: **274**

Singular Reflectances:

2.89	2.00	2.50	2.58	2.69
2.81	1.29	2.07	3.03	2.05
2.17	3.79	1.88	2.77	2.46
2.60	2.34	1.88	2.74	3.62
2.62	2.58	2.53		

Class	n	n%	Sn	Sn%
1.2	1	4.35	1	4.35
1.8	2	8.70	3	13.04
2.0	3	13.04	6	26.09
2.1	1	4.35	7	30.43
2.3	1	4.35	8	34.78
2.4	1	4.35	9	39.13
2.5	4	17.39	13	56.52
2.6	3	13.04	16	69.57
2.7	2	8.70	18	78.26
2.8	2	8.70	20	86.96
3.0	1	4.35	21	91.30
3.6	1	4.35	22	95.65
3.7	1	4.35	23	100.00

Re = 2.52 **s = 0.55** **R< = 1.62** **R> = 3.70** **N = 23** **MVR = 10.7**

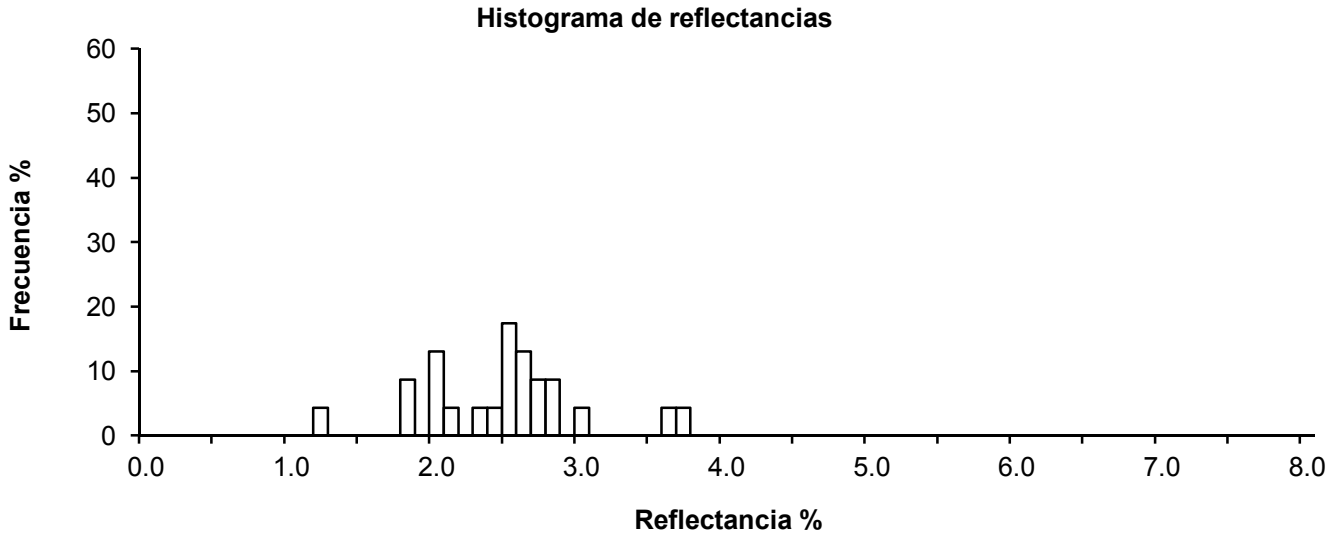

Analysis realized in: **MPV-1 Combi-Leitz**

Sample: **SMO-01**
Objective: **50x**
Pattern: **274**

Singular Reflectances:

3.38	3.72	3.59	3.42	3.34
2.99	3.12	3.16	3.42	2.99
3.46	3.46			

Class	n	n%	Sn	Sn%
2.9	2	16.67	2	16.67
3.1	2	16.67	4	33.33
3.3	2	16.67	6	50.00
3.4	4	33.33	10	83.33
3.5	1	8.33	11	91.67
3.7	1	8.33	12	100.00

Re = 3.34 **s = 0.23** **R< = 2.99** **R> = 3.68** **N = 12** **MVR = 6.8**

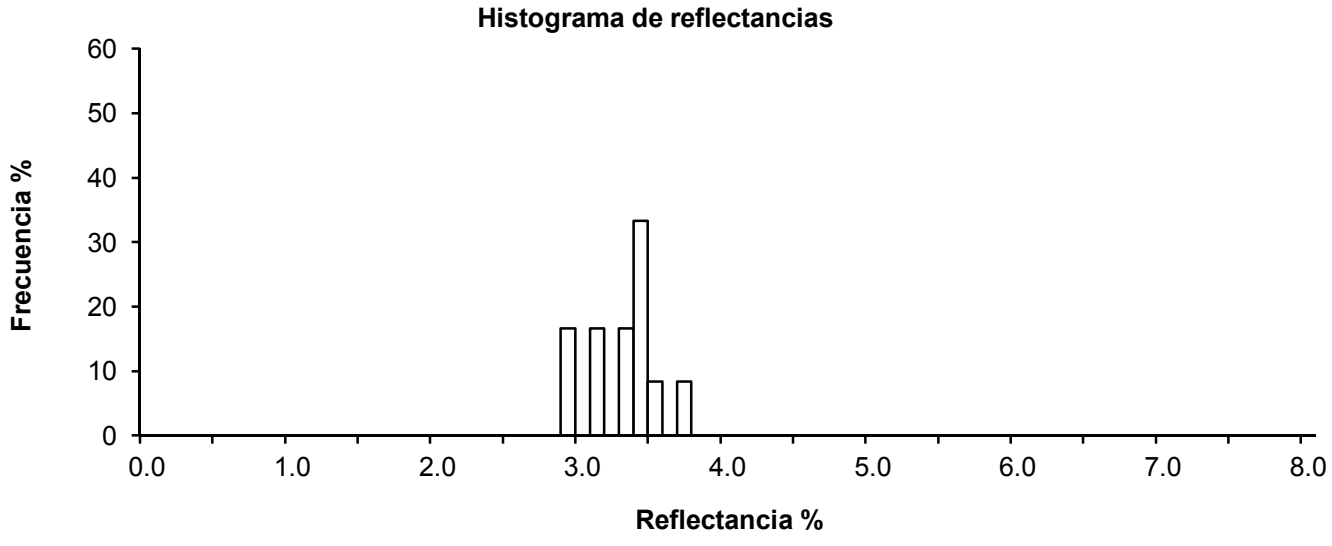

Analysis realized in: **MPV-1 Combi-Leitz**

Sample: **SMO-0**
Objective: **50x**
Pattern: **274**

Singular Reflectances:

3.74	5.01	4.69	4.43	4.52
4.84				

Class	n	n%	Sn	Sn%
3.7	1	16.67	1	16.67
4.4	1	16.67	2	33.33
4.5	1	16.67	3	50.00
4.6	1	16.67	4	66.67
4.8	1	16.67	5	83.33
5.0	1	16.67	6	100.00

Re = 4.54 **s = 0.44** **R< = 3.83** **R> = 4.99** **N = 6** **MVR = 4.2**

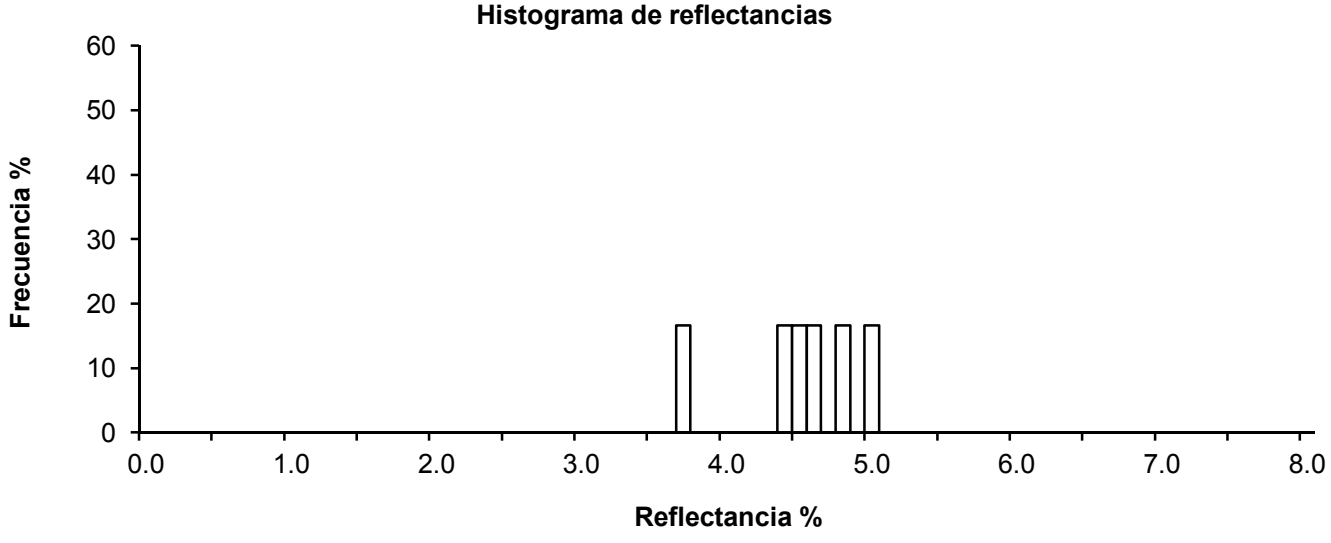

Analysis realized in: **MPV-1 Combi-Leitz**

Sample: SIC-1
Objective: 50x
Pattern: 274

Singular Reflectances:

1.54	2.40	2.63	3.01	3.34
3.38	3.57	3.61	3.64	3.64
3.95	4.02	4.06	4.10	4.21
4.21	4.25	4.25	4.28	4.36
4.51				

Class	n	n%	Sn	Sn%
1.5	1	4.76	1	4.76
2.4	1	4.76	2	9.52
2.6	1	4.76	3	14.29
3.0	1	4.76	4	19.05
3.3	2	9.52	6	28.57
3.5	1	4.76	7	33.33
3.6	3	14.29	10	47.62
3.9	1	4.76	11	52.38
4.0	2	9.52	13	61.90
4.1	1	4.76	14	66.67
4.2	5	23.81	19	90.48
4.3	1	4.76	20	95.24
4.5	1	4.76	21	100.00

Re = 3.66 **s = 0.75** **R< = 1.97** **R> = 4.43** **N = 21** **MVR = 6.4**

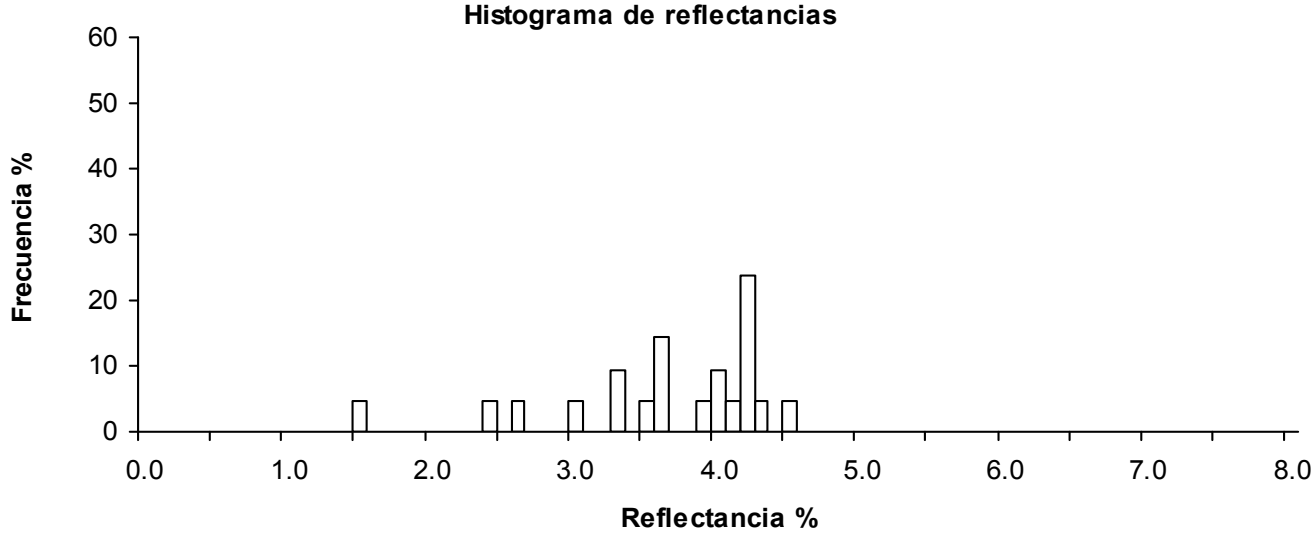

Analysis realized in: **MPV-1 Combi-Leitz**

Sample: SIC-2
Objective: 50x
Pattern: 274

Singular Reflectances:

3.31	3.46	3.51	3.53	3.61
3.61	3.66	3.76	3.83	3.85
3.89	3.93	3.96	4.04	4.08
4.08	4.08	4.08	4.08	4.10
4.13	4.15	4.17	4.19	4.19
4.21	4.21	4.21	4.23	4.23
4.25	4.28	4.34	4.40	4.40
4.43	4.43	4.45	4.51	4.60

Class	n	n%	Sn	Sn%
3.3	1	2.50	1	2.50
3.4	1	2.50	2	5.00
3.5	2	5.00	4	10.00
3.6	3	7.50	7	17.50
3.7	1	2.50	8	20.00
3.8	3	7.50	11	27.50
3.9	2	5.00	13	32.50
4.0	6	15.00	19	47.50
4.1	6	15.00	25	62.50
4.2	7	17.50	32	80.00
4.3	1	2.50	33	82.50
4.4	5	12.50	38	95.00
4.5	1	2.50	39	97.50
4.6	1	2.50	40	100.00

Re = 4.06 **s = 0.31** **R< = 3.46** **R> = 4.51** **N = 40** **MVR = 5.1**

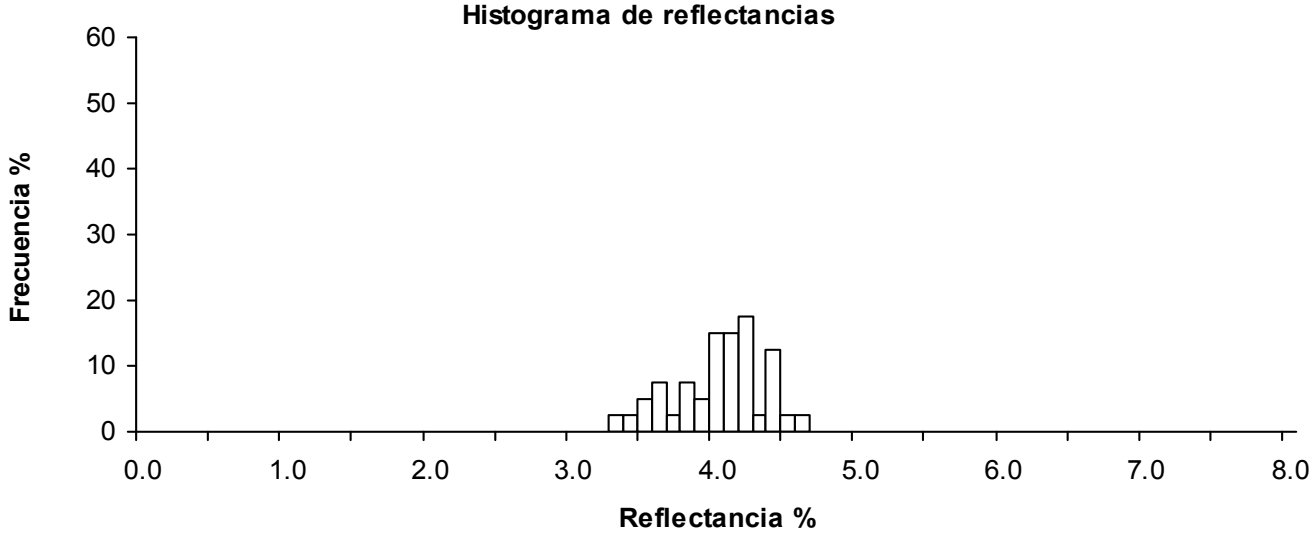

Analysis realized in: **MPV-1 Combi-Leitz**

Sample: SCGT-413
Objective: 50x
Pattern: 274

Singular Reflectances:

1.52	1.92	2.23	2.33	2.33
2.39	2.45	2.48	2.57	2.60
2.67	2.73	2.79	2.79	2.85
3.01				

Class	n	n%	Sn	Sn%
1.5	1	6.25	1	6.25
1.9	1	6.25	2	12.50
2.2	1	6.25	3	18.75
2.3	3	18.75	6	37.50
2.4	2	12.50	8	50.00
2.5	1	6.25	9	56.25
2.6	2	12.50	11	68.75
2.7	3	18.75	14	87.50
2.8	1	6.25	15	93.75
3.0	1	6.25	16	100.00

Re = 2.48 **s = 0.37** **R< = 1.67** **R> = 2.95** **N = 16** **MVR = 10.4**

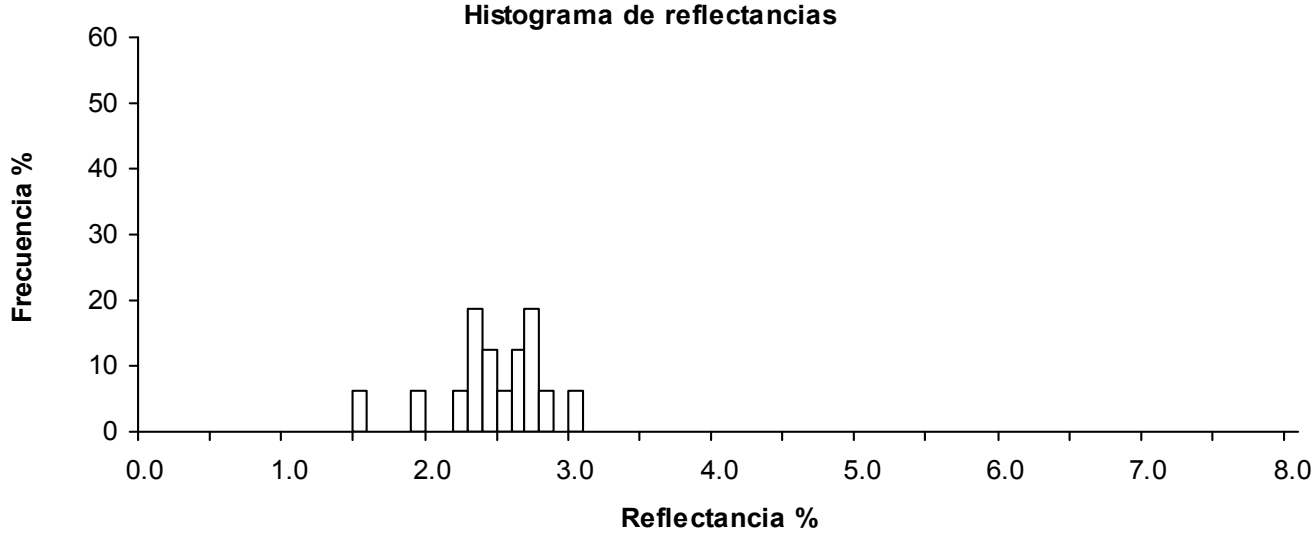

Analysis realized in: **MPV-1 Combi-Leitz**

Sample: CG-2
Objective: 50x
Pattern: 274

Singular Reflectances:

2.78	2.81	2.81	2.94	2.96
2.98	3.00	3.07	3.09	3.09
3.15	3.22	3.24	3.26	3.28
3.31	3.31	3.37	3.37	3.39

Class	n	n%	Sn	Sn%
2.7	1	5.00	1	5.00
2.8	2	10.00	3	15.00
2.9	3	15.00	6	30.00
3.0	4	20.00	10	50.00
3.1	1	5.00	11	55.00
3.2	4	20.00	15	75.00
3.3	5	25.00	20	100.00

Re = 3.12 **s = 0.20** **R< = 2.79** **R> = 3.38** **N = 20** **MVR = 7.5**

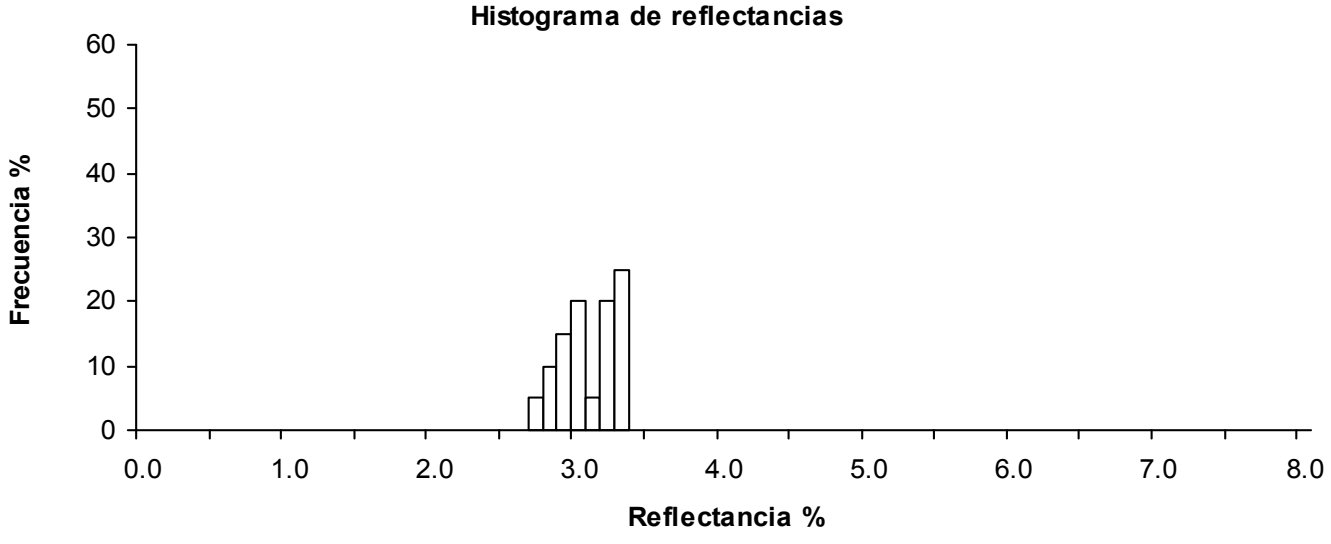

Analysis realized in: **MPV-1 Combi-Leitz**

Sample: CG-103
Objective: 50x
Pattern: 274

Singular Reflectances:

2.22	2.81	2.92	3.06	3.10
3.14	3.17	3.32	3.39	3.54
3.57	3.65	3.68		

Class	n	n%	Sn	Sn%
2.2	1	7.69	1	7.69
2.8	1	7.69	2	15.38
2.9	1	7.69	3	23.08
3.0	1	7.69	4	30.77
3.1	3	23.08	7	53.85
3.3	2	15.38	9	69.23
3.5	2	15.38	11	84.62
3.6	2	15.38	13	100.00

Re = 3.20 **s = 0.40** **R< = 2.40** **R> = 3.67** **N = 13** **MVR = 7.3**

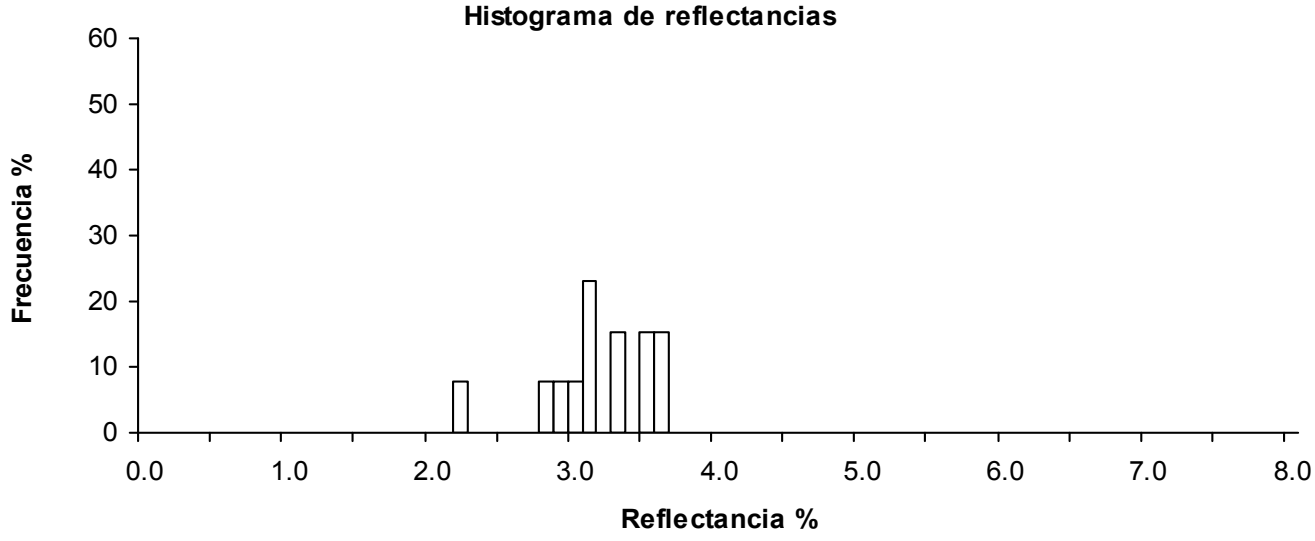

Analysis realized in: **MPV-1 Combi-Leitz**

Sample: FM-N2
Objective: 50x
Pattern: 274

Singular Reflectances:

2.94	2.64	2.91	3.10	3.42
3.15	3.32	3.37	3.48	2.45
2.94	2.78	3.37	3.05	3.37
2.94	2.40	2.24	2.80	

Class	n	n%	Sn	Sn%
2.2	1	5.26	1	5.26
2.4	2	10.53	3	15.79
2.6	1	5.26	4	21.05
2.7	1	5.26	5	26.32
2.8	1	5.26	6	31.58
2.9	4	21.05	10	52.63
3.0	1	5.26	11	57.89
3.1	2	10.53	13	68.42
3.3	4	21.05	17	89.47
3.4	2	10.53	19	100.00

Re = 2.98 **s = 0.37** **R< = 2.31** **R> = 3.45** **N = 19** **MVR = 8.0**

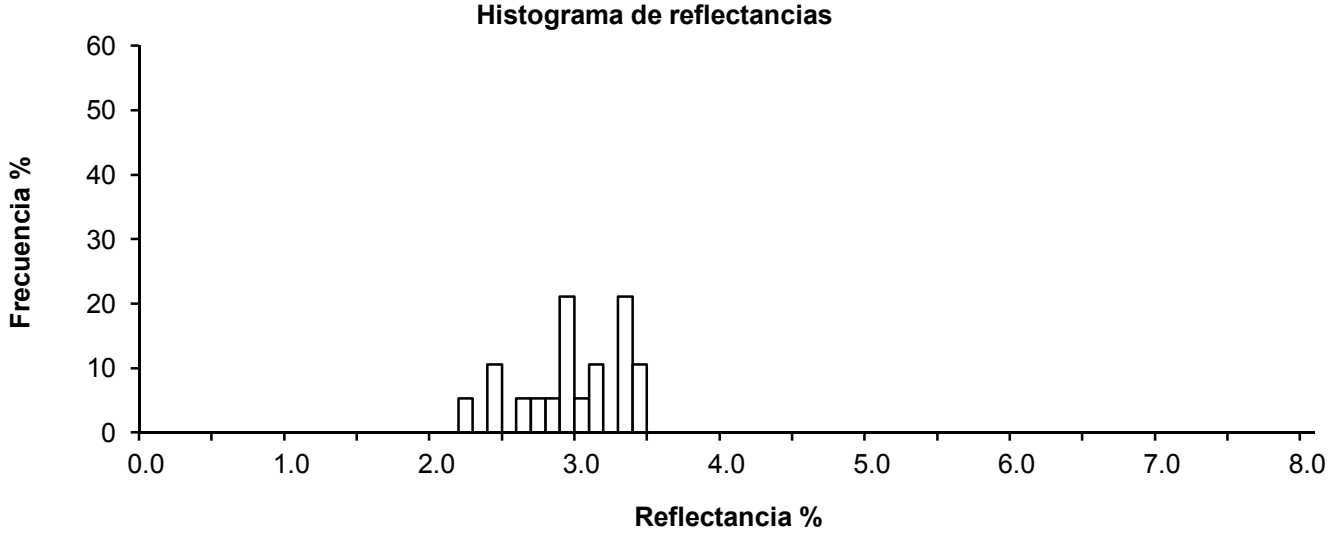

Appendix 4

Appendix 4

MICROSCOPE PHOTOGRAPHS OF THE ORGANIC MATTER OF THE BASIN

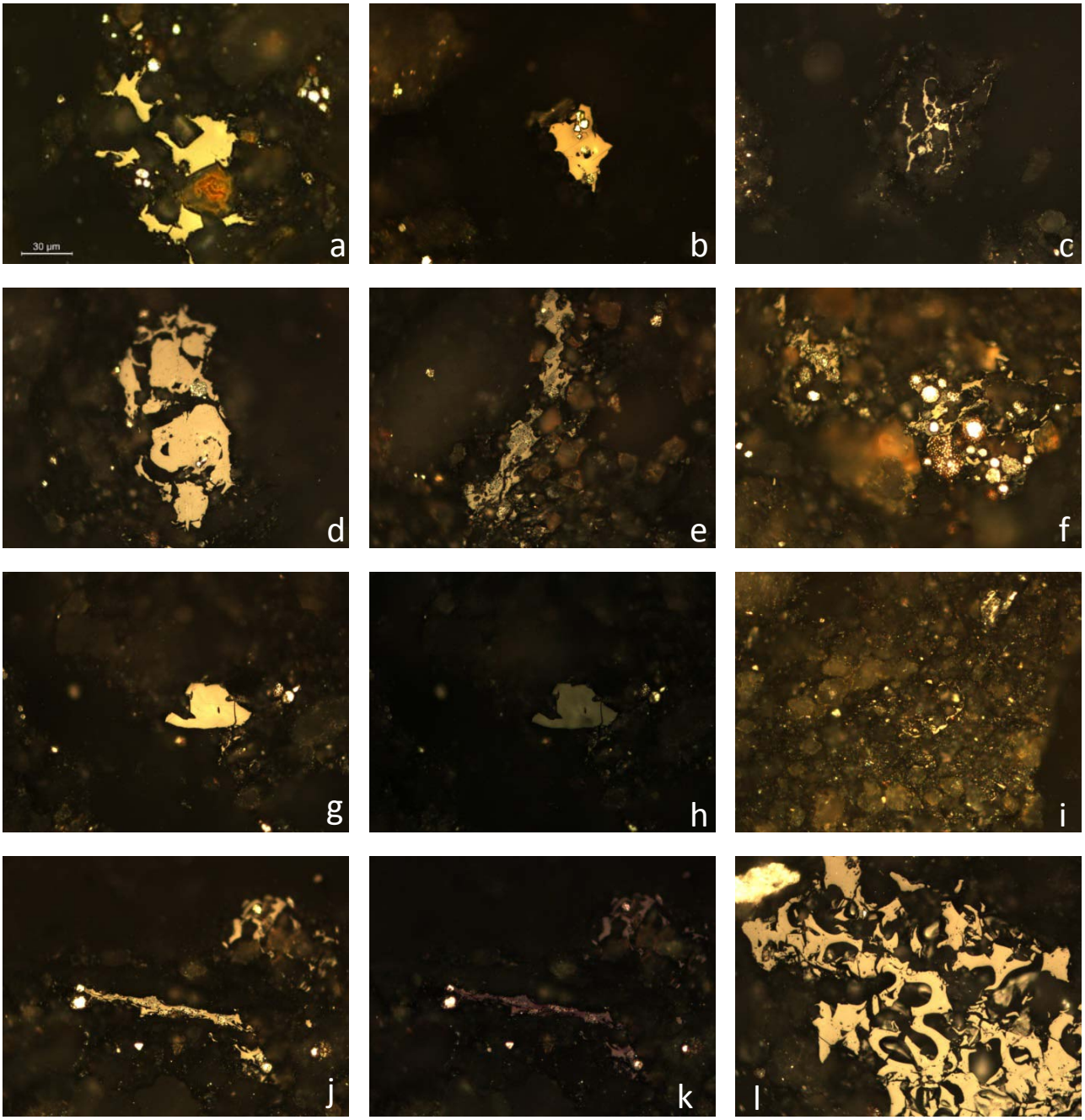

Plate 1: Optical microscopy. Photomicrographs taken in reflected white light. Polarized light in photographs (h) and (m), with a 1 λ retarder plate in (m).
(a) Solid bitumen particle rounded mineral borders (SIC-1); (b) solid bitumen particle with concave-convexe borders and degassing vacuous (SIC-1); (c) solid bitumen in the mineral matrix (SIC-1); (d) solid bitumen with vacuous (SIC-1); (e) solid bitumen partially replaced with pyrite (SIC-1); (f) Organic matter rest partially replaced with pyrite (SIC-1); (g) vitrinite particle with anisotropy (h) (SIC-1); (i) Organic matter rests; (j) vitrinite with stressed optical anysotropy (k) (SIC-1); (l) inertinite (SIC-1).
Width of the long dimension of the pictures: 200 µm

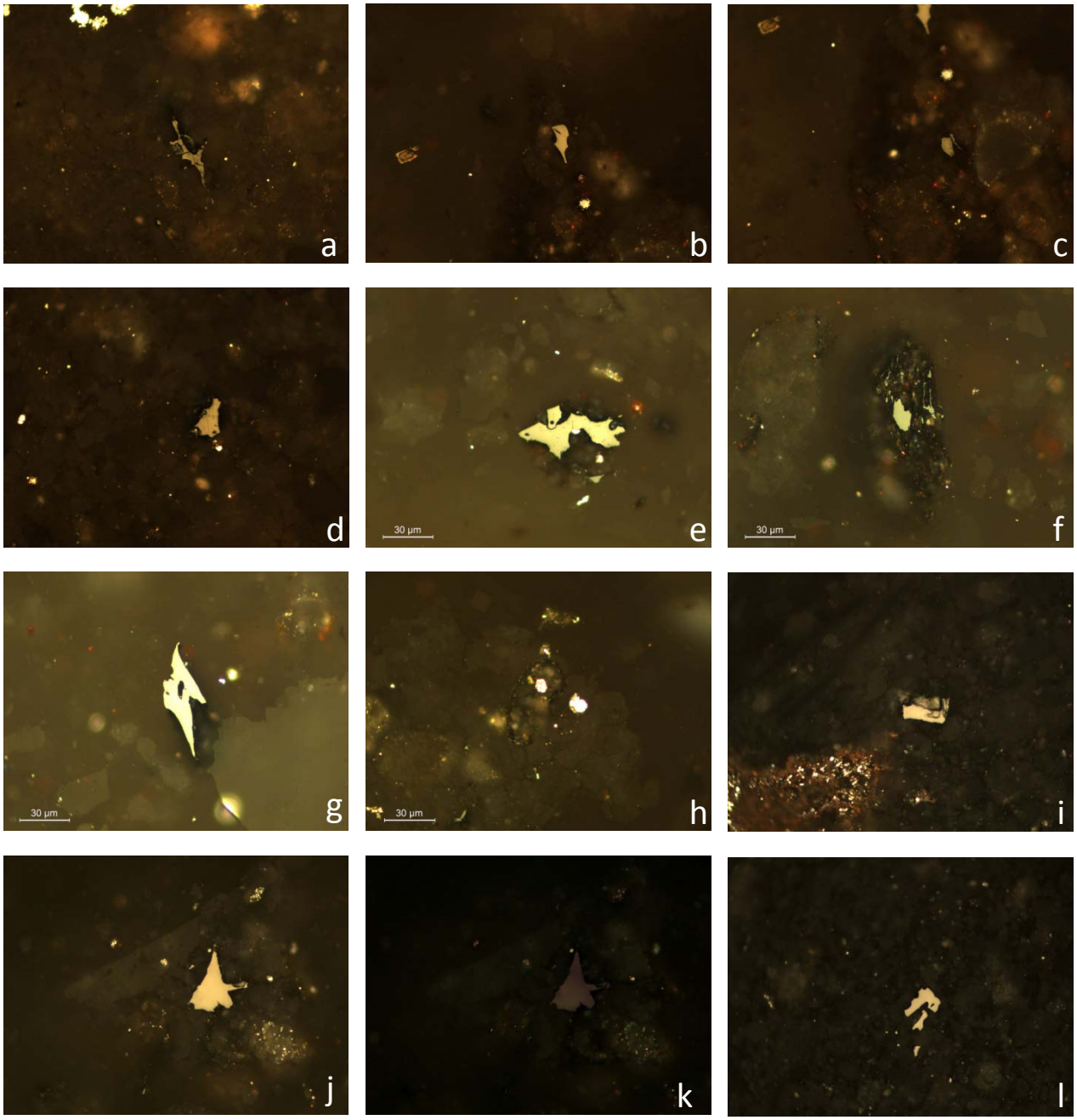

Plate 2: Optical microscopy. Photomicrographs taken in reflected white light. Polarized light, with a 1 λ retarder plate, in photograph (m).
(a) Solid bitumen particle rounded mineral borders (CGT-413); (b), (c) and (d) vitrinite particles (CGT-413); (e) solid bitumen particle (CG-2); (f) Organic matter rest partially altered (CG-2); (g) inertinite (h) (CG-2); (i) Inertinite (CG-2); (j) vitrinite with optical anisotropy (k); (l) inertinite (SMO-0).
Width of the long dimension of the pictures: 200 µm

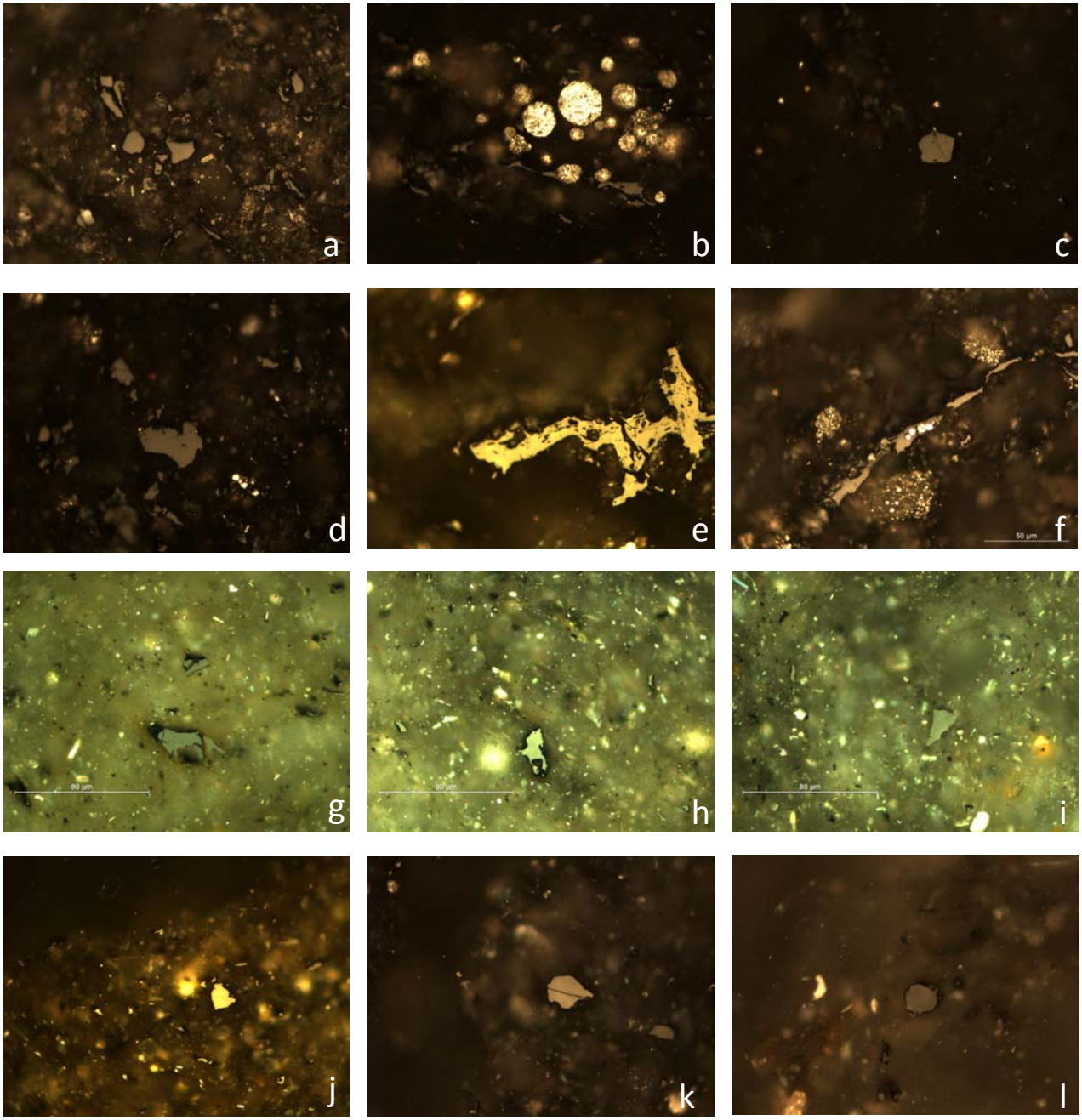

Plate 3: Optical microscopy. Photomicrographs taken in reflected white light.
(a) Inertinite (SMO-01); (b) vitrinite with framboidal pyrite (SMO-01), (c) and (d) vitrinite (SMO-01); (e) inertinite-fusinite (SMO-01); (f) vitrinite with framboidal pyrite (SMO-01); (g) vitrinite (SMO-1); (h) solid bitumen (?) (SMO-1); (i) vitrinite (SMO-1); (j) vitrinite with high reflectance (SMO-2); (k) and (l) vitrinite (SMO-2b).
Width of the long dimension of the pictures: 200 µm

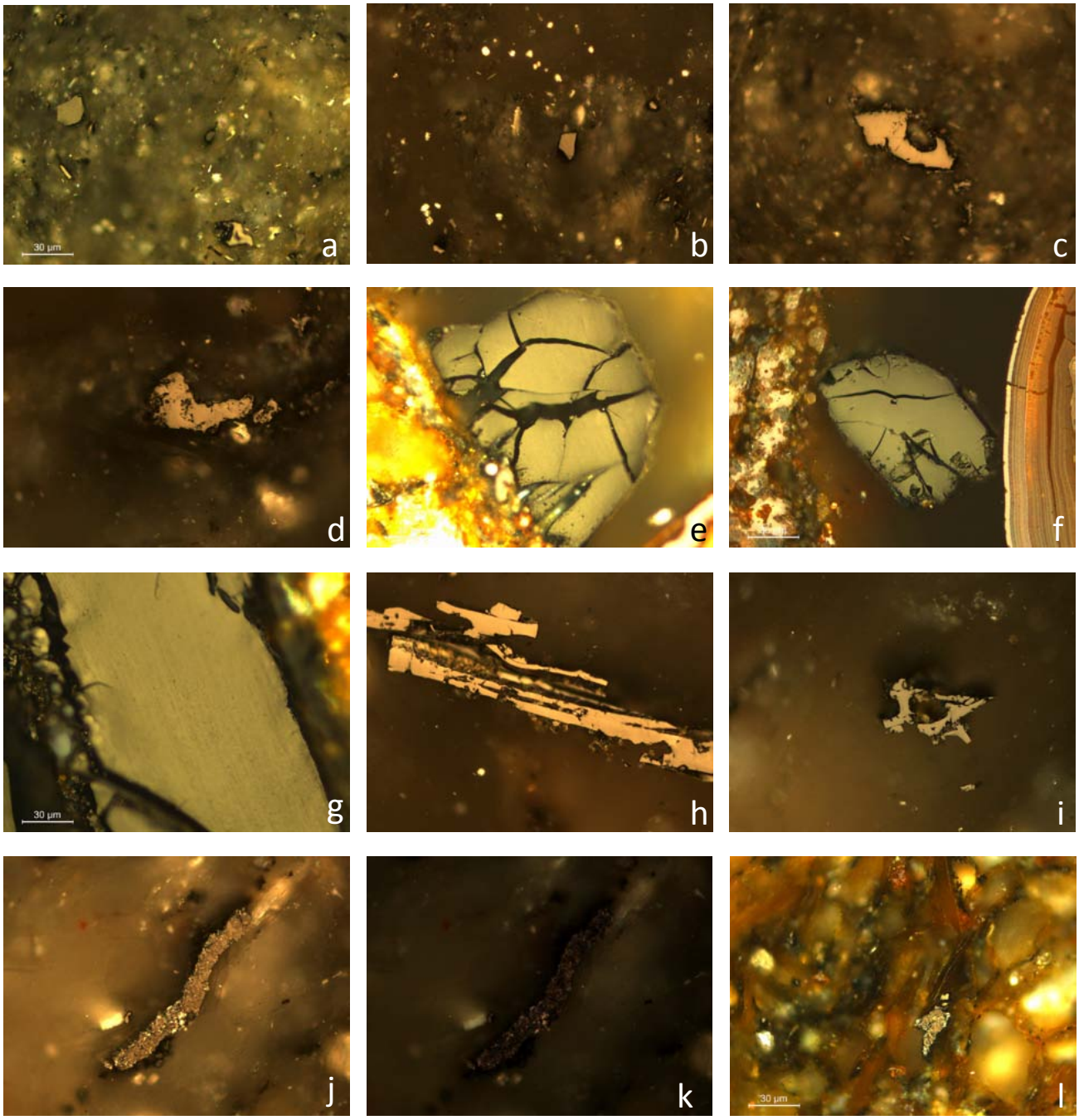

Plate 4: Optical microscopy. Photomicrographs taken in reflected white light. Polarized light, with a 1 λ retarder plate, in photograph (m).
(a) Vitrinite on the left, intertinite on the right (SPOV-1); (b) vitrinite (SPOV-1), (c) and (d) solid bitumen particles (SPOV-1); (e) and (f) vitrinite oxidized (SPOV-3t); (g) vitrinite (SPOV-3t); (h) and (i) inertinite (SPOV-3); (j) Vitrinite particle with fine coke texture, with optical anisotropy (k) (SPOV-3); (l) Vitrinite particle with fine coke texture (SPOV-3).
Width of the long dimension of the pictures: 200 µm

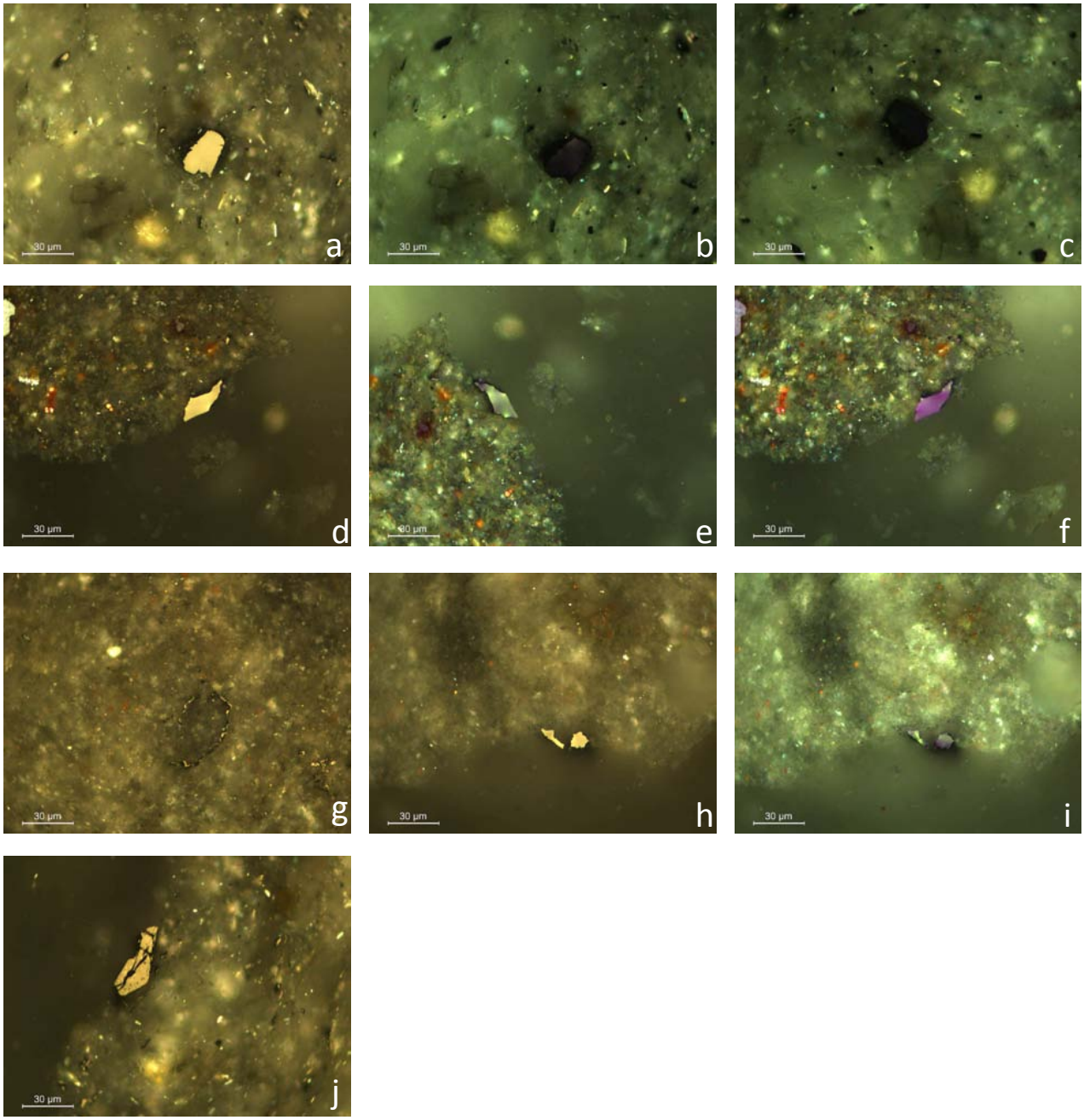

Plate 5: Optical microscopy. Photomicrographs taken in reflected white light. Polarized light, with a 1 λ retarder plate in photographs (b, c, e, f and i).
(a) Vitrinite with stressed optical anisotropy (b and c) (SPO-2); (b) Vitrinite with stressed optical anisotropy (e and f) (SCL-1); (g) Rest of organic matter (polen or spore) thermally transformed in hydrocarbons (SCL-1); (h) Vitrinite vitrinite with with stressed optical anisotropy (i) (SCL-1); (j) solid bitumen particle (?) (SPO-2).
Width of the long dimension of the pictures: 200 µm

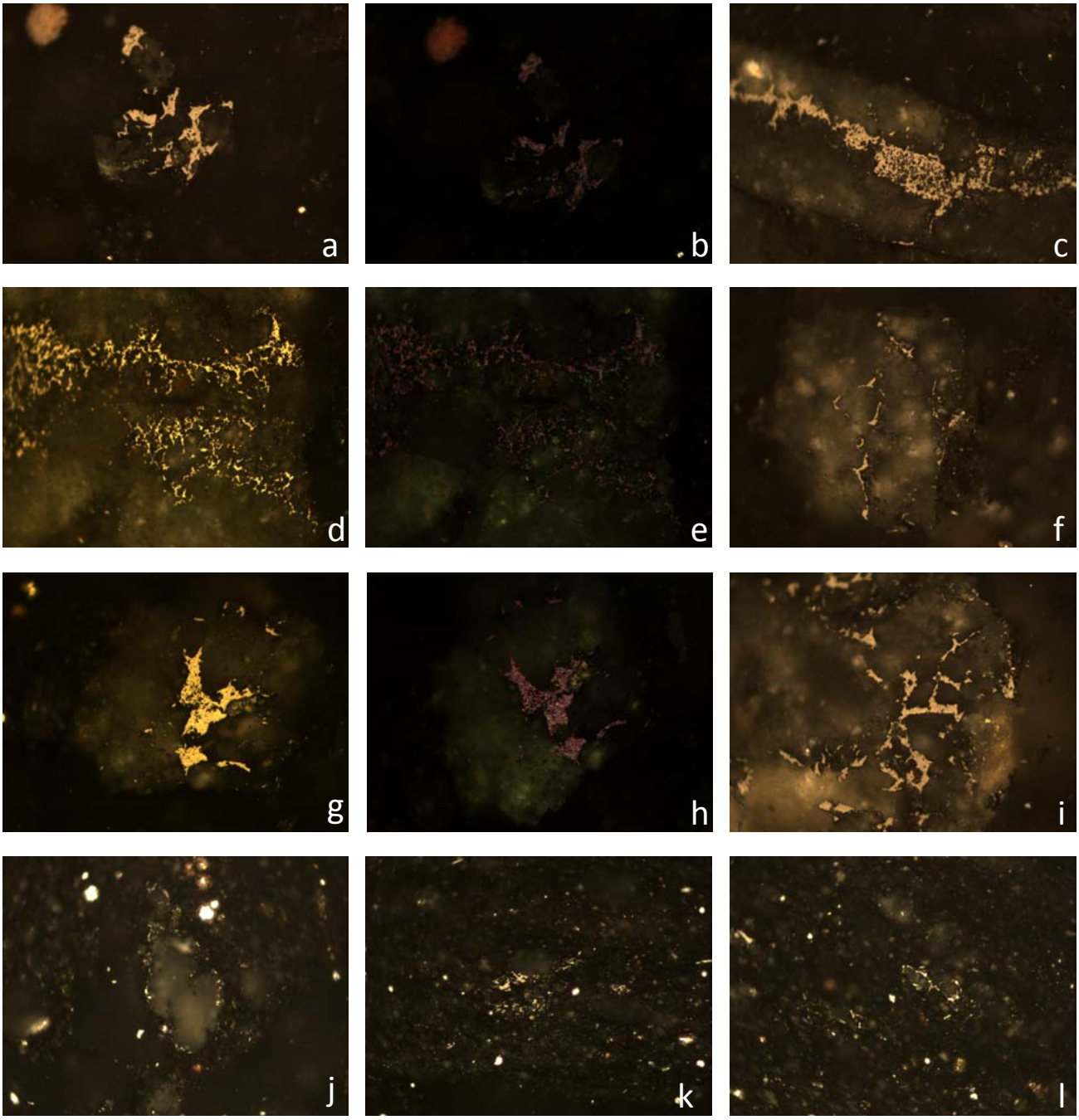

Plate 6: Optical microscopy. Photomicrographs taken in reflected white light. Polarized light, with a 1 λ retarder plate, in photographs (b, e and h).
(a), (c), (d), (f), (g) and (i) High reflectance solid bitumen filling mineral porosity, with coke mosaic texture; the mosaic texture has a stressed optical anisotropy (b, e and h) (SMO-3b); (j), (k) and (l) Fine-grained carbons left as result of liptinite thermal alteration (SMO-3b).
Width of the long dimension of the pictures: 200 μm

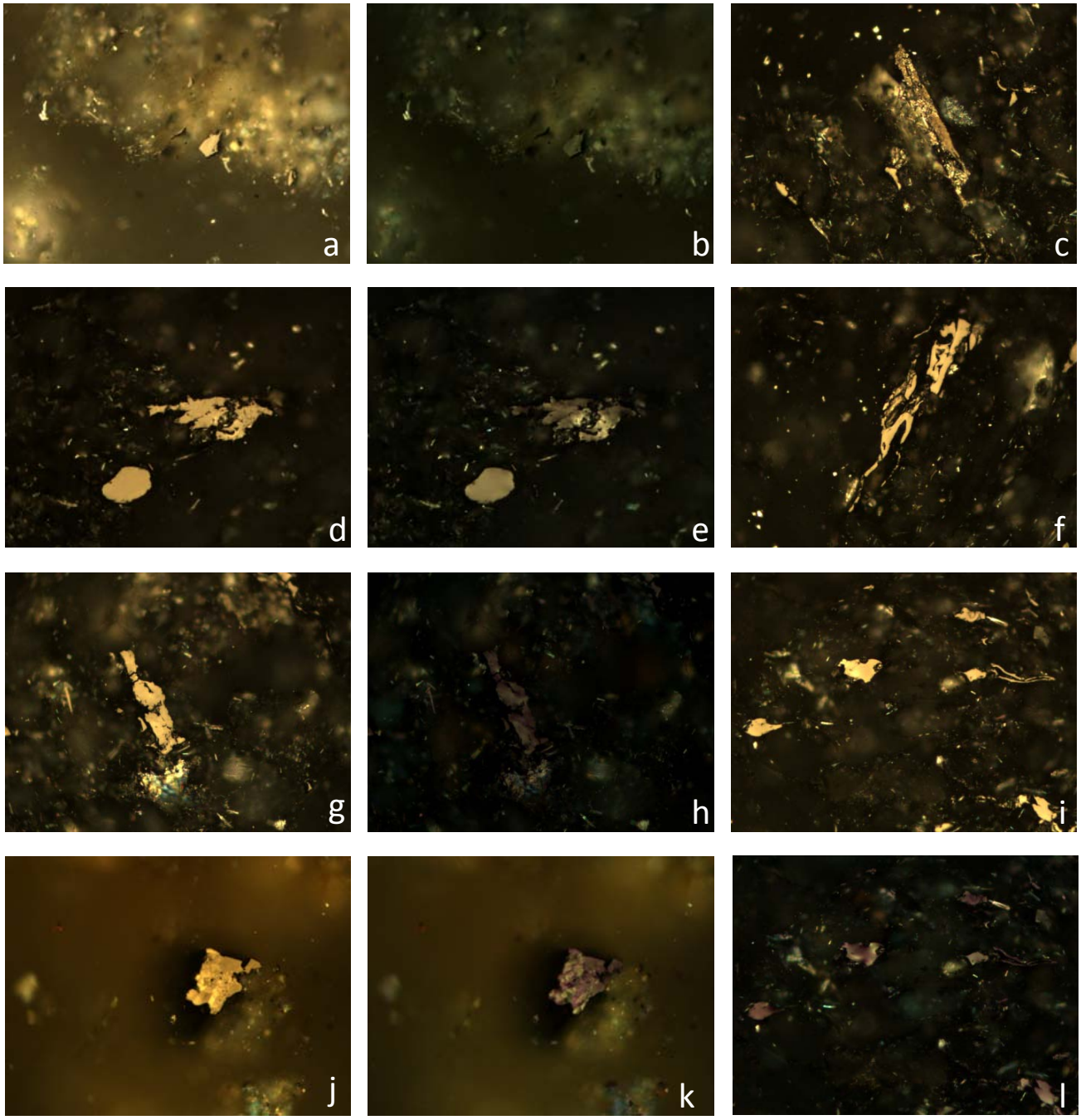

Plate 7: Optical microscopy. Photomicrographs taken in reflected white light. Polarized light photographs (b and e) and with the addition of a 1 λ retarder plate in photographs (h, m and n).
(a) Vitrinite with stressed optical anisotropy (b) (SPOV-7); (c) vitrinite with coke texture (TORMO-2); (d) Vitrinite with stressed optical anisotropy (e) (TORMO-2); (f) inertinite (TORMO-2); (g and i) Vitrinite with stressed optical anisotropy (h and l respectively) (TORMO-2); (j) solid bitumen particle with mesophase, with optical anisotropy (k) (SPOV-7.
Width of the long dimension of the pictures: 200 µm

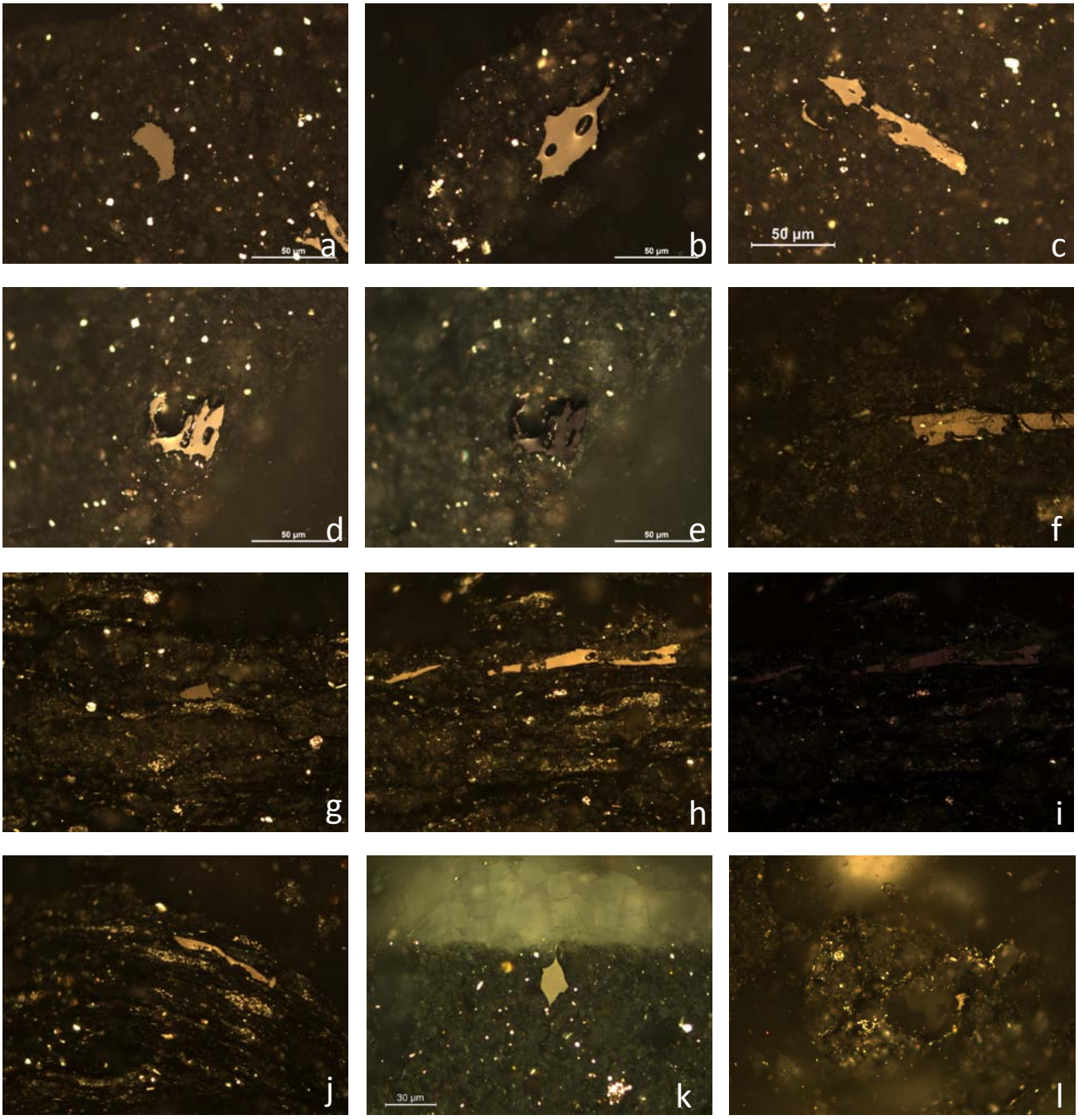

Plate 8: Optical microscopy. Photomicrographs taken in reflected white light. Polarized light with a 1 λ retarder plate in photograph (e).
(a) Vitrinite (SOH-1); (b) solid bitumen particle (SOH-1); (c) inertinite (SOH-1); (d) Vitrinite or solid bitumen particle, with stressed optical anisotropy (e) (SOH-1); (f) inertinite (SOH-2); (g, h and j) Fine-grained carbon left as result of liptinite (laminar algae?) thermal alteration. In (h) vitrinite has optical anisotropy (i) (SOH-3); (k) Planar vitrinite (YN-B04); (l) Fine-grained carbon left as result of liptinite (algae, spore or polen?) thermal alteration (YN-B010).
Width of the long dimension of the pictures: 200 µm

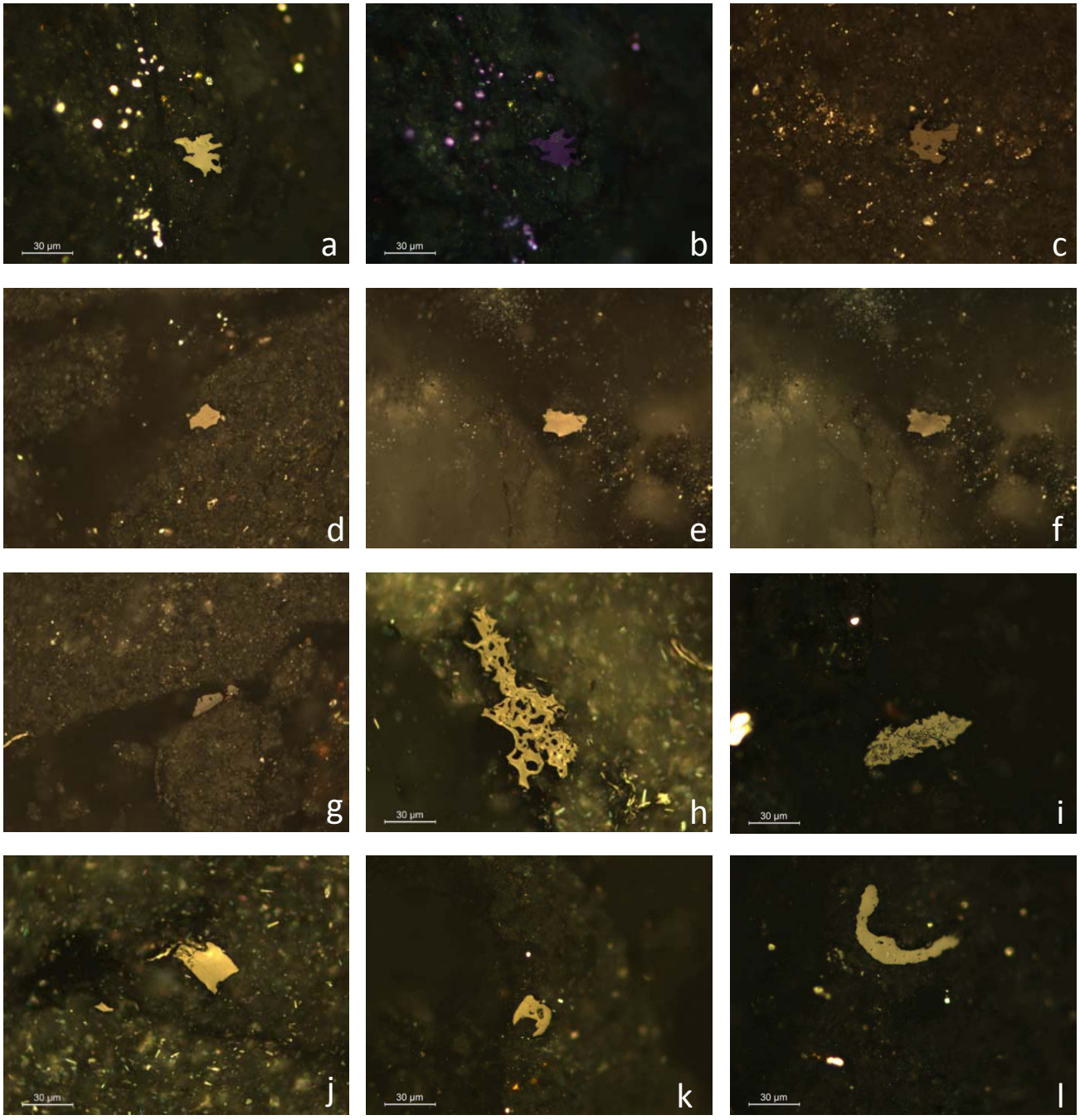

Plate 9: Optical microscopy. Photomicrographs taken in reflected white light. Polarized light in photograph (f).
(a) Vitrinite with a part with coke texture, which has a mosaic anisotropy (b) (SHDL-1); (c) solid bitumen particle with degassing vacuous (SOO-1); (d) vitrinite (SOO-2); (e) solid bitumen particle with degassing vacuous , with optical anisotropy (f) (SOO-2); (g) vitrinite (SOO-2); (h) Fusinite (SOY-3); (i) solid bitumen particle in the mineral matrix (SOY-3); (j) vitrinite (SOY-3); (k and l) solid bitumen particles with degassing vacuous (SHDL-1).
Width of the long dimension of the pictures: 200 µm.

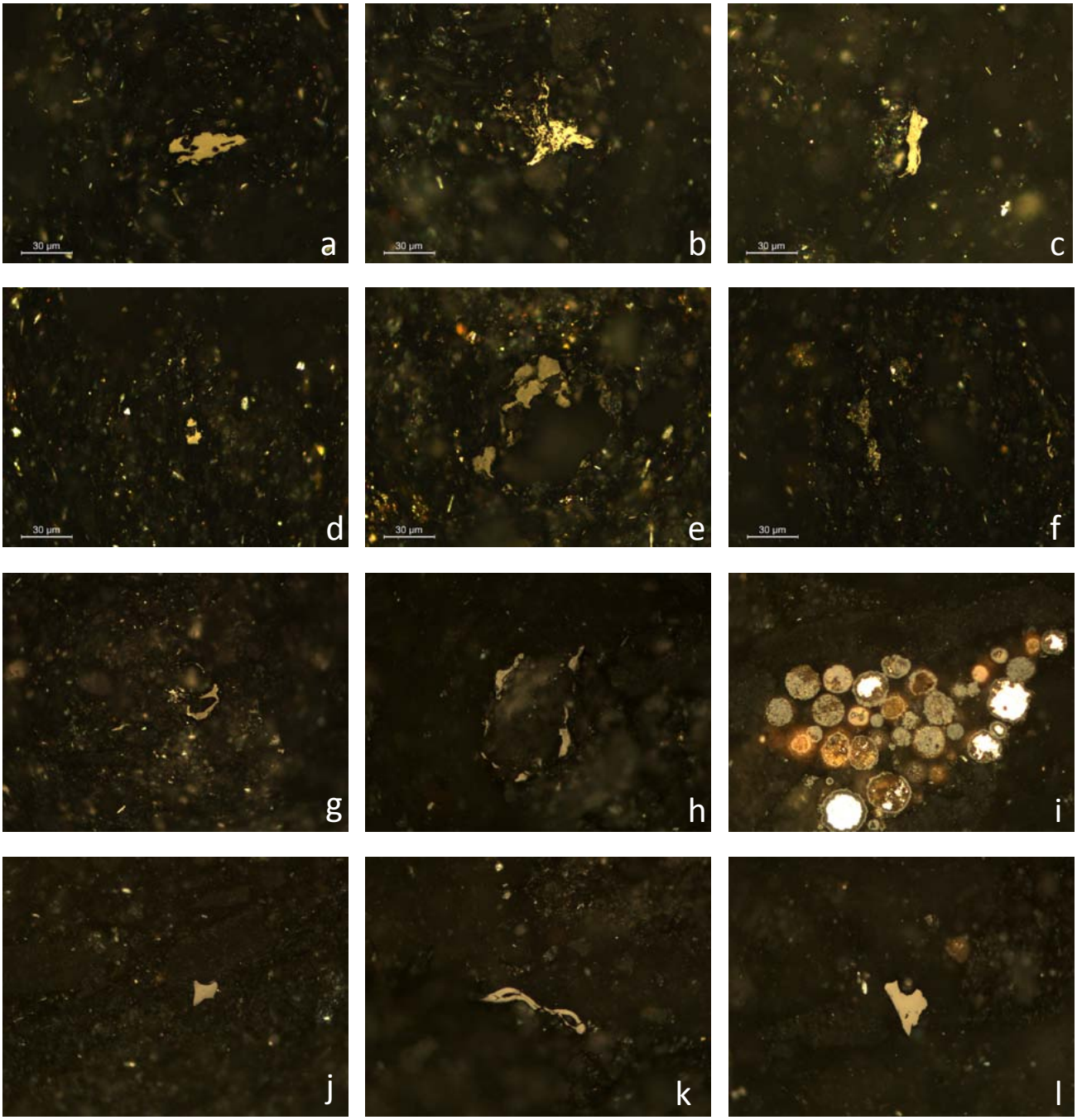

Plate 10: Optical microscopy. Photomicrographs taken in reflected white light.
(a) Solid bitumen particle (URB-2); (b) high reflectance vitrinite with stressed optical anisotropy (URB-2); (c) high reflectance vitrinite (URB-2); (d) high reflectance vitrinite (SEN-5); (e) solid bitumen particle (SEN-5); (f) vitrinite with coke texture (SEN-5); (g) solid bitumen particle (SEN-3); (h) rest of organic matter which has been thermally altered (SEN-3); (i) Framboidal pyrite (SEN-3); (j) vitrinite (SEN-3); (k) inertinite (SEN-3); (l) vitrinite (SEN-3).
Width of the long dimension of the pictures: 200 µm.

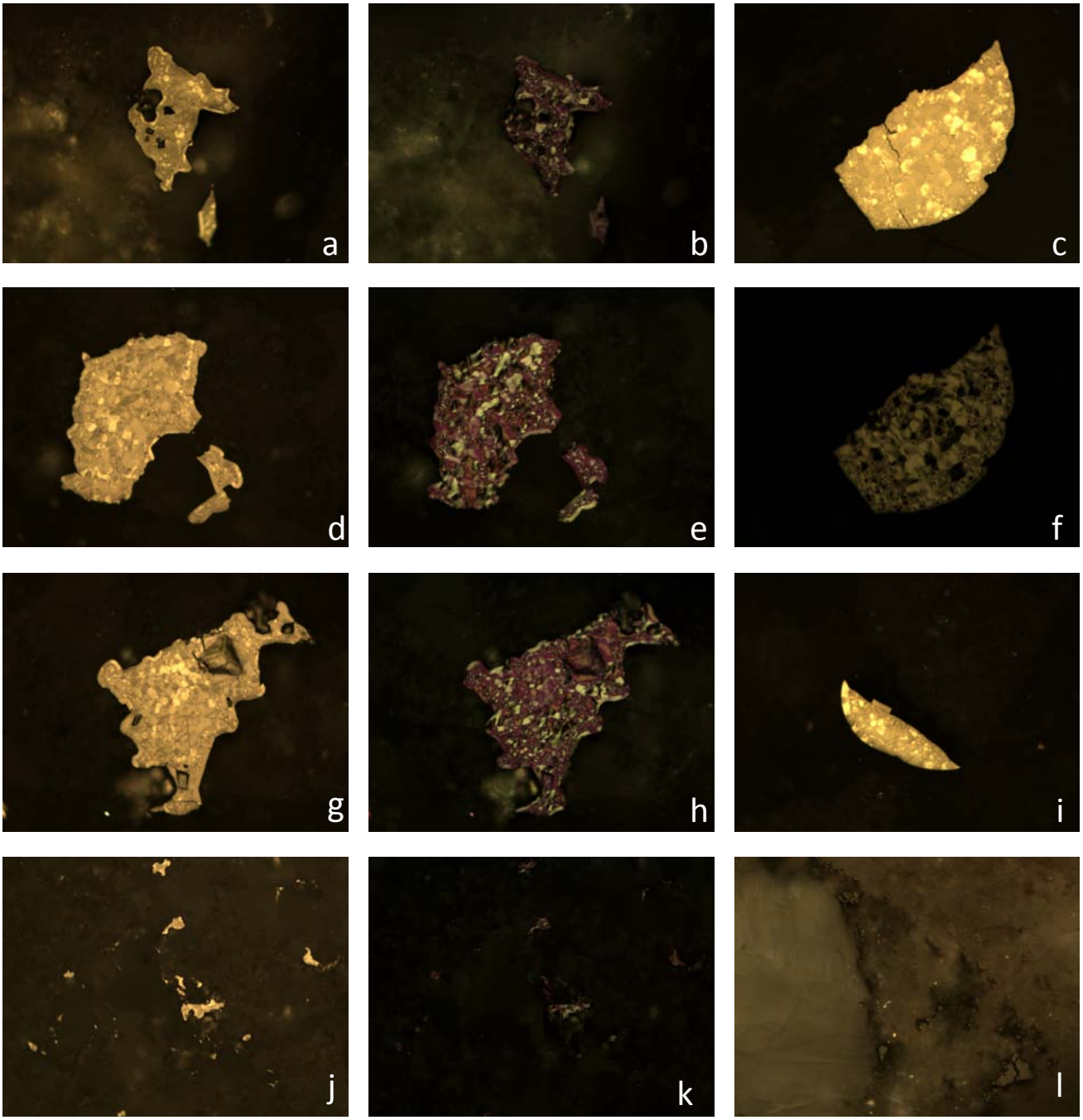

Plate 11: Optical microscopy. Photomicrographs taken in reflected white light. Polarized light photographs (b, e, f and k) and with the addition of a 1 λ retarder plate in photographs (e, h and k).
(a, c, d, g and i) Large solid bytumen particles with mesophaseof different size, testifyng a liquid-gas transition. Polarized light evidences the anisotropy of the mesophases (b, f, e and h respectively) (PR-11P); (j) Solid bitumen particles with mesophases in the mineral matrix, with optical anisotropy (k) (PR-11P); (l) solid bitumen particles in the diagenetic quartz overgrowth (PR-11P).
Width of the long dimension of the pictures: 200 µm.

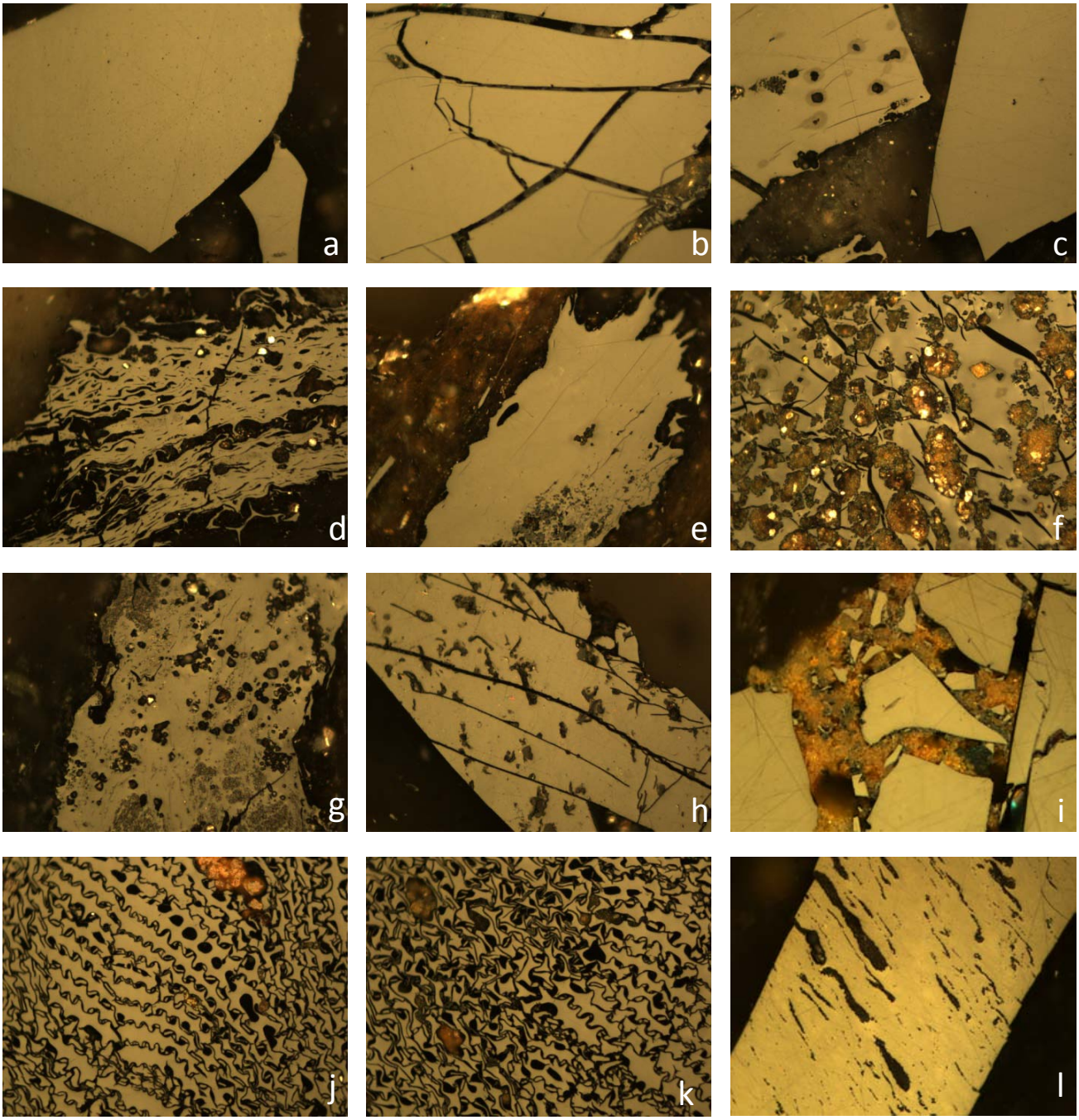

Plate 12: Optical microscopy. Photomicrographs taken in reflected white light.
(a, b and c) Large vitrinite particle with high reflectance (ROB-13); (d) fusinite (ROB-13); (e) vitrinite partially altered (ROB-13); (f, g and h) vitrinite with porosity filled with mineral matter (ROB-13); (i) vitrinite fractured by veins, filled with calcite cement (ROB-13); (j and k) fusinite (OLI-200); (l) vitrinite particles including narrow cavities, originally formed by sporinite, subsequently replaced by mineral cement.
Width of the long dimension of the pictures: 200 µm.

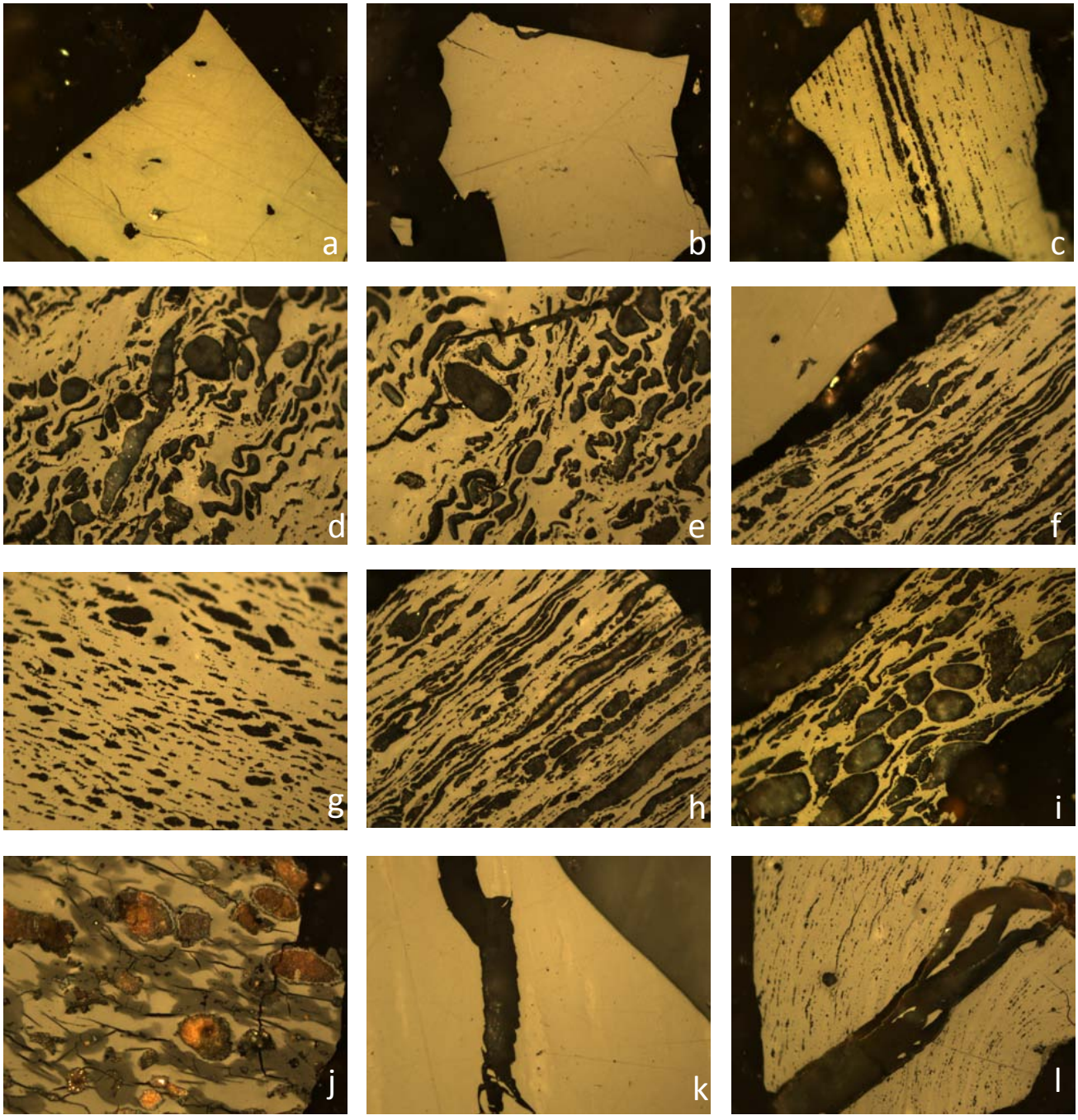

Plate 13: Optical microscopy. Photomicrographs taken in reflected white light.
(a and b) Large vitrinite particle with high reflectance (ROB-100); (c, d, e, f, g, h and i) vitrinite particles including elongated cavities, possibly originally formed by sporinite, subsequently replaced by mineral cement (ROB-100); (j) altered vitrinite (ROB-100); (k and l) vitrinite fractured by veins, filled with calcite cement (ROB-100).
Width of the long dimension of the pictures: 200 µm.

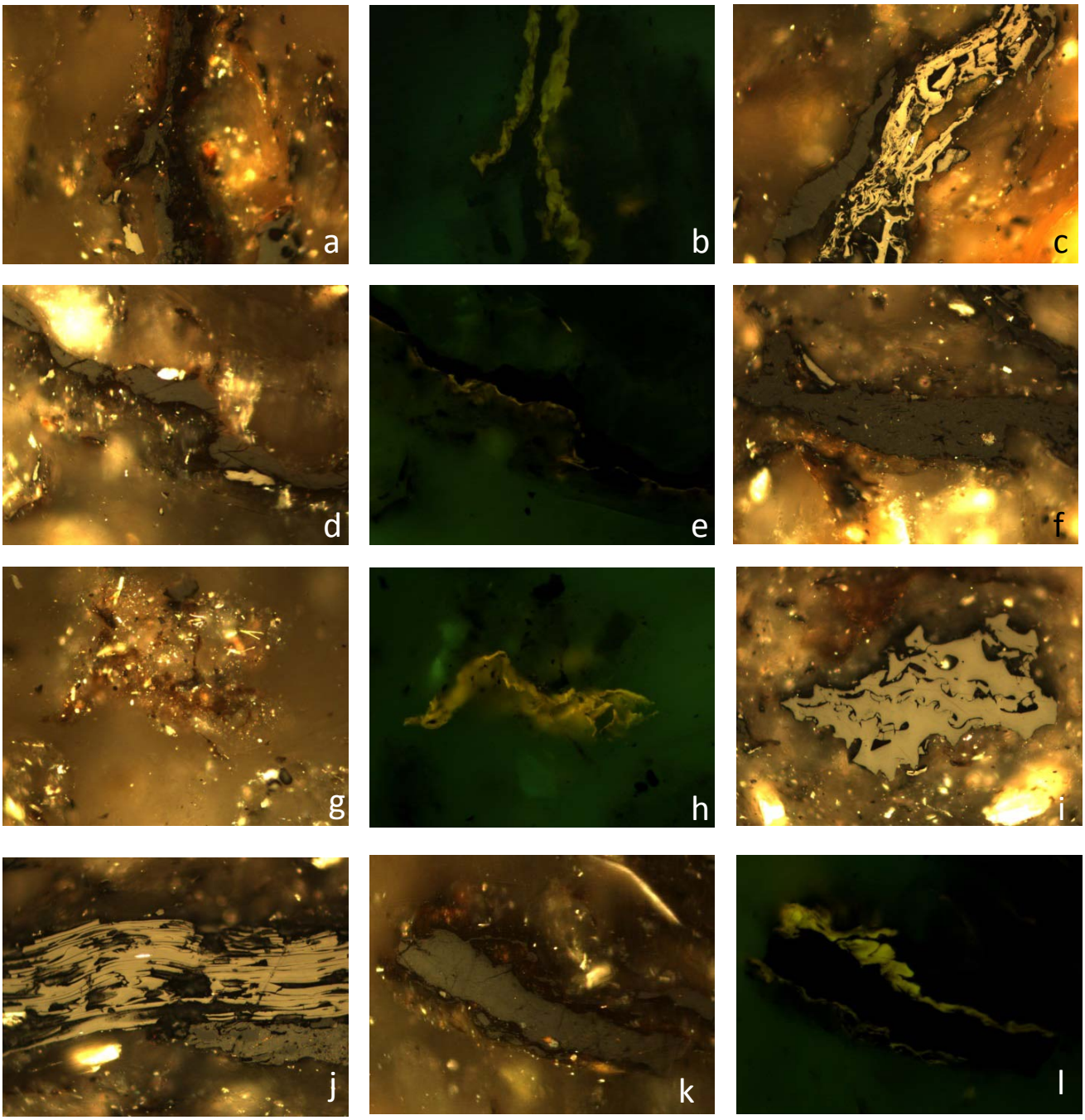

Plate 14: Optical microscopy. Photomicrographs taken in reflected white light. Fluorescence mode in photographs (b, e, h and l).
(a, d and k) Huminite (ulminite) rimmed by liptinite. In the fluorescence mode (b, e and l rispectively) the liptinite appears as a cutinite (STFC-0); (c) huminite (dark) and fusinite (white) (STFC-0); (f) Huminite (textinite) mixed with mineral material (STFC-0); (g) liptinite in mineral matter, which in fluorescence mode (h) appears as algae (STFC-0); (i) fusinite/semifusinite (STFC-0); (j) fusinite (white) and vitrinite (dark) partially oxidized (STFC-0).
Width of the long dimension of the pictures: 200 µm.

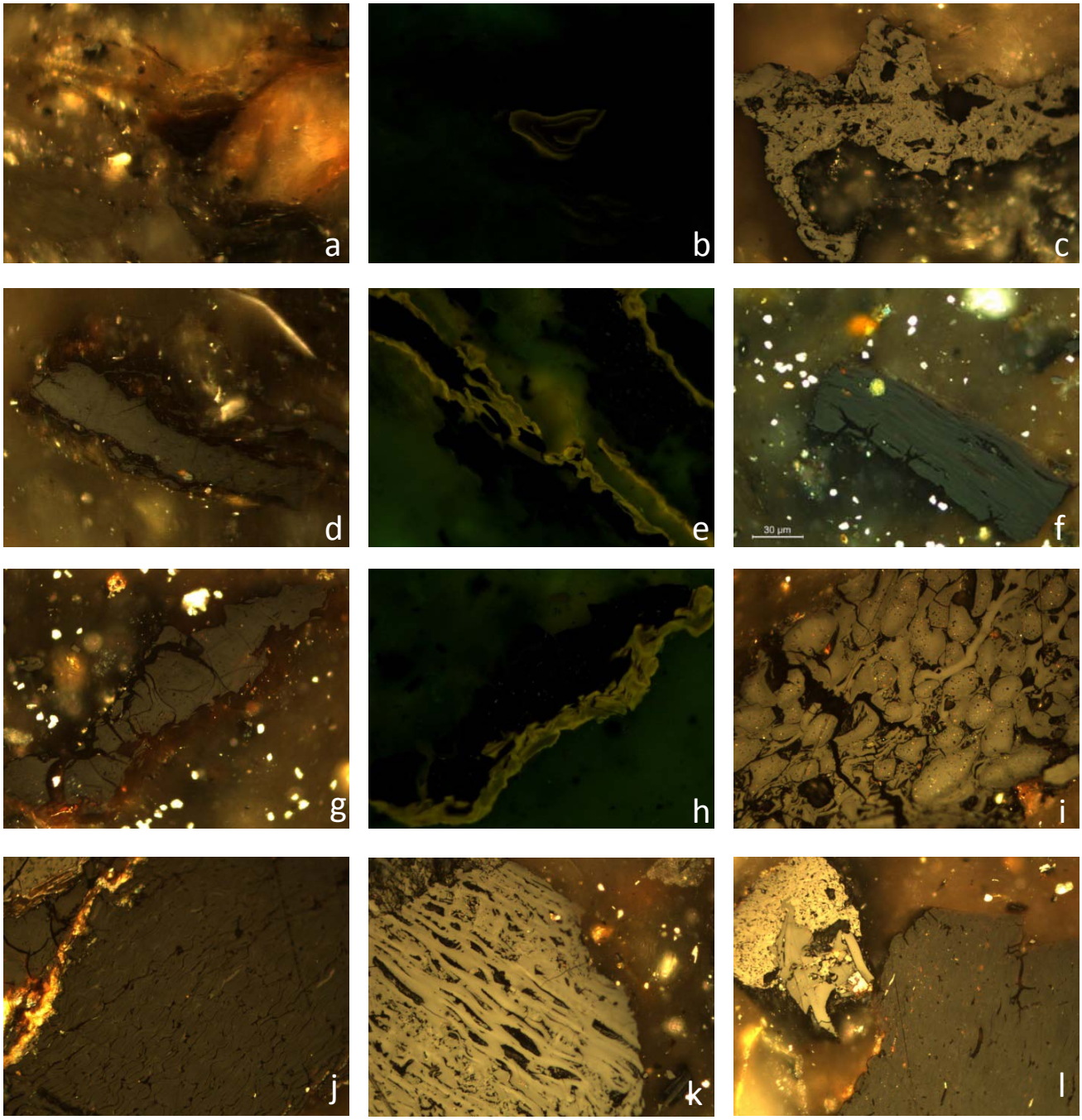

Plate 15: Optical microscopy. Photomicrographs taken in reflected white light. Fluorescence mode in photographs (b, e and h).
(a) Liptinite, which in fluorescence mode (b) appears as algae (STFC-0); (c) semifusinite (STFC-0); (d and g) Huminite (ulminite) rimmed by liptinite. In the fluorescence mode (e and h rispectively) the liptinite appears as a cutinite (STFC-1); (f) huminite (STFC-1); (i) Semifusinite/fusinite with recognizable cell walls (STFC-1); (j) Huminite (textinite) (STFC-1); (k) fusinite (STFC-1); (l) fusinite (white) and uminite (l) (STFC-1).
Width of the long dimension of the pictures: 200 µm.

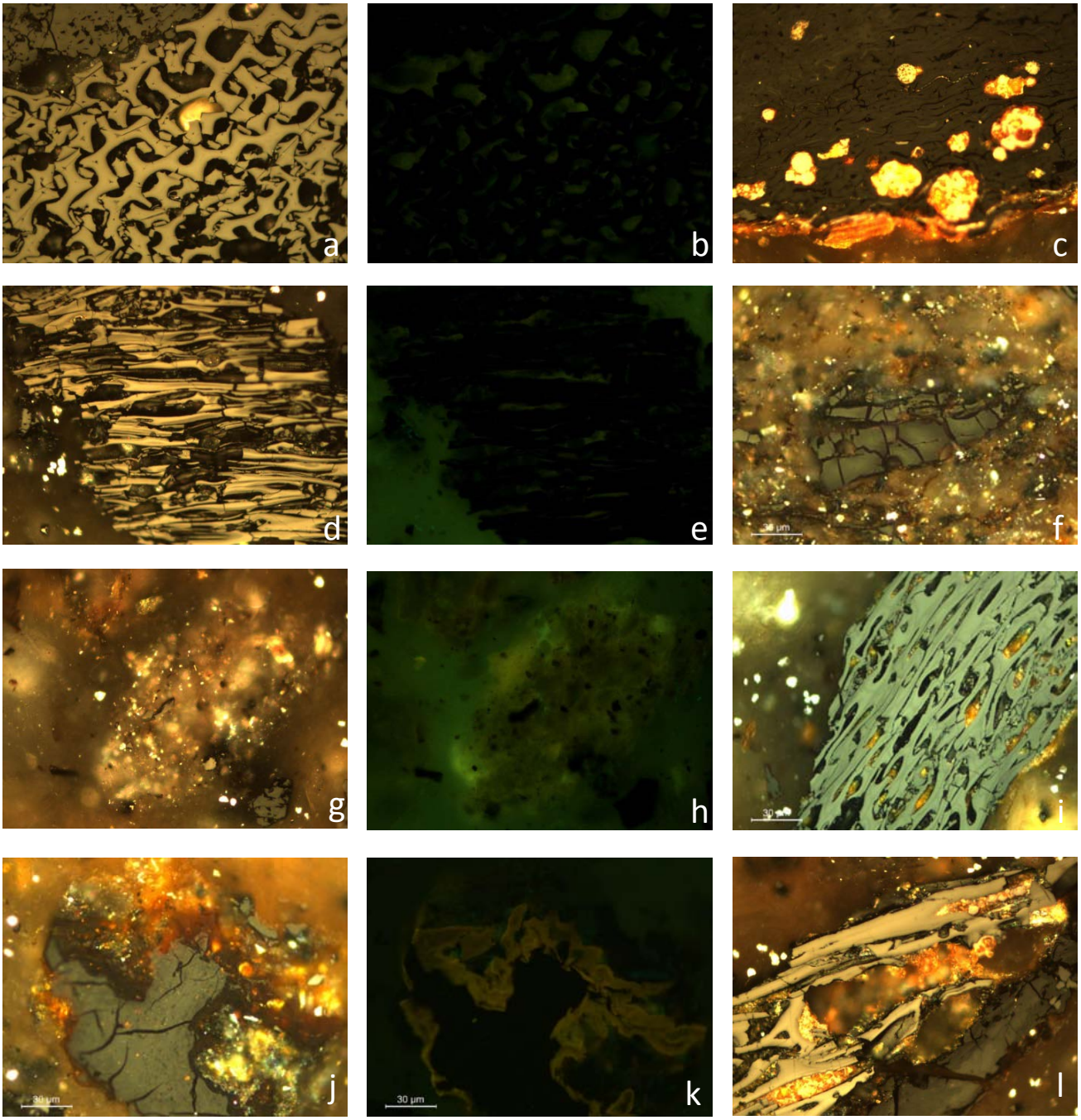

Plate 16: Optical microscopy. Photomicrographs taken in reflected white light. Fluorescence mode in photographs (b, e, h and k).
(a) Fusinite with liptinite filling cells walls, visible in fluorescence mode (b) (STFC-1); (c) huminite (textinite) mixed with mineral material (STFC-1); (d) Fusinite-semifusinite and liptinite, visible in fluorescence mode (e) (STFC-1); (f) altered (oxidized) vitrinite (STFC-2); (g) liptinite in organic material, which in fluorescence mode (h) appears as dispersed organic matter (STFC-1); (i) fusinite (STFC-1); (j) Altered vitrinite (oxidized), rimmed by liptinite. In the fluorescence mode (k) the liptinite appears as a cutinite (STFC-2); (l) fusinite and vitrinite (STFC-1).
Width of the long dimension of the pictures: 200 µm.

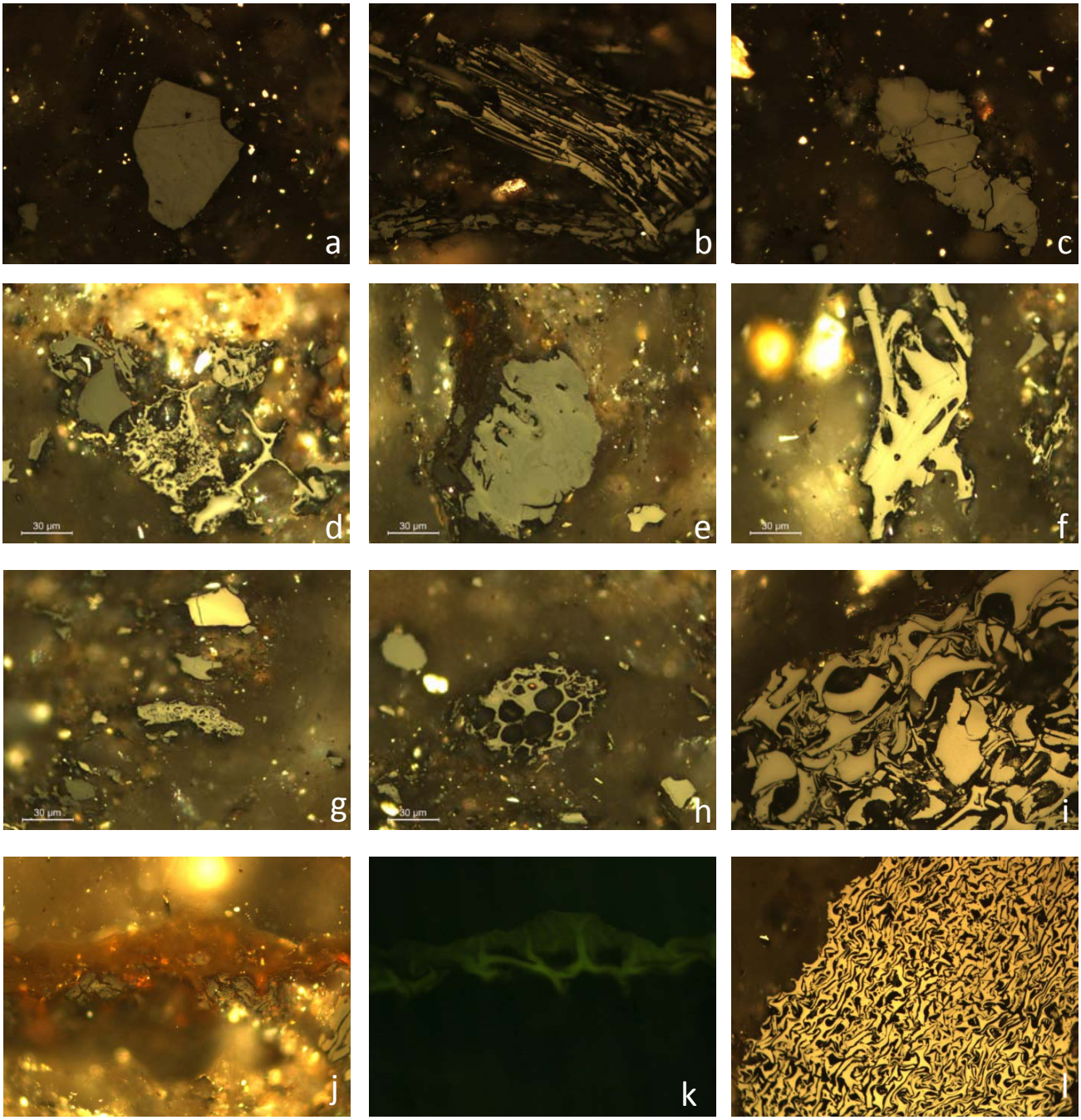

Plate 17: Optical microscopy. Photomicrographs taken in reflected white light. Fluorescence mode in photograph (k).
(a) Vitrinite (telinite) (STFC-3); (b) Fusinite mixed with semifusinite and vitrinite (STFC-3b); (c) vitrinite partially transformed in semifusinite (STFC-2); (d) Vitrinite (dark), fusinite (white) and solid bytumen rounding minerals borders (STFC-4); (e) Semifusinite (STFC-4); (f) fusinite (STFC-4); (g) From the top: inertinite, inertodentrinite, semifusinite and vitrinite (STFC-4); (h) Fusinite with well preseved cells walls (STFC-4); (i) Fusinite (white) and semifusinite (grey) (STFC-4b); (j) liptinite which in fluorescence mode (k) appears as cutinite (STFC-4b); (i) fusinite (STFC-4b);
Width of the long dimension of the pictures: 200 µm.

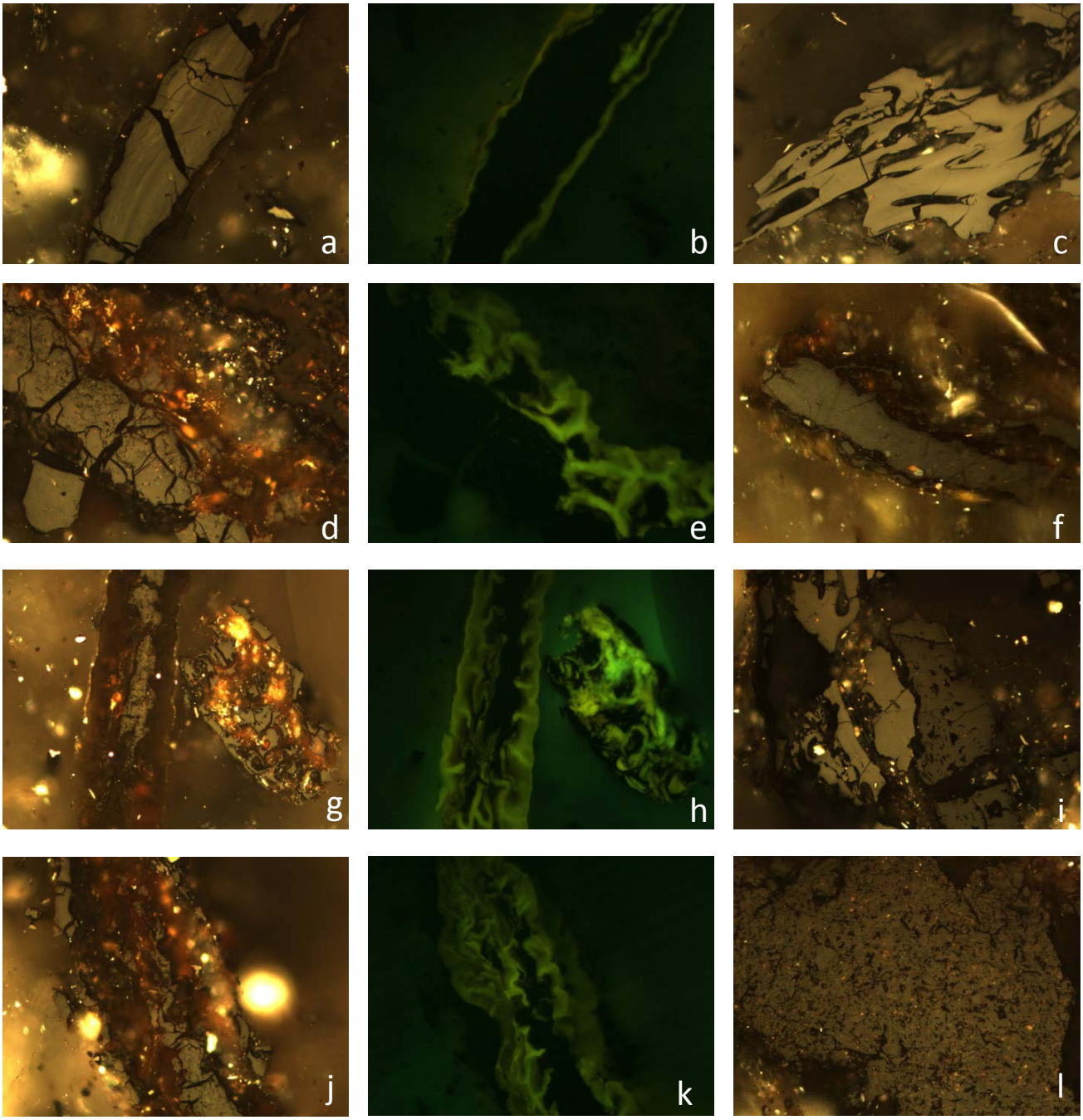

Plate 18: Optical microscopy. Photomicrographs taken in reflected white light. Fluorescence mode in photographs (b, e, h and k).
(a, d, g and j) Huminite rimmed by liptinite, which in fluorescence mode (b, e, h and k respectively) appears as cutinite (STFC-b); (c) semifusinite (STFC-4b); (f) Huminite (STFC-4b); (i) semifusinite (light grey) and huminite (dark grey) (STFC-4b); (l) huminite poorly gelified mixed with mineral material (STFC-4b);
Width of the long dimension of the pictures: 200 µm.

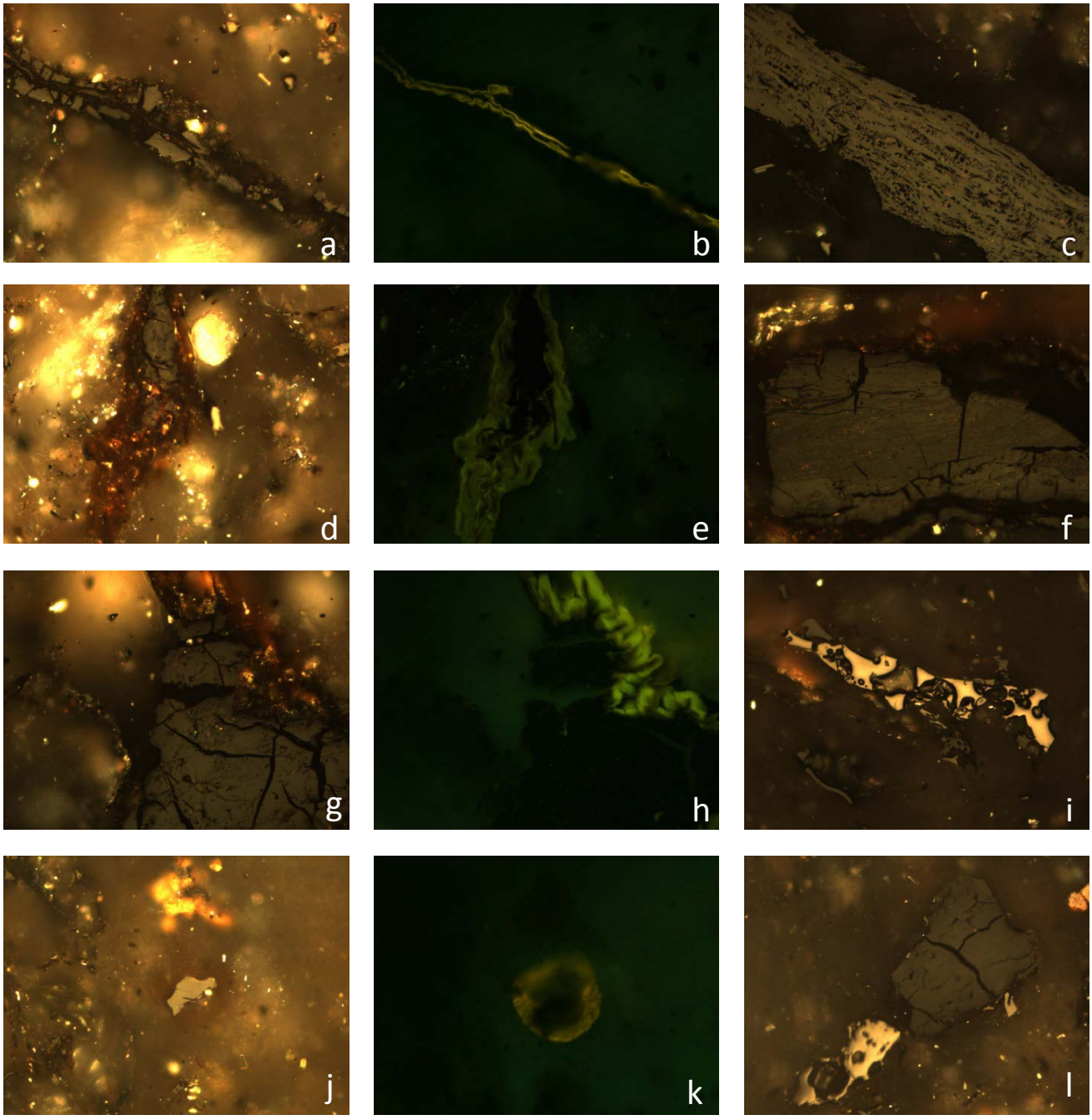

Plate 19: Optical microscopy. Photomicrographs taken in reflected white light. Fluorescence mode in photographs (b, e, h and k).
(a, d and g) Huminite rimmed by liptinite, which in fluorescence mode (b, e, h respectively) appears as cutinite (STFC-b); (c) semifusinite (STFC-4b); (f) Huminite partially altered (STFC-4b); (i) vitrinite mixed with solid bitumen (STFC-4b); (j) vitrinite superimposed to liptinite, wich in fluorescence mode appears as an algae (STFC-4b); (l) huminite (dark) and solid bitumen particle (white) (STFC-4b);
Width of the long dimension of the pictures: 200 µm.

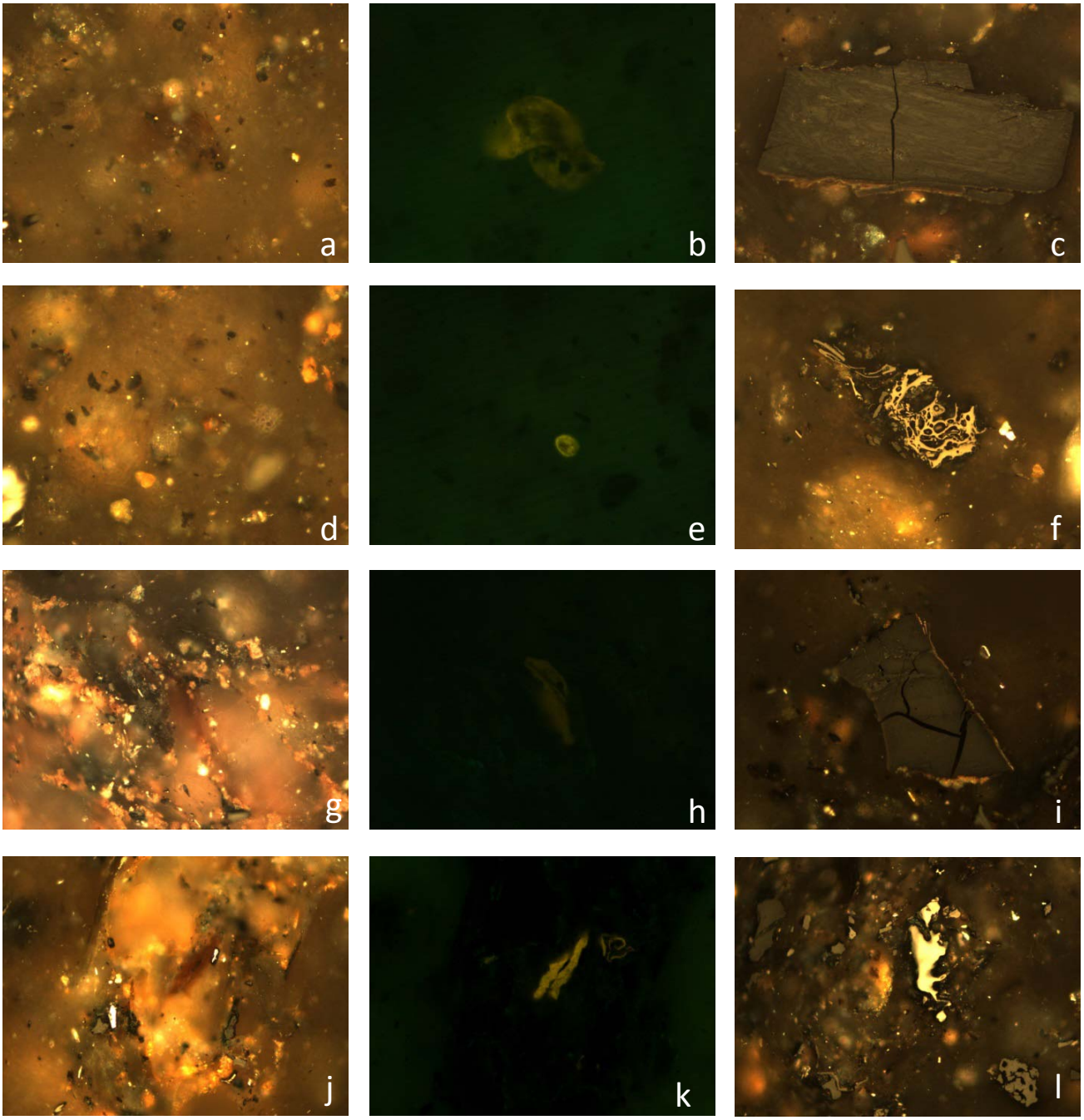

Plate 20: Optical microscopy. Photomicrographs taken in reflected white light. Fluorescence mode in photographs (b, e, h and k).
(a) Liptinite, which in fluorescence mode (b) appears as algae (PIG-1); (c) Vitrinite with recongizable cell walls (PIG-1); (d) liptinite, which in fluorescence mode (e) appears as spore or algae (?) (PIG-1); (f) fusinite (PIG-1); (g and j) liptinite in mineral material. liptinite in fluorescence mode appears as algae (h and k, respectively) (PIG-1); (l) solid bitumen particle (white) (PIG-1).
Width of the long dimension of the pictures: 200 µm.

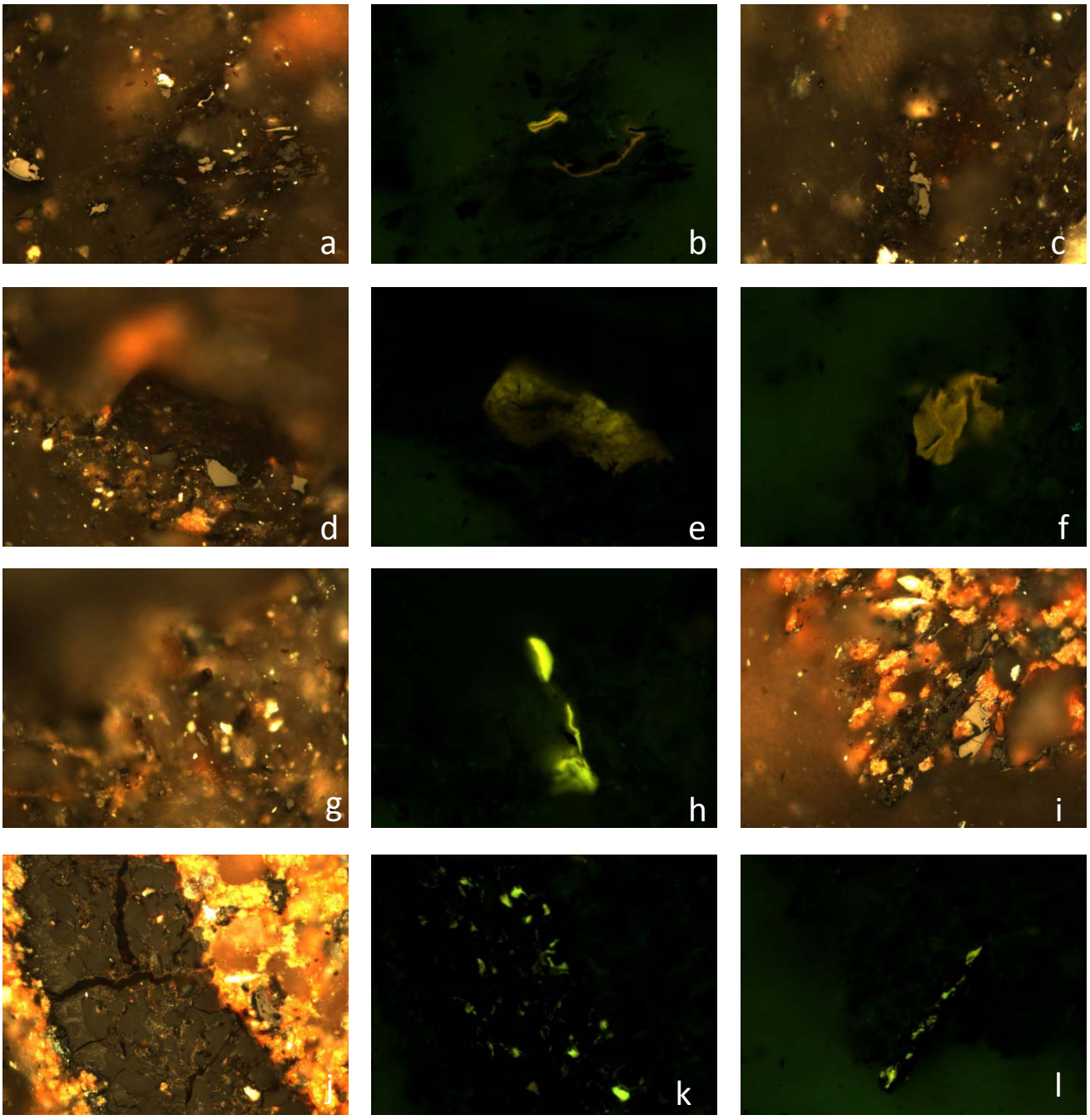

Plate 21: Optical microscopy. Photomicrographs taken in reflected white light. Fluorescence mode in photographs (b, e, f, h, k and l).
(a, c and g) Liptinite in mineral material. Liptinite in fluorescence mode (b, f, and e) respectively) appears as algae (PIG-1); (g and h respectively) Oil/hydrocarbons (exsudatinite) in form of green-yellow fluorescent droplets associated to liptinite material (PIG-1); (i and J) Vitrinite filled in the porosity by oil/hydrocarbons (exsudatinite) (k and l respectively) (PIG-1).
Width of the long dimension of the pictures: 200 µm.

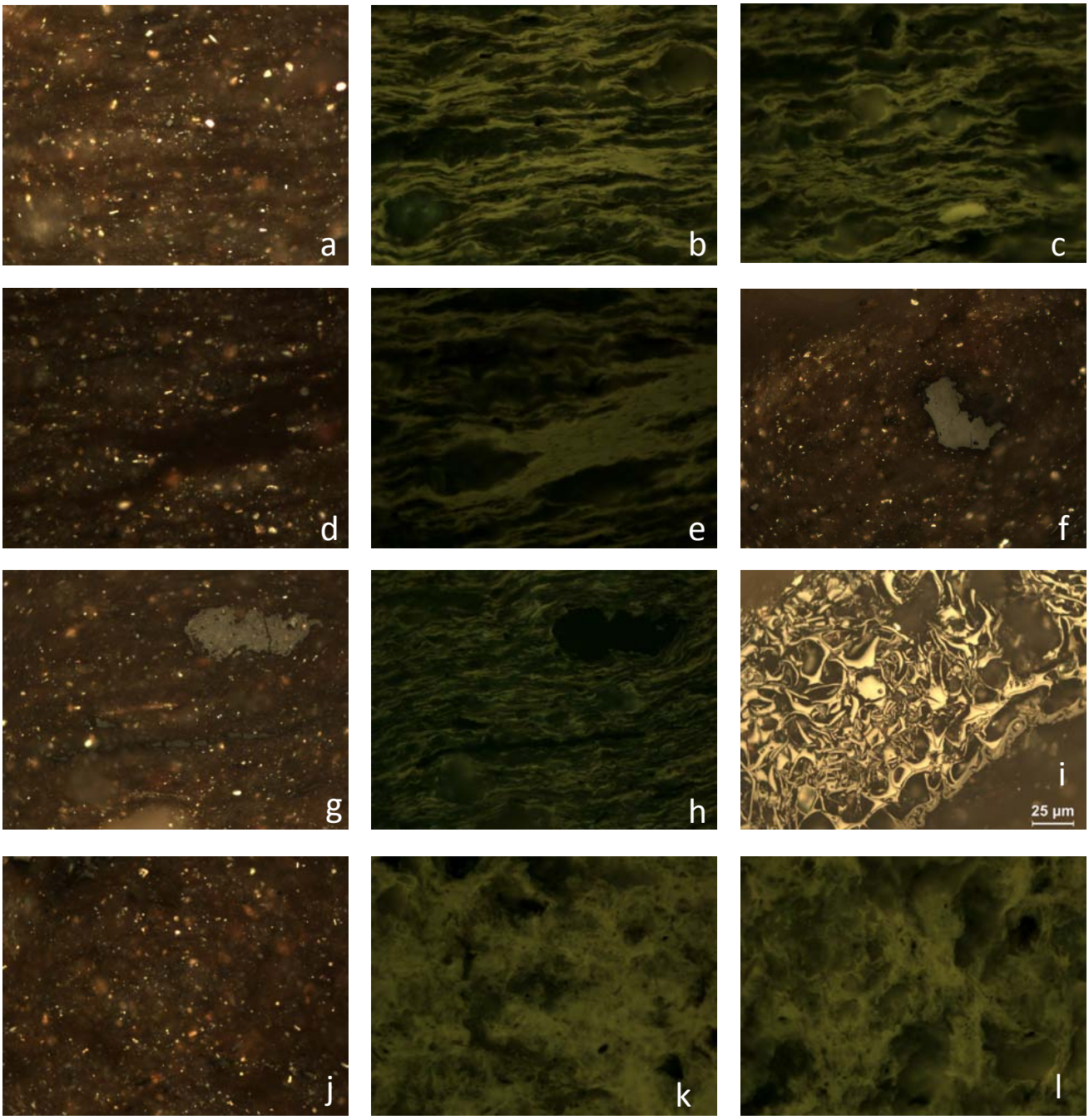

Plate 22: Optical microscopy. Photomicrographs taken in reflected white light. Fluorescence mode in photographs (b, c, e, h, k and l).
(a and d) Liptinite in mineral material. Liptinite in fluorescence mode (b and e respectively) appears as algae oriented in laminae (lamalginites) (CAS-2); (c) algae oriented in laminae (lamalginites) and and algal bodies (telalginites) such as Botryococcus (CAS-2); (f) vitrinite with low reflectance (cAS-2); (g) large vitrinite mixed with mineral material in liptinite. Liptinite in fluorescence mode (h) appears as algae oriented in laminae (lamalginites) (CAS-2); (i) fusinite (CAS-2); (J) lilptinite in mineral material, which in fluorescence mode (K) appears as amorphous organic matter (CAS-2); (l) amorphous organic matter (CAS-2).
Width of the long dimension of the pictures: 200 µm

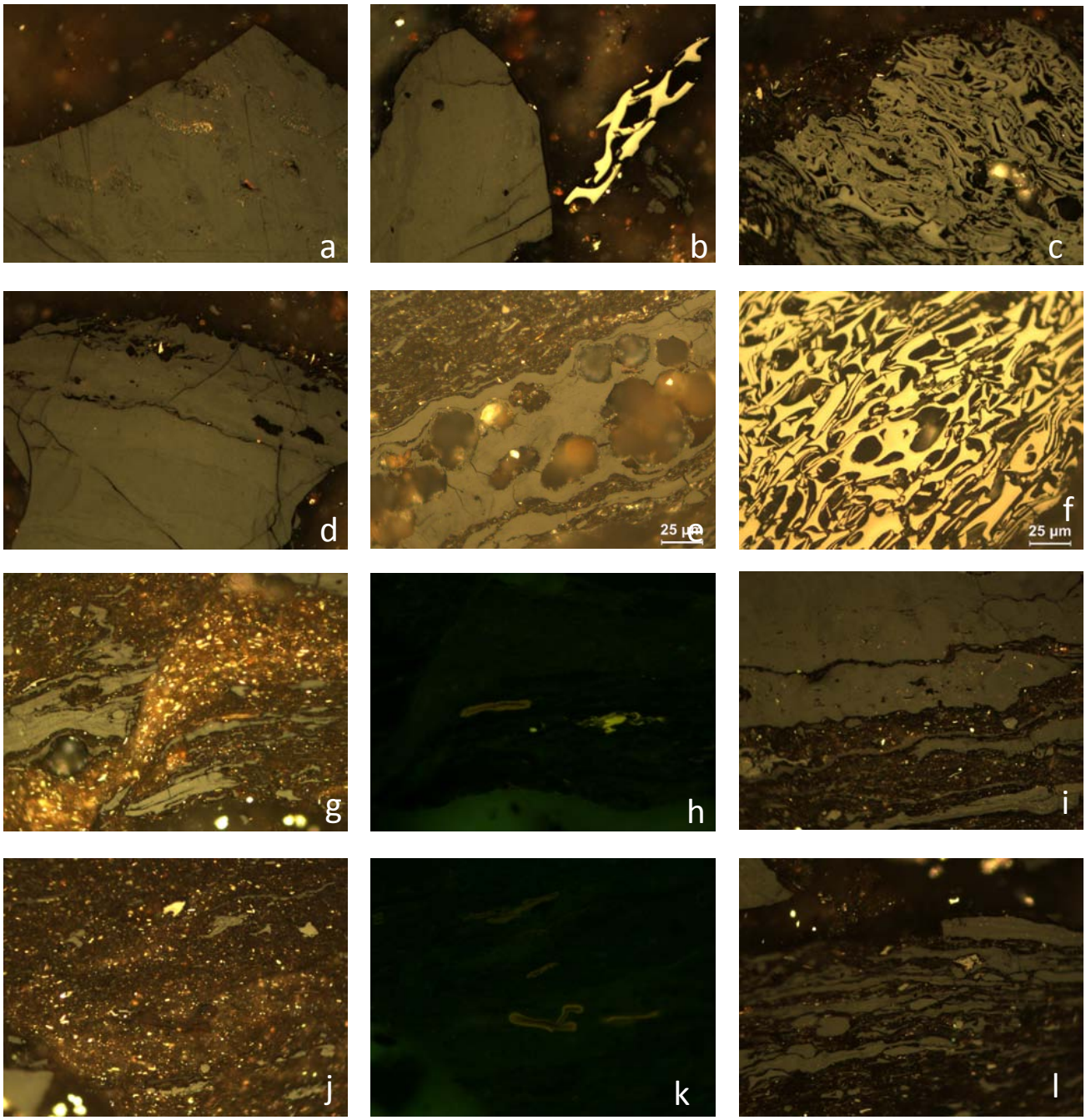

Plate 23: Optical microscopy. Photomicrographs taken in reflected white light. Fluorescence mode in photographs (h and k).
(a and d) Large vitrinite particle (PRJ-10); (b) large vitrinite particle (dark) and fusinite (white) (PRJ-10); (c) semifusinite (PRJ-10); (e) vitrinite with pores (ESC-PEÑ); (f) fusinite (ESC-PEÑ); (g) vitrinite and liptinite in mineral material. Liptinite in fluorescence mode (h) appears as algae (ESC-PEÑ); (i) vitrinite (ESC-PEÑ); (j) liptinite and small fragments of vitrinite and fusinite in mineral material. Liptinite in fluorescence mode (k) appears as algae (ESC-PEÑ); (l) elongated vitrinite (ESC-PEÑ).
Width of the long dimension of the pictures: 200 µm.

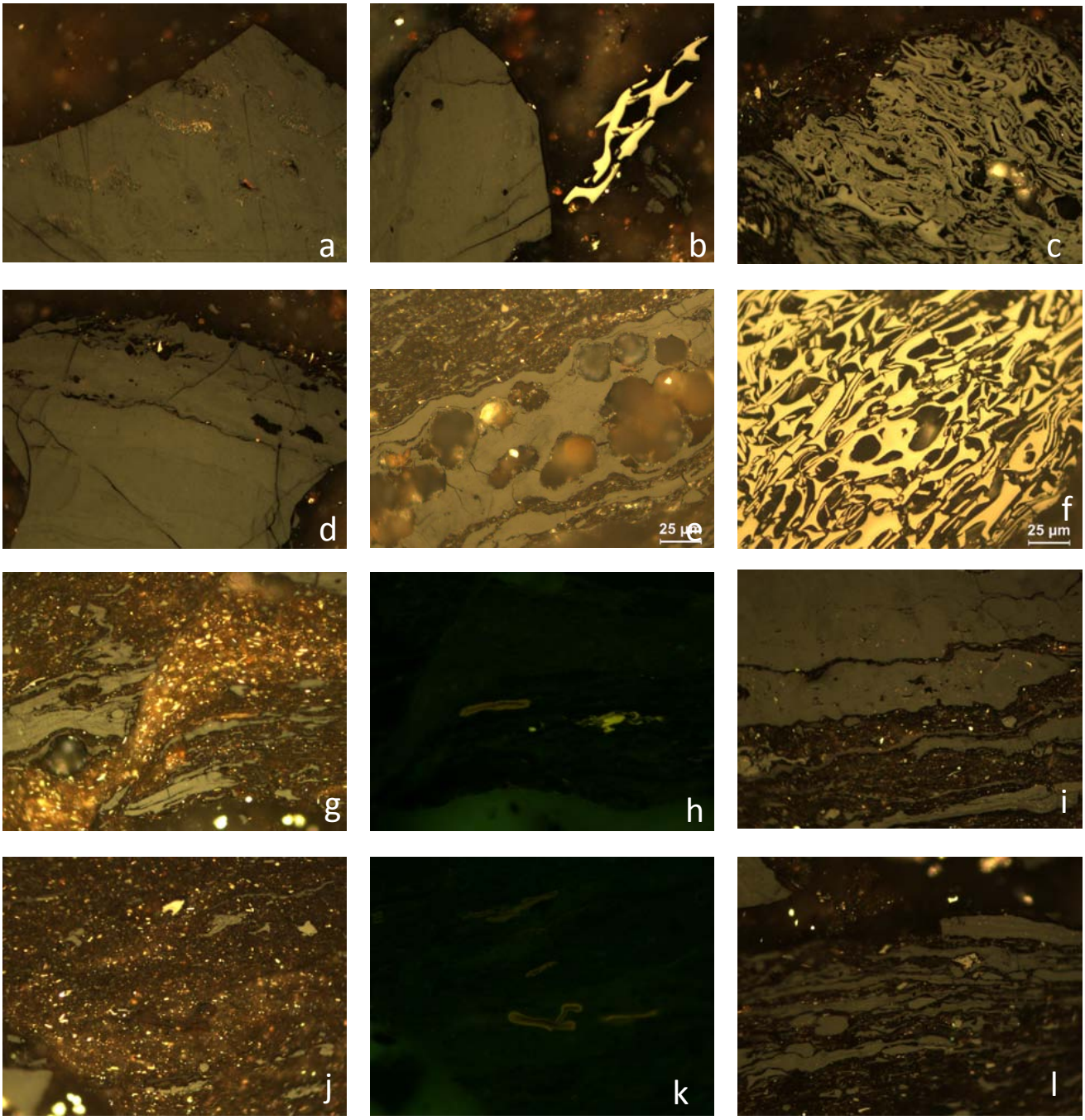

Plate 24: Optical microscopy. Photomicrographs taken in reflected white light. Fluorescence mode in photographs (h and k).
(a and d) Large vitrinite particle (PRJ-10); (b) large vitrinite particle (dark) and fusinite (white) (PRJ-10); (c) semifusinite (PRJ-10); (e) vitrinite with pores (ESC-PEÑ); (f) fusinite (ESC-PEÑ); (g) vitrinite and liptinite in mineral material. Liptinite in fluorescence mode (h) appears as algae (ESC-PEÑ); (i) vitrinite (ESC-PEÑ); (j) liptinite and small fragments of vitrinite and fusinite in mineral material. Liptinite in fluorescence mode (k) appears as algae (ESC-PEÑ); (l) elongated vitrinite (ESC-PEÑ).
Width of the long dimension of the pictures: 200 µm.

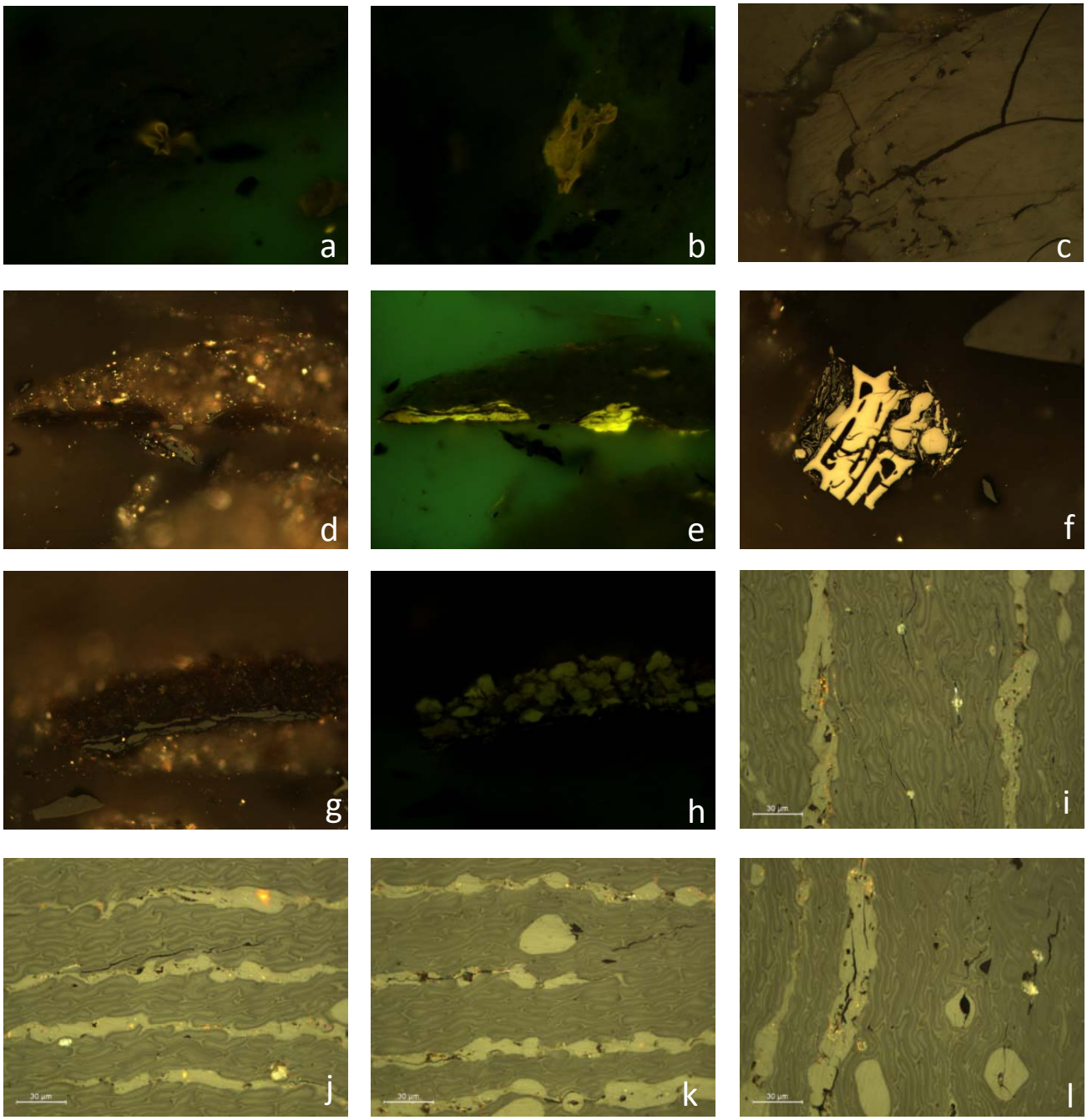

Plate 25: Optical microscopy. Photomicrographs taken in reflected white light. Fluorescence mode in photographs (a, b, e, and h).
(a) Liptinite, spore (PRJ-18); (b) liptinite, alga (PRJ-18); (c) large vitrinite (PRJ-18); (d) liptinite in mineral material, which appears in fluorescence mode (e) as algae (PRJ-18); (f) fusinite (PRJ-18); (g) vitrinite and fluorescent hydrocarbons (exsudatinite) (h) (PRJ-18); (i, j, k and l) vegetal tissue (vitrinite) with recognizable cell walls. Darker grey - corpohuminite, lighter grey – telinite (PRJ-10).
Width of the long dimension of the pictures: 200 µm.

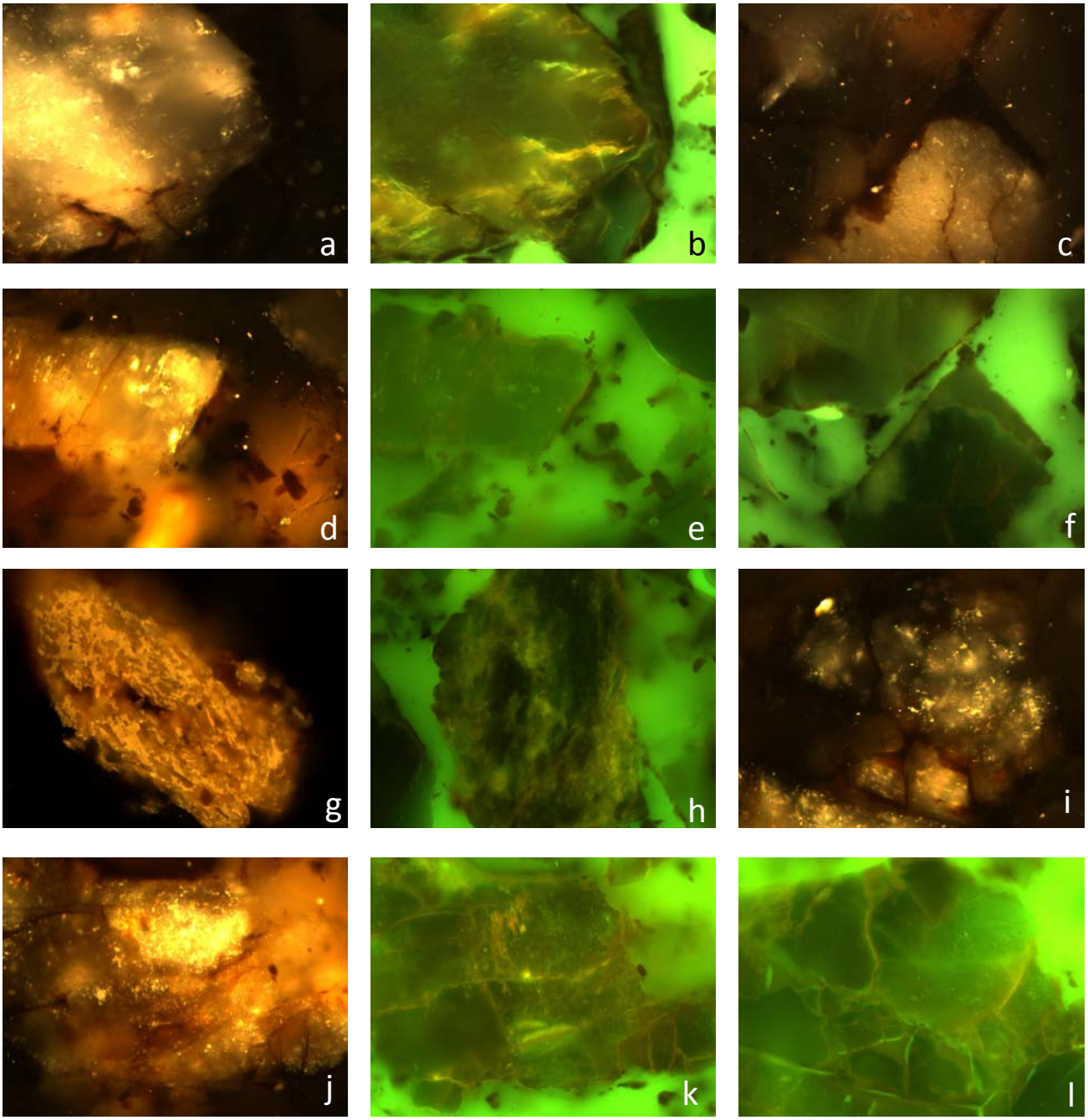

Plate 26: Optical microscopy. Photomicrographs taken in reflected white light. Fluorescence mode in photographs (b, e, f, h, k and l).
(a, c, d, g, i and j) Dark brown bytumens impregnated in the mineral fracture and veins, with yellow fluorescence (b, f, e, h, l and k respectively) (RFT-0, RFT-1 and RFT-2).
Width of the long dimension of the pictures: 200 µm.

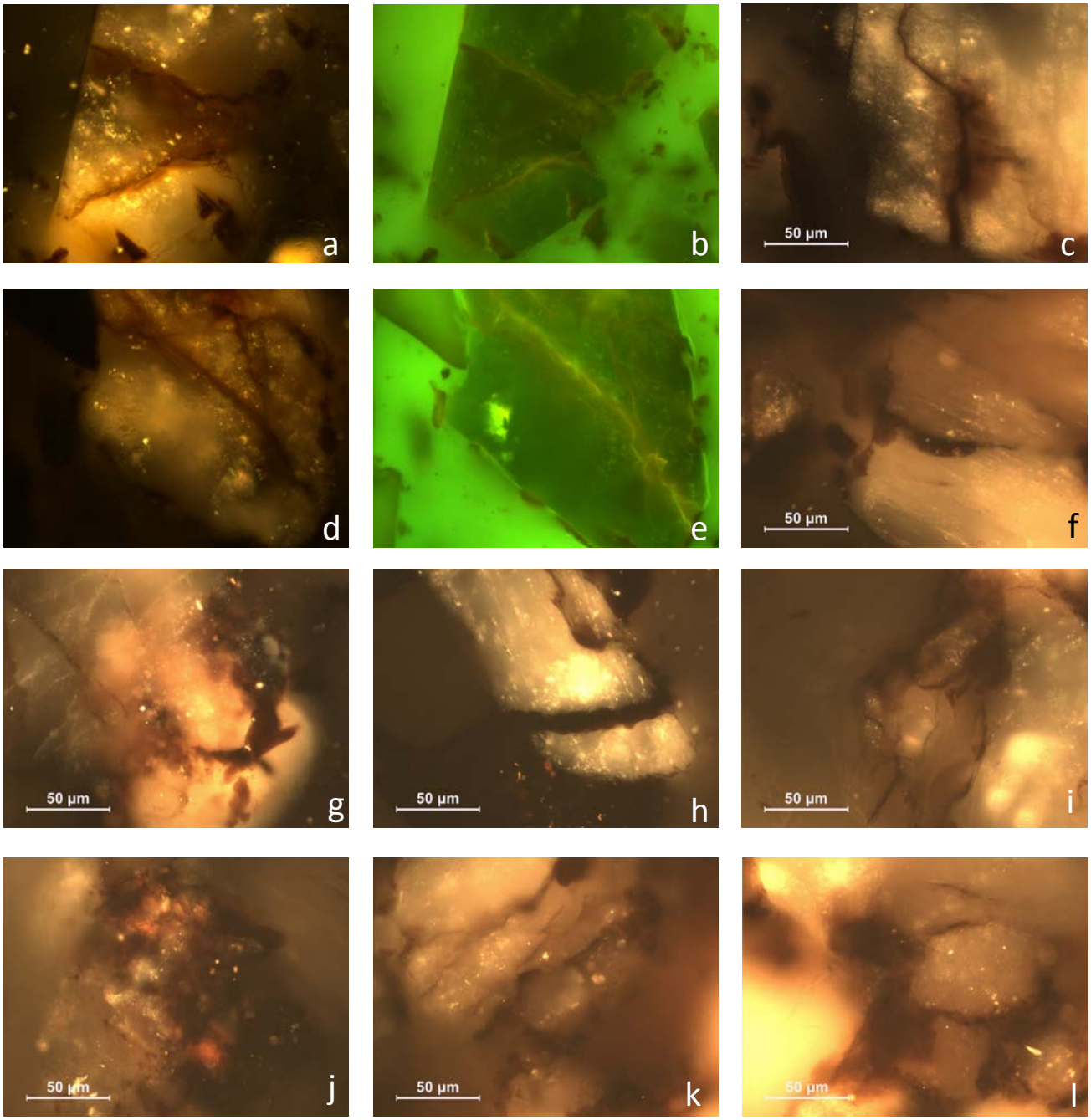

Plate 27: Optical microscopy. Photomicrographs taken in reflected white light. Fluorescence mode in photographs (b, e, f, h, k and l).
(a and d) Dark brown bitumens impregnated in the mineral fracture and veins, with yellow fluorescence (b and e respectively) (RFT-0 and RFT-1); (c, f, g, h, i, j, k and l) dark brown bitumens impregnated in the mineral fracture and veins (RFT-1 and RFT-2).
Width of the long dimension of the pictures: 200 µm.